Large scale, long term, physically based modelling of the effects of land cover change on forest water yield

PhD dissertation

Fred G. R. Watson

March 9, 1999

Abstract

The question was asked: is it possible to realistically and spatially simulate the water balance of forests at large scales for long periods in a way which responds to land cover change. The answer to this question was pursued by attempting to construct a new model and applying it to a 163 km^2 catchment area near Melbourne, Australia.

The new model is called Macaque and is a daily model which inherits much from previous models. It employs a modification to the distribution function modelling (DFM) approach termed 'limited DFM' where lateral subsurface redistribution of water is achieved implicitly by means of a distribution function at a rate controlled by a 'lateral redistribution factor'. Vertical flux is modelled using a three layer Penman-Monteith scheme similar to previous physically based evapotranspiration schemes. A detailed micro-meteorological component is included.

The model was described in detail, with frequent consideration to the physical realism of the processes which are represented. It has some 72 parameters, and values for each were based as much as possible on physical observations through either direct field measurement, or constrained calibration against observations of internal variables.

Key spatial parameters were identified as those associated with topography, precipitation, vegetation leaf area index (LAI), and soil. Chapters are given on each of the first three of these, including analyses of the accuracy of each spatially mapped parameter. In particular, advances were made in the use of ground-based LAI data from different aged forests in combination with remote sensing data and maps of forest species and age to produce spatio-temporal maps of total and canopy LAI for the study area. Attempts to map soil parameters failed, and so these parameters had to be held constant in space, leading to uncertainty in model realism in parts of the study area with unrepresentative soils.

Predictions of key internal model variables were tested against observed time series of temperature, humidity, radiation, transpiration, soil moisture, and water table levels. Whilst errors were present, realistic model operation was generally indicated for all tested processes. The combination of these processes led to accurate predictions of the hydrograph for a small experimental

catchment. The fact that this was done without free calibration of parameters solely against hydrographs is an encouraging sign that the model was operating realistically.

Scaling up to the full study area necessitated re-calibration of three key sub-surface parameters to achieve accurate hydrographs, a need most likely related to the lumping of sub-surface/soil parameters. A number of long term simulations were run over an 84 year period in order to test the model's ability to simulate the hydrological effects of the devastating 1939 wildfires. The first simulation assumed constant forest cover. Inter-annual streamflow variability was well predicted, but as expected, the differences in water yield between the pre- and post-1939 period was not predicted. A second simulation included the large changes in LAI across the study area caused by the 1939 fires, and resulted in part prediction of the associated differences in water yield. The influence of other factors was suggested to cause the remaining differences. Of these, a change in maximum leaf conductance was selected for inclusion in a third run, resulting in an accurate simulation of the change in water yield.

These results indicate that realistic, large scale simulation of changes in water yield following land cover change is possible. Many improvements are possible, from areas such as improved and more efficient representation of individual processes to improved mapping of each of the spatial parameters.

In the long term simulations of annual water yield, an approximately 20% error was typical. Sensitivity analyses were conducted with the key lumped and spatial parameters and model inputs. Precipitation parameters and inputs were particularly sensitive both with respect to the spatial pattern of precipitation simulated by the model, and the source of temporal precipitation data used to drive the model. Inaccuracies in precipitation estimation could easily account for the observed 20% errors in predicted streamflow.

Improved daily estimation of precipitation over complex terrain incorporating better use of limited daily precipitation observations was highlighted as the primary avenue of improvement for future work.

Declaration

This dissertation is submitted in total fulfilment of the requirements of the degree of Doctor of Philosophy to the University of Melbourne, Australia.

I declare that the dissertation and the work it describes is entirely my own, and has not been submitted for any other degree. It contains less than 100 000 words, exclusive of figures, tables, equations, footnotes, reference lists, and appendices.

Acknowledgements

I gratefully acknowledge the following people:

my partner, Tanya Singleton,

my supervisors: Dr Rob Vertessy, Dr Rodger Grayson, Professor Tom McMahon, and Associate Professor Ian Bishop,

for ongoing intellectual association with the project: Professor Larry Band, Dr Richard Benyon, Professor Keith Beven, Dr Rob Lamb, Dr Richard Silberstein, Dr Andrew Western, Dr George Kuczera,

for intermittent intellectual discussions: Bob Abrahart, Associate professor Günter Blöschl, Ian Calder, Irena Creed, Frank Dunin, Richard Fernandez, Dr Stewart Franks, Dr John Gallant, Dr Alex Held, Dr David Jupp, Richard Lammers, Dr Scott Mackay, Professor Russell Mein, Pat O'Shaughnessy, Dr Paul Quinn, Dr Murugesu Sivapalan, Dr Nigel Tapper, Dr Q.J. Wang, Dr Mark Wigmosta,

for moral support in the office: Dr Robin Allison, Murray Peel, Phil Scanlon, Sandra Roberts, and Chinthaka Karunaratne,

for secretarial help and worldly advice: Jacqui Wise,

for IT help: Bevan Anderson, Craig Beverly, Tony Butt, Chris Chu, Andrew Disseldorp, Trevor Dowling, Dr Leslie Hodgson, Nick Moore, Kate Ord, Paul Stephens, Bert Thompson, Thomas Weichert,

for help with and facilitation of fieldwork: Bill Butcher, Richard Campbell, John Cazanis, Simon Cornish, Jacinta Duncan, Paul Gribben, Jamie Hall, Mark Judd, Karl Landorf, Frank Lawless, Tom Mitchell,

Contents

III Parameter mapping

6 Topographic mapping   151

List of Figures

List of Tables

Part I

Introduction

Chapter 1

Introduction

Contents

1.1 A water resource issue

The reliable supply of water to ever growing urban populations is a challenge facing water resource managers around the world. In Melbourne, Australia, the challenge is particularly interesting, owing to the hydrologic characteristics of Melbourne's forested water supply catchments. Under normal circumstances with mature forest cover, a high water yield is collected from the catchments. However if the forest is cleared, a regeneration process begins and sub-mature forests are present for a number of decades. Langford (1974, 1976) and Kuczera (1985, 1987) found that significantly lower water yields are collected from the regenerating forests. The implication of these findings is that excessive clearing may threaten the reliability of Melbourne's water supply.

Two agents may cause the forest to be cleared and regenerated - timber harvesting and wildfire. Both of these are a threat to the catchments. The wildfires of 1939 razed a large proportion of southeast Australian forests including large areas of Melbourne's water supply catchments (Paine, 1982). This may occur again although it is less likely due to modern fire-warning
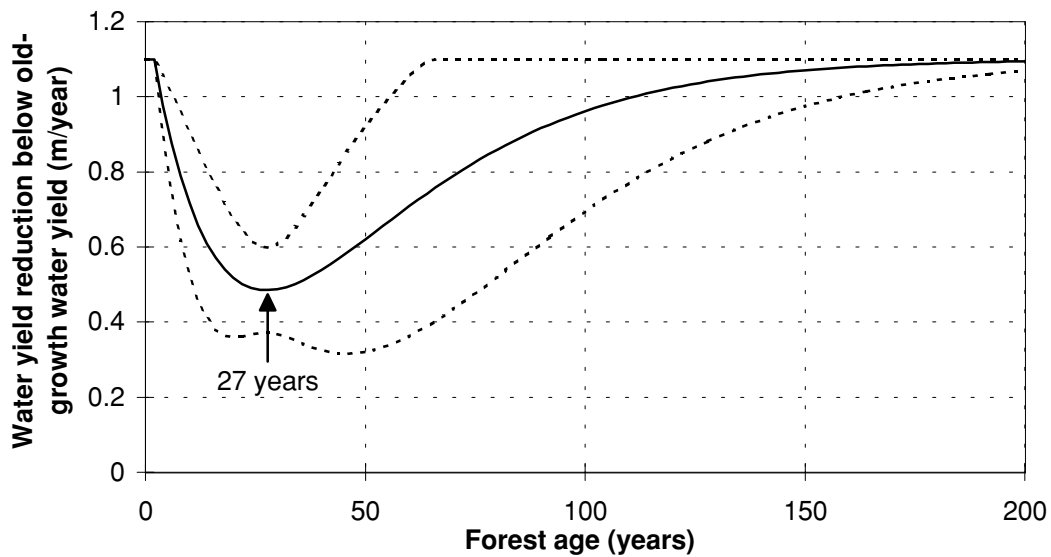
Figure 1.1: The Kuczera curve (with 90% confidence limits) predicting water yield decline from forest age in *Eucalyptus regnans* forests (after Kuczera, 1985, Fig. 6-7; also Kuczera, 1987, Equations 17 to 20).

and fire-fighting technology (Tolhurst, 1994). The timber supported by the catchments is of significant economic value to the timber industry, a fact which resulted in joint investigations by the former Department of Conservation and Natural Resources (DCNR) and Melbourne Water into the relative economic worth of timber harvesting and water harvesting within the catchments (Read Sturgess & Associates, 1992). Initial findings indicated that timber harvesting in the catchments is economically unwise. This sparked some controversy and led to further investigations which throw some doubt on the initial findings (Read et al., 1994; Ferguson, 1995).

Early analytical work in the Maroondah catchments (Langford 1974, 1976) discovered the relationship between forest age and streamflow yield which was hypothesised to be caused by higher water consumption by regenerating forests and is the driving fact behind the present project. Langford's work was extended by Kuczera (1985, 1987) who formed the often cited 'Kuczera Curve' which quantifies the relationship within given error bounds (Figure 1.1).

The Kuczera curve is used operationally by the Department of Natural Resources and Environment (DNRE) in the management of the Thomson catchment with regard to planning the location of new logging coupes (Lau et al., 1994, 1995, 1996). The curve is used to predict the effects of planned forestry operations. However, the same curve is used for all Ash type forests regardless of other environmental influences on water yield such as precipitation

and radiation. Precipitation has a range of well over 1000 mm within Mountain Ash forests, and radiation varies greatly between north and south facing slopes. Thus, current management, such as the management of logging in the Thomson, is limited by inaccuracy in water yield prediction resulting from the assumption of spatial invariance of the yield/age relationship. Ash forest management could be improved by allowing for large scale, spatially variable responses of hydrology to forestry operations.

Climate change may be another source of change in catchment conditions. Climate change scenarios for south eastern Australia may involve changes in precipitation and temperature leading to changes in runoff in the order of $\pm 20\%$ (Chiew et al., 1996; CSIRO Division of Atmospheric Research, 1996). The interaction between precipitation and temperature and streamflow is both complex and spatial, and hence, predictions of the effects of climate change on water yield would benefit by being made on a spatial basis.

1.2   The need for a predictive model

A predictive spatial model of the effects of land cover change and climate change on long term water yield is needed in order to better manage water supply catchments subject to these changes.

Such prediction is the focus of this dissertation.

For simplicity, the dissertation focuses on predicting the effects of land cover change, although it is mindful of parallel needs to predict climate change at some stage.

We know that water yield reduction is caused by increased evapotranspiration from regrowth forest after logging and/or wildfire, but we have only basic means of predicting the effects on water yield of possible future impacts on land cover. We have especially little idea about where in the catchment area are the risks greatest. In what species? What climate?

Given such a large, diverse catchment area, a spatially lumped solution is of little help; land cover changes are not uniform spatially and the response of large areas to partial land cover change is unlikely to be linearly proportional to the extent of land cover change. Spatial heterogeneity of both land cover change and catchment response to this change results in non-linear responses observed at the catchment scale (Band et al., 1993). A prediction scheme is needed which takes account of differing environments within the catchment area and how these interact and combine to influence water yield.

A spatial predictive model is implied, specifically a large scale spatial model (LSSM). The ideal model would provide the following:

- simulation of catchment water yield

- identification of important locations for catchment management, e.g. areas which should be vigorously protected from logging and/or wildfire,

- large scale (> 100 km^2) simulation [1],

- long term (> 100 years) simulation,

- simulation of changes in water balance resulting from changes in land cover,

- realistic simulation, i.e. where everything represented by the model reflects something within the real world, and is tested to ensure this,

- a framework for the organisation of our understanding of the physical processes and spatial variability thereof which govern the water balance of catchments,

- parsimonious simulation, where duplication and redundancy in representation is minimised.

A model so constructed will solve the problem outlined.

1.3   Research question

The question addressed by this dissertation is then:

Is it possible to realistically and spatially simulate the water balance of forests at large scales for long periods in a way that responds to land cover change?

This question is answered first by attempting to construct the ideal model outlined above, and then by assessing whether the exercise was successful.

---

[1]Scales which are considered 'large' vary amongst the earth sciences (see Blöschl and Sivapalan, 1995; Trenberth, 1992; Colls and Whitaker, 1990). The definition adopted here (> 100 km^2) is typical amongst physically based hydrological modelling studies.

1.4   Specific aims - implement a new model

It is asserted herein that no existing model is entirely suitable, so the development of a new model is warranted. The new model is called Macaque.

The development and application of a new LSSM comprises several major tasks, expressed here as the specific aims of the present research:

- design the structure of the model based on a perceptual model of catchment processes as well as related elements from existing models,

- measure as many parameters as possible,

- construct maps of key spatially variable parameters,

- run the model on test sites and calibrate remaining free parameters against observations of internal and external variables,

- validate as many internal and external predictions as possible using observed data from test sites, or where this is not available, using expectations based on the perceptual model of catchment behaviour,

- apply the model to a large scale, long term scenario.

1.5   Dissertation structure

This dissertation is divided into parts comprised of one or more chapters.

Part I, which contains the present chapter, concludes with a second chapter describing the study area and past research within it.

Part II has three chapters: on model theory, development, and operation respectively. The first describes some theoretical aspects of relevance, including the development of a new form of distribution function model. The next chapter details the full development and structure of Macaque. It is organised in terms of processes, both horizontal and vertical. The last chapter of this part describes the operation of the model through a description of the meaning, function, measurement, and calibration of each parameter. Model testing is left until Part IV, after parameter mapping has been presented.

Part III focuses on parameter mapping, the other half of the LSSM problem. Mapping is described in chapters on each of the main spatial parameter

groups: topography, precipitation, and vegetation. Each chapter investigates what parameters are required by the model, how previous studies have mapped them, what data are available or have been collected for the present study, how previous techniques are applied and improved, and how accurate the results are.

In Part IV, the model is tested and applied using long term historical input data. The chapter on testing describes testing of individual model components and testing of overall model response to different spatial inputs respectively. A second chapter, on model application, describes the application of the model to the key historical scenario of land cover change in Melbourne's water supply catchment area, the 1939 fires. Predictions and observations of the hydrological effects of these fires are presented and discussed.

Finally in Part V, the results of the work are summarised and used as a basis for answering the research question stated above.

Appendices include reference tables on: publications, data, symbols, constants, acronyms, and plant species names amongst other things.

Chapter 2

The study area and previous investigations within it

Contents

This chapter has two short sections. The first describes the study area. The second briefly reviews some of the extensive experimental and modelling work which has been undertaken within the study area in the past few decades.

2.1   Study area

The core study area comprises five water supply catchments, collectively referred to as the Maroondah catchments (163 km^2) (Figures 2.1 to 2.3). These form part of the total catchment area (1040 km^2) supplying the city of Melbourne, Australia (pop. 3.25 million). The largest of the Maroondah catchments contains the Maroondah storage reservoir (surface area 1.9 km^2 and storage of 22 GL at full supply level), which lies just upstream of the town of Healesville, about 55km north east of Melbourne.

The area is a long term hydro-ecological research site featuring 18 small gauged experimental catchments within and around the water supply catchments (Figure 2.3). Three experimental catchments (Picaninny, Blue Jacket,
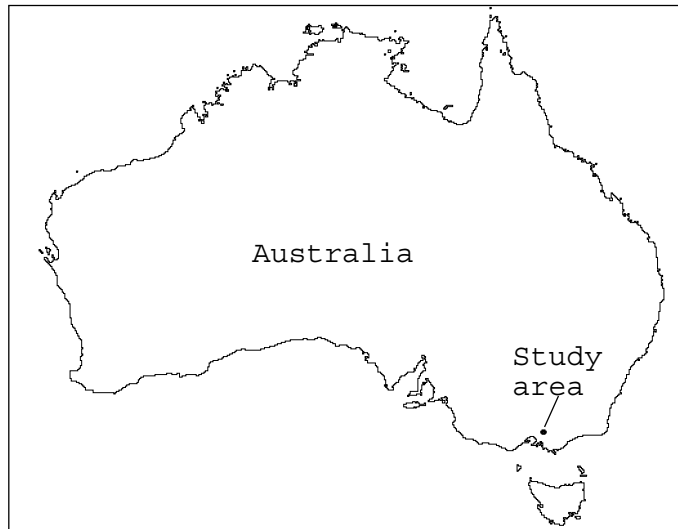
Figure 2.1: Location of the Maroondah study area within Australia.
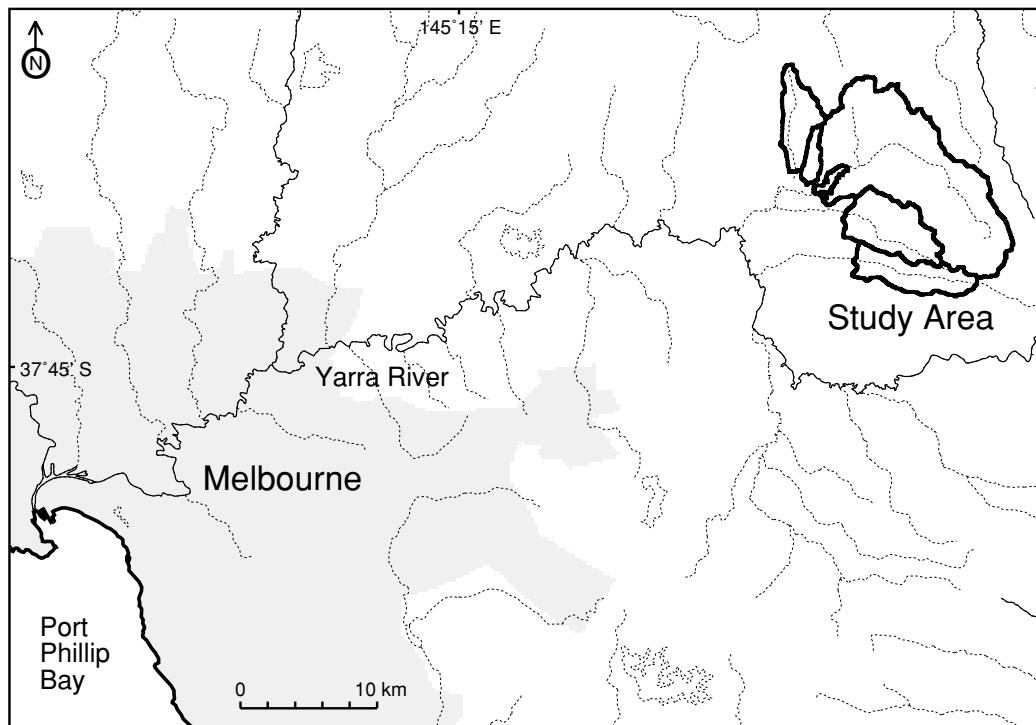
Figure 2.2: Location of the Maroondah study area 55 km east-north-east of Melbourne.
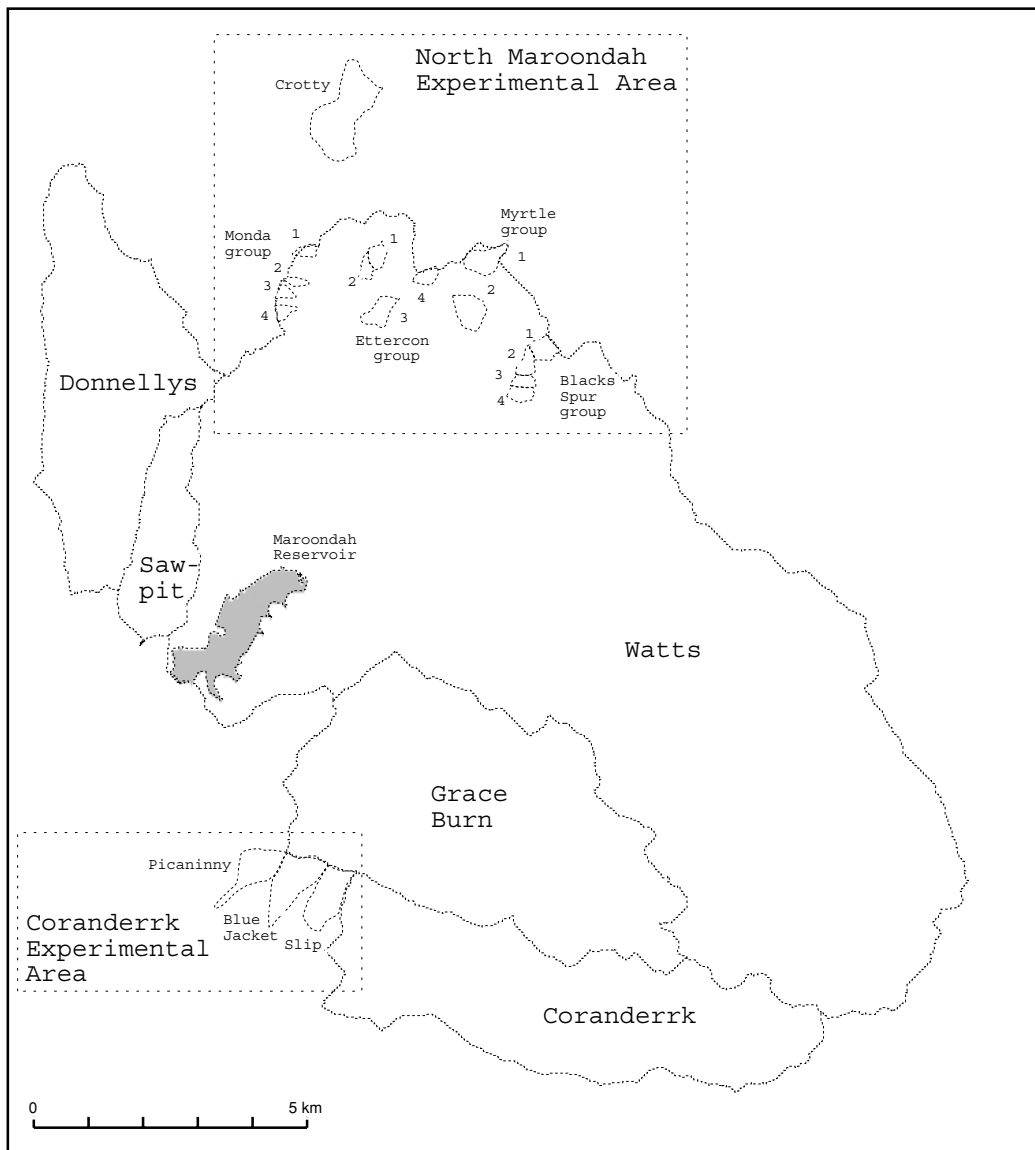
Figure 2.3: The Maroondah Catchments. The core study area is the five water supply catchments: Donnellys, Sawpit, Watts, Grace Burn, and Coranderrk. Also shown are 18 experimental catchments both within and adjacent to the core study area.
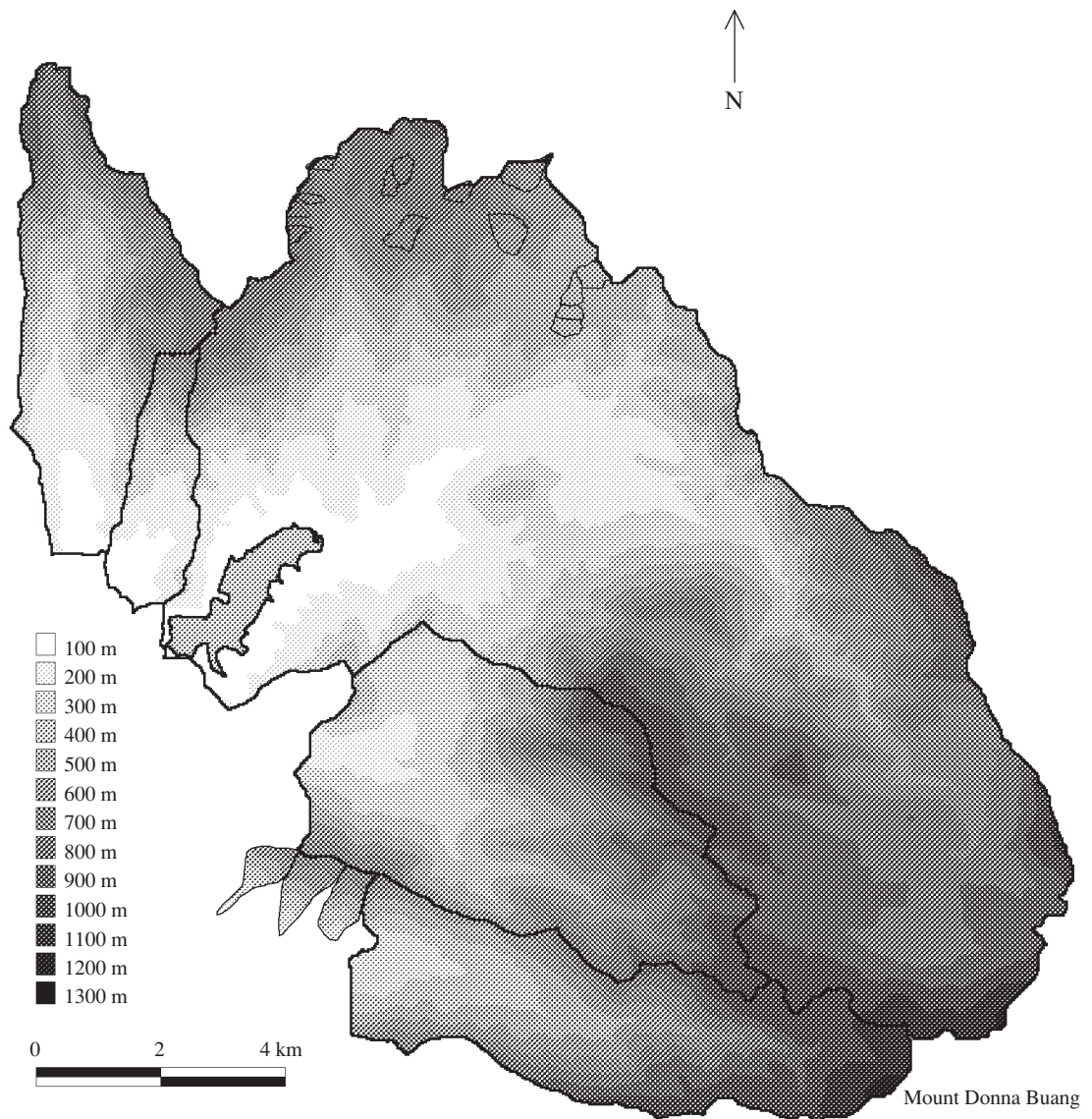
Figure 2.4: Digital elevation model of the study area.

and Slip) lie outside and to the south west of the water supply catchments (Figure 2.3) and are included as part of the greater study area.

The area exhibits steep, deeply incised terrain with laterally confined stream lines and a relative relief of over 1000 m (Figure 2.4). Mean annual precipitation (MAP) varies markedly from around 1100 mm at lower elevations to over 2800 mm on the highest mountain top. Most of the precipitation falls as rain. In mid-winter, snow is common above 1000 m but rarely accumulates to more than 30 cm deep.

The catchments are almost entirely forested and are dominated by pure stands of tall wet-sclerophyll Ash type forest. Forest species include 59%

Mountain Ash (*Eucalyptus regnans*), 7% other Ash type species, 22% dry-sclerophyll 'Mixed Species' eucalypt forest, and 5% cool temperate rainforest. Only the Ash forest has been studied in detail.

The 'Guiness Book of Records 1998' states that the area was the site of the tallest tree ever measured, the 'Ferguson Tree', an *E. regnans* measured at 132.6 m in 1872 but estimated to have topped 150 m before its crown was either blown off or struck by lightning (Guiness Publishing, 1997, p. 228; Crawford, 1995). A number of recent summaries of Australian tall trees omit the Ferguson Tree (Ashton, 1975; Griffiths, 1992; Lindenmayer, 1996) and even the Guiness Book of Records contradicts itself by omitting this tree from its note on tall trees in an 'Australian Supplement' (Guiness Publishing, 1997, p. 020). The specimens which survive today are considerably shorter than 150 m, and some tens of metres shorter than their *Sequoia sempervivens* counterparts in California. A definitive documentation of all candidates is in progress (B. Mace, pers. comm.).

The area is characterised by very deep, permeable soils leading to deep, static water tables away from streams and shallow, dynamic, and hydrologically significant water table response near streams (Campbell, in prep.). Shallow soils occur on certain ridge-tops and north facing slopes. The underlying geology is almost entirely late Devonian acid-volcanic, with very small areas of Silurian sediments in the west (Edwards, 1932; McLaughlin, 1988).

Streamflow originates from and responds to longitudinally extensive saturated areas which enlarge significantly during wet periods (Finlayson & Wong, 1982; Duncan and Langford, 1977). A high and relatively constant proportion of baseflow to total flow is maintained throughout the year. Mean annual runoff for the three largest water supply catchments in the period 1910-1992 is 802 mm. This can be divided into pre- and post-1939 means of 879 mm and 760 mm respectively (a decrease in runoff despite increased precipitation in the latter part of the century both locally and regionally, Pittock, 1975, 1983).

2.2 Previous work within the study area

2.2.1 Experimental work

Considerable experimental work in the study area has focused on understanding the exact cause of streamflow decline in regenerating forests. This has included fog-drip studies (O'Connell & O'Shaughnessy, 1975), intercep-

tion studies (Langford & O'Shaughnessy, 1978; Duncan et al, 1978; Haydon et al, 1996), transpiration studies (Brookes & Turner, 1963; Langford & O'Shaughnessy, 1979b; Moran & Ronan, 1978; Legge, 1980; Dunn & Connor, 1991, 1993; Jayasuriya et al, 1993), and water balance studies (Moran & O'Shaughnessy, 1984).

Summarising Vertessy et al's (1994a) review of these studies, interception and transpiration have been identified as two hydrologic processes strongly determinant of the forest-age/ water-yield relationship in Ash forests. Increased transpiration by younger forests is the dominant cause of streamflow decline during forest regeneration - increased interception being a subdominant cause. Current work links these processes to conveniently measurable stand parameters such as leaf area index, trunk diameter, and sapwood area (Vertessy et al, 1994b, 1995a, 1997).

Hillslope hydrologic processes beneath the forests have received less research attention. Some basic soil hydrologic properties have been measured by Langford and O'Shaughnessy (1980a) and Davis (Davis, in prep.; Davis et al., 1996, 1997), and basic streamflow characteristics have been discussed by Duncan and Langford (1977), Duncan (1980), Jayasuriya (1994b), and Lacey (1996) who outline a hydrographic pattern dominated by annually periodic baseflow but with distinct stormflow peaks appearing above the baseflow. Stormflow has been shown to originate largely from saturated areas which border most streams in the catchment (Finlayson and Wong, 1982; Duncan & Langford, 1977; Duncan, 1980). No other surface flow appears to occur except on compacted areas after logging (Duncan, 1980; Langford & O'Shaughnessy, 1980a). The situation immediately after fire may vary from this (see Attiwill & Leeper, 1987, p. 192; Zierholz, 1994).

Water entering the soil can be stored in large amounts for long periods of time owing to the high water holding capacity of the deep soils of the catchment (Langford & O'Shaughnessy, 1980a) and moisture acquired from winter rainfall can remain for use by plants in the coming summer (Langford & O'Shaughnessy, 1979b).

Whilst evapotranspiration from the soil is relatively well understood (McJannet et al., 1996), drainage through it is not (Kuczera, 1983a). It is accepted that high moisture storage in the soil mass explains the high, steady baseflow in streams (Howard & O'Shaughnessy, 1971; Melbourne and Metropolitan Board of Works, 1980; O'Shaughnessy et al., 1981; Jayasuriya, 1994a) but the processes governing this phenomena have only recently received specific research attention (Davis, in prep.; Campbell, in prep.).

2.2.2 Modelling work

The earliest modelling work relevant to the study area was conducted by Porter and McMahon (1975), who applied the conceptual model HYDROLOG to the Blue Jacket experimental catchment as part of a study using six diverse catchments from around Australia. Their work simply demonstrated that hydrographs from the study area could be simulated from climate data using a water balance modelling approach.

The Soil Dryness Index (SDI) model originated by Mount (1972) is a lumped-parameter, conceptual model and has been used to predict monthly streamflow in the study area over a number of years (Langford et al, 1978; Kuczera, 1983a, b, 1984, 1988a, b; Duncan et al, 1977, 1979, 1980; Duncan & Heeps, 1980; Haydon, 1993; Kuczera et al., 1993; Jayasuriya, 1994a). The model has performed well - any limitations usually being attributed to inadequacies in input data and not the model itself (Langford et al, 1978). Kuczera et al. (1993) compared its performance with a slightly more detailed model, CAT-PRO, applied to predicting changes in streamflow following strip thinning at Crotty Creek. They found that CATPRO, through its more process-oriented representation of 'quickflow', was better able to simulate the effects of the treatment after both models were calibrated on only the pre-treatment record.

More recently, the Topog model has been applied to the Myrtle 2 and Picaninny experimental catchments within the study area (Vertessy et al, 1993, 1995b). Topog is a detailed, physically based, distributed parameter model normally applied to small, first order basins. It is described more fully in Section 3.2.4. At Myrtle 2 it was used to predict water yield over a 12 year period as an initial test of the model's newly enhanced representation of ET processes. At Picaninny, a forest growth modelling component was added and tested against observed forest growth data available for the 23 years following forest clearing. Whilst too detailed to extend to the full study area at this stage (see Section 3.2.4), experience and parametric information gained from Topog applications within the study area are invaluable for the present study.

The conceptual model IHACRES has also been used within the study area, essentially as an analytical tool for examining changes in water yield following various forest treatments (Post et al., 1993, 1996, 1997). The model simulates yield using a time-series analysis approach with no representation of physical or conceptual catchment structures (though physical meaning is 'attached' to each of the model parameters). Apart from demonstrating the ability to

reproduce observed hydrographs from climatic inputs, the model is of limited relevance here.

2.3 A note about time series data

Numerous time series data are used within this dissertation. A database was set up to store these data employing a cataloguing system with unique identification numbers for each record. The numbers are referred to as F-numbers and are all of the form: "F####", where '#' is a numeral. An example is F1195 which is the long term daily precipitation record from the Warburton Post Office. F-numbers are cited throughout the dissertation for cross-reference and to clarify exactly which record is used for which purpose. Appendix B summarises all the records which have been used.

Part II

Model development

Chapter 3

Model review and theory

Contents

3.1 Introduction

Our understanding of catchment hydrological processes is generally founded on observations at scales of 0.1 to 100 metres. Large scale spatial models (LSSMs) deal with catchments much larger than this scale and, in the absence of analytical solutions to the problem of integration to larger scales (Jensen

and Mantoglou, 1992), must broach the gap in scales by dividing catchments into many smaller elementary spatial units (ESUs), each of which represents an area within which physical processes are simulated. The description of a given ESU is made through a number of parameters which must be mapped across the catchment in order that each ESU may be modelled correctly. This may be viewed as a three goaled system. The first goal is the representation of detailed processes within an ESU. The second goal is the division of the catchment into appropriate ESUs, and the third goal is the mapping of the parameters which distinguish and control the individual behaviour of those ESUs throughout the catchment. The achievement of a *realistic* simulation depends on all three goals being attained. It is questionable whether any LSSM modelling project to date has done this.

In this chapter, some aspects of the first two goals are considered, the third goal being the focus of Part III. In Section 3.2, a selection of existing models is reviewed with respect to both the level of detail of process representation implemented within each ESU, and the way in which catchments are divided into ESUs. It is shown that a number of models implement detailed process representation which is suitable for the present study, and at least one model offers a promisingly parsimonious disaggregation of catchments into ESUs using distribution function modelling concepts. However, the finer points of current distribution modelling practice require extension before being suitable here. Section 3.3 specifically addresses approaches to the spatial aspects of hydrological modelling, leading to the introduction of a new approach to distribution function modelling.

3.2   Existing models

Several water balance models were examined in detail in various aspects of the present study. To avoid repeated citations to model authors throughout this dissertation a table is given listing all model names referred to throughout the dissertation, and references to each (Table 3.1). In addition to citations which are directly relevant to the present work, citations are given for some of the key papers on each model. Throughout the present dissertation specific citations to model references are not given unless there is ambiguity as to which reference is of relevance.

A number of the models listed in Table 3.1 were examined in detail in order to identify those which best matched the ideal model characteristics listed in Section 1.2. A detailed report on this examination would detract from the

Model name	Reference/s relevant to this dissertation
ALSIS	Munro et al., 1997; Shao et al., 1997a, b
ARNO	Todini, 1996
BATS	Dickinson et al., 1986, 1991; Sellers, 1991
BIOMASS	McMurtie et al., 1990a, b; Leuning et al., 1991; McMurtie et al., 1992a, b; McMurtie, 1993
BROOK,BROOK90	Federer and Lash, 1978; Federer, 1995
CATPRO	Kuczera et al., 1993; Mroczkowski and Kuczera, 1996
CLATTER	Roberts and Rosier (1994)
COUPLES	Silberstein and Sivapalan, 1993, 1995, 1996
CREAMS	Knisel and Williams, 1995
DHVM	Wigmosta et al., 1994
Famiglietti et al's model	Famiglietti et al., 1992
FOREST-BGC	Running and Coughlan, 1988; Running and Gower, 1991; Hatton et al., 1993
HBV	Bergström, 1995
HYDROLOG,- MODHYDROLOG,- Monash model	Porter and McMahon, 1971, 1975; Moore and Mein, 1975; Chiew and McMahon, 1990a, b, 1994; Chiew et al., 1992, 1993
HYMAS	Hughes and Sami, 1994
IHACRES	Jakeman et al., 1990, 1992; Jakeman and Hornberger, 1993; Chiew et al., 1993; Post et al., 1993, 1996, 1997; Post and Jakeman, 1996; Sefton et al., 1993
LASCAM	Sivapalan and Viney, 1994a, b; Sivapalan et al., 1996a, b, c
Naden et al's model	Naden et al., 1996
Penman combination and Penman-Monteith ET models	Penman (1948); Monteith (1965); Roberts and Rosier (1994); Teixeira Filho et al. (1996)
Polarski's model	Polarski, 1997
PRMS	Leavesley and Stannard, 1995
RHESSys	Band, 1993; Band et al., 1991, 1993; Running and Hunt, 1993; Nemani et al., 1993b; Scuderi et al., 1993; Mackay and Band, 1997
SDI	Langford et al., 1977, 1978, 1982; Mount, 1980; Kuczera and Mein, 1982; Kuczera, 1983a, b, 1984, 1988a,b; Jayasuriya and O'Shaughnessy, 1988; Haydon and Jayasuriya, 1993; Kuczera et al., 1993
SHE,MIKE SHE, SHETRAN	Beven, 1985; Abbott et al., 1986a, b; Bathurst, 1986; Bathurst and O'Connell, 1992; Dunn and Mackay, 1995; Bathurst et al., 1995; Refsgaard and Storm, 1995; Shah et al., 1996a, b; Storm and Refsgaard, 1996; Refsgaard, 1997
SiB	Sellers et al., 1986; Dickinson et al., 1991; Sellers, 1991
SLURP	Kite, 1995
SRM	Rango, 1992
SWRRB	Arnold and Williams, 1995
THALES	Grayson et al., 1992a, b; Grayson and Moore, 1992
TOPMODEL	Beven and Kirkby, 1979; Beven et al., 1995; Obled et al., 1994; Ostendorf et al., 1995; Lamb, 1996; Lamb et al., 1996, 1997; Lamb and Beven, 1997
Topog	Hatton et al., 1992; Vertessy et al., 1991, 1993, 1994c, 1995b, 1996; Dawes and Hatton, 1993; Dawes et al., 1997
UBC	Quick, 1995
WAVES	Hatton et al., 1995
WBM	Vörösmarty and Moore, 1991
Xinanjiang	Zhao et al., 1980; Zhao, 1992

Table 3.1: List of water balance models referred to within this dissertation.

focus of this work. Rather, a few models were selected for comment.

Some philosophical points are touched upon first.

No models currently satisfy *all* the characteristics listed in Section 1.2. Obviously, several provide 'simulation of catchment water yield'. Many, including most fully distributed models, offer spatially distributed simulation involving either separate or linked simulation of numerous elementary (horizontal) spatial units (ESUs). Most of these could be used for 'identification of important locations for catchment management'. By the time the 'large scale' and 'long term' requirements are introduced, the field of contenders reduces considerably, to maybe ten or so published models.

But it is the combination of the 'large scale' and 'long term' aims with the additional requirements for 'realistic' 'simulation of changes in ... land cover', or *the three 'L's*, that brings the field down to one or two serious contenders. There are a few models which adopt a highly detailed, often multi-layered, representation of evapotranspiration from geometrically complex canopies. Some of these include multi-layered, multi-dimensional representation of unsaturated and saturated water flow within the soil. It is this level of detail in vegetation and soil representation that is often purported by model authors to enable realistic simulation of the water balance, the factors by which it is influenced, and as a corollary, the changes in water balance resulting from changes in land cover (e.g. Abbott et al., 1986a; Bathurst and O'Connell, 1992). However, only a few attempts have been made to turn this style of modelling to large scale application. Such attempts require careful consideration to parsimony and must avoid blind reductionism, even with 1997 computing technology.

Following some criticisms of the physically based approach to hydrological modelling (Beven, 1989; Grayson et al., 1992b), emphasis has been placed on internal testing of physically based models as a means of establishing their realism (in particular: Beven, 1996a; but also: Beven, 1985; Anderson and Rogers, 1987; Bergström, 1991; Grayson et al., 1992; Jensen and Mantoglou, 1992). The exercise is a vital component in physically based modelling studies, such as the present study, which seek to use models not only as a tool for prediction of the effects of future land cover scenarios, *but also as a vehicle for obtaining a better understanding of the processes linking land cover to hydrological change.*

Only a few studies have undertaken internal testing, validation, or calibration in earnest (Beven, 1996a), typically using soil moisture as the observed internal variable. An early example using a conceptual model is given by

Kuczera and Mein (1982) who were able to better constrain the parameters of the SDI model by calibrating against observed soil moisture as well as streamflow. Using TOPMODEL, Ostendorf et al. (1995) were able to validate predictions of water table depth in a limited sense using time domain reflectometry (TDR) data. Using a particularly detailed water table data set, Lamb et al. (Lamb, 1996; Lamb et al., 1996, 1997) were able to validate TOPMODEL's predictions of saturation deficit, but only by generalising a key equation within the model. McMurtie et al. (1990a, b) successfully validated predictions of soil moisture and photosynthesis dynamics using the BIOMASS model against observations of soil moisture and basal area increment. Refsgaard (1997) validated piezometric head predicted by MIKE SHE against observations of the same, with the result that predictions at independent testing sites were poor compared with predictions at sites used for model calibration. The topic is becoming more central in contemporary research, being a key theme of meetings such as the special session of the 13th General Assembly of the European Geophysical Society titled 'Process representation in hydrological models - Can it be achieved?', which calls for 'examples of calibration or validation of hydrological models using internal catchment processes'.

Four models are singled out for discussion: RHESSys, DHVM, SHE, and Topog. As elaborated below, all four use a Penman-Monteith representation of evapotranspiration with different levels of complexity. However, each differs in its representation of spatial heterogeneity. DHVM and SHE are fully distributed models based on a regular gridded representation of topography with lateral Darcian flow between the elements. Topog is also fully distributed, but uses an irregular grid defined by contours and drainage lines. RHESSys is a distribution function model (DFM) employing an outwardly more parsimonious disaggregation of horizontal space based on sub-basins and, within these, intervals of a statistical distribution function of a topographic wetness index.

3.2.1 RHESSys

RHESSys simulates both water balance and forest growth in a spatially distributed, physically-based manner. A key feature is its parsimonious representation of spatial heterogeneity based around the distribution function modelling concepts introduced by TOPMODEL. Large (c. 500 km^2, Nemani et al., 1993b) catchments are broken into numerous small catchments or 'hillslopes' enabling a spatially distributed representation of broad-scale variables such as precipitation and radiation. Smaller scale, sub-hillslope heterogene-

ity in variables such as soil moisture and land cover is represented by further dividing 'hillslopes' into 'intervals' of a topographic wetness index designed to quantify the range of soil moisture and related conditions observed within each hillslope. Parsimony is achieved because the intervals, i.e. the elementary spatial units (ESUs) of the model, represent homogenous land units of varying size, which together, are able to describe the key spatial heterogeneity observed within large catchments. The representation of intra-hillslope spatial variability is notionally statistical, avoiding explicit association of ESUs with specific parts of space, and with neighbouring ESUs.

Within each hillslope, lateral redistribution of water is accomplished using a distribution function which, at each time step, accumulates hillslope water into a single variable, and then re-distributes it to each ESU according to its wetness index relative to the wetness index of the other ESUs in the hillslope. ESUs with the highest wetness index receive more water than the others. Lateral redistribution of water downslope is therefore accomplished implicitly, as opposed to explicitly by simulating some gravity based process such as Darcian flow between explicitly connected ESUs. These ideas are discussed in detail in Section 3.3.

The overall approach embodied within RHESSys is ideally suited to the present study. However, a number model details are inappropriate. Firstly, the distribution function is taken directly from TOPMODEL and therefore inherits some limitations of TOPMODEL when applied to deep-soiled regions such as the study area. These are discussed in detail in Section 3.3. Secondly, RHESSys represents only one vegetation layer. In the coniferous forests of North America, this may be adequate. But in the study area, it is suspected the balance of understorey and canopy vegetation follows a long term dynamic that is an important influence of long term water balance. Hence, a two layer representation of vegetation is more desirable. A final, pragmatic, yet crucial limitation of RHESSys is in the code itself, which is largely un-documented, un-referenced, and difficult for outsiders to follow. These difficulties preclude its adoption in the present study, which requires a model which in part may be used as tool for development of new ideas. It should be noted that such difficulties apply to all foreign model code which was examined in detail by the author for the present study (including RHESSys, Topog, and TOPMODEL).

3.2.2 DHVM

DHVM is a more recent model with more detail in its representation of ET than RHESSys, and a conceptually simpler, less constraining representation of horizontal space and sub-surface lateral flow between ESUs. A three layered (canopy, understorey, soil) representation of ET is employed, using similar Penman-Monteith concepts as in RHESSys. The model also adopts what is becoming a standard array of multi-layered vegetation parameters and processes in physically based models, including propagation of short-wave and net radiation through the vegetation layers, and assumed wind profiles within the vegetation leading to aerodynamic resistance terms for the Penman-Monteith equation.

The chief concern with DHVM in relation to the present study is the regular grid based representation of spatial heterogeneity. Essentially, the level of disaggregation of space is determined by the computational ability of the host computer. If the computer is fast, small grid cells may be used. Otherwise, large ones must be used. In practice, Wigmosta et al. (1994) used 200×200 metre cells in a 2900 km^2 catchment. Such cells are much larger than the valley bottoms of the study area which contain extensive dendritic patterns of soil moisture, flow generation, and gully vegetation typically about 10 to 20 metres wide. At the same time, they are considerably smaller than many of the expansive upslope areas which appear to be completely homogeneous from the water yield modelling point of view. DHVM does not allow for this naturally multi-scaled heterogeneity of catchments, and therefore cannot take advantage of it by dividing ESUs only at points of observed heterogeneity. Such advantage is exactly that which is gained by the representation of space employed within RHESSys. The extent and resolution of spatial representation (*sensu* Blöschl and Sivapalan, 1995) is determined more by computational ability than by natural heterogeneity.

Protagonists of the spatially reductionist approaches employed within models such as DHVM, SHE, and Topog might argue that computing technology has progressed to the point that computational speed, and hence the number of ESUs is no longer a limiting factor in model design. However, so too has the scale at which models are being applied, and most importantly, has the degree to which reductionism's dissenters stress that models must be scrutinised through various forms of sensitivity analysis requiring multiple simulation runs (Refsgaard, 1996). A classic example is the generalised likelihood uncertainty estimation (GLUE) methodology introduced by Beven and Binley (1992) which is becoming a standard feature in applications of TOPMODEL (Beven, 1993, 1996a; Piñol et al., 1997; Freer et al., 1996; Franks

et al., 1997). GLUE is a very useful procedure which examines parameter uncertainty quantitatively and graphically through typically 10 000 to 50 000 Monte Carlo simulations. To date it has only been applied to TOPMODEL, partly because TOPMODEL is very simple and runs quickly. It has not been applied to complex models such as SHE and DHVM because these models run much slower than TOPMODEL and a sufficient number of Monte Carlo simulations could not be completed on most modern computers in reasonable time. This practical limitation has intellectual consequences because it has limited our understanding of the uncertainty in complex models relative to simpler ones.

3.2.3   SHE

SHE has been a focus of many of the concerns about (Anderson and Rogers, 1987; Beven, 1985, 1989, 1996a) and defences of (Abbott et al., 1986a; Bathurst and O'Connell, 1992; Jensen and Mantoglou, 1992; Storm and Refsgaard, 1996) physically based, distributed parameter models. Like DHVM, it has a regular-grid based structure and, having been applied to catchments ranging in area from 30 m^2 to 5000 km^2 with grid spacings up to 2 km (Bathurst et al., 1995), it is subject to the same 'lack of parsimony' arguments outlined above. It implements a simpler, two-layered (vegetation and soil) representation of ET which, as also outlined above, is unsuitable for the present study which requires an understorey. The focus of the development and application of SHE has been on lateral flow aspects involving stream hydraulics and combination with sediment transport and contaminant migration models (Bathurst et al., 1995; Refsgaard and Storm, 1995), with little work on the ET aspects which are of importance in the present context. Also, SHE is a commercial model and so access to source code is limited.

3.2.4   Topog

Topog is a very detailed, physically based model. In terms of spatial representation, it is unsuitable for the present study. The contour based ESUs used within Topog are typically about 20 × 20 metres in size, numbering about 1000 for the small, first order basins to which Topog is typically applied (e.g. Vertessy et al., 1993). A great deal of computation is involved in routing subsurface flow downslope through networks of this size. Arguably, the terrain analysis procedures used in the initial disaggregation of catchments could be

optimised to provide more parsimonious representation applicable at large scales, but this has not yet been attempted. Further limitations with respect to the needs of the present study include a typically greater than 10 layered representation of the soil with numerical solution of the Richard's equation used to simulated vertical soil water flux. This sort of computational demand would be cumbersome in large scale applications which would almost certainly involve many more ESUs than in previous applications (although it should be noted that ALSIS is an, albeit un-validated, continental scale, distributed soil moisture model which uses the Richard's equation).

Topog does, however, implement a suitable level of detail in ET. It is of the same school as DHVM in this respect. Differing mainly by the additional representation of increased humidity as one moves down from above the canopy to the soil level. Such representation provides some negative feedback limiting ET in situations where it may reach saturation levels. Such situations are likely in the study area, which has abundant moisture, radiation, and nutrients supporting the tallest flowering plants in the world (*Eucalyptus regnans*). The model has repeatedly been applied to the study area and future modelling studies will benefit from knowledge of parameters and other specifics of these past applications.

3.3 Approaches to spatial modelling

Approaches to spatial modelling can be classified according to the manner in which a catchment is divided into ESUs, and the means by which lateral surface and subsurface flow is moved between these units, if at all. Two existing approaches are described: fully distributed modelling and distribution function modelling. Then, a generalised expression of distribution function modelling concepts is presented, and a new modification to the distribution function approach is introduced: termed *limited distribution function modelling*.

3.3.1 Fully distributed models (FDMs)

Fully distributed models (FDMs) are commonly used. Recent descriptions and reviews appear in Singh (1995), Abbott and Refsgaard (1996), and Moore et al. (1993). The characteristic of FDMs that is most important here is that they use relatively small ESUs and redistribute water laterally by implementing *explicit* lateral flow between neighbouring units.

FDMs offer spatial and temporal flexibility, and in principle, the ability to model processes in great detail. They are limited however by the complexity which accompanies this flexibility. It is computationally impractical to model large basins using many fully distributed models (DHVM is an exception). Also, the detailed spatial parameterisation requirements of FDMs are often unrealistic (Grayson et al., 1993) unless parameters are lumped across many ESUs, in which case many ESUs become redundant. Model complexity both within and between spatial units is often greater than that which can be examined by the user, and this leads to uncertainty about the realism of the model.

3.3.2   Distribution function models (DFMs)

Distribution function modelling (DFM) is a more recent approach to large scale spatial modelling, chiefly designed to be more parsimonious in both parametric and computational needs. The key observation underpinning distribution function modelling is that spatial patterns of moisture distribution repeat themselves in time, depending on the mean moisture status of the catchment. A functional relation is used to predict moisture status at a specific location given some measure of location and of mean catchment moisture status. In this way, moisture distribution patterns are modelled *implicitly* without the need for an *explicit* implementation of lateral flow between spatial units.

Distribution function modelling was popularised by applications of the TOP-MODEL framework (Beven and Kirkby, 1979) to numerous small catchments throughout the world (see Beven et al., 1995). DFM concepts have been implemented at a variety of levels from large scale spatial models utilising the TOPMODEL framework (e.g. RHESSys; and the models of Famiglietti et al., 1992, and Obled et al., 1994) to more lumped models emphasising statistical aspects (e.g. the Xinanjiang model, HYMAS, ARNO, and models reviewed by Moore, 1985).

The operation of RHESSys exemplifies the DFM approach to large scale spatial modelling. RHESSys first divides a catchment into a number of *hillslopes* defined by the stream and ridge network. Each hillslope is thought of as a conceptual soil catena running from a relatively dry ridge top to a relatively moist valley bottom. A *wetness index* based on slope and accumulated upslope area is calculated for all areas within the hillslope, and is used to quantify the location of each area within the conceptual catena. Areas of similar wetness index are deemed hydrologically similar and grouped

to form single ESUs, termed *intervals*. A typical hillslope might be represented by ten to twenty ESUs of varying size and shape ranging from 'dry' to 'wet'. Conventional vertical hydrological fluxes are implemented for each ESU. Lateral flow between the ESUs is implemented implicitly using a distribution function whereby, at each time step, the saturation deficit (a measure of moisture status) of a given ESU is calculated as a function of the wetness index of the ESU, the mean wetness index of the hillslope, and the mean saturation deficit of the hillslope.

The fact that explicit lateral fluxes between adjoining ESUs are not implemented enables a conceptual detachment of modelled spatial units from one another and from the notion of their having a location in space. The representation of spatial variability within hillslopes becomes a partly statistical one where the specific location of, for example, dry areas is not of so much concern as their total area relative to the area of the hillslope. This places fewer demands on the parameter mapping process.

A number of limitations come with the convenience and simplicity offered by DFMs. Assigning physical meaning to distribution functions is difficult because they require over-simplified assumptions about subsurface systems. For instance, the assumptions made within the TOPMODEL framework result in predicted water table profiles which do not change shape but rather, move slowly up and down by the same amount throughout the hillslope. Unless the water table is near the soil surface throughout the entire catchment, the dynamic behaviour of near stream water tables cannot be made to reflect periods of rapid recharge and drawdown (typical of shallow water tables) during storm events.

Additionally, the theory behind TOPMODEL inextricably links assumptions about the vertical profile of hydraulic conductivity with both the shape of the water table and the manner of baseflow recession. This would be very convenient if the model were able to predict simultaneously these three aspects of catchment hydrology. However, the few attempts which have been made at simultaneous validation have been unsuccessful (see citations in Section 3.3.6 below). Pilot applications of RHESSys/TOPMODEL for the present study (not described) were no exception, with reasonable hydrograph prediction at the Ettercon 3 experimental catchment achievable only with grossly unrealistic water table predictions, and vice versa. Lamb et al. (1996, 1997) dispensed with the rigour of the original TOPMODEL theory (Beven and Kirkby, 1979) and resorted to a modification termed 'generalised TOPMODEL' in order to achieve complimentary hydrograph and water table simulation. Below, a novel, alternative generalisation of distri-

bution function modelling concepts is introduced which does not chain itself to the TOPMODEL framework.

3.3.3   A generalised distribution function (GDF)

Almost all applications of DFMs to date have utilised the distribution function associated with the TOPMODEL framework. It is important to realise however, that there are other functions which may be used by DFMs but that there are constraints imposed by the DFM approach which preclude the use of completely arbitrary functions. The notion of a *generalised distribution function* (GDF) was developed for the present study and is introduced as a means of exactly describing the form which all distribution functions must take if they are to be used in a conventional manner.

A conventional distribution function determines the moisture status of a point as a function of the mean moisture status of the catena to which it belongs and some measure of the location of the point within the catena. As stated previously, it is convenient to represent catenas as hillslopes, to use a wetness index as a measure of location within the hillslope, and to represent moisture status as saturation deficit.

Because the wetness index is used in the initial spatial disaggregation of the hillslope, it must be static. A dynamic wetness index (which changes over time, e.g. Barling et al., 1994) would require run-time changing of the spatial representation of the catchment, or perhaps two wetness indices - one for spatial disaggregation and one for use in the distribution function. Both of these possibilities would necessitate additional complexity which is not covered here. An index based on topography alone is suitable as a static wetness index but other static components may be included such as soil heterogeneity or mean annual precipitation. Examples include the topography-soils index (Sivapalan et al., 1987; Beven, 1986), the linear wetness 'parameter' of O'Loughlin (1986), the subsurface flow index of Woods et al. (1997), and topographic curvature (Zaslavsky and Sinai, 1981). The exact form of the wetness index is otherwise unconstrained. However it is most useful if it is chosen so that its spatial distribution mimics observed spatial moisture patterns.

The essential form of the distribution function, f, is:

$$s_{sat,dist} = f(\bar{s}_{sat}, i_{wet}) \tag{3.1}$$

where $s_{sat,dist}$ is the saturation deficit of a point as determined by the distribution function, $\bar{s}_{sat}$ is the mean saturation deficit of the hillslope, and i_{wet} is the wetness index of the point.

The function may be constrained by imposing a condition of water balance continuity. In order that water is not lost in the redistribution of hillslope water, the mean of distributed saturation deficits must equal the original mean saturation deficit from which they were derived. Functionally:

$$\frac{1}{A_{hill}} \int_0^{A_{hill}} s_{sat,dist} \, dA \;=\; \bar{s}_{sat} \tag{3.2}$$

where A_{hill} is the area of the hillslope.

This leads to:

$$\frac{1}{A_{hill}} \int_0^{A_{hill}} f(\bar{s}_{sat}, i_{wet}) \, dA \;-\; \bar{s}_{sat} \;=\; 0 \tag{3.3}$$

For this equality to hold, the integral must yield an '$A_{hill} \cdot \bar{s}_{sat}$' term and no other terms containing $\bar{s}_{sat}$. Any other $\bar{s}_{sat}$ terms would not be negated outside the integral giving a non-zero left hand side. The integrand, f, must therefore contain an '$\bar{s}_{sat}$' term and no other terms containing $\bar{s}_{sat}$. It must be of the form:

$$f(\bar{s}_{sat}, i_{wet}) \;=\; \bar{s}_{sat} + g(i_{wet}) \tag{3.4}$$

where g is some function of wetness index alone.

The equality now reduces to:

$$\frac{1}{A_{hill}} \int_0^{A_{hill}} g(i_{wet}) \, dA \;=\; 0 \tag{3.5}$$

For this new equality to hold, the wetness index could be constructed to have a mean of zero, in which case $g(i_{wet}) = i_{wet}$. However, it is more convenient to perform the construction within the distribution function by supplying g with a second parameter: the mean wetness index of the hillslope, $\bar{i}_{wet}$. In this way, g must be of the form:

$$g(i_{wet}, \bar{i}_{wet}) \;=\; \Delta_{sat}\,(i_{wet} - \bar{i}_{wet}) \tag{3.6}$$

where the mean value of $i_{wet} - \bar{i}_{wet}$ is by definition zero, and the only remaining degree of freedom is multiplication by a scaling parameter, Δ_{sat} .

The distribution function must then be:

$$\begin{aligned}
s_{sat,dist} &= f(\bar{s}_{sat}, i_{wet}, \bar{i}_{wet}) \\
&= \bar{s}_{sat} + \Delta_{sat}\,(i_{wet} - \bar{i}_{wet})
\end{aligned} \tag{3.7}$$

This is what shall be termed a generalised distribution function (GDF), which operates with any chosen wetness index. It makes no assumptions about subsurface flow within hillslopes but relies on the user choosing a wetness index which reflects observed moisture distribution patterns or water table profiles.

The distribution function used by TOPMODEL is of this form and uses the familiar $\ln(\frac{a}{\tan \beta})$ wetness index, where a is upslope area per unit contour length and β is the surface slope. The m parameter (or $\frac{1}{f}$ in the 'z-based' version) of TOPMODEL is a special case of Δ_{sat}. The TOPMODEL distribution function is derived analytically from a number of assumptions about subsurface hillslope flow. In many situations, these assumptions do not hold, and the user of TOPMODEL is led into a vicious circle of compromise between striving for physical reality in parameterisation and achieving accurate hydrograph predictions.

3.3.4 A new development: limited distribution function modelling

A modification to the DFM approach, referred to as *limited* distribution function modelling (limited DFM), was developed for the present study and is introduced here.

From the point of reference of a single ESU, the operation of a conventional DFM can be thought of as an implicit simulation of lateral flow occurring between the ESU and the remainder of the hillslope. Once the distribution function has been applied, the saturation deficit of each ESU will reflect the value specified by the distribution function, regardless of any local variation

brought about during the previous time step. Notionally, water will flow between the individual and the whole. Water tables simulated by conventional DFMs are always the same shape with respect to the catena. This does not necessarily reflect reality (e.g. Bren, 1997).

The modification introduced by limited DFMs allows individuality amongst spatial units by limiting the amount of flow between individuals and the whole according to a *lateral redistribution factor*. At the point at which the distribution function is applied to a spatial unit, the amount of implicit flow between the spatial unit and the remainder of the hillslope is calculated. Instead of implementing the entire flow, a fraction dictated by the lateral redistribution factor is implemented. Thus, mounds or troughs can develop in the water table relative to its shape as determined by the distribution function, in response to particular circumstances in the vertical component of the model. Hence, the shape of the water table can change.

Limited DFMs have distinct advantages over conventional DFMs. By allowing the shape of the water table to change, the subsurface response of the system can be sped up allowing dynamic behaviour of the water table near saturated areas of a catchment even when the water table away from these areas is inactive. This enables the DFM approach to be applied in a physically realistic manner to deep-soiled catchments where previously this was not possible.

3.3.5   Operation of a limited DFM

Practically, the operation of a limited DFM proceeds as follows.

Each ESU within each hillslope is modelled separately, having its own unsaturated and saturated soil water stores, the latter being implemented as a saturation deficit. At the beginning of each time step for a given ESU, the mean saturation deficit of the hillslope is known from accounting following the end of the previous time step. This is presented to the GDF which estimates a new saturation deficit, $s_{sat,dist}$. In a conventional DFM, this value is immediately adopted as the new saturation deficit, s_{sat}, implying an instantaneous lateral flow between the ESU and the remainder of the hillslope, and forcing the water table profile to follow that predicted by the wetness index. In the limited DFM proposed here, the implicit lateral flow, q_{redist}, is limited according to a lateral redistribution factor, δ, as follows:

$$q_{redist} = \delta \left(s_{sat,dist} - \text{previous } s_{sat} \right) \qquad (3.8)$$

$$s_{sat} = \text{previous } s_{sat} + q_{redist} \qquad (3.9)$$

where s_{sat} is the actual saturation deficit (as opposed to $s_{sat,dist}$, which is that dictated by the GDF).

The effect of the δ parameter can be thought of as slowing down the redistribution process, changing the response time of local water table levels relative to those of the rest of the hillslope, or allowing the water table of individual intervals to rapidly respond to influences from the vertical flux system. The parameter is conceptually related to the effective lateral hydraulic conductivity and hydraulic gradient of the saturated zone.

Once the new value of s_{sat} has been set, the implementation of lateral processes is complete and vertical processes are implemented.

3.3.6 Choice of wetness index and disaggregation of hillslopes

The wetness index typically performs two functions within a DFM. Firstly, a wetness index is required for use within the distribution function as a proxy for the spatial variation in water table depth. Secondly, the disaggregation of hillslopes into ESUs is usually made by identifying areas of a hillslope within specific ranges or *intervals* of the wetness index. This is the case for TOPMODEL and RHESSys. There are many ways in which a suitable wetness index may be chosen.

Many modelling studies have used analytically derived wetness indices based on assumptions about subsurface processes, such as the $\ln(\frac{a}{\tan\beta})$ index (see Beven et al., 1995) and the $\frac{a}{\tan\beta}$ index implicit in O'Loughlin (1986) (a being upslope area per unit contour length, and $\tan\beta$ being downslope gradient). Numerous investigations have thrown doubt on many of the assumptions inherent in these studies and on their spatial predictions of hillslope moisture distribution (Ambroise et al., 1996b; Lamb et al., 1997; Barling et al., 1994; Petch, 1988; Jones, 1986; Moore and Thompson, 1996; Woods et al., 1997; Moore et al., 1988; McDonnell et al., 1996; Burt and Butcher, 1985; Jackson, 1991) (although admittedly some of these studies have worked with

unsaturated moisture content instead of water table levels). Some studies have validated certain assumptions (e.g. Moore et al., 1996) and certain elements of moisture distribution (e.g. O'Loughlin, 1986; Moore et al., 1986, 1988; Troch et al., 1993; Merot et al., 1995), whilst others have provided promising analytical (Ambroise et al., 1996a; Woods et al., 1997), empirical (Lamb and Beven, 1997), and dynamic (Barling et al., 1994) alternatives to conventional indices. But, to my knowledge, there has been no successful validation of spatial and dynamic predictions of saturated area and moisture distribution (e.g. water table depth) made using an *analytically derived* wetness index.

An empirical rather than analytical approach is suggested here whereby an arbitrary wetness index is chosen such that the GDF approximately reproduces observed spatial patterns of water table depth. This approach is explored within the chapter on model operation and parameterisation (Section 5.2.3).

Chapter 4

Model description

Contents

4.1 Introduction

This chapter, and the appendices to which it refers, are intended to be a self contained and complete description of the Macaque model. It is a long chapter which illustrates the true complexity of physically based models. It is the author's experience from comparisons between published model descriptions and model code that shorter descriptions, which are common in the literature, conceal many influential auxiliary algorithms.

The description of each simulated process (i.e. each sub-component of the model) begins with a brief summary of the role of the process within the greater simulated hydrological system, as well as some background on the way in which the process is simulated in other models. This is followed by the process description itself, and finally, where appropriate some comments on the limitations of the process as represented and suggested future improvements. The operation of the model (as opposed to its description) is described in the following chapter, which includes a detailed description of each parameter.

Macaque is a large scale spatial model intended for physical process based hydrological modelling of large forested catchments. It is based on RHESSys (Band et al., 1993), from which it differs in the following ways. It employs a limited DFM approach to spatial modelling instead of a conventional DFM

approach. Baseflow is generated specifically from each saturated interval and not from hillslopes as a whole, forcing a more spatially realistic implementation of streamflow production. It has a more sophisticated vertical structure, including two vegetation layers. Much of the vertical structure is derived from Topog and COUPLES. From a programming point of view, its spatial data structure and algorithms are more highly refined than in RHESSys and Topog. Features include: recursive, generic code for simulating different levels of spatial disaggregation (catchments, hillslopes, intervals etc.); hierarchical parameter inheritance between these levels; the ability to specify the value of any parameter at any spatial level at run time; and automatic spatio-temporal accounting and output of any model variable (including all inputs, outputs, stores, parameters, and intermediate working variables). The code is completely original and is written in the `C` programming language ($>$ 7800 lines including comments).

The description is given in two sections. The first deals with *horizontal* structure and flux, including aspects such as the horizontal spatial disaggregation of the catchment into smaller spatial units, and the means of laterally redistributing water between these units. The second section deals with *vertical* structure and flux, including the representation of all processes which occur within a single ESU, and which tend to be oriented vertically.

A general overview of the model structure is given in Figure 4.1.

All symbols and units used are described in detail in Appendix C.

4.2 Horizontal structure and fluxes

4.2.1 The generic spatial unit

The fundamental building block of Macaque is a *spatial unit*, a horizontally defined part of the landscape. Examples of spatial units include the entire region of interest, catchments within that region of interest, and at the smallest end of the scale, elementary spatial units (ESUs). Any particular application of Macaque may operate with an arbitrary range of spatial units. The definition of the types of units to be used as well as the units themselves occurs only at run time. For example, the concept of, say, a catchment is not hard-coded into Macaque, but rather introduced to the model by the user at run time.
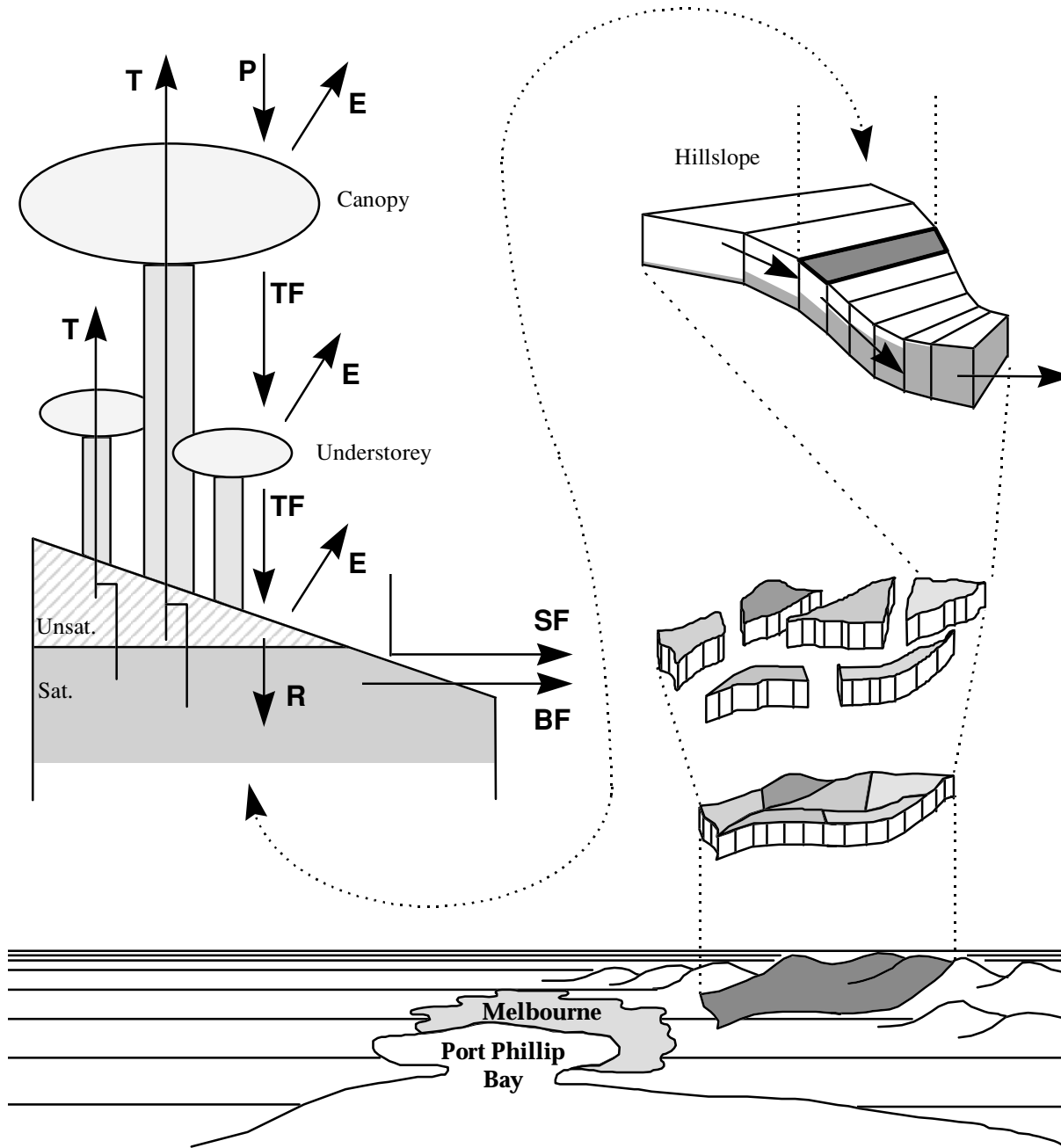
Figure 4.1: A simple representation of the essential horizontal and vertical structure of the Macaque model.

4.2.1.1 Spatial hierarchy

Spatial units are hierarchical. At run time, larger spatial units can be defined to contain smaller spatial units, and so on. This leads to the use of the term *spatial level* or just *level*. All spatial units exist within a given level of the hierarchy. There is a single top-level unit, and there may be any number of levels of spatial units defined below this. Bottom-level units are termed *elementary spatial units*.

For example, the applications of Macaque described in this dissertation define the following spatial levels: `world`, `region`, `catchment`, `hillslope`, and `ESU`. The `world` level does nothing but contain everything else. The `region` level is used to organise `catchments` into two groups containing well gauged and poorly gauged catchments respectively. For the Maroondah study area, `catchments`, typically contain about ten or twenty `hillslopes` each. Finally, each `hillslope` contains, on average, fourteen `ESUs`. As an illustration of the versatility of this system, if it was decided to remove the concept of a region, the `region` level could be removed from the run time header file in about a minute and no further adjustments would be necessary to banish `regions` for ever.

4.2.1.2 Generic and specific code for manipulating spatial units

The code of Macaque is generic with respect to the manipulation of spatial units. Code that manipulates spatial units operates irrespective of the level to which the unit belongs. The code for `regions` is the same code as that for `hillslopes`. This is a very powerful programming feature, made possible through object oriented programming techniques. For example, accounting of model variables amongst spatial units is performed by a single section of code. The average value of *any* model variable can be queried by the user for *any* spatial unit at *any* spatial level, all using the same code. A second example involves inheritance of parameters from larger units to their 'children' (see Section 4.2.2), which is implemented by a single piece of code.

To the user, this feature means that many normal modelling decisions do not have to be made until run time, and significantly more information may be extracted from the model than is normally the case. Decisions as to how a study area should be structured can be made at any stage, and not at the outset. Decisions as to which parameters should be defined at which spatial scale can also be made at any stage. Queries about the internal workings of the model can be made at any level of spatial detail, and about any part of

any physical process represented by the model.

The only part code which operates with a specific spatial level is the core hydrological modelling code which implements horizontal and vertical fluxes at the level of ESUs. The level-specific code in question comes into effect when the vertical flux for an ESU is just about to be run. At this point, the ESU queries its parent (ostensibly a hillslope) for the mean saturation deficit of the hillslope, and uses this value to compute its own saturation deficit. The specific algorithms are described in Section 4.2.3.

4.2.2 Variables, inheritance, and accounting

Macaque uses five distinct types of 'variables'. These are: 'parameters', 'working variables', 'fluxes', 'states/stores', and 'areas'. In the code, these types are recognised by the first letter of the variable name, which may be p, w, f, s, or a (see Appendix C). The different types behave differently within the model.

Because of a unique way of storing the variables, a number of useful model features can be implemented. Parameters are inherited from larger spatial units to smaller sub-units. This economises parameter storage both in memory and on disk. It also allows parameters to be defined at any spatial level (be it catchment-wide, hillslope-wide, etc.) at run time and removes the requirement on programmers to make decisions about the resolution or spatial variability of any given parameter. Working variables, fluxes, states, and areas are accumulated from smaller spatial units to their parent, overlapping spatial units. This enables *any* such variable to be accounted at any *spatial* resolution. For example, the user can observe the catchment average of a specific internal working variable, or look at it on a per hillslope, or per interval basis.

Additionally, accumulated or average values of any parameter at any spatial level can be reported at a number of *temporal* resolutions i.e. daily, weekly, monthly, yearly, water-yearly, or on a per-run basis. As with the above features, this automatic temporal accounting is accomplished by a single section of model code which operates with any variable at any spatial level.

All variables active at a given point in the simulation are in fact held within a single variable array. The code knows which way to treat them by looking at the first letter of the name. The variable names used in the code are not actually C variables. Rather they are C macros, defined to appropriately index the variable array.

4.2.3   Hillslopes and ESUs

The lowest two spatial levels in applications of Macaque presented here are *hillslopes* and *ESUs*. Hillslopes represent all parts of space between (and including) the top and bottom of a catena along which lateral flow of water occurs. Hillslopes are divided into ESUs. Typically, a hillslope may represent a small sub-basin, or one side of a large sub-basin. ESUs may be defined by some wetness index, whereby each ESU represents all parts of the hillslope within a certain range of the wetness index. There is no restriction on the exact space defined to be a hillslope except that no water can flow laterally downward into the top-most ESU and no water can flow laterally downward from the bottom-most ESU except as stream flow (which is described in Section 4.3).

Once parts of space are associated with an ESU within Macaque, their location loses much of its relevance. Instead, a statistical significance is given to the ESU as a whole. An ESU is thought of as having a certain total area and mean value for its parameters, but knowledge of its location is not essential. This allows the user to *explicitly* deal with uncertainty in parameterisation because the representation of space is less specific than if parameter values were assigned to every part of space. Of course, when constructing maps of model outputs, knowledge of the locations in space occupied by each ESU is useful. However the user must be wary when associating physical observations at a point in space with model predictions for the ESU which (in part) represents that point.

There is no code which deals explicitly with hillslopes. All functions of hillslopes are generic functions of all spatial units. In particular, the accumulation of saturated zone water to a hillslope total is implemented by the generic code which accumulates and averages all stores, working variables, fluxes, and areas from all spatial units to their parent units.

There are two sections of code which deal specifically with ESUs. These are executed serially. The first handles the redistribution of water amongst ESUs and depends on variables for the total hillslope water. This code also reports to a routine that checks for water balance violations during the redistribution process. The second piece of ESU-specific code is the code for the vertical part of Macaque (radiation, vertical water flux, etc.).

The redistribution code implements the following algorithm (which, for the sake of keeping the present description self-contained, partly reproduces material from the previous chapter).

The average amount of saturated zone water in the hillslope is determined from the area-weighted average saturation deficits of all ESUs in the hillslope at the end of the previous time step:

$$\bar{s}_{sat} = \frac{\sum\limits^{N} A \text{ previous} s_{sat}}{\sum\limits^{N} A} \tag{4.1}$$

The distribution function is then evaluated at the wetness index of the current ESU (from Equation 3.7):

$$s_{sat,dist} = \bar{s}_{sat} + \Delta_{sat} \left(i_{wet} - \bar{i}_{wet} \right) \tag{4.2}$$

This is the saturation deficit prescribed for the ESU by the distribution function. The difference between this and the previous saturation deficit of the ESU implies lateral flow to or from some other part of the hillslope. Conventional distribution function models such as TOPMODEL use $s_{sat,dist}$ directly to calculate the saturation deficit of an ESU prior to the execution of vertical flux for the timestep. Macaque adds a further step whereby the implicit lateral flow is scaled by a redistribution factor:

$$q_{redist} = \delta \left(s_{sat,dist} - \text{previous } s_{sat} \right) \tag{4.3}$$

This flow is then applied to the saturation deficit of the current ESU:

$$s_{sat} = \text{previous } s_{sat} + q_{redist} \tag{4.4}$$

Finally, for reporting only, the degree to which the saturated zone 'mounds' above the level prescribed by the distribution function is calculated:

$$s_{sat,mound} = s_{sat,dist} - s_{sat} \tag{4.5}$$

This completes the redistribution algorithm, which is tested against water table level observations in Section 10.2.11.1. Execution now passes to the vertical component of the model.

4.3 Vertical structure and fluxes

4.3.1 Summary

The description of vertical structure and flux is long. Therefore, a summary is presented first, accompanied by Figure 4.2 which summarises the interactions between the key vertical components of the model.

Vertical flux is implemented from the top down starting with precipitation, interception, and infiltration, followed by streamflow generation, and ending in transpiration from the canopy and understorey and evaporation from the soil. A daily time step is used.

The major structures implemented are a canopy and an understorey layer of vegetation, a snowpack, an unsaturated soil water store, and a saturation zone modelled as a saturation deficit.

Daily precipitation input is driven by daily data from a base station and distributed spatially using a mean monthly precipitation index (MMPI) which is supplied as a mapped parameter (see Chapter 7). This involves an assumption that spatial precipitation patterns are stationary at daily to annual time scales. Precipitation is deemed rain or snow depending on temperature and intercepted successively by the canopy and understorey using an interception store approach based on Rutter et al. (1971).

Snow is *not* a major feature of the hydrology of the study area. Only a few falls are recorded at the highest point, Mount Donna Buang, each year and snow rarely persists on the ground for more than a few days. Snowpack accumulation and melting processes are included in Macaque only for completeness and are modelled using a degree-day algorithm (see Gray and Prowse, 1993) borrowed directly from RHESSys.

A portion of each ESU may be saturated to the surface. The saturated proportion is calculated from the saturation deficit using a derivative of the generalised distribution function (defined in Section 3.3.3).

All water falling (or melting) onto the *unsaturated* portion infiltrates into the soil, from whence it may evaporate, be transpired, or recharge the saturated zone. Recharge is calculated using a Van Genuchten estimation of the unsaturated hydraulic conductivity of the soil (see Rawls et al., 1993) based on soil water tension measurements.

All water falling (or melting) onto the *saturated* portion of the soil immediately becomes saturation excess runoff. Baseflow is also released from the

RADIATION

Interception, absorption, and propagation of solar and longwave radiation

EVAPOTRANSPIRATION

Transpiration and soil evaporation into specific atmospheric layers

HUMIDITY

Humidity of specific atmospheric layers and its control of ET

PRECIPITATION

Interception of precipitation.

Snowpack processes

LEGEND

→ Downward water flux
→ Evapotranspiration
→ Solar radiation
→ Longwave radiation
⋯▸ Functional controls

Longwave

Solar

Reference level atmosphere

Evaporation

Humidity control

Canopy radiation interception

Radiation control

Canopy transpiration

Canopy atmosphere

Canopy precip. interception

Canopy throughfall

Humidity control

Understorey radiation interception

Radiation control

Understorey transpiration

Understorey atmosphere

Underst. precip. interception

Understorey throughfall

Humidity control

Snowpack irradiation

Radiation control

Surface atmosphere

Snowpack accumulation

Soil irradiation

Soil evaporation

Snowmelt

Infiltration

Unsaturated zone

Saturation excess flow

Recharge

Saturated zone

Baseflow

Figure 4.2: Key components of Macaque's vertical structure

saturated portion at a constant rate determined as the product of the surface vertical saturated hydraulic conductivity and a parameter expressing the effective hydraulic gradient of the saturated zone when it is at or near the surface. Thus total hillslope baseflow can only rise or fall as the ESUs within the hillslope become more or less saturated. The generation of runoff is thus inextricably and explicitly linked to the spatial distribution of moisture, and hence to the topography of the hillslope. The model cannot simulate the undesirable situation of a dynamic hydrograph whilst moisture patterns remain static. This is a significant difference to RHESSys and TOPMODEL which calculate baseflow at the hillslope level as an exponential function of mean hillslope saturation deficit, irrespective of whether appropriate saturation areas (from which all baseflow must emerge) are represented.

Transpiration from the canopy and understorey and evaporation from the soil are implemented using Penman-Monteith schemes based largely on Topog and RHESSys but improved by ideas from COUPLES. Running and Coughlan's (1988) leaf conductance model is used, parameterised to be most sensitive to variations in vapor pressure deficit (VPD) and soil moisture, with maximum levels set by data from Connor et al. (1977). VPD is modelled using theory set out by Jarvis and McNaughton (1986). Choudhury and Monteith's (1988) soil resistance model is used with a modification that estimates the effective depth to an evaporating layer from modelled unsaturated zone moisture content. As in most physically based models, LAI is a major control of all evapotranspiration systems, influencing leaf conductance, canopy conductance, radiation interception, and precipitation interception. Net radiation is also a major control. It is calculated primarily from temperature range using a novel combination of equations from Bristow and Campbell (1984), Dingman (1994), Iqbal (1983), and Linacre (1992), and calibrated using data from the nearby Tarrawarra catchment (Western and Grayson, 1997).

Time-series inputs to the system are precipitation and maximum and minimum temperature at a base station. From these inputs are estimated a number of further driving variables such as radiation and humidity.

The following sections describe the vertical structure and fluxes in complete detail, as close as possible to the order of computation.

A reminder. *All symbols and units used are described in detail in Appendix C.*

4.3.2 Topography

Most topographic variables, such as elevation and slope, are input directly into Macaque as parameters. Aspect, however, is input as the separate sine and cosine of the aspect. This is done in order that the automatic spatial averaging procedures employed in importing data from the GIS to Macaque do not erroneously average the aspect value itself. For example, if an aspect of $0°$ was naively averaged with $300°$, the result would be $150°$, which is nonsense. The correct result should be $330°$. By separating aspects into their sines and cosines, averaging these, and then recombining them, the correct spatially averaged aspects are obtained. The basic recombination equation used within Macaque is:

$$\phi = \arctan\left(\frac{\sin\phi}{\cos\phi}\right) \tag{4.6}$$

However, as with any use of the arctan function, there are a number of special cases and a more complex equation is necessary:

$$\phi = \begin{cases} \mathrm{mod}\left(\arctan\left(\frac{\sin\phi}{\cos\phi}\right) + 360, 360\right) & \cos\phi > 0 \\ \mathrm{mod}\left(\arctan\left(\frac{\sin\phi}{\cos\phi}\right) + 180, 360\right) & \cos\phi < 0 \\ 90 & \cos\phi = 0, \sin\phi > 0 \\ 270 & \cos\phi = 0, \sin\phi <= 0 \end{cases} \tag{4.7}$$

4.3.3 Vegetation

4.3.3.1 Vegetation age

A number of model processes depend on the age and LAI of the vegetation. The age is calculated as the time in years since the last fire or logging. The calculation of this time involves first calculating the fractional current year:

$$t_{date} = t_{year} + \frac{t_{day} - 1}{364 + leapyear(t_{year})} \tag{4.8}$$

where the function $leapyear()$ is 1 day for leap years and 0 days otherwise. From this is subtracted the most recent of three supplied (already fractional) origin dates:

$$y_{age} = \begin{cases} t_{date} - y_{origin,1} & t_{date} > y_{origin,1} \\ t_{date} - y_{origin,2} & y_{origin,1} \geq t_{date} > y_{origin,1} \\ t_{date} - y_{origin,3} & y_{origin,2} \geq t_{date} > y_{origin,3} \end{cases} \qquad (4.9)$$

where $y_{origin,1}$ is the most recent origin date, which is preceded respectively by $y_{origin,2}$ and $y_{origin,3}$.

The ages of the canopy and understorey are assumed to be identical. This assumption may occasionally be violated, for example in cool temperate rainforest gullies where a moist understorey is jumped by a fire and remains whilst a younger canopy species grows around it, or where low intensity fires burn the understorey beneath a relatively unscathed canopy. Complications arising from succession of understorey plant communities are not considered.

4.3.3.2   LAI

Both total and canopy LAI are spatio-temporal parameters within Macaque. The temporal dependence requires that the calculation of these parameters be coded into the model in order that they may be determined for each ESU at each time step. For the sake of continuity, the associated algorithms are described here, whilst the origins of the key equations are dealt with in later chapters. Note that temporal variation of LAI is limited to dependence on vegetation age. In *E. maculata* forests generally drier than those of the study area, Pook (1984a, b, 1985) has observed marked *seasonal* and *drought* related variation in LAI. Currently, such variation is not accounted for within Macaque because the forests of the study area are predominantly not water limited.

Firstly, total LAI may be supplied directly as a parameter, in which case the value used within the model is taken from the parameter:

$$LAI_{tot} = LAI_{tot,param} \qquad (4.10)$$

Typically however, the value is calculated according to canopy species using a lookup table coded into the model (this course of action being invoked by setting $LAI_{tot,param}$ to some negative value). The lookup table can return a direct LAI value which is used in the model, subject to modification by a sigmoid function which emulates continuous growth from zero LAI at age

zero, asymptoting at the lookup value within a few years (from Equation 9.12):

$$LAI_{tot} = LAI_{tot,lookup} \left(\frac{2}{1 + e^{\left(\frac{-AGE}{\tau_{tot,C}} \right)}} - 1 \right) \qquad (4.11)$$

Alternatively, the lookup table can return a negative value which directs the model to calculate LAI using an equation specially parameterised for the species in question (from Equation 9.11):

$$LAI_{tot} = (LAI_{tot,P} - LAI_{tot,C} - LAI_{tot,D}) \frac{e}{\tau_{tot,P}} AGE \, e^{\left(\frac{-AGE}{\tau_{tot,P}} \right)} +$$
$$(LAI_{tot,C} + LAI_{tot,D}) \left(\frac{2}{1 + e^{\left(\frac{-AGE}{\tau_{tot,C}} \right)}} - 1 \right) + \qquad (4.12)$$
$$LAI_{tot,D} \left(e^{\left(\frac{-AGE}{\tau_{tot,D}} \right)} - 1 \right)$$

where parameters $LAI_{tot,P}$, $LAI_{tot,D}$, $LAI_{tot,C}$, $\tau_{tot,P}$, $\tau_{tot,D}$, and $\tau_{tot,C}$ are species specific and are described in Sections 9.5.2.5 and 9.5.2.7.

A similar approach is adopted for canopy LAI, except that the lookup table returns one of only two possible values. One indicates that canopy LAI should be calculated simply as a constant fraction of total LAI:

$$LAI_c = \frac{1}{2} LAI_{tot} \qquad (4.13)$$

and the other indicates that an equation dependent on vegetation age should be used:

$$LAI_c = 11.014 \, y_{age}^{-1.624} \, (y_{age} - 5.04)^{1.180} \, 3.592^{[(y_{age} - 5.04)^{-0.319}]} \qquad (4.14)$$

The choice of the two is discussed in Section 9.6.

Understorey LAI is calculated as total LAI minus canopy LAI:

$$LAI_u = \max(LAI_{tot} - LAI_c, \, 0) \qquad (4.15)$$

4.3.4 Temperature

A number of temperature variables are required. Firstly base temperatures must be scaled from the input data recorded at the base station to give values applicable to the current ESU. Simple linear environmental lapse rates for maximum and minimum temperatures, $\Delta_{T,max}$ and $\Delta_{T,min}$, are used:

$$T_{max} = T_{max,stn} + \Delta_{T,max}(h - h_{stn}) \tag{4.16}$$

$$T_{min} = T_{min,stn} + \Delta_{T,min}(h - h_{stn}) \tag{4.17}$$

$$T_{min,tom} = T_{min,tom,stn} + \Delta_T(h - h_{stn}) \tag{4.18}$$

Note that careful attention is paid to matching a given maximum or minimum temperature reading to the day to which it applies. For example, today's 9 a.m. reading of maximum temperature usually tells us about yesterday's maximum temperature. Curiously, climate records can contain periods describing a maximum recorded on one day which is lower than the minimum recorded on the previous day. The model warns the user when this occurs, and switches the values.

Twenty-four hour mean air temperature is used in continuous 24 hour systems such as snowpack energy accumulation. It is calculated as:

$$\bar{T} = \frac{T_{max} + T_{min}}{2} \tag{4.19}$$

Daytime mean air temperature is used either directly or indirectly in many predominantly daytime processes such as transpiration, and evaporation. It is calculated assuming a sinusoidal daily temperature trace after Parton and Logan (1981) and validated by Running et al. (1987, p. 475):

$$\bar{T}_{day} = 0.606\, T_{max} + 0.394\, T_{min} \tag{4.20}$$

Night-time mean temperature is used to determine whether precipitation is rain or snow. After Running et al. (1987, p. 475), it is estimated as:

$$\bar{T}_{night} = \frac{\bar{T}_{day} + T_{min}}{2} \tag{4.21}$$

Soil temperature is used in the calculation of leaf water potential, and soil resistance to evaporation. It is estimated from the 24 hour mean temperature:

$$T_{soil} = \bar{T} \tag{4.22}$$

Possibilities exist for more sophisticated temperature estimation, such as the spline interpolation used by Hutchinson (Hutchinson, 1983; Hutchinson et al., 1997) who fitted a non-linear surface to monthly mean maximum and minimum temperature data using latitude, longitude, and elevation as independent variables. Hutchinson noted that the greatest predictive errors using this method occurred for winter minimum temperatures which were suggested to be influenced by cold air drainage, which is not well represented by the chosen independent variables (Hutchinson, 1983, 1995b).

A number of temperature predictions are tested against observed data in Section 10.2.3, including maximum, minimum, and daytime mean temperature.

4.3.5 Humidity

Dewpoint temperature is used as the initial humidity variable from which other quantifications of humidity are derived. This is done because dewpoint remains relatively constant throughout the course of a day (Linacre & Hobbs, 1977, Fig. 6.5). Dewpoint is estimated from daily minimum temperature following Linacre (1992, p. 86), Running et al. (1987, p. 476), and McMurtie et al. (1990a):

$$T_{dew} = T_{min} \tag{4.23}$$

More complex estimations can be made using temperature range as well as minimum temperature. Given that humidity is a sensitive input to the model and that both Running et al's data (1987) and data from the present study (see Section 10.2.4) show over-estimations of a few degrees, these more complex techniques should be investigated in the future.

Saturation vapor pressure (SVP) can be estimated by a variety of equations (Linacre, 1992 p. 315), one of the most popular being the Clausius-Clapeyron

equation of Tetens (1930) (also offered by Smith, 1990, p. 43; Murray, 1967, p. 204; Dingman, 1994, p. 516; and Monteith and Unsworth, 1990, p. 10). An estimation of mean daily SVP is obtained by using $\bar{T}_{day}$ as the temperature term in the Clausius-Clapeyron equation:

$$e_{sat} = 611 \, \exp\left(\frac{17.27 \, \bar{T}_{day}}{\bar{T}_{day} + 237.3}\right) \tag{4.24}$$

By substituting the dewpoint temperature into the SVP equation, we obtain the vapor pressure of the air, which should remain relatively constant throughout the day:

$$e = 611 \, \exp\left(\frac{17.27 \, T_{dew}}{T_{dew} + 237.3}\right) \tag{4.25}$$

This enables vapor pressure deficit (VPD), the key humidity variable used by Macaque, to be calculated:

$$D_{ref} = e_{sat} - e \tag{4.26}$$

This value is calculated using screen temperatures, and so is a screen-height estimate of VPD. The value we require is the VPD of the air at some reference level within the boundary layer above the canopy. We thus make the assumption here that screen temperatures have been measured in a clearing whose atmosphere approximates that of the atmosphere above a canopy. This assumption has yet to be tested, although the screen-height prediction of both dewpoint and VPD at locations remote from the base station is tested against observed data in Section 10.2.4.

4.3.6   Radiation

A number of radiation inputs are used by Macaque, and are estimated solely from temperature range, time of year, and topography using a *novel* combination of various relationships. *Solar* radiation is estimated using various geometrical and empirical climatological formulae. It is then intercepted and absorbed successively by the canopy, understorey, snowpack, and soil. Solar radiation is used directly only in the calculation of leaf conductance. The

balance of terrestrially emitted and atmospherically emitted *long-wave* radiation is then found and intercepted and absorbed in a similar manner to solar radiation. Solar radiation is then summed with longwave radiation to give *net* radiation. Net radiation is used for evapotranspiration and snowmelt. The details of the radiation calculation, interception and absorption processes are explained as follows.

4.3.6.1   Solar radiation

Total daily solar radiation incident above the canopy

Global daily solar radiation incident above the canopy is calculated as a function of the time of year, the slope and aspect of the terrain, and the daily temperature range, which is used as a proxy for cloudiness. Formulae given by Dingman (1994, App. E) are used to estimate extra-terrestrial radiation incident on a sloping surface above the atmosphere. The ratio between observed radiation and extra-terrestrial radiation is called the transmission. Bristow and Campbell (1984) give a model for predicting the transmission from temperature range. A modified version of this model was calibrated to local observed radiation data using extra-terrestrial radiation incident on a *horizontal* surface. Using a formula from Linacre (1992, p. 155), the predicted radiation incident on a horizontal surface is split into direct and diffuse components. The direct component is modified to be incident on a sloping surface, and then re-combined with the diffuse component to give the global radiation incident on a sloping surface. The details follow.

The mean radiation incident above the atmosphere over the course of a year is termed the *solar constant* (I_{con}). The solar constant varies both periodically and aperiodically over time scales greater than one year but has been 'fixed' by the WMO as (Linacre, 1992 p. 152):

$$I_{con} = 1367 \text{ W m}^{-2} \tag{4.27}$$

The irradiance above the atmosphere at any time throughout the year is called the *solar parameter* (I_{par}). Because of the slightly eccentric, elliptical orbit of the earth, the solar parameter varies almost sinusoidally throughout the year. An eccentricity correction is applied to the solar constant to give the solar parameter, as a function of the *day angle* (Γ). The day angle is an angular measure of Earth's location relative to the sun (Dingman, 1994, Eqn. E-1):

$$\Gamma = \frac{360\,(t_{day} - 1)}{365} \tag{4.28}$$

and the *eccentricity* is (Dingman, 1994, Eqn. E-2):

$$
\begin{aligned}
ecc =\, &1.000110 \\
&+0.034221\cos(\Gamma°) + 0.001280\sin(\Gamma°) \\
&+0.000719\cos(2\Gamma°) + 0.000077\sin(2\Gamma°)
\end{aligned} \tag{4.29}
$$

Note the use of the ° symbol in this and the following equations. This is a reminder that angles within Macaque are stored and expressed in degrees for ease of interpretation. However, when used in trigonometric functions they should be converted to radians. In part, this is obvious, but at some points (e.g. Equations 4.33 and 4.44) the equations are the results of integration and the need for a conversion is not so obvious. One can think of the ° symbol as meaning 'multiply by $\frac{\pi}{180}$'.

The solar parameter is then:

$$I_{par} = I_{con}\, ecc \tag{4.30}$$

The declination of sun's observed path can be expressed in a number of ways, including (Dingman, 1994, Eqn. E-3; see also Linacre, 1992, p. 148):

$$
\begin{aligned}
d = \frac{180}{\pi} \Big[&0.006918 \\
&-0.399912\,\cos(\Gamma°) + 0.070257\,\sin(\Gamma°) \\
&-0.006758\,\cos(2\,\Gamma°) + 0.000907\,\sin(2\,\Gamma°) \\
&-0.002697\,\cos(3\,\Gamma°) + 0.00148\,\sin(3\,\Gamma°) \Big]
\end{aligned} \tag{4.31}
$$

The time of sunset for a horizontal surface is calculated as the time when the solar zenith angle is zero (Dingman, 1994, Eqn. E-5b):

$$
t_{hor,set} = \begin{cases}
0 & \tan lat\ \tan d° < -1 \\
43\,200 & \tan lat\ \tan d° > 1 \\
\frac{\arccos(-\tan d°\ \tan lat°)}{rot°} & otherwise
\end{cases} \tag{4.32}
$$

where 43200 is the number of seconds in half a day, and $rot = 4.167 \times 10^{-3\circ}$ s^{-1}) is the angular speed of rotation of the earth. The specified conditions apply at certain times of year for sites above the arctic circle or below the Antarctic circle. The time of sunrise for a horizontal surface is the negative of the time of sunset (Dingman, 1994, Eqn. E-5a).

The extra-terrestrial solar radiation incident on a horizontal surface is (Dingman, 1994, Eqn. 7):

$$
\begin{aligned}
I'_{ex} = 2\, I_{con}\, ecc \Bigg(&\cos d^\circ\ \cos lat^\circ \\
&\times \frac{\sin(rot^\circ\, t_{hor,set})}{rot^\circ} \\
&+ t_{hor,set}\ \sin d^\circ\ \sin lat^\circ \Bigg)
\end{aligned}
\tag{4.33}
$$

Note that Dingman's version of the above equation contains an error whereby sunrise time is used instead of sunset time.

Extra-terrestrial radiation is attenuated by various atmospheric components before becoming radiation incident above a horizontal canopy. The ratio between the two is called the *transmission* (Linacre, 1992, p. 160):

$$
\text{observed } \tau_{atm} = \frac{\text{observed } S'_{tot}}{I'_{ex}}
\tag{4.34}
$$

The transmission is influenced by cloud, water vapor, aerosols, and the thickness of the atmosphere. Numerous equations exist for predicting the latter three from standard geometric and meteorological variables (e.g. Dingman, 1994, App. E; Linacre, 1992, p. 156). However, expressions predicting the effect of clouds from commonly measured data such as temperature range (as opposed to sparsely measured data such as cloud cover) are rare.

Bristow and Campbell (1984) present a method for estimating the transmission, including cloud effects, from the temperature range (although they refer to it as the 'transmission coefficient', which is different according to Linacre *op cit*). The essential equation of their method is:

$$
\tau_{atm} = a \left[1 - \exp\left(-b\ (T_{max} - T_{min})^c \right) \right]
\tag{4.35}
$$

where the parameters a, b, and c should be calibrated for each region of interest. Bristow and Campbell used variously more complex forms for the

temperature range term (here: $T_{max} - T_{min}$) involving temperatures from a number of different days and a scaling for rainy days. They also calibrated the parameters by hand and included a separate equation for b in terms of monthly mean temperature range. The present experience is that this complexity is a hindrance and not necessary.

Here the standard equation above is used with a *novel* automatic parameterisation scheme based on observed global radiation data as follows. The a parameter sets the maximum transmission and is thus set to the maximum observed τ_{atm}. This leaves two parameters, b and c, which can be estimated by linear regression after linearising Equation 4.35:

$$\ln\left[-\ln\left(1 - \frac{\tau_{atm}}{a}\right)\right] = \ln b + c \, \ln(T_{max} - T_{min}) \qquad (4.36)$$

where $\ln[-\ln(1 - \frac{\tau_{atm}}{a})]$ is the dependent term, $\ln(T_{max} - T_{min})$ is the independent term, $\ln b$ is the intercept, and c is the slope.

Currently, no account is taken for the effect of varying site elevation on transmission. In general, transmission increases with elevation due to the reduced thickness of the atmosphere (Linacre, 1992, p. 156). However, so too does cloudiness in many regions, which decreases transmission. Data from a wider range of sites will be analysed before an elevation component is added to the transmission model. It is possible that this omission may be significant, due to the under-estimation of ET caused by under-estimation of radiation in high elevation, high precipitation areas where ET is radiation-limited (as opposed to moisture-limited).

Inverting Equation 4.34, the global solar radiation incident above a horizontal canopy is then:

$$S'_{tot} = I'_{ex} \, \tau_{atm} \qquad (4.37)$$

Linacre (1992, p. 155) cites several equations for estimating the diffuse proportion of global radiation from the transmission, and fits his own quadratic equation to the median values predicted by the others. This allows us to split global radiation (above) into direct and diffuse components:

$$S_{dif} = S'_{tot} \left(1 - 1.2 \, \tau_{atm} + 0.13 \, \tau_{atm}^2\right) \qquad (4.38)$$

$$S'_{dir} = S'_{tot} - S'_{dif} \qquad (4.39)$$

Diffuse radiation is assumed to be uniformly distributed across the sky and hence it is not necessary to simulate a difference between diffuse radiation incident on horizontal or sloping surfaces. Sloping surfaces 'see' less of the sky (they have a lower *view factor*, *sensu* Dozier et al., 1981; Moore et al., 1993) but at this stage this is not taken into account.

The direct component *is* modified when incident on a sloping surface. This modification is assumed to be proportional to the ratio between extra-terrestrial radiation incident on sloping and horizontal surfaces. The calculation of extra-terrestrial radiation incident on a sloping surface is taken from Dingman (1994). Solar geometry relative to a sloping surface is calculated using the principle of *equivalent slope*, where the calculations are made for a point on Earth which, horizontally, faces in the same direction relative to the sun as the slope of interest. Some equivalent geometric variables are calculated for this purpose.

The difference in longitude between the current location and the equivalent slope is (Dingman, 1994, Eqn. E-22):

$$\Delta_{lon} = \arctan\left(\frac{\sin\beta° \, \sin\phi°}{\cos\beta° \, \cos lat° \, \cos\phi°}\right) \qquad (4.40)$$

The latitude of the equivalent slope is (Dingman, 1994, Eqn. E-23):

$$lat_{eqiv} = \arcsin(\sin\beta° \, \cos\phi° \, \cos lat° + \cos\beta° \, \sin lat°) \qquad (4.41)$$

Times of sunrise and sunset for the sloping surface are calculated in a similar way to those for a horizontal surface with an adjustment according to the difference in longitude between the current site and the equivalent slope (Dingman, 1994, Eqn. E-24b). Additional constraints are imposed to ensure that the magnitudes of the sunrise and sunset times thus calculated do not exceed those for the horizontal surface:

$$t_{slop,rise} =$$

$$\begin{cases} 0 & \tan d^\circ \ \tan lat^\circ_{eqiv} - \Delta^\circ_{lon} < -1 \\ \max(-t_{horiz,set}, -43200) & \tan d^\circ \ \tan lat^\circ_{eqiv} - \Delta^\circ_{lon} > 1 \\ \max\left(-t_{horiz,set}, \frac{-\arccos(-\tan d^\circ \ \tan lat^\circ_{eqiv}) - \Delta^\circ_{lon}}{rot^\circ}\right) & \text{otherwise} \end{cases}$$

$$(4.42)$$

$$t_{slop,set} =$$

$$\begin{cases} 0 & \tan d^\circ \ \tan lat^\circ_{eqiv} - \Delta^\circ_{lon} < -1 \\ \min(t_{horiz,set}, 43200) & \tan d^\circ \ \tan lat^\circ_{eqiv} - \Delta^\circ_{lon} > 1 \\ \min\left(t_{horiz,set}, \frac{+\arccos(-\tan d^\circ \ \tan lat^\circ_{eqiv}) - \Delta^\circ_{lon}}{rot^\circ}\right) & \text{otherwise} \end{cases}$$

$$(4.43)$$

Note that Dingman's versions of the above equations contain errors. Dingman puts the first sign of the numerator in front of the whole equation, and the right parenthesis before the Δ_{lon} term after it.

No account is taken of shading by higher surrounding terrain and the associated elevation of the effective horizon observed from a site. Methods exist for inclusion of these factors in the future (e.g. Dozier et al., 1981; Dozier and Frew, 1989; Varley et al., 1996) although apparently no-one has determined the sensitivity of hydrological models to such improvements.

The above variables are combined to yield an expression for the total extra-terrestrial radiation incident on a sloping surface over the course of a day (Dingman, 1994, Eqn. E-25):

$$
\begin{aligned}
I_{ex} = I_{con} \ ecc \ \Bigg(& \cos d^\circ \ \cos lat^\circ_{eqiv} \\
& \times \frac{[\sin(rot^\circ \ t_{slop,set} + \Delta^\circ_{lon}) - \sin(rot^\circ \ t_{slop,rise} + \Delta^\circ_{lon})]}{rot^\circ} \\
& + (t_{slop,set} - t_{slop,rise}) \ \sin d^\circ \ \sin lat^\circ_{eqiv} \Bigg)
\end{aligned}
\qquad (4.44)
$$

Direct radiation on a horizontal surface is then modified by the ratio of sloping to horizontal extra-terrestrial radiation to give direct radiation incident on a horizontal surface:

$$S_{dir} = S'_{dir} \ \frac{I_{ex}}{I'_{ex}} \qquad (4.45)$$

Combined with diffuse radiation, this gives the global solar radiation incident on a sloping surface:

$$S_{tot} = S_{dir} + S_{dif} \qquad (4.46)$$

Both net radiation and global solar radiation predictions are tested against observed data in Section 10.2.5.

Propagation of solar radiation through vegetation

The solar radiation incident above the canopy is intercepted, transmitted, and absorbed by the two vegetation layers in succession, and the remainder is absorbed by either snow or soil at the forest floor. These processes are modelled using Beer's Law (Monteith and Unsworth, 1990, p. 33, 73, 88) making certain assumptions about the random distribution of leaves within a canopy.

The canopy intercepts the incident radiation in non-linear proportion to its LAI and an associated radiation extinction coefficient. Some of the intercepted radiation is reflected back upward and some is transmitted through the canopy. The remainder is absorbed. Currently, Macaque models canopy reflection and absorption but not transmission. This practice is inherited from other models but could be reviewed in the future. One could argue that interception by a layer of upward reflection from the layer below (which is not modelled) roughly balances transmission through the first layer. Transmission coefficients for leaves are usually similar to or slightly less than reflection coefficients (Monteith and Unsworth, 1990, p. 86; Oke, 1987, p. 118). Note that the term 'reflection coefficient' is used instead of 'albedo' *sensu* Monteith and Unsworth (1990, p. 80). The symbol often used for albedo, α, is retained to avoid confusion of Monteith and Unsworth's symbol for reflection coefficient, ρ, with density.

Thus, canopy absorbed solar radiation is modelled as:

$$S_{a,c} = S_{tot}(1 - \exp(-k_{R,c}\,LAI_c))\,(1 - \alpha_c) \qquad (4.47)$$

where the exponential term is the Beer's Law term, and the last term expresses reflection and absorption.

Understorey absorbed solar radiation is modelled in a similar way, except that the understorey incident solar radiation is that which is left over after canopy interception:

$$S_{a,u} = S_{tot} \, \exp(-k_{R,c} \, LAI_c) \, (1 - \exp(-k_{R,u} \, LAI_u)) \, (1 - \alpha_u) \qquad (4.48)$$

where the first exponential term accounts for the reduction by previous canopy interception, the second exponential term is the interception by the understorey, and the final term expresses understorey reflection and absorption.

The propagation of radiation continues in a similar manner to the surface, be it snow or soil. If a snowpack is present, it is assumed the soil receives no solar radiation and the snowpack absorbs the following amount:

$$S_{a,snow} = S_{tot} \, \exp(-k_{R,c} \, LAI_c) \, \exp(-k_{R,u} \, LAI_u) \, (1 - \alpha_{snow}) \qquad (4.49)$$

Conversely, if snow is not present, the soil absorbs solar radiation as:

$$S_{a,soil} = S_{tot} \, \exp(-k_{R,c} \, LAI_c) \, \exp(-k_{R,u} \, LAI_u) \, (1 - \alpha_{soil}) \qquad (4.50)$$

4.3.6.2   Longwave radiation

Longwave radiation can be thought of as originating from two main sources: the atmosphere, and all the terrestrial surface layers (canopy, understorey, snowpack, soil). The driving variable in longwave radiation is the temperature of the emitting body. All of the surface layers are treated as having the same temperature and emittance and so emit longwave radiation equally and upward in proportion to their exposure to the sky above. Empirically, the atmosphere is effectively about 20°C cooler than the surface (Monteith and Unsworth, 1990, p. 53). It emits longwave radiation downward such that each surface layer receives an amount in proportion to its exposure to the sky. This symmetrical situation enables us to think of longwave radiation as a single flux, either upward or downward depending on the balance of terrestrially emitted and atmospherically emitted fluxes. The part of that balance which each surface layer gains or loses is proportional to its exposure to the sky, which in turn can modelled using Beer's Law (as for solar radiation). The details are explained as follows.

Longwave radiation balance

The balance of longwave fluxes is estimated from net radiation, which in turn is estimated from global solar radiation incident on a horizontal surface. Net radiation is estimated from global solar radiation using a general equation documented by Linacre (1992, Eqn 3.20):

$$R = \Delta_R S'_{tot} + C_R \qquad (4.51)$$

The parameters of this equation are important determinants of whether or not net radiation is positive, especially in winter.

The longwave radiation balance in the downward direction is then:

$$L_b = R - S'_{tot} \qquad (4.52)$$

Alternative methods exist for the calculation of longwave radiation. Linacre (1992) and Monteith and Unsworth (1990) give several equations, predominantly based on temperature. These were trailed in the initial development of Macaque but comparison with observed data (from Tarrawarra, Western and Grayson, 1997) showed them to be inferior to the correlation method described above.

Finally, longwave radiation is assumed to be independent of the slope of the terrain. The value calibrated against horizontal global solar radiation is used for all slopes.

Propagation of longwave radiation through the vegetation layers

The propagation of longwave radiation through the vegetation layers is modelled in a similar manner to that for solar radiation. A key difference is that at long wavelengths, leaf (and for that matter all wet surface) reflection and transmission coefficients are very close to zero (Oke, 1987, p. 118) and so it is assumed that all longwave radiation is absorbed when incident upon surface layers.

This gives canopy absorbed longwave radiation as:

$$L_{a,c} = L_b \left(1 - \exp(-k_{R,c}\, LAI_c)\right) \qquad (4.53)$$

The remainder from canopy intercepted longwave radiation becomes potentially incident on the understorey and is absorbed as:

$$L_{a,u} = L_b \, \exp(-k_{R,c} \, LAI_c) \, (1 - \exp(-k_{R,u} \, LAI_u)) \qquad (4.54)$$

Propagation continues downward to the snowpack or soil. The snowpack, if present, absorbs:

$$L_{a,snow} = L_b \, \exp(-k_{R,c} \, LAI_c) \, \exp(-k_{R,u} \, LAI_u) \qquad (4.55)$$

Otherwise, the soil absorbs the same amount:

$$L_{a,soil} = L_b \, \exp(-k_{R,c} \, LAI_c) \, \exp(-k_{R,u} \, LAI_u) \qquad (4.56)$$

4.3.6.3 Net radiation

Solar and longwave radiation are summed to give net radiation absorbed by each layer:

$$
\begin{aligned}
R_{a,c} &= S_{a,c} + L_{a,c} & (4.57) \\
R_{a,u} &= S_{a,u} + L_{a,u} & (4.58) \\
R_{a,snow} &= S_{a,snow} + L_{a,snow} & (4.59) \\
R_{a,s} &= S_{a,s} + L_{a,s} & (4.60)
\end{aligned}
$$

4.3.6.4 Allocation of net radiation

Net radiation absorbed by each layer may be 'used' in a variety of ways. For the canopy and understorey, the radiation is first used in the evaporation of any intercepted precipitation. The remainder is then used for transpiration. For the snowpack, radiation is used to melt snow (along with temperature), and for the soil, radiation is used in the evaporation of soil water.

In the case of the canopy and understorey, a radiation budget is modelled whereby the absorbed radiation is transferred to an available-for-transpiration

variable. This variable may be reduced by evaporation of intercepted precipitation before being passed to the transpiration routine. Thus, *initially*:

$$R_{tran,c} = R_{a,c} \tag{4.61}$$

$$R_{tran,u} = R_{a,u} \tag{4.62}$$

4.3.7 Daylength

A number of evapotranspiration calculations require estimates of the length of the day. This is calculated as the difference between sunset and sunrise time (for sloping surfaces):

$$dayl = t_{slop,set} - t_{slop,rise} \tag{4.63}$$

This calculation is tested against an independent equation in Section 10.2.6.

4.3.7.1 Preliminary evapotranspiration variables

A number of preliminary variables used by the evapotranspiration routines are calculated first. Note that many of these variables depend on temperature. The mean daytime temperature is used because evapotranspiration is assumed to occur only during daylight hours.

The worth of using equations for these variables instead of constants is open to question. RHESSys (Band et al., 1993) often uses equations, which is why equations are usually used here. It is possible that future sensitivity analyses will reveal that these equations present undue complexity and can be replaced with constants.

The slope of the saturation vapor pressure curve with respect to temperature is used in the Penman combination equation. It is calculated simply by evaluating the Clausius-Clapeyron expression (see Section 4.3.5) for SVP at either side of the mean daytime temperature:

$$\Delta_{e_{sat}} =$$
$$611 \left[\exp \left(\frac{17.27(\bar{T}_{day} + 0.5)}{(\bar{T}_{day} + 0.5) + 237.3} \right) - \exp \left(\frac{17.27(\bar{T}_{day} - 0.5)}{(\bar{T}_{day} - 0.5) + 237.3} \right) \right] \tag{4.64}$$

The density of air is also used in the Penman combination equation and varies with temperature. A simple linear equation has been fitted here to tabular data given by Monteith and Unsworth (1990, p. 268). The slope of the line is most accurate at about 15°C:

$$\rho_{air} = 1.292 - 0.0042\,\bar{T}_{day} \tag{4.65}$$

The latent heat of vaporisation of water is another variable used in the Penman combination equation. As with air density, an equation has been fitted from tabular data, this time from Oke (1987, p. 392), with the slope being most accurate at around 15°C. Note that a similar table in Monteith and Unsworth (1990, p. 268) has an error for values calculated at 20°C and above, in addition to minor variations from Oke's table. The equation is:

$$\lambda = 2.501 \times 10^6 - 2.4 \times 10^3\,\bar{T}_{day} \tag{4.66}$$

A final Penman combination variable is the psychrometer constant (also known as the psychrometric constant). Once again, an equation is fitted from a table in Oke (1987, p. 392) with the slope most accurate at about 15°C. Note that, as with the latent heat of vaporisation of water, Monteith and Unsworth's (1990, p. 268) table is erroneous for 20°C and above. The equation is:

$$\gamma = 64.9 + 0.06\,\bar{T}_{day} \tag{4.67}$$

The humidity reduction algorithms below make use of a dimensionless variable, ϵ, which saves some calculation time:

$$\epsilon = \frac{\Delta_{e_{sat}}}{\gamma} \tag{4.68}$$

4.3.8 Precipitation

Precipitation is the only source of water to the model. Daily precipitation at any given location is estimated by scaling daily precipitation data from a base station using a three dimensional spline surface of mean monthly *relative*

precipitation values fitted across the study area as described in Chapter 7. The spline surface data are input to the model as mean monthly precipitation index (MMPI) values for each spatial unit. Thus by dividing the MMPI of the spatial units by the MMPI of the base station, a scaling value for the base station data is obtained. This method is intended to be more accurate than simple linear precipitation/elevation correlations in common use, and is tested in Sections 7.5.3 and 10.2.7. The estimation equation is:

$$q_P = q_{P,stn} \, \frac{MMPI}{MMPI_{stn}} \tag{4.69}$$

Note that the value $q_{P,stn}$ is the reading for today's precipitation which will be taken tomorrow at 9:00 a.m.

Daily precipitation predictions are tested against independent observed data in Section 10.2.7.

4.3.9   Rainfall, snowfall, and interception

Once all preliminary vegetation and climate variables have been calculated, the flux of water begins.

Rain or snow falling on the canopy and understorey are partially intercepted and vaporised or sublimated back into the atmosphere. These processes are limited by a number of factors. Firstly, each vegetation layer can intercept and store water up to a maximum level scaled by the LAI of the vegetation. Excess water falls through the layer to the layer below. Secondly, the amount of stored water which is either vaporised or sublimated back into the atmosphere is limited by potential evaporation, and hence radiation and VPD.

On a given day, all precipitating or stored water is assumed to be liquid or solid depending on whether the mean night-time temperature is above or below zero degrees Celsius (after RHESSys, SLURP, CREAMS, SWRRB, and UBC). Additionally, stored water is assumed to change state if the temperature crosses zero between days. Note that Auer (1974), as cited by Dingman (1994, p. 99), indicated from *c.* 1000 observations that a more appropriate value might be 2.5° C (instantaneous screen temperature), whilst Todini (1996) suggests analysis of site-specific historical data to determine the crossover temperature.

4.3.9.1 Rainfall and its interception by the canopy and understorey

Simulation of rainfall interception is based on the principle of Rutter et al. (1971) whereby interception is controlled by both interception storage capacity and potential evaporation as determined by the Penman combination equation. This approach has been used in physically based models such as SHE, BIOMASS, and DHVM.

In the case where the mean night-time temperature is above zero ($\bar{T}_{night} > 0$), the following sequence of rainfall and rainfall interception processes is implemented. Firstly, precipitation is converted to rainfall and snowfall is set to zero:

$$
\begin{aligned}
q_{rain} &= q_P & (4.70)\\
q_{snow} &= 0 & (4.71)
\end{aligned}
$$

Rainfall, if any, is first added to the canopy interception storage which has a capacity dependent on the LAI of the canopy. Any water exceeding that capacity falls through the canopy:

$$
q_{thru,c,rain} = \max(0, \text{ previous } s_c + q_{rain} - k_{rain}\, LAI_c) \qquad (4.72)
$$

$$
s_c = \text{previous } s_c + q_{rain} - q_{thru,c,rain} \qquad (4.73)
$$

Some or all of the storage may be vaporised according to the Penman combination equation as driven by canopy absorbed net radiation (where this is positive) and reference level VPD. Firstly the *potentially* vaporised amount is calculated (negative net radiation is 'maxed' to zero to prevent dew or frost - which would need to be modelled separately if at all):

$$
q_{vap,pot,c} = dayl \times \frac{\Delta_{e_{sat}} \frac{\max(0, R_{a,c})}{dayl} + c_p\, \rho_{air}\, D_{ref} \frac{1}{r_{aero,c,ref}}}{\lambda\, \rho_w (\Delta_{e_{sat}} + \gamma)} \qquad (4.74)
$$

Then this is limited by the interception storage to yield the actually vaporised amount:

$$q_{vap,c} = \min\left(s_c, q_{vap,pot,c}\right) \tag{4.75}$$

The vaporised amount is removed from the canopy:

$$s_c = \text{previous } s_c - q_{vap,c} \tag{4.76}$$

Next, the amount of radiation used in the vaporisation process is calculated as the total canopy absorbed radiation scaled by the ratio of actual to potentially vaporised rain:

$$R_{vap,c} = \begin{cases} 0 & q_{vap,pot,c} = 0 \\ R_{a,c}\frac{q_{vap,c}}{q_{vap,pot,c}} & \text{otherwise} \end{cases} \tag{4.77}$$

which is removed from the amount remaining for transpiration:

$$R_{tran,c} = \text{initial } R_{tran,c} - R_{vap,c} \tag{4.78}$$

Finally, given that it is raining not snowing, the snow equivalents of all the above quantities should be zero. If there is no precipitation at all, all these quantities should also be zero.

$$q_{thru,c,snow} = 0 \tag{4.79}$$
$$q_{sub,c} = 0 \tag{4.80}$$
$$R_{sub,c} = 0 \tag{4.81}$$

Canopy interception predictions are tested against observed data in Section 10.2.8.

Understorey interception is modelled in the same way as canopy interception except that the input to the understorey is the throughfall from the canopy. The relevant equations are:

$$q_{thru,u,rain} = \max\left(0, \text{ previous } s_u + q_{thru,c,rain} - k_{rain} \, LAI_u\right) \tag{4.82}$$

$$s_u = \text{previous } s_u + q_{thru,c,rain} - q_{thru,u,rain} \tag{4.83}$$

$$q_{vap,pot,u} = dayl \times \frac{\Delta_{e_{sat}}\frac{\max(0,R_{a,u})}{dayl} + c_p\,\rho_{air}\,D_{ref}\frac{1}{r_{aero,c,ref}+r_{aero,u,c}}}{\lambda\,\rho_w(\Delta_{e_{sat}} + \gamma)} \tag{4.84}$$

Note that, in the above equation, reference level VPD is used to drive evaporation of understorey intercepted water through summed resistance expressions for the canopy and understorey. This differs from the processes modelled for transpiration, where a separate, reduced canopy level VPD is calculated. It constitutes an inconsistency in the model which should be addressed at a later stage.

$$q_{vap,u} = \min(s_u, q_{vap,pot,u}) \tag{4.85}$$

$$s_u = \text{previous } s_u - q_{vap,u} \tag{4.86}$$

$$R_{vap,u} = \begin{cases} 0 & q_{vap,pot,u} = 0 \\ R_{a,u}\frac{q_{vap,u}}{q_{vap,pot,u}} & \text{otherwise} \end{cases} \tag{4.87}$$

$$R_{tran,u} = \text{initial } R_{tran,u} - R_{vap,u} \tag{4.88}$$

$$q_{thru,u,snow} = 0 \tag{4.89}$$
$$q_{sub,u} = 0 \tag{4.90}$$
$$R_{sub,u} = 0 \tag{4.91}$$

4.3.9.2 Snowfall and its interception by the canopy and understorey

In the case where the mean night-time temperature is equal to or below zero ($\bar{T}_{night} <= 0$), a sequence of snowfall and snowfall interception processes is

implemented. Night-time temperature is used on the (un-tested) assumption that, because of cooler temperatures at night, winter orographic precipitation is more likely to occur at night. The simulated interception processes are similar to that for rainfall, except that the Penman combination equation is not used. This is because the validity of this equation may be uncertain when applied to sublimation of snow instead of evaporation of liquid water. Instead, radiation alone is used to limit sublimation (instead of both radiation and VPD, as in the combination equation). The maximum sublimatable snow is calculated using the volumetric latent heat of sublimation (2.83×10^9 J m^{-3}, Oke, 1987, p. 392). The relevant equations are:

$$q_{snow} = q_P \tag{4.92}$$
$$q_{rain} = 0 \tag{4.93}$$

$$q_{thru,c,snow} = \max(0, \text{ previous } s_c + q_{snow} - k_{snow} \, LAI_c) \tag{4.94}$$

$$s_c = \text{previous } s_c + q_{snow} - q_{thru,c,snow} \tag{4.95}$$

$$q_{sub,c} = \min \left[s_c, \frac{\max(0, R_{a,c})}{2.83 \times 10^9} \right] \tag{4.96}$$

$$s_c = \text{previous } s_c - q_{sub,c} \tag{4.97}$$

$$R_{sub,c} = q_{sub,c} \, 2.83 \times 10^9 \tag{4.98}$$

$$R_{tran,c} = \text{initial } R_{tran,c} - R_{sub,c} \tag{4.99}$$

$$q_{thru,c,rain} = 0 \tag{4.100}$$
$$q_{vap,c} = 0 \tag{4.101}$$
$$R_{vap,c} = 0 \tag{4.102}$$

$$q_{thru,u,snow} = \max(0, \text{ previous } s_u + q_{thru,c,snow} - k_{snow} \, LAI_u) \qquad (4.103)$$

$$s_u = \text{previous } s_u + q_{thru,c,snow} - q_{thru,u,snow} \qquad (4.104)$$

$$q_{sub,u} = \min \left[s_u, \ \frac{\max(0, R_{a,u})}{2.83 \times 10^9} \right] \qquad (4.105)$$

$$s_u = \text{previous } s_u - q_{sub,u} \qquad (4.106)$$

$$R_{sub,u} = q_{sub,u} \, 2.83 \times 10^9 \qquad (4.107)$$

$$R_{tran,u} = \text{initial } R_{tran,u} - R_{sub,u} \qquad (4.108)$$

$$q_{thru,u,rain} = 0 \qquad (4.109)$$
$$q_{vap,u} = 0 \qquad (4.110)$$
$$R_{vap,u} = 0 \qquad (4.111)$$

4.3.9.3 Total interception

Total interception (matched by vaporisation/sublimation) is calculated for reporting purposes only as:

$$q_{int} = q_{vap,c} + q_{sub,c} + q_{vap,u} + q_{sub,u} \qquad (4.112)$$

4.3.10   Snowpack accumulation and melting

The snowpack is modelled using a simple formulation borrowed directly from RHESSys. The depth of snow is modelled as an equivalent depth of water. There is no layering of snow or concept of snow density. The energy stored within the snowpack is modelled abstractly using a 'degree day' concept (Gray and Prowse, 1993) as used by SRM (Rango, 1992). This is the simpler alternative to a range of physical energy balance approaches (see Engman, 1995). A balance is recorded of the accumulated temperature of the air above the snowpack. Days above zero degrees add to this value, days below subtract from it, in direct proportion to how far above or below zero the temperature is. The degree day value is used to control snow melt, which can only occur if both the air temperature *and* the snowpack degree days are above zero. Two types of snowmelt can occur however, that caused by radiation and that caused by temperature, both of which result in water falling out of the snowpack onto the soil. The details are as follows.

Snow falling through the understorey is accumulated directly onto the snowpack:

$$s_{snow} = \text{previous } s_{snow} + q_{thru,u,snow} \tag{4.113}$$

If a snowpack is present, its degree days are accumulated according to the mean daily temperature. A minimum value, $O_{dd,min}$, is enforced, reflecting an abstract idea that there is a limit to how cold a snowpack can get:

$$O_{dd} = \max(\text{previous } O_{dd} + \bar{T}, O_{dd,min}) \tag{4.114}$$

Once a snowpack is completely melted, the degree day value is reset to zero.

Two kinds of snowpack melting can occur. Melt caused by positive temperatures in both the air and snowpack is modelled using a simple temperature-melt coefficient, $\mu_{snow,T}$, as:

$$q_{melt,T} = \begin{cases} \mu_{snow,T}\,\bar{T} & \bar{T} > 0,\ O_{dd} >= 0 \\ 0 & \text{otherwise} \end{cases} \tag{4.115}$$

Mean daily temperature is used because this kind of melt can occur at all times. Melting caused by radiation will normally occur only during daylight so a mean daylight temperature is used below.

Melting caused by radiation is controlled either by the latent heat of fusion of water at zero degrees (0.334×10^9 J m^{-3}, Oke, 1987, p. 392, used if both air and snowpack are above 0°C), or by the latent heat of vaporisation of water at zero degrees (2.83×10^9 J m^{-3}, used otherwise). If net radiation is below zero, nothing occurs, i.e. no frost or dew is modelled. The equation is:

$$q_{melt,R} = \begin{cases} \frac{\mu_{snow,R} \ R_{a,snow}}{0.334 \times 10^9} & \bar{T}_{day} > 0,\ O_{dd} >= 0 \\ \\ \frac{\mu_{snow,R} \ R_{a,snow}}{2.83 \times 10^9} & \text{otherwise} \end{cases} \tag{4.116}$$

The total snowmelt is the sum of these two, limited by the amount of snow in the snowpack:

$$q_{melt} = \min(q_{melt,T} + q_{melt,R},\ s_{snow}) \tag{4.117}$$

The snowpack is thus reduced by the snowmelt:

$$s_{snow} = \text{previous } s_{snow} - q_{melt} \tag{4.118}$$

4.3.11 Soil water fluxes

Soil water flux begins with the determination of how much water is falling onto the soil, what proportion (areally) of the soil is saturated to the surface, and how close to saturation is the remaining proportion. These three variables determine the amount of saturation excess runoff and baseflow exfiltration that occurs. Water falling on the saturated proportion immediately becomes saturation excess runoff. Water falling on the unsaturated proportion infiltrates into the soil, which may, in turn, saturate completely and cause more saturation excess flow. Baseflow is exfiltrated from the saturated proportion. If the unsaturated zone contains some free water, some of this will flow as recharge to the saturated zone. The infiltration capacity of the soil is assumed to be limited only by the available space in the unsaturated zone.

In principle, the algorithms for soil water flux (saturation excess runoff, recharge, and baseflow) are simple. In practice there are a number of conditions which occur from time to time which require additional complexity in

the model if it is to be robust. The exact nature of these complexities will become clear below.

It should be re-iterated that the saturated zone is modelled as a deficit, not as a conventional store. The variable, s_{sat}, which will be referred to as the 'saturation deficit', is zero when the water table is at the surface and positive when it is below the surface. Strictly speaking, the term 'saturation deficit' is not accurate. The true deficit from saturation deficit would be lower because of water in the unsaturated zone above the water table, which does no affect the value of s_{sat}.

4.3.11.1   Preliminary soil water calculations

Some preliminary calculations are made before key soil water flux occurs.

Recharge occurs at various points in the code. A recharge variable is used to keep track of the total recharge. Here, it is initialised to zero:

$$q_{rech} = 0 \qquad (4.119)$$

Similarly, saturation excess flow occurs at various points in the code and is initially zero:

$$q_{xs} = 0 \qquad (4.120)$$

It is possible during lateral redistribution of water (Section 4.2), that the water table can rise above the surface where it was formerly below the surface, *and* that the unsaturated store will contain water at this time. If this occurs (which is quite rare), the unsaturated store should be drained because, effectively, recharge has occurred. Thus, if the above condition occurs the following assignments are invoked:

$$s_{sat} = \text{previous } s_{sat} - s_{unsat} \qquad (4.121)$$

$$q_{rech} = \text{previous } q_{rech} + s_{unsat} \qquad (4.122)$$

$$s_{unsat} = 0 \tag{4.123}$$

The total water falling on the soil is the sum of understorey throughfall (rain only) and snowpack melt:

$$q_{fall} = q_{thru,u,rain} + q_{melt} \tag{4.124}$$

Finally, we calculate the maximum available volumetric water content, which could alternatively be called the effective porosity. At this point, it should be noted that the saturation deficit and the unsaturated store are measures of the amount of water held within the effectively porous volume. They do not quantify the total water content. For example, when the unsaturated store, s_{unsat}, is zero, residual moisture (that which can never be freed from the soil) remains in the unsaturated zone.

$$\theta_{avail,max} = \theta_{sat} - \theta_{res} \tag{4.125}$$

4.3.11.2 The concept of saturated proportion

For the purposes of saturation excess flow and baseflow generation, a given ESU can be thought of as having a *horizontally* separate saturated 'proportion' and unsaturated 'proportion', either of which may be zero. As shown in Figure 4.3, this is not the same as the modelling of *vertically* separate saturated and unsaturated 'zones'. As the saturation deficit decreases, the saturated zone gets closer to the surface until the point that some part of the ESU is saturated. An ESU is thought of as having a small amount of relief, so that the lower parts will saturate first. As the saturated zone continues to rise, more of the ESU will saturate and the saturated proportion will rise accordingly. The function relating the level of saturation deficit to the saturated proportion is the saturated water distribution function (Equation 3.7), the same function that is used to distribute water amongst a number of ESUs representing a hillslope.

Early versions of the model did not incorporate partial saturation of ESUs. Because of the explicit link between surface saturation and streamflow generation within the model (see below), this lead to undesirable discrete jumps in simulated streamflow as individual ESUs 'turned on and off'.
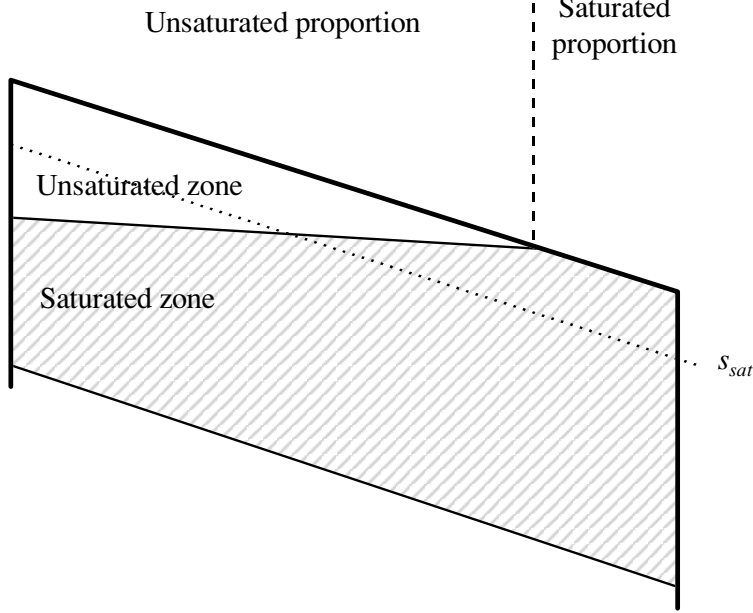
Figure 4.3: The difference between *horizontal* saturated/unsaturated *proportions* of an ESU, and *vertical* saturated/unsaturated *zones* within an ESU.

In simulation of soil evaporation and plant transpiration, the saturated proportion concept does not currently apply and ESUs are regarded as homogenous.

Calculation of the saturated proportion begins with calculation of the saturation deficit at which the ESU *just* becomes partially saturated, $s_{sat,0}$. The Δ_{sat} variable is the nominal slope of the water table relative to the surface slope (calculated with respect to wetness index and not horizontal distance). This can be multiplied by the range of wetness index values occurring within an ESU to give the corresponding range of water table depths. The mean saturation deficit of the ESU, s_{sat}, is assumed to lie in the middle of the range of depths, and so when the shallowest depth in the range is zero and the ESU just becomes partially saturated, s_{sat} will be equal to half of the slope times the range, or $s_{sat,0}$. The range term is supplied as a parameter, $i_{wet,range}$, which is calculated as the range of wetness index values which *actually occur* within the the upper and lower limits of wetness index used to define the extent of the ESU in the first place. Thus the saturation deficit at *just* zero exfiltration/saturation is *initially*:

$$s_{sat,0} = -\Delta_{sat}\,\frac{i_{wet,range}}{2} \tag{4.126}$$

with the negative sign adjusting for the fact that saturation deficits decrease as wetness index values increase.

In practice, the above equation does not work. Upslope ESUs are found to have high wetness index ranges and thus become partially saturated and produce flow even when their mean water table level is very deep. The equation does not take account of mounding of the water table above or below the level prescribed by the distribution function, $s_{sat,mound}$, which clearly alters the slope of the water table relative to the surface. An interim correction is applied until a more reasonable scheme is developed. The correction simply divides wetness index ranges by four, a value chosen by trial and error (this change is reflected in Equation 4.127).

A further, but less significant complication occurs for very small wetness index ranges. Mean water table depth within ESUs tends to align closely with the depth at which saturation just occurs (i.e. s_{sat} is often close to $s_{sat,0}$). ESUs with small wetness index ranges will exhibit water table depths of similarly small magnitude to the depth of water which is able to exfiltrate from the ESU as baseflow in a single time step. This leads to numerical instabilities associated with the sampling of time at discrete, coarse intervals. A further correction is applied where wetness index ranges corrected as above are 'maxed' to 0.1, a value determined by trial and error. The final equation for the saturation deficit at zero exfiltration is thus:

$$s_{sat,0} = -\Delta_{sat} \ \max\left(\frac{i_{wet,range}}{2 \times 4}, \ 0.1\right) \tag{4.127}$$

The above formulation operates satisfactorily but crudely. It should be improved in the future.

Continuing, the saturated proportion of the spatial unit is then the ratio of how far the saturated zone is above the zero level to the zero level itself:

$$p_{sat} = \begin{cases} \max(0, \min(1, \frac{s_{sat,0} - s_{sat}}{s_{sat,0}})) & s_{sat,0} > 0 \\ 1 & s_{sat,0} <= 0, \ s_{sat} <= 0 \\ 0 & s_{sat,0} <= 0, \ s_{sat} > 0 \end{cases} \tag{4.128}$$

with the conditions on $s_{sat,0}$ and s_{sat} being necessary to avoid division by zero in undesirable and unintended situations such as where ESUs have zero or negative wetness index ranges.

Saturated area predictions are tested against observed data in Section 10.5 (in particular, Section 10.5.3).

4.3.11.3 Saturation excess flow

Saturation excess flow occurs at two points in the code. The first is when water falls on the already-saturated proportion of an ESU. The second is when water falling on the unsaturated proportion (which may be the whole unit), causes the saturated area of the unit to increase, although at present, the additional area only produces additional flow if full saturation of the ESU occurs.

As stated above, the first point of saturation excess flow is from water falling onto the already saturated proportion of a spatial unit:

$$q_{xs} = \text{previous } q_{xs} + p_{sat} \, q_{fall} \tag{4.129}$$

The remaining water is added to the unsaturated store:

$$s_{unsat} = \text{previous } s_{unsat} + q_{fall} - q_{xs} \tag{4.130}$$

If this additional water causes the spatial unit to become completely saturated, the following condition is true:

$$- \max(0, s_{sat}) + s_{unsat} > 0 \tag{4.131}$$

and the additional water should be converted to either recharge or further saturation excess flow as follows:

$$
\begin{aligned}
q_{rech} &= \text{previous } q_{rech} + s_{sat} & (4.132) \\
q_{xs} &= \text{previous } q_{xs} + s_{unsat} - s_{sat} & (4.133) \\
s_{sat} &= 0 & (4.134) \\
s_{unsat} &= 0 & (4.135)
\end{aligned}
$$

Additionally, a number of auxiliary soil variables adopt some default values for saturated situations:

$$K_{sat,wt} = K_{sat,surf} \qquad (4.136)$$

$$K_{wt} = K_{sat,wt} \qquad (4.137)$$

$$\theta = 1 \qquad (4.138)$$

$$\Theta = 1 \qquad (4.139)$$

If, on the other hand, the additional water leaves the unsaturated proportion of the spatial unit unsaturated, then further saturation excess flow does not occur, but unsaturated recharge to the saturated zone does.

4.3.11.4 Recharge from the unsaturated zone to the saturated zone

Recharge from the unsaturated zone to the saturated zone is calculated according to the unsaturated vertical hydraulic conductivity of the soil at the depth of the water table. This calculation makes use of the Van Genuchten model of unsaturated conductivity as well as some assumptions about the vertical profile of saturated hydraulic conductivity.

Given a situation where, after infiltration, the spatial unit is not completely saturated, this part of the code assumes that the water table lies at a uniform depth beneath the surface throughout the spatial unit. Thus the saturated proportion concept described above is not employed here. It is uncertain as to whether this inconsistency matters.

The depth of water table is calculated from the saturation deficit and the maximum available volumetric water content (effective porosity):

$$z_{wt} = \frac{\max(0, s_{sat})}{\theta_{avail,max}} \qquad (4.140)$$

Observations of saturated hydraulic conductivity in the study area (5.3.11.4) suggest that a combination constant/exponential function of saturated hydraulic conductivity with depth is appropriate. Thus, the saturated vertical hydraulic conductivity at the water table is estimated as:

$$K_{sat,wt} = K_{sat,min} + (K_{sat,surf} - K_{sat,min}) \exp(-f z_{wt}) \qquad (4.141)$$

The volumetric water content of the unsaturated zone overlying the water table is calculated from the ratio of the content of the unsaturated store to its size, which is given by the saturation deficit (of the saturated zone, not the combined zones):

$$\theta = \frac{s_{unsat}}{s_{sat}}\theta_{avail,max} + \theta_{res} \tag{4.142}$$

This value can be normalised with respect to the maximum available volumetric water content giving:

$$\Theta = \frac{\theta - \theta_{res}}{\theta_{avail,max}} \tag{4.143}$$

Given the saturated hydraulic conductivity at the water table, and the normalised volumetric water content of the soil immediately above the water table (and throughout the unsaturated zone), a number of models can be employed to predict unsaturated hydraulic conductivity at the water table (Rawls et al., 1993). Based on fits to preliminary soil water tension data from the study area made by Campbell (in prep.), the Van Genuchten model (Rawls et al., 1993) was chosen:

$$K_{wt} = K_{sat,wt} \sqrt{\Theta} \left[1 - \left(1 - \Theta^{\frac{n}{n-1}}\right)^{1-\frac{1}{n}}\right]^2 \tag{4.144}$$

This value is measured in units of water flux (m day^{-1}) and so directly gives further recharge from the unsaturated zone to the saturated zone, as well as the corresponding adjustments to the unsaturated store and saturation deficit:

$$
\begin{aligned}
q_{rech} &= \text{previous } q_{rech} + \min(K_{wt}, s_{unsat}) & (4.145) \\
s_{sat} &= \text{previous } s_{sat} - \min(K_{wt}, s_{unsat}) & (4.146) \\
s_{unsat} &= \text{previous } s_{unsat} - \min(K_{wt}, \text{previous } s_{unsat}) & (4.147)
\end{aligned}
$$

Soil moisture (s_{unsat}) predictions are tested against observed data in Section 10.2.11.2.

4.3.11.5 Infiltration

If the saturated proportion (above) was less than one, infiltration may have occurred during the processes described above. The amount of infiltration is calculated for reporting purposes only as:

$$q_{inf} = q_{fall} - q_{xs} \tag{4.148}$$

4.3.11.6 Baseflow

Regardless of saturation excess flow and recharge processes, if the saturated proportion is greater than zero, some baseflow is exfiltrated from the soil. Currently, a constant hydraulic gradient is assumed to operate at the surface and thus, according to Darcy's Law (e.g. Shaw, 1994), baseflow is simply the product of this gradient and the saturated hydraulic conductivity at the surface:

$$q_{base} = p_{sat} \, K_{sat,surf} \, \Delta_z \tag{4.149}$$

With the saturation deficit being adjusted accordingly:

$$s_{sat} = \text{previous } s_{sat} + q_{base} \tag{4.150}$$

4.3.11.7 Total flow

Total flow from the spatial unit is then summed for reporting purposes only as:

$$q_{flow} = q_{xs} + q_{base} \tag{4.151}$$

4.3.12 Transpiration and soil evaporation

Transpiration and evaporation are calculated for canopy, understorey, and soil layers separately using the Penman-Monteith equation (Monteith, 1965).

The meteorological parts of the equation are driven primarily by humidity and net radiation. Net radiation is calculated separately for each layer through a Beer's Law formulation as described in Section 4.3.6. Humidity (specified as vapor pressure deficit, VPD) at a reference level within the atmospheric boundary layer is estimated from temperature data in Section 4.3.5. VPD at the level of each layer is reduced according to evapotranspiration conditions. This is an integral part of the calculations below. For the canopy and understorey, transpiration is dependent on leaf conductances which are calculated to be dependent on soil water, VPD, solar radiation, and temperature using the model of Running and Coughlan (1988). Soil evaporation is controlled by a soil resistance term which is dependent on soil water according to Choudhury and Monteith (1988).

There are numerous considerations regarding this system which remain open. In particular, there is considerable uncertainty as to what factors control the leaf conductance of a given species, and in what way. The Topog model (Vertessy et al., 1996) uses a quite different formulation of leaf conductance based on Ball et al. (1987) and Leuning (1995). A similar formulation may be adopted within Macaque in the future. However, more detailed field investigations and examination of the literature are required.

It is also an open question whether to use a Penman-Monteith approach at all. Sufficient feedback may be present within the transpiration/conductance system of large eucalypt forests that conductance is always such that transpiration occurs at some potential, or at least solely radiation-determined rate. In which case schemes based on potential evaporation using equations without conductance or humidity terms may be appropriate (e.g. Priestley and Taylor, 1972; Morton, 1965, 1969, 1975, 1983). The Penman-Monteith approach is however the paradigm, being used in such models as SHE, DHVM, RHESSys, Topog, CLATTER, and the model of Teixeira Filho et al. (1996). It is not the place of the present work to defy this paradigm.

4.3.12.1 VPD reduction within the boundary layer

Experience with the Topog model suggests that the simulation of tall forest evapotranspiration processes can be particularly sensitive to the representation of VPD (R. Vertessy and R. Silberstein, pers. comm., CSIRO Land and Water, Canberra). This is supported by physical observations of the dependence of leaf conductance on humidity in *Eucalyptus maculata* forest (Wong and Dunin, 1987). Particular attention is paid here to the reduction of VPD from relatively high (dry) values at the reference level above the

canopy to lower (humid) values within the evapotranspiring layers. Specifically, understorey transpiration is lower than it would be otherwise relative to canopy transpiration because of the humid atmosphere that the canopy imposes above the understorey. Jarvis and McNaughton (1986), in a study of the relative control that stomatal conductance has on transpiration at different scales, present a means of estimating the VPD within a transpiring layer. The VPD so calculated may be used to drive the transpiration of the immediately lower layer, with an appropriate aerodynamic resistance between the two layers. This approach of propagating successively decreasing VPDs down through the vegetation was developed within WAVES (Hatton et al., 1995) and Topog (Vertessy et al., 1996) and improved within Macaque with the assistance of R. Silberstein (CSIRO Land and Water, Canberra).

There is some circularity in the system. Canopy conductance is dependent on canopy VPD, and vice versa. Additionally, understorey transpiration is dependent on canopy VPD, but also influences canopy VPD, and so too for soil evaporation. These inter-dependencies can be resolved either by analytical solution of the relevant simultaneous equations, by iterative solution of the equations until equilibrium is reached, or by treating the results of the first iteration as a sufficient prediction of evapotranspiration and humidity conditions. Ideally, the analytical solution would be used, owing to its accuracy and speed. The extent to which it is possible remains to be seen. The iterative solution, would also be accurate but requires some additional algorithmic complexity. The first-guess solution is algorithmically simplest, and probably sufficiently accurate at this stage given the uncertainty in providing accurate reference level VPD inputs, and the uncertainty in the conductance model. Presently, both Topog and Macaque adopt the first-guess scheme.

Within both Topog and Macaque, leaf conductance is calculated first using reference level VPD, and then canopy VPD is calculated in terms of both reference level VPD and canopy conductance. This ordering is logical because the uncertainty in calculating conductance in terms of reference level VPD instead of canopy VPD is likely to be less than the error in calculating canopy VPD in terms of some arbitrary conductance value. Further, the conductance models used in both Topog and Macaque are somewhat less well constrained than the Penman-Monteith model itself. It is simple to adjust the VPD parameter within either conductance model to compensate for an inaccurate VPD input.

An iterative solution to simultaneous calculation of canopy VPD and canopy conductance has been investigated briefly. A simple spreadsheet analysis (not shown) revealed that equilibrium is reached after one or two iterations and

that, under typical conditions, canopy conductance calculated on the first iteration can be in error by about 20%, and VPD by a few percent. Future modifications to Macaque may implement this iterative scheme, which may prove useful in ensuring that an appropriate balance of stomatal and meteorological control of evapotranspiration is obtained (Jarvis and McNaughton, 1986). For now, a 20% error is acceptable when compared with the uncertainty surrounding the overall conductance model.

A corresponding iterative solution involving interactions between all three evapotranspiring layers has not been addressed. The importance of such a solution should be investigated in the future.

In the detailed description of transpiration that follows, each layer's conductance is calculated in terms of the VPD of the layer above (instead of the VPD of its own atmosphere).

4.3.12.2 Canopy transpiration

Transpiration calculations are made separately for each vegetation layer. Firstly, a number of calculations estimate the water available to the roots of the vegetation. This is used to estimate pre-dawn leaf water potential (LWP), which is a primary control on leaf conductance. Subsequent leaf conductance calculations include modifications according to temperature, humidity, and radiation. In modelling within the study area to date, water has not been found to be a limiting factor, and temperature and radiation influences on conductance have been de-sensitised. Thus humidity is the primary control which has been examined. Canopy conductance is calculated as the product of leaf conductance and LAI. This value is used as a control on both transpiration (via Penman-Monteith) and the reduction of VPD down through the canopy (according to Jarvis and McNaughton, 1986), which in turn controls the transpiration of lower layers. Then, the Penman-Monteith equation is used to combine the above variables and calculate transpiration. Finally, a novel algorithm determines from which soil zones the transpiration should be drawn. The details follow.

Soil water availability

Water-limited transpiration is likely to be only a small component of the overall transpiration of the study area, which is generally very wet. Therefore the representation of soil water availability is relatively crude in comparison with models which take factors such as soil water tension into account (e.g.

Topog and COUPLE).

The water available to canopy roots is calculated as the amount of water in the depth of soil which contains canopy roots. This is calculated separately for the saturated and unsaturated zones. Firstly, the water table depth and volumetric water content of the soil must be recalculated because they may have changed since Section 4.3.11.4:

$$z_{wt} = \frac{\max(0, s_{sat})}{\theta_{avail,max}} \tag{4.152}$$

$$\theta = \frac{s_{unsat}}{s_{sat}} \theta_{avail,max} + \theta_{res} \tag{4.153}$$

The saturated water available to canopy roots is then the amount of water in the saturated zone which is penetrated by canopy roots:

$$s_{sat,c} = \begin{cases} \theta_{avail,max}(z_{c,max} - z_{wt}) & z_{c,max} > z_{wt} \\ 0 & \text{otherwise} \end{cases} \tag{4.154}$$

and the unsaturated water available to canopy roots is the free water in the unsaturated zone up to the depth of the water table or the canopy roots, whichever is shallower:

$$s_{unsat,c} = \min(z_{c,max}, z_{wt}) (\theta - \theta_{res}) \tag{4.155}$$

The total available to canopy roots is thus:

$$s_{tot,c} = s_{sat,c} + s_{unsat,c} \tag{4.156}$$

and the maximum that this value could attain is:

$$s_{tot,c,max} = z_{c,max} \, \theta_{avail,max} \tag{4.157}$$

Leaf water potential (LWP)

Leaf water potential can be thought of as a measure of the availability of water within the leaves of a plant (Salisbury and Ross, 1992, Ch. 3). In some species, *pre-dawn* LWP (i.e. the maximum daily value, usually attained just before dawn) is a control on daily potential maximum leaf conductance, with actual daytime values often being un-correlated (Körner, 1994). Hydrological models generally implement pre-dawn LWP as a (possibly species specific) function of soil water status. But additional influences are clearly operative, such as root depth (Crombie et al., 1988) and tree height (Connor et al., 1977). The above variables pertaining to the availability of soil water enable canopy pre-dawn LWP to be estimated using an algorithm borrowed from RHESSys which, in turn, originates from FOREST-BGC. The estimation involves a simple scaling of LWP according to relative soil water availability (the ratio between available soil water and maximum available soil water), and truncation by specified minimum (stomatal closure) and maximum values. The algorithm is flawed in that it takes no account of the height of the vegetation, which clearly affects LWP (Connor et al., 1977; Salisbury and Ross, 1992, p. 111). However, given the uncertainty surrounding the possible variation in stomatal response to LWP at differing heights (Connor et al., 1977), the algorithm is retained intact for the time being. A slope parameter, $\Delta_{\psi,l}$, is included, as is an adjustment by a factor of two if the soil temperature is at or below zero.

$$\psi_{cl} =
\begin{cases}
\max\Big[\psi_{cl.close}, \\
\quad \min\Big(\psi_{cl,max}, \Delta_{\psi,l}\dfrac{s_{tot,c,max}}{s_{tot,c}}\Big) \times
\begin{Bmatrix}
1 & T_{soil} > 0 \\
2 & T_{soil} <= 0
\end{Bmatrix}\Big] & s_{tot,c} > 0 \\
\psi_{cl,close} & \text{otherwise}
\end{cases}$$

$$(4.158)$$

Note that the above equation prohibits ψ_{cl} from being less than $\psi_{cl,close}$ which is not strictly appropriate because there is no reason to expect that LWP itself should depend upon the way in which leaves respond to changes in LWP. However, this has no functional effect because the canopy conductance model (below) is not sensitive to values of ψ_{cl} below the closure value.

Canopy leaf conductance and canopy conductance

At least three classes of canopy conductance model have emerged in the literature. These could be termed: *successive*, *product*, and *linked* models respectively. Each implements a different way of determining leaf conductance in terms of factors such as LWP, temperature, humidity, and radiation.

The *successive* method sets an initial conductance in terms of one variable (e.g. LWP), then modifies that value according to the influence of another variable (e.g. air temperature), and so on for any other desired variables (e.g. VPD, radiation). The result is usually successive reduction from the prescribed maximum leaf conductance according to how far each controlling variable deviates from its optimal value. The method has been used in FOREST-BGC and its family of related models (Running and Hunt, 1993), RHESSys (which inherited it from FOREST-BGC), as well as early versions of BIOMASS (McMurtie et al., 1990a; Leuning et al., 1991). The method is limited by the difficulty of de-convoluting the successive modification procedure in order to determine the sensitivity of each of the variables, and whether or not this is independent of the order in which the modifications are applied.

The *product* method is conceptually more elegant. Simple optimality functions (usually ranging from zero to one) are formed for each controlling variable, and then all the functions are multiplied together to form a single optimality value which is used to scale the prescribed maximum leaf conductance. Clearly, each controlling variable has equal opportunity to limit conductance and the manner in which this influence is applied is conveniently visualised by examining the individual optimality curves. The method is adopted within the global land surface schemes BATS and SiB, as well as the conifer ET model of Stewart (1988).

The *linked* method is a more recent derivative of combined forest growth and water balance models such as recent versions of Topog (Vertessy et al., 1996) and BIOMASS (McMurtie et al., 1992a, b). It involves calculating rates of CO_2 assimilation using various empirical models of radiation and respiration influence. Canopy conductance is then *linked* to the CO_2 assimilation value with a further empirical equation that includes the influence of humidity and CO_2 concentration (Ball et al., 1987).

Various publications provide measured or inferred curves relating either maximum, potential, or actual leaf conductance to variables such as LWP, VPD, radiation, soil temperature, and air temperature (Körner, 1994; Hookey et al., 1987; Dingman, 1994). Such curves are species specific and are of only

indicative use in regions such as the study area where responses for the appropriate species have been only partially examined. They are also dependent on the time scales over which conductance is to be quantified (Körner, 1994).

In terms of the ability to simulate the response of leaf conductance to environmental variables, the three methods *may* be equivalent, which leaves the choice of method to be based on practical considerations. The linked method is only suitable in situations where forest growth is being modelled. Of the remaining two, the product method is more convenient and more user-friendly than the successive method. However, Macaque uses the successive method due to inheritance from RHESSys and FOREST-BGC. The adopted algorithm starts by calculating an initial canopy leaf conductance as a function of canopy LWP. This value is then modified three times in succession according to temperature, canopy VPD, and canopy absorbed solar radiation respectively. All of the calculations involved are simple linear scalings between specified limits according to the relevant controlling variable. A scaling parameter is involved in each case.

The initial canopy leaf conductance, as set by canopy LWP, is:

$$g_{cl,1} = \max\left[g_{cl,min},\ g_{cl,max}\left(1 - \frac{\psi_{cl} - \psi_{cl,max}}{\psi_{cl,close} - \psi_{cl,max}}\right)\right] \qquad (4.159)$$

This implies a linear relationship, which, judging by leaf conductance/LWP curves given for a variety of eucalypts by Hookey et al. (1987, Fig. 6), is not too great a distortion of reality. Within the BIOMASS model, Leuning et al. (1991) converted Hookey et al's data into a simple truncated ramp expression which might be adopted in a future version of Macaque.

The initial conductance is modified by minimum temperature to give the second canopy leaf conductance:

$$g_{cl,2} = \max\left[g_{cl,min},\ \begin{cases} g_{cl,1} + \Delta_{g,T}T_{min} & T_{min} < 0 \\ g_{cl,1}(1 + \Delta_{f,T}(T_{min} - 10)) & \text{otherwise} \end{cases}\right] \qquad (4.160)$$

Note that two different forms of slope parameter are used in the above equation. The equation used under freezing temperatures uses a slope of *absolute* leaf conductance versus temperature, $\Delta_{g,T}$. The equation used under non-freezing temperatures uses a *relative* leaf conductance slope, $\Delta_{f,T}$. This is a rather peculiar legacy of the RHESSys algorithm upon which the present code is based. It will probably be simplified in a future re-specification of

the leaf conductance algorithms used by Macaque. As discussed in Section 5.3.12.3, a non-linear relationship might also be more appropriate in future versions.

A third value modifies the second according to the VPD at reference level and a scaling parameter, $\Delta_{f,cl,D}$. As discussed in Section 4.3.12.1, canopy level VPD would be used ideally, but a circularity prevents this:

$$g_{cl,3} = \max[g_{cl,min}, \, g_{cl,2}(1 + \Delta_{f,cl,D} \, D_{ref})] \tag{4.161}$$

The final canopy leaf conductance includes a modification according to canopy absorbed solar radiation:

$$g_{cl} = g_{cl,3} \times \begin{cases} \min\left(1, \frac{\frac{S_{a,c}}{LAI_c}}{S_{thresh,c}}\right) & S_{thresh,c} > 0 \\ 1 & \text{otherwise} \end{cases} \tag{4.162}$$

The condition on $S_{thresh,c}$ is included to avoid divisions by zero.

Canopy conductance is leaf conductance multiplied by LAI (Singh and Sceicz, 1980; Dingman, 1994; Dickinson et al., 1991), further multiplied by two for symmetrical amphistomatous leaves:

$$g_c = LAI_c \, g_{cl} \times \begin{cases} 2 & amphistomatous(V_c) \\ 1 & \text{otherwise} \end{cases} \tag{4.163}$$

where $amphistomatous(V_c)$ is true for species (V_c) with stomata distributed equally on both sides of leaves.

Penman-Monteith

The transpiration rate (in m s^{-1}) for the canopy as predicted by the Penman-Monteith combination equation (Monteith, 1965) is then:

$$E_c = \frac{\Delta_{e_{sat}} \frac{\max(0, R_{tran,c})}{dayl} + c_p \, \rho_{air} \, D_{ref} \frac{1}{r_{aero,c,ref}}}{\lambda \, \rho_w (\Delta_{e_{sat}} + \gamma \, (1 + \frac{1}{r_{aero,c,ref} \, g_c}))} \tag{4.164}$$

Note that radiation is forced to be positive or zero to obviate the uncertain validity of the Penman-Monteith equation when net radiation is negative, i.e. the balance of longwave radiation *upwards* for the canopy exceeds the absorbed solar radiation which is available for transpiration (after possible use for evaporation/sublimation of intercepted precipitation).

Integrated over the daylight hours this gives the day's canopy transpiration as:

$$q_{tran,c} = E_c \, dayl \qquad (4.165)$$

Of course, most of the quantities calculated above as influencing this value are not constant during the daylight hours. Indeed all values are effective daylight means differing from instantaneous or maximum values as a result of temporal scaling. The effect of this scaling was not investigated. In one sense, there should be few undesirable consequences because the parameters controlling transpiration response are quantified empirically using daily data. On the other hand, the non-linearity of both the Penman-Monteith equation and the associated equations for canopy conductance does not guarantee that the behaviour of instantaneous transpiration response to environmental controls will be preserved following temporal aggregation to the daily scale, even if the parameters are scaled to be 'effective' daily parameters. The issue left as another source of uncertainty in an already imperfect representation of canopy conductance and transpiration.

Canopy transpiration predictions are tested against observed data in Section 10.2.10.

Soil water extraction

It is not immediately obvious from which parts of the soil water system to extract the calculated canopy transpiration. It was decided to bias the relative proportions of transpiration from the saturated and unsaturated zones according to two influences: the relative availability of water from the two zones, and a parameter quantifying the extent to which the transpiring species is phreatic (able to draw water from the saturated zone). This can be thought of as a nominal proportion of water to be drawn from the saturated zone. The biasing system quantifies the two influences and multiplies them together, giving weights for saturated zone and unsaturated zone transpiration. The respective weights are then divided by their sum and multiplied by total transpiration to give the actual transpiration drawn from each zone.

Thus, initially, the two influences are quantified and multiplied giving a 'weighted saturated zone canopy transpiration factor' and a 'weighted *un*saturated zone canopy transpiration factor':

$$\omega_{c,sat} = p_{c,sat} \frac{s_{sat,c}}{s_{tot,c}} \qquad (4.166)$$

$$\omega_{c,unsat} = (1 - p_{c,sat}) \frac{s_{unsat,c}}{s_{tot,c}} \qquad (4.167)$$

where the first term in each equation is the nominal proportion to which the respective zone should be used, and the second term gives the relative availability of water from that zone.

The actual canopy transpiration from each zone is then the total canopy transpiration multiplied by the weight for the zone divided by the sum of weights:

$$q_{tran,c,sat} = q_{tran,c} \frac{\omega_{c,sat}}{\omega_{c,sat} + \omega_{c,unsat}} \qquad (4.168)$$

$$q_{tran,c,unsat} = q_{tran,c} \frac{\omega_{c,unsat}}{\omega_{c,sat} + \omega_{c,unsat}}$$

$$= q_{tran,c} - q_{tran,c,sat} \qquad (4.169)$$

These fluxes are then applied to their respective store/deficit:

$$s_{sat} = \text{previous } s_{sat} + q_{tran,c,sat} \qquad (4.170)$$

$$s_{unsat} = \text{previous } s_{unsat} - q_{tran,c,unsat} \qquad (4.171)$$

Finally, checks are made as to whether the calculated fluxes are too large. If canopy transpiration from the saturated zone is larger than the water available from this zone, an error is reported. If canopy transpiration from the unsaturated zone causes the unsaturated zone to become negative, the offending amount is added back to the store, and removed from the accounted transpiration flux.

In future, an alternative to this scheme could be employed making use of the soil water tension information represented within the sub-model of unsaturated hydraulic conductivity. The operative notion being that water is extracted from parts of the soil in inverse proportion to the tension with which it is held within the soil. This could eliminate the $p_{c,sat}$ parameter and its counterpart for understorey transpiration, $p_{u,sat}$.

VPD reduction

As described in Section 4.3.12.1, canopy transpiration causes a drop in VPD within the canopy layer relative to the above-canopy reference level. The canopy VPD is used to drive understorey transpiration and is calculated according to Jarvis and McNaughton (1986). Firstly, an equilibrium VPD is calculated assuming an infinite degree of aerodynamic de-coupling between the canopy and the reference level:

$$D_{eq,c} = \frac{\Delta_{e_{sat}} \frac{\max(0, R_{tran,c})}{dayl}}{(\epsilon + 1) \, c_p \, g_c \, \rho_w}$$

(4.172)

The degree to which the canopy and the reference level are *actually* aerodynamically de-coupled is then calculated:

$$\Omega_{ref,c} = \frac{\epsilon + 1}{\epsilon + 1 + \frac{1}{r_{aero,c,ref} \, g_c}}$$

(4.173)

These are linked to give the canopy level VPD:

$$D_c = \Omega_{ref,c} \, D_{eq,c} + (1 - \Omega_{ref,c}) \, D_{ref}$$

(4.174)

4.3.12.3   Understorey transpiration

Understorey transpiration is calculated in the same manner as canopy transpiration. Whereas canopy transpiration is driven by VPD at the reference level, understorey transpiration is driven by canopy VPD. Additionally, the aerodynamic component of the resistance to water vapor transfer for the understorey is expressed as a resistance between the understorey and the canopy. Whilst canopy transpiration influences understorey transpiration via the reduction of VPD, the reverse is not modelled. Additional VPD reduction in the canopy is likely to be associated with understorey transpiration. The extent to which this is so has not been investigated here. Because canopy vegetation is much better able to transpire more than understorey vegetation, a downward propagation of VPD reduction, as modelled, is most likely to be suitable.

In the following sections, equations leading to understorey transpiration are generally presented without accompanying descriptions, which are as for canopy transpiration. Comments are included where necessary.

Soil water availability

Water table depth and volumetric water content are calculated here for the third time:

$$z_{wt} = \frac{\max(0, s_{sat})}{\theta_{avail,max}} \tag{4.175}$$

$$\theta = \frac{s_{unsat}}{s_{sat}}\theta_{avail,max} + \theta_{res} \tag{4.176}$$

$$s_{sat,u} = \begin{cases} \theta_{avail,max}(z_{u,max} - z_{wt}) & z_{u,max} > z_{wt} \\ 0 & \text{otherwise} \end{cases} \tag{4.177}$$

$$s_{unsat,u} = \min(z_{u,max}, z_{wt})(\theta - \theta_{res}) \tag{4.178}$$

$$s_{tot,u} = s_{sat,u} + s_{unsat,u} \tag{4.179}$$

$$s_{tot,u,max} = z_{u,max}\,\theta_{avail,max} \tag{4.180}$$

$$\psi_{ul} =$$
$$\begin{cases} \max(\psi_{ul.close}, \min(\psi_{ul,max}, \Delta_{\psi,l}\frac{s_{tot,u,max}}{s_{tot,u}}) \times \left\{ \begin{array}{ll} 1 & T_{soil} > 0 \\ 2 & T_{soil} <= 0 \end{array} \right\}) & s_{tot,u} > 0 \\ \psi_{ul,close} & \text{otherwise} \end{cases} \tag{4.181}$$

Canopy leaf conductance and canopy conductance

$$g_{ul,1} = \max\left[g_{ul,min}, \ g_{ul,max}\left(1 - \frac{\psi_{ul} - \psi_{ul,max}}{\psi_{ul,close} - \psi_{ul,max}}\right) \right] \tag{4.182}$$

$$g_{ul,2} = \max\left[g_{ul,min}, \begin{cases} g_{ul,1} + \Delta_{g,T}T_{min} & T_{min} < 0 \\ g_{ul,1}(1 + \Delta_{f,T}(T_{min} - 10)) & \text{otherwise} \end{cases}\right] \quad (4.183)$$

VPD at canopy level is used here. Ideally, VPD at understorey level would be used.

$$g_{ul,3} = \max[g_{ul,min}, \ g_{ul,2}(1 + \Delta_{f,ul,D} \ D_c)] \quad (4.184)$$

$$g_{ul} = g_{ul,3} \times \begin{cases} \min\left(1, \frac{\frac{S_{a,u}}{LAI_u}}{S_{thresh,u}}\right) & S_{thresh,u} > 0 \\ 1 & \text{otherwise} \end{cases} \quad (4.185)$$

$$g_u = LAI_u \ g_{ul} \times \begin{cases} 2 & amphistomatous(V_u) \\ 1 & \text{otherwise} \end{cases} \quad (4.186)$$

Penman-Monteith

$$E_u = \frac{\Delta_{e_{sat}}\frac{\max(0,R_{tran,u})}{dayl} + c_p \ \rho_{air} \ D_c\frac{1}{r_{aero,u,c}}}{\lambda \ \rho_w(\Delta_{e_{sat}} + \gamma \ (1 + \frac{1}{r_{aero,u,c} \ g_u}))} \quad (4.187)$$

$$q_{tran,u} = E_u \ dayl \quad (4.188)$$

Soil water extraction

$$\omega_{u,sat} = p_{u,sat} \ \frac{s_{sat,u}}{s_{tot,u}} \quad (4.189)$$

$$\omega_{u,unsat} = (1 - p_{u,sat}) \ \frac{s_{unsat,u}}{s_{tot,u}} \quad (4.190)$$

$$q_{tran,u,sat} = q_{tran,u} \ \frac{\omega_{u,sat}}{\omega_{u,sat} + \omega_{u,unsat}} \quad (4.191)$$

$$q_{tran,u,unsat} = q_{tran,u} \ \frac{\omega_{u,unsat}}{\omega_{u,sat} + \omega_{u,unsat}}$$

$$= q_{tran,u} - q_{tran,u,sat} \quad (4.192)$$

$$s_{sat} \quad = \quad \text{previous } s_{sat} + q_{tran,u,sat} \tag{4.193}$$

$$s_{unsat} \quad = \quad \text{previous } s_{unsat} - q_{tran,u,unsat} \tag{4.194}$$

VPD reduction

VPD reduction within the understorey layer is calculated in order that understorey VPD may be used to calculate soil evaporation. The de-coupling which is calculated is between the canopy and the understorey.

$$D_{eq,u} = \frac{\Delta_{e_{sat}} \frac{\max(0, R_{tran,u})}{dayl}}{(\epsilon + 1)\, c_p\, g_u\, \rho_w} \tag{4.195}$$

$$\Omega_{c,u} = \frac{\epsilon + 1}{\epsilon + 1 + \frac{1}{r_{aero,u,c}\, g_u}} \tag{4.196}$$

$$D_u = \Omega_{c,u}\, D_{eq,u} + (1 - \Omega_{c,u})\, D_c \tag{4.197}$$

4.3.12.4 Soil evaporation

Soil evaporation is calculated using the Penman-Monteith equation, as for canopy and understorey transpiration, combined with a modification of Choudhury and Monteith's (1988) expression of soil resistance. The modification relates to the method of determining water availability, the modelling of the soil surface as the evaporating layer, and the extraction of water from the soil. As with the relation between understorey and canopy, soil evaporation will influence the transpiration of overlying layers, but this has not been modelled. Rather, a downward communication of VPD levels is implemented as with the understorey and canopy. The VPD of the understorey layer drives the soil evaporation, and the associated aerodynamic resistance to water vapor transfer is expressed between the soil and the understorey.

Soil water availability

Soil water availability is determined as a first step towards determining the depth of air dry soil (required by the Choudhury and Monteith (1988) model) and the soil resistance to water vapor transfer.

Water table depth and volumetric water content are calculated here for the fourth time:

$$z_{wt} = \frac{\max(0, s_{sat})}{\theta_{avail,max}} \quad (4.198)$$

$$\theta = \frac{s_{unsat}}{s_{sat}} \theta_{avail,max} + \theta_{res} \quad (4.199)$$

To determine the soil water available for soil surface evaporation, a nominal 'evaporation depth', $z_{s,max}$ is specified. This is analogous to the rooting depths expressed for the canopy and understorey. Saturated, unsaturated, and total water availability are calculated within this depth as for the canopy and understorey routines:

$$s_{sat,s} = \begin{cases} \theta_{avail,max}(z_{s,max} - z_{wt}) & z_{s,max} > z_{wt} \\ 0 & \text{otherwise} \end{cases} \quad (4.200)$$

$$s_{unsat,s} = \min(z_{s,max}, z_{wt})(\theta - \theta_{res}) \quad (4.201)$$

$$s_{tot,s} = s_{sat,s} + s_{unsat,s} \quad (4.202)$$

$$s_{tot,s,max} = z_{s,max}\,\theta_{avail,max} \quad (4.203)$$

Soil resistance

Choudhury and Monteith (1988) give a model for soil resistance which is primarily controlled by a 'depth of air dry soil' term. Their model assumes an air dry ($\theta = \theta_{res}$) soil overlying a water table, and the depth to this water table is the depth of the air dry layer. Here, a partially saturated soil overlying a water table is modelled, and so some modification is necessary.

The effective depth of the air dry layer of soil is estimated as the nominal evaporation depth used above, scaled by the relative availability of water within this depth:

$$z_{s,eff} = \begin{cases} z_{s,max}\left(1 - \frac{s_{tot,s}}{s_{tot,s,max}}\right) & s_{tot,s} > 0 \\ \frac{s_{sat}}{\theta_{avail,max}} & \text{otherwise} \end{cases} \quad (4.204)$$

Note the condition where there is no water within the evaporation depth, which occurs where the unsaturated store is dry and the water table is not shallow. The depth of the air dry layer is set to the depth of the water table in this case.

The soil resistance is then calculated according to Choudhury and Monteith (1988):

$$r_s = \frac{\tau \, z_{s,eff}}{\theta_{avail,max} \, d_v} \quad (4.205)$$

where d_v, the molecular diffusion coefficient for water vapor, is taken from Monteith and Unsworth (1990, p. 21) as:

$$d_v = 21.2 \times 10^{-6}(1 + 0.007 \, T_s) \quad (4.206)$$

This estimation procedure is not ideal. In practice, the evaporation depth must be set to a few centimetres or less in order to generate significant soil evaporation, but it is likely that the true evaporating layer extends deeper than this. The procedure is under review, and may be changed in future to a simpler conceptual model, such as that of Schaap and Bouten (1997), which is more in keeping with our limited physical understanding of soil evaporation from the forest floor.

Penman-Monteith

The Penman-Monteith equation is used to calculate the soil evaporation rate as for the canopy and understorey. A check is made for zero available water, which occurs according to the condition described for Equation 4.204. It may be more realistic to omit this check and allow soil evaporation from deeper than the nominal evaporation depth if the soil above this depth is dry. This possibility is left for future development.

$$E_s = \begin{cases} \frac{\Delta_{e_{sat}} \frac{\max(0,Ra,s)}{dayl} + c_p \, \rho_{air} \, D_u \frac{1}{r_{aero,s,u}}}{\lambda \, \rho_w (\Delta_{e_{sat}} + \gamma \, (1 + \frac{r_s}{r_{aero,s,u}}))} & s_{tot,s} > 0 \\ 0 & \text{otherwise} \end{cases} \quad (4.207)$$

$$q_{evap} = E_s \, dayl \qquad (4.208)$$

Soil water extraction

Water for soil evaporation is extracted from the soil in a different way to the understorey and canopy. Water is extracted preferentially from the unsaturated zone, and then from the saturated zone if the unsaturated store becomes dry:

$$q_{evap,unsat} = \min(s_{unsat}, \, q_{evap}) \qquad (4.209)$$
$$q_{evap,sat} = q_{evap} - q_{evap,unsat} \qquad (4.210)$$

$$s_{unsat} = \text{previous } s_{unsat} - q_{evap,unsat} \qquad (4.211)$$
$$s_{sat} = \text{previous } s_{sat} - q_{evap,sat} \qquad (4.212)$$

It is not necessary to check whether these fluxes are too large. The flux from the unsaturated store cannot exceed the size of the unsaturated store by definition. The flux from the saturated zone simply increases the saturation deficit and is unlimited. The flux could take the water table below the nominal evaporation depth, but this is not considered a problem.

VPD reduction

VPD reduction at the soil surface is calculated for validation purposes. The quantity is not used by other model processes, but is easily (although rarely) measured and included for convenience. De-coupling is calculated between the understorey and the soil.

$$D_{eq,s} = \begin{cases} \dfrac{\Delta_{esat} \frac{\max(0, R_{a,s})}{dayl} r_s}{(\epsilon+1) \, c_p \, \rho_w} & r_s > 0 \\ 0 & \text{otherwise} \end{cases} \qquad (4.213)$$

$$\Omega_{u,s} = \frac{\epsilon + 1}{\epsilon + 1 + \frac{r_s}{r_{aero,s,u}}} \qquad (4.214)$$

$$D_s = \Omega_{u,s} \, D_{eq,s} + (1 - \Omega_{u,s}) \, D_u \qquad (4.215)$$

4.3.12.5   Total evapotranspiration

Total evapotranspiration is calculated for reporting purposes only as:

$$q_{et} = q_{int} + q_{tran,c} + q_{tran,u} + q_{evap} \qquad (4.216)$$

4.4   Summary

A new, physically based model of forested catchment hydrology was described. The model, named Macaque, is intended for application to large areas (> 100 km^2) and operates within a combined statistical/specific disaggregation of catchments enabling a parsimonious representation of catchment spatial heterogeneity. Lateral redistribution of subsurface water is achieved using a novel approach termed *limited distribution function modelling* (limited DFM).

Modern computer programming techniques have been applied throughout which greatly enhance the power and utility of the model relative to its contemporaries. These include:

- a hierarchy of spatial units (regions, catchments, hillslopes, etc.) which is defined at run time and can be changed easily,

- recursive, generic code which operates with *all* spatial units irrespective of where it sits within the hierarchy,

- inheritance of all variables (parameters, states, fluxes, and internal variables) up and down through the hierarchy,

- and the ability to account and output information on *any* model variable, at *any* spatial level, at *any* degree of temporal aggregation as either a map or a time series.

A detailed vertical structure is implemented for each elementary spatial unit (ESU) of the model. This is centred around a three layered (canopy, understorey, and soil) representation of evapotranspiration (ET) using the Penman-Monteith equation. All ET is designed to respond to changes in LAI, which is the key descriptor of land cover within the model. Standard ET processes are represented, including: interception storage; dependence

of canopy conductance on soil moisture, temperature, humidity, and radiation; direct control of transpiration by radiation and humidity as well as canopy conductance; and propagation of radiation down through the vegetation layers). Additionally, some less commonly represented processes are represented, such as reduction of vapor pressure deficit due to evapotranspiration at one layer lowering the humidity gradient experienced by lower layers.

Overall, the level of detail of evapotranspiration representation reflects the processes within the study area which are thought to be operative in effecting long term changes in water balance associated with changes in land cover.

The core model is prefixed with a detailed system of micro-meteorological components which take, as input, precipitation and maximum and minimum temperature and output a host of driving variables relating to temperature, humidity, radiation, rainfall, and snowfall. These components are considered part of, and intrinsic to Macaque.

A relatively simple array of modelled vertical subsurface flow processes operate within a two-layered soil structure and are linked together by lateral flow modelled implicitly as part of the limited DFM approach noted earlier. This simplicity reflects both our limited ability to test more detailed subsurface models, and the assumed insensitivity of ET to soil moisture which is thought to be generally not limiting within the study area.

Finally, it should be noted that a number of model components (such as snow accumulation and melting, and soil evaporation) are noted as having obvious limitations which reflect the perennial, continual progression of development which characterises physically based modelling. These components relate to relatively insensitive parts of the model.

Chapter 5

Model operation

Contents

5.1   Introduction

This chapter describes the scientific methods involved in applying Macaque
to the study area. These range from methods of spatial disaggregation of
the study area to quantification of the many detailed physical parameters.
Frequent links are made to the relevant chapters and sections in Part III
which deals with the mapping of spatial parameters.

5.2   Spatial disaggregation

5.2.1   Overall structure

The first step in the operation of Macaque is to decide upon a suitable spatial
structure for representing the study area as a hierarchy of spatial levels. Five

levels were chosen with a structure as illustrated in Figure 5.1. The top level, `world`, contains a single spatial unit defining the full extent of the study area (Figure 5.2). This unit is attributed with default values for all model parameters, including all parameters which are not spatially distributed. As discussed in Section 4.2, spatial units in all levels below `world` inherit the `world` default parameter values and then have the option of redefining them if they are specifically mapped at that level. The inheritance recurs down to the lowest spatial level, `ESU`.

A second level, named `region`, was chosen to divide the `world` into gauged and ungauged catchments (Figure 5.3) and a third level, `catchment`, defined the five water supply catchments of the study area, two in one `region` and three in another (Figure 5.4). These three levels serve mainly as accounting units to facilitate the analysis of accumulated model outputs such as stream-flow and evapotranspiration at large spatial scales. The next two levels relate more to model function, specifically the operation of the limited DFM.

5.2.2 Hillslopes

The fourth spatial level contains `hillslopes` which, by way of containing a number of `ESU`s each, are the structure within which lateral redistribution of water occurs due to the distribution function (Figure 5.5). The terrain analysis procedures and (modified) code of Lammers and Band (1990) were used to divide the study area into hillslopes. The method begins by delineating a stream network and defines hillslopes as areas bounded by stream segments, stream intersections, and ridge lines. The mean hillslope size may be prescribed *a priori*. Band (1993) and Wood et al. (1988, 1990) explored the effects of differing scales of spatial disaggregation in large scale spatial modelling with the general finding that there is little to be gained by delineating every conceivable hillslope. Here, the largest possible hillslope size was specified that did not represent known importantly heterogeneous areas as single hillslopes. Practically, this meant choosing the largest hillslope size that did not result in a single hillslope representing the entire southern flank of the Coranderrk catchment, which exhibits precipitation variation greater than a factor of two. Clearly, this was a subjective choice and there is much scope for improvement. Automated maximisation of between-hillslope heterogeneity and within-hillslope homogeneity could be implemented. Additionally, non-topographic factors, such as precipitation, could be explicitly introduced into the hillslope disaggregation process prior to the application of Lammers and Band's procedure.

Spatial levels

Level 0: world

Level 1: region

Level 2: catchment

Level 3: hillslope

Level 4: ESU

Spatial units in each level

World 0
Entire study area

Region 0
Poorly gauged catchments

Region 1
Well gauged catchments

Catchment 0
Donnellys

Catchment 1
Sawpit

Catchment 0
Watts

Catchment 1
Grace Burn

Catchment 2
Coranderrk

Hillslopes 0 to 5

Hillslopes 0 to 1

Hillslopes 0 to 97

Hillslopes 0 to 17

Hillslopes 0 to 5

About 14 ESUs
in each hillslope

About 14 ESUs
in each hillslope

About 14 ESUs
in each hillslope

About 14 ESUs
in each hillslope

About 14 ESUs
in each hillslope

Figure 5.1: The structure of spatial levels, and units within those levels, used to represent the study area.
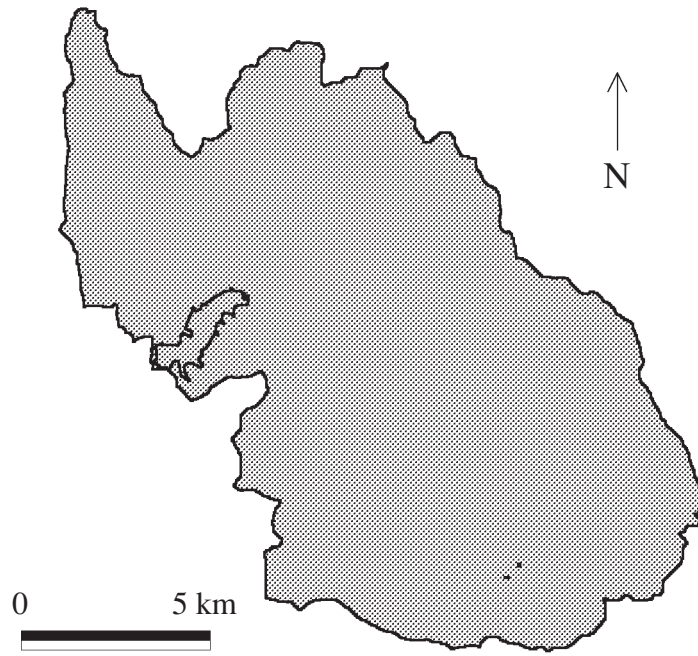
Figure 5.2: The `world` spatial unit.

Poorly gauged
Well gauged
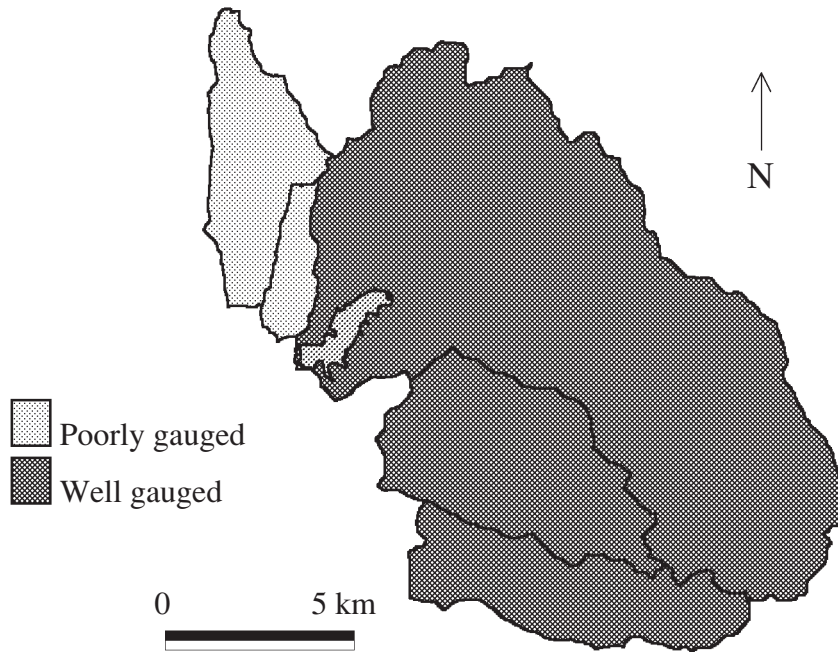
Figure 5.3: Spatial units at the `region` level.
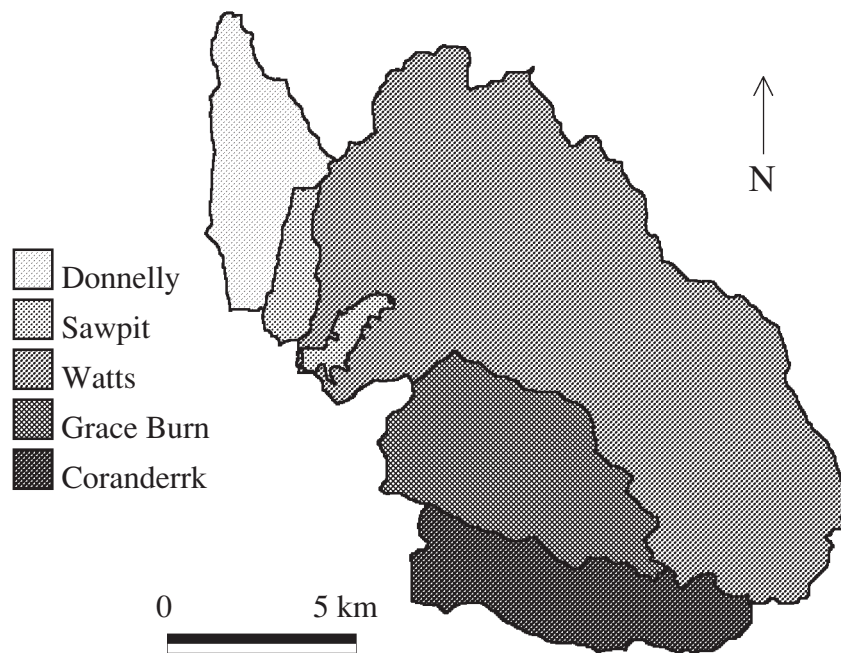
Figure 5.4: Spatial units at the `catchment` level.

Figure 5.5 shows the final disaggregation into hillslopes. The mean area of the 131 hillslopes is 123 ha (1.23 km^2), the median is 89 ha, and the range is 0.75 ha to 491 ha.

5.2.3 ESUs and wetness indices

The `ESUs` themselves are the fifth level. These were defined as the areas occupied by specific intervals of a wetness index, i.e. areas of similar wetness index were lumped together to form each ESU. As with `hillslopes`, any factors can be used to define `ESUs`. Initially however, a wetness index is the most suitable choice.

Four topographic wetness indices were investigated: a, $\ln(a)$, $\frac{a}{\tan\beta}$, and $\ln(\frac{a}{\tan\beta})$; where a is upslope area per unit contour length, and β is the terrain slope, specifically the contour length weighted average of downward slopes. Figures 6.7 and 6.8 show $\ln(a)$ and $\ln(\frac{a}{\tan\beta})$ mapped over the study area based on the 25 $\times$ 25 metre DEM described in Chapter 6. The $\ln(\frac{a}{\tan\beta})$ index has been used extensively in applications of TOPMODEL (Beven et al., 1995).

The four indices were fitted to observations of water table depth made in the Ettercon 3 experimental catchment using piezometers (see Section 10.2.11.1) and the detailed topographic survey described in Chapter 6. The $\ln(\frac{a}{\tan\beta})$ index produced a qualitatively better fit than the other indices and was
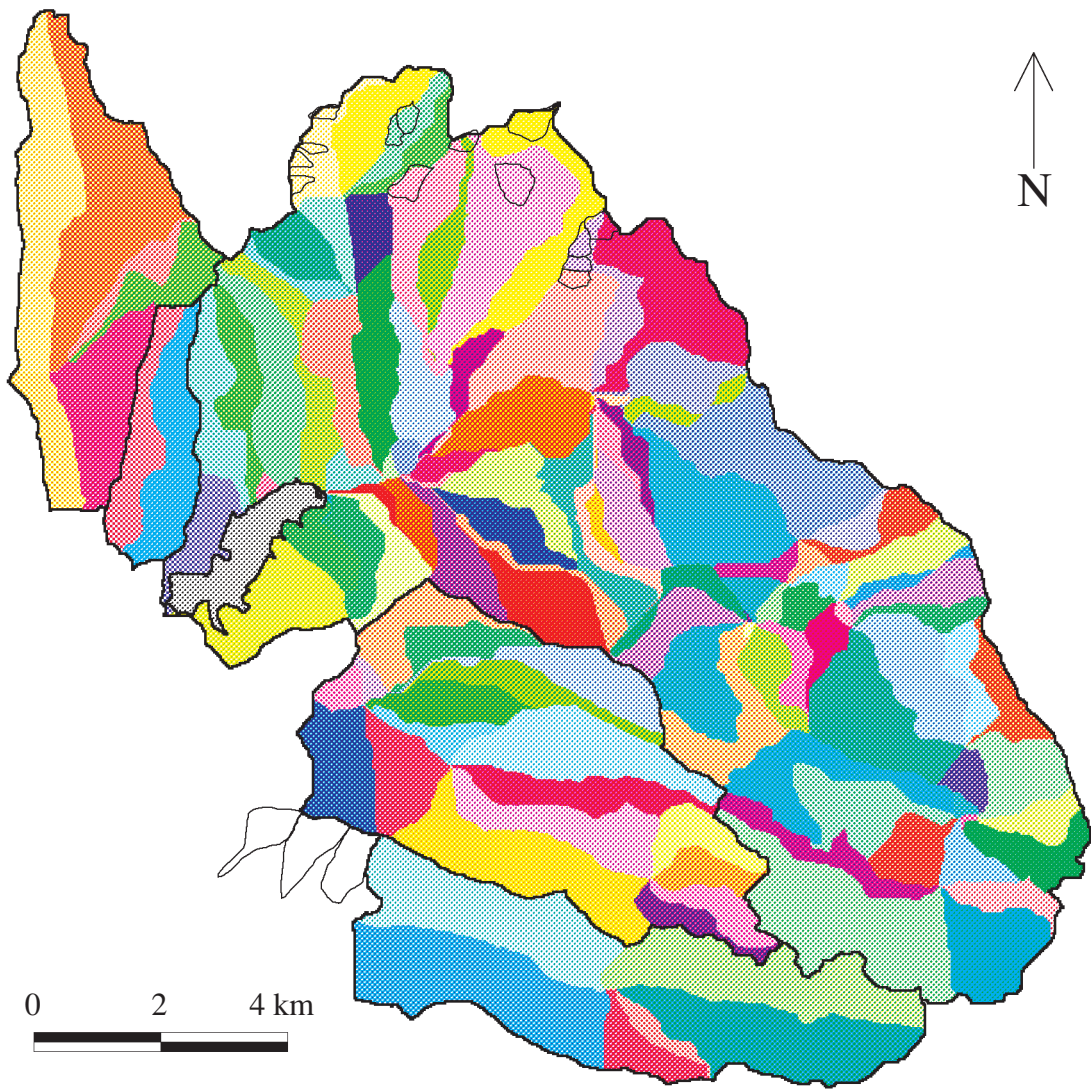
Figure 5.5: Spatial units at the `hillslope` level.

adopted henceforth. It is important to stress that the choice was made empirically using observations about catchment moisture distribution and not analytically using subsurface flow theory (as is the case for TOPMODEL and RHESSys). The assumptions about subsurface flow processes inherent in TOPMODEL are avoided, including the necessary linkage between baseflow recession and the decline in saturated hydraulic conductivity with depth.

Values of the $\ln(\frac{a}{\tan \beta})$ index range from 3.3 to 22.6 within the study area although visualisation with the GIS suggests that most spatial heterogeneity is likely to occur in areas where this index ranges from about 6 to 12. Values less than 6 are confined to the upper portions of hillslopes which are assumed to be relatively homogeneous. Similarly, values greater than 12 are associated with permanently saturated streams which can also be considered a homogeneous unit. Consequently, spatial disaggregation of `hillslope`s into `ESU`s was concentrated in the intervening wetness index range. Table 5.1 lists the wetness index intervals which were used to define each `ESU` within each `hillslope`. The definition of `ESU`s according to these ranges resulted in the map of `ESU`s shown in Figure 5.6. There are 1848 `ESU`s in the entire study area (ranging from 0.6 to 168 ha with a mean area of 8.7 ha and a median of 3.5 ha) and hence an average of 14 `ESU`s per `hillslope`.

Note that there is no reason why an individual `ESU` within a `hillslope` must be contiguous. Indeed the amorphous, disconnected, but same-coloured shapes in close proximity to each other in Figure 5.6 indicate that that many `ESU`s are quite discontiguous. Conceptually they are thought of as lying one above the other along a conceptual soil catena, but actually, they are statistical representations of the amount of area within each hillslope at different points along the wetness index gradient.

5.3   Parameters

This section describes the parameters of Macaque and is organised into subsections which, for ease of reference, closely match the structure of the model description in Chapter 4. Each parameter description attempts to answer the following questions:
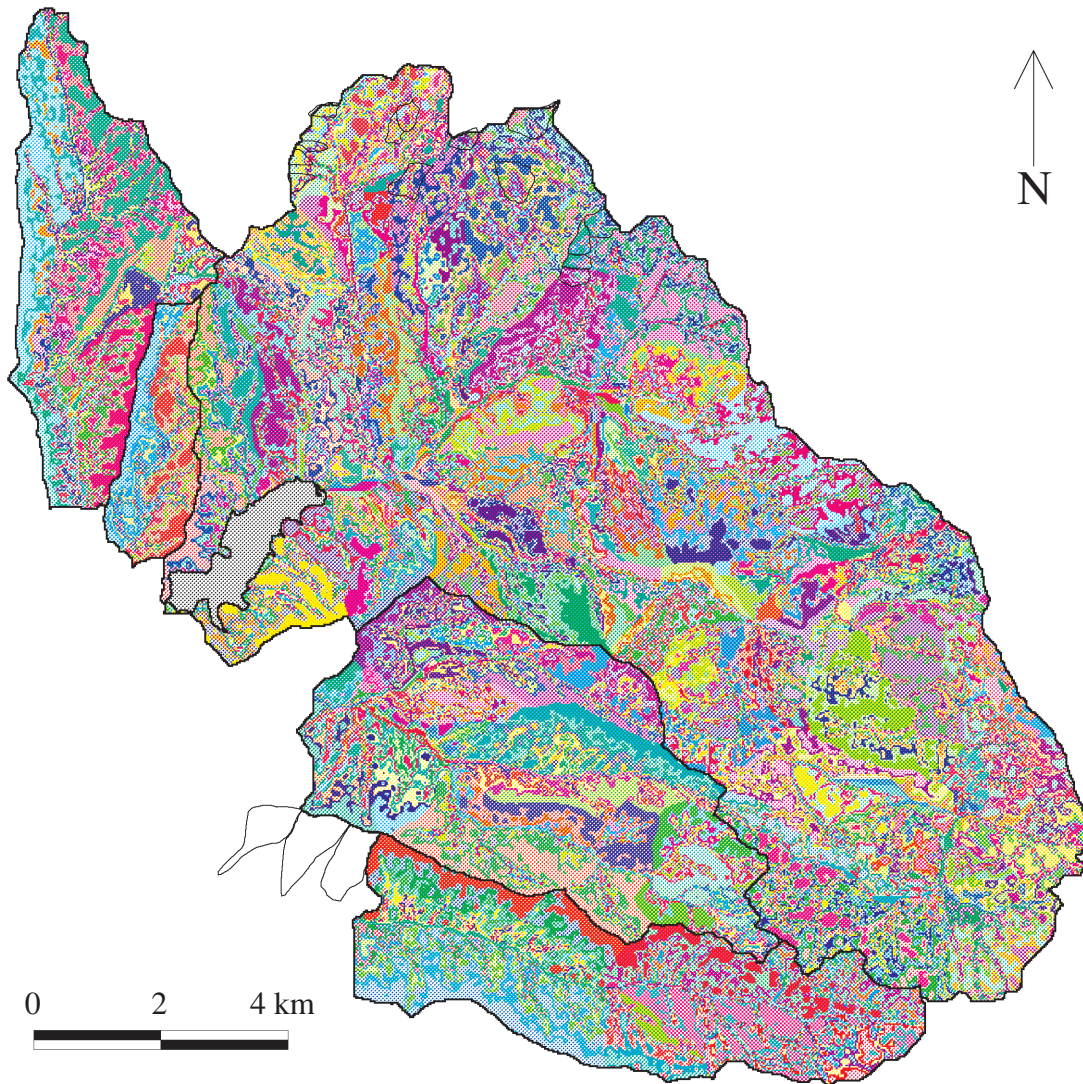
Figure 5.6: Spatial units at the ESU level. The colours have no meaning except to enable the shape and extent of each of the 1848 ESUs to be discerned.

Interval	ESU number
0 - 6	1
6 - 6.5	2
6.5 - 7	3
7 - 7.5	4
7.5 - 8	5
8 - 8.5	6
8.5 - 9	7
9 - 9.5	8
9.5 - 10	9
10 - 10.5	10
10.5 - 11	11
11 - 11.5	12
11.5 - 12	13
12 - 15	14
15 - 30	15

Table 5.1: Intervals of the $\ln(\frac{a}{\tan \beta})$ wetness index which were used to define separate ESUs within each hillslope.

- What does the parameter represent physically?

- How does the parameter control model operation?

- What is the acceptable range of values for the parameter?

- How certain is this range?

- What information is available to quantify the parameter?

A table summarising the key information for each parameter is presented first in Table 5.2. There are very many parameters. All of them have some effect on model operation, although many have very little effect when varied within acceptable ranges of uncertainty. This may be because they are generally insensitive within a wide range of values (e.g. minimum leaf conductance), or because their range of uncertainty is small (e.g. topographic aspect). Such parameters are listed in the table as having 'low' sensitivity relative to certainty.

More important are the parameters listed as having 'medium' sensitivity relative to certainty. These parameters can have a big effect on model operation but generally do not do so because they have been sufficiently constrained by either physical measurement or calibration against measurements of internal variables.

Most important are the 'highly' sensitive parameters. Some of these are rather conceptual and exhibit high sensitivity within a more or less unconstrained range of values (e.g. the parameters surrounding the lateral

re-distribution of subsurface water). Others are physical, but are difficult to measure and exert great influence on model operation. Classic examples are MMPI which is the strongest control of water being input to the system, and maximum canopy leaf conductance which is the strongest control of water being output from the system. These are the biggest tuning 'knobs' of the model, and there are eight of them.

Table 5.2: Summary of standard parameter set used by Macaque in the present study. Note that parameters listed as having 'spatial' standard values are mapped parameters whose value is specified independently for each ESU.

Symbol	Standard value	Origin	Sensitivity relative to certainty
Hillslope and ESU			
i_{wet}	spatial	measured	med.
$i_{wet,range}$	spatial	measured	med.
$\bar{i}_{wet}$	spatial	measured	med.
Δ_{sat}	-6.5 m i_{wet}^{-1}	internally calibrated	**high**
δ	0.001 day^{-1}	internally calibrated	**high**
Topographic			
h	spatial	measured	low
h_{stn}	spatial	measured	low
$\sin\phi$, $\cos\phi$	spatial	measured	low
β	spatial	measured	low
β_E, β_W	0 °	not set	low
Vegetation			
$y_{origin,1}$, $y_{origin,2}$, $y_{origin,3}$	spatial	measured	med.
V_c	spatial	measured	low
V_u	spatial	not set	low
$LAI_{tot,param}$	spatial	not set	med.
$LAI_{tot,P}$	spatial	measured	med.
$LAI_{tot,D}$	spatial	measured	med.
$LAI_{tot,C}$	spatial	measured	med.
$\tau_{tot,P}$	spatial	measured	med.
$\tau_{tot,D}$	spatial	measured	med.
$\tau_{tot,C}$	spatial	measured	med.
Temperature			
$\Delta_{T,max}$	0.006 °C m^{-1}	measured	**high**
$\Delta_{T,min}$	0.006 °C m^{-1}	measured	med.
Daylength			
lat	-37.625°	measured	low
Radiation			
a	0.766	internally calibrated	med.
b	0.0327	internally calibrated	med.

c	1.46	internally calibrated	med.
$k_{R,c}$	0.37	meas. in literature	med.
$k_{R,u}$	0.93	meas. in literature	med.
α_c	0.19	meas. in literature	low
α_u	0.13	meas. in literature	low
α_{soil}	0.10	meas. in literature	low
α_{snow}	0.65	meas. in literature	low
Δ_R	0.612	internally calibrated	med.
C_R	9.74×10^5 J m^{-2} day^{-1}	internally calibrated	med.
Precipitation			
$MMPI$	spatial	measured	**high**
$MMPI_{stn}$	spatial	measured	low
Rainfall, snowfall, interception			
k_{rain}	0.0008 m LAI^{-1}	internally calibrated	med.
k_{snow}	0.0008 m LAI^{-1}	internally calibrated	med.
Snowpack			
$O_{dd,min}$	-30 °C.days	internally calib. in literature	low
$\mu_{snow,T}$	0.001 m (water) °C^{-1} day^{-1}	internally calib. in literature	low
$\mu_{snow,R}$	0.12	internally calib. in literature	low
Soil			
θ_{sat}	0.67 m (water) m^{-1} (soil)	measured	low
θ_{res}	0.20 m (water) m^{-1} (soil)	measured	low
$K_{sat,surf}$	5.0 m day^{-1}	measured	med.
$K_{sat,min}$	0.40 m day^{-1}	measured	med.
f	2.0 m^{-1}	measured	med.
n	1.25	meas. and internally calibrated	med.
Δ_z	0.005	meas. and internally calibrated	**high**
Evapotranspiration			
$z_{c,max}$	4.0 m	measured	low
$z_{u,max}$	2.0 m	measured	low
$\psi_{cl,max}$	-0.5×10^5 Pa	measured	low
$\psi_{cl,close}$	-2.3×10^5 Pa	measured	low
$\psi_{ul,max}$	-0.5×10^5 Pa	defaulted from canopy value	low
$\psi_{ul,close}$	-2.3×10^5 Pa	defaulted from canopy value	low
$\Delta_{\psi,l}$	-1.0×10^5 Pa	internally calib. in literature	low
$g_{cl,max}$	0.005 m s^{-1}	meas. and externally calib.	**high**
$g_{cl,min}$	0.0002 m s^{-1}	measured	low
$g_{ul,max}$	0.005 m s^{-1}	defaulted from canopy value	**high**
$g_{ul,min}$	0.0002 m s^{-1}	defaulted from canopy value	low
$\Delta_{g,T}$	0.0002 m s^{-1} °C^{-1}	internally calib. in literature	med.

$\Delta_{f,T}$	0.0003 °C^{-1}	internally calib. in literature	med.
$\Delta_{f,cl,D}$	-0.0003 Pa^{-1}	meas. and externally calib.	med.
$\Delta_{f,ul,D}$	-0.0003 Pa^{-1}	defaulted from canopy value	med.
$S_{thresh,c}$	0 J m^{-2} day^{-1} LAI^{-1}	not set	low
$S_{thresh,u}$	0 J m^{-2} day^{-1} LAI^{-1}	not set	low
$r_{aero,c,ref}$	15 s m^{-1}	meas. in literature	med.
$r_{aero,u,c}$	15 s m^{-1}	meas. in literature	med.
$r_{aero,s,u}$	15 s m^{-1}	meas. in literature	med.
$p_{c,sat}$	0.1	inferred from obs. in literature	med.
$p_{u,sat}$	0.5	inferred from obs. in literature	med.
$z_{s,max}$	0.003 m	internally calibrated	**high**
τ	2	calib. in literature	low

Most of the parameter values given in Table 5.2 are fixed for all simulations reported. However, some are calibrated for specific executions of the model as described in Sections 10.2.11.3, 10.4, and 11.2. The associated alternate values are: $\Delta_{sat} = -10.5$, $\delta = 0.0002$, $\Delta_z = 0.01$, and $g_{cl,max} = g_{ul,max} = 0.0023$.

5.3.1 Hillslope and ESU parameters

5.3.1.1 Wetness index and mean wetness index

The wetness index parameter, i_{wet}, was discussed in Section 5.2.3. For consistency with the present section on individual parameter descriptions, some summary points are brought together here. The index represents the distance down the conceptual soil catena occurring within each mapped hillslope. For a given ESU, the value of i_{wet} relative to the mean value for the hillslope, $\bar{i}_{wet}$, controls the depth to the water table prescribed by the distribution function (the actual value being allowed to vary from this to some extent). In Section 5.2.3, the index was chosen as the topographic function $\ln(\frac{a}{\tan\beta})$ because of the correlation of this function with a limited number of water table depth observations. Values for $\ln(\frac{a}{\tan\beta})$ are derived from the DEM using well established digital terrain analysis procedures (Section 6.5) and range from 3.3 to 22.6 within the study area (mean hillslope values range from 5.73 to 15.0). Whilst there are a variety choices in the exact method of calculation (Freeman, 1991; Holmgren, 1994; Quinn et al., 1995; Costa-Cabral and Burges, 1994), the model is not considered sensitive to the resulting values relative to the uncertainty associated with these methodological choices.

5.3.1.2 Wetness index range

The wetness index range parameter, $i_{wet,range}$, quantifies the amount of the conceptual soil catena (above) represented by a particular ESU. Specifically it is the range of wetness index values *actually observed* within the upper and lower limits used to define the ESU. Within the model, it is used to indicate the range of water table depths that are expected within an ESU by means of the relationship between saturation deficit (related to water table depth) and wetness index. Because the saturation deficit at which exfiltration begins is calculated directly from the wetness index range, the parameter is a control of saturation deficit itself. For example, a water table below the exfiltration point may rise under favourable recharge conditions to the exfiltration level, at which point exfiltration commences thereby limiting the rate of further

rise. In practice, saturation deficit is very sensitive to wetness index range. However, values are easily and accurately derived through digital terrain analysis (Section 6.5) and therefore the parameter is listed in Table 5.2 as having only 'medium' sensitivity *relative to certainty* (values range from 0 to 7.639). Greater sensitivity is associated with choices in the model structure itself with respect to the calculation of saturated proportion.

Values for $i_{wet,range}$ within each ESU are taken directly from the maps of wetness index and ESUs (Section 6.5).

5.3.1.3 Saturation deficit slope

This parameter (Δ_{sat}) and the lateral redistribution factor (δ) described in the following section are considered to be primarily 'hillslope' parameters. To some extent, they are also soil parameters and some discussion of their role as such is included in the relevant section (Section 5.3.11).

The slope of the saturation deficit of ESUs with respect to their wetness index, Δ_{sat}, is a conceptual, integrated representation of quantities such as soil depth, soil porosity, and the slope of various layers within the regolith. Within the study area, all of these quantities control the rate at which the water table deepens as one moves up the soil catena away from the stream. Their combined influence is quantified by Δ_{sat}. The parameter influences not only saturation deficit and water table depth, but also hydrograph shape through the changed dynamics of saturated area expansion which result when the near stream water table is made deeper or shallower. Useful values typically range from 1.0 m i_{wet}^{-1}, which leads to a relatively shallow water table, to 15.0 m i_{wet}^{-1}, which predicts a water table which deepens rapidly with distance away from streams. Ideally, different values would be assigned to each hillslope, depending mostly on soil depth. However, both the physical realisation of the parameter and the spatial measurement of soil depth is too uncertain to enable such mapping. Instead, dual calibration against hydrographs and expected water table levels must be employed. This approach to constraining distribution function models has recently been applied in the TOPMODEL literature (Lamb et al., 1996, 1997). The Δ_{sat} parameter is considered highly sensitive relative to its certainty.

5.3.1.4 Lateral redistribution factor

The hillslope lateral redistribution factor, δ, is a conceptual representation of the lateral hydraulic conductivity of the aquifer within which the water table

lies. Within the model, it controls the rate at which lateral redistribution of water is applied between each ESU and the remainder of its parent hillslope through the imposition of the distribution function. This results in a control of the degree to which near stream water tables may dynamically mound above or dip beneath the relative static value prescribed by the distribution function. In turn, this affects hydrograph shape by altering the dynamics of saturated area expansion. Values for δ are calibrated against both hydrograph shape and observations and expectations of near stream water table mounding and typically range from about 0.01 to 0.0001 day^{-1}. The model is co-dependent on δ and Δ_{sat} and so δ, like Δ_{sat}, is listed as having 'high' sensitivity relative to certainty.

5.3.2 Topographic parameters

The topographic parameters elevation, slope, and aspect (h, h_{stn}, β, $\sin\phi$, $\cos\phi$) are key spatial parameters within Macaque and are discussed separately in Chapter 6.

5.3.3 Vegetation parameters

5.3.3.1 Species

Values for the canopy species parameter, V_c, are canopy codes used within lookup tables in the determination of LAI and canopy conductance. The choice between temporally constant canopy LAI and total LAI and a range of temporal functions for canopy LAI and total LAI is made according to canopy species. Additionally, a lookup table indicates whether a given canopy species is amphistomatous (i.e. its leaves have stomata on both sides), in which case canopy conductance should be multiplied by an additional factor of two. The parameter is a mapped parameter and is addressed separately in Chapter 9. It has 'low' sensitivity relative to certainty.

The understorey species parameter mostly serves as a place-holder for cases where more is known about understorey distribution and behaviour. In the present study, it is set to a single generic value which is only used in a lookup function for the amphistomatous property.

5.3.3.2 Vegetation origin

Historical dates of forest origin ($y_{origin,1}$, $y_{origin,2}$, and $y_{origin,3}$) are used to calculate vegetation age, upon which LAI depends. Dates applicable to contemporary forest are accurately known, whilst dates applicable to past stands are poorly known. On average, these parameters are listed as having 'medium' sensitivity relative to certainty. They are mapped parameters as discussed in detail in Chapter 9.

5.3.3.3 LAI

Excluding the parameter for constant total LAI, $LAI_{tot,param}$, which is generally not used, six parameters control the magnitude and timing of LAI changes with vegetation age ($LAI_{tot,P}$, $LAI_{tot,D}$, $LAI_{tot,C}$, $\tau_{tot,P}$, $\tau_{tot,D}$, and $\tau_{tot,C}$). These are the primary spatio-temporal parameters of the model and strongly influence long term changes in water balance. Their measurement is described in detail in Chapter 9.

5.3.4 Temperature parameters

The only parameters of the temperature sub-model are the maximum and minimum temperature/elevation lapse rates, $\Delta_{T,max}$ and $\Delta_{T,min}$, which represent the decrease in temperature with increased elevation. These parameters strongly influence temperature estimates at all locations vertically removed from the base station. They thus affects humidity, radiation, and leaf conductance estimates as well as whether precipitation is deemed rain or snow.

Barry (1992) discusses world-wide ranges of lapse rates in some detail and highlights the limited utility of a single lapse rate which is constant in time and space. Locally, Ruddell et al. (1990) give annual and seasonal maximum and minimum temperature lapse rates separately for Victoria and the Snowy Mountains. These rates are mainly based on data from the snow country a few hundred kilometres north east and were tested for initial use in the study area. For Victoria, the values given for annual maximum and minimum temperature lapse rates are 0.0081 °C m^{-1} and 0.0033 °C m^{-1} respectively.

Limited temperature data from within and around the study area were assembled in order to test temperature predictions made using Ruddell et al's lapse rates. The data were expressed in terms of mean temperature difference from the Melbourne Regional Office meteorological station (the temperature station used for long term simulations, see Appendix B), and plotted against

elevation in Figure 5.7 using solid red circles for the maximum temperature data and blue stars for the minimum temperature data.

In preparing this Figure, it was noticed that two of the temperature records used (the CRCCH records from Murrindindi and Upper Coranderrk, the highest two sites in Figure 5.7) had very short periods which were biased to the summer months. These records plotted higher than expected in Figure 5.7, and were investigated further. It was ascertained that strong seasonality exists in observed daily lapse rates. This is shown in Figure 5.8 which plots differences in maximum and minimum temperatures between the Blacks' Spur (F1820) and Melbourne Regional Office (F2540) meteorological stations. Strong seasonality is observed in the maximum data but not in the minimum data. To quantify this more concisely, sine curves were objectively fitted to the data as shown. A factor of three difference in maximum temperature lapse rate between summer and winter is inferred.

The seasonality of lapse rate can be treated in two ways. Firstly, the parameters of the sine curve could be input as elevation dependent parameters of the model. For this study, this was unfeasible given the limited temperature data and the variability of the three parameters involved (mean, amplitude, and phase). The amplitude in particular varied significantly amongst three records examined. Alternatively, a single mean (non-seasonal) lapse rate could be used, and the data upon which the mean is based could be adjusted for any seasonal bias. This latter option was chosen, resulting in two adjusted values (open red circles) for maximum data in Figure 5.7 (the values for the highest two stations).

Returning to Figure 5.7 and the testing of Ruddell et al's values, the adjusted maximum data (solid and open red circles) are reasonably well predicted using Ruddell et al's maximum temperature lapse rate (thick dashed red line), but the line of best fit to this data (thick solid red line) suggests a lower lapse rate. The data for minimum temperature lapse rates (blue stars) and the corresponding line of best fit (thin solid blue line) are poorly predicted by Ruddell et al's lapse rate for minimum temperatures (thin dashed blue line).

It was decided to abandon use of Ruddell et al's values and simply use the slopes of the lines of best fit from Figure 5.7 as lapse rates. The slope for both maximum and minimum temperature data is $\Delta_{T,max} = \Delta_{T,min} = 0.006$ ° C m^{-1}. Note that significant scatter is observed about these lines, but that a similar degree of scatter was observed by Ruddell et al. (1990, Figure 3.4) from a much larger number of stations. The scatter is most likely caused by factors such as differences in aspect, and topographic location with
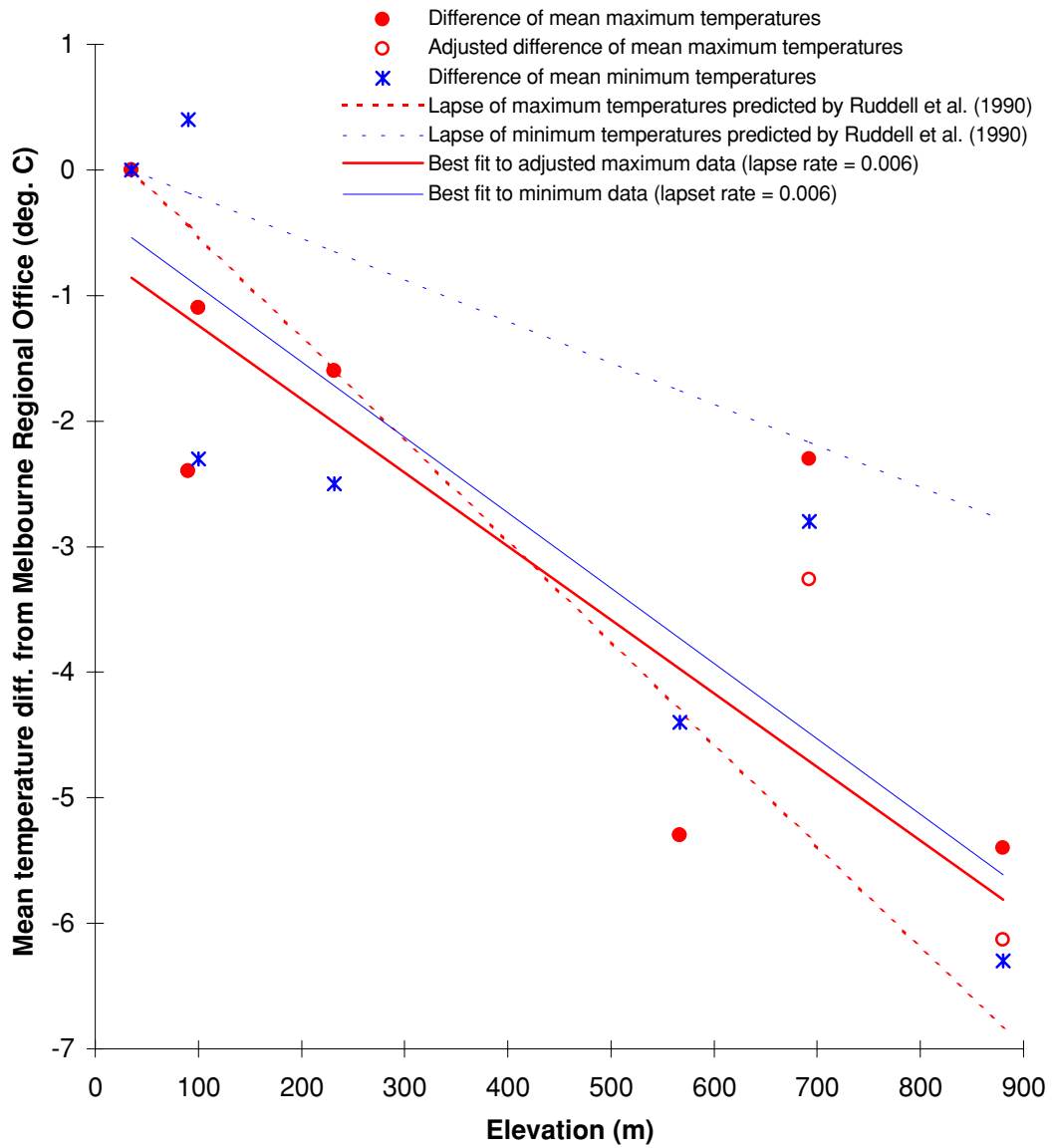
Figure 5.7: Temperature lapse rate as expressed by mean maximum and minimum temperature difference between various stations and the Melbourne Regional Office meteorological station versus elevation.
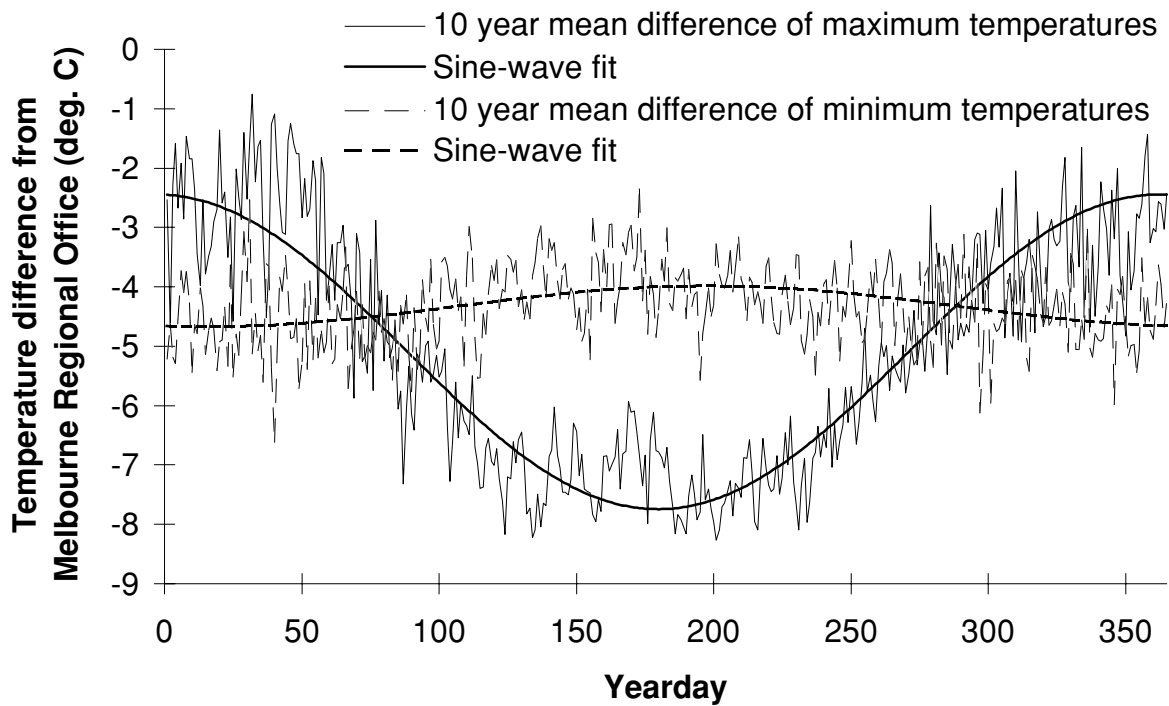
Figure 5.8: Seasonal variation in lapse expressed as the difference in maximum and minimum temperatures between the Blacks' Spur and Melbourne Regional Office meteorological stations (532 m vertical separation). The value for each yearday is the average for the same yearday from a 10 year period (1975-1984).

respect to cold air drainage patterns.

5.3.5 Humidity parameters

There are no parameters associated with the humidity sub-model.

5.3.6 Daylength parameters

There are no specific daylength parameters. However, the latitude of the study area, $lat = -37.625°$, is used in daylength and radiation calculations. It is simply read from a map and is negative in the southern hemisphere.

5.3.7 Radiation parameters

5.3.7.1 Incident solar radiation parameters

The estimation of global solar radiation incident on a sloping surface above the canopy involves three model parameters: the a, b, and c parameters from Bristow and Campbell's (1984) model of atmospheric transmission versus temperature range (Equations 4.35 and 4.36).

Daily global incident solar radiation data were available from three sites: Upper Coranderrk (F0430), Murrindindi (F1510), and Tarrawarra (F1064). The first of these was used for parameter calibration and the other two were used for testing (Section 10.2.5). In order to produce 'observations' of transmission, the observed incident radiation data had to be divided by estimates of extra-terrestrial solar radiation produced according to Dingman (1994, App. E) as described in 4.3.6.1.

As noted in Section 4.3.6.1, the a parameter was set to the maximum observed transmission of 0.766, and $b = 0.0450$ and $c = 1.39$ were estimated by linear regression of the transformed Bristow and Campbell (1984) equation. The subsequent predictions made using Equation 4.35 are plotted alongside observed transmission versus temperature range in Figure 5.9.

5.3.7.2 Radiation/vegetation parameters

There are six parameters associated with the propagation of solar and long-wave radiation through the vegetation layers. Two of these, $k_{R,c}$ and $k_{R,u}$
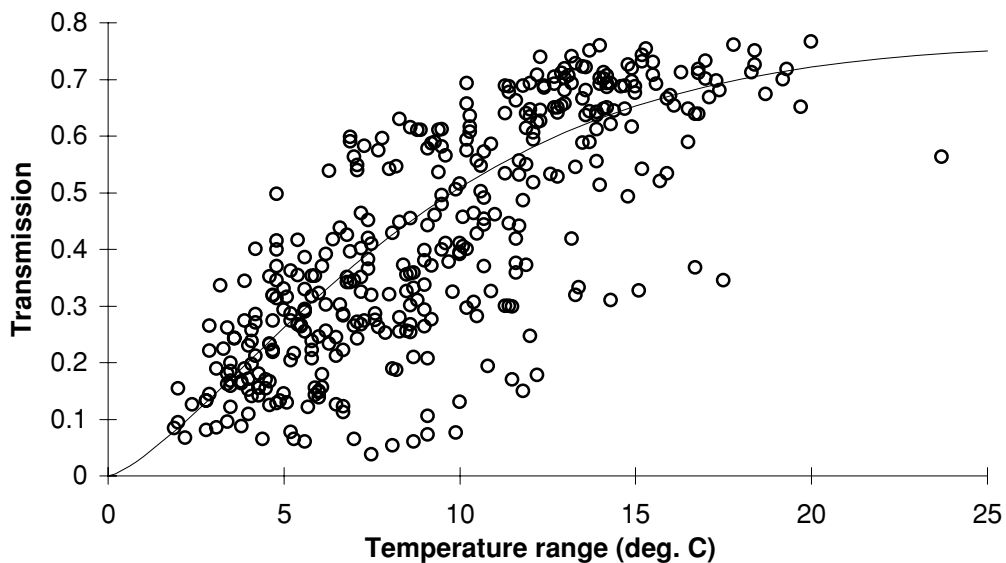
Figure 5.9: Predicted (curved line) and observed (open circles) atmospheric transmission of solar radiation versus temperature range at Upper Coranderrk.

are general radiation extinction coefficients for the canopy and understorey respectively. The remaining four, α_c, α_u, α_{soil}, and α_{snow} are solar radiation reflection coefficients (analogous to albedos) for the canopy, understorey, soil, and snow respectively.

Radiation interception coefficients

The radiation coefficient for a small leaf area is the ratio of the radiation intercepted by that leaf area to that which would be intercepted if the leaves faced directly toward the source of radiation (Monteith and Unsworth, 1990). It may be used within Beer's Law to estimate the amount of radiation intercepted by a vegetation layer with given LAI. The coefficients for the canopy and understorey, $k_{R,c}$ and $k_{R,u}$, therefore directly (and non-linearly) scale all forms of evapotranspiration by controlling the allocation of above-canopy incident radiation to each of the respective layers.

There are few data on radiation interception derived from direct measurement within eucalypt forests and hence, modelling studies tend to use general values from a rather sparse literature or values calibrated to give apparently realistic results (e.g. Running and Coughlan, 1988; Silberstein and Sivapalan, 1996; Vertessy et al., 1993, 1996). An exception is found in Hatton et al. (1993) where the above/below canopy radiation ratio was measured.

Interception coefficients depend on the vertical and azimuthal distribution of the leaves (Monteith and Unsworth, 1990). In the simplest case, a top-

lit conical distribution can be assumed with random azimuth, fixed vertical angle, and the sun shining from above. In this case, we may measure the angle, and take the cosine to give the interception coefficient. Anderson (1981) measured leaf angles for a variety of eucalypts including *E. rossii*, *E. maculata* and *E. gummifera* and noted that angles from the horizontal of 60-80°are typical for the genus. For *E. maculata* forest at Kioloa, Pook (1985) cited Anderson and took the cosine of 65° to give an interception coefficient of 0.42. Hatton et al. (1993) used 0.42 in modelling studies at Kioloa, noting measurements of the ratio of below to above-canopy radiation at this site of 0.3 which roughly matches the value of 0.25 predicted for the site using Beer's Law with an LAI of 3.3 and an interception coefficient of 0.42. The value 0.42 was also used in Topog modelling studies of *E. regnans* forest by Vertessy et al. (1993, 1996), along with an un-sourced understorey value of 0.6. Ashton (1976) provides some measurements of leaf angle for *E. regnans* and a common associated understorey species, *Pomaderris aspera* of 68°±10°and 22°±18°respectively. The corresponding cosines are $k_{R,c} = 0.37$ and $k_{R,u} = 0.93$ and these are the values used here.

Its well known that eucalypts are able to orient their leaves toward and away from the sun according to their needs and this confounds the random conical assumption implicit in the above values. From observations, it is also appears likely that many of the understorey leaves of the study area are distributed as an oblate spheroid and not a cone, a further confounding factor. Further, interception can depend heavily on solar elevation (Monteith and Unsworth, 1990), a factor which is not easily accounted for by a daily model.

Other modelling studies citing interception coefficients include McMurtie et al. (1990a) and McMurtie (1993) where the un-sourced value 0.5 is used with an assumption of spherical leaf distribution in BIOMASS applications to *Pinus radiata* plantations.

The values chosen above can be considered interim values pending a more thorough investigation of the radiation environment of eucalypt stands. More use could be made of observations described by Ashton (1976) as well as improved measurement techniques. For example, Welles and Norman (1991) note that leaf angle can be measured with the Li-Cor plant canopy analyser used in the present study for measuring LAI. If enough measurements were made from each of the five differently inclined rings of the Li-Cor LAI-2000, a simple model dependent on mean daily solar elevation could be constructed.

Reflection coefficients

The canopy, understorey, soil, and snow reflection coefficients for solar radiation (α_c, α_u, α_{soil}, and α_{snow}) represent the proportion of radiation intercepted by surfaces within these layers which is reflected back upward. Hence, they are an inverse control on all evapotranspiration processes.

Suitable values were taken from Monteith and Unsworth (1990, p. 80-84), Gates (1980), Lee (1980), Oke (1987), and Dingman (1994) as: 0.19 for '*Eucalyptus*', used for the canopy; 0.13 for 'tropical rainforest', used for the understorey; 0.1 for 'soils with a high organic matter content', used for all soils within the study area; and 0.65 for 'fresh, high density snow', used for all snow. The accuracy of these values is probably sufficient, given the narrow range of values cited for a wide range of natural surfaces (0.1 to 0.3, excluding snow). Howard (1991) describes spectral reflectance and transmittance curves for a variety of eucalypt leaves in detail but unfortunately omits a simple characterisation of these as single, spectrally integrated values.

5.3.7.3   Net radiation parameters

The nearest source of net radiation data to the study area is the lowland pasture field site at Tarrawarra, some 10 km distant from the study area (Western and Grayson, 1997).

Two parameters, Δ_R and C_R, quantify the relation between net radiation and global solar radiation. In summer, when both solar and net radiation are high, the parameters are not particularly sensitive relative to their certainty. But in winter, net radiation can become very low or negative and the two parameters are sensitive in determining this. They are hence a strong control of winter ET. Linacre (1992, p. 98) discusses general values for the parameters ($\Delta_R = 0.63$ and $C_R = 3.46 \times 10^6 \text{J m}^{-2}$ day $^{-1}$) and these were initially input to Macaque. However, this led to negative predicted net radiation far more often than was observed at Tarrawarra. Thus new values were obtained by linear regression of observed net and solar radiation at Tarrawarra ($\Delta_R = 0.612$ and $C_R = 9.74 \times 10^5 \text{J m}^{-2}$ day $^{-1}$, $r^2 = 0.88$, $n = 842$ days). At least at the 24 hour average level, these are likely to be applicable to nearby forests such as those of the study area (pers. comm., F. Dunin, CSIRO Plant Industry, Perth). The values are tested in Section 10.2.5.2.

5.3.8 Precipitation parameters

The precipitation parameters, $MMPI$ and $MMPI_{stn}$, are key parameters within Macaque and are discussed in detail in Chapter 7.

5.3.9 Rainfall, snowfall, and interception parameters

The only parameters of the rainfall, snowfall, and interception sub-models are the interception coefficients for rain and snow, k_{rain} and k_{snow}. These control the amount of precipitation that is intercepted by the vegetation and, hence, limit the amount of water that is input to the soil. Conceptually, the values are representations of the capacity, in metres of water per unit LAI, of each vegetation layer to store water. Functionally however, temporal scaling by models (i.e. discretisation of time) requires that higher than realistic values be used in order to achieve sufficient long term interception totals.

An *hypothetical upper bound* for the scaling effect on interception storage capacity can be estimated as follows. Assume a very hot dry summer period followed by a day of continual rain. Potential evaporation remains constant throughout the day at say 3.5 mm day^{-1} (even during the rain, as observed by Dunin et al., 1988). Rain falls at the continuous rate of 3.5 mm day^{-1}. The *instantaneous* interception storage capacity of the forest is 0.35 mm (also as observed by Dunin et al., 1988). Because rainfall is matched by evaporation, all rain is caught by the leaves and immediately evaporated. Daily interception is thus 3.5 mm. If this were modelled using a *daily* Rutter model (Rutter et al., 1971), interception would be limited by the storage capacity to only 0.35 mm, 10 times less than 'reality'. If a half-day time step were used, interception would double to 0.7 mm; and so on down to a time step of two hours when modelled interception would reach the true value of $10 \times 0.35 = 3.5$ mm. Conversely, to achieve an accurate estimate of interception using a daily time step, the storage capacity would need to be set at 3.5 mm, 10 times higher than reality.

Obviously, this situation would rarely, if ever, occur. Evaporation during rainfall would rarely be so high, and rain rarely falls continuously for an entire day. However, there are many situations where the above conditions are *approached* leading to unrealistically high storage capacity parameters in models.

Dunin et al. (1988) give an instantaneous value for interception storage capacity of 0.35 mm in eucalypt forest with an LAI of about 3.0, i.e. 0.12 mm LAI^{-1}. Modelling studies use higher values. Leuning et al. (1991) used 0.3 mm LAI^{-1}

as a general value for eucalypts within the BIOMASS model. Using Topog, Hatton et al. (1992) and Vertessy et al. (1996) cited Dunin et al. (1988) as a source but used values of 0.15 and 0.30 mm LAI^{-1} respectively. Vertessy et al. (1993) also cited Dunin et al. but, after calibration of their hourly model against cumulative throughfall totals, used 0.68 mm LAI^{-1} for *E. regnans*. This reflects the hypothetical situation outlined above.

In *Pinus radiata* plantations, McMurtie et al. (1990a) used 0.5 mm LAI^{-1} within the BIOMASS model. This information might be useful in future for parameterisation of the (very) limited areas of pine forest within the study area. However, k_{rain} is treated as a lumped parameter at this stage as there are no consistent data on how it might be distributed.

The outcome of the above discussion is that it should not be unexpected that a daily model such as Macaque might require values for interception storage capacity several times larger than instantaneous values such as those measured by Dunin et al. (1988). A corollary is that values will also depend on the particulars of the model involved, e.g. whether evaporation of intercepted water is controlled by radiation alone, as in RHESSys, or by more realistic concepts such as potential evaporation, as in SHE, DHVM, BIOMASS, and Macaque, which use a Rutter et al. (1971) scheme.

In the present study, a value for $k_{rain} = 0.0008$ m LAI^{-1} was derived by manual calibration against long term ratios of interception to precipitation given by Langford and O'Shaughnessy (1978, p. 63). As summarised by Haydon et al. (1996), more data are available from a range of *E. regnans* forests of different ages and these could be used to improve calibration (and testing) in the future. There are no data on snow interception in *Eucalyptus* forests, and little data on snow interception relative to rain interception in any forest type (Gray & Prowse, 1993), so the value for snow was set to be equal to that for rain.

5.3.10 Snowpack accumulation and melting parameters

As stated earlier, snow processes are of minor importance within the study area and hence, snowpack accumulation and melting parameters are simply taken from the literature as follows.

There are three simple parameters to the snowpack sub-model: the minimum snowpack 'energy', $O_{dd,min}$; and temperature and radiation melt coefficients, $\mu_{snow,T}$ and $\mu_{snow,R}$. These parameters are the principal controls of snowmelt

in Macaque. Gray and Prowse (1993) give a discussion of temperature melt coefficients and from this a median value of $\mu_{snow,T} = 0.001$ m (water) $^\circ$C^{-1} day^{-1} was taken. Values for the other two parameters were inherited from RHESSys and FOREST-BGC (e.g. Scuderi et al., 1993) as: $\mu_{snow,R} = 0.12$ and $O_{dd,min} = -30$ $^\circ$C.days. Whilst there are extensive snowpack data for Australia (Ruddell et al., 1990), including one gauge within the study area, no validation of Macaque's snowpack sub-model has been undertaken to date. It remains a low priority given the limited influence of snow on the hydrology of the study area. Gray and Prowse (1993) do, however, recommend site specific calibrations of snowmelt models.

5.3.11 Soil parameters

5.3.11.1 Introduction

A number of studies have investigated the soils of the Maroondah Catchments and these have built up a picture of the typical soil of the *E. regnans* forests within the study area as a deep, gradational clay loam (Langford & O'Shaughnessy, 1980a; Vertessy et al., 1991; Campbell, in prep.; Davis, in prep.; Lorieri et al., in prep.). There is, however, very little information on the spatial variability of soil parameters at large scales so the present study initially focused on mapping simple properties such as soil depth.

5.3.11.2 Preliminary investigations

Traditionally, soils have been mapped according to named soil types (Bouma, 1985), which is appropriate where a range of distinct types exist. However, Australia's mountainous forested regions do not tend to exhibit a range of distinct types (Northcote, 1961) but rather continual variation in soil properties. More modern techniques concentrate on mapping distinct physical properties, either by spatial interpolation of measurements made at a large number of sampling sites, or by relating measurements to environmental variables and performing the interpolation in *environment space* (e.g. McKenzie and Austin, 1993). Once a property is mapped in environment space, its value is estimated at any given site from the environmental characteristics of that site.

In the study area, a number of environmental controls on soil property distribution are likely to be operative:

leaching and weathering In areas of high precipitation (such as the study area), leaching of soluble and colloidal elements from the soil is a dominant soil forming process, and may account for increased clay concentrations and decreased hydraulic conductivity both with depth, and with distance down the soil catena towards the streams (Leeper and Uren, 1993, p. 38). The extent of such leaching may be related to moisture controls such as the amount of precipitation and radiation received by a hillslope, as well as topographic controls within the hillslope such as upslope area and surface slope. Weathering of parent material is also environmentally controlled. 'The most effective agent in weathering is warm water' (Leeper and Uren, 1993, p. 47), and so temperature (and hence elevation) are cited as further controls.

geology The relatively homogeneous acid-volcanic geology of the study is unlikely to be a strong control of soil properties. Leeper and Uren (1993, p. 48) note that in krasnozem soils (which dominate the study area) severe leaching obliterates the compositional influence of geology.

surface erosion The existence of incised mountainous terrain implicates erosion as a major influence on the physical structure of the study area - including the soil. Landslides, mud-slides, and soil creep have all been observed in the study area as agents of significant downslope soil movement (Langford and O'Shaughnessy, 1980a, p. 105; Evans and Joyce, 1974; Hills, 1975; Cecil, 1977). Erosion leads to structural reorganisation of the soil. An example of this is the scattering of floaters throughout some profiles, which is explained by Langford and O'Shaughnessy (1980a) as the detritus of erosive events. Additionally, mixed soil horizons, loose surface rocks, and thin A1 horizons are evidence of erosion. Environmental controls of erosion include surface slope and moisture.

vegetation The soil and vegetation of the study area are inter-related through nutrient cycling (Feller, 1978, 1980, 1981). In the surface horizons, vegetation influences soil nutrient supply. A tree which is better able to circulate large quantities of nutrients is better able to keep these nutrients from being available for leaching out of the soil. A dynamic equilibrium occurs where less degraded soils occur beneath more productive forests (Leeper and Uren, 1993, p. 45). This phenomenon has been observed in the study area (Langford and O'Shaughnessy, 1980a, p. 41). An additional connection between vegetation and soil arises from the macropores which are left in place of decomposed roots and which are a strong influence on soil hydraulic conductivity (Davis, in prep.).

animals Apart from the myriad macro-invertebrates and microscopic organisms which manipulate the organic horizons, at least three large species are well known for causing bulk soil movement. Both wombats and freshwater yabbies excavate holes which become preferred paths for water movement. Adamson et al. (1983) report lyre birds near Sydney turning over 63 tonnes of debris per hectare per year and therefore being a significant geomorphic agent. Lyre birds are abundant within the study area. The environmental controls which apply to the distribution of these animals therefor apply also to soil property distribution.

logging and fire There are at least two influences of logging and fire on soil properties. Firstly, the high conductivity of deep krasnozems despite their high clay content is explained partly by clay chemistry (Leeper and Uren, 1993, p. 76), and partly by the abundance of water stable aggregates in these soils (Attiwill and Leeper, 1987, p. 8). Water stable aggregates may break down following logging (decreasing conductivity) (Attiwill and Leeper, 1987, p. 8) or they may be increased in number following fire (increasing conductivity) (Attiwill and Leeper, 1987, p. 192). Secondly, soil compaction at log landings reduces the infiltration capacity of the soil (Langford and O'Shaughnessy, 1980a). The distribution of logging is environmentally controlled through the avoidance of steep areas, near-stream areas, and un-productive forests. Fire distribution is controlled by factors such as moisture and temperature.

Where soil properties are relatively easily measured, standard interpolation techniques such as kriging, splines, and generalised linear modelling (GLM) may be used to map the properties with respect to environmental controls such as those flagged above (e.g. McKenzie and Austin, 1993). However, in deep soiled, forested areas soil properties can be very difficult to measure reliably (Davis, in prep.). Alternatives to measurement based interpolation include expert based approaches, where the knowledge of a local soil expert is formally recorded and used in place of measurements. Fuzzy set theory (Zimmerman, 1991) can be applied in this sense as an expert based approach to soil mapping (Droesen and Geelen, 1993; Zhu, 1994; Zhu and Band, 1993). The method works with soil 'types' which are defined continuously (as opposed to discretely with sharp boundaries) over the landscape and from which soil properties may be inferred. It suffers however from the problem of making objective classifications of soil type (see for example Powell et al., 1994; and McBratney et al, 1992) and the possibility that there may be no expert who has sufficient knowledge of controls on soil property or type distribution in the area of interest.

In the present study it was decided to commence a soil mapping investigation, starting by measuring some simple soil properties across a range of environmental gradients. The properties chosen initially were soil depth and transmissivity (the depth integral of conductivity). The environmental gradients of interest were precipitation, elevation, vegetation, surface slope, upslope area, and distance from streams. The following field investigations were conducted:

hand augering Hand augering was trialed as a means of both measuring soil depth and transmissivity (in conjunction with Campbell's work at Ettercon 3, in prep.). Whilst in some areas of Ettercon 3 holes were able to be augered to over ten metres depth, the norm was to encounter numerous floaters in the first few metres of the soil profile. In other parts of the study area, shallow floaters were repeatedly encountered in areas where the soil was expected to be very deep. Hand augering was therefore abandoned.

seismic survey Seismic survey was used by Langford and O'Shaughnessy (1980a, p. 43) to measure soil depth beneath a short section of road within the study area. For the present study, in conjunction with Campbell (in prep.), a 12 channel seismograph was trialed at Ettercon 3 for the same purpose. Depth measurement was conducted at four locations. Each measurement used 12 geophones placed along a 200 m survey line parallel to the contours. A large sledge hammer and iron plate were used as the vibration source. Suitably strong reflections were recorded digitally from all 12 geophones. In the subsequent laboratory analysis it was difficult to separate bedrock reflections from ground water and saprolite reflections. It was inferred that there is no clear soil/bedrock interface, and any interfaces which do occur exhibit strong spatial variability. Nevertheless, approximate measurements were obtained from the data (as used for testing of water table level predictions in Section 10.2.11.1). Unfortunately however, the method was found to be too cumbersome and time-consuming to be practical in a large scale mapping context.

roadside cutting survey Given the unsuitability of other techniques, a crude but simple survey of roadside cuttings within the study area was undertaken. Every road within the study area (some hundreds of kilometres) was searched for high roadside cuttings. The higher cuttings were around 8 metres high, occasionally exposing fractured bedrock. At each significant cutting a systematic survey of the vertical profile was undertaken using techniques drawn from McDonald and Isbell (1990).

Rope abseils were used for access to high parts of the profile. Attention was paid to quantifying the relative volumetric extent of floaters, and hand measuring the texture of the intervening soil with a view to estimating hydraulic conductivity using tables and charts given by Rawls and Brakenseik (1989) (note that there are numerous problems associated with inferring hydraulic conductivity from soil texture, Greacen and Williams, 1983, p. 512). The exercise was considered exploratory and results are only reported briefly here. Numerous profiles contained a dense layer of floaters at about one metre from the surface, above about 5-10 metres of relatively floater-free gradational red clay loam. These are clearly the floaters which confound hand augering surveys. The bottom of the soil was often very difficult to locate. In most cases, an irregular and overlapping gradation through soil, saprolite, decomposed bedrock, and fractured bedrock was observed before anything which could be considered solid bedrock was encountered. In the complete absence of soil, roots up to about 10 mm in diameter were frequently observed penetrating fractures within what might otherwise be considered solid bedrock. This indicates, as supported by Heislers (1993), that the water table frequently lies far from the surface within deep, fractured bedrock. Within one profile a mass of rock about 2 metres deep was encountered *above* further soil layers (sandy clays). Shallow rock and out-cropping occurred in seemingly un-predictable locations. This confounded attempts to relate profile depth to environmental variables. No clear relationships were evident.

Following these preliminary investigations, the soil mapping exercise was deemed unsuccessful given the time available. Hence, it was decided to treat soil parameters as lumped parameters.

As described below, some of the soil parameters within Macaque, such as those describing volumetric water content limits and vertical hydraulic conductivity, are relatively insensitive and will not be greatly affected by this decision. The parameters which *will* be affected significantly are those which relate to terrain slope, lateral hydraulic conductivity, and soil depth such as the hydraulic gradient (Δ_z), the lateral redistribution factor (δ), and the slope of the saturation deficit with respect to the wetness index (Δ_{sat}). The latter two are not strictly soil parameters but rather 'hillslope' parameters (see Sections 5.3.1.3 and 5.3.1.4) whose values is largely determined by deep lateral hydraulic conductivity and soil depth. All three (Δ_z, δ, and Δ_{sat}) exert a strong influence on hydrograph shape (Chapters 10 and 11). In the absence of spatial information on soil depth, these two parameters must be

included in the list of highly sensitive parameters (Table 5.2) and calibrated against observed streamflow hydrographs from various catchments as well as expected water table levels (Chapters 10 and 11). Calibrated values vary with catchment size and terrain although the systematism of this relationship has not been quantified.

A description of the (lumped) parameterisation of soil parameters follows. Most of the data used are based on measurements from the Ettercon 3 experimental catchment and are biased as such. Ettercon 3 exhibits a deep, gradational soil typical of the region but is not as steep as many of the slopes of the study area.

5.3.11.3   Volumetric water content

The volumetric water content of the soil at saturation and at air-dryness, θ_{sat} and θ_{res}, essentially relate soil water depth to true soil depth. Macaque mainly works with soil water depth, and true depth is only occasionally used (e.g. vegetation rooting depth). Given the conceptual, calibrated nature of the sub-surface representation within Macaque, it is unlikely that the overall model operation is particularly sensitive to these parameters.

Values of 0.67 m(water) m^{-1}(soil) for θ_{sat}, and 0.2 m(water) m^{-1}(soil) for θ_{res} were used following analyses presented by Campbell (in prep.) using soil moisture tension data collected by Davis (in prep.). The data do not clearly point to specific values but indicate a range of values from about 0.4 to 0.7 for θ_{sat} and 0.1 to 0.3 for θ_{res}. Similar ranges may be inferred from Langford and O'Shaughnessy (1980a).

5.3.11.4   Hydraulic conductivity

Parameters characterising both saturated and unsaturated hydraulic conductivity are required by Macaque.

The vertical profile of saturated hydraulic conductivity is expressed by: a surface or maximum value, $K_{sat,surf}$; a minimum value, $K_{sat,min}$; and a shape parameter, f, which controls the rate of exponential decline from the surface to the minimum with increasing soil depth (measured as saturation deficit). The surface value is used in the calculation of baseflow, along with the hydraulic gradient parameter, Δ_z. Whilst it directly controls baseflow, it can be effectively set to some physically realistic value whilst the gradient can be calibrated to produce appropriate baseflow characteristics.

The other sub-model where the three saturated hydraulic conductivity parameters are used is in the calculation of recharge from the unsaturated zone to the saturated zone, where they are used to calculate the saturated vertical hydraulic conductivity at the depth of the water table. This value is then combined with the single parameter for unsaturated hydraulic conductivity, n, in the Van Genuchten model of unsaturated hydraulic conductivity to estimate the recharge. Many aspects of this sub-model are uncertain, such as the sensitivity of water balance and associated dynamics to these parameters, and the realism of the sub-model. Simulations to date indicate that none of the parameters are as sensitive as their counterparts in fully distributed models (FDMs). In FDMs such as Topog and SHE, hydraulic conductivity parameters are used to control lateral redistribution of water and hence water table levels, whereas in Macaque, this control and the associated sensitivity is transferred to the conceptual hillslope and lateral redistribution parameters, Δ_{sat} and δ. It appears that whilst changing the hydraulic conductivity parameters changes the amount of water in the unsaturated zone, the rest of the model is not greatly affected by this. Recharge, and hence baseflow, *is* affected by changes to n.

Values for $K_{sat,surf} = 5.0$ m day^{-1}, $K_{sat,min} = 0.40$ m day^{-1}, and $f = 2.0$ m^{-1} were fitted to measurements made by Vertessy et al. (1991), Davis (in prep.), and Lorieri et al. (in prep.) within the deep soils of the study area using both a constant head well permeameter (CHWP) and the auger hole method (van Beers, 1983) as shown in Figure 5.10. CHWP and auger hole techniques are least likely to be affected by confounding factors such as macropores, unconnected soil pipes, and related small scale heterogeneity. Other measurement techniques have been used by Campbell (in prep.), Davis (in prep.), and Langford and O'Shaughnessy (1980a), yielding a wide range of values.

Campbell (in prep.) fitted Van Genuchten soil moisture tension curves to data collected by Davis (in prep.), yielding values for the n parameter of 1.374 and 1.166 for two soil depths at Ettercon 3. These values were used as seeds within Macaque and subsequently calibrated within the range 1.1 to 2.0 to match observations of soil moisture made by Langford and O'Shaughnessy (1979b) as well as expected temporal recharge and baseflow patterns. A final value of 1.25 proved satisfactory, typically predicting volumetric water content in the range 30% to 50%.
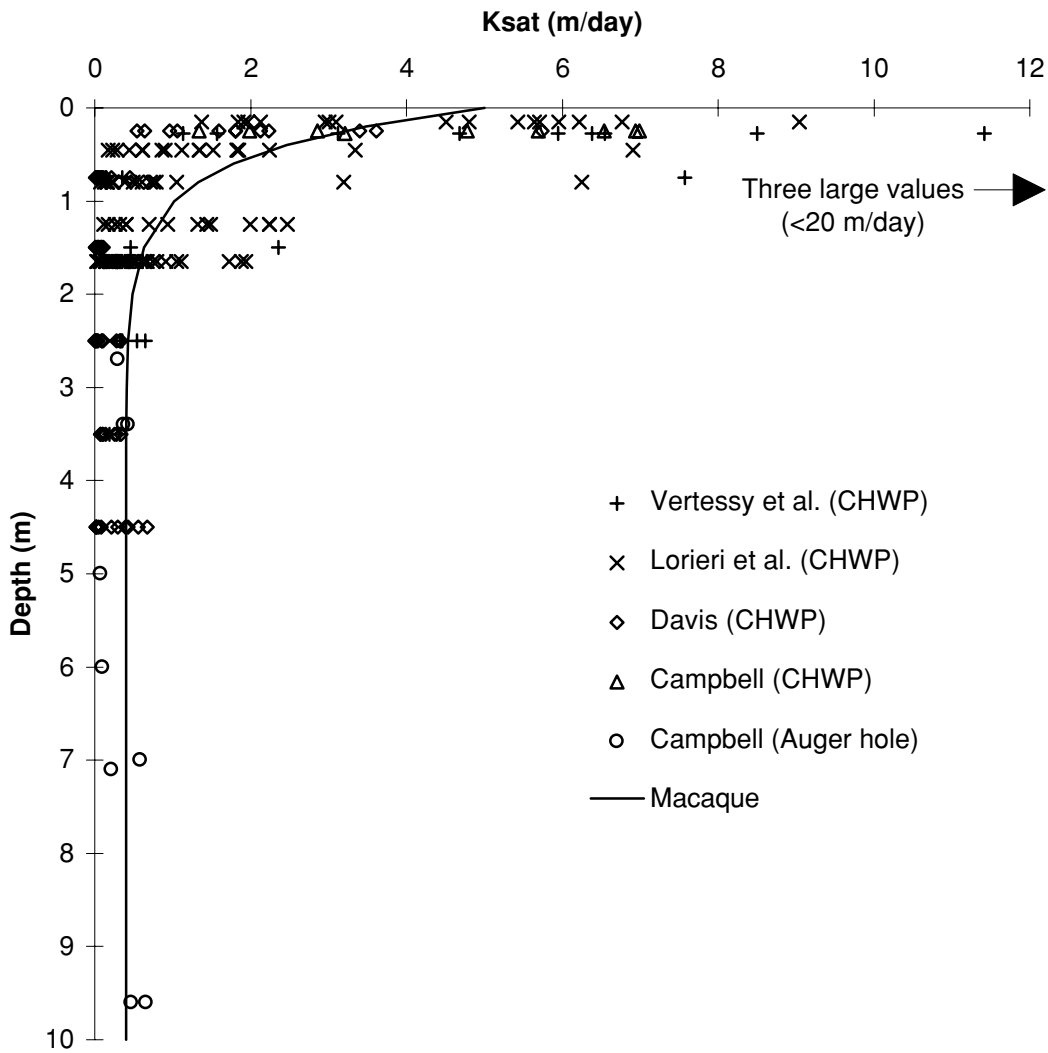
Figure 5.10: Measurements of saturated hydraulic conductivity made by Vertessy et al. (1991), Campbell (in prep.), Davis (in prep.), and Lorieri et al. (in prep.) at Ettercon 3, overlaid with the conductivity profile implemented within Macaque. Note that an outlier from Campbell's data at 7.15 metres depth was removed because the corresponding auger hole barely penetrated the water table (R. Campbell, pers. comm.)

5.3.11.5 Hydraulic gradient

The hydraulic gradient within the saturated zone at the point of exfiltration of baseflow, Δ_z, controls the rate of baseflow exfiltration per unit saturated area. Because evapotranspiration in the study area is predominantly *not* water limited, evapotranspiration controls the water balance and, by subtraction, net streamflow. Thus, changing the parameters that affect baseflow simply changes the saturated area required to release an unchanging total flow. Typically, reducing Δ_z will result in increased saturated area and decreased baseflow index (the ratio of baseflow to total flow).

An initial value for the hydraulic gradient was taken from water table gradients measured at Ettercon 3 by Campbell (in prep.) between about 0.0 and 0.1, with summer values typically around 0.015 and winter values typically around 0.05. The model value was calibrated to optimise both saturated area and baseflow index using visual observations of hydrographs and maps of typical winter and summer saturated areas across the study area. A value of $\Delta_z = 0.005$ was used in the standard parameter set for use with the Ettercon 3 experimental catchment, whilst a value closer to those measured, $\Delta_z = 0.01$, was used in full catchment simulations.

5.3.12 Evapotranspiration parameters

5.3.12.1 Vegetation rooting depth

The vegetation rooting depths for the canopy and understorey, $z_{c,max}$ and $z_{u,max}$, determine the depth of soil from which the vegetation is able to withdraw water. In the non-water limited areas which comprise most of the study area, the values do not affect transpiration greatly, but have an influence on the shape of the water table. In water limited areas, the values should be a control on transpiration.

Data on *Eucalyptus regnans* rooting depths can be inferred from a number of sources. Using piezometers, Campbell (in prep.) observed daily water table fluctuations from 56 year old trees at depths up to 6.0 m. Whilst the amplitude of the fluctuations (c 4 cm) is comparable to that which may be due to variations in barometric pressure (1.5-6 cm; Freeze and Cherry, 1979, p. 234; Turk, 1975) the consistency of the sinusoidal pattern reported by Campbell suggests that they are caused by evapotranspiration rather than atmospheric changes, which would be more variable. Below this, no effect was observed. This implies that the roots of these trees can draw water from

up 6.0 m depth either directly, or through capillary rise. This concurs with observations by Ashton (1975) of *sinker* roots extending to 2.1 m beneath 40 to 80 year old trees, and fine roots extending to 5.0 m beneath mature (> 100 year old.) trees. Also, Langford and O'Shaughnessy (1979b, p. 29) observed roots to 5.5 m depth for 40 year old trees.

Ashton (1975) observed understorey rooting depths beneath *E. regnans* to be much shallower than for *E. regnans* itself. A typical species, *Pomaderris aspera*, was observed to have roots descending to 65 cm.

No data on rooting depths for other canopy species were obtained.

Values of 4.0 m for canopy roots and 2.0 m for understorey roots were used in Macaque, regardless of species. In future, these values should be chosen to vary with species, and age. Ashton's (1975) observations, for example, provide data on age variations of rooting depth within *E. regnans* forest.

5.3.12.2 Leaf water potential

Leaf water potential (LWP) is an inverse measure of the water stress of leaves and its dependence on soil moisture (Salisbury and Ross, 1992). The representation of leaf water potential provides an intermediate physical step between soil water and its effect on leaf conductance. In a manner inherited by Macaque from FOREST-BGC, parameters are defined expressing the maximum and minimum (stomate closing) potentials for both canopy and understorey leaves: $\psi_{cl,max}$, $\psi_{cl,close}$, $\psi_{ul,max}$, and $\psi_{ul,close}$, and a slope parameter $\Delta_{\psi,l}$ which controls how quickly LWP descends from maximum toward closure values with decreasing relative soil water availability. In the absence of detailed observations of LWP, the effect of the slope parameter can be countered by changing the maximum and closure parameters, and hence the remainder of the model is not sensitive to the *absolute* values of these parameters. However, limited observations of LWP can be used to set realistic values for the maximum and minimum values, leaving the slope parameter as a strong control on LWP and leaf conductance in water limited situations.

Particularly within tall forests such as *E. regnans* forests, LWP varies markedly with height above the ground or phreatic surface (Connor et al., 1977). Thus, model values must represent some effective mean. Their quantification and interpretation in physical terms is confounded by the different heights at which measurements are taken, and the fact the trees of different ages have different heights. For *E. regnans*, Connor et al. (1977) measured maximum

LWP values near the top of the canopy of around -0.5×10^5 Pa. They also observed an instance of stomatal closure at -2.2×10^5 Pa but another instance of non-closure at the more water stressed value of -2.4×10^5. Thus, canopy values of $\psi_{cl,max} = -0.5 \times 10^5$ and $\psi_{cl,close} = -2.3 \times 10^5$ are used for this study. This is consistent with the range of values used in RHESSys and FOREST-BGC modelling studies (Running and Coughlan, 1988; Hatton et al., 1993; Scuderi et al., 1993; L. Band, Dept. of Geography, Univ. of Toronto, pers. comm.) as well as a wide range of LWP measurements from various eucalypt forests (Journet, 1979; Sinclair, 1980; Pook, 1985; Hookey et al., 1987; Crombie et al., 1988). There are no data to suggest that different values be applied to different *Eucalyptus* species within the study area. There are also few comparative data on the LWP of canopy and understorey species at a site. In water stressed understorey species beneath eucalypt forests slightly drier than those of the study area, Crombie et al. (1988) observed LWP slightly lower than that observed in the eucalypts. However, in the rarely water stressed environment of the study area, there are no data to suggest using different LWP parameters for understorey and canopy. Hence, the understorey parameters, $\psi_{ul,max}$ and $\psi_{ul,close}$, were set to the same values as for the canopy.

Based solely on previous values used within FOREST-BGC (0.2 MPa used by Running and Coughlan, 1988; 0.05 MPa used by Scuderi et al., 1993), the slope parameter was set to a value of $\Delta_{\psi,l} = -1.0 \times 10^5$ Pa (0.1 MPa).

5.3.12.3   Leaf conductance

Macaque requires maximum and minimum (cuticular) leaf conductances for the canopy and understorey: $g_{cl,max}$, $g_{cl,min}$, $g_{ul,max}$, and $g_{ul,min}$. Transpiration is very sensitive to the maximum values and hence these are two of the most important parameters in the model. Maximum leaf conductance values vary with species and, in some cases, with leaf age (Dingman, 1994, Tab. 7-5). Values ranging from around 0.0029 to 0.025 m s^{-1} are reported although, on average, there is little difference between the major vegetation types of the world (Körner, 1994, Tab. 22.2; Kelliher et al, 1995).

From a variety of observations made on six separate days, Connor et al. (1997) observed a maximum leaf conductance for *E. regnans* of 0.0091 m s^{-1} (although, inexplicably, Korner cites Connor et al's maximum as a value which converts from mmol m^{-2} s^{-1} to about 0.0043 m s^{-1}). In a similar study in South Australia, the maximum conductance measured by Sinclair (1980) for *E. obliqua* was about 0.002 m s^{-1} (although Korner cites this study as

reporting a maximum of 0.0055 m s^{-1}). In modelling studies in *E. regnans* forests using Topog, Vertessy et al. (1993) used a values of 0.0039 m s^{-1}.

There are limited data on maximum understorey conductance. The best indications to date are from recent work in the study area by R. Vertessy and J. Buckmaster (CSIRO Land and Water, Canberra) which found that water use per unit leaf area of a typical understorey to *E. regnans* was 37% lower than for the canopy. Whilst environmental factors particular to the understorey (such as increased aerodynamic resistance and decreased radiation) may partly explain this difference, they are unlikely to effect the full reduction. Rather, it is likely that maximum understorey leaf conductance is lower than for the canopy. This concurs with data from Northern Hemisphere deciduous forest (Roberts and Rosier, 1994). Some numerical experimentation would be required in order to quantify the reduction. In the present study, which pre-dates the above work, understorey and canopy values were set to be equal and the possibility of reduced understorey values is acknowledged in the discussion of results.

Minimum conductance for eucalypts is very small (Aston, 1984). The minimum value measured for *E. regnans* by Connor et al. (1977) was 0.00035 m s^{-1}, which is consistent with the general *Eucalyptus* value given by Körner (1994) (0.0002 m s^{-1}).

In the present study, the maximum conductance parameters were used to ensure a realistic water balance and hence were calibrated with consideration of the above values. This resulted in a final value of 0.005 m s^{-1} for both $g_{cl,max}$ and $g_{ul,max}$. The minimum values, $g_{cl,min}$ and $g_{ul,min}$, were set to Körner's value of 0.0002 m s $^{-1}$.

The effect of air temperature, VPD, and radiation on leaf conductance is expressed using a number of parameters taken directly from the Running and Coughlan (1988) model upon which Macaque's leaf conductance submodel is based. These parameters are conceptual parameters which must be calibrated using experimental leaf conductance data, and against the overall operation of the model:

Two separate parameters, $\Delta_{g,T}$ and $\Delta_{f,T}$, express the dependence of leaf conductance on air temperature for above and below freezing conditions respectively. Their values, $\Delta_{g,T} = 0.0002$ m s^{-1} °C^{-1} and $\Delta_{f,T} = 0.0003$ °C^{-1} have been taken directly from North American applications of RHESSys (L. Band, Dept. of Geography, Univ. of Toronto, pers. comm.). Practically, they induce little effect on leaf conductance, which is probably of little consequence for temperatures between about 5 and 30° C but inappropriate otherwise.

At temperatures around 0° C, Slatyer (1976) observed stomatal closure in the alpine species, *E. pauciflora*. For intermediate temperatures between 15 and 25° C, Wong and Dunin (1987) observed no temperature/conductance response in *E. maculata*. And at the other end of the scale, observations made by Pietsch (1975) and Legge (1985) indicated stomatal closure of *E. regnans* at high temperatures (*c.* 32° C). These observations imply a modal temperature/conductance model as opposed to the monotonic model currently implemented for Macaque and inherited from FOREST-BGC (which was developed in cold climates). In future, an alternative model such as that reviewed by Dingman (1994) may be more appropriate. The current model does not preclude the sensible operation of Macaque as a whole within the study area considering that ameliorative temperatures persist at most sites for most of the year.

A further two parameters, $\Delta_{f,cl,D}$ and $\Delta_{f,ul,D}$, express the influence of VPD on leaf conductance for the canopy and understorey respectively. Applications of Topog within the study area have suggested that, in this way, VPD is an important control on seasonal variations in transpiration. Initial trials with Macaque have followed similar lines, with strongly negative (e.g. -0.0004 Pa^{-1}) values for the two parameters being necessary to prevent winter transpiration being too low relative to summer transpiration. Whether a causal relation for *E. regnans* is implied by these observations cannot be determined without more detailed investigation.

Hookey et al. (1987, e.g. Fig. 3) provide the most detailed data on leaf conductance/VPD relations for eucalypts. They give curves for over 20 eucalypt species in a Western Australian plantation which indicate a uniformly strong dependence. When scaled by maximum conductance, all curves exhibit approximately the same non-linear shape which can easily be approximated by a linear model as in Macaque. The only species studied by Hookey et al. which is found in the study area is *E. viminalis*. By fitting a straight line over the curve pertaining to *E. viminalis*, a value for the *relative* change in leaf conductance per unit VPD of $\Delta_{f,cl,D} = -0.00018$ Pa^{-1} was inferred. Also drawing on Hookey et al's data, Leuning et al. (1991) effectively used the same value in a slightly different conductance/VPD expression within the BIOMASS model. Alternate data were drawn by Hatton et al. (1993), in a FOREST-BGC modelling study, from physical measurements made by Wong and Dunin (1987). After conversion from absolute humidity to vapor pressure units (Monteith and Unsworth, 1990, Eqn 2.26), Hatton et al's value for *E. maculata* and *E. populnea* woodland becomes -0.00031 Pa^{-1} (assuming an air temperature of 10° C). This is similar to the original value used by the authors of FOREST-BGC (Running and Coughlan, 1988; see also,

Scuderi et al., 1993) which converts to -0.00038 Pa^{-1}, but almost twice as high as the value implied by Hookey et al's data. Here, an approximate median value of $\Delta_{f,cl,D} = -0.0003$ Pa^{-1} is taken initially, but some calibration against streamflow and transpiration data is expected. As usual, there is no information on understorey species so the value of $\Delta_{f,ul,D} = -0.0003$ Pa^{-1} is tied to that for the canopy.

Two final parameters, $S_{thresh,c}$ and $S_{thresh,u}$, allow for low radiation to limit leaf conductance of the canopy and understorey respectively according to a threshold mechanism. Wong and Dunin (1987) provide some data on the dependence of CO_2 assimilation rates (which can be converted to conductances) on radiation. At some stage, data such as these should by used to quantify the above parameters. To date, this exercise has not been undertaken so the parameters were set to zero, indicating no limit of conductance by daytime radiation levels.

5.3.12.4 Aerodynamic resistance

The aerodynamic resistance to the transfer of water vapor from vegetation to the atmosphere above is a conceptual measure of the degree to which factors such as calm winds and rough vegetation slow the atmospheric mixing processes which cause water vapor to diffuse upwards, away from the humid environment of a vegetated surface. Within Macaque, aerodynamic resistance is represented by three variables, $r_{aero,c,ref}$, $r_{aero,u,c}$, and $r_{aero,s,u}$, which act *in series* to quantify resistances progressively from the soil through the understorey and the canopy to a reference level within atmosphere above.

By assuming that boundary layer processes controlling the transfer of water vapor and momentum (and heat) are the same, a theory can be developed which allows the estimation of aerodynamic resistance based on measurements and of assumptions of vertical wind speed profiles (Thom, 1975; Campbell, 1977; Shuttleworth and Wallace, 1985; Oke, 1987, App. A2; Choudhury and Monteith, 1988; Choudhury, 1989; Shuttleworth, 1991a, b, 1993). Typically, a logarithmic wind speed profile is assumed down to a critical height within the vegetation at which wind speed is zero.

Numerous authors have made use of this theory. Values for forests of about 5 to 12.5 s m^{-1} for a variety of wind speeds are given in tables and charts by Oke (1987, Tab. 4.2), Choudhury (1989), and Dingman (1994, Fig. 7-9). Modelling studies have used a similar range of values (10 s m^{-1}, Connor et al., 1977; 10 to 30 s m^{-1}, Aston, 1984; 6.8 s m^{-1}, McMurtie et al., 1990a; 12 s m^{-1}, Hatton et al., 1992, 1993; 12 s m^{-1}, Vertessy et al., 1991; 15

s m^{-1}, Vertessy et al., 1996). Only some of these either reproduce or cite the essential theory and assumptions (e.g. Silberstein and Sivapalan, 1996; Hatton et al., 1995).

All the above citations effectively assume a logarithmic wind profile. This breaks down when one considers aerodynamic resistance from the soil and understorey to higher layers because the soil and understorey usually lie below the point at which wind speed is assumed to be zero. Only a few modelling studies have described aerodynamic resistance for multi-layered forests (e.g. Wigmosta et al., 1994; McMurtie et al., 1990a). Citing complex theory presented by van de Griend and van Boxel (1989), Vertessy et al. (1996) used values in *E. regnans* forest which translate to: $r_{aero,c,ref} = 15$ to 20 s m^{-1}, and $r_{aero,u,c} = 15$ s m^{-1}. No value was given for $r_{aero,s,u}$. With unreferenced parameters, McMurtie et al. (1990a) chose a greater difference between understorey and canopy. Their values translate to $r_{aero,c,ref} = 6.8$ s m^{-1} and $r_{aero,u,c} = 75$ s m^{-1}.

A number of authors cite the important point made by McNaughton and Black (1973) that, relative to leaf resistance, aerodynamic resistance is generally small and hence is only a weak control on evapotranspiration in both reality and in models using the Penman-Monteith equation (Aston, 1984; Connor et al., 1977). However, it has not been investigated whether this insensitivity remains over long periods, such as throughout the life of an *E. regnans* forest growing from zero to > 100 m in height with accompanying changes in the relative densities of canopy and understorey leaves. Additionally, if the high understorey values given by McMurtie et al. (1990a) are to be believed, then aerodynamic resistance *can* approach similar values to leaf resistance.

In the present study, the following values for aerodynamic resistance were adopted, largely following Vertessy et al. (1996) and assuming equal resistance between the soil and understorey as between the understorey and canopy: $r_{aero,c,ref} = 15$ s m^{-1}, $r_{aero,u,c} = 15$ s m^{-1}, and $r_{aero,s,u} = 15$ s m^{-1}. Improved values might be obtained by combining the theory cited above with measurements of vertical profiles of wind speed in different vegetation types within the study area. Use might also be made of data on larger scale variations in wind speed and wind run given by Hutchinson et al. (1984).

5.3.12.5 Soil water extraction

The parameters $p_{c,sat}$ and $p_{u,sat}$ indicate the *nominal* proportions of canopy and understorey transpiration that should be drawn from the saturated zone

as opposed to the unsaturated zone. They influence the moisture content of the unsaturated zone, as well as the shape of the water table. In water limited situations, they should also influence transpiration by controlling the manner in which the soil is dried, thereby limiting water availability and transpiration. Values range from zero, indicating a phreatophobic plant drawing no water from the saturated zone, to one, indicating a phreatophyte which only draws water from the saturated zone.

For *E. regnans*, Ashton (1975) observed that roots do not penetrate the summer water table, indicating that the species is not particularly phreatophytic. This is supported by Incoll's (1969) observation that 96% of the root weight of *E. regnans* occurs in the upper 60 cm of soil. Ashton also observed some understorey species, *Leptospermum lanigerum* and *Acacia melanoxylon*, as having roots penetrating 60 to 75 cm into permanently saturated soil.

Based on this limited data, a low (phreatophobic) value of $p_{c,sat} = 0.1$ and a higher (more phreatophytic) value of $p_{u,sat} = 0.5$ was set for all canopy and understorey species respectively.

5.3.12.6 Soil evaporation

The nominal evaporation depth, $z_{s,max}$, is used to control the availability of soil water for evaporation. The value is calibrated to give estimates of soil evaporation contributing 10% to 15% of total evapotranspiration according to measurements made in *E. regnans* forest by McJannet et al. (1996). A typical value is $z_{s,max} = 0.003$ m, which is much smaller than might be expected. A validation of the physical realism of the soil evaporation sub-model is necessary.

The soil tortuosity factor, τ, is a parameter introduced by Choudhury and Monteith (1988), apparently representing the path length that water vapor must travel to move through a unit depth of soil. Choudhury and Monteith's value of $\tau = 2$ is used in Macaque.

5.4   Summary

The operation of Macaque within the study area was described in two parts, respectively on the spatial disaggregation of the study area into elementary spatial units (ESUs), and the description and quantification of the model parameters.

A spatial structure was defined comprising a hierarchy of spatial levels: `world`, `region`, `catchment`, `hillslope`, and `ESU`. The first three of these exist for accounting and reporting, whilst the remaining two have a functional significance. Hillslopes were defined from the terrain using a stream network. Each hillslope is thought of as representing a conceptual soil catena from ridge top to valley bottom. Hillslopes were further divided along the conceptual catena into ESUs defined by intervals of a topographic wetness index. The hillslope/ESU combination is intended to be a parsimonious structure representing the key lines of heterogeneity and areas of homogeneity within the study area.

Macaque defines over seventy parameters and each of these must be quantified on either a lumped or distributed basis. The distributed parameters are dealt with in Part III below. Each parameter was described in terms of: what it represents physically, its role within the model, its acceptable range and likely value qualified by some estimate of uncertainty. The level of detail in these descriptions and its review of data sources exceeds perhaps any other description in the literature on physically based hydrological modelling. This is intended as a response to concerns in the literature about parameter uncertainty and lack of realism (Beven, 1996; Refsgaard, 1997).

A rough breakdown of the data sources is as follows. Thirty-two parameters were derived from local measurements, and nine from measurements reported in the literature. Ten parameters were calibrated against internal model variables, and seven from internal calibration reported in the literature. Of the remainder, five were not used, five defaulted from values given for other parameters, two were inferred from observations reported in the literature, and two were quantified through a mixture of measurement and internal calibration.

None of the parameters were calibrated solely against streamflow hydrographs, and every parameter was in some way related to physical measurements. This is a unique, desirable, and deliberate situation, once again intended as a response to concerns in the literature about the lack of attention to the internal validity of models.

However, wholesale optimism is not entirely due. There remain eight parameters which are listed in the parameter summary in Table 5.2 as having 'high sensitivity relative to certainty'. Whilst they may be related to physical measurements, they are only loosely so. A detailed discussion of the effects of this uncertainty is given in the summary to Chapter 10, after the model is tested.

Part III

Parameter mapping

This part describes the mapping of parameters which are supplied to Macaque as spatial maps. There are chapters for each major class of parameters: topography, precipitation, and vegetation. There are two chapters on vegetation. The first deals with the specific issue of estimating the leaf area and leaf area index of *E. regnans* at different ages. The second integrates all aspects of spatial vegetation mapping. It is quite long, owing to the extensive investigations into LAI variability in time and space.

The GRASS GIS, augmented by an array of *original* purpose-written GRASS-compliant GIS software, was used throughout all the spatial operations described herein.

Chapter 6

Topographic mapping

Contents

6.1 Introduction

At large scales in mountainous regions, topography is the dominant control on terrestrial water movement, precipitation, radiation, temperature, and vegetation species distribution. Any physical modelling of these regions must start with some representation of topography. A digital elevation model (DEM) must be constructed, from which model parameters such as elevation, slope, and aspect may be extracted.

This chapter describes the construction of a large DEM for the study area, and its validation against a small DEM constructed using detailed ground data.

As discussed by Moore et al. (1991), DEMs may be constructed in variety of forms (e.g. regular grids, triangulated irregular networks, and contour based networks) using a variety of means (e.g. splines, kriging, polynomials). Spline interpolation over a regular grid has emerged as a popular method in hydrological and geomorphological studies, particularly at large scales. The method has been used in the construction of a variety of standard large scale DEM products available in Australia and elsewhere (e.g. Hutchinson and Dowling, 1991). Following the mathematical development of spline techniques (Wahba and Wendelberger, 1980), the work of Hutchinson (1983, 1987, 1988, 1989, 1991a,b, 1993, 1995a,b; Hutchinson and Bischof, 1983; Hutchinson and Gessler, 1994) and Mitasova (Mitasova and Hofierka, 1993; Mitasova and Mitas, 1993) has been largely responsible for the method becoming more accessible. A surprising number of published distributed hydrological modelling applications omit mention of the methods used to construct the DEMs around which they are based (e.g. Wigmosta et al., 1994; Bathurst, 1986; Band et al., 1993; Polarski, 1997; Vörösmarty and Moore, 1991). Of those studies where DEM origins *are* explained, spline interpolation prevails - e.g. in applications of Topog (Vertessy et al., 1993) and THALES (Grayson et al., 1992a).

At least in Australia, spline interpolation is the *de facto* standard and is used here.

The next section of this chapter describes the construction of a DEM for the whole study area, and is followed by a section on testing the accuracy of this DEM using a smaller, more detailed DEM. The final two sections deal with pit and flat removal and terrain analysis procedures based on the main DEM.

6.2   Full study area DEM

6.2.1   Data

Initially, coarse resolution point data commensurate with the scale of 1:250 000 topographic mapsheets were obtained from AUSLIG, the national mapping agency. A gridded DEM was interpolated over the study area using these data but the resulting representation of terrain (not shown) appeared too coarse and too inaccurate when compared with the data used in previous applications of large scale models such as RHESSys.

Subsequently, 20 metre digital contour data used in the production of 1:25 000 topographic mapsheets were obtained from the Victorian Division of Survey

and Mapping via Melbourne Water. These data were derived using air-photo interpretation (API). The data were converted from the original Intergraph MicroStation GIS format to a format suitable for import to the GRASS GIS using *original* purpose-written MicroStation macro software. The data were stored in GRASS as a list of 235509 three dimensional point co-ordinates. This included some hand-digitised hypothetical points beneath Maroondah Reservoir to ensure that flat terrain was not artefactually represented around the boundary of the reservoir.

6.2.2   DEM interpolation

The point data were then input to a 2D thin-plate smoothing spline interpolation routine written for the GRASS GIS by Mitasova and Hofierka (1993) to produce a regular gridded 25×25 metre DEM.

The interpolation routine takes several parameters which affect the shape of the interpolated surface, and hence the representation of topography. Three of these, `dmin`, `segmax`, and `npmin`, are not sensitive within sensible ranges. A fourth, `smooth`, is always set to a low value (0.01) indicating that no smoothing of 'errors' is desired. The `tension` parameter, however, is an important and sensitive control of the shape of the surface. Its effect can be likened to the tension in a thin rubber sheet being stretched over the data points. High tension can lead to 'steps' in the surface between the locations of the original digital contours. Low tension can lead to 'overshoots' in incised terrain.

It appears to be impossible to choose a tension value which gives a suitable representation of both smooth and rough terrain without steps or overshoots. Using a variety of *ad-hoc* visualisation techniques, a tension of 20 was chosen as the best compromise.

The resulting elevation map was presented earlier in Section 2.1 as Figure 2.4. Accompanying the elevation map are maps of slope and aspect produced by the interpolation procedure (Figures 6.1 and 6.2). The steps in the DEM can clearly be seen in the slope map as curvilinear, contour-like features, especially in steep terrain.
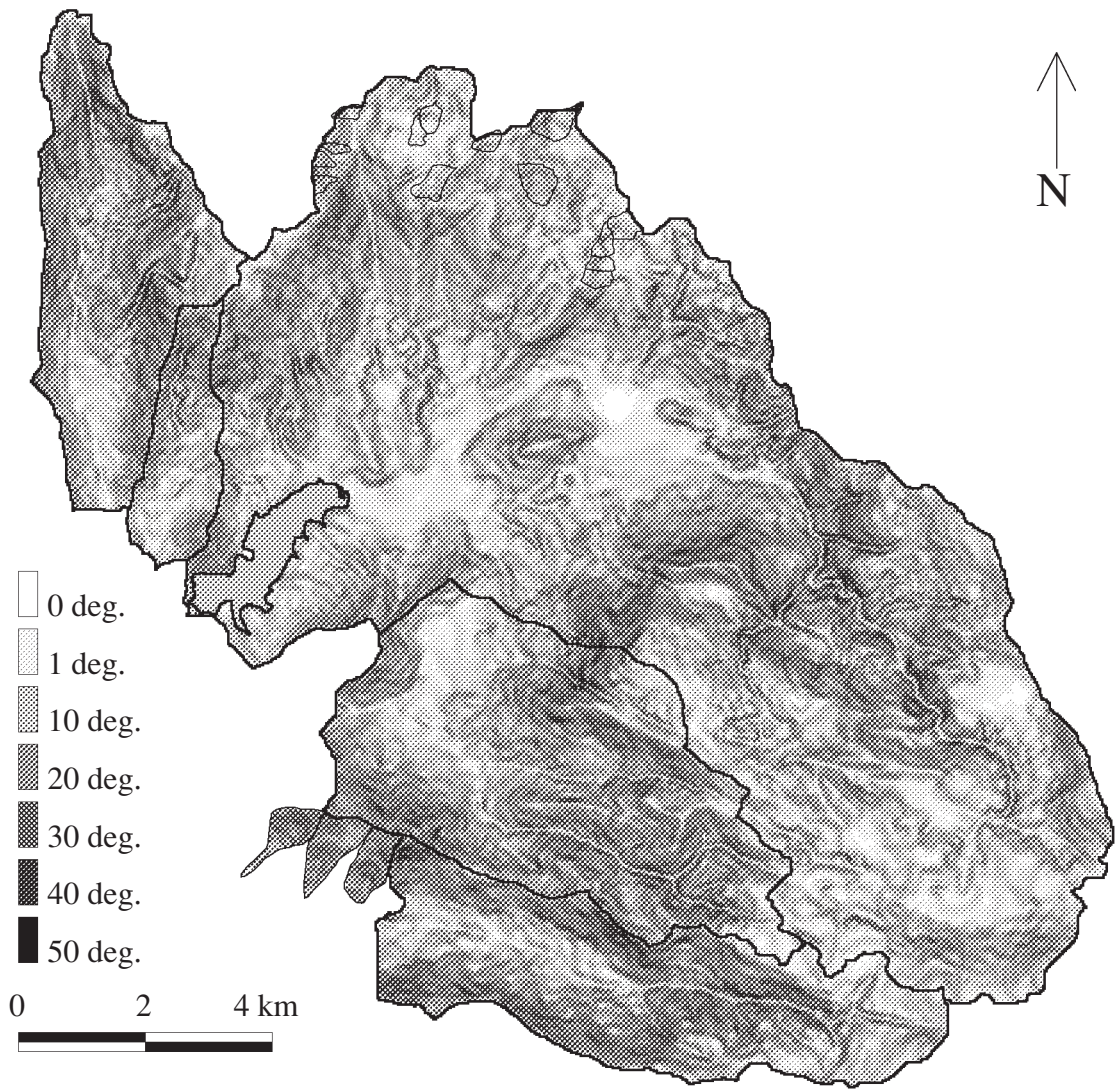
Figure 6.1: Map of terrain slope throughout the study area.
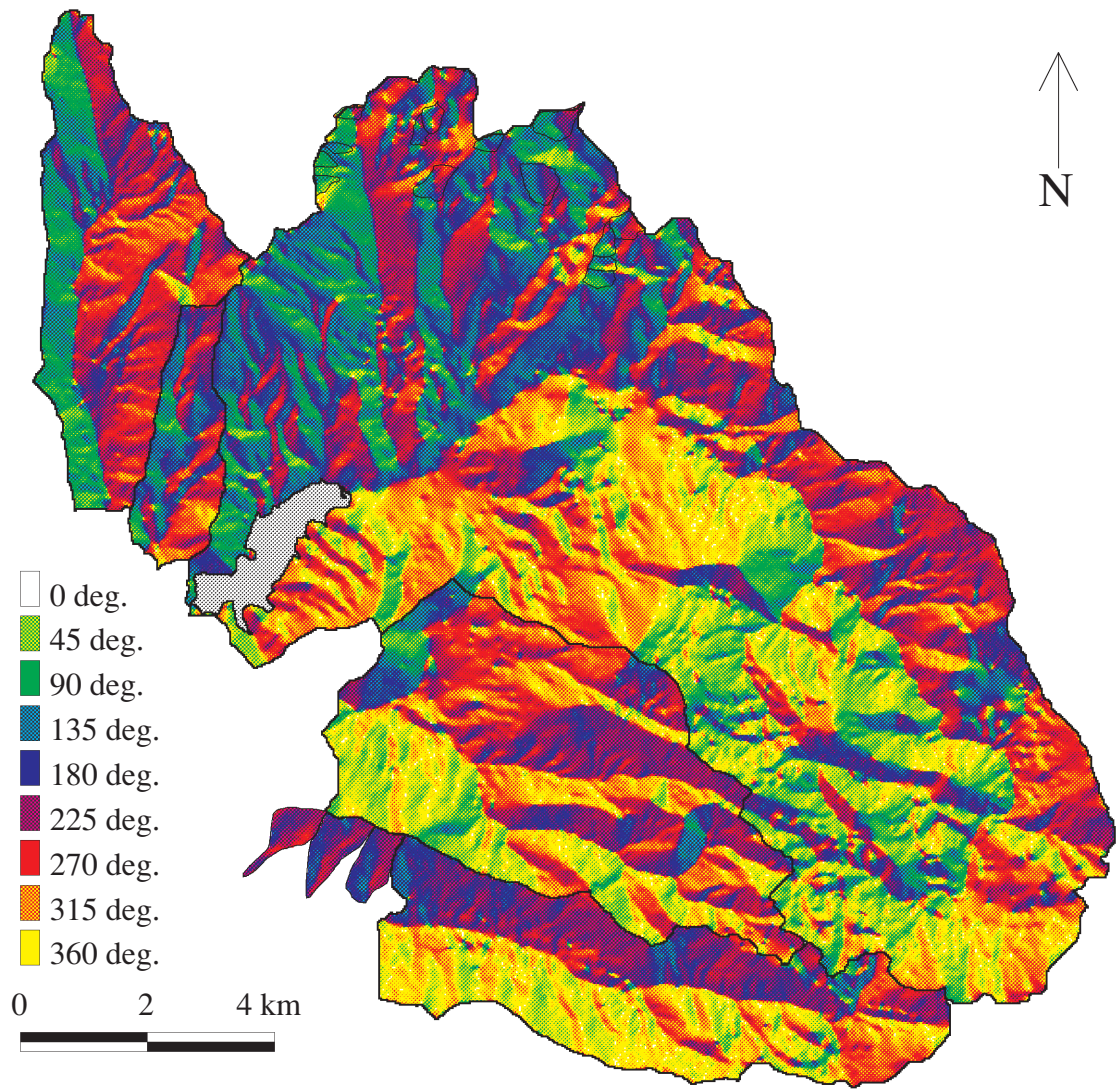
Figure 6.2: Map of terrain aspect throughout the study area.

6.3 Testing the study area DEM

Despite the large number of closely spaced data points typically used to construct large area DEMs, they can be quite inaccurate representations of terrain (Wise, 1995). The accuracy of the study area DEM was tested by conducting a detailed ground survey of a small catchment, fitting a detailed DEM using the survey data, and comparing the two. The Ettercon 3 experimental catchment (15 ha.) was chosen as a suitable site as it exhibited typical relief, and is the site of broader field investigations. The location of Ettercon 3 is shown in Figure 2.3.

Note that parts of this work have been previously published as a conference paper (Watson et al., 1996).

6.3.1 Detailed ground data

A detailed topography survey was made for Ettercon 3 using modern electronic surveying equipment (theodolites, electronic distance measurers (EDMs), prisms, etc.). Control for an arbitrary co-ordinate system was set up using two star pickets driven deeply into the ground. Control traverses were made around the circumference, along the stream, and at various auxiliary points within the catchment. A total of 59 survey stations were installed using star pickets. As many sightings as possible were made from each station to natural surface points within the catchment using a five metre staff. The sightings were extremely difficult due to the dense vegetation. As often as possible, stations were located atop large fallen logs about 2 metres high to promote visibility. Low cloud and persistent rain also limited the range of the EDM. A total of 609 natural surface points were surveyed. The relative error in the co-ordinates determined for these points is locally around ± 0.1 m but as high as ± 0.8 m over large distances. This is poor by surveyors' standards but adequate for the task at hand given the time available (about 20 days in the field).

The surveyed points were coded according to the underlying features such that a feature map could be constructed as well as a DEM. The resulting map is shown in Figure 6.3.
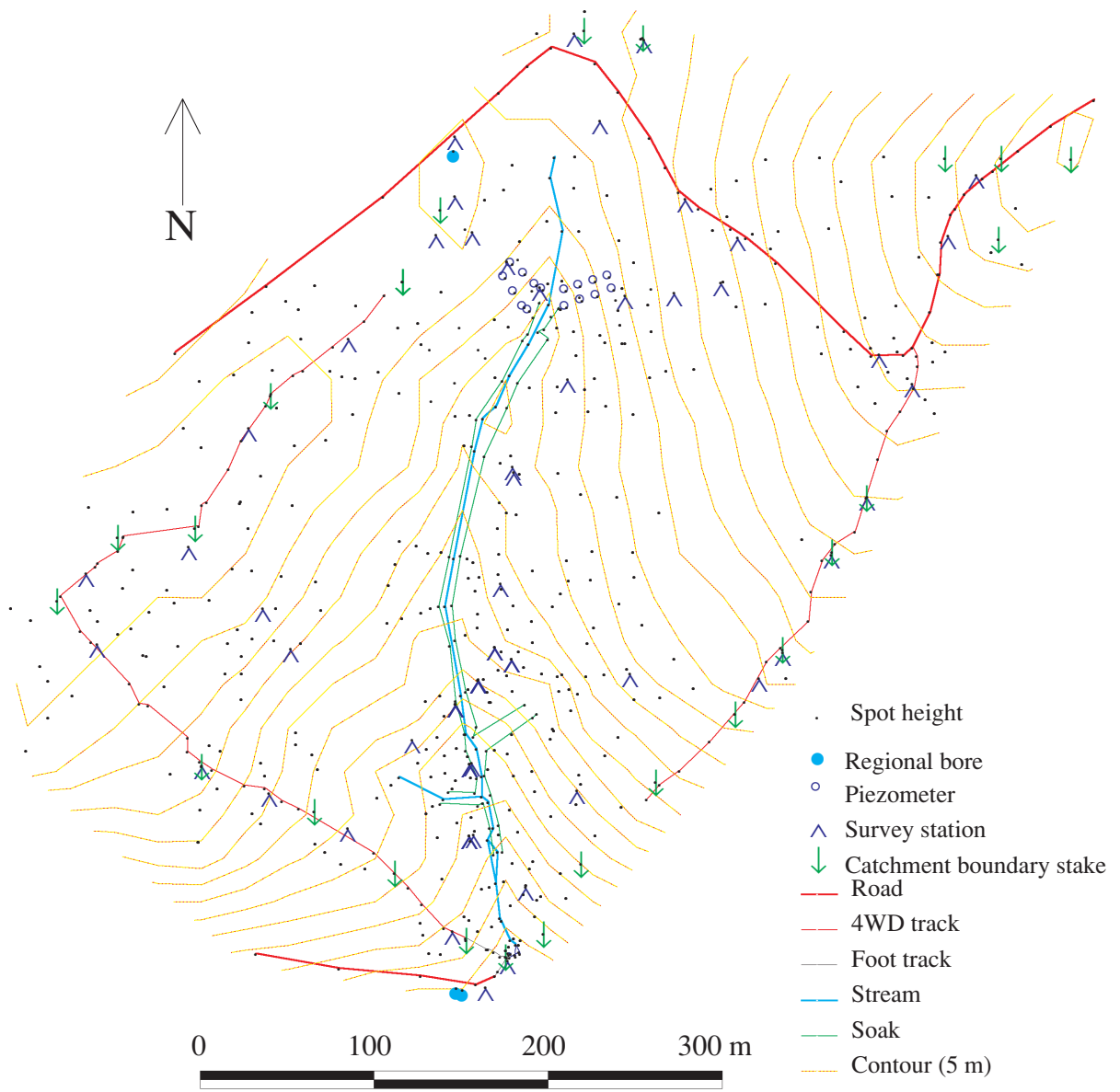
Figure 6.3: Map of the Ettercon 3 experimental catchment constructed using detailed topographic survey.

6.3.2   Detailed DEM interpolation

The data were used to construct a detailed DEM using the interpolation procedure described in Section 6.2.2. Five metre contours were calculated from the DEM and are included in Figure 6.3.

6.3.3   Comparison of the two DEMs

The large DEM and the detailed DEM can be compared in a number of ways. Firstly, contours from each DEM can be overlaid. Figure 6.4 shows the detailed DEM overlaid with the original 20 metre 1:25 000 digital contours from the Division of Survey and Mapping, 5 metre contours derived from the study area DEM (the API DEM), and 5 metre contours from the detailed DEM. Every fourth 'derived' 5 m contour closely follows the corresponding original 20 m contour indicating that the API DEM for the study area is an accurate representation of the topographic information contained in the original contours. However, the 5 m contours from the detailed DEM often diverge significantly from their API 'derived' counterparts, particularly near the stream. The large DEM represents the gully as being much smoother than reality, which is more accurately represented by the detailed DEM.

This gully smoothing was examined using a second comparison of the two DEMs made by examining vertical sections through the DEMs. Figure 6.4 shows the location of a transect extending 500 m west to east across Ettercon 3. The elevations predicted by the two DEMs along this transect are plotted in Figure 6.5. The gully represented by the large DEM is distinctly smoother than that represented by the detailed DEM. Additionally, the relative reliefs of the two sections differ.

This exercise shows that the API DEM for the study area, whilst derived from recent, high quality 1:25 000 topographic data, represents smoother terrain than reality, particularly for gullies. Intuitively, this is likely to have a significant effect on hydrological processes related to streamflow. In the study area, stormflow and baseflow production are directly linked to the saturated areas in gullies (Finlayson and Wong, 1982; Duncan and Langford, 1977). One would expect that by changing the representation of gullies, changes in modelled streamflow would result. This sensitivity is investigated in Section 10.5.3 and presently, no correction to the large DEM is attempted.
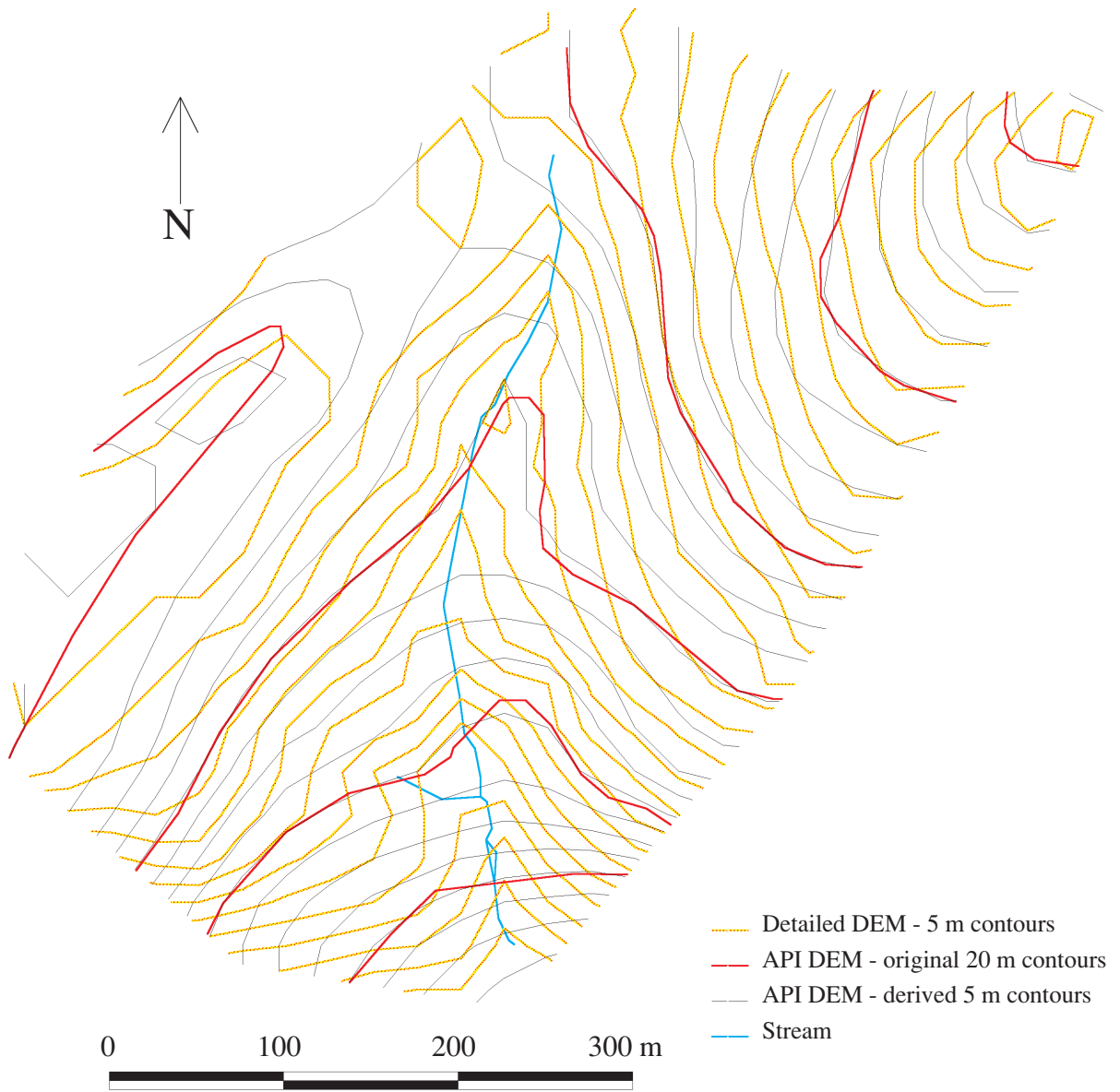
Figure 6.4: Map comparing contours associated with the two different DEMs - see text.
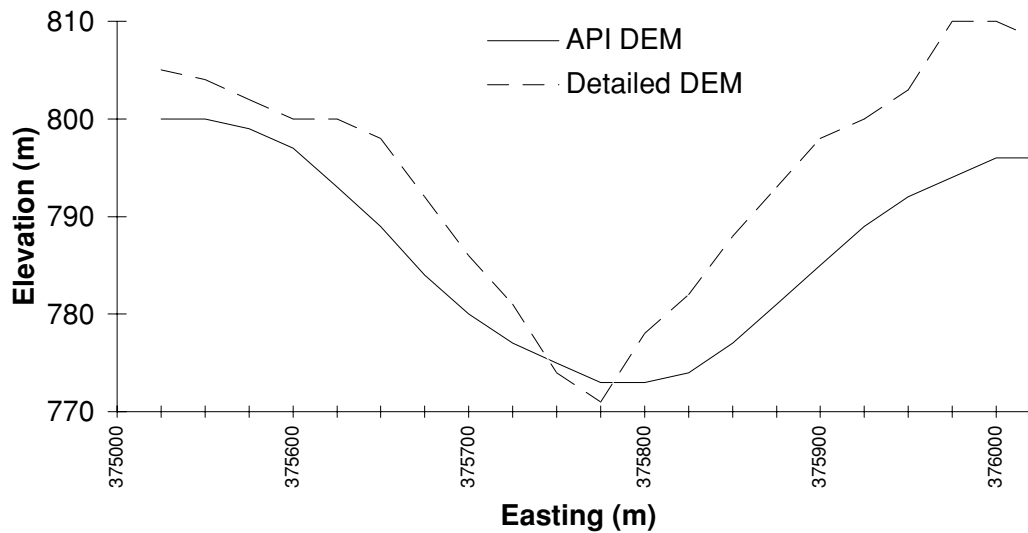
Figure 6.5: Transect through Ettercon 3 showing elevation profiles predicted by the API (large) DEM and the detailed DEM.

6.4 DEM pit, dam, and flat removal

In its raw form, the large DEM contains additional inaccuracies in the form of *pits*, *dams*, and *flats*. A 'pit' is an artefactual localised depression in the DEM usually occurring along streamlines where the gradient is close to zero. A 'dam' is effectively the same thing except that it is an artefactual localised high point, usually in an incised gully, which leads to an extended depression upstream. A 'flat' is just that, a DEM cell neighboured by other cells with the same elevation, but none with lower elevations where water should flow. Except in karst regions, it is rare to find such surface features in real terrain. However, they are common in DEMs produced by interpolation schemes which generally have no built-in concept of gravity or water flowing down hill. Pit removal algorithms are required in order that gravity-sensitive analyses such as the calculation of upslope areas (below) can be accomplished.

Some GRASS-compliant pit removal code was specially developed because existing schemes (e.g. Hutchinson, 1988, 1989, 1993) were felt to be inadequate or too time consuming to incorporate into GRASS. The code implements an *original* and very simple algorithm. In as many passes over the DEM as are required, cells with no downslope neighbour are identified. If they have no equipotential neighbour, they are pits, and a unit increment is added to their elevation. If they have an equipotential neighbour, they are flats, *but their elevation is not incremented unless they also have an upslope neighbour.* This ensures that flats are filled from the edge inwards instead of in some arbitrary way totally determined by the order in which cells are

scanned. A valley-like terrain is constructed in place of the flat. Eventually, after many passes over the DEM, all the pits will slowly rise to become flats, and across all the flats will slowly grow promontories, until no pits or flats are left and all cells have downslope neighbours except the catchment outlets at the edge of the DEM. The algorithm is 'brute force', but only needs to be done once.

Figure 6.6 shows the results of the procedure, expressed as the amount of fill required to removed all artefacts. The maximum fill required was 20.5 m. This occurred at the large filled area in the east of the figure where a large, long flat area drained through a relative constriction in a gully. The constriction was a dam, and in the flat area a negative overshoot was produced by the interpolation procedure leading to a large pit. The combined result of these factors required a lot of filling. On close inspection (not shown) the final representation of terrain in the area appears as good as can be inferred from the original contour data. Typically, the filled areas occupy flat valley bottoms in the Watts catchment.

At present, the total filled area is not considered large enough to necessitate more sophisticated algorithms. Future improvements might include 'dam cutting' instead of pit filling, as well as interpolating elevation values along mapped streams and including this data in the original DEM interpolation. In all analyses to date, the location of streams is inferred from the contour data.

6.5   Upslope area calculation

Given a depressionless and flatless DEM, maps relating to upslope area can be calculated. These are commonly used in wetness index calculations (see Section 5.2.3). The essential variable of these maps is the upslope area per unit contour length, a. Quinn et al. (1995) review methods for its calculation. Here, a multiple flow direction algorithm was used following Freeman (1991) and Holmgren (1994) with a power of 1.1 and a 0.75:1 weighting between diagonal and cardinal flow. Some *original* GRASS-compliant code was specifically written for the purpose using recursive calculation. Acknowledgement is due here to S. Mackay and R. Lammers (Dept. of Geography, Univ. of Toronto) for key ideas embodied within the code.

The variable, a, has a very highly skewed distribution and is difficult to represent on a map. Instead, the natural logarithm $\ln(a)$ is mapped in Figure 6.7.
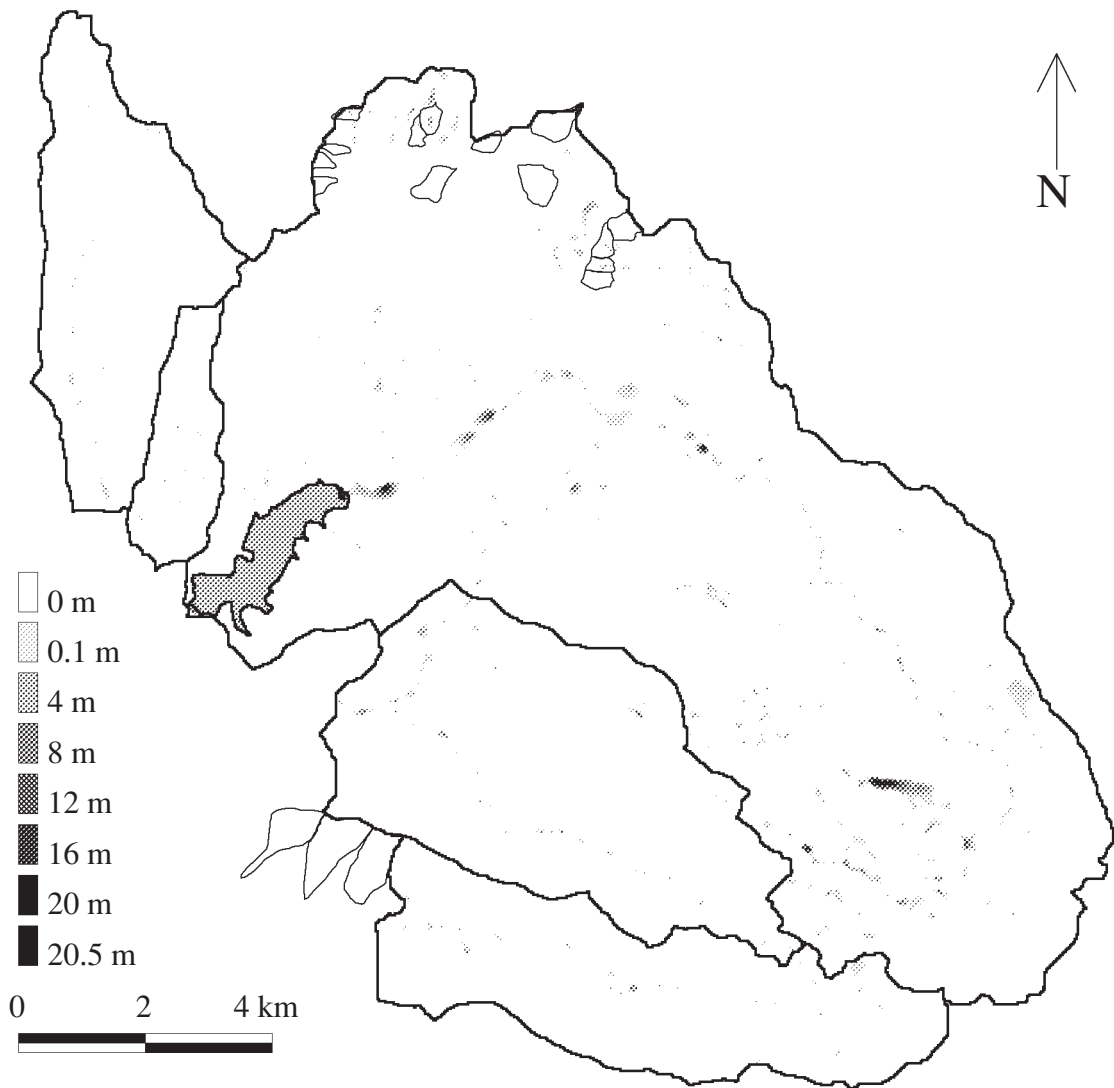
Figure 6.6: Pit, dam, and flat removal: a map of the amount of fill required to remove all such artefacts.
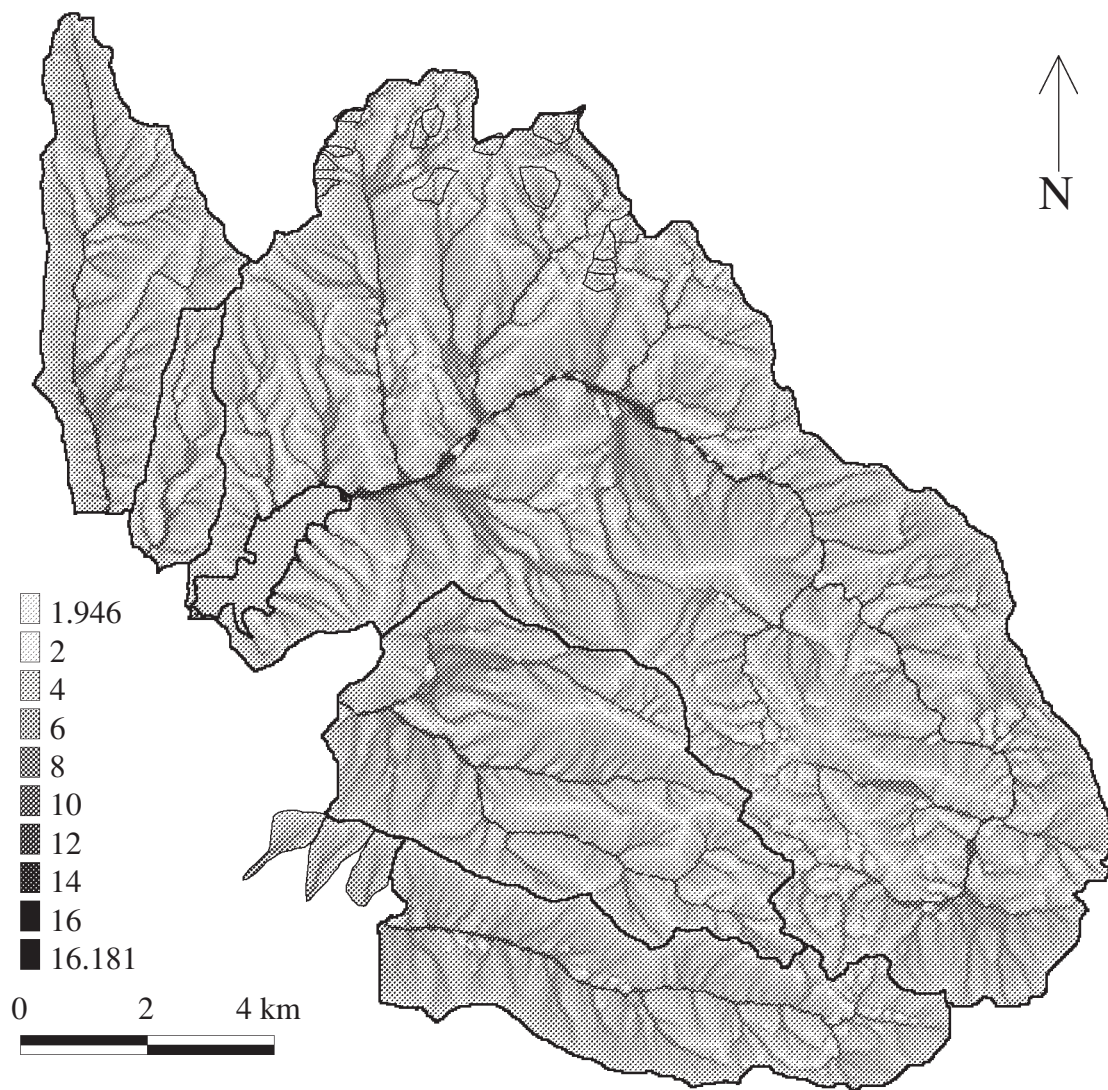
Figure 6.7: ln(a) mapped over the study area.
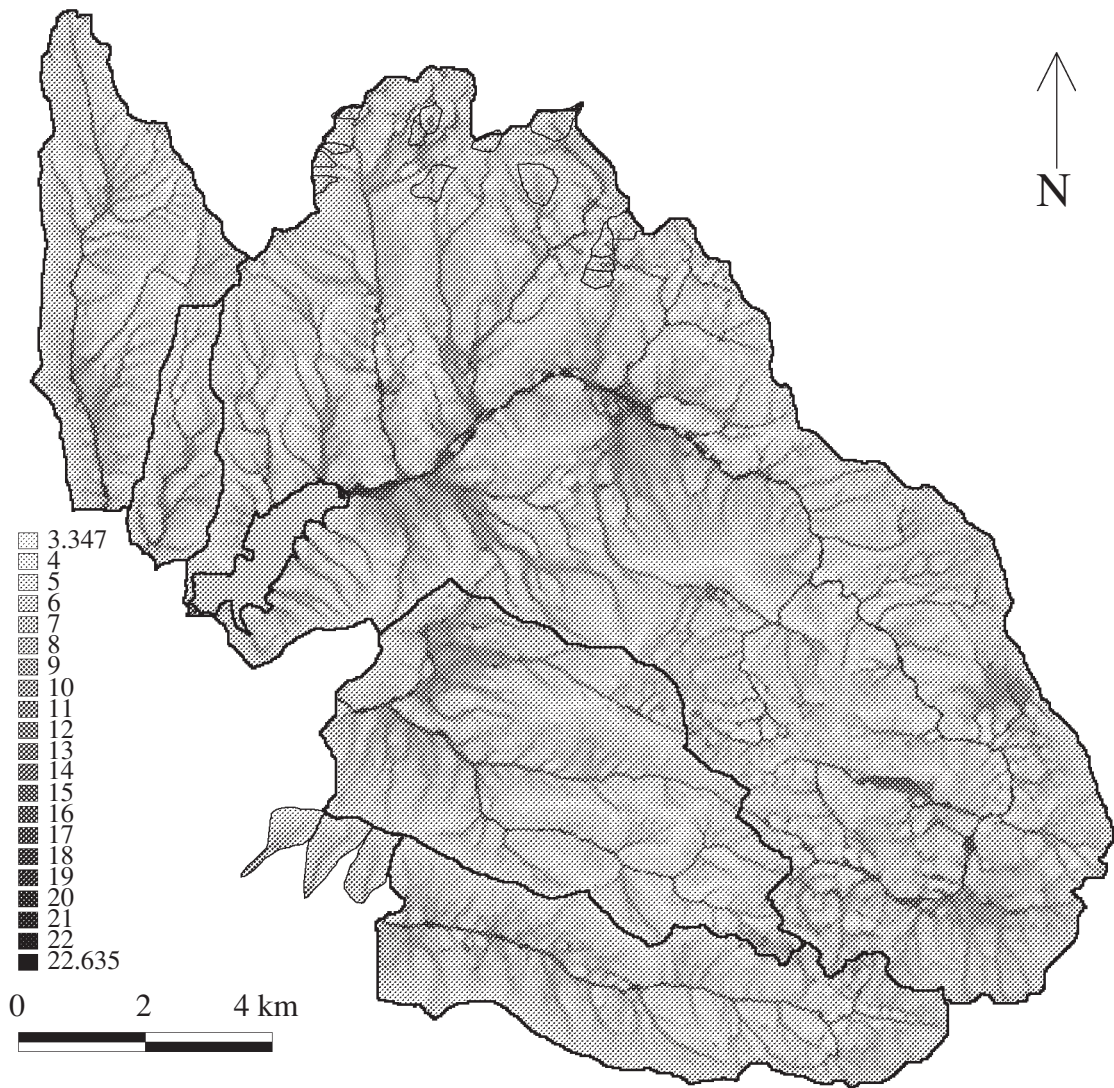
Figure 6.8: $\ln(\frac{a}{\tan\beta})$ mapped over the study area (TOPMODEL's or 'Kirkby's' wetness index).

An additional variable, $\ln(\frac{a}{\tan\beta})$, is used to represent topographic convergence and location within hillslope catenas (see Section 5.2.3). The β part of this index represents the terrain slope as a proxy for the degree to which a location is well drained. Because drainage occurs downslope, β is calculated as the average over all downslope directions from a cell, weighted by the contour length in each direction. It is a *contour length weighted average of downward slopes*. It is thus different to slopes conventionally calculated within GISs using, for example, Horn's (1981) method. Figure 6.8 shows $\ln(\frac{a}{\tan\beta})$ mapped over the study area.

6.6 Summary

The construction and testing of a large area DEM and associated terrain analysis was described.

Based on 20 metre digital contour data derived from air-photo interpretation, the large area DEM was interpolated over the study area using a $25{\times}25$ metre grid and an established 2D spline interpolation algorithm.

For testing purposes, a detailed topographic survey of a 15 ha experimental catchment was conducted. The resulting data were interpolated to construct a detailed DEM which is considered to be an accurate representation of the terrain down to a horizontal resolution of about 5 metres.

Comparison of the two DEMs using contour overlays and sections determined that the large area DEM exhibited a smoother representation of terrain than reality, particularly in incised gullies which are common in the study area. A rectification procedure was not suggested. Rather, the effect of having a smooth representation of terrain is considered in DEM sensitivity analysis later in the chapter on model testing (Section 10.5.3).

An original algorithm for pit and flat removal was implemented and applied to the large area DEM to ensure hydrological soundness. Some large fills were required, but at this stage, these are not considered a great problem. Future work should remedy them.

Finally, original terrain analysis software was used to construct wetness index maps of $\ln(a)$ and $\ln(\frac{a}{\tan\beta})$ for the study area.

Chapter 7

Precipitation mapping

Contents

7.1 Introduction

Accurate spatio-temporal quantification of precipitation is of vital importance in hydrological modelling, perhaps most so in large scale studies. Observed precipitation patterns can be highly variable with respect to the information offered by sparse gauge networks (Obled et al., 1994; Goodrich et al., 1995). Where tested, high model sensitivity to precipitation inputs is normally observed (Kuczera, 1988; Obled et al., 1994; Faures et al., 1995; Shah et al., 1996b).

Macaque requires a daily precipitation estimate for every ESU in the study area. Precipitation data are typically available in daily form from only a few stations, and in monthly form from a larger number of stations. Careful consideration must be given to the means of converting the data into the required spatial precipitation estimates. The problem can be divided into spatio-temporal aspects (interpolation of precipitation at locations between gauging sites) and temporal aspects (estimating appropriate temporal patterns of precipitation at each location).

7.2 Review

The literature relating to daily spatial precipitation estimation over large areas is reviewed in two sections, respectively on *observation* and *prediction*.

7.2.1 Observation

7.2.1.1 Point measurement

Perhaps the most fundamental characteristic of precipitation observation is that accurate *measurement* of precipitation at a single point is no easy matter.

In mountainous areas, high winds commonly induce eddies around rain gauges causing under-estimation of at least 10% (Linacre, 1992; Dingman, 1994). Much larger effects were observed in Tasmania by Morris et al. (1995) for wind-speeds greater than about 2.5 m s^{-1}. Various wind-correction schemes have been developed (see Moore et al., 1991; Dingman, 1994) but these of course require some form of wind measurement, which is also difficult in mountainous, forested areas.

Suitable clearings in forested areas are not usually available for the siting of gauges. This necessitates either deliberate clearing or the use of tower-mounted gauges, both of which have been used in and near the study area (De Laine, 1969; Wu et al., 1984, Fiske et al., 1977; Howard and O'Shaughnessy, 1971). Almost all of the rain gauges in and near the study area were visited by the author. The great majority of them do not meet the 2:1 and 4:1 clearing/tree-height ratios suggested by Colls and Whitaker (1990) and Linacre (1992) respectively. Inadequate clearings may shield gauges from precipitation, or due to lower wind-speed within the clearing, increase precipitation measured relative to 'normal' gauges.

7.2.1.2   Expected patterns

The study area experiences two main forms of precipitation. Precipitation associated with east moving frontal depressions occurs mainly in the winter, whilst summer precipitation can be brought about by thunderstorm activity or on-shore southerlies associated with large high pressure systems west of Victoria (Linacre and Hobbs, 1977; Ruddell et al., 1990). The area is at the western, windward edge of Australia's alpine region, the Great Dividing Range, which makes it particularly susceptible to winter frontal orographic precipitation (Colls and Whitaker, 1990). Topography is the major control on precipitation distribution (Ruddell et al., 1990). Within the study area, precipitation can be expected to be greatest at eastward locations which are closer to the main mass of the Great Divide.

The influence of elevation on precipitation is of course widespread, being cited, for example, by Dingman et al. (1988), Blöschl and Sivapalan (1995), and Givone and Meignien (1990). However, it is not omni-present, even in similar topographic and synoptic situations to the present (Loukas and Quick, 1996; Creutin and Obled, 1982).

7.2.1.3   Spatial variability

Spatial variability of precipitation is gaining increasing prominence in the literature as a confounding factor in spatial hydrological modelling. A number of studies report significant and essentially random spatial variability in observable precipitation patterns, despite concomitant predictable, deterministic controls (Obled et al., 1994; Goodrich et al., 1995). At time scales of the order less than one hour, very dense gauge networks (<100 m spacing) are required to observe this variability whilst, at the daily level, gauge spacings

well over 5 km may be adequate (Obled et al., 1994). It is thus important, in designing procedures for spatio-temporal precipitation estimation using data from sparse gauges, to ask questions such as: 'What is the correlation length (*sensu* Blöschl and Sivapalan, 1995) of a daily precipitation gauge in a temperate mountainous region?'

7.2.2   Prediction

Macaque requires rather finely distributed daily precipitation estimates. Because precipitation observations are not distributed at the required level of detail simultaneously in both space and time, this necessitates spatial and temporal interpolation. The literature on spatial, temporal, and spatio-temporal interpolation using either empirical and process-based based methods is briefly reviewed.

7.2.2.1   Spatial interpolation

Splines and kriging

Spatial interpolation of precipitation, typically mean monthly or annual precipitation, is one of the classic problems of hydrology. A wide range of techniques are available. Their respective proponents have by no means reached consensus on the best techniques. Rather, a duplicity emerges in the literature comprising two actively evolving techniques: splines and kriging.

Techniques addressed in reviews of the 1970's and 1980's included: the arithmetic mean, Thiessen polygons (nearest-neighbour), distance weighting, isohyetal and hypsometric methods, trend surface analysis, polynomial interpolation, multiquadric interpolation, optimal interpolation, spline interpolation, and kriging (Shaw and Lynn, 1972; Creutin and Obled, 1982; Tabios and Salas, 1985; Lebel et al., 1987). In the 1990's, the dominance of the latter two (splines and kriging) in the literature indicates that these are *the* two modern interpolation techniques.

Splines, in the three dimensional case, are compound mathematical functions fitted to input data points so as to minimise the curvature of the resulting surface. Spline interpolation has been applied to precipitation mapping by Hutchinson (1983, 1995a), Hutchinson and Bischof (1983), Lebel et al. (1987), Mitchell (1991), and Cheesman and Petch (1996).

Kriging procedures are rooted more in statistics, whereby a surface is con-

structed as a weighted sum of the input data points with the weights adjusted to minimise the variance of the prediction error at each data point. The technique has been applied to precipitation estimation by Lebel et al. (1987), Dingman et al. (1988), Martinez-Cob (1996), Hevesi et al. (1992a), Craigie (1981), and Cheesman and Petch (1996),

The separate literatures relating to splines and kriging only occasionally interact. Tabios and Salas (1985) reviewed seven, and Craigie (1981) reviewed four techniques including kriging but excluded splines. Conversely, Shaw and Lynn (1972) included six techniques, including splines, in their analysis, but excluded kriging. A number of authors ponder the alternatives within the broad domain of kriging without reference to splines (Dingman et al., 1988; Hevesi et al., 1992a,b; Martinez-Cob, 1996). Hutchinson has long promoted spline interpolation and whilst making strong efforts to bring the two fields together, does not appear to have ever *used* kriging (Hutchinson, 1983, 1987, 1991, 1995a,b; Hutchinson and Bischof, 1983; Hutchinson and Gessler, 1994). The problem is related to the difficulty of implementing either method from scratch. The present author's observation is that most users appear to obtain a software package for one or other method (e.g. the spline package ANUSPLIN, anon., 1995); and the kriging package GEOPACK, Yates and Yates, 1990), and never use anything else.

Of the authors who have compared splines and kriging (Creutin and Obled, 1982; Lebel et al. 1987; Dingman, 1994), almost none have been prepared to make concise, general statements as to which is better. There are at least four reasons for this. First, the two techniques perform similarly (e.g. Creutin and Obled, 1982; Hutchinson, 1987, 1991; Cheesman and Petch, 1996). Second, their description and interpretation involves much statistical jargon and is written by specialists who rarely succeed in enlightening the broader readership with application-oriented conclusions (e.g. Myers, 1994). Third, there are increasingly many mathematical and practical variants of the two techniques, so comparisons are dependent upon which combination of variants was used (Creutin and Obled, 1982). Fourth, the performance of specific techniques can depend upon the quantity being interpolated (Hutchinson and Gessler, 1994), which is not always precipitation.

Those author's who *do* find in favour of a particular method do not agree. 'Spline analyses appear to be marginally superior ... ' (Hutchinson and Gessler, 1994). 'The comparative studies reviewed have unanimously concluded that optimal-interpolation/kriging methods provide the best estimates ... ' (Dingman, 1994). Dingman's comment is confounded by his citation of Creutin and Obled (1982) who state: 'kriging ... does not seem

to work better than the others, and may not be, in our case, worth its computational burden ... '.

Another difficulty for the uninitiated would-be interpolator is that comparisons are not always made using real data. Shaw and Lynn (1972) compared performance on synthetic precipitation fields. Myers (1994) mathematically compared the two techniques. Hutchinson and Gessler (1994) make a large number of reasoned, but effectively anecdotal, comparative statements.

Perhaps, the most useful statement made to date regarding the choice between splines and kriging is from Hutchinson (1995b): 'kriging and thin plate spline methods can give rise to results of similar accuracy (Laslett, 1994; Hutchinson and Gessler, 1994), *in which case the chief advantage of splines is their operational simplicity*' (my emphasis).

Elevation and spatial interpolation

Of particular interest is the inclusion by many studies of elevation as an independent variable in precipitation interpolation (Blöschl and Sivapalan, 1995). Its use requires a DEM.

At the simplest level, elevation is the *only* independent variable used in the linear model offered by Running et al. (1987). Similarly, the UBC water balance model combines elevation and temperature as predictors in another simple linear model (Quick, 1995). The PRISM model (Garen and Daly, 1996) uses separate precipitation elevation regressions for each topographic 'facet' within an area. Hevesi et al. (1992a,b) and Dingman et al. (1988) compared kriging methods with and without elevation as a third variable (in addition to two variables describing horizontal location) and found the tri-variate version to be superior. Hutchinson and Bischof (1983) introduced a line of work demonstrating the benefits of three dimensional spline interpolation of precipitation with elevation as the third dimension. An interesting development is suggested by Michaud et al. (1995) and, to an extent, Garen and Daly (1996), whereby elevation operates as a larger scale control than other variables, and hence should be smoothed or averaged spatially before being input to interpolation routines.

Validation of spatial interpolation

Validation of spatial interpolation has been achieved using at least three approaches. Analysis of the difference between synthetic data fields and interpolated surfaces derived from sampled points within the fields was used

by Shaw and Lynn (1972), but the approach seems to have gone out of vogue. More contemporary workers tend to use either split samples, where about half the data points are reserved for comparison with estimates made using the other half (e.g. Martinez-Cob, 1996; Creutin and Obled, 1982); or cross validation, where each single data point in turn is removed from the data set and compared with the prediction made in its place (e.g. Hevesi et al., 1992a; Hutchinson, 1995a). According to Creutin and Obled (1982), cross validation is 'biased and too optimistic', the bias being toward locations similar to those where gauges tend to be sited (e.g. valley bottoms).

Methods used in catchment modelling

Despite the existence of proven, sophisticated spatial interpolation methods described above, inferior methods are common in hydrological modelling studies. There appears to be a lag of 10 to 20 years between the acceptance of sophisticated methods in the interpolation literature and the widespread availability of software enabling catchment modellers to use such methods.

Numerous modelling studies assume uniform (areal mean) precipitation over quite large (often > 100 km^2) areas where better spatial data are available (Knisel and Williams, 1995, CREAMS; Arnold and Williams, 1995, SWRRB; Naden et al. 1996; Polarski, 1997; Bathurst, 1986, SHE; Colosimo and Mendicino, 1996; Porter and McMahon, 1971, Chiew and McMahon, 1990a, b, 1994, Chiew et al., 1992, HYDROLOG and MODHYDROLOG).

Often, data from only a single site is used in the estimation of mean precipitation. In a 518 km^2 catchment, Kuczera (1988) compared this practice with the use of multiple gauges in the calculation of areal means and found the single gauge method to be seriously deficient. Similar sensitivity was observed by Faures et al. (1995) who used 5 separate gauges in turn to drive catchment simulations of a 4.4 ha catchment.

Where interpolation *is* undertaken, it is often done using out-dated methods. Theissen polygons and distance weighting are used in many models (Federer and Lash, 1978, BROOK; Porter and McMahon, 1971, Chiew and McMahon, 1990a, b, Chiew et al., 1992, HYDROLOG and MODHYDROLOG; Bergström, 1995, HBV; Price, 1996; Hughes and Sami, 1994, HYMAS).

Some authors offer vague descriptions of what appear to be completely subjective gauge weighting techniques (e.g. Leavesley and Stannard, 1995, PRMS). Others, including almost the entire TOPMODEL literature (Beven et al., 1995, about 30 papers checked) give no indication of their means of obtain-

ing catchment precipitation estimates.

More progressive thinking is demonstrated by authors of models implementing precipitation/elevation correlation, such as: HBV (Bergström, 1995), Topog (Hatton et al., 1992; Dawes and Hatton, 1993), and RHESSys (Band et al., 1993).

The present author could find only two studies which used either splines or kriging. These were Famiglietti et al's (1992) use of kriged precipitation estimates, and Obled et al's (1994) comparison of the effect of different estimation techniques, including spline interpolation, on the predictions made by TOPMODEL over a large area divided into sub-basins. The latter authors concluded that, despite the strong sensitivity reported in the literature, the model was insensitive to spatial differences in precipitation, but sensitive to the aggregated differences in *total* precipitation.

In the literature on stochastic estimation, Shah et al. (1996b) have examined the behaviour of the SHE catchment model when supplied with data from a new spatio-temporal stochastic precipitation model. They concluded that high sensitivity and non-linearity in runoff response for a 10.55 km^2 catchment occurs under dry catchment conditions, but under wet conditions the model is insensitive to spatial precipitation patterns.

7.2.2.2 Temporal aspects

There are a number of ways to incorporate temporal disaggregation into spatial precipitation estimation methods. The simplest are simple deterministic methods. There is a large literature on stochastic methods, and a limited degree of mixing of the two.

Perhaps, the simplest possible deterministic method is to use the measured temporal signal from some reference site to modulate temporal means estimated for other sites using a spatial interpolation to give complete spatio-temporal estimates for the area of interest. An example of this is given by Kuczera (1984) who scaled daily precipitation at a reference site according to a catchment areal mean to estimate daily areal precipitation. Other examples are implemented by Federer and Lash (1978) and Porter and McMahon (1971).

A related method is implemented by the PRISM model (Garen and Daly, 1996) where precipitation/elevation regressions are constructed for a range of daily sites, in some cases *for each day or each storm*. Thus the interpolation is performed many times.

Stochastic methods acknowledge the scarcity of distributed temporal data and generate completely synthetic, yet statistically representative time-series of precipitation data. Foufoula-Georgiou and Georgakakos (1991) give a comprehensive review. Many methods simply generate data for a single site or group of correlated sites (e.g. Richardson, 1978; Hanson and Woolhiser, 1990; Hutchinson, 1990; Cowpertwait et al., 1996a). Hutchinson (1987, 1995a) notes that the parameters associated with these methods can be spatially interpolated to yield spatio-temporal data (see also Cowpertwait et al., 1996b). More complex, *inherently* spatio-temporal stochastic models generate realistic temporally and spatially varying patterns in one step (e.g. Valdes et al., 1985; Costa et al., 1996; Shah et al., 1996a, b).

Ideally, in many modelling scenarios, temporal data from a reference site would be used to drive the estimation of spatio-temporal patterns which are statistically representative of the spatial variability expected for a catchment whilst retaining the real time-series from the reference site (or sites). This is termed *conditional simulation*. Shah et al. (1996a) present such a technique by combining a stochastic spatio-temporal precipitation model with kriging. The technique is tested by Shah et al. (1996b) using the SHE model.

Additional contributions include such diverse technologies as neural net forecasting of spatio-temporal rainfall fields (French et al., 1992), the use of satellite observations of cloud cover over very large areas to estimate precipitation patterns (Roberts, 1993; Engman, 1995), and the use of rainfall radar systems (Liu and Krajewski, 1993).

Finally, links can be made to *process based* orographic precipitation models (e.g. Barros and Lettenmaier, 1994; Hay et al., 1993; Hay and Knapp, 1996; Munro et al., 1997; Shao et al., 1997a, b), which could be used to provide input to surface hydrological models such as Macaque, but at the cost of significant additional complexity.

7.3   Data

All precipitation data were sought for a 40x40 km region centred on the study area. The data were available from a number of sources including: CRCCH internally, BOM, Melbourne Water, DNRE Marysville, DNRE Toolangi, and R. Furmston (retired, Melbourne Water, Healesville). Data were obtained from about 80 sites. Most data are monthly precipitation records from various parts of the century.

Very few sites were located at high elevation, a common limitation of precipitation gauging networks (e.g. Schulze, 1976), so it was decided to install additional gauges to reduce the bias. Eight bulk gauges were installed within the study area in clearings maintained for wildfire observation purposes. These were read monthly for a year. Such widely spaced readings are not standard practice. However, investigations with paired rain gauges by Melbourne Water (J. Snodgrass, Melbourne Water, Healesville, pers. comm.) indicated that evaporation from within a standard bulk rain gauge during one month would lead to acceptably small errors, relative to the many other sources of error in the precipitation estimation procedure.

Figure 7.1 shows the location of *monthly* precipitation gauging sites. The sites are coded depending on whether: data for the site have been measured but are no longer available (1), data are available but were not acquired for this project (2), data were acquired but not used (3), data were used for model input and parameterisation (4), or data were used for model validation (5). In total 73 sites were used for spatial precipitation mapping (see below), including 65 existing sites and 8 installed for the present study. A further 14 (codes 1, 2, and 3) were not used for various reasons including lateness in acquisition, poor location information, and patchy consistency where better sites were nearby. One site was used for independent testing (Section 10.2.7). In hindsight, more sites should have been retained for this purpose.

Figure 7.2 shows the location of those sites for which *daily* data have been measured. The same codes are used as for Figure 7.1. There are 46 reliably located sites in total. Four were used as input to various model runs (see below) and one was used for model validation. Many of the remaining 41 sites would be suitable for future model validation.

7.4 Mean monthly precipitation index (MMPI)

Table 7.1 provides summary information for the monthly precipitation sites and Figure 7.3 shows their periods of record. It is clear that the data from these sites come from a wide range of time periods, and are often discontinuous and not coextensive. In Figure 7.3, the sites are arranged (and numbered) roughly from earliest to latest, except for the gauges numbered 56 to 87 which are the core gauges associated with the Melbourne Water (formerly MMBW) Catchment Hydrology Research programme. Note that the record for gauge number one spans all the records for all the other gauges.

Table 7.1: Summary of monthly precipitation sites.

F-num.	Gauge number from Figure 7.3	Record name	Months of data	MMPI relative to F0700	Used for MMPI mapping?
F1190	1	Warburton Post Office rainfall	1363	1.181	Yes
F0700	2	Maroondah dam (nearby) rainfall	1202	1.000	Yes
F0790	3	Marysville Post Office rainfall	1073	1.195	Yes
F0970	4	Mount St Leonard (summit - just south) rainfall	655	1.049	Yes
F1910	5	North Maroondah Site 15 rainfall	979	1.472	Yes
F1020	6	Narbethong rainfall	814	1.046	Yes
F0710	7	Maroondah dam (nearby) rainfall	648	0.998	No
F0590	8	Healesville (Muragal) rainfall	375	0.747	Yes
F0600	9	Healesville (Nyora) rainfall	463	1.148	Yes
F1130	10	Toolangi rainfall	123	1.166	Yes
F0570	11	Blacks Spur (Hermitage) rainfall	285	1.338	Yes
F1160	12	Warburton (Fernleigh) rainfall	246	1.085	Yes
F1140	13	Toolangi (Mount Sale Stn.) rainfall	91	1.228	Yes
F0650	14	Healesville (Sanctuary) rainfall	624	0.894	Yes
F0800	15	Millgrove rainfall	67	1.204	Yes
F0680	16	Launching Place rainfall	67	0.987	Yes
F0610	17	Healesville (The Wattles) rainfall	93	0.828	No
F1025	18	Narbethong Nursery rainfall	214	1.108	Yes
F1010	19	Mount Toole Be Wong rainfall	71	1.091	Yes
F0690	20	Launching Place - Don Valley rainfall	26	0.996	Yes
F1170	21	Warburton East rainfall	26	1.158	Yes
F1060	22	Taggerty (Thendara) rainfall	11	0.962	No
F0900	23	Mount St Leonard (potato farm) rainfall	466	1.294	Yes
F0270	24	Coranderrk Site 10 rainfall	456	1.152	Yes
F0607	25	Healesville (Ron Furmston) rainfall	314	0.883	Yes
F1150	26	Wandin North rainfall	138	0.918	Yes
F1600	27	North Maroondah Site 1 rainfall	173	1.623	No
F1210	28	Yarra Glen rainfall	205	0.760	Yes
F1200	29	Warburton watersheds rainfall	83	1.292	Yes
F1040	30	Poley Range rainfall	232	1.817	Yes
F1000	31	Mount Strickland rainfall	181	1.606	Yes
F0820	32	Mount Donna Buang rainfall	188	2.417	Yes
F2035	33	North Maroondah Site 18 rainfall	137	0.982	Yes
F0865	34	Mount Juliet (heli-pad) rainfall	106	1.806	Yes
F0550	35	Ben Cairn rainfall	57	1.638	Yes
F0530	36	North Maroondah Site 17 (Crotty Creek) rainfall ?	212	1.597	Yes
F0860	37	Mount Juliet (heli-pad) rainfall	57	1.895	No
F2040	38	North Maroondah Site 19 rainfall	138	1.280	Yes
F2050	39	North Maroondah Site 20 rainfall	156	1.643	Yes
F2060	40	North Maroondah Site 21 rainfall	150	1.644	Yes
F2020	41	North Maroondah Site 18 rainfall	97	0.976	No
F1180	42	Warburton East (Arabri) rainfall	92	1.257	Yes
F1100	43	Tarrawarra Monastery rainfall	88	0.738	Yes
F0580	44	Fernshaw rainfall	55	1.379	Yes
F0850	45	Mount Juliet (heli-pad) rainfall	49	1.681	No
F1220	46	Yarra Junction rainfall	11	1.391	No
F0542	47	Acheron Valley rainfall	8	1.518	Yes
F1141	48	Vantage Point C1 rainfall	8	1.730	Yes
F1142	49	Vantage Point F rainfall	7	1.951	Yes
F1143	50	Vantage Point H rainfall	9	1.268	Yes
F1144	51	Vantage Point J rainfall	8	1.602	Yes
F1145	52	Vantage Point L rainfall	9	1.334	Yes
F1146	53	Vantage Point N rainfall	9	1.012	Yes

F1147	54	Vantage Point S rainfall	9	1.230	Yes
F0050	56	Coranderrk Site 1 rainfall	192	1.068	Yes
F0060	57	Coranderrk Site 2 rainfall	192	1.146	Yes
F0150	58	Coranderrk Site 3 rainfall	192	1.002	Yes
F0160	59	Coranderrk Site 4 rainfall	192	1.338	Yes
F0190	60	Coranderrk Site 5 rainfall	292	1.252	Yes
F0200	61	Coranderrk Site 6 rainfall	292	1.162	Yes
F0210	62	Coranderrk Site 7 rainfall	192	1.280	Yes
F0220	63	Coranderrk Site 8 rainfall	192	1.230	Yes
F0230	64	Coranderrk Site 9 rainfall	292	1.309	Yes
F0260	65	Coranderrk Site 10 rainfall	292	1.146	No
F0350	66	Coranderrk Site 11 rainfall	292	1.337	Yes
F0460	67	Coranderrk Site 12 rainfall	168	1.360	Yes
F0470	68	Coranderrk Site 13 rainfall	228	1.104	Yes
F1610	69	North Maroondah Site 1 rainfall	255	1.591	Yes
F1640	70	North Maroondah Site 2 rainfall	255	1.738	Yes
F1660	71	North Maroondah Site 3 rainfall	155	1.684	Yes
F1670	72	North Maroondah Site 4 rainfall	255	1.625	Yes
F1720	73	North Maroondah Site 5 rainfall	255	1.548	Yes
F1730	74	North Maroondah Site 6 rainfall	155	1.568	Yes
F1740	75	North Maroondah Site 7 rainfall	255	1.477	Yes
F1750	76	North Maroondah Site 8 rainfall	155	1.506	Yes
F1760	77	North Maroondah Site 9 rainfall	253	1.452	Yes
F1810	78	North Maroondah Site 10 rainfall	255	1.457	No
F1840	79	North Maroondah Site 11 rainfall (for TF only)	149	1.390	Yes
F1850	80	North Maroondah Site 12 rainfall	148	1.458	Yes
F1860	81	North Maroondah Site 13 rainfall	131	1.356	Yes
F1870	82	North Maroondah Site 14 rainfall	232	1.359	Yes
F1900	83	North Maroondah Site 15 rainfall	233	1.420	No
F1970	84	North Maroondah Site 16 rainfall	230	1.379	Yes
F0540	85	North Maroondah Site 17 (Crotty Creek) rainfall ?	206	1.576	No
F2030	86	North Maroondah Site 18 rainfall	40	0.999	No
F1790	87	North Maroondah Site 10 rainfall	268	1.441	Yes

Spatial precipitation mapping exercises typically use mean annual precipitation (MAP) data as input to the mapping procedure. However comparison between, and mapping using MAP values for the sites listed in Figure 7.3 would be adversely affected by the inconsistent time periods to which the data apply. For example, an erroneously low MAP compared to other sites would be estimated for a gauge which happened to operate only during a dry part of the century (e.g. gauge numbers 17 to 19 in the 1940's). The long term precipitation records from the region (not shown) show that such periods have indeed occurred (e.g. the 1940's). Therefore, rather than discard data from sites with difficult periods of record, a *mean monthly precipitation index* (MMPI) was devised which makes use of almost all data from all sites. This means that a maximum amount of spatial information was used in the precipitation mapping process.

Every site was calculated to have a *single* MMPI value as follows. A continuous long term gauge was chosen as a *base station*. For every month where a site had data, its monthly precipitation total was divided by the total for
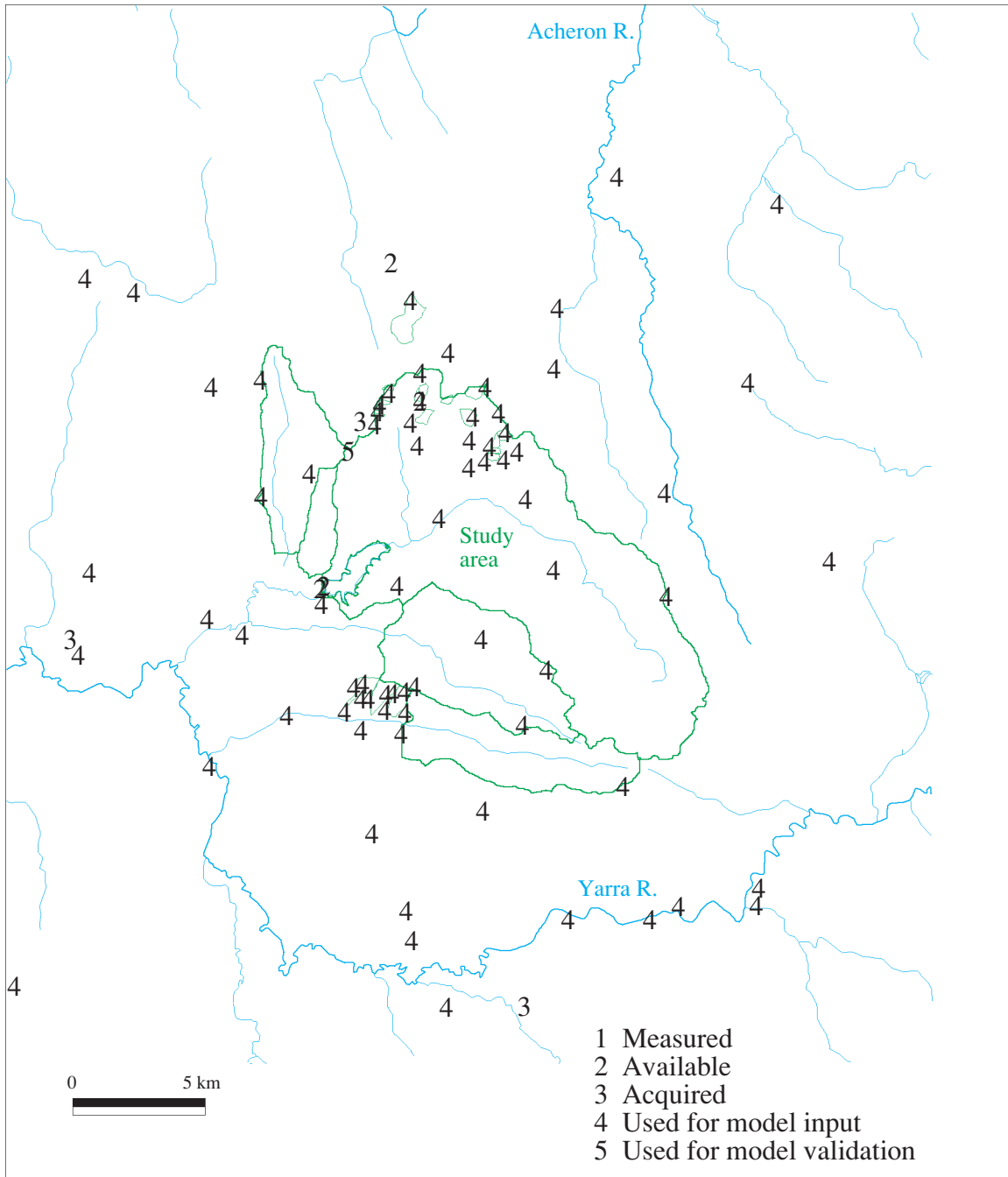
Figure 7.1: Sites of all monthly precipitation data in and near the study area. An explanation of the legend is given in the text (Section 7.3).
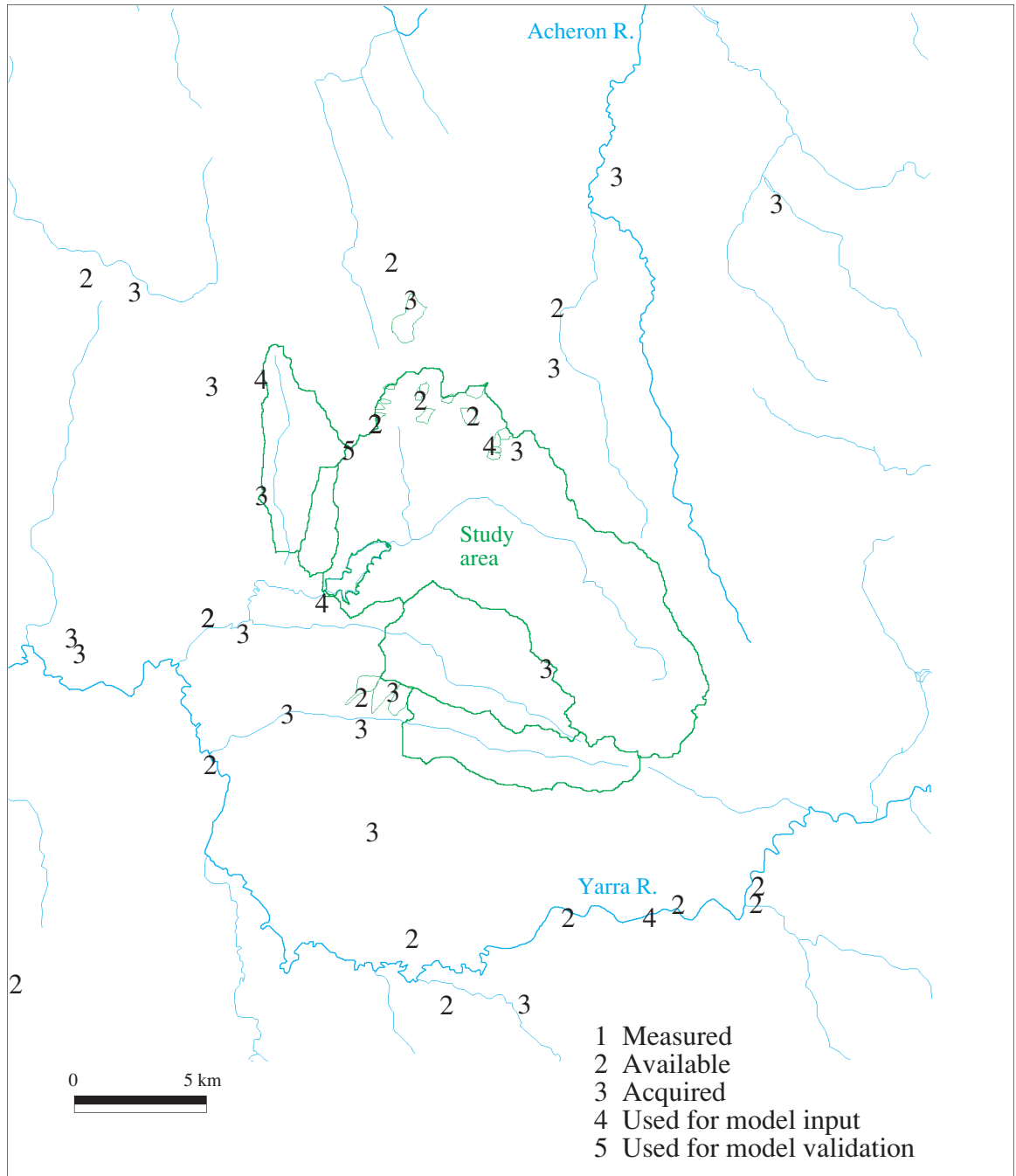
Figure 7.2: Sites of all daily precipitation data in and near the study area. An explanation of the legend is given in the text (Section 7.3).
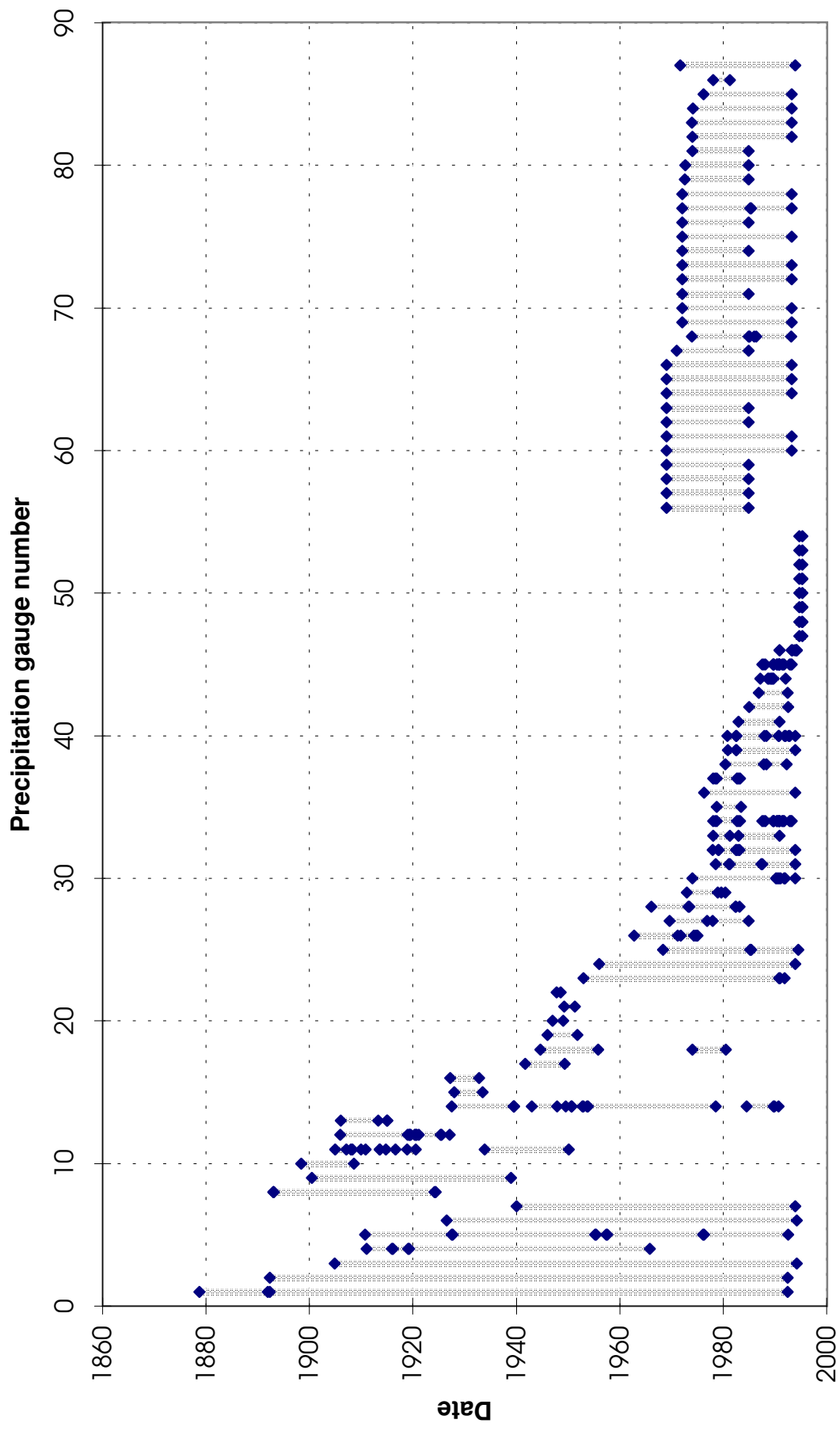
Figure 7.3: Periods of record of monthly precipitation data used for MMPI mapping.

the corresponding month from the base station. This yielded a time series of monthly precipitation index (MPI) values for the site. Another term for these could be *relative* monthly precipitation values. The MMPI is simply the mean of all MPI values, and is an expression of the mean, long term precipitation status of the site. A number of assumptions are inherent in this statement:

- The spatial distribution of monthly total precipitation is assumed to be *stationary throughout the year*. Specifically, MPI is assumed to be stationary throughout the year. If a bias exists where data are missing for certain months of the year, calculated MMPI values are assumed to be unaffected. This assumption is known to be invalid as preliminary analysis (not shown) shows mean winter spatial precipitation patterns to be different to mean summer spatial precipitation patterns. The effect of these variations is not tested but is included in the discussion of results. In future work, twelve MMPI values could be calculated for each for site (one for each month). This was not done initially because of the additional complexity it would introduce, and the possibility of inconsistencies introduced by gauges for which data are not available for certain months.

- A related assumption operates at longer time scales: that the spatial distribution of a given month's total precipitation is *stationary from year to year*. Specifically, MPI for each month is assumed to be stationary. It is possible that global long term climate trends affect precipitation patterns over the study area, but the effects are likely to be small relative to other influences and are ignored for the time being.

The index was chosen to be based on monthly data for two reasons. If a yearly time unit were used, the analysis would be supported by a great deal less data because many sites have single months missing from many years. And, if a weekly or daily time unit were used, a great deal fewer sites could be used in the mapping process because there are not many long term daily or weekly records.

A gauge near the dam wall of Maroondah reservoir was selected as the base station. Monthly data from the gauge (F0700) are available from May 1892, and daily data (F0710) are available from January 1940. The monthly and daily records relate to the same gauge although, for inexplicable reasons, monthly totals from daily data are slightly different to the monthly data at times. This sort of problem is typical of the early climate data for the region.

Very occasionally, the base station records no precipitation in a given month. These months are omitted from the calculation of MMPI in order to avoid division by zero. The resulting bias is negligible.

MMPI values relative to the base station (F0700) were calculated for all the sites summarised in Table 7.1. As noted above, 73 of these sites were selected for use in spatial mapping of MMPI, as indicated in the table.

7.5 MMPI mapping

Two methods of mapping MMPI over the study area are presented. The first, referred to as '1D linear interpolation', is a common method used in large scale modelling studies. It involves correlating mean precipitation (here, MMPI) with elevation using linear regression analysis and applying the resulting regression equation to the DEM (Figure 2.4) to obtain a map of mean precipitation. The second method, referred to as '3D spline interpolation', is presented as a superior alternative and involves fitting a thin-plate smoothing spline surface (see Section 7.2.2.1) with three independent variables to the MMPI data. Surprisingly, this method has been used only rarely in hydrological modelling studies. The two methods are presented in detail and compared in the following sections.

7.5.1 1D linear interpolation of MMPI

In mountainous terrain, the strongest control of long term precipitation is usually topography, often due to orographic uplift and associated cooling of moist air-streams (Barros and Lettenmaier, 1994). At large enough horizontal scales relative to the speed of the air-stream and the height of the mountains, elevation alone can be expected to be a powerful predictor of precipitation, as opposed to other topographic variables quantifying rain shadow effects.

Figure 7.4 shows that a good correlation between MMPI and elevation is observed in the study area, as represented by the linear regression equation:

$$MMPI = 0.906 + 0.755 \times 10^{-3} \times h \quad r^2 = 0.586 \qquad (7.1)$$

The regression equation was applied to the DEM (Figure 2.4), giving the map of MMPI shown in Figure 7.5. By definition, the map is simply a re-scaling
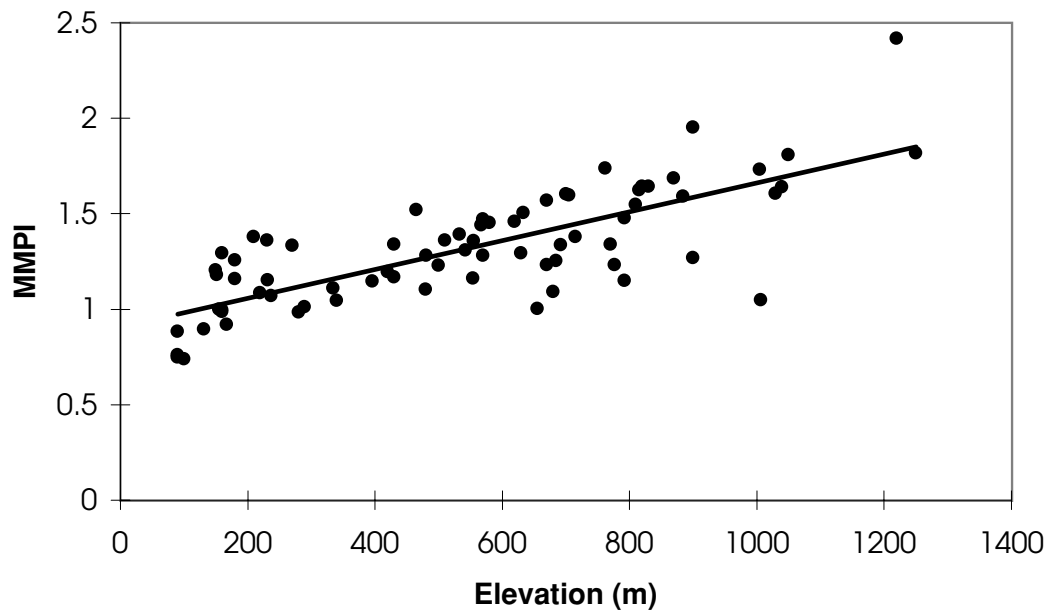
Figure 7.4: The relationship between MMPI and elevation for the study area and surrounds, including the line of best fit expressed by Equation 7.1.

of the DEM. Its features are discussed in Section 7.5.3.

7.5.2   3D spline interpolation of MMPI

Whilst a strong control on precipitation, elevation is not the only major control. In the study area, it is hypothesised that broad scale horizontal influences are also present - such as proximity to the large mountain ranges to the east of the study area. These influences can be included in the precipitation interpolation procedure as extra independent variables (dimensions), specifically easting and northing. Additionally, the likelihood of non-linear relationships between precipitation and location is also allowed for, and a 3D non-linear, or spline interpolation is performed.

Easting, northing, elevation, and MMPI data from the 73 sites used earlier were input to the ANUSPLIN software package developed by Hutchinson (1995a, Anon., 1996). The software produced a number of spline functions which were then applied to the DEM to produce a map of MMPI as shown in Figure 7.6.
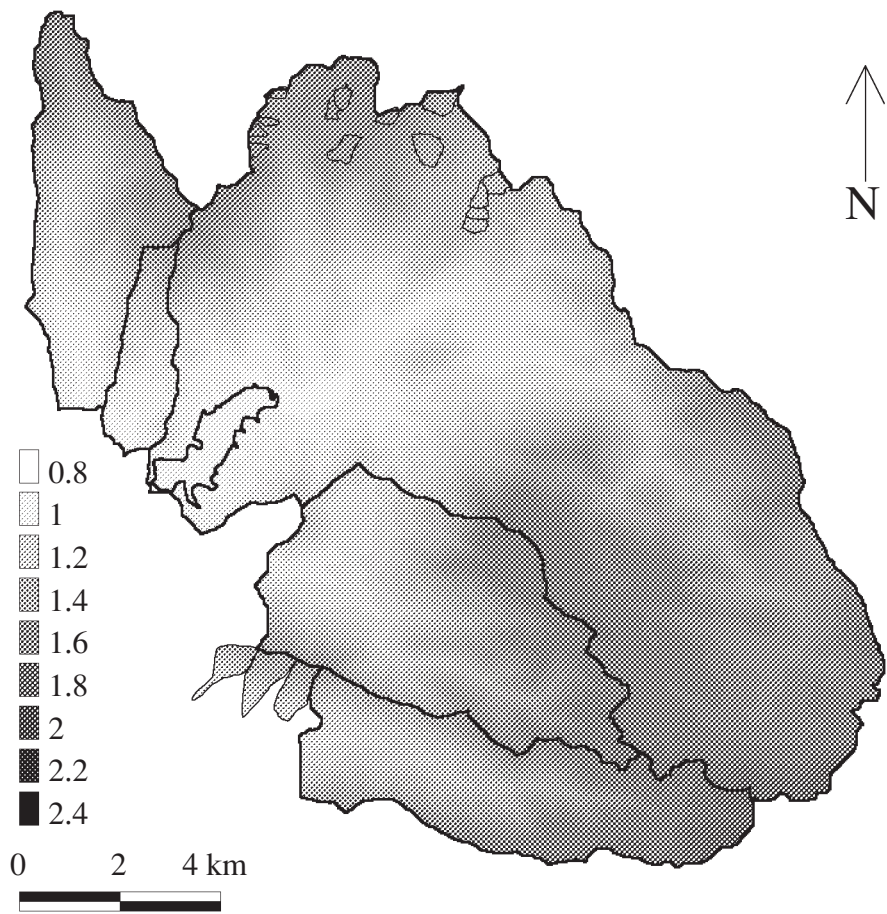
Figure 7.5: MMPI mapped over the study area using 1D linear interpolation.
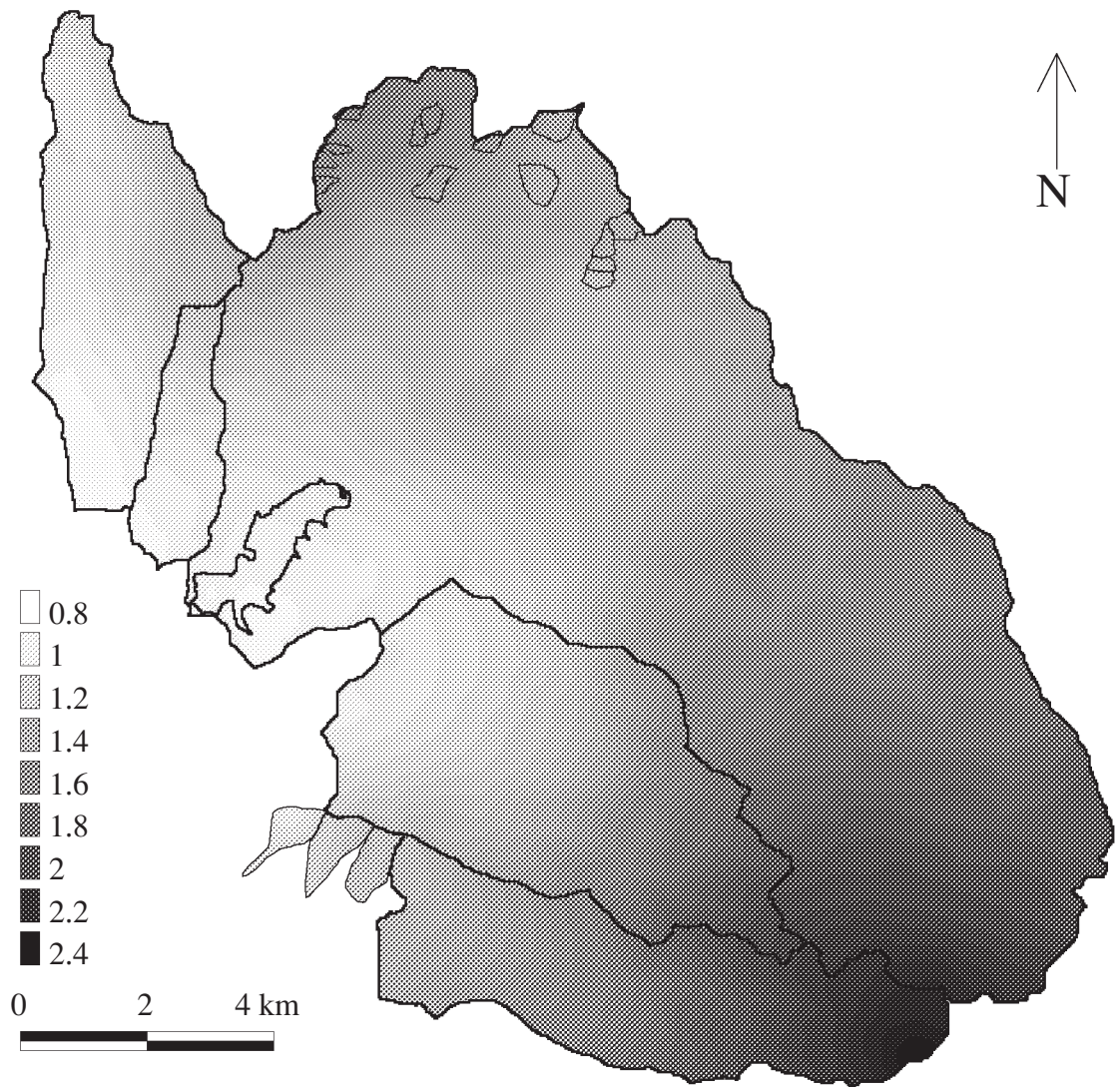
Figure 7.6: MMPI mapped over the study area using 3D spline interpolation.

7.5.3 Comparison

Qualitatively, two key observations can be made about the two maps of MMPI. Firstly, the 3D spline map is smoother than the 1D map. This is because the relative importance of elevation as a controlling factor is allowed to decrease under the 3D method when other independent variables are introduced. This is a desirable feature because detailed analysis of the clusters of precipitation records in the Coranderrk and North Maroondah experimental areas (not shown) suggests that *at small scales of the order of less than one kilometre*, elevation is not a strong control of precipitation. Rather, a larger scaled (smoothed) elevation surface appears to be a better fit to the data.

Secondly, whilst areas of equal elevation are predicted by the 1D method to have equal MMPI values, the same is clearly not so for the 3D method. Under the 1D method, Mount St Leonard at the far north west of the study area is predicted to have an MMPI of about 1.6, as are all areas of the same elevation (*c.* 1000 m). Under the 3D method, Mount St Leonard is predicted to have a much lower MMPI of around 1.2 whilst similarly elevated areas in the south east have higher MMPIs of around 1.8. This reflects a precipitation gradient operating in the west/east direction concomitant with *but independent* of elevation, and associated with a departure from the hinterland to the west of the study area toward larger, higher mountain ranges to the east of the study area. Once again, such prediction is a desirable feature which better reflects the data, and better represents all of the known influences on precipitation distribution in the region.

The 3D spline interpolation method properly supersedes the 1D linear method and is far less constrained. Purely one-dimensional linear data can be modelled using both methods, but higher-dimensional non-linear data can only be modelled using the 3D method. The 3D method is thus superior (see Hutchinson, 1995a).

This can be shown using a simple graphical comparison between MMPI values predicted for the gauging sites themselves and the original measured values. Predicted versus measured values *for sites within the study area* are plotted in Figure 7.7. Values predicted using the 1D linear method show considerable scatter about the 1:1 line, whereas those for the 3D spline method fall very close to the 1:1 line. This confirms that the 3D method is better able to fit the data than the 1D method. Of course, the plot reveals nothing, directly, about the relative interpolative power of the two methods at locations *between* gauging sites. Although it is clear that in order to produce a smooth, continuous precipitation map (Figure 7.6) *and* better fit the original
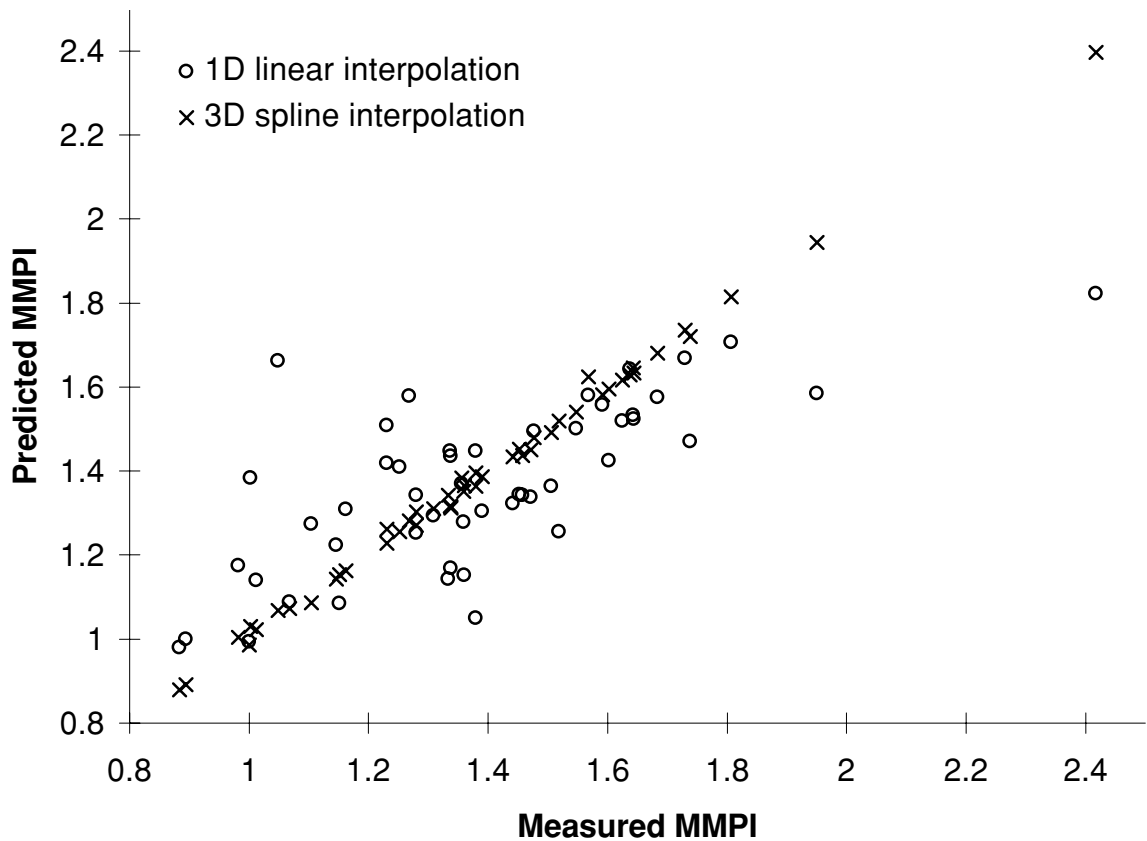
Figure 7.7: MMPI predicted by each of the two interpolation methods versus that measured at each of the gauging sites.

data points, the 3D method must be more accurate for ungauged as well as gauged locations.

A further comparison between the methods is made in Figure 7.8 which plots predictions from the 3D method against those of the 1D method for every GIS cell in the study area (excluding Maroondah reservoir). If the two methods were similar, all the dark shading would lie near the 1:1 line. The fact that most of the dark shading lies above the 1:1 line indicates that for most of the study area, the 1D method significantly under-estimates MMPI relative to the 3D method. This is especially so for areas with high MMPI values. Numerically, these differences result in mean MMPI values predicted by the 1D and 3D methods respectively of 1.369 and 1.496 respectively. Scaling by the mean annual precipitation of the base station (F0710, 1176 mm) gives 1610 mm and 1759 mm respectively. In percentage terms, the 3D method yields a 9.3% higher mean, than the 1D method which yields an 8.5% lower mean.
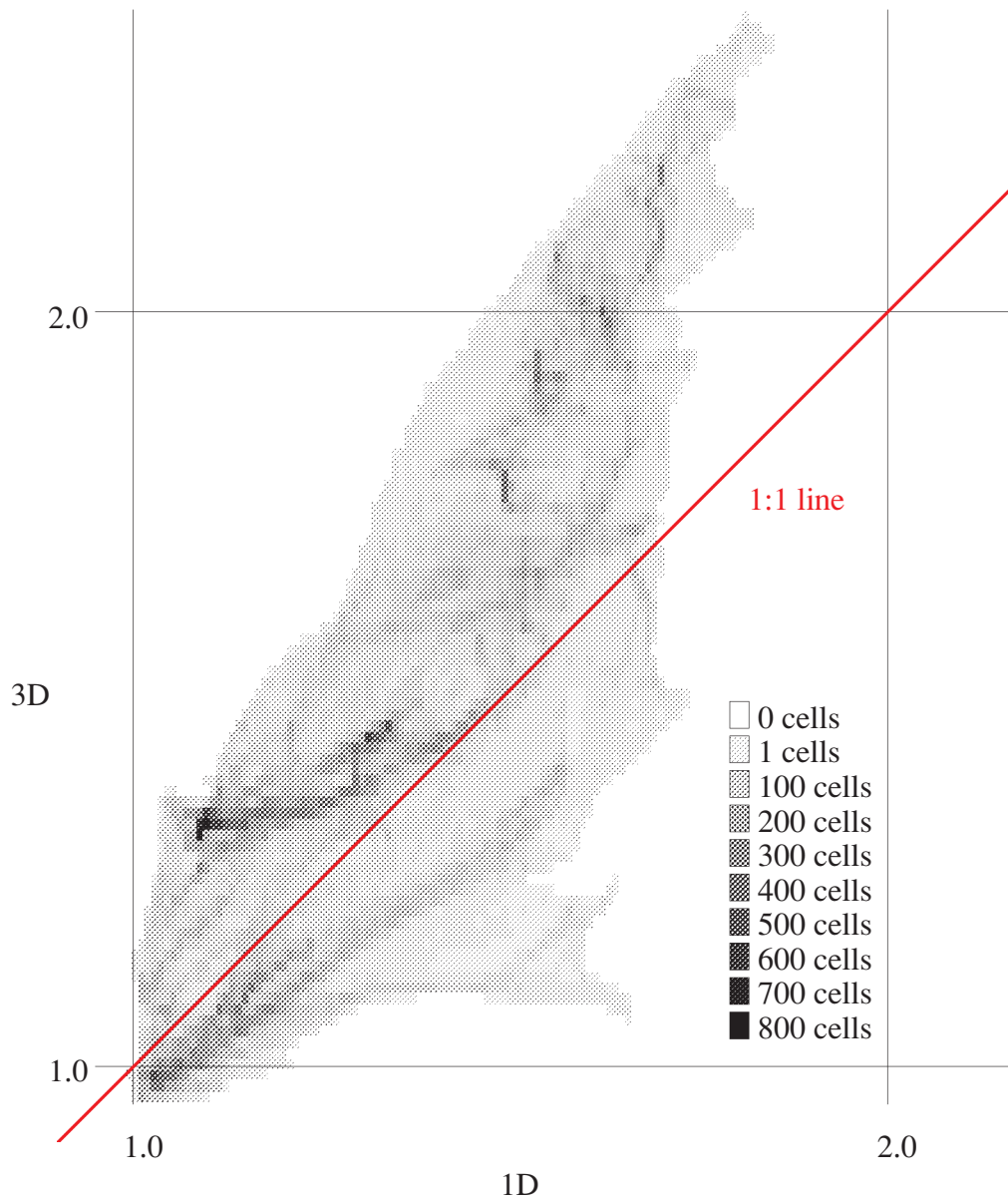
Figure 7.8: Enhanced XY scatter plot of 3D spline interpolated MMPI versus 1D linear interpolated MMPI for each of 0.25 million GIS cells in the study area. Because there are too many 'dots' to enter on a normal scatter plot without loosing clarity, the diagram is shaded according to how many dots fall on top of each other.

7.6 Daily precipitation estimation

The second stage of precipitation estimation considers *temporal* aspects. MMPI maps were constructed in the previous section as a means of estimating long term *spatial* patterns of precipitation. Here, it is assumed that:

- the relative spatial distribution of daily precipitation does not vary within a month.

When coupled with the assumptions made in Section 7.4, it is thus assumed that spatial patterns of precipitation never change from the daily scale upwards.

Given the above assumption, daily data from a base station is used to modulate the MMPI estimates for each location in the study area giving daily estimated precipitation for each location in the study area, according to the equation:

$$q_P = q_{P,stn} \frac{MMPI}{MMPI_{stn}} \tag{7.2}$$

This is presented as an initial procedure which makes use of the few very long term precipitation records for the region. A number of improvements are possible, some requiring more data, and some requiring alternative analysis of existing data. One improvement could utilise a number of base stations in concert with precipitation estimates weighted according to proximity to the respective base stations. Alternatively, a stochastic element could be introduced as discussed in the review at the start of this chapter (e.g. Shah et al., 1996a, b).

Testing of daily precipitation estimation against independent data is presented in Section 10.2.7.

7.7 Future improvements

A number of improvements to the methods described above are possible:

- In keeping with the idea that precipitation responds to elevation at large ($>$ 1 km) scale and not small ($<$ 1 km) scales, elevation data

from a smoothed elevation surface could be input as an independent variable instead of the raw elevation data. This idea was explored by Michaud et al., (1995).

- Closer examination of the data from individual gauges might be included in the analysis. For example, the high precipitation predicted in the south-east is largely due to high readings from a single gauge atop Mount Donna Buang. This gauge is sited in a highly sheltered location and may record more precipitation than other gauges due to reduced wind (or, vice versa, other gauges may record less precipitation due to increased wind).

- Separate maps of MMPI could be constructed for each month of the year, or each season (for instance, the January map would map 'mean January precipitation index'). Difficulties which would need to be overcome include the absence of data for particular months from gauges with very short records. Some exploration of these ideas was undertaken (but not described) and there were indications that spatial patterns of mean monthly precipitation vary throughout the year.

- Hutchinson's spline interpolation software (*op cit*) is able to take account of the uncertainty in individual data points through associated estimates of variance (Mitchell, 1991; Hutchinson and Gessler, 1994). Such estimates could be supplied to the software based on the sample variance and length of record for each MMPI site in order to improve the accuracy of the overall interpolation.

- A more detailed independent testing procedure should be employed than the limited testing described in Section 10.2.7. A good example is set by Martinez-Cob (1996) who used 132 stations for modelling precipitation patterns, withholding a further 50 for independent validation.

7.8   Summary

A means was presented of obtaining spatio-temporal daily precipitation estimates for each 25 × 25 metre grid-cell in a large area.

Beforehand, a review of the literature on precipitation observation and prediction highlighted the following points. There are many sources of error in both observation and measurement. The errors start with simple point measurement of precipitation in mountainous, forested areas. Both over and under-estimation can be expected due to wind, and the difficulty of siting

gauges in appropriate clearings. A benefit of working in these areas is that spatial precipitation patterns can be expected to be strongly correlated with elevation, an easily measured variable. Although, even mountainous areas exhibit strong, apparently random spatial variability in precipitation which is very difficult to measure.

Large scale spatial interpolation of mean precipitation is typically based on spline or kriging methods, apparently depending on which software is most readily available to the authors. There is disagreement and contradiction regarding which is best, although spline interpolation is stated to be easier to use. A number of techniques, including those simpler than splines or kriging, involve elevation as an independent variable in spatial precipitation estimation.

Hydrological modellers lag significantly behind the contemporary interpolation literature in their use of interpolated precipitation estimates in models. Very few studies to date have used either splines or kriging, despite clear evidence that hydrological models are very sensitive to spatial precipitation estimation techniques, and that splines and kriging are superior to traditional methods being used by hydrological modellers.

The incorporation of daily temporal information in precipitation estimation may be done either deterministically, by using a simple daily 'modulation' gauge which directly scales spatial mean precipitation estimates; or stochastically, where a wide range of techniques have been put forward which include statistically realistic temporal variations in predicted spatial patterns. The 'conditional simulation' examined by Shah et al. (1996a, b), which combines deterministic estimation at gauged sites with stochastic estimation at interpolated sites, holds promise as the way forward for contemporary hydrological modelling where precipitation estimation is being increasingly stressed as a bottleneck restricting the accuracy of hydrological models.

In the present study, following an extensive data-sourcing campaign, data were obtained from a relatively dense network of 87 gauges within and around the study area. These provided an excellent basis for the testing of various aspects of precipitation estimation. A limited amount of time was available, so there are very many, often simple, improvements and adjuncts to the procedures described below which could be implemented. A number of useful ideas gleaned from the literature review were not able to be incorporated.

The procedure adopted for estimating daily precipitation at any site began with the calculation of the mean monthly precipitation index (MMPI) for each gauged site. The MMPI is an *original* index of the mean precipitation

status of a site, independent of bias introduced by the period of record for the site, which may have occurred during relatively dry or wet parts of the century. Its use as such assumes that mean spatial patterns of precipitation are the same for each month of the year, and for each year of the century.

In order to facilitate precipitation sensitivity analysis later in the dissertation, two maps of MMPI were constructed for the study area. The first used a simple linear regression between MMPI and elevation which, when applied to the DEM, yielded a '1D linear' map of MMPI. The second map used 3D spline interpolation, and therefore differed by including two extra independent variables specifying horizontal location (easting and northing), and by allowing for non-linear patterns of MMPI with respect to the three independent variables. It is considered to be more accurate than the 1D map because it has more degrees of freedom, but can also reproduce 1D linear patterns if that is what is observed. Comparison of the two maps indicates that the 3D map better reproduces the dominant controls on mean precipitation in the study area, which are elevation and proximity to the main mass of the Great Dividing Range.

Temporal patterns of precipitation at any location are estimated using a relatively simple method which necessitates the assumption that spatial patterns of daily precipitation do not change within a month. When coupled with the previous assumptions, it is then assumed that precipitation distribution is stationary from the daily scale upwards, a clearly invalid, but workable assumption. A single, long term daily precipitation gauge is used as a base station. Its daily precipitation is used as a temporal signal which modulates the MMPI value estimated for each location within the study area.

Within Macaque, the procedure can be summarised as follows. Each ESU has an MMPI parameter expressing the mean precipitation status of the ESU. Its value is supplied to the model from the chosen map of MMPI (either 1D linear or 3D spline). During its execution for a given time step, the ESU receives the precipitation value from the base station as an input, and multiplies that by its own MMPI value to get its own daily estimate of precipitation.

As noted earlier, numerous improvements to this method are possible and should be investigated in the future. The methods described are biased towards the use of sophisticated spatial interpolation techniques (i.e. splines) and an imbalance exists due to the simplistic assumptions inherent in the use of a single base station to provide the temporal precipitation signal.

Chapter 8

Estimation of *E. regnans* LAI versus age

Contents

8.1   Prologue

The mapping of LAI over the study area requires the separate consideration of canopy species distribution and LAI estimation for canopy species, understorey species, and the sum of the two. These matters are brought together in Chapter 9. Here, one aspect of LAI mapping is dealt with in detail: the variation with forest age of the LAI of *E. regnans*. This variation is strongly linked to changes in water yield from Ash forests (Vertessy et al., 1994a), which are the driving issue behind this dissertation.

This chapter reproduces, almost verbatim, material published by Watson and Vertessy (1996). The work was conceived, completed, and written-up by the present author. R. Vertessy supervised the work and wrote the introductory paragraphs.

8.2   Abstract

A model is presented enabling the prediction of the leaf area of an individual *E. regnans* tree given both the diameter at breast height (DBH) of the tree

and the mean ln(DBH) of all trees in the stand from which the tree came. The model was calibrated using linear regressions on natural log data obtained through destructive measurement of the leaf areas of 78 trees.

Predictions of the leaf area of individual trees and of the total leaf area of a sample of trees were tested using destructive leaf area measurements from a further 88 trees. Tests of individual predictions showed that the model was able to accurately reproduce the dominant patterns of intra-stand variability in leaf area. Tests of total leaf area predictions revealed that the model could predict the leaf area index (LAI) of stands with errors ranging from 10% to 32% for trees younger than 60 years old, to a maximum of 88% for old-growth trees (225 years old).

The model was applied to a database of 2079 DBH measurements from 17 *E. regnans* stands. This application proceeded in two ways. Firstly, in a direct application of the model, individual tree leaf area predictions were made from each of the 2079 DBH measurements, and summed over respective stand areas to give LAI predictions for the 17 stands. When plotted against stand age and adjusted for variations in stocking rate, LAI predictions followed an expected pattern peaking at just under 4 m^2 m^{-2} for 10 to 20 year old forest and decreasing to less than 2 m^2 m^{-2} for old-growth stands.

A more general application of the model was to combine analytically the key model equation, predicting leaf area from DBH and mean ln(DBH), with regression equations describing age-related variation in the stem diameters of *E. regnans* forest. In particular the variation with age of mean stand ln(DBH), intra-stand distribution of DBH, and stocking rate were characterised. The combination of these equations produced an equation relating LAI to stand age which predicted a similar pattern of variation with age to the direct LAI predictions. This equation provided continuous estimates of LAI over a wide range of ages of *E. regnans* forest.

8.3   Introduction

In the *E. regnans* forests of south east Australia, stand age is a major determinant of catchment runoff rate. It is now well documented that regrowth *E. regnans* yields significantly less runoff than old-growth *E. regnans* (Langford, 1976; Kuczera, 1987; Jayasuriya et al., 1993). These water yield patterns have been attributed *inter alia* to transpiration differences caused by age-dependent changes in forest density and structure (Vertessy et al., 1994a). A great deal has been revealed about the hydro-ecological functioning of *E.*

regnans forests through investigations on root development (Ashton, 1975), stand structure (Ashton, 1976), tree water relations (Connor et al., 1977) and nutrient cycling (Feller, 1981; Polglase and Attiwill, 1992; Polglase et al., 1992a, 1992b). However, comparatively little has been reported on the leaf area index of *E. regnans*.

Leaf area index (LAI) is the ratio of leaf area of a forest stand to the area on the ground which it occupies. It is a major determinant of a number of hydrologic processes in forests including rainfall interception, transpiration and radiation partitioning. For these reasons, LAI is a key parameter in most process-based catchment hydrological models, being frequently used as the 'change parameter' to represent vegetation cover dynamics and its effect on water balance (Band et al., 1993; Vertessy et al., 1993, 1996).

In this chapter, a simple allometric technique is described to estimate LAI from stem diameter at breast height over bark (DBH) measurements. The model is an empirical one, being based on a limited sample of measurements collected in the *E. regnans* forests of the Victorian Central Highlands. However, the model performs well when tested against several independent data sets collected from the same area. Further, by combining the model with relationships between mean stem diameter, stocking rate and age, an analytical expression is developed that predicts LAI for different ages of *E. regnans*. This expression helps to elucidate the mechanisms behind the stand age/ water yield relationship reported by Langford (1976) and Kuczera (1987).

8.4 Previous allometric measurement of *Eucalyptus* LAI

A general description of techniques for LAI estimation is given in Section 9.2.1. Here, the focus is on allometric estimation of LAI.

In the Maroondah Catchments, Vertessy et al. (1995a, 1997) have fitted power-function curves to measurements of leaf area (LA) and DBH from a *sample* of trees within plots of known area. Figures 8.1 to 8.3 illustrate the relationships which were found for 4 year old, 16 year old[1], and 56 year old *E. regnans* forest respectively. The corresponding regression equations

---

[1]Vertessy et al. (1995a) report the age as 15 years, which is calculated using the date of seeding as the origin of the stand. In this report, the date of cessation of logging and burning is used as the origin date, in order that the ages of seeded and un-seeded stands (e.g. those burnt by wildfire) are consistent. This results in an age of 16 years for this stand.
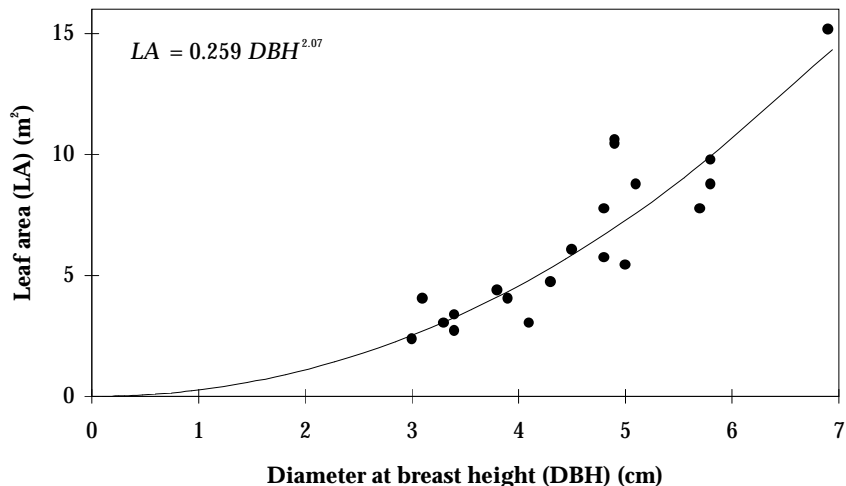
Figure 8.1: Power function fitted to LA versus DBH data for 4 year old forest in the Murrindindi catchment by Vertessy (unpub.).

predicting the LA of individual trees were as follows:

4 year old forest (Vertessy, unpub.)

$$\widehat{LA} = 0.259\,DBH^{2.07} \qquad r^2 = 0.81 \qquad n = 20 \tag{8.1}$$

16 year old forest (Vertessy et al., 1995a)

$$\widehat{LA} = 0.003\,DBH^{2.99} \qquad r^2 = 0.93 \qquad n = 19 \tag{8.2}$$

56 year old forest (Vertessy et al., 1997)

$$\widehat{LA} = 0.005\,DBH^{2.51} \qquad r^2 = 0.66 \qquad n = 11 \tag{8.3}$$

For a given stand, the LAI was calculated by applying the fitted relationship to DBH measurements for all trees in a plot to estimate the LA for every tree. The leaf areas were then summed and divided by the plot area to give LAI.

The method is useful for measuring the LAI of a plot by converting destructive LA measurements of a sample of trees to stand LAI, but it has two key limitations:

1. The process of directly fitting power functions is sensitive and not robust with respect to the software used to fit the curve. Vertessy et al. (1995a) used Macintosh-based Cricket Graph and Kaleidagraph software. While these yielded similar fits, different PC-based curve fitting software produced different equations.
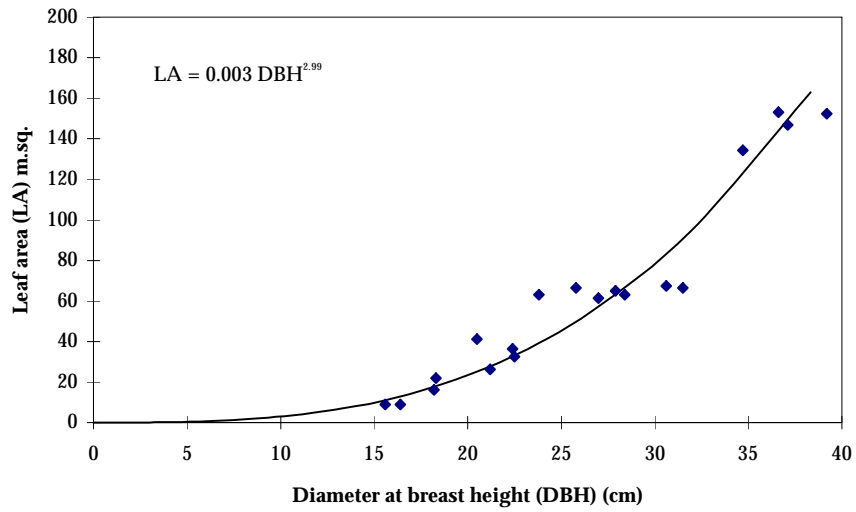
Figure 8.2: Power function fitted to LA versus DBH data for 15 year old forest near the Monda experimental catchments by Vertessy et al. (1995a).
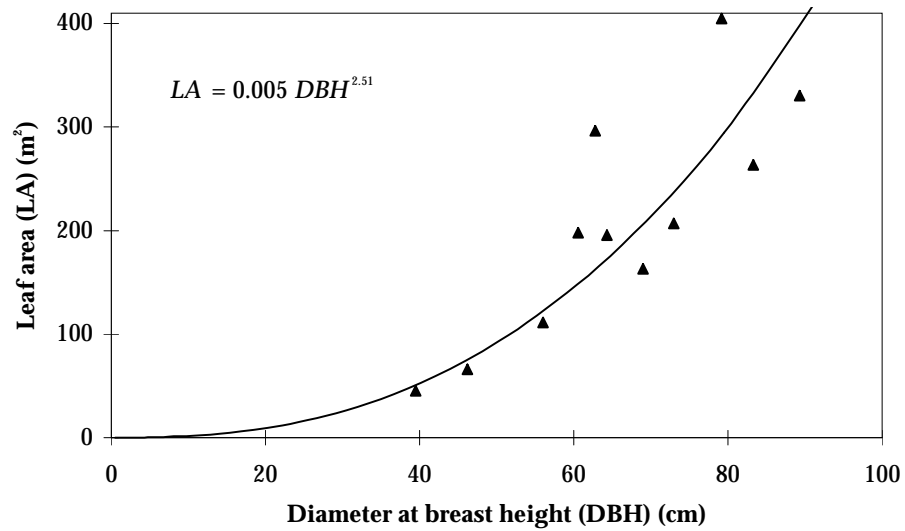
Figure 8.3: Power function fitted to LA versus DBH data for 56 year old forest near the Blacks' Spur experimental catchments by Vertessy et al. (1997).

2. A different curve must be constructed for different aged stands and the method offers no means of generalising to new stands where LA has not been measured.

8.5   Data used in this study

8.5.1   The database

A number of data sets based on destructive sampling of *E. regnans* leaf area are available. These are used in the calibration and testing of the model (Sections 8.7 and 8.8). Four of these data sets were collected by the research group of which the present author is a member. The remainder were collected as part of previous studies by other workers. Table 8.1 summarises these data sets which are reproduced in full in the Appendix to Watson and Vertessy (1996).

Additionally, a number of data sets comprised solely of DBH measurements were collected by a variety of authors. These are used in the general characterisation of forest structural variation with age (Section 8.6) and in the application of the model to predict LAI variation with age (Section 8.9).

8.5.2   Data representation and notation

The 'calibration' and 'testing' data sets above are represented as follows:

Data were acquired for a number of stands of trees occupying known areas. Within each stand, the DBH of every tree has been recorded. Also, within a sample of trees in each stand, the LA has been measured destructively. The data from the sampled trees are of the form:

$$(DBH_{s,i}, LA_{s,j}) \qquad\qquad (8.4)$$

... where $s = 1, ..., S$, S is the number of stands, $j = 1, ..., n_s$, n_s is the number of trees in the measured sample from stand s, $i = 1, ..., N_s$, and N_s is the number of trees in the whole population of stand s.

The distributions of $(DBH_{s,i}, LA_{s,j})$ data are highly skewed. Both $LA_{s,j}$ measurements and $DBH_{s,i}$ measurements are concentrated towards lower values and sparse at higher values. Additionally, the data are heteroscedastic.

Table 8.1 — Summary of the data sets used in this study.

Age	Name	Principal investigator(s)	Location	No. of DBHs	No. of LAs	Use	References
4	Vert4	Vertessy & O'Sullivan	Murrindindi catch.	20	20	Testing	Beringer (1994), Ord (1985)
5	Vert5	Vertessy & O'Sullivan	Murrindindi catch.	143	42	Calibration	
8	Ber8	Beringer	Myrtle 2 catch.	340	NA	Testing	
9	OS9	O'Sullivan	Myrtle 2 catch.	105	0	Application	O'Sullivan (in prep.)
11	Vert11	Vertessy & O'Sullivan	Myrtle 2 catch.	128	30	Testing	
14	Orr14	Orr	Picaninny catch.	18	18	Testing	Orr et al. (1986, App. 2)
14	Orl14	Orr	Picaninny catch.	29	0	Application	Orr et al. (1986, App. 3, 'Dense' plots only)
15	Ber15	Beringer	Monda 2/3 catch.	103	0	Application	Beringer (1994)
16	OS16	O'Sullivan	Monda 2/3 catch.	127	0	Application	O'Sullivan (in prep.)
16	Vert16	Vertessy & O'Sullivan	Monda 2/3 catch.	164	19	Calibration	Vertessy et al. (1994b, 1995a), O'Sullivan (in prep.)
21	Ber'21	Beringer	Picaninny catch.	249	0	Application	Beringer (1994)
22	OS22	O'Sullivan	Picaninny catch.	104	0	Application	O'Sullivan (in prep.)
38	Ron38	Ronan	Blacks' Spur 1 catch.	15	15	Testing	Ronan (1984)
50	Dun50	Dunn	Monda Road	44	0	Application	Dunn & Connor (1991, 1993)
50	Dun50	Dunn	Monda Road	1	0	Mixed age	Dunn & Connor (1991, 1993)
50	Dun150	Dunn	Myrtle 1 catch.	10	0	Mixed age	Dunn & Connor (1991, 1993)
50	Dun230	Dunn	Blacks' Spur catch.	153	0	Application	Dunn & Connor (1991, 1993)
54	Ber54	Beringer	Blacks' Spur catch.	59	0	Application	Beringer (1994)
55	OS55	O'Sullivan	Ettercon 3 catch.	94	0	Application	O'Sullivan (in prep.)
56	Vert56	Vertessy & O'Sullivan	Blacks' Spur catch.	17	11	Calibration	Vertessy et al. (1997), O'Sullivan (in prep.)
90	Dun90	Dunn	Monda Road	1	0	Mixed age	Dunn & Connor (1991, 1993)
90	Ron225	Ronan	Myrtle 2 catch.	3	3	Testing	Ronan (1984)
150	Dun150	Dunn	Monda Road	13	0	Application	Dunn & Connor (1991, 1993)
150	Ron225	Ronan	Myrtle 2 catch.	1	1	Testing	Ronan (1984)
150	Dun150	Dunn	Myrtle 2 catch.	1	0	Mixed age	Dunn & Connor (1991, 1993)
154	Berl54	Beringer	Monda Road	54	0	Mixed age	Beringer (1994)
212	MW212	Melbourne Water	Myrtle 2 catch.	29	0	Application	(Pure 'overmature' plots only)
225	Ron225	Ronan	Myrtle 2 catch.	7	7	Calibration	Ronan (1984)
230	Dun230	Dunn	Myrtle 1 catch.	8	0	Mixed age	Dunn & Connor (1991, 1993)
235	OS235	O'Sullivan	Myrtle 1 catch.	41	0	Mixed age	O'Sullivan (in prep.)
Sum				2079	166		

Table 8.1: Summary of the data sets used in this study. The complete data sets appear in Watson and Vertessy (1996). The 'use' column denotes how the data are used in this report. 'Calibration' data are used to calibrate the LA versus DBH model. 'Testing' data are used to test the model. 'Application' data are used in the example applications of the model. 'Mixed-age' data are data where the age of individual trees is in doubt and are only used in Figure 8.4.

By taking logarithms of the data, the data can be analysed using ordinary least squares analysis. The following notation will be adopted:

$$x_{s,i} = \ln(DBH_{s,i}) \qquad (8.5)$$

... and:

$$y_{s,j} = \ln(LA_{s,j}) \qquad (8.6)$$

Note that values such as $y_{s,j}$ are often estimated in the course of the following analyses. In such cases, a 'hat' is used to denote 'estimated value', e.g. $\hat{y}_{s,j}$.

DBH measurements were taken for the entire population. In the log domain these are the $x_{s,i}$ values from Equation 8.5. The sample mean of $x_{s,i}$ is $\bar{x}_s$ and the population mean is μ_s, both of which can be calculated directly from the data. LA measurements were taken only for a sample of the population of trees. From Equation 8.6 these are the $y_{s,j}$ values in the log domain. The sample mean of $y_{s,j}$ is $\bar{y}_s$ which is calculated directly from the data. The population mean of y_s is ν_s is unknown but is estimated below as $\hat{\nu}_s$.

From this point onwards, all analysis of LA and DBH data is performed on the logged data, that is, in terms of $x_{s,i}$ and $y_{s,j}$ instead of $DBH_{s,i}$ and $LA_{s,j}$. Conversions back to the original scale occur for some plots and results.

When taking a mean of log-transformed data the value $\bar{x}_s$, for example, is referred to in the text as 'mean ln(DBH)' - not 'mean DBH'. When mean ln(DBH) is plotted, the exponential is taken, transforming it back into linear units as what is here termed 'exp-mean-ln DBH'. This back-transformed value is then plotted on standard log axes. Hence the data are displayed on a log scale as desired, but the units on the axes are meaningful and as originally measured. Note that natural logarithms are used despite the fact that the axes are marked in powers of ten.

Additionally, residuals about means of log data are referred to as 'exp-residual-ln' values.

8.6 Observations of DBH and stocking rate variation

8.6.1 General DBH distribution characteristics

Figure 8.4 shows histograms of DBH values for each stand. The DBHs were measured from a population of trees from a plot of known area. These histograms illustrate how the distributions of DBH within stands varies with the age of the stands. The DBH classes were constructed along a log scale to enable stands of all ages to be viewed within the same domain with approximately uniform variance. Note that the DBH classes for the youngest trees in the Vert5 stand are smaller than the precision of measurement. As a result, the histogram for these classes displays more peaks than are present in the data. This is of negligible consequence. The following observations are made:

- The mean ln(DBH) increases with age, an observation which is explored in Section 8.6.2.

- Many of the distributions are multi-modal, reflecting plot sizes which are too small to accurately characterise the distribution shape. However, many of these can be assumed to follow a normal distribution. This observation is explored in Section 8.6.3.

- The youngest three distributions appear systematically bi-modal, perhaps indicating that the forest originates by two waves of germination in successive years, and that by about 10 years of age, competition and other forces obscures this pattern. Perhaps more plausibly, based on observations of growth and water use of *Eucalyptus grandis*, Benyon[2] (pers. comm.) suggests that competition itself may cause the bi-modality and that at about four or five years of age, the stand separates into distinct dominant and suppressed size classes, the suppressed trees eventually dying. Similar observations were made by Ashton (1976). Some older distributions are also bi-modal or even multi-modal, due partly to under-sampling, and partly to the sampling of mixed-age stands where the authors of the data have been unable to assign ages to individual trees and have simply recorded the age of the oldest trees in the stand.

---

[2]Richard Benyon, Post-doctoral fellow, CSIRO Forestry and Forest Products, Canberra

- Some stands, in particular the Ber154 and the OS235 stands, are clearly of mixed age, having trees from a much wider range of DBH classes than most stands. Data from these stands are of little use unless the trees can be separated into age classes. The mixed-age stands are included in Table 8.1 and Figure 8.4 to illustrate the need to consider whether DBH data are from a single-aged stand or a mixed-aged stand. In the remainder of this chapter however, mixed-age data are not considered unless the ages of all trees in the data set are known. In cases where the age of trees in old-growth, mixed-age stands *is* known, only data for the oldest stratum is used, unless otherwise stated. This is because the growth of sub-dominant trees in a mixed-age stand is likely to be different to that of trees of the same age in a single-age stand. The converse may be true to some extent for dominant trees in a mixed-age stand but, as *all* old-growth stands in the database are of mixed-age, use must be made of data from old-growth trees in mixed-age stands if the old-growth data are to be of any use.

8.6.2   Relationship between DBH and age

Some of the leaf area data used in this study were not collected in conjunction with DBH measurements from an *entire population* of trees within a plot of known area. In these cases, the population mean ln(DBH) cannot be calculated directly. As will become clear, the population mean ln(DBH) is an important quantity. Its variation with age is examined here, primarily for the purposes of constructing a simple relationship between DBH and age. This relationship can be used for situations where the mean ln(DBH) is not known.

Figure 8.5 shows exp-mean-ln DBH against stand age. Only stands exhibiting single-aged trees are included. Additionally, some stands in the Orr14 data set were excluded because they were part of particularly low stocked, poorly regenerated forest documented by Langford and O'Shaughnessy (1980b). Non-linearity and non-uniformity are evident in the data and can be rectified by re-plotting against log age as shown in Figure 8.6. The now uniform distribution of points along the x-axis indicates a strongly linear relationship for all but the youngest two stands.

If forest structural development is assumed not to commence until some years after age zero (here taken as the end of burning due to either wildfire or logging), then it is reasonable to consider not 'age' but 'age minus some
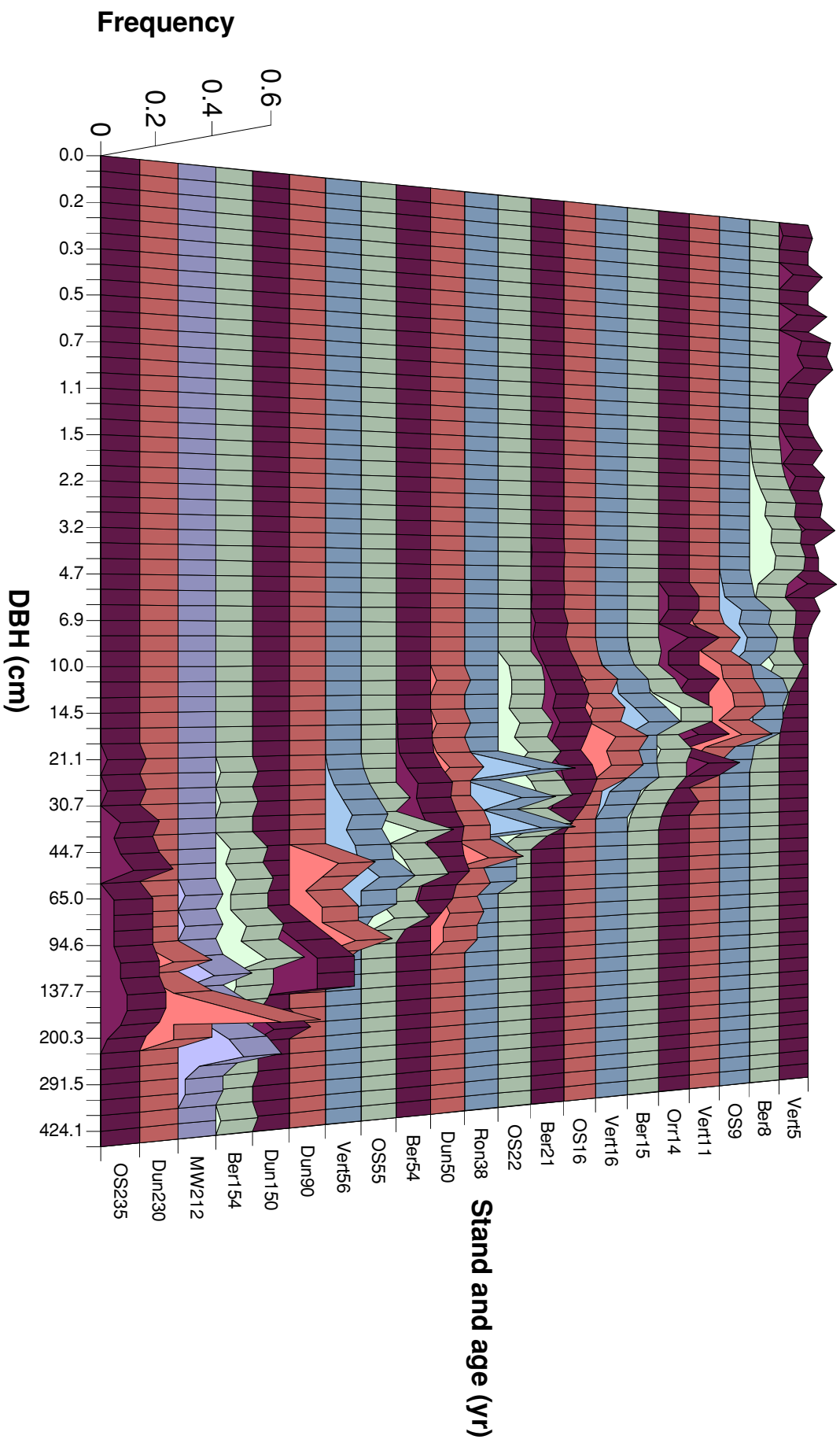
Figure 8.4: Histograms of DBH values for each stand in the database. DBH classes are calculated and plotted along a natural logarithmic scale.
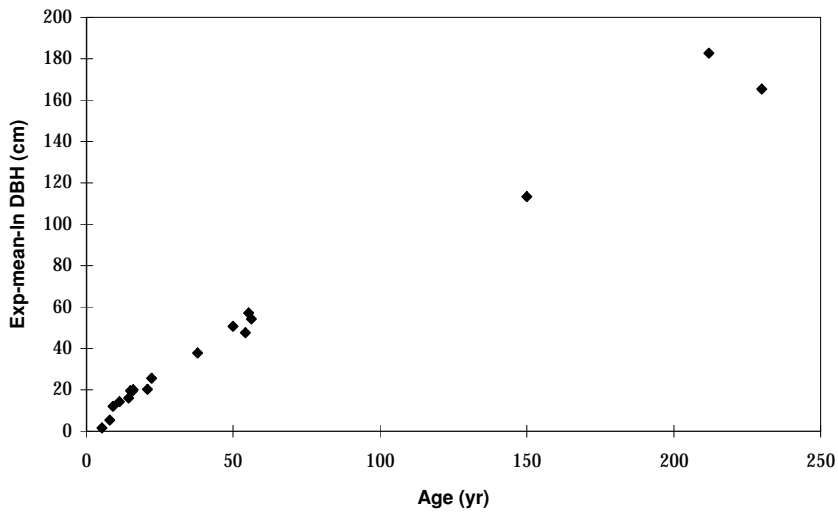
Figure 8.5: Linear plot of exp-mean-ln DBH versus forest age for all healthy, single-aged stands where all DBHs in a plot or plots of known area have been measured

value' as the independent variable. Hence, the following equation relating exp-mean-ln DBH to age was constructed:

$$\hat{\mu}_s = d_1 + d_2 \ln(AGE_s - d_3) \qquad (8.7)$$

The parameters d_1 and d_2 were obtained using ordinary least squares linear regression, adjusting d_3 to maximise the associated r^2 value. The estimated parameters, resulting in $r^2 = 0.987$, were:

$$d_1 = 1.206 \qquad (8.8)$$
$$d_2 = 0.719 \qquad (8.9)$$
$$d_3 = 5.04 \qquad (8.10)$$

Figure 8.7 shows the line of best fit for the data after adjustment of age (i.e. $AGE - d_3$). The two youngest stands have been 'pulled into line' by the age adjustment though the model will not reliably predict exp-mean-ln DBH for forests younger than or close to $d_3 = 5.04$ years old. The calibrated value of 5.04 for d_3 is higher than would be expected given the earlier hypothesis of delayed forest structural development. Forests younger than five years old are frequently well developed. Clearly, more data from young forests are required if the age adjustment approach is to be consolidated. Presently, Equation 8.7 is used in latter parts of this chapter despite some reservations

about the degree to which it is appropriate. It reflects a meaningful approach to modelling DBH versus age relationships but could be improved with more data, which would probably reduce the calibrated value of d_3.

For *E. regnans* in other areas, Ashton (1976) gives the relation:

$$\log(D\hat{B}H) = 1.02 \log(AGE)$$

with some ambiguity as to whether means or individual trees were used to construct the relationship. Using the form of Ashton's equation in the present study area, the following regression equation was obtained:

$$\log(\overline{\hat{DBH}}_s) = -0.029 + 1.002 \log(AGE_s), \ r^2 = 0.906$$

for mean values, which is very similar to Ashton's equation.

8.6.3 DBH distribution shape

Figure 8.8 shows histograms of standardised ln(DBH) data from all single-aged healthy stands overlaid upon one another[3]. A standard normal probability density function (PDF) is overlaid upon these histograms, indicating that the ln(DBH) values are approximately normally distributed. Exceptions arise for stands where a small number of trees were measured, and plotted distributions appear irregular, multi-modal, and peaked.

8.6.4 Stocking rate versus age

Figure 8.9 shows stocking rate plotted against age on log/log axes for the same stands as above. A strong pattern of forest thinning is evident from 5 year old to 230 year old forest. This information provides a useful background to the remainder of the chapter, particularly in helping determine whether

---

[3]The standardisation follows the equation:

$$z = \frac{x_{s,i} - \mu_s}{\sigma_s} \tag{8.11}$$

where z is the standardised value of $x_{s,i}$ and σ_s is the population standard deviation of $x_{s,i}$.
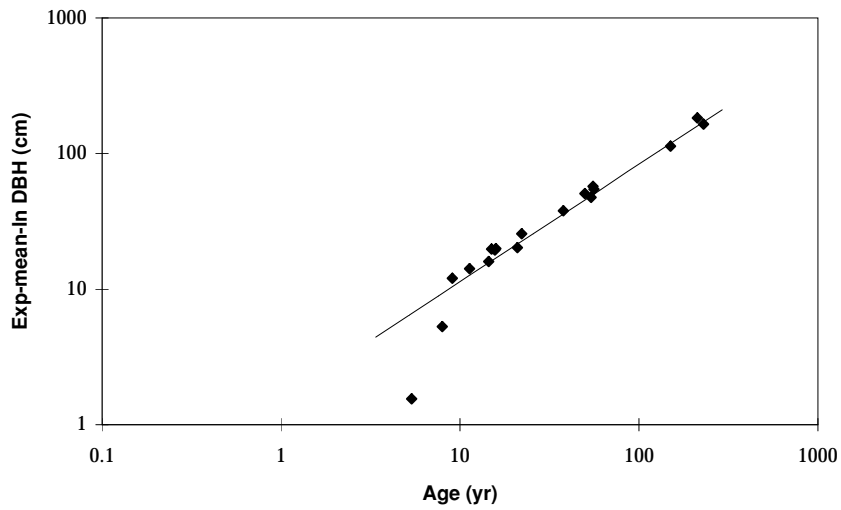
Figure 8.6: Logarithmic plot of exp-mean-ln DBH versus age with the line of best fit obtained by ordinary linear regression.
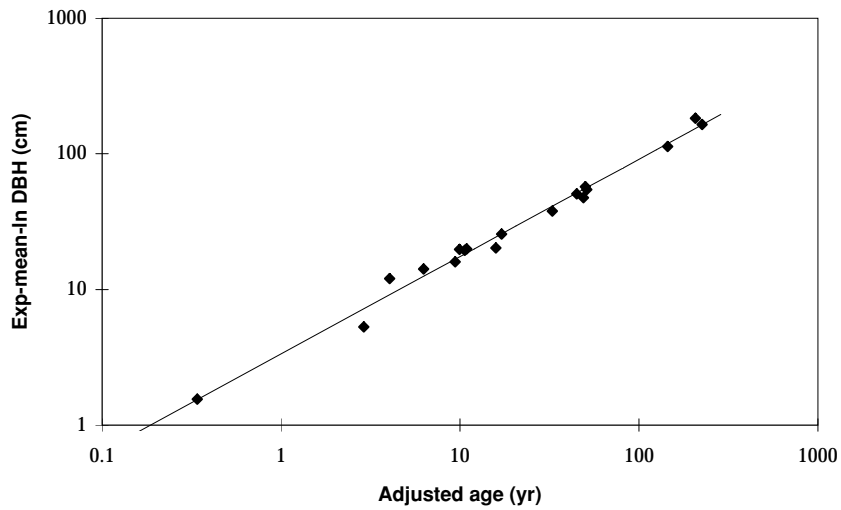
Figure 8.7: Logarithmic plot of exp-mean-ln DBH versus *adjusted* age, including the line of best fit obtained by ordinary linear regression.

variations in leaf area index with age are due to variations in stocking rate, or some other influence. The following regression has been fitted to the stocking rate data:

$$\ln(\widehat{SR_s}) = r_1 + r_2 \ln(AGE_s) \tag{8.12}$$

which becomes, after estimation of regression parameters:

$$\ln(\widehat{SR_s}) = 11.610 - 1.624 \ln(AGE_s) \quad r^2 = 0.921 \tag{8.13}$$

where $\widehat{SR_s}$ is an estimate of SR_s, the stocking rate of a stand.

8.7 A new, generalised model for estimating LAI from stem diameter measurements

8.7.1 Introduction

In this section, a new model is described which linearises the observed relationship between LA and DBH, and generalises it to a wide range of *E. regnans* stands. The model was developed using data from four *E. regnans* stands and then tested using data from several other stands (refer to Table 8.1).

The calibration data are plotted on linear axes in Figure 8.10 and on log/log axes in Figure 8.11. Figure 8.10 clearly shows the variance increasing with LA and DBH, and the non-uniform distribution of points along each axis. Logarithmic transformations of both LA and DBH resulted in a more constant variance and uniformity in both variables (see Figure 8.11). Figure 8.11 illustrates clustering of the data into four groups, corresponding to the four stands which were sampled. There appears to be some variability amongst observations within a cluster, though the mean values of each cluster align linearly. The relationships between ln(LA) and ln(DBH) in the three youngest stands, can be represented quite well by linear regressions.

The model predicting LA from DBH measurements was derived in two parts. Firstly, the relationship between population mean LA and population mean
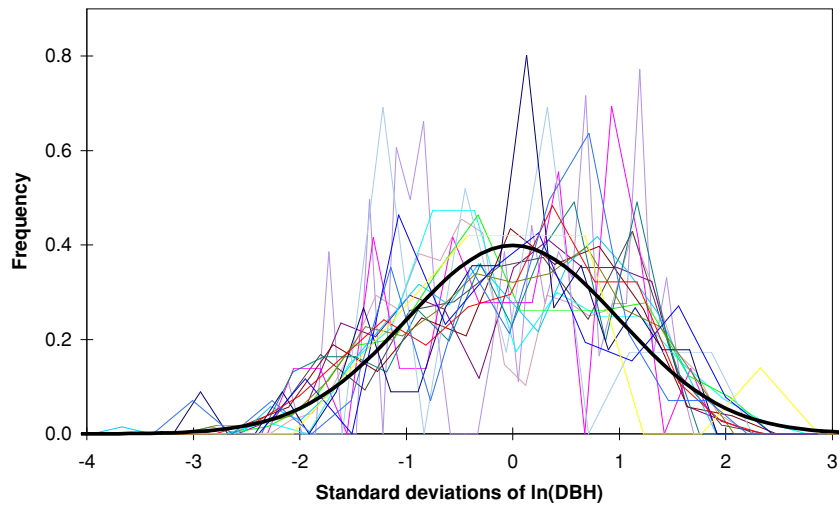
Figure 8.8: Histograms of ln(DBH) values within each stand, standardised and scaled to have zero mean, unit standard deviation, and unit area. A standard normal PDF has been overlaid to demonstrate that the distribution of ln(DBH) for any given stand tends towards a normal distribution. For clarity, the histograms have been plotted using lines instead of bars.
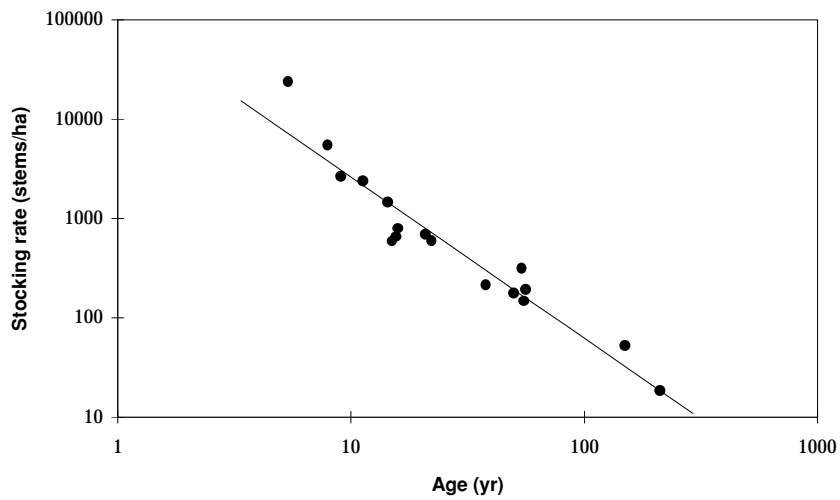
Figure 8.9: Stocking rate versus age for a number of forest stands, plotted on log/log axes, including the line of best fit obtained by ordinary linear regression.
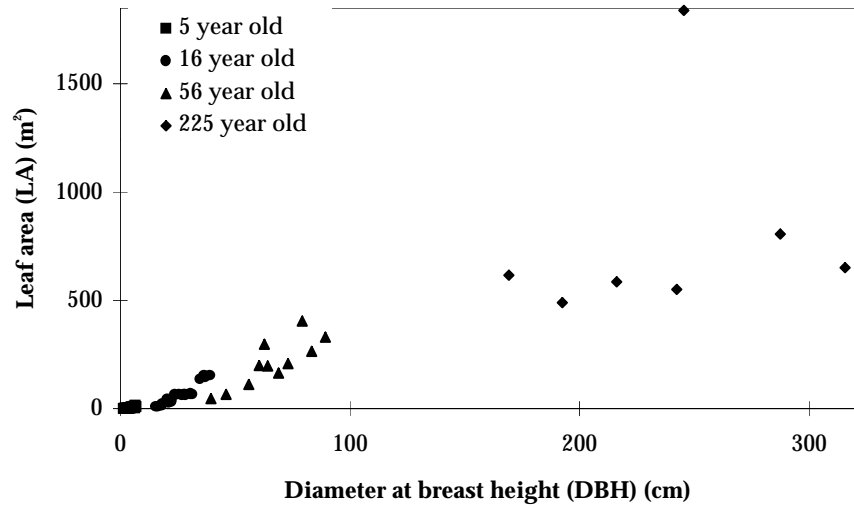
Figure 8.10: Sampled LA versus DBH for the four 'calibration' stands - plotted on linear axes
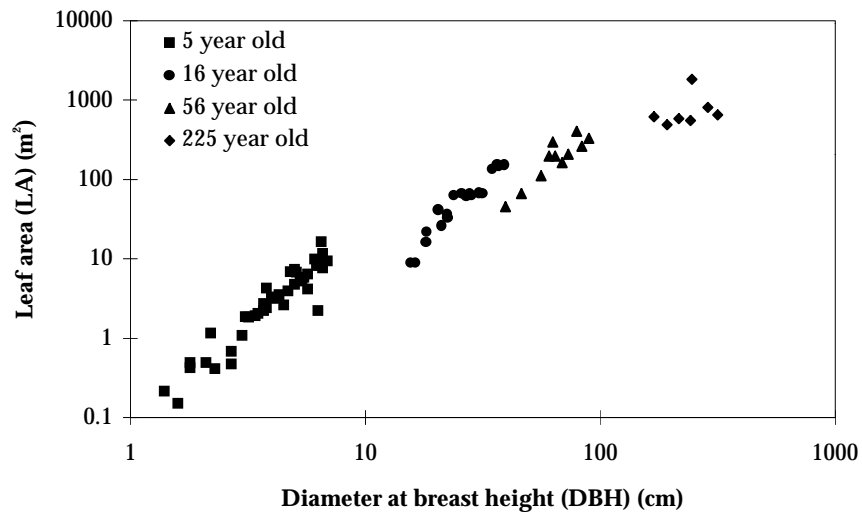
Figure 8.11: Sampled LA versus DBH for the four 'calibration' stands - plotted on log axes

DBH was obtained. Secondly, a relationship was developed between residual LA and DBH *within* each stand. In the following two sections, these procedures are described in full.

8.7.2 Calculation of mean stand LA versus mean stand DBH

To relate mean LA to mean population DBH in the log domain, a linear regression of $\hat{\nu}_s$ on μ_s was performed. Values of μ_s were calculated directly, and values of $\hat{\nu}_s$ were estimated. This was accomplished using separate linear regressions on the $(x_{s,j}, y_{s,j})$ data from each stand as follows:

In Figure 8.11, a linear relation between $y_{s,j}$ and $x_{s,j}$ is evident within each stand. It was assumed that the sampled ln(DBH) values were uniformly distributed and that, for each value of ln(DBH), measurements of ln(LA) were normally distributed about their mean. This assumption is independent of the observation in Section 8.6.3 that *populations* of ln(DBH) values are approximately normally distributed. Figure 8.11 shows that the sampled ln(DBH) values are not always uniformly distributed within each stand. The following ordinary least squares analyses are limited to some degree by this fact. Four separate linear regressions of the form:

$$\hat{y}_{s,j} = \gamma_s + \delta_s x_{s,j} \tag{8.14}$$

... were fitted to the data in each stand. Estimates of $y_{s,i}$ were obtained by substituting $x_{s,i}$ values into the resulting linear equation. The linear regressions calculated for each stand were:

Stand 1: 5 year old

$$\hat{y}_{1,i} = -2.502 + 2.526\, x_{1,i} \quad r^2 = 0.898 \tag{8.15}$$

Stand 2: 16 year old

$$\hat{y}_{2,i} = -5.780 + 2.987\, x_{2,i} \quad r^2 = 0.929 \tag{8.16}$$

Stand 3: 56 year old

$$\hat{y}_{3,i} = -5.293 + 2.513\, x_{3,i} \quad r^2 = 0.836 \tag{8.17}$$
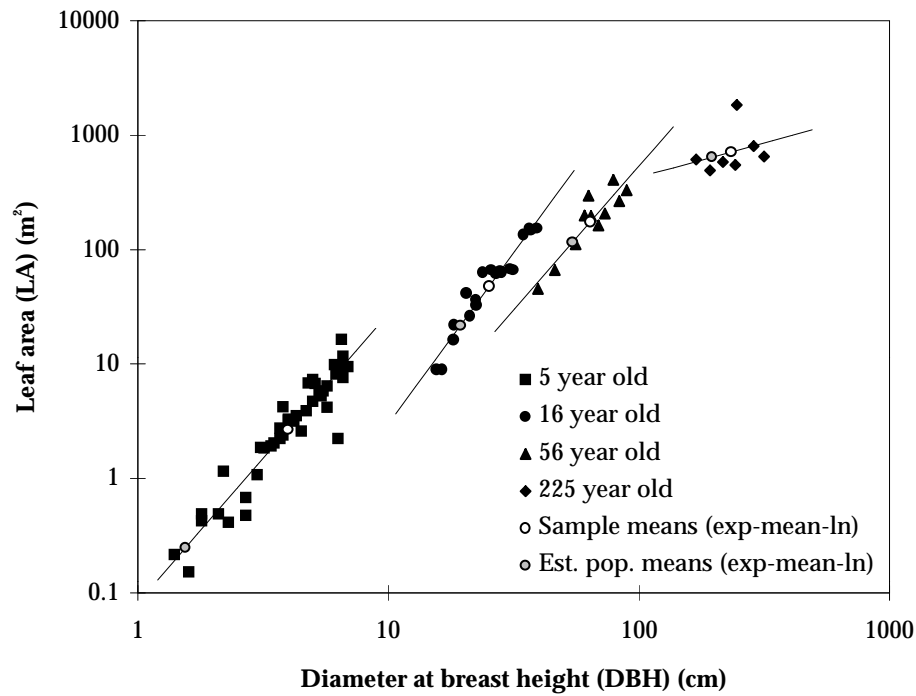
Figure 8.12: Estimating the population mean ln(LA) of stands: four separate regression lines are fitted; the white circles are sample means; the grey circles are population means estimated from the sample regression equations.

Stand 4: 225 year old

$$\hat{y}_{4,i} = 3.313 + 0.597\, x_{4,i} \qquad r^2 = 0.085 \qquad (8.18)$$

These relationships are graphed in Figure 8.12.

Log/log relationships between LA and DBH have been recognised by other authors. For five tree species in Western Australia including two eucalypts, Hingston et al. (pers. comm.[4]) obtained $\log_{10}/\log_{10}$ relationships between *leaf weight* and DBH. These relationships, although using base-ten logarithms instead of natural logarithms, and leaf weight instead of leaf area, can be compared to the present LA versus DBH relationships by adjusting the intercept, γ_s, in Equation 8.14. The slope term in Equation 8.14, δ_s, is directly comparable without adjustment. Hingston et al's slopes range from 1.62 to 2.06, slightly lower than those found here. Attiwill (1962), in *E. obliqua* forest, formed a $\log_{10}/\log_{10}$ relationship between dry leaf weight and *branch* girth with a slope of 1.66, also lower than those found here. In *E. regnans*, Attiwill (1991) formed several ln/ln relationships between dry leaf weight and DBH but only provided an equation for one, which had a

---

[4]Hingston, F.J., Galbraith, J.H., & Jones, M.S., CSIRO Division of Forestry and Forest Products, W.A. Divisional Research Group, Western Australia

slope of 2.38, being similar to the present values. Feller (1980) obtained slopes ranging from 1.7 to 6.8 for ln/ln relationships between leaf weight and DBH in three eucalypt species. Ronan (1984) and Teskey and Sheriff (1996) obtained linear regressions between LA and *basal area* for *E. regnans* and *Pinus radiata*, respectively. Because basal area is proportional to the square of DBH, a linear LA versus basal area relationship translates into the log/log domain as a LA versus DBH relationship with $\delta_s = 2$. Conversely, relationships such as those presented above and Hingston et al's, where δ is approximately equal to two, will appear linear if basal area is used as the independent variable instead of DBH. However, the log/log domain is preferred to Ronan's and Teskey and Sheriff's linear approach because: it allows for cases where δ_s is not equal to two; it forces the relationship through zero, thus avoiding negative leaf areas; it reduces non-uniformity in the distribution of the independent variable (here ln(DBH)); and it reduces heteroscedasticity in the dependent variable (here ln(LA)). Ronan's basal area values are non-uniformly distributed, which biases his ordinary linear regression towards low values. Pook (1984b) adopted a quadratic model for a regression on untransformed LA versus basal area data. His Figure 4 shows non-uniformity which suggests that data transformation could improve the model.

The sample mean ln(LA) and sample mean ln(DBH) can be calculated for each stand, but estimation of the mean relationship between LA and DBH should be based on the population means and not the sample means. This is necessary for the method to be independent of the sampling procedure. Thus, the population mean ln(LA), ν_s, was estimated for each stand using Equations 8.15 to 8.18, by substituting in the population mean ln(DBH), μ_s, for each stand:

$$\hat{\nu}_s = \gamma_s + \delta_s \mu_s \tag{8.19}$$

The sample means $(\bar{x}_s, \bar{y}_s)$ and population means $(\mu_s, \hat{\nu}_s)$ for each stand are plotted in Figure 8.12. There is a clear offset between sample and population means for each stand. This indicates that the samples are not representative of the populations for each stand, because of the bias to sample larger trees, hence justifying the separate consideration of sample and population means. The population means do, however, fall within the domain of the sampled trees, thus validating the estimation of population mean ln(LA) from the sample data.

A further linear regression is performed on the estimated population means giving the relationship between mean stand ln(LA) and mean stand ln(DBH)
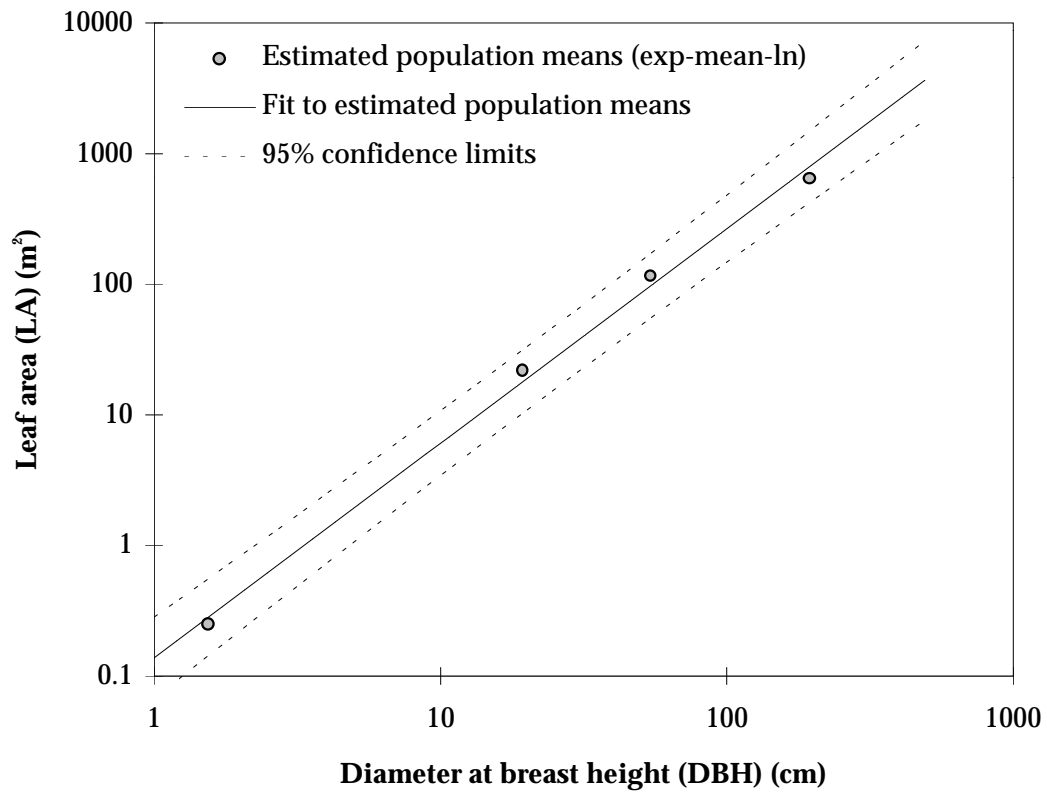
Figure 8.13: Estimated variation in (estimated) population mean ln(LA) between stands.

represented by the solid line in Figure 8.13 (i.e. the line of best fit to the grey circles in Figure 8.12). Note that the estimate of population mean ln(LA) produced here is an *estimate derived from an estimate*, written as $\hat{\hat{\nu}}_s$, which occurs in the general regression equation:

$$\hat{\hat{\nu}}_s = \alpha + \beta \mu_s \tag{8.20}$$

The resulting line of best fit in Figure 8.13 is:

$$\hat{\hat{\nu}}_s = -1.980 + 1.642 \mu_s \quad r^2 = 0.996 \tag{8.21}$$

The estimate, $\hat{\hat{\nu}}_s$, for stands of *E. regnans* described by Equation 8.20 is subject to regression errors which are calculated in Section G.1. The 95% confidence limits were subsequently calculated and plotted in Figure 8.13. All points fall within the confidence limits. There are additional errors in the measurement of leaf area and in the estimation of population means

from sample means. The magnitude of these is not explicitly investigated here but is implicit in the errors discussed in Section 8.8. In the following section, a relationship describing the intra-stand variability of leaf area is described which assumes that ν_s is known. This intra-stand relationship is thus subject not only to its own errors, but also the error in the mean relationship, or $\hat{\nu}_s - \nu_s$.

8.7.3 Calculation of LA versus DBH within each stand

As discussed in Section 8.7.1, a linear relationship between $y_{s,j}$ and $x_{s,j}$ is evident *within* each stand. The calculated residuals about the estimated population means for each tree in each stand, $(x_{s,j} - \mu_s, y_{s,j} - \hat{\nu}_s)$, are plotted in Figure 8.14.

The line of best fit represents the relationship between the residuals. However, a *single* linear regression is not suitable for this data because it is biased towards stands with more trees. Instead, separate regressions fitted earlier for each stand (Equations 8.15 to 8.18) were used. The slope of the line of best fit for all residuals, $\bar{\delta}$, is taken as the mean of the slopes of the separate regressions, δ_s. The intercept is zero because the population means about which the residuals are calculated are defined to lie *on* the separate regression lines from Equations 8.15 to 8.18. Taking the mean slope is equivalent to performing a single regression on unbiased data for the zero-intercept case.

The r^2 for the 225 year old forest (Equation 8.18) is very low. The strong intra-stand relationship between leaf area and DBH observed in the younger stands does not hold for older forest. It is suggested that the intra-stand patterns observed for the younger forest are a result of thinning processes within the stand. If a tree has a DBH significantly lower than the mean DBH of the stand, it is most likely to become a victim of natural thinning. As such, it is in sub-optimal health, and its leaf area will be lower than would be predicted by the inter-stand relationship described in Section 8.7.2. The converse applies to trees of larger DBH than the stand mean. This argument leads to a LA versus DBH relationship which is steeper within stands than between stands, which is what is observed in Figure 8.12. Once a forest begins to senesce (i.e. branches which are destroyed by the elements are not replaced), thinning through competition amongst trees is perhaps less prevalent and the steep intra-stand LA versus DBH relationship will weaken. The structure of the forest will be primarily influenced by more random controls such as catastrophic crown damage in storms and so forth.
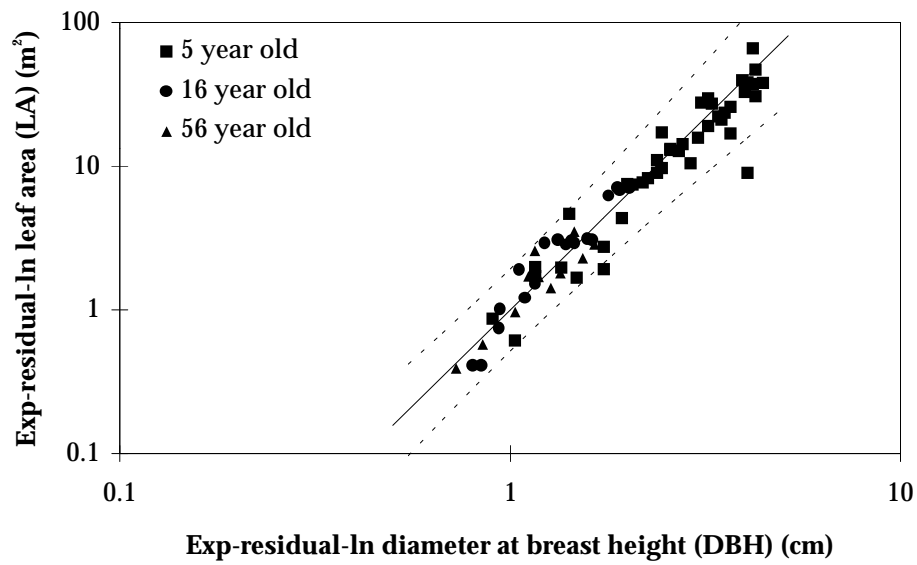
Figure 8.14: Mean of three separate regressions on residual LA versus DBH variation within each stand. Dashed lines indicate 95% confidence limits for the mean regression.

Because of the weak intra-stand pattern in the 225 year old forest, the slope of the mean line of best fit to the residuals was calculated as the mean of the slopes for the *three younger stands only*. The resulting mean line of best fit to the residuals is plotted in Figure 8.14 and described by the following equation:

$$\hat{y}_{s,i} - \hat{\nu}_s = \gamma + \bar{\delta}(x_{s,i} - \mu_s) \quad s = 1, 2, 3 \tag{8.22}$$

By substituting in parameter values of $\gamma = 0$ and $\bar{\delta} = \frac{1}{3}\sum_{s=1}^{3}\delta_s = 2.675$ the following equation was obtained:

$$\hat{y}_{s,i} - \hat{\nu}_s = 2.675(x_{s,i} - \mu_s) \tag{8.23}$$

At this point the specific regression slopes, δ_s, for each stand could have been used. However, the slopes for each stand are quite similar and a general relationship with only one slope, $\bar{\delta}$, is more useful. The improvement in predictive accuracy offered by separate regressions of the residuals was briefly tested (not shown) and it was found that the improvement is not so large as to offset the benefits of a general relationship.

The estimate of $y_{s,i} - \hat{\nu}_s$ described by Equation 8.22 is subject to regression errors which are calculated in Section G.2. They are subsequently used in

the calculation of the 95% confidence limits which are plotted in Figure 8.14. All but two of the 72 data points fall within the confidence limits, indicating that the limits are a valid characterisation of the error in the fit to residuals. Additional errors arise in the use of a single fit to approximate the fits for stands of different ages, and in the extrapolation of the residual relationship to forests older than 56 years. The model of residuals assumes that the population mean ln(LA) values for each stand is accurate, an assumption which itself is subject to the errors noted in Section 8.7.2. The total magnitude of the error in $\hat{y}_{s,i} - \hat{\nu}_s$ is implicit in the errors discussed in Section 8.8.

8.7.4 The full model

The relationship between ln(LA) and ln(DBH) was obtained by substituting Equation 8.20 into Equation 8.22, giving:

$$\hat{y}_{s,i} = \alpha + \beta\mu_s + \gamma + \bar{\delta}(x_{s,i} - \mu_s) \tag{8.24}$$

and:

$$\hat{y}_{s,i} = -1.980 + 1.642\mu_s + 2.675(x_{s,i} - \mu_s) \tag{8.25}$$

once the appropriate parameter values were substituted.

Back-transformation of these equations gave:

$$\widehat{LA}_{s,i} = e^{\alpha + \beta\mu_s + \gamma + \bar{\delta}(\ln DBH_{s,i} - \mu_s)} \tag{8.26}$$

and:

$$\widehat{LA}_{s,i} = e^{-1.980 + 1.642\mu_s + 2.675(\ln DBH_{s,i} - \mu_s)} \tag{8.27}$$

once the appropriate parameter values were substituted.

Equations 8.26 and 8.27 were simplified as:

$$\widehat{LA}_{s,i} = e^{\alpha+\gamma} \, M_s^{\beta-\delta} \, DBH_{s,i}^{\delta} \tag{8.28}$$

and:

$$\widehat{LA}_{s,i} = 0.138 \ M_s^{-1.033} \ DBH_{s,i}^{2.675} \tag{8.29}$$

once the following substitution was made:

$$M_s \ = \ e^{\mu_s} \ = \ e^{\frac{1}{N_s}\sum_{i=1}^{N_s}\ln(DBH_{s,i})} \tag{8.30}$$

The relationship between LA and DBH described by Equation 8.29 is plotted in Figure 8.15 on log/log axes for each of the for stands, and on linear axes in Figure 8.16. The model enables the prediction of the leaf area of any tree in a stand of *E. regnans* given $x_{s,i}$, the natural log of the DBH of the tree, and M_s the exponential of the mean of the natural logs of the DBHs of all trees in the stand. Values for M_s can be estimated from the age of stand as discussed in Section 8.6.2. The model can also predict the LAI of a stand if the area of the stand is known and the DBHs of all trees in the stand are known.

The estimate of $LA_{s,i}$ described by Equation 8.29 is subject to the sum of the errors described in Sections 8.7.2 and 8.7.3, including the regression errors calculated in Section G.3. These regression errors are represented as 95% confidence limits in Figures 8.15 and 8.16. All but one of the points from the first three stands fall within the confidence limits, indicating that the limits are an accurate representation of the regression errors in the full model. Three of the seven points for the 225 year old stand fall outside the limits, which relates to the earlier observation that patterns of intra-stand variability in LA are weakened for old-growth forests. Predictions of *individual* tree LA for stands older than 56 years are *extrapolations*, the true confidence limits for which would be significantly wider than shown in Figures 8.15 and 8.16. The following section tests the model predictions using some additional leaf area data.

8.8 Model testing

Leaf area measurements from samples within four forest stands were used to construct and calibrate a general model for predicting the leaf area of a tree given its DBH and the mean ln(DBH) of the population of trees from which it came. In this section, a further five sets of leaf area measurements are
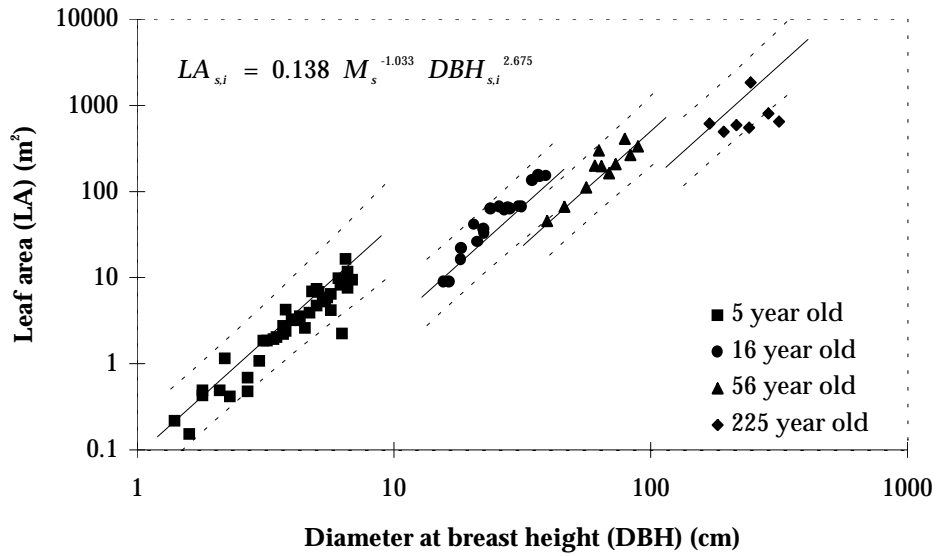
Figure 8.15: Final model of LA versus DBH for the four stands, plotted on log axes with 95% confidence limits (dashed lines).
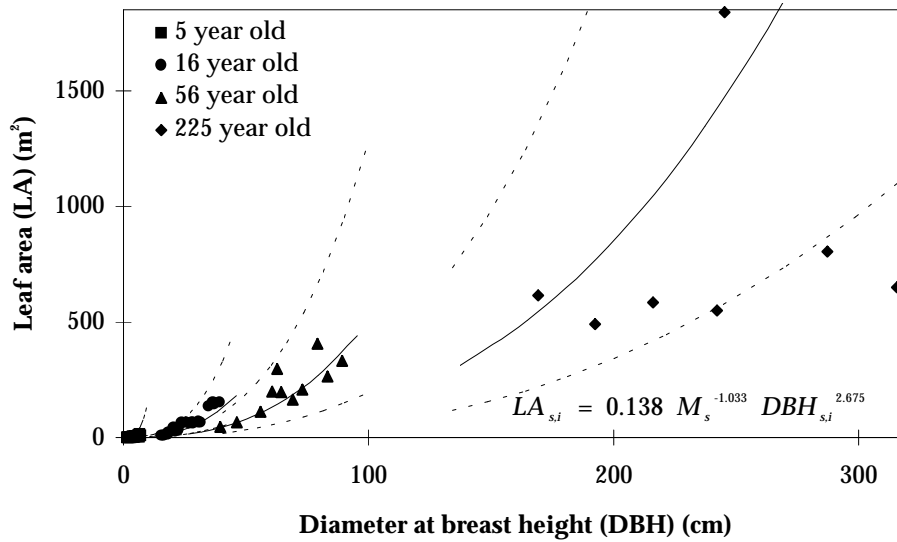
Figure 8.16: Final model of LA versus DBH for the four stands, plotted on linear axes with 95% confidence limits (dashed lines).

used to independently test the model. Firstly, the prediction of individual tree leaf area is assessed and secondly, the prediction of the total leaf area of sampled trees is assessed.

8.8.1   Testing of individual tree leaf area predictions

Data from five forest stands are available for testing individual tree leaf area predictions (see Table 8.1). Two of these data sets were collected as part of the current research programme. The remaining three were collected as part of two previous research efforts in the same region. The five data sets are named after the chief researcher in each case and are examined separately as follows:

8.8.1.1 The Vertessy & O'Sullivan Murrindindi 4 year old data set

This data set was obtained by the destruction and leaf area measurement of 20 trees in the Murrindindi basin during July 1995. Unfortunately, DBH measurements were taken only for the destroyed trees and not for an entire population from a known area. This means that the data can only be used to test the intra-stand prediction of leaf area variation and not the mean leaf area of the stand in relation to other, older stands.

For the purposes of display, the population mean ln(DBH) was calibrated so that the total prediction error for the stand is zero. Modelled versus measured leaf area for this data set is plotted in Figure 8.17. The points are closely scattered around the 1:1 line at a similar slope. The overall proximity of the points to the line is of no consequence - being a result of calibration. However, the similarity in slope indicates that the model accurately predicts the intra-stand variability of leaf area for this stand.
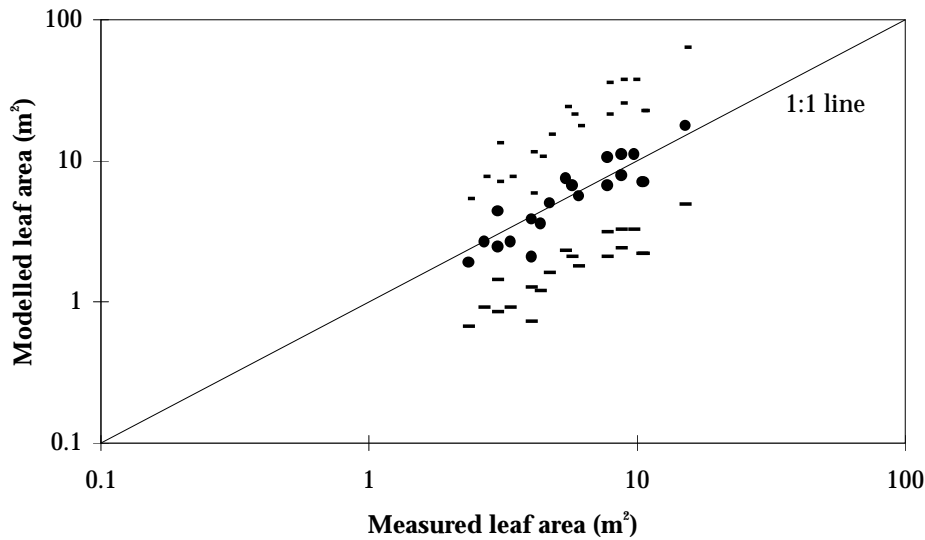
Figure 8.17: Modelled versus measured leaf area for the 'Vertessy & O'Sullivan Murrindindi 4 year old' data set. Dashes indicate 95% confidence limits for each prediction.

8.8.1.2 The Vertessy & O'Sullivan Myrtle 11 year old data set

This data set was obtained by the destruction and leaf area measurement of 30 trees from a 540 m^2 plot in the recently logged Myrtle 2 experimental catchment during July 1996. Additionally, DBH was measured for the full population of 128 trees in the plot, enabling the calculation of a population mean ln(DBH).

Modelled versus measured leaf area for this data set is plotted in Figure 8.18. The points are closely scattered along the 1:1 line at a similar but slightly shallower slope. The plot demonstrates that the model has accurately predicted both the mean leaf area of these 11 year old trees and the pattern of their intra-stand leaf area variability. The 95% confidence limits for two of the predictions fall away from the 1:1 line, approximately the number expected from a sample size of 30.
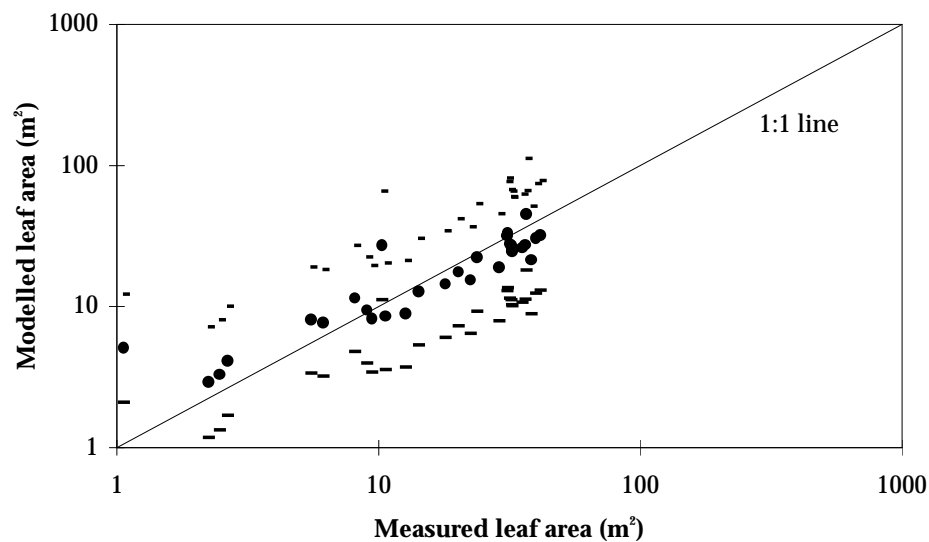
Figure 8.18: Modelled versus measured leaf area for the 'Vertessy & O'Sullivan Murrindindi 11 year old' data set. Dashes indicate 95% confidence limits for each prediction.

8.8.1.3   The Orr Picaninny 14 year old data set

This data set was obtained by Orr et al. (1986) in 1986 and involved the destruction and leaf area measurement of 18 trees from scattered locations bordering the Picaninny experimental catchment. Because of the scattered location of the trees, a population mean ln(DBH) cannot be calculated directly. Instead, a mean was obtained from the total population of six permanent growth plots[5] at Picaninny, surveyed by Melbourne Water in 1986. Use of this proxy mean is not ideal, owing to the patchy regeneration at Picaninny (Langford and O'Shaughnessy, 1980b). However, it should be sufficient to enable the use of Orr et al's data to test the model.

Modelled versus measured leaf area for this data set is plotted in Figure 8.19. The points are less aligned with the 1:1 line than for the two previous examples. The mean location of points is slightly below the line, which may be partly due to the use of a proxy mean ln(DBH). Also, the slope of the line of best fit through the points is not as steep as the 1:1 line, in a similar manner to the Vertessy & O'Sullivan Myrtle 11 year old data. The 95% confidence limits for two of the predictions fall away from the 1:1 line. This is about twice the number expected from a sample size of 18.
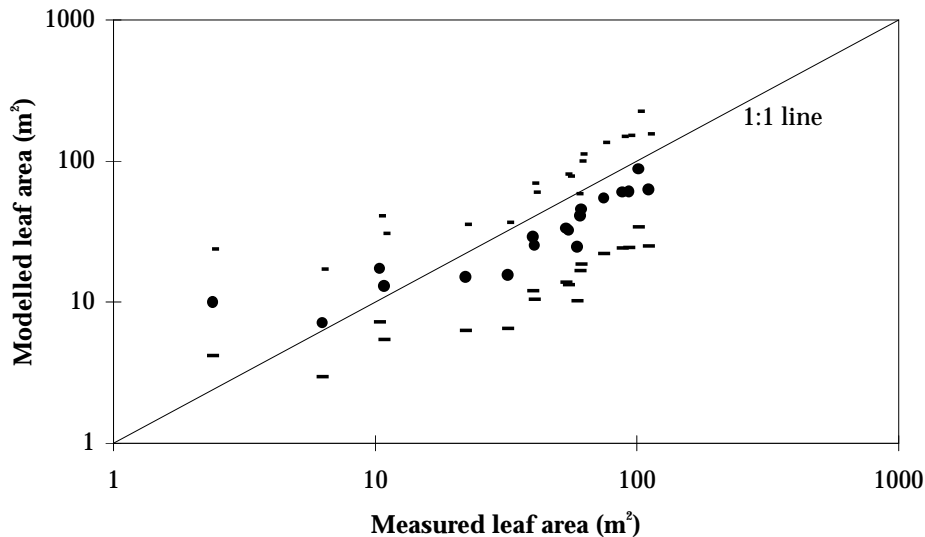
Figure 8.19: Modelled versus measured leaf area for the 'Orr Picaninny 14 year old' data set. Dashes indicate 95% confidence limits for each prediction.

---

[5]45 plots are surveyed at Picaninny every 5 years. A subset is surveyed every year.

8.8.1.4   The Ronan Blacks' Spur 38 year old data set

This data set was obtained by Ronan (1984) in around December 1976. Fifteen 38 year old *E. regnans* trees comprising the total population of a plot of known area were felled for leaf area measurement; the DBH of each tree was also recorded.

Modelled versus measured area for this data set is plotted in Figure 8.20. A similar pattern to the above data is observed - with the mean leaf area being modelled accurately and a slope slightly lower than the 1:1 line. The 95% confidence limits for one of the predictions fall away from the 1:1 line, as would be expected from a sample size of 15. These data strongly support the model.
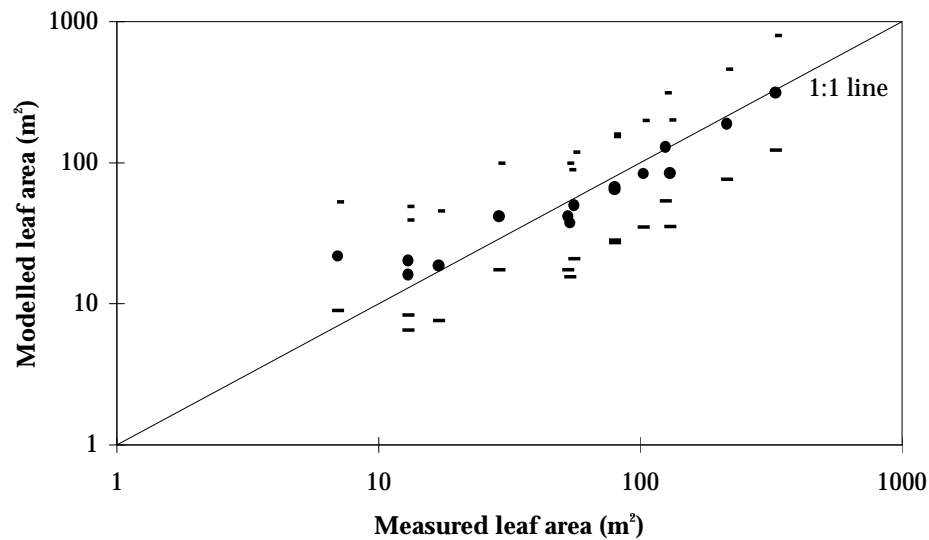
Figure 8.20: Modelled versus measured leaf area for the 'Ronan Blacks' Spur 38 year old' data set. Dashes indicate 95% confidence limits for each prediction.

8.8.1.5 The Ronan Myrtle 225 year old data set

Data from the 225 year old trees in this data set were used in the initial calibration of the model. Additionally, Ronan (1984) measured one 150 year old and three 90 year old trees from the same location. The data from these sub-dominant trees are examined here. Population mean ln(DBH) for both ages was derived from the DBH versus age relation given in Equation 8.7. Estimating the mean DBH in this manner may lead to some additional uncertainty in the estimation of mean leaf areas.

Modelled versus measured leaf area for this data set is plotted in Figure 8.21. The modelled leaf area for the 150 year old tree is accurate, but as there is only one observation, this offers no statistical support for the accuracy of the model. Both the mean and the trend of LAs for the 90 year old stand are poorly estimated. This may be due to the small sample size, inaccuracy in the estimated population means, and the fact that the trees are sub-dominants and have spent their entire lives beneath larger and older trees. The 95% confidence limits for two out of the three LA predictions for 90 year old trees fall away from the 1:1 line.
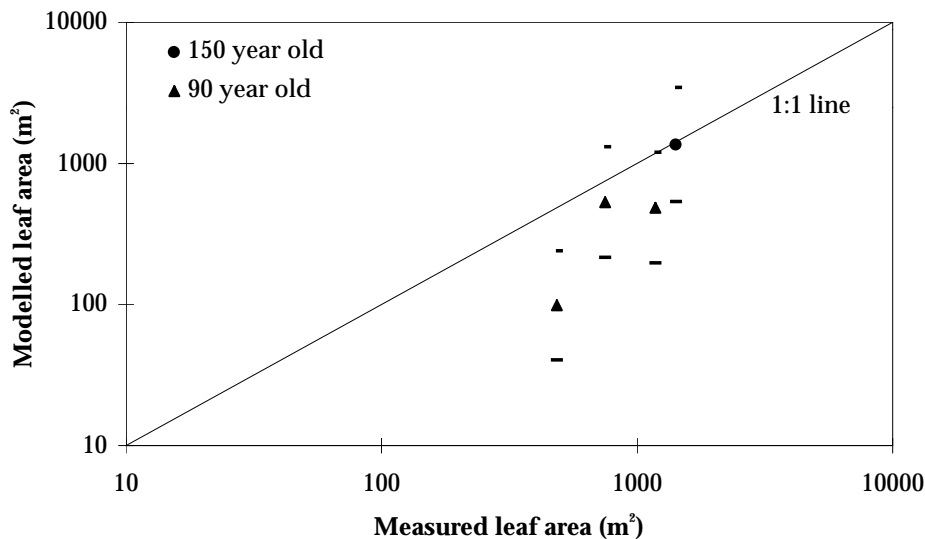
Figure 8.21: Modelled versus measured leaf area for the 'Ronan Myrtle 150 and 90 year old' data set. Dashes indicate 95% confidence limits for each prediction.

8.8.2 Testing of total sample leaf area and LAI predictions

The prediction of total leaf area for stands can be evaluated by summing measured and modelled leaf areas for all the trees in a sample from a stand. However, in most cases, only a sample of trees from a plot or plots within each stand had their leaf areas measured. Thus, bias between sampled trees and the full population of a plot will lead to differences between the error in total LA estimated from the sample and the true error which would be calculated if the whole population had their leaf areas measured. However, these differences are likely to be small.

Figure 8.22 shows the percentage error in the sample sum of modelled leaf areas for each stand, calculated as $100(\frac{Total\,modelled\,LA}{Total\,measured\,LA} - 1)$. These values are a good approximation to the percentage errors in LAI estimation which would be made if total population leaf area was measured. In two cases (the Beringer 8 year old stand and the Ronan 38 year old stand), total population LA *was* measured, so the error in LAI is exactly the same as the error in sample sum LA as plotted in Figure 8.22 (-26% and -10%, respectively). For stands younger than about 60 years old, the maximum percentage error observed was +32%, with three of these stands displaying a percentage error less than ±13%. For the 90 year old stand of sub-dominant trees, an error of -54% was obtained. The 225 year old stand was modelled least accurately with an error of +88%. There was no dependence of error magnitude on whether the stand was part of the calibration or test data sets. This indicates that the model, as structured, was calibrated as well as possible, and that the observed errors are inherent in the data. As mentioned before, a more complex model could be constructed but it is felt that the present model achieves a desirable balance between predictive ability and simplicity.

8.9 LAI versus age

There are a number of ways in which the model may be used. Here the model is used to construct curves relating LAI to age, both by applying the model to individual tree data, and to relationships expressing the variation in DBH and stocking rate with age, and the distribution of DBH values within stands.
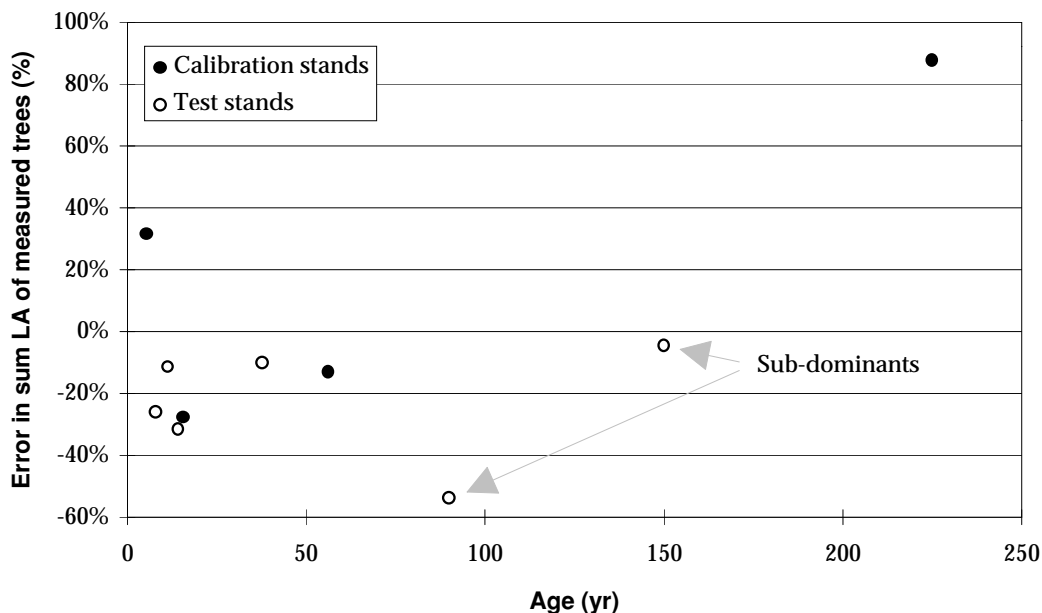
Figure 8.22: Percentage error in sample summed leaf area for both the calibration and testing stands. The values plotted are approximate percentage errors in predicted LAI, the differences being solely attributable to sample bias in each stand.

8.9.1 Constructing an LAI versus age curve from individual tree measurements

Having constructed, calibrated, and tested a model enabling the prediction of LAs of individual trees, LAI can be predicted by applying the model to populations of DBH measurements from a number of stands. The DBH database assembled for this study is large, but some ages of forest are poorly represented. The use of these data to predict LAI at a number of ages is presented chiefly as a *demonstration of the application of the model*. A much larger forest assessment database is available which will be the subject of future work.

From the database, data were selected for all stands exhibiting healthy, single-aged *E. regnans* for which the DBH was recorded for all trees in plots of known area. The population exp-mean-ln DBH was calculated for each stand. Estimates of LA were calculated using Equation 8.29. The resulting LA predictions were summed for each stand and divided by the area of the measurement plot to give LAI predictions for each stand (Figure 8.23).

A great deal of scatter is evident, as are some expected features such as a peak in LAI for very young forest and a gradual decrease in LAI as the forest ages. Given the high accuracy with which the model can predict leaf areas,
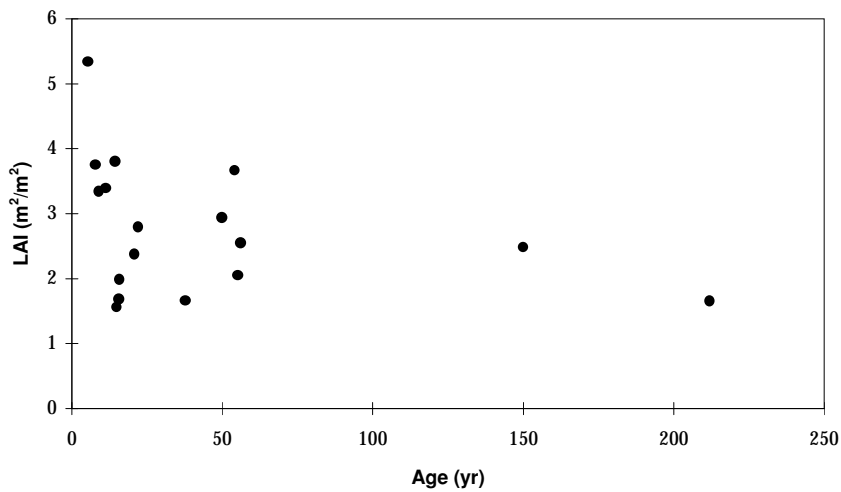
Figure 8.23: Predicted LAI versus age for each healthy, single-aged stand (uncorrected).

the scatter in Figure 8.23 was unexpected. The most likely cause is variability in the stocking rates of stands from the general relationship between stocking rate and age described in Section 8.6.4. To correct for this, the predicted LAI was divided by a 'stocking rate deficit', calculated as measured stand stocking rate divided by the rate predicted by Equation 8.13 as follows:

$$Corrected \; \widehat{LAI}_s = \frac{\widehat{LAI}_s}{\frac{SR_s}{\widehat{SR}_s}} \tag{8.31}$$

This correction essentially replaces the actual stocking rate of the experimental plot with the rate expected for a stand of the particular age. This results in Figure 8.24 which shows considerably reduced scatter and describes an LAI versus age relationship which peaks at just under 4 m^2 m^{-2} for 10 to 20 year old forest and then declines gradually to below 2 for old-growth forest.

8.9.2 Constructing an LAI versus age curve from previously derived relationships

An equation can be derived that mimics the relationship shown in Figure 8.24 using a number of the equations derived throughout this report. Firstly, LAI is expressed as the product of mean LA and stocking rate (adjusted to use the same units):
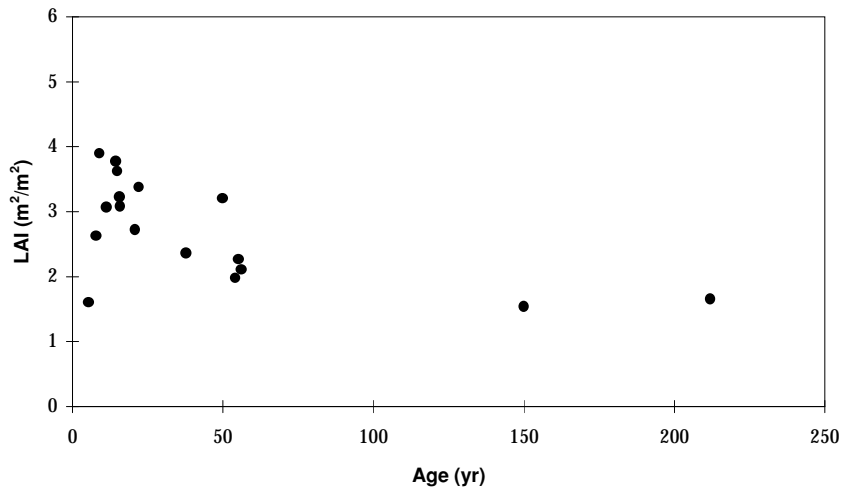
Figure 8.24: Predicted LAI versus age for each healthy, single-aged stand (corrected for variability in stocking rate).

$$\widehat{LAI}_s = \frac{\widehat{SR_s}\,\overline{\widehat{LA_s}}}{10000} \tag{8.32}$$

$\widehat{SR_s}$ can be easily obtained from Equation 8.13 and $\overline{\widehat{LA_s}}$, can be estimated by making some assumptions about the distribution of $x_{s,i}$ values within any given stand. Assume that the distribution of $x_{s,i}$ for all stands follows the shape of a standardised probability density function (PDF), $g(z)$, where z is the standardised value of $x_{s,i}$:

$$z = \frac{x_{s,i} - \mu_s}{\sigma_s} \tag{8.33}$$

By substituting Equation 8.33 into the PDF $g(z)$, and dividing by σ_s to ensure the integral of the function remains equal to unity, the distribution of $x_{s,i}$ values for any particular stand can be written as the PDF $f(x_{s,i})$:

$$\begin{aligned} f(x_{s,i}) &= \frac{1}{\sigma_s}\, g\left(\frac{x_{s,i} - \mu_s}{\sigma_s}\right) \\ &= \frac{g(z)}{\sigma_s} \end{aligned} \tag{8.34}$$

where σ_s is the population standard deviation of $x_{s,i}$.

Treating $x_{s,i}$ as a continuous random variable distributed according to the PDF $f(x_{s,i})$, an expression for the expected or mean value of $\widehat{LA}_{s,i}$, itself a function of $x_{s,i}$, can be written:

$$\overline{\widehat{LA_s}} = \int_{-\infty}^{\infty} \widehat{LA_s} f(x_{s,i}) dx_{s,i} \tag{8.35}$$

Substituting into this the equation for the leaf area of a single tree (Equation 8.26), and the equation for the PDF of $x_{s,i}$ (Equation 8.34), gives:

$$
\begin{aligned}
\overline{\widehat{LA_s}} &= \int_{-\infty}^{\infty} e^{\alpha+\beta\mu_s+\gamma+\bar{\delta}(x_{s,i}-\mu_s)} \frac{1}{\sigma_s} g(\frac{x_{s,i}-\mu_s}{\sigma_s}) dx_{s,i} \\
&= e^{\alpha+\beta\mu_s+\gamma} \int_{-\infty}^{\infty} e^{\bar{\delta}\sigma_s(\frac{x_{s,i}-\mu_s}{\sigma_s})} \frac{1}{\sigma_s} g(\frac{x_{s,i}-\mu_s}{\sigma_s}) dx_{s,i} \\
&= e^{\alpha+\beta\mu_s+\gamma} \int_{-\infty}^{\infty} e^{\bar{\delta}\sigma_s z} \frac{g(z)}{\sigma_s} \frac{dx_{s,i}}{dz} \frac{dz}{dx_{s,i}} dx_{s,i} \\
&= e^{\alpha+\beta\mu_s+\gamma} \int_{-\infty}^{\infty} e^{\bar{\delta}\sigma_s z} g(z) \, dz \tag{8.36}
\end{aligned}
$$

The mean estimated LA of trees in a given stand depends on an integral involving both the standardised PDF and the standard deviation of the $x_{s,i}$ values for the stand. As noted in Section 8.6.3, ln(DBH) values follow an approximately normal distribution. Therefore:

$$g(z) = \frac{1}{\sqrt{2\pi}} e^{-\frac{1}{2}z^2} \tag{8.37}$$

Substituting this into Equation 8.36 gives:

$$
\begin{aligned}
\overline{\widehat{LA_s}} &= e^{\alpha+\beta\mu_s+\gamma} \int_{-\infty}^{\infty} e^{\bar{\delta}\sigma_s z} \frac{1}{\sqrt{2\pi}} e^{-\frac{1}{2}z^2} \, dz \\
&= e^{\alpha+\beta\mu_s+\gamma} \frac{1}{\sqrt{2\pi}} \int_{-\infty}^{\infty} e^{-\frac{1}{2}z^2+\bar{\delta}\sigma_s z} \, dz \\
&= e^{\alpha+\beta\mu_s+\gamma} \frac{e^{\frac{1}{2}(\bar{\delta}\sigma_s)^2}}{\sqrt{2\pi}} \int_{-\infty}^{\infty} e^{-\frac{1}{2}(z^2-2\bar{\delta}\sigma_s z+(\bar{\delta}\sigma_s)^2)} \, dz \\
&= e^{\alpha+\beta\mu_s+\gamma} \frac{e^{\frac{1}{2}(\bar{\delta}\sigma_s)^2}}{\sqrt{2\pi}} \int_{-\infty}^{\infty} e^{-\frac{1}{2}(z-\bar{\delta}\sigma_s)^2} \, d(z-\bar{\delta}\sigma_s) \tag{8.38}
\end{aligned}
$$

The right hand portion of this equation:

$$\frac{1}{\sqrt{2\pi}} \int_{-\infty}^{\infty} e^{-\frac{1}{2}(z-\bar{\delta}\sigma_s)^2} \, d(z-\bar{\delta}\sigma_s) \tag{8.39}$$
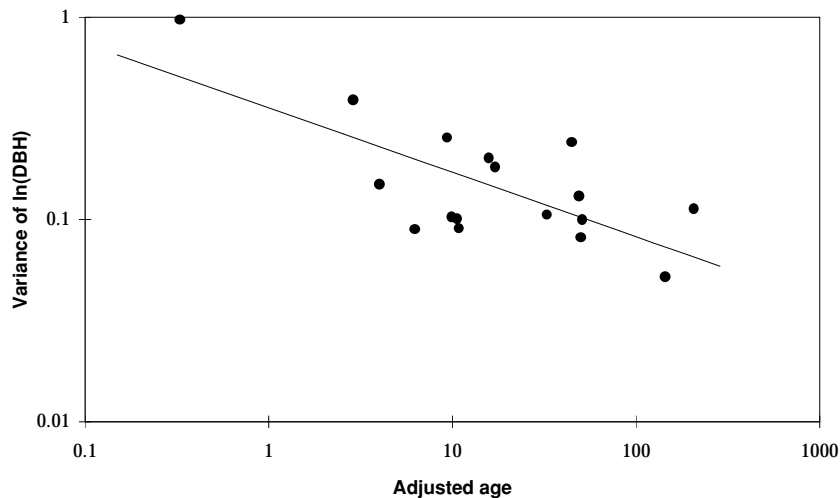
Figure 8.25: Line of best fit for variance of ln(DBH) versus age for each stand.

is the integral of a standard normal PDF for $z - \bar{\delta}\sigma_s$. By definition this integral is unity. Thus:

$$
\begin{aligned}
\widehat{\overline{LA_s}} &= e^{\alpha + \beta\mu_s + \gamma}\, e^{\frac{1}{2}(\bar{\delta}\sigma_s)^2} \\
&= e^{\alpha + \beta\mu_s + \gamma + \frac{1}{2}\bar{\delta}^2\sigma_s^2}
\end{aligned}
\tag{8.40}
$$

There are two unknowns in Equation 8.40: μ_s and σ_s^2. An estimate of μ_s can be obtained from Equation 8.7. An estimate of σ_s^2 is not so easily calculated. Figure 8.25 shows σ_s^2 (the variance of ln(DBH) values within a stand) plotted on log/log axes with respect to adjusted age. The same age adjustment is used as in Equation 8.7. The regression of σ_s and AGE_s is given in Equation 8.41 and is drawn in Figure 8.25.

$$
\ln(\widehat{\sigma_s^2}) = v_1 + v_2 \ln(AGE_s - d_3)
\tag{8.41}
$$

Substituting in d_3 from Equation 8.10 and estimating v_1 and v_2 by regression gives:

$$
\ln(\widehat{\sigma_s^2}) = -1.029 + -0.319 \ln(AGE_s - 5.04), \quad r^2 = 0.504
\tag{8.42}
$$

The low r^2 value indicates that the regression of the variance of ln(DBH) on age does not fit the data well. As Figure 8.8 suggests, there are enough

data points within each stand to characterise accurately the mean ln(DBH), but there are too many 'spikes' in the observed distributions to accurately characterise the variance. In future, it is intended to process more available data to remedy this situation. At present, use is made of Equation 8.41 which is substituted along with Equation 8.7 into Equation 8.40 giving:

$$\widehat{\overline{LA_s}} = e^{\alpha + \beta[d_1 + d_2 \ln(AGE_s - d_3)] + \gamma + \frac{1}{2}\bar{\delta}^2 e^{[v_1 + v_2 \ln(AGE_s - d_3)]}} \tag{8.43}$$

Substituting Equations 8.13 and 8.43 into Equation 8.32 gives:

$$
\begin{aligned}
\widehat{LAI_s} &= \frac{e^{r_1 + r_2 \ln(AGE_s)} \, e^{\alpha + \beta(d_1 + d_2 \ln(AGE_s - d_3)) + \gamma + \frac{1}{2}\bar{\delta}^2 e^{[v_1 + v_2 \ln(AGE_s - d_3)]}}}{10000} \\
&= \frac{e^{r_1 + \alpha + \beta d_1 + \gamma}}{10000} e^{r_2 \ln(AGE_s)} \, e^{\beta d_2 \ln(AGE_s - d_3)} \, e^{\frac{1}{2}\bar{\delta}^2 e^{[v_1 + v_2 \ln(AGE_s - d_3)]}} \\
&= \frac{e^{r_1 + \alpha + \beta d_1 + \gamma}}{10000} AGE_s^{r_2} \left(AGE_s - d_3\right)^{\beta d_2} \left(e^{\frac{1}{2}\bar{\delta}^2 e^{v_1}}\right)^{[(AGE_s - d_3)^{v_2}]} \tag{8.44}
\end{aligned}
$$

If estimates of the regression parameters are then substituted into Equation 8.44, the following fully specified model of *E. regnans* LAI versus age is obtained:

$$\widehat{LAI_s} = 11.014 \; AGE_s^{-1.624} \; (AGE_s - 5.04)^{1.180} \; 3.592^{[(AGE_s - 5.04)^{-0.319}]} \tag{8.45}$$

The relationship between LAI and age (Equation 8.45) is plotted in Figure 8.26 along with the modelled LAI estimates for each stand. It is important to note that this equation was not directly fitted to the points plotted in Figure 8.26 (i.e. LAI values 'measured' using the LA versus DBH model given in Equation 8.29). Rather Equation 8.45 has been derived as a combination of equations representing approximations to the various factors that influence LAI variation with age, namely: stocking rate of trees in a stand; exp-mean-ln DBH of trees within a stand; variance of ln(DBH) values of trees within a stand; an assumption of normally distributed ln(DBH) values within each stand; and finally, the model predicting the leaf area of an individual tree in a stand given the DBH of the tree and the exp-mean-ln DBH of the stand. Figures 8.27 and 8.28 summarise these steps.

The relationship expressed in Equation 8.44 is simple, except for the last term, the nested power function. This term originates from the regression relating variance of ln(DBH) to stand age, which was not a good fit to the
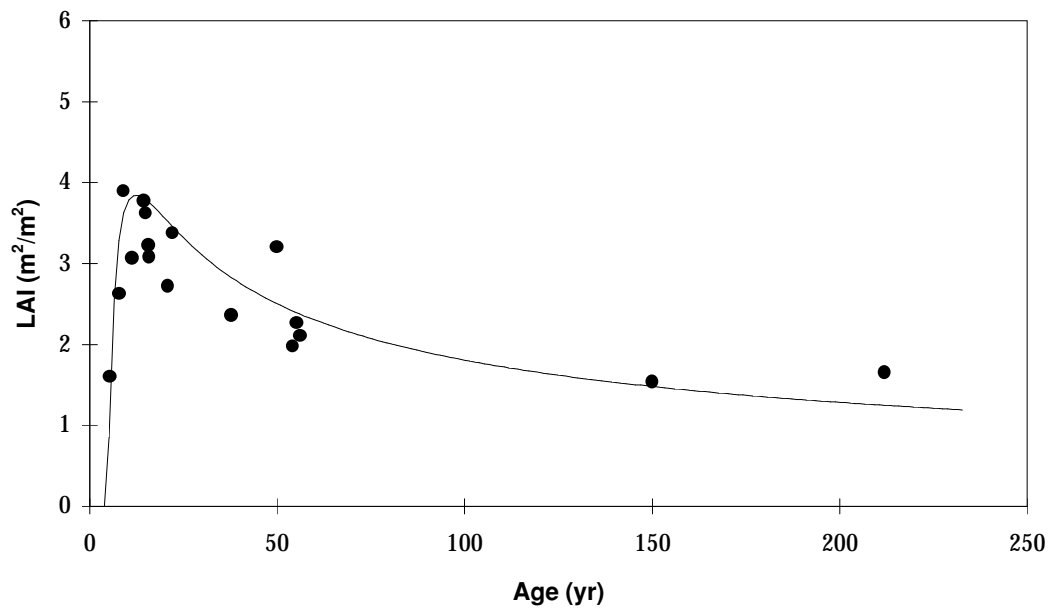
Figure 8.26: Predictions of LAI variation with stand age derived from Equation 8.45 plotted over individual (stocking-corrected) model predictions of LAI for all single-aged healthy stands in the database.
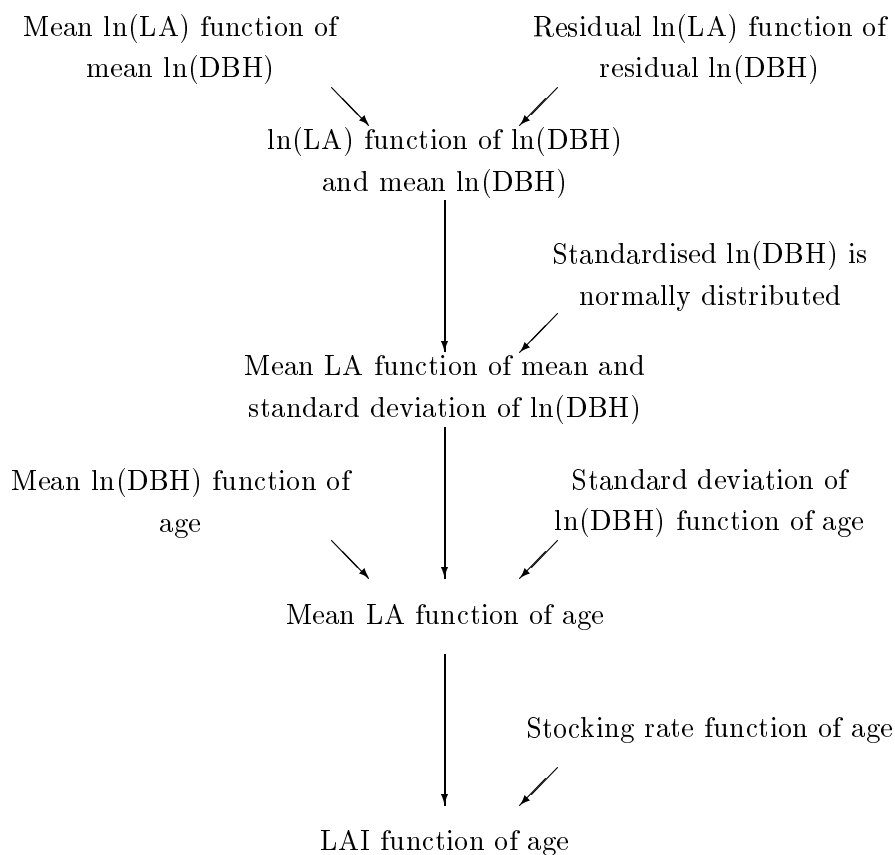
Figure 8.27: Flow chart summarising the steps taken to establish the relationship between LAI and age. A symbolic version is given in Figure 8.28.

$\nu = f(\mu),$ (8.20)

$y - \nu = f(x - \mu),$ (8.22)

$y = \ln(LA) = f(x, \mu),$ (8.24)

PDF($\frac{x-\mu}{\sigma}$) is normal, (8.37)

$\overline{LA} = f(\mu, \sigma^2),$ (8.40)

$\mu = f(AGE),$ (8.7)

$\sigma^2 = f(AGE),$ (8.41)

$\overline{LA} = f(AGE),$ (8.43)

$SR = f(AGE),$ (8.13)

$LAI = f(AGE),$ (8.44)
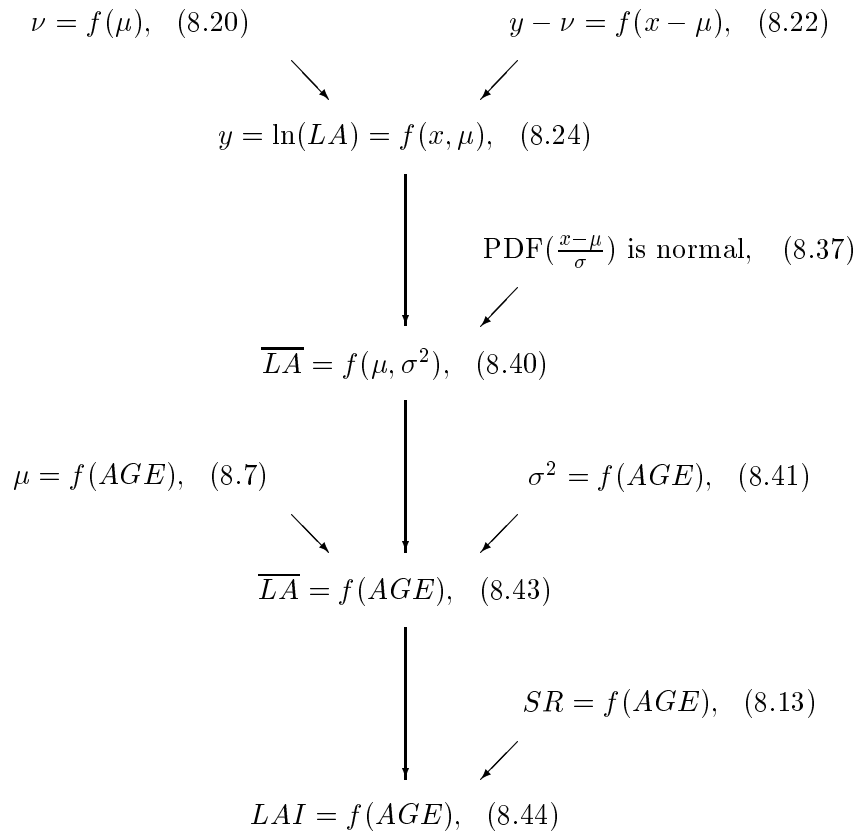
Figure 8.28: Symbolic version of Figure 8.27. Subscripts and 'hats' have been removed from variables for simplicity.

data. Investigations of this regression will follow. One hypothesis is that if a linear/log regression is fitted to the variance data, the nested power function would disappear, being subsumed into the third term of Equation 8.44.

Further improvements are expected to result from the use or more detailed data for young stands. Presently, the LAI model is very sensitive to perturbations in the regression fits to young aged stands, in particular to perturbations of $a_3 = d_3$, the age adjustment value.

The form of the curve is similar to that offered for a wide range of ages of *E. regnans* by Jarvis and Leslie (1988) in some preliminary and exploratory work. It is also supported by Haydon et al's (1996) plot of stand sapwood area versus *E. regnans* forest age, due to the relationship between leaf area and sapwood area (see Section 9.2.1.3).

8.10 Summary

A large amount of data on the stem diameter and leaf area (LA) of *E. regnans* (*Eucalyptus regnans*) at various ages was collected - both through fieldwork conducted as part of the present study, and from a variety of other sources. The resulting database was organised by forest stand into two groups of data: that where diameter at breast height (DBH) only was measured; and that where both DBH and LA were measured. For each stand of the 'DBH only' data, DBH measurements were recorded for every tree in one or a number of plots of known area. For the 'DBH and LA' data, destructive leaf area measurements were recorded from either a sample of trees in a plot or a number of scattered trees. DBH measurements were occasionally made for the sampled trees only, but usually from all the trees in the plot.

Simple observations of the variation in mean ln(DBH) and stocking rate with age revealed clear organisation within the forest. A strong positive correlation was observed between DBH and age for all except the youngest ages of forest. This correlation was very similar to that observed by Ashton (1976). A strong negative correlation was observed between stocking rate and age. These observations are useful background to the analysis of leaf area patterns in *E. regnans* forest.

As previously noted by others, clear relationships were also shown between LA and DBH - both amongst stand mean values, and within the trees of each stand. Mean ln(LA) is linearly related to mean ln(DBH). Also, within each stand, individual tree ln(LA) and ln(DBH) exhibit separate linear rela-

tionships within each stand, with steeper slopes than the mean relationship. These relationships support observations made by Hingston et al. (pers. comm.), Feller (1980), Pook (1984b), Ronan (1984), Attiwill (1962, 1991), and Teskey and Sheriff (1996) in both *E. regnans* forests and other forests. Pook (1984b), Ronan (1984) and Teskey and Sheriff (1996) report linear and quadratic relationships using basal area as the independent variable. It is suggested that these relationships could be re-derived in the log/log domain to give similar slopes to those found here, with the advantage that the data in the log/log domain would exhibit reduced non-uniformity and reduced heteroscedasticity. The steeper sloped relationships given for the intra-stand variability are likely to be governed by natural thinning resulting from competition amongst trees. The relationship weakens within the oldest (225 year old) forest whose intra-stand variability appears to be governed by intermittent catastrophic structural influences such as lightning strikes.

The above observations were used to construct a model enabling the prediction of the leaf area of any tree given its DBH and the mean ln(DBH) of the population of trees from which it came. Data from four stands, aged between 5 and 225 years old, were used in the construction and calibration of the model. The model was constructed using a number of linear regressions on natural log DBH and LA data. Four separate regressions (one for each stand) were computed in order to estimate population mean ln(LA) for each stand, with population mean ln(DBH) being calculated directly from the data. Then, a single regression was computed on the four population means, yielding a line of best fit to the inter-stand variability in mean ln(LA) versus mean ln(DBH). Finally, the mean slope of the separate regressions for the three youngest stands was used to give the slope of a line of best fit to the residual intra-stand variability in ln(LA) versus ln(DBH). The two lines of best fit were added together to give the final model, which may be written in two alternate forms (reproduced from Equations 8.27 and 8.29):

$$\widehat{LA}_{s,i} = e^{-1.980 + 1.642\mu_s + 2.675(\ln DBH_{s,i} - \mu_s)} \tag{8.27}$$

$$\widehat{LA}_{s,i} = 0.138 \, M_s^{-1.033} \, DBH_{s,i}^{2.675} \tag{8.29}$$

where $\widehat{LA}_{s,i}$ is the estimated leaf area of tree i from stand s, $\ln(DBH_{s,i})$ is the natural log DBH of tree i from stand s, μ_s is the population mean ln(DBH) of stand s, and M_s is e^{μ_s}.

Plots of modelled versus measured LA showed that the model could reproduce the intra-stand and inter-stand leaf area relationships of the calibration data set. As expected, intra-stand variability was not well predicted for the 225 year old trees which, as described above, are subject to different structural influences to the younger forest.

Five further data sets were introduced to independently test the model. Some of these data sets lacked a population mean ln(DBH), so the DBH versus age relationship constructed earlier was used to fill in the missing values. The model was able to predict the intra-stand and inter-stand variability of the test data set, with some qualifications. For mid-aged forests, the slope of the intra-stand LA versus DBH pattern was over-predicted by the model. Perhaps a more complex model could take account of this variation, but it is suggested that more data would be needed to justify such complexity (which would probably require an extra parameter in the model). Prediction of leaf areas for 90 year old trees which were sub-dominant to 225 year old trees in a mixed-age stand was not accurate. Amongst other influences, this could be because the trees were sub-dominants and thus no assertion is made as to the model's validity as a predictor of the leaf area of sub-dominant trees. Overall, considering the wide range of ages and locations of the forest stand data, the model performed well on independent tests against individual tree leaf area measurements.

Tests of the model's ability to predict *total* LA and LAI were also possible. Most of the 'DBH & LA' data sets do not include destructive LA measurements for all trees in a plot of known area, so the percentage error in the model's prediction of LAI cannot usually be calculated. However, the percentage error in predictions of the total LA of measured trees is an estimator of LAI error - the differences being essentially due to sample bias. LAI errors thus estimated ranged from -10% to ±32% for trees younger than 60 years old. The errors for 90 and 150 year old sub-dominant trees were -54% and -5% respectively. As noted above, these values are influenced by the trees' sub-dominance. For the oldest trees (225 years old), the error increased to +88%.

Two example applications of the model were presented. The first involved applying the model to DBH measurements from all trees in all single-aged, healthy stands where a population of trees from a plot of known area was measured. The model predictions were summed and divided by the plot areas to yield LAI estimates for 17 plots. When plotted against age, a scattered pattern was observed. This was improved by applying a correction to the LAI predictions based on deviations in stocking rate for each stand from the

pattern of stocking rate versus age constructed earlier. This is a sensible correction because many plots contained too few trees to give an adequate reflection of stocking rate for the corresponding stand. The corrected LAI data, when plotted against age, were much less scattered and followed an expected trend; LAI increasing to a peak of just under 4 m^2 m^{-2} for 10 to 20 year old forest then gradually decreasing to less than 2 m^2 m^{-2} for old-growth stands.

The second example application of the LA versus DBH model involved deriving an equation predicting LAI variation with age by combining the LA versus DBH model with expressions of DBH and stocking rate variation with age and an expression of the distribution of DBH values within each stand. The combined expressions included: the regression of stocking rate against age; the regression of exp-mean-ln DBH against age; a new regression of variance in ln(DBH) against age; an assumption that ln(DBH) values within each stand are always normally distributed; and the LA versus DBH model itself. The analytical combination of these expressions yielded the following equation for LAI versus age (reproduced from Equation 8.45):

$$\widehat{LAI}_s = 11.014 \; AGE_s^{-1.624} \; (AGE_s - 5.04)^{1.180} \; 3.592^{(AGE_s-5.04)^{-0.319}} \quad (8.45)$$

where $\widehat{LAI}_s$ is an estimate of the LAI of stand s and AGE_s is the age of stand s.

The plot of this equation (Figure 8.26) showed that analytically predicted LAI varied both as expected, and in the same manner as the points derived from explicit application of the model to individual DBH measurements. It is hoped to replace the awkward final term of the equation, representing the effect of changing variance in ln(DBH) values, with a more simple expression upon processing further DBH data. Finally, it is noted that Equation 8.45 (reproduced above) is very sensitive to changes in the expression of forest structural descriptors (such as stocking rate) *for young aged forest stands*.

8.11   Epilogue

As stated in the Prologue, this chapter reproduces a previously published report by Watson and Vertessy (1996), the result being an equation predicting *E. regnans* LAI from forest age. This equation is an integral part of the overall LAI mapping procedures which are brought together in the following chapter on vegetation mapping, specifically in Section 9.6.

Chapter 9

LAI mapping

Contents

9.1   Introduction

This chapter chiefly describes spatio-temporal mapping of both total and canopy LAI across the study area.

Strictly speaking, the mapping of LAI only occurs when the model is run, at which point mapped species and origin parameters are combined *within the model* with date information and species-specific equations predicting LAI from forest age.

In this way, LAI is initially the only means by which long term changes in catchment condition are communicated to the model (later, in Chapter 11, changes in other parameters are explored). The realistic long term, large scale spatio-temporal characterisation of LAI is of obvious importance in a study, such as the present, which is *about* land cover change and its effect on hydrology.

9.2   Review

9.2.1   LAI estimation techniques

There is a wide range of techniques for measurement and estimation of LAI, from the fundamental direct and destructive measurement of individual leaf areas, to theoretical determination of the maximum LAI which can be supported under given environmental conditions. The techniques are described as follows:

9.2.1.1   Destructive sampling

Destructive sampling typically involves felling trees, stripping and weighing all their leaves, and measuring the leaf area of a weighed sub-sample of leaves

using a planimeter (e.g. Vertessy et al., 1995a). It is the most accurate means of measuring the leaf area (LA) of individual trees. The LAI can be calculated if all the trees in a known area are felled. Alternatively, a sample may be felled and LAs for the remaining trees estimated using allometry (see below).

A variant on this method was used in a monitoring study by Pook (1985) who repeatedly counted individual leaves, classified them as mature or immature, and estimated leaf areas from destructive measurements of 50-100 sub-sampled leaves (see also, Wong and Dunin, 1987).

9.2.1.2 Calibrated visual estimation (CVE)

A variety of techniques rely on a number observers' visual estimation of the LAI of trees or parts of trees (Carbon et al., 1979a, b; Ronan, 1984; Hookey et al., 1987; McVicar et al., 1996a). Each observer's estimates are typically calibrated against a smaller number of destructive estimates. In some cases, such as the 'module' method of Andrew et al. (1979), a structured scheme of stratified sampling is used.

9.2.1.3 Allometry

Allometry, from the latin prefix *allo* meaning 'other', is the estimation of one quantity (e.g. LAI) through measurement of another (e.g. DBH). Either DBH or sapwood area are typically used as estimators of LAI as follows:

DBH

Diameter at breast height (DBH) measurements are far more convenient to make than destructive leaf area measurements. During destructive LAI measurement, an *allometric* relation can be constructed between LA and DBH for individual trees of a given species. This enables LAI estimation for the same species to be made at other locations by measuring the DBHs of all trees in a known area and applying the LA/DBH relation to each. This method has been used extensively for conifers in the Northern Hemisphere by Gholtz et al. (1976), Waring et al. (1978), Running et al. (1986), Peterson et al. (1987), Spanner et al. (1990a, b), Herwitz et al. (1990), Curran et al. (1992), Nemani et al. (1993a). These authors typically estimated LAI in a two step process, first predicting biomass from DBH measurements, and then LAI from biomass. In Australia, allometry has been applied to *E. regnans* by Vertessy et al. (1995a, 1997) who used power-function relationships between

LA and DBH (see Section 8.4), to *E. sieberi* by Roberts (in prep.) also using power functions, to *E. marginata* and *E. calophylla* by Carbon et al. (1979a,b) using simple linear functions, and to *Pinus radiata* by Teskey & Sheriff (1996) who used a linear relationship. Additionally, Whitford et al. (1995) used DBH in combination with three crown variables to estimate the LAI of *E. marginata*, citing the method as being superior to light interception analysis methods (see below). Allometric estimation of LAI using DBH was the focus of the previous chapter.

Sapwood area

Sapwood area can be used in a similar way to DBH for predicting LAI. The technique has the advantage that sapwood area is a measure of living conductive tissue in the stem which is likely to be more closely related to LAI than DBH. It has the disadvantage that sapwood area is less easily measured than DBH. Authors who have used sapwood area as a scalar include: Grier and Waring (1974), Rogers and Hinckley (1979), Kaufmann and Troendle (1981), Brack et al., (1985). Jarvis & Leslie (1988) predicted LAI from sapwood area in old-growth *E. regnans* forest using a weak ($r^2 = 0.657$) leaf area/sapwood area regression given by Ronan (1984).

9.2.1.4 Light interception analysis

A variety of techniques can be used to estimate LAI by measuring the amount of light beneath the canopy relative to that in the open, given the following assumptions:

- leaves are black and do not reflect or transmit any light from the sky or sun above,

- leaves are small, and many appear within the field of view of the light measurement device concerned,

- leaves are randomly oriented with respect to azimuth (but their orientation is unconstrained with respect to inclination),

- leaves are uniformly distributed within the plant canopy.

A summary of the necessary calculations is given by Lacaze (1996) and the relevant techniques are briefly described below.

Hemispherical photographic analysis (HPA)

HPA involves taking a photograph of the sky hemisphere looking upward through the forest canopy (Anderson, 1981; Rich 1990, Rich et al. 1993; Whitford et al., 1995). Photographs are digitally scanned and the LAI of the stand is calculated from digital measurements of the amount of sky obscured by vegetation using some assumptions about leaf geometry and distribution within the canopy. This worked successfully in young *E. regnans* forest (Vertessy et al., 1995).

Light meters

Various instantaneous light meters may be used to compare radiation incident above the canopy with that which is received beneath the canopy. The ratio of above-canopy to below-canopy radiation reflects the integrated effect of obstruction of light by vegetation - from which an estimate of LAI can be made using similar logic to HPA. Specialised units are available for such measurements, including the Li-Cor LAI-2000 Plant Canopy Analyser (PCA) (Welles and Norman 1991), the Sunfleck Ceptometer (Pierce and Running 1988, Lathrop and Pierce, 1991, Rich et al. 1993), and the DEMON (Lang et al. 1985, Whitford et al. 1995).

Comparison

Light interception analysis techniques are not without their problems. For example, Anderson (1981) notes that eucalypts can be both brighter and darker than the sky when viewed from below, which violates the 'black leaf' assumption which is typically made. Also, in sparse vegetation, heterogeneity due to large canopy gaps can lead to problems in LAI estimation using DEMON and HPA (Whitford et al., 1991). In a comparison of LAI measurement techniques in low LAI forest using destructive sampling, DEMON, HPA, and allometry, Whitford et al. (1995) found that allometric estimates compared well with destructive measurement, but that light interception techniques overestimated LAI by between 20% and 132% depending on the particulars of each technique. Much smaller over-estimation relative to destructive measurements was observed by Vertessy et al. (1995a) who were able to account for the over-estimation in terms of light interception by tree stems and branches. Lacaze (1996) cited several further European comparisons of the techniques. Of these, one found no consistency between methods, two reported under-estimation by light interception methods, one reported

over-estimation. The PCA method was noted to be more precise, but not necessarily more accurate than other light interception methods. Lacaze concluded with the recommendation that, in a given study, a *single* method and accompanying analytical techniques should be used.

9.2.1.5 Remote sensing

Remote sensing of LAI involves correlating multispectral satellite or aerial imagery with ground based measurements of LAI. The correlations can be used to predict the spatial distribution of LAI from the imagery where there are no ground measurements. The approach has been used successfully and extensively in coniferous forests but has had limited application to broadleaf forests. Section 9.2.5.2 reviews remote sensing of vegetation in detail. Traditionally, ground-based LAI measurement techniques have been used to calibrate and validate remote sensing estimation of LAI, but there are cases where satellite remote sensing is suggested to be more accurate than certain ground-based techniques, such as allometry (Herwitz et al., 1990).

9.2.1.6 Hydrological equilibrium theory

In 1982, Eagleson posed a theory of 'hydrologic equilibrium' which formally stated the interdependencies of soil, plant, water, and radiant energy. Over short time scales the solution of these interdependencies eliminated the need for quantification (parameterisation) of the plant characteristic controlling water use (e.g. LAI), and indirectly enabled such a quantity to predicted in terms of the other controlling variables of the system. Over longer time scales, the soil term also dropped out, enabling both soil and plant properties to be predicted from water and radiation inputs. A number of authors have explored the idea that the climax LAI of vegetation is determined wholly by environmental factors such as radiation, precipitation, and soil conditions. Examples include: Waring et al., (1978) who assumed environmentally determined climax LAI in their analysis of the maximum LAI of conifers at a variety of locations in Oregon; Nemani and Running (1989) and Nemani et al. (1993a) who specifically addressed the prediction of LAI from climate and soil inputs; and Woodward (1987) who formed a simple, spatial Penman combination model of evapotranspiration at a global scale and used feedback from droughts which occurred during simulation to adjust and hence predict (and validate) equilibrium or climax LAI across the globe. Given the immensity of the task of direct spatial mapping of LAI (see this chapter), and the simple elegance of equilibrium based methods for doing the same, it is

surprising that hydrologic equilibrium theory has not received more attention from spatial modellers. Recently Hatton (Hatton and Wu, 1995; Hatton et al., 1998) has attempted to revive this line of inquiry with a comprehensive discussion of it origins, experience, and future.

9.2.2   LAI values

The LAI of forests can vary between zero and about 20, the maximum values being observed in the conifers of the Pacific north west of the USA (Gholtz et al., 1976; Waring et al., 1978; see also Dingman, 1994; Anderson, 1981). Note that this value, and all others in the present dissertation, applies to *projected* LAI, which is a term used in relation to conifers, where the *total* leaf area is about 2.3 -2.6 times greater than the projected area due to in-rolling of needles.

The LAI of *Eucalyptus* forests and woodlands ranges from less than one to over six, and at the continental scale is strongly dependent on precipitation. Some values are summarised in Table 9.1. In water limited situations, eucalypt LAI can also vary greatly according to water availability (Pook, 1984a, b, 1985).

Table 9.1: A sample of *Eucalyptus* and other Australian LAI values reported in the literature. All LAI values are for the stated stratum only unless otherwise noted. Some of the values reported by Anderson (1981) are from 'poor quality' stands. The values reported by Aston (1979) assume a closed canopy and are therefore anomalously high.

Species	Age (yrs)	MAP (mm)	LAI	Method	Reference
E. regnans	150 - 250	*c.* 1700	3.5 - 2.5	allometry	Jarvis and Leslie (1988)
E. regnans	*c.* 130	?	3.2	allometry	Legge (1985)
E. regnans	56	1660	2.85	allometry	Vertessy et al. (1997)
E. regnans	56	1660	2.6	Li-Cor	Vertessy et al. (1997)
E. regnans	37	*c.* 1700	2.3	not stated	Ronan (unpub. data) cited by Jarvis and Leslie (1988)
E. regnans	37	*c.* 1700	1.85	destructive	Ronan (1984)
E. regnans, dense	15	*c.* 1300	4.54	allometry	Orr et al. (1986)
E. regnans	15	1713	2.1	destructive	Vertessy et al. (1995a)
E. regnans + mid-storey	15	1713	4.0	destructive	Vertessy et al. (1995a)
E. regnans + mid-storey	15	1713	4.2	Li-Cor	Vertessy et al. (1995a)
E. regnans + mid-storey	15	1713	4.4	HPA	Vertessy et al. (1995a)
E. regnans + mid-storey	various	various	various	Li-Cor	O'Sullivan (in prep.)
E. regnans + understorey	8	*c.* 1680	6.21	Li-Cor	Beringer (1994)
E. regnans no understorey	8	*c.* 1680	3.88	Li-Cor	Beringer (1994)
E. regnans understorey only	8	*c.* 1680	2.33	Li-Cor	Beringer (1994)
E. regnans + understorey	8	*c.* 1680	5.74	destructive	Beringer (1994)
E. regnans no understorey	8	*c.* 1680	5.07	destructive	Beringer (1994)
E. regnans understorey only	8	*c.* 1680	0.67	destructive	Beringer (1994)
E. maculata from drought to non-drought conditions	16-27	*c.* 946	0.7 - 5.0	destructive	Coops et al., 1997
E. maculata dominated forest	10-13	580-1530	*c.* 3.0	not stated	Dunin et al. (1988)
E. maculata and *E. globoidea*	12	*c.* 946	3.3	destructive	Wong and Dunin (1987)
E. maculata + all other trees	11	*c.* 946	4.9	destructive	Aston (1985)
E. maculata	*c.* 9	*c.* 946	3.5-4	destructive	Aston (1984)
E. maculata	7-9	*c.* 946	2-3	not stated	Dunin and Mackay (1982)
E. maculata as a co-dominant	5-7	*c.* 946	*c.* 2.5-3.3	various	Pook (1984b)
E. maculata + other canopy spp.	5-7	*c.* 946	*c.* 3.6	various	Pook (1984b)
E. maculata + other canopy spp. + understorey	5-7	*c.* 946	*c.* 4	various	Pook (1984b)
E. maculata + understorey, drought affected	8-9	*c.* 946	4.3→0.8	various	Pook (1985)
E. maculata + understorey, maximum	8-9	*c.* 946	5.1	various	Pook (1985)
E. maculata small individual tree	v. young	not stated	13.4	destructive	Aston (1979)
E. maculata/*E. gummifera*	?	> 1000	1.06 - 1.96	HPA	Anderson (1981)
E. rossii/*E. maculata*	?	dry	0.81 - 1.24	HPA	Anderson (1981)
E. populnea	?seeRoss89	dry	0.40-0.77	not stated	Hatton and Wu (1995)
E. viminalis small individual tree	v. young	not stated	4.1	destructive	Aston (1979)
E. dives small individual tree	v. young	not stated	4.1	destructive	Aston (1979)
E. mannifera subsp. *maculosa* small individual tree	v. young	not stated	2.9	destructive	Aston (1979)
E. cinerea small individual tree	v. young	not stated	3.6	destructive	Aston (1979)
E. pauciflora small individual tree	v. young	not stated	4.2	destructive	Aston (1979)
E. diversicolor	6	1060	2.9	CVE	Carbon et al., (1979b)
E. diversicolor	mature	1060	1.3	CVE	Carbon et al., (1979b)
E. marginata/*E. calophylla*	1	600-1200	0.3	CVE	Carbon et al. (1979b)
E. marginata/*E. calophylla*	5	600-1200	1.7	CVE	Carbon et al. (1979b)
E. marginata/*E. calophylla*	40	600-1200	1.3	CVE	Carbon et al. (1979b)
E. marginata/*E. calophylla*	various	600-1200	0.5-2.4	CVE	Carbon et al. (1979b)

E. marginata/E. calophylla	?	1200	1.8	CVE	Carbon et al. (1979b)
E. marginata/E. calophylla	?	700	1.2	CVE	Carbon et al. (1979b)
E. marginata	?	-	0.2 - 2.3	HPA	Wallace (1996)
E. marginata	?	?	1.05	destructive	Whitford et al. (1995)
E. melliodora	6-7	750	1.79-2.16	Li-Cor?	Hookey et al. (1987)
E. microcarpa	6-7	750	1.58-2.02	Li-Cor?	Hookey et al. (1987)
E. botryoides	6-7	750	1.54-1.90	Li-Cor?	Hookey et al. (1987)
E. sideroxylon (E. saligna hybrid)	6-7	750	2.05-2.54	Li-Cor?	Hookey et al. (1987)
Acacia dealbata in understorey	15	1713	0.1	destructive	Vertessy et al. (1995a)
Acacia frigescens in understorey	15	1713	1.8	destructive	Vertessy et al. (1995a)
Acacia longifolia small individual tree	v. young	not stated	7.6	destructive	Aston (1979)
Pinus radiata small individual tree	v. young	not stated	13.1	destructive	Aston (1979)
Pinus radiata	?	dry	1.56	HPA	Anderson (1981)

9.2.3 Spatial LAI patterns

Numerous papers from the conifer forests of the Pacific north west report a clear pattern of LAI varying both within and between species according to environmental gradients of water stress and temperature growth index (Gholtz et al., 1976; Grier and Running, 1977; Waring et al., 1978; Gholtz, 1982).

Variation of LAI within and between *Eucalyptus* species is less well understood. In the study area, there are obvious differences between the high LAI of the wet sclerophyll species such as *E. regnans*, and the low LAI of the dry sclerophyll species such as *E. obliqua*. However, it is not known whether LAI within a species is relatively constant and significant changes are only observed at geographical species boundaries, or whether LAI changes continuously along environmental gradients irrespective of species.

Measurements from *E. marginata* forests in Western Australia have shown significant variation (0.2 - 2.3) of LAI within this species (Wallace, 1996). Similar variability was reported in regrowth *E. maculata* forest in New South Wales by Coops et al. (1997).

9.2.4 Temporal LAI Patterns

LAI varies over time as well as space, although the literature on such temporal variations is relatively sparse. The previous chapter described the significant long term (> 100 years) variation in the LAI of *E. regnans*. At much shorter time scales, Pook (1985) and Coops et al. (1997) observed large variations in the LAI of *E. maculata* during periods of drought at the Kioloa site in New

South Wales. Additionally, Hatton and Wu (1995) described the continual adjustment of LAI at any given site towards some environmentally determined equilibrium value. Clearly then, it is important to note that a single LAI value for a site will not necessarily be a lasting, definitive indication of the vegetative status of the site.

9.2.5 Remote sensing of vegetation

9.2.5.1 Vegetation indices and spectral response

Numerous remote sensing platforms have been developed to measure radiance within useful bands of the electro-magnetic (EM) spectrum. Examples include: the Multi-spectral Scanner (MSS) and Thematic Mapper (TM) carried by the Landsat satellites, the Advanced Very-High Resolution Radiometer (AVHRR)carried by National Oceanic and Atmospheric Administration (NOAA) weather satellites; and the Daedalus Airborne Thematic Mapper (ATM) carried by various aircraft (often high altitude, *c.* 20 km) (Barrett and Curtis, 1992; Running et al., 1986; Tian, 1989). The bands measured by these sensors and typically used in vegetation analysis include: blue (B), green (G), red (R), near infra-red (NIR), and middle infra-red (MIR).

Much has been studied about the colour of vegetation, or more precisely, the spectral response of vegetation and the propagation of light within plant canopies (e.g. Guyot, 1990; Ross, 1981; Howard, 1991). With respect to remote sensing, this has led to the development of a number of *vegetation indices* which combine measurements of vegetation reflectance from one or more bands of the EM spectrum into a single quantification of some aspect of vegetation (Leblon et al., 1993; Lacaze, 1996). Most of these indices involve the NIR and R bands because red radiation is absorbed by chlorophyll and NIR radiation is scattered by internal leaf structure and hence reflected by canopies as a whole (Running et al., 1986). Vegetation indices exploit the positive correlation between vegetation amount and NIR reflectance, and the negative correlation with red reflectance. The most popular index is the normalised difference vegetation index (NDVI) originated by Rouse et al. (1973, 1974). But there are many others, as summarised here (see reviews by Lacaze, 1996; Nemani et al., 1993a; Howard, 1991; and Tian, 1989):

- standard difference

$$SD = NIR - R \qquad (9.1)$$

- ratio vegetation index (RVI) or standard ratio (SR)

$$RVI = SR = \frac{NIR}{R} \tag{9.2}$$

- log ratio (LR)

$$LR = 0.5 \log(SR) \tag{9.3}$$

- normalised difference vegetation index (NDVI)

$$NDVI = \frac{NIR - R}{NIR + R} \tag{9.4}$$

- MIR corrected NDVI (NDVIc)

$$NDVIc = NDVI \left(1 - \frac{MIR - MIR_{min}}{MIR_{max} - MIR_{min}}\right) \tag{9.5}$$

- transformed vegetation index (TVI)

$$TVI = \sqrt{NDVI + 0.5} \tag{9.6}$$

- perpendicular vegetation index (PVI)

$$PVI = \frac{1}{\sqrt{k_1^2 + 1}}(NIR - k_1 R - K_2) \tag{9.7}$$

- greenness vegetation index (GVI)

$$GVI = k_1.B + k_2.G + k_3.R + k_4.NIR \tag{9.8}$$

where k_n are equation-specific constants, and subscripts 'max' and 'min' denote maximum and minimum observed reflectances from an area of study.

9.2.5.2 Vegetation indices and LAI

Above-canopy remote sensing of LAI is very commonly conducted using empirical correlations between LAI and various vegetation indices. The earliest work originated from crop studies such as that of Asrar et al. (1984) who formed equations predicting wheat LAI from ground-based measurements of NDVI over Arizona. Crop studies have also been applied in Australia (McVicar et al., 1996b, c).

Soon after the work of Asrar et al., a large body of work began to emerge from the conifer forests of the Pacific north west of the USA. Initially this

work found strong relationships between ATM RVI and LAI (Peterson et al., 1986, 1987). This was extended to larger scale satellite based studies relating AVHRR NDVI to LAI (Nemani and Running, 1989; Running et al., 1989; Spanner et al., 1990b) and small scale, transect-based studies using TM RVI (Lathrop and Pierce, 1991). Spanner et al. (1990a) investigated a wider range of EM bands and vegetation indices, paving the way for the MIR corrected NDVI (NDVIc) of Nemani et al. (1993a). This was introduced to enable predictions of the widest possible range of conifer LAI values from both open and closed canopy forests.

In the coniferous forests of Florida, Curran et al. (1992) successfully related TM NDVI to LAI, whilst in Massachusetts, Herwitz et al. (1990) found no correlation between either RVI or NDVI and LAI. The latter authors cited small image samples and inaccurate ground based LAI measurements as possible reasons for the lack of correlation.

LAI remote sensing in broad-leaved and other non-coniferous forests is, by comparison to the conifer work, under-represented. Using a ground-based sensor above grasses, shrubs, and small trees in California, Gamon et al. (1995) found good correlation between NDVI and LAI. In the similar climate of southern France, Teixeira Filho et al. (1996) cite an equation relating LAI to TM NDVI based on Li-Cor PCA data.

Studies of remote sensing of *Eucalyptus* LAI have only recent emerged. Over a large tract of New South Wales, McVicar et al (1996a) measured LAI values between 0.0 and 4.4 and reported good correlations with AVHRR RVI. One of the resulting equations was applied to estimation of LAI over the entire Australian continent by Shao et al. (1997a). At the Kioloa site in New South Wales, Coops et al. (1997) found temporal changes in LAI sampled 13 times over a 9 year period were well predicted by MSS NDVI. In Western Australia, Wallace (1996) found a reasonable correlation between TM NDVI with LAI measured using HPA in *E. marginata* forest ranging in LAI from 0.2 to 2.3. Additionally, Swaminathan (1994) made some preliminary investigations in *E. regnans* forest using TM indices and very limited ground-based LAI data, with correlation being observed with the RVI.

It is perhaps too early for *general* LAI/vegetation index relations to emerge although some progress has been made by Baret et al. (1989, cited by Lacaze, 1996) who presented the transformed NDVI (TNDVI) which is calibrated to directly predict LAI:

$$LAI = TNDVI = -\frac{1}{k}\ln\left(\frac{NDVI_\infty - NDVI}{NDVI_\infty - NDVI_{back}}\right) \qquad (9.9)$$

where k is a shape parameter, $NDVI_{back}$ is the NDVI observed for background surface with no vegetation, and $NDVI_\infty$ is the saturation NDVI observed for 'infinite' vegetation. Lacaze (1996) and Leblon et al. (1993) provided a range of values for these parameters.

9.2.5.3 Saturation

The relationships between vegetation indices and LAI observed in the above studies are often non-linear. A feature of the relationships is that they tend to asymptote or 'saturate'. Beyond the point of saturation, increases in LAI are not matched by corresponding increases in remotely sensed indices. This is important because it restricts the range of LAI values over which accurate predictions may be made. Coniferous forests exhibit the highest saturation levels, on the order of 8-10 for RVI and 5-6 for NDVI (Peterson et al., 1987; Spanner et al., 1990). Lacaze (1990, 1996) noted that crops saturate at LAI values of about 2-4, and *Quercus* spp. forests did not saturate by LAI values of 4. In dry woodlands, Gamon et al. (1995) described saturation of NDVI at LAI values as low as 2. Saturation has not been described for *Eucalyptus* spp. but could be an important limit on the range of applicability of remote sensing of *Eucalyptus* LAI. Coops et al. (1997) noted that no saturation was apparent in *E. maculata* forest up to their maximum recorded LAI value of 5.

9.2.5.4 Image correction

A further feature of the literature on remote sensing of vegetation is the range of image corrections which are applied. The simplest correction is termed *radiometric correction* which simply converts the *digital numbers* representing radiation observed by a sensor (typically in the range 0 to 255) to physical units (typically W m^{-2} sr^{-1}, sr = steradian). Radiometric correction does not necessarily improve observed relationships, but rather promotes easy comparison between sensors and described relationships using a standard set of units (Lacaze, 1996). For example, NDVI calculated from radiometrically corrected data yields different values from that calculated from un-corrected data. A more complex correction is *atmospheric correction* where the effects of the atmosphere are taken into account in a manner dependent on the general clarity and temperature of the atmosphere at the time of measurement,

and on the elevation of the sensed surface and hence the thickness of atmosphere through which observations are made (Peterson et al., 1987). *Terrain correction* corrects for the differing illumination and viewing angles associated with inclined surfaces in areas of variable topography. A related correction deals with image *hot spots* where the sun and sensor are aligned such that observed trees and leaves obscure their shadow and a relative brightness in the image results (Jupp and Strahler, 1991).

Radiometric correction is commonly performed using published sensor calibrations such as those of Arino et al. (1995), Clark (1986), Markham and Barker (1986), Teillet (1986), Rao (1987), and Gu (1988) (Teixeira Filho et al., 1996; Pierce et al., 1990; Paltridge and Mitchell, 1990; Herwitz et al., 1990; Curran et al., 1992; Running et al., 1986; Spanner et al. 1990a; Lathrop and Pierce, 1991; Nemani et al., 1993a). There are also cases where vegetation indices such as NDVI have been calculated using radiometrically un-corrected data (e.g. Wallace, 1996).

A variety of theoretical/physical atmospheric correction schemes involving descriptions of atmospheric scattering and optical depth have been used, including those of Paltridge and Mitchell (1990), Herwitz et al. (1990), and Spanner et al. (1990). A conceptually simple yet expensive atmospheric correction was used by Running et al. (1986) and Peterson et al. (1987) whereby high-altitude aircraft data were corrected by regression against simultaneously collected low-altitude helicopter data at a small number of sites. Interestingly and pleasingly, the degree of correction was *observed* to be elevation dependent. Over very large areas using the NOAA AVHRR, Spanner et al. (1990b) used *maximum value compositing* which involves taking the maximum observed reflectance for each pixel from a large number of images, assuming that eventually, each pixel will be observed under optimal atmospheric and geometric conditions. Herwitz et al. (1990), Curran et al. (1992), Nemani et al. (1993), and Coops et al. (1997) used the assumption that deep clear lakes are ideal radiation sinks and hence define 'black' or background atmospheric effects which can then be subtracted from the imagery. Some authors have opted to omit atmospheric correction (e.g. Lathrop and Pierce, 1991). Nemani and Running (1989) cited the clear air over Montana as a reason for this, although it is uncertain whether their optimism regarding the lack of atmospheric effects is well founded.

Terrain correction is very simple when the observed surface is assumed to be Lambertian, reflecting incident radiation equally in all directions. In this case the correction simply accounts for the illumination angle, the angle of incidence of the sun on the surface (e.g. Spanner et al., 1990). Where the

Lambertian assumption is not valid, as is usually the case (Lacaze, 1996), a variety of correction schemes are possible, such as the simple, regression-based method of Smith et al. (1980) based on Minnaert (1941), and more physically based methods (Paltridge and Mitchell, 1990).

It should be noted that the NDVI is itself an image corrector, being the standard difference of NIR and R divided by the sum of NIR and R. The division is included to remove terrain and atmospheric effects which are assumed to equally affect both NIR and R (e.g. Peterson et al., 1987).

Comparisons of correction schemes and between corrected and un-corrected data have rarely been made in earnest. Peterson et al. (1987) observed slight improvement in LAI prediction using terrain corrected RVI instead of either NDVI or un-corrected RVI. Spanner et al. (1990a) concluded that atmospheric correction was a 'necessary' part of their regional scale analysis of LAI patterns. Gamon et al. (1995) found that NDVI was marginally superior to RVI for sensing the LAI of dry Californian vegetation. Paltridge and Mitchell (1990) suggested that atmospheric correction was superior to the correction implicit in the NDVI in an Australian investigation of grassland fuel moisture content.

9.2.5.5   Temporal variation

Remote sensing approaches provide a convenient means of assessing vegetation changes over time, provided appropriate corrections are made for time variant radiometric and atmospheric effects. Examples include: the analysis of natural seasonal LAI variation in coniferous forests (Spanner et al., 1990b; Curran et al., 1992) and eucalypt forests (Coops et al., 1997); the detection of LAI changes associated with thinning treatments in coniferous forests (Herwitz et al., 1990); and an attempt to examine the changes in LAI with eucalypt forest age (Swaminathan, 1994).

9.2.5.6   Site/image registration

It can be very difficult to accurately locate a ground measurement site on an aerial or satellite image. Many of the authors cited above make mention of various schemes for accomplishing this site/image registration, and some are confounded by it. Lathrop and Pierce (1991) were effectively prevented from detailed quantitative analysis of an excellent comparison of ground and satellite based transect data because of navigational difficulties. These included errors in pacing the distance between sites in inclined, forested terrain, and

errors due to lateral, non-uniform distortion of imagery due to variation in relief of the observed surface.

Many authors sample 'patches' of imagery rather than individual pixels to compensate for registration uncertainty (e.g. Paltridge and Mitchell, 1990). Out-dated GIS technology has limited some authors in this respect (Greaves and Spencer, 1993).

9.2.5.7 Use of homogeneous sites

Many studies restrict their analyses to homogeneous parts of an otherwise heterogeneous landscape in order to observe optimal correlation between remotely sensed and ground data (e.g. Walker et al., 1986; Wallace, 1996). These authors note that the relationships they observe are unlikely to be valid throughout the landscape. The implication is that greater difficulties are likely to be encountered in a highly heterogeneous landscape such as the present study area than are evident at a glance from the literature.

9.2.5.8 Use in hydro-ecological modelling

Remotely sensed LAI data are still finding their way into hydro-ecological modelling studies (Curran, 1994). Not surprisingly, the idea is absent from Rango's (1985) early discussion of remote sensing input to hydrological models. However, by the time of Stewart and Finch's (1993) and Engman's (1995) reviews of recent advances in remote sensing in hydrology, there was still no mention. A few examples are briefly mentioned here. In parallel with the pioneering development of remote sensing of LAI in the Pacific north-western USA (see above), Running et al. (1989) incorporated AVHRR LAI data into large scale studies with FOREST-BGC. Curran (1994) made brief mention of work which was in progress in Wales in 1994 on driving FOREST-BGC with ATM LAI data. In a more recent pilot study, Teixeira Filho et al. (1996) used TM LAI data to drive a simple distributed Penman-Monteith transpiration model of a 31 km^2 catchment in southern France.

9.2.5.9 Vegetation attributes other than LAI

It is worth mentioning that remote sensing is routinely applied, with varying degrees of success, to the estimation of a range of vegetation and surface attributes other than LAI. These include: vegetation type (Sadek, 1997), surface temperature (Sader, 1986), structural and phenological attributes

(Walker et al., 1986; Niemann, 1993), fuel moisture content (Paltridge and Mitchell, 1990), photosynthetically absorbed radiation (PAR) (Myeni and Williams, 1994), plant water stress (Steven et al., 1990; Pierce et al., 1990; McVicar, 1997), and the extent of fire damage (Smith and Woodgate, 1985). Some reviews discuss this type of work (e.g. Stewart and Finch, 1993; Engman, 1995; Roberts, 1993; McVicar, 1997).

There is some indication that remote sensing of vegetation attributes in *Eucalyptus* forest can be successful in drier forests (Lees and Ritman, 1991; McCloy and Hall, 1991) but less successful in wetter forests (Lees and Ritman, 1991; Greaves and Spencer, 1993). The study of Lees and Ritman (1991) supplemented remote sensing data with environmental data to achieve a successful classification of vegetation types in reasonably dry, predominantly eucalypt forest. Remote sensing of *Eucalyptus* in general is likely to be more difficult than for other broad-leaved species owing to the inter-species similarity of reflectance spectra, as shown by Howard (1991, Figure 3.11).

9.3 Data and preliminary analysis

In the present study, the mapping of vegetation parameters, in particular LAI, makes opportunistic use of any and all types of data which could be made available for the study area. These include: resource management inventories of forest species and age maps; destructive and Li-Cor measurements of LAI both within the study area and within other eucalypt forests, the LAI versus age relationship derived in Chapter 8 for *E. regnans*, and aerial and satellite remote sensing data. These data are described as follows:

9.3.1 Species distribution data

Perhaps the most fundamental information pertaining to vegetation distribution in forests is the distribution of different canopy species.

In recent years, the Victorian Department of Natural Resources and Environment (DNRE) participated in a detailed survey of the habitat of the endangered Leadbeater's Possum (Lindenmayer, 1996). This included digital mapping of canopy species and age throughout the Central Highlands, including the study area. The survey method was based on air-photo interpretation (API) validated by field reconnaissance (Smith et al., 1996).

The data for the study area were obtained from DNRE in ARC/INFO vector

Species	Area	% of study area
Mixed species forest	36.24	21.95%
Eucalyptus delegatensis	10.46	6.33%
Eucalyptus nitens	4.07	2.46%
Eucalyptus regnans	96.01	58.15%
Eucalyptus sieberi	0.36	0.22%
Pinus spp.	0.25	0.15%
Rainforest spp.	7.89	4.78%
Acacia spp.	0.26	0.15%
Acacia dealbata	3.48	2.1%
Acacia melanoxylon	0.19	0.11%
Fern	0.01	0%
Leptospermum spp.	0.42	0.26%
Shrubland	1.88	1.14%
Grassland	0.04	0.02%
Agricultural land	0.02	0.01%
Water	1.97	1.19%
Rocky	0.08	0.05%
Not vegetated	0.19	0.12%
No data	0.84	0.51%
Unknown	0.47	0.28%

Table 9.2: Areas occupied by each canopy species.

format and exported to GRASS format using purpose-designed macro code. Once imported to GRASS, the data were rasterised to the standard 25×25 m grid used in the present study.

The resulting raster map of canopy species is shown in Figure 9.1, and Table 9.2 shows the area occupied by each species. Auxiliary land cover classes (e.g. 'fern', 'water', etc.) were included in the original data. *E. regnans* dominates the study area (58.15%), with other eucalypts (including 'mixed species') occupying 30.96%, *Acacia* occupying 2.77%, and cool temperate rainforest occupying 4.78%.

9.3.2 Forest age data

The dates of origin of the vegetation ($y_{origin,1}$, $y_{origin,2}$, and $y_{origin,3}$) are used in the calculation of vegetation age, which is the input to the LAI versus age model for *E. regnans*. Three dates are used corresponding to the three most recent dates of regeneration (i.e. logging or fire) for a given site. As the simulation proceeds, the current forest age is calculated relative to the origin date which most recently precedes the current simulation date. Table 9.3 shows a set of example values for the three parameters. The site described

Legend:
- Mixed species forest
- Eucalyptus delegatensis
- Eucalyptus nitens
- Eucalyptus regnans
- Eucalyptus sieberi
- Pinus spp.
- Rainforest spp.
- Acacia spp.
- Acacia dealbata
- Acacia melanoxylon
- Fern
- Leptospermum spp.
- Shrubland
- Grassland
- Agricultural land
- Water
- Rocky
- Not vegetated
- No data
- Unknown
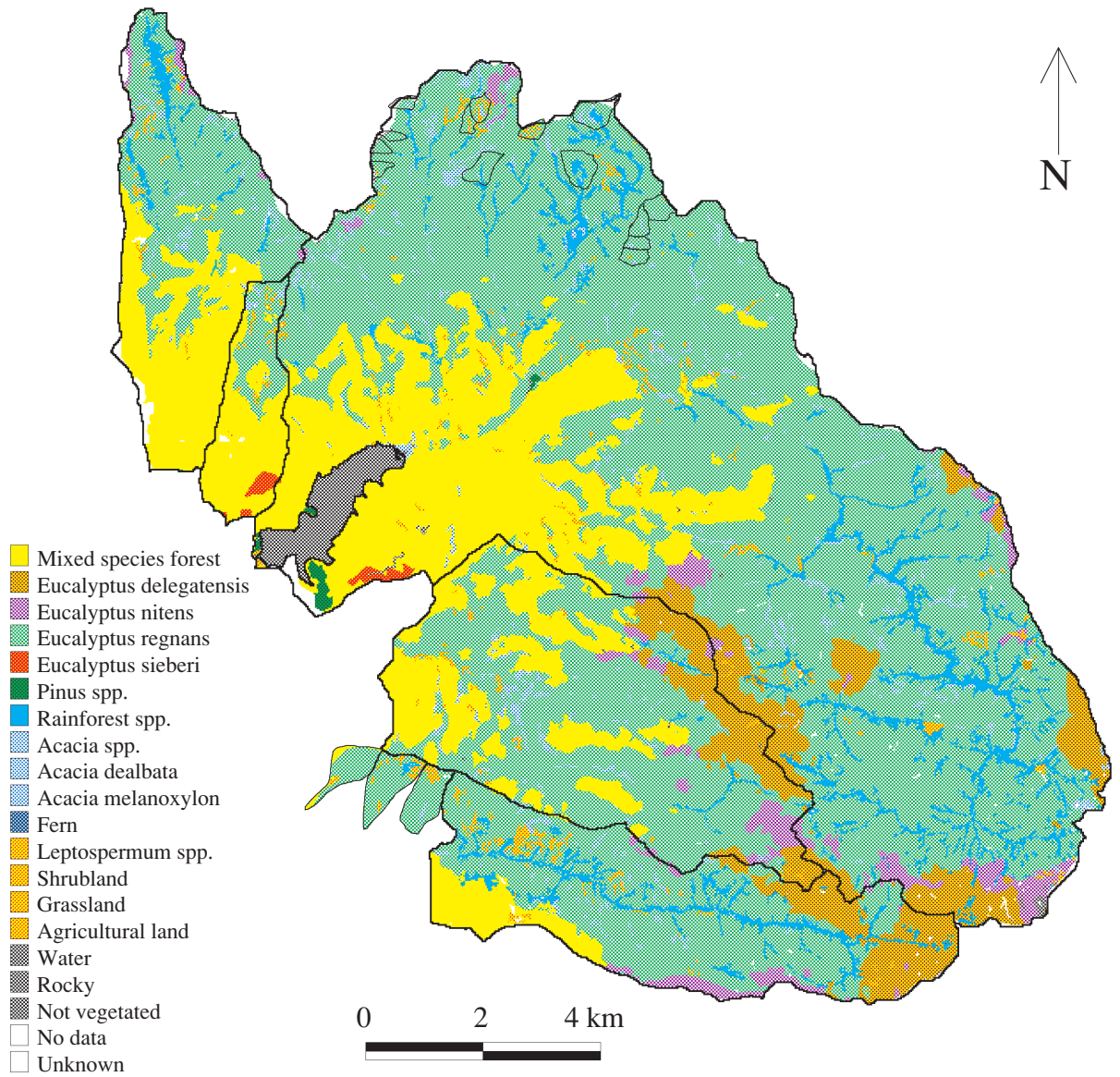
Figure 9.1: Map of canopy species for the study area derived from air-photo interpretation by DNRE.

Parameter	Value
$y_{origin,1}$	1939.033
$y_{origin,2}$	1898.085
$y_{origin,3}$	1759

Table 9.3: Typical values for the three vegetation origin parameters. To simplify the representation, dates within a year are given as fractions of a year. For example, the 13th of January is 3.3% of the way through the year and so is represented as 0.033 above.

by these values was most recently burnt on Black Friday (13th Jan. 1939). Prior to then, it was burnt on Red Tuesday (1st Feb. 1898), before which it was assumed to have originated from a known large scale fire in the region in about 1759[1].

A number of references list the dates and extent of major fires in the region since European habitation (*c.* 200 years ago). These include The Sun News Pictorial (1939), Foley (1947), King (1963), Paine (1982), and Gigliotti et al. (1994). Further dates are suggested by Banks (1993) from dendrochronological analysis of a single *E. regnans* in the Watts Catchment. Table 9.4 lists these dates and the intervals between them. It is unlikely that every listed fire affected every part of the study area. Ashton and Attiwill (1994) indicate that the minimum separation of tree ages (and hence origin dates) is approximately 25 years, owing to the reduced ability of younger trees to withstand fires. Banks (1993) calculated the mean separation of fires as 36 years. A number of the fires listed in Table 9.4 are separated by much less than 25 years, implying that these fires were not coincident in space, or that some of them did not affect the study area at all, the latter being more likely.

Further forest origin dates arise from the experimental logging undertaken in the Maroondah Catchments. These are also listed in Table 9.4.

Forest origin dates were mapped across the study area recently by DNRE as described in Section 9.3.1. The maps were used in combination with the information in Table 9.4 to produce maps of the three most recent origin dates for all parts of the study area. A certain amount of reasoning was involved in deciding pre-1939 origin dates for current 1939 regrowth forests. Typically, an origin of 1759 was assigned where doubt existed (see explanation above). Figures 9.2 to 9.4 show the resulting maps for each parameter.

---

[1]Based on dendrochronological work by Ronan, 1984, Ronan, pers. comm., and Banks, 1993.

Date	Banks?	Ronan?	Gigliotti et al.?	DNRE?	Used?	Name	Description
1480±8	•						Origin of Banks' tree
1578±6	•						
1643±6	•						
1705±6	•						
1736±6	•						
1757±6	•						
1759		•			•		
1781±6	•						
1791±6	•						
1800				•			
1808±6	•						
1850				•			
6/2/1851			•		•	Black Thursday	'widespread destruction'
1/2/1898			•		•	Red Tuesday	'large fires in Gippsland'
12/3/1914			•				' ... Healesville'
1919				•			
22/2/1923			•				' ... Healesville'
27/1/1926			•	•	•		' ... Healesville'
13/1/1939	•		•	•	•	Black Friday	'large areas of state' (incl. Healesville)
26/2/1973					•		Picaninny logging
1/1/73					•		Blue Jacket logging
1/3/77					•		Blacks' Spur logging
1/4/78					•		Monda logging
20/3/85					•		Myrtle logging
20/2/91					•		Murrindindi logging

Table 9.4: Logging dates and *possible* fire dates for the Maroondah Catchments. From: Banks (1993), Gigliotti et al. (1994, Tab. 3.2), Langford & O'Shaughnessy (1977, p. 271), Langford & O'Shaughnessy (1979a, p. 61), Langford & O'Shaughnessy (1980b, p. 27, 35), Ord (1985), Watson & Vertessy (1996, App. B), and G. Dash (DNRE, Toolangi, pers. comm.).
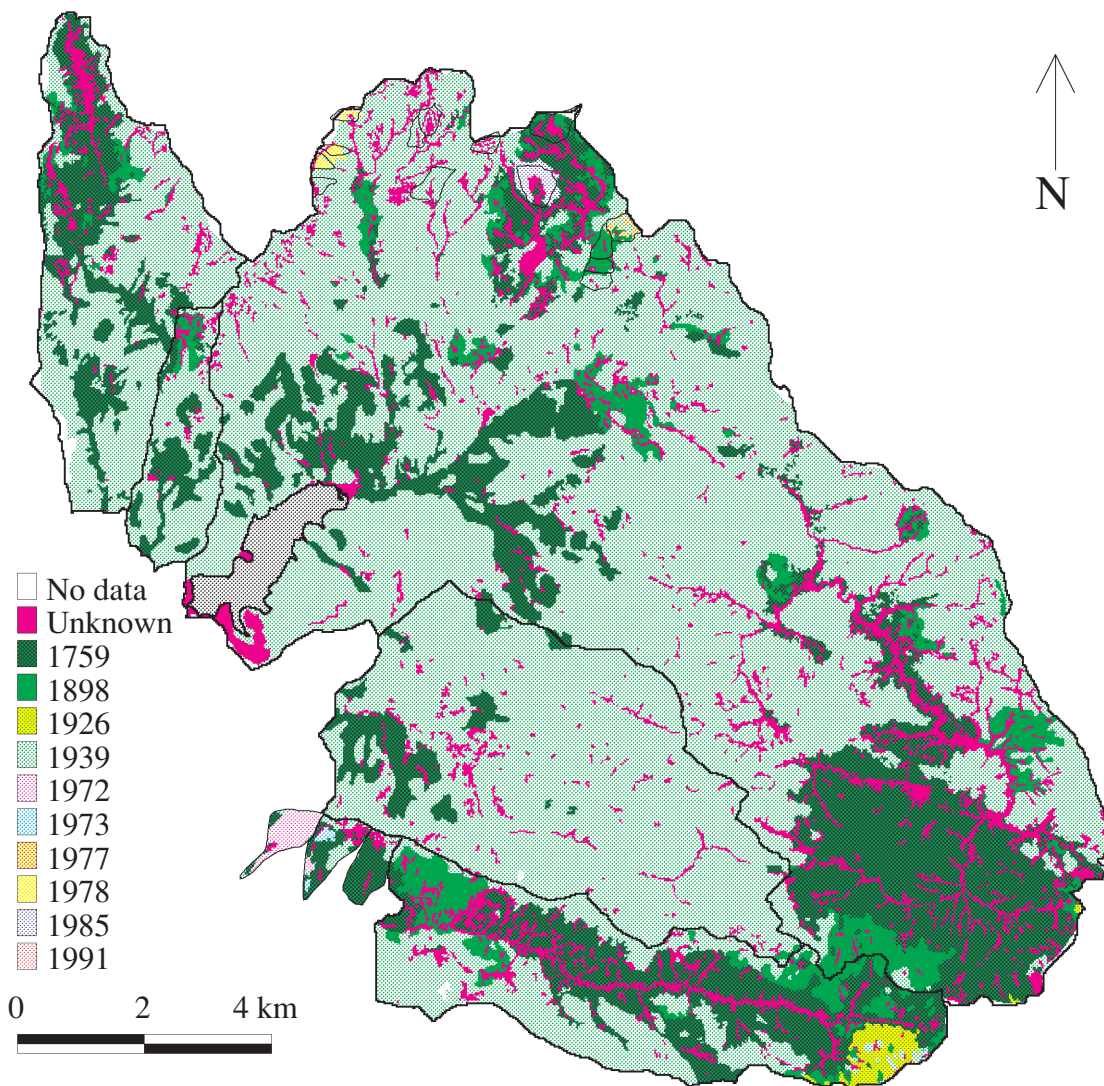
Figure 9.2: Map of the $y_{origin,1}$ parameter, showing the latest historical forest origin dates.

N

No data
Unknown
1759
1898
1926
1939
1972
1973
1977
1978
1985
1991

0   2   4 km
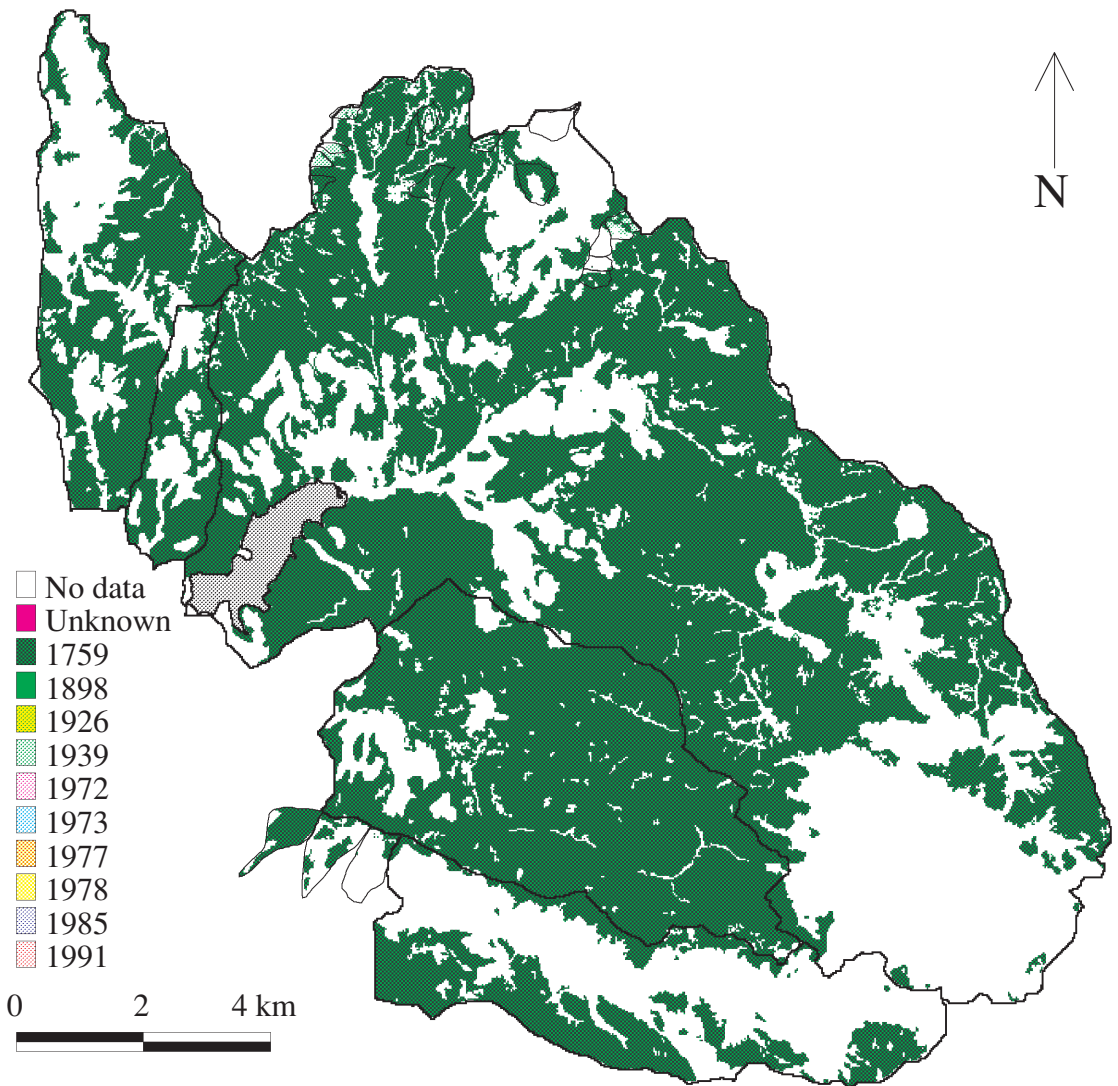
Figure 9.3: Map of the $y_{origin,2}$ parameter, showing the 2nd latest historical forest origin dates.
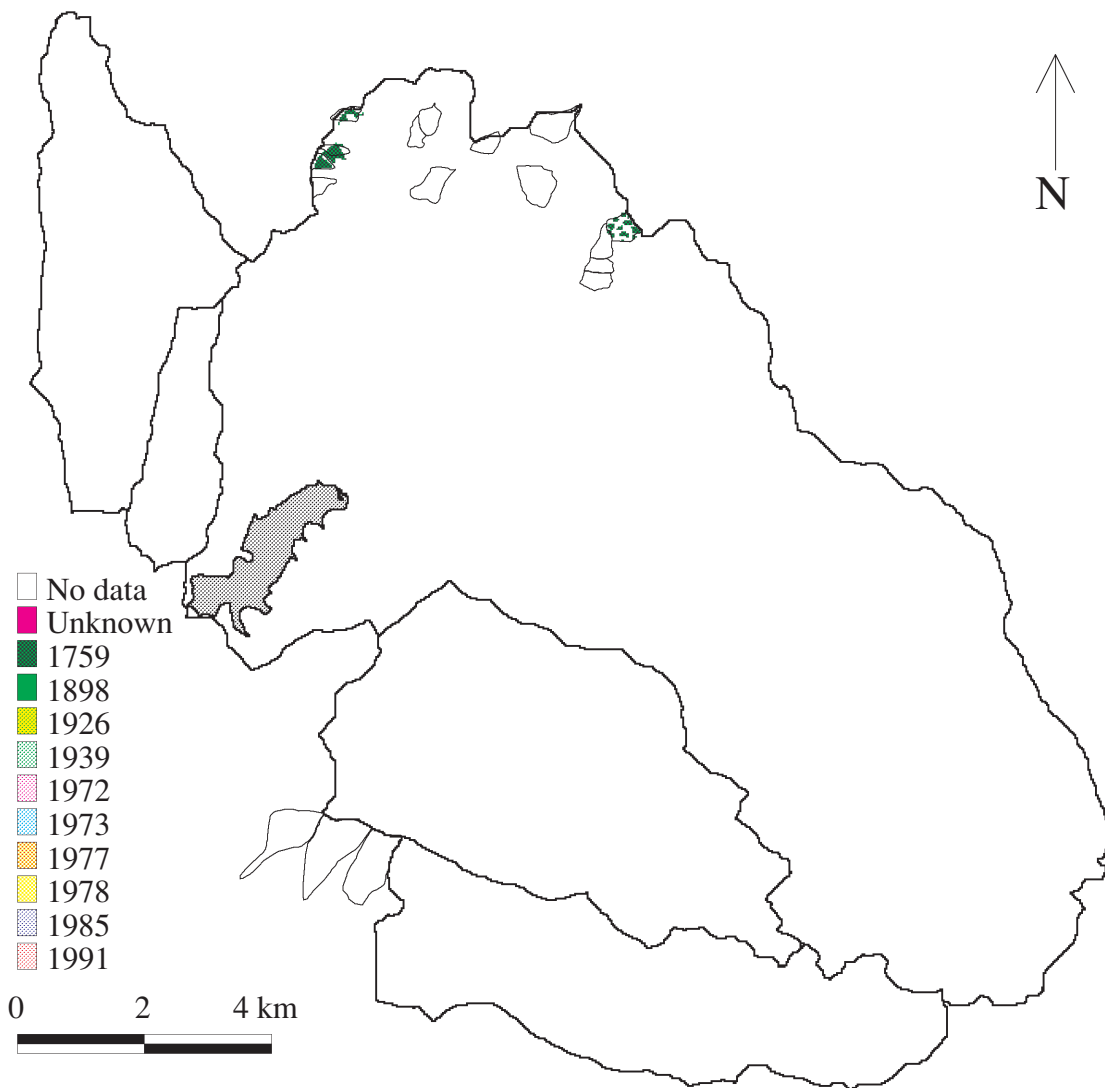
Figure 9.4: Map of the $y_{origin,3}$ parameter, showing the 3rd latest historical forest origin dates.

9.3.3 LAI data

The description of LAI data is organised into sections on: canopy LAI for Ash type forests, canopy LAI for other forest types, understorey LAI, and total LAI.

9.3.3.1 Canopy LAI data for *E. regnans* and other Ash type species

Owing to their morphological similarity, three species are dealt with together as the 'Ash type' species: *E. regnans*, *E. delegatensis*, and *E. nitens*. It is likely that leaf area response differs between these species, but there is no information to separate them quantitatively. Data are available only for *E. regnans* and are assumed to apply to each of the Ash type species.

All available destructive data were used in the development and testing of an allometric model of LAI variation with forest age in Chapter 8. This is the most accurate general source of information on *canopy* LAI for these species and is used here.

9.3.3.2 Canopy LAI data for non-Ash type species

Apart from the data developed from remote sensing later in this chapter, there are no direct data on canopy LAI for the non-Ash type species found within the study area. The data in Table 9.1, particularly for the dry sclerophyll species *E. maculata* which itself is not found in the study area, suggest that the 'mixed species' eucalypt forest in the drier parts of the study area should exhibit about one unit (i.e. $1 \text{ m}^2 \text{ m}^{-2}$) lower LAI than the Ash-type species.

9.3.3.3 Understorey LAI data

The only direct data on understorey LAI within the study area were collected beneath 8 year old *E. regnans* by Beringer (1994), who destructively measured an LAI of 0.67 as the total from a number of species, and beneath 15 year old *E. regnans* by Vertessy et al. (1995a) who destructively measured LAI values of 0.1 for *Acacia dealbata* and 1.8 for *Acacia frigescens*. Understorey LAI can be inferred from the difference between total and canopy LAI and this is addressed later in this chapter.

Source	Location	Technique	Age	Mean LAI value	No. of measurements	No. of sites	No. of days
present study	Acheron	Li-Cor PCA	0.00	0.00	1	1	1
Beringer (1994)	Myrtle 2	destructive	7.94	5.74	1	1	1
Beringer (1994)	Myrtle 2	Li-Cor PCA	7.94	6.21	322	1	2
O'Sullivan (in prep.)	Myrtle 2	Li-Cor PCA	9.75	4.40	25	1	1
Vertessy et al. (1994b)	Monda 2	destructive	15.66	4.0	1	1	1
Vertessy et al. (1994b)	Monda 2	Li-Cor PCA	15.66	4.30	1119	6	?
O'Sullivan (in prep.)	Monda 2	Li-Cor PCA	16.79	3.70	25	1	1
O'Sullivan (in prep.)	Monda 2	Li-Cor PCA	17.19	4.00	25	1	1
O'Sullivan (in prep.)	Picaninny (upper)	Li-Cor PCA	22.6	4.77	25	1	1
O'Sullivan (in prep.)	Picaninny	Li-Cor PCA	22.69	4.70	25	1	1
O'Sullivan (in prep.)	Picaninny	Li-Cor PCA	23.10	4.50	25	1	1
O'Sullivan (in prep.)	Ettercon 3	Li-Cor PCA	55.97	3.90	200	1	2
O'Sullivan (in prep.)	Blacks' Spur	Li-Cor PCA	56.16	2.45	125	1	5
O'Sullivan (in prep.)	Ettercon 3	Li-Cor PCA	56.37	4.47	100	1	1
Pfeiffer and Watson (see text)	Ettercon 3	Li-Cor PCA	56.97	3.63	1650	33	2
Pfeiffer and Watson (see text)	Mount Riddell (North)	Li-Cor PCA	56.97	3.13	650	13	2
O'Sullivan (in prep.)	Myrtle 1	Li-Cor PCA	235	3.60	25	1	1
Pfeiffer and Watson (see text)	Mount Riddell (South)	Li-Cor PCA	237	3.66	275	11	1

Table 9.5: Summary of total LAI data for *E. regnans* forests in the study area. Typically the values given are means from measurements made over one or more days, along transects or segments of a transect at one or more sites.

9.3.3.4 Total

Limited data on *total* LAI of *E. regnans* forest are available, as summarised in Table 9.5. Most of these data were collected using the Li-Cor PCA. Some destructive data are given by Beringer (1994) and Vertessy et al. (1995a) and these compare well with Li-Cor PCA measurements from the same sites. Additionally, very limited Li-Cor PCA data for mixed species forest were collected by Pfeiffer and Watson (1996).

Many of the data in Table 9.5 were collected as part of other published studies and are described elsewhere. However, the Li-Cor PCA data of 'Pfeiffer and Watson' were collected as part of the present study and are explained

as follows (more information is contained in a draft report by Pfeiffer and Watson, 1996). To assess various aspects of spatial variability, two sampling strategies were employed:

In the first, a regular array of transects was delineated over the Ettercon 3 experimental catchment (15 ha), which exhibits a regrowth stand of pure *E. regnans* interrupted by a narrow band of rainforest species along a central stream. Precipitation and radiation are unlikely to vary greatly over the catchment, but a topographically induced soil moisture gradient is observed, concentrated around the first-order stream that runs from it. Six transects were surveyed at approximately 100 m spacings perpendicular to the stream. The transects followed those used by Melbourne Water in their Continuous Forest Inventory (CFI) programme. Every 50 m along each transect, a 25 m segment was marked. Along each segment, Li-Cor PCA readings were taken at 1 m intervals.

The second strategy involved measurements on either side of a steep mountain in the drier, south west part of the study area. Two transects were surveyed over Mount Riddell. One of these was on the steep south slopes rising 474 m from 302 m to 776 m, and the other was on the north slopes rising 412 m from 319 m to 731 m. The south transect ran through old-growth *E. regnans* forest and the north transect ran through both *E. regnans* and 'mixed species' regrowth forest. Measurements were taken at one metre intervals along 25 m segments spaced every 100 m along the two transects.

9.3.4 Aerial photography

Colour aerial photography for the study area was flown by DNRE as part of their forest type mapping programme. This photography was obtained and compiled into a large mosaic poster at a scale of approximately 1:16 000.

The photography promoted familiarisation with the vegetation of the study area, highlighting patterns of homogeneity and heterogeneity. It gave an indication of what could be expected to be discerned from satellite imagery.

9.3.5 Satellite imagery

Four images from the Landsat 5 Thematic Mapper (TM) were obtained for the study area. The images were acquired on clear summer days from 1990 to 1994 (29th Dec. 1990, 3rd Mar. 1991, 19th Jan. 1993, 22nd Jan. 1994). The 1994 image shows some small patches of cloud but the others are completely

clear. Each image was comprised of seven EM bands: 1-Blue, 2-Green, 3-Red, 4-Near infrared, 5-Middle infrared, 6-Thermal infrared, and 7-Far infrared.

9.4   Image processing

A variety of image processing operations were performed on the satellite data before further use. These are described as follows.

9.4.1   Geocoding correction

The images were obtained as a 'Level 8' Landsat product. This means that they were re-sampled to be geocoded in the Australian Map Grid (AMG) with 25 metre pixels. The re-sampling was performed solely using geometrical information about the shape of the AMG and the location of the satellite at the time of acquisition. Ground control was not used, nor was any account taken of the varying elevation of the study area and associated displacement of pixels due to parallax error. Simple calculations (not shown) indicate that the latter results in miss-coding of pixels by as much 100 metres horizontally. The Level 10 Landsat product is planned to use a DEM to correct for elevation distortion at the time of re-sampling.

A procedure could have been designed to correct for elevation distortion using a geometrical re-sampling of the (already) re-sampled imagery. However this would probably lead to an unacceptable loss of image resolution.

Instead, a simpler, *novel* correction was devised which did not involve more re-sampling. Because the images are dominated by topographic shading, their alignment with other cartographic information (such as the DEM) can be verified by correlation with a theoretical shading image calculated for a surface of uniform reflectance draped over the DEM. Further, the correlation with the theoretical shading image may be optimised by *translating the satellite images in all directions by multiples of one pixel-width*. The translation which leads to the best correlation is that which offers the best registration between the imagery and other cartographic data associated with the DEM.

The method of Smith et al. (1980) was used to calculate theoretical shading images and associated coefficients of correlation, R, with the imagery. This method avoids the assumption of Lambertian reflectance which limits simpler methods.

Typical results are illustrated in Table 9.6 which lists the R^2 values obtained

Northing translation	Easting translation						
	-75	-50	-25	0	25	50	75
-75	0.631	0.658	0.658	0.629	0.582	0.534	0.493
-50	0.671	0.704	0.698	0.655	0.595	0.537	0.490
-25	0.706	0.739	0.724	0.671	0.601	0.534	0.483
0	0.719	*0.746*	0.728	0.670	0.596	0.527	0.473
25	0.706	0.727	0.706	0.652	0.582	0.517	0.464
50	0.676	0.691	0.672	0.625	0.566	0.508	0.458
75	0.640	0.649	0.633	0.597	0.550	0.500	0.454

Table 9.6: R^2 values obtained by correlating satellite imagery with theoretical (non-Lambertian) shading images for a range of orthogonal translations of the satellite imagery. Results are shown for Band 4 of the 1990 image.

by a series of translations of Band 4 of the 1990 image. The best correlation ($R^2 = 0.746$) was achieved for a due-east translation of 50 m (two pixels). Optimal translations were usually the same for different bands within a given image, but differed between images.

All seven bands of all four images were optimally translated before further analysis.

9.4.2 Radiometric correction

Radiometric correction was applied to all but the thermal infrared band using the in-flight calibrated gain and offset data published on the World Wide Web by Arino et al. (1995). These data are superior to those published from pre-launch calibrations (see Section 9.2.5.4). The correction equation is:

$$L = \alpha_0 + \alpha_1 \, Q_{cal} \qquad (9.10)$$

where L (W m^{-2} sr^{-1} μm^{-1}) is the spectral radiance at the satellite, Q_{cal} is the raw digital number of the data as obtained (already calibrated such that each sensor within the satellite gives the same digital number for a given radiance), and α_0 and α_1 are offset and gain correction coefficients respectively. The gain and offset data are given in Table 9.7.

Band	Gain	Offset
1	0.7314	-1.5
2	1.3533	-3.1
3	0.9714	-2.7
4	1.0686	-2.5
5	0.1429	-0.45
6	NA	NA
7	0.0757	-0.30

Table 9.7: In-flight calibrated gain and offset values for Landsat 4 and 5 Thematic Mapper data as published by Arino et al. (1995).

9.4.3 Atmospheric correction

Atmospheric correction is more complicated than radiometric correction and was not able to be performed in the time available. It is likely that this will limit the strength of the ensuing analysis but will not preclude conclusions regarding the feasibility or otherwise of satellite remote sensing of eucalypt LAI.

9.4.4 Visualisation

As will become clear below, effective visualisation of the imagery proved to be crucial in identifying logging coupes north and east of the study area and designing a strategy for making optimal use of the imagery in remote sensing of LAI.

True-colour images were initially printed by assigning the radiometrically corrected Blue, Green, and Red image data to the like-named colours of an inkjet printer. This proved unsatisfactory because, for each band, almost all of the measured radiance values fell within a narrow range relative to the total measurable range. In simple terms, the relatively homogeneous forest scene exhibited very low contrast.

Hence, a *novel* objective scheme for contrast enhancement was designed. Specific upper and lower percentiles were calculated for each band within each image. The radiances were scaled such that all radiances lower than or equal to the calculated lower percentile were given the minimum printable value. All radiances higher than or equal to the upper percentile were given the maximum printable value, and radiances between these limits were scaled linearly between minimum and maximum printable values. Table 9.8 shows

Band	Lower cut-off percentile	Upper cut-off percentile
1	0.005	0.95
2	0.001	0.90
3	0.001	0.90

Table 9.8: Lower and upper cut-off percentiles applied in objective contrast enhancement of radiometrically corrected true colour TM imagery.

the percentiles used for each band. These were determined by trial and error but used consistently to allow objective comparison between images.

Finally, gamma correction ($\gamma = 3.0$, Foley et al., 1990) was applied to enhance the contrast of darker regions such as forest.

Figure 9.5 shows the resulting contrast-enhanced true colour image from 1993. Maroondah Reservoir is clearly visible. The forest of the south east of the study area appears slightly reddish. This is the area covered by *E. delegatensis* (see Figure 9.1). To the north and east of the study area can be seen a number of logging coupes in various stages of regeneration. The rural areas to the west and the north east are saturated to white due to the contrast enhancement. Topographic shading between north facing and south facing slopes dominates all of the mountainous areas. At the time of acquisition, the sun was 47.75° above the horizon at 79.00° east of north.

The 1990 and 1994 true colour images (not shown) are similar to the 1993 image, with similar solar positions. The 1991 image is slightly different, being acquired later in summer with a lower solar elevation and, consequently, more pronounced shading.

9.4.5 NDVI

Analysis was conducted for both RVI and NDVI but, for the sake of brevity, only the analysis of NDVI images is presented here. For the record, RVI behaved very similarly to NDVI with respect to image characteristics and subsequent correlation with ground LAI data. NDVI was preferred because of greater popularity in the literature and the existence of the general form for LAI/NDVI relationships cited by Lacaze (1996) and Leblon et al. (1993) (see below).

The 1993 NDVI image is shown in Figure 9.6. Note that in this image, and a number of subsequent ones in this chapter, linear grey-scales have been used. These lead to low contrast throughout much of the image, *which is*
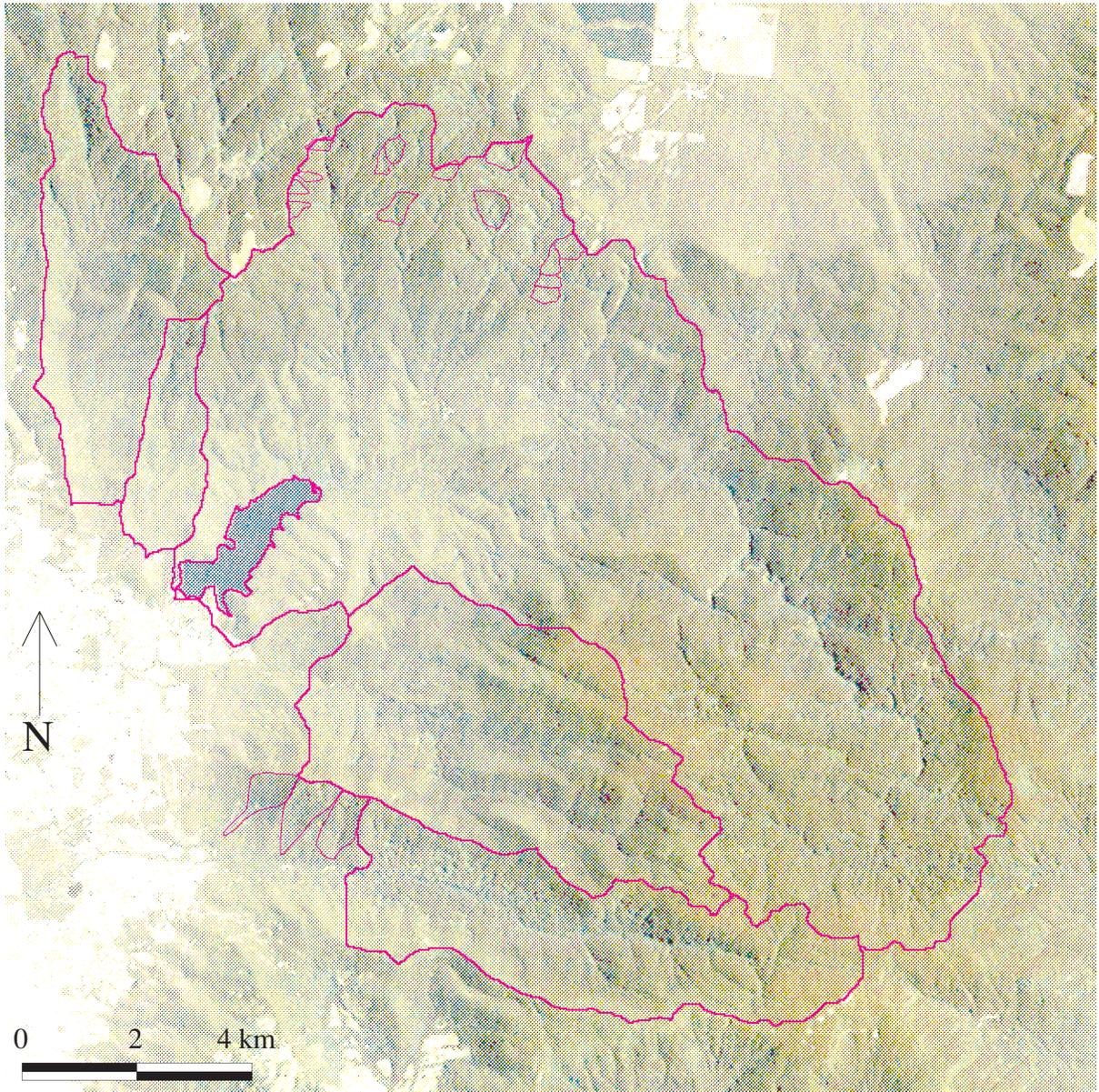
Figure 9.5: Landsat 5 TM true colour image of the study area for 19th Jan. 1993 after objective linear contrast enhancement.

exactly the point of the exercise. Non-linear, contrast enhancing scales could be used (as for the true colour imagery), but these would create the false impression of heterogeneity in the vegetation of the area. As will be seen, both NDVI and LAI are relatively homogeneous within eucalypt forest and it is the intention of the displayed Figures to show this.

The 1993 NDVI image in Figure 9.6 shows a number of desirable features. Most obviously, low NDVI is observed for Maroondah Reservoir, and for a large logging coupe just outside the north east boundary of the study area. Some smaller coupes can be seen to the north of the study area. Additionally, lower NDVI than for surrounding areas is generally observed in the south east of the study area, which is covered by *E. delegatensis* and old growth *E. regnans*, both which may be expected to exhibit lower LAI than the regrowth *E. regnans* which occupies most of the study area. An undesirable feature of the image is that, despite the intention that NDVI corrects for largely band-independent effects such as topographic shading, some topographic effects are still evident in the image (e.g. alternating light and dark hillslope facets on either side of water courses).

9.4.6   Shading correction

Explicit shading correction (as opposed to that implicit in NDVI) was performed on each band using the Minnaert method employed by Smith et al. (1980). As noted earlier, this method avoids the Lambertian reflectance assumption of simpler methods such as that of Harrison and Jupp (1990). The method uses a least squares regression procedure to compute a theoretical shading image which would be observed if there were a uniform ground cover. The shade-corrected reflectance is then the ratio of observed reflectance to the shading image. Figure 9.7 shows the shading image for Band 3 of the 1993 observed image. An indication of the efficacy of the method is given by noting the similarities between the shading apparent in the true colour image (Figure 9.5) and the shading image.

Figures 9.8 and 9.9 show the true colour image and NDVI image for 1993 constructed using the shade-corrected bands. In both cases, topographic effects were greatly reduced.

Note that the correction procedure employed accounted for shading due to the varying angle of incidence of the sun on the terrain. It did *not* account for shading due to obstruction of sunlight. This can occur for a number reasons, such as: when a slope cannot 'see' the sun at all because it is inclined steeply
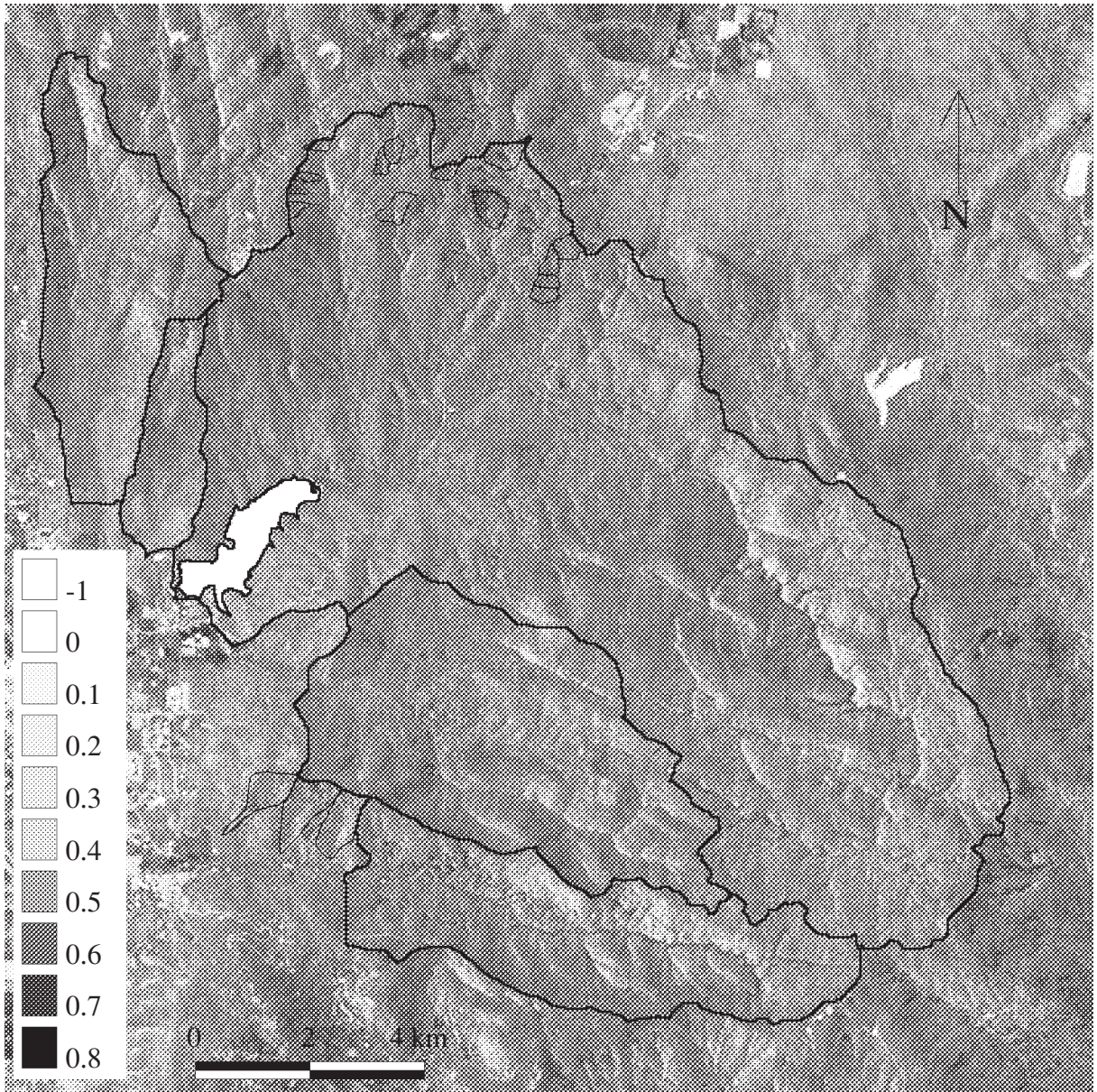
Figure 9.6: Landsat 5 TM NDVI image of the study area for 19th Jan. 1993.
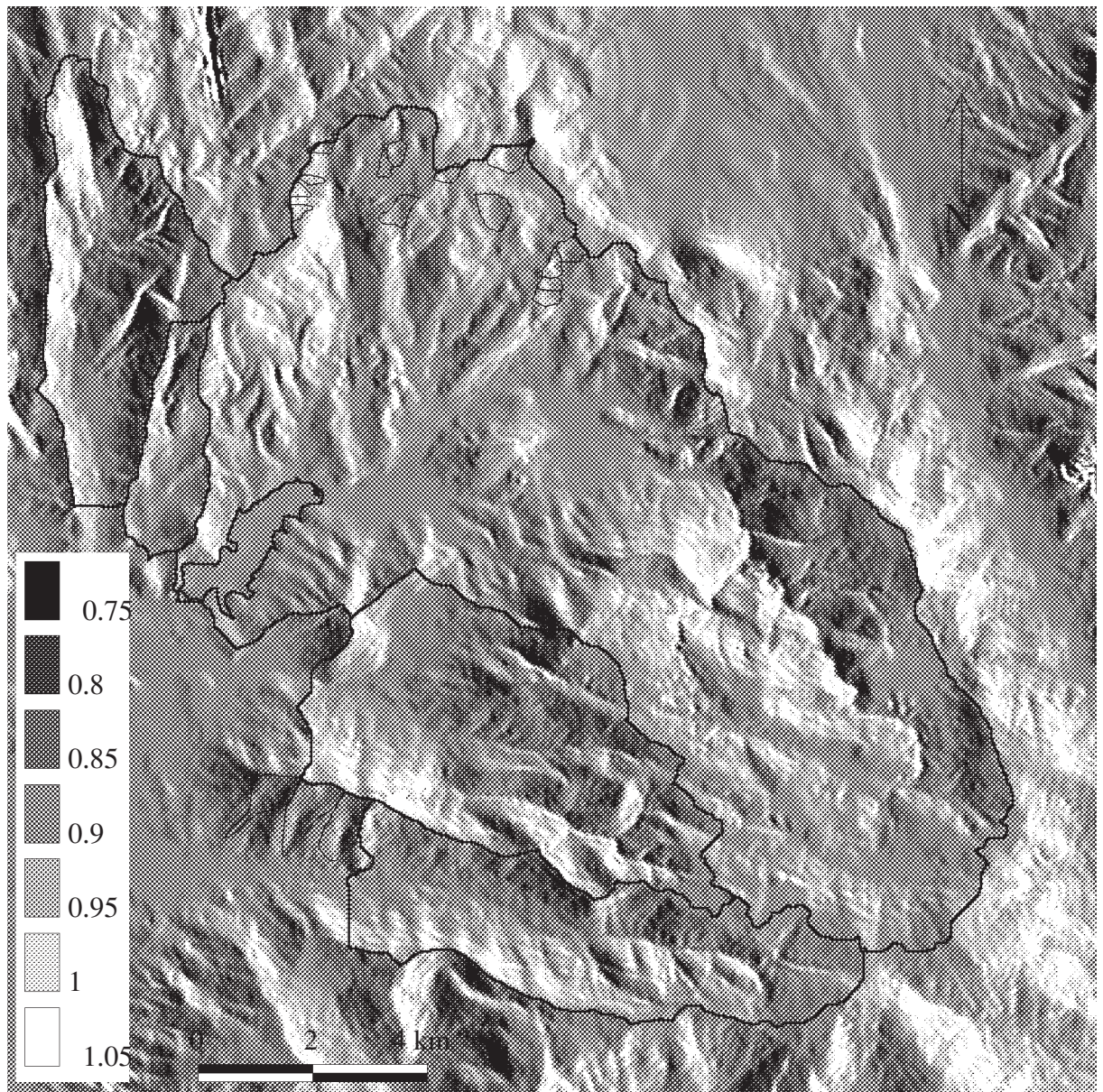
Figure 9.7: Theoretical non-Lambertian shading image of the study area calculated for Band 3 of the TM image acquired on 19th Jan. 1993.
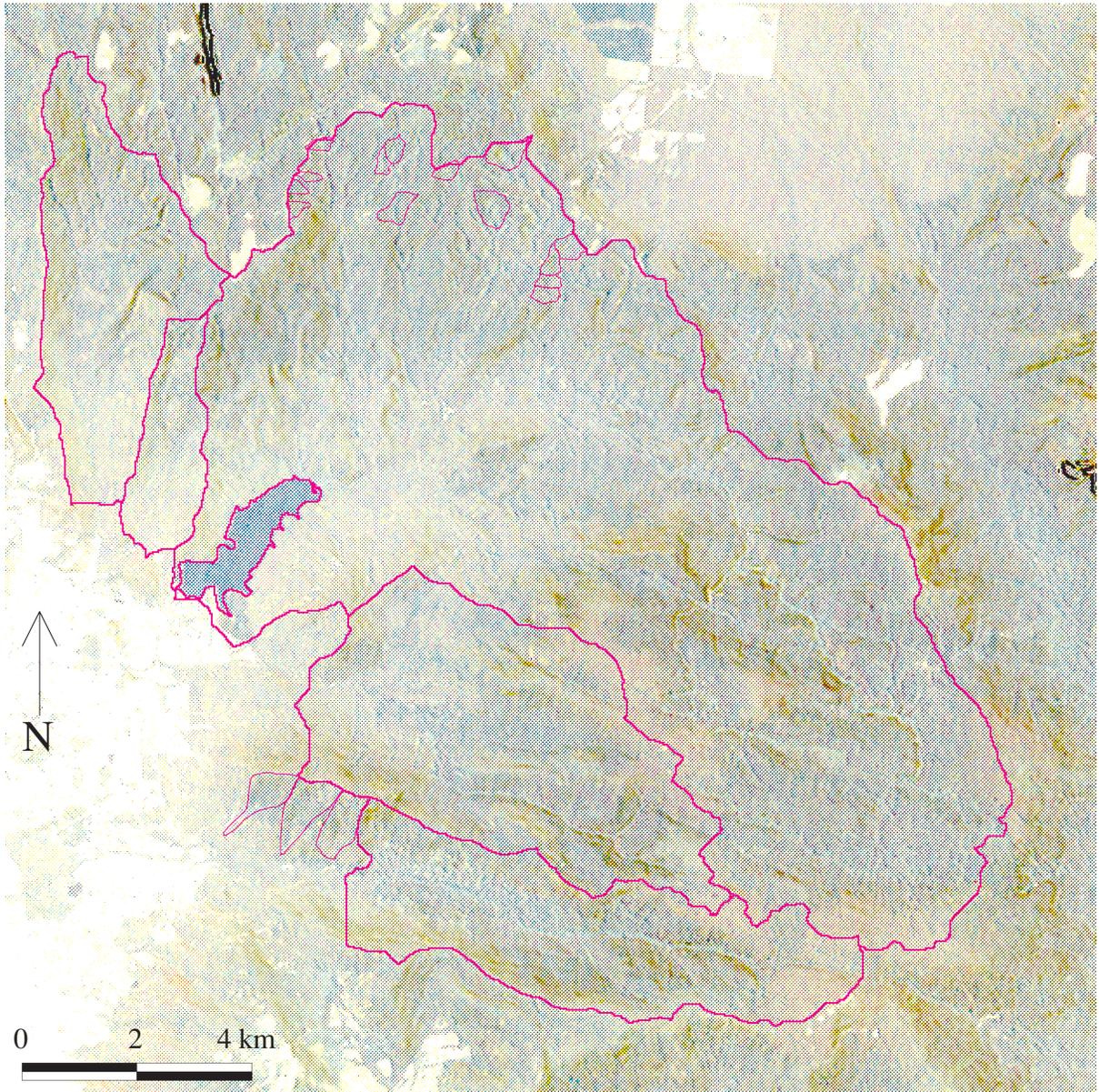
Figure 9.8: Shade-corrected Landsat 5 TM true colour image of the study area for 19th Jan. 1993 after objective linear contrast enhancement.
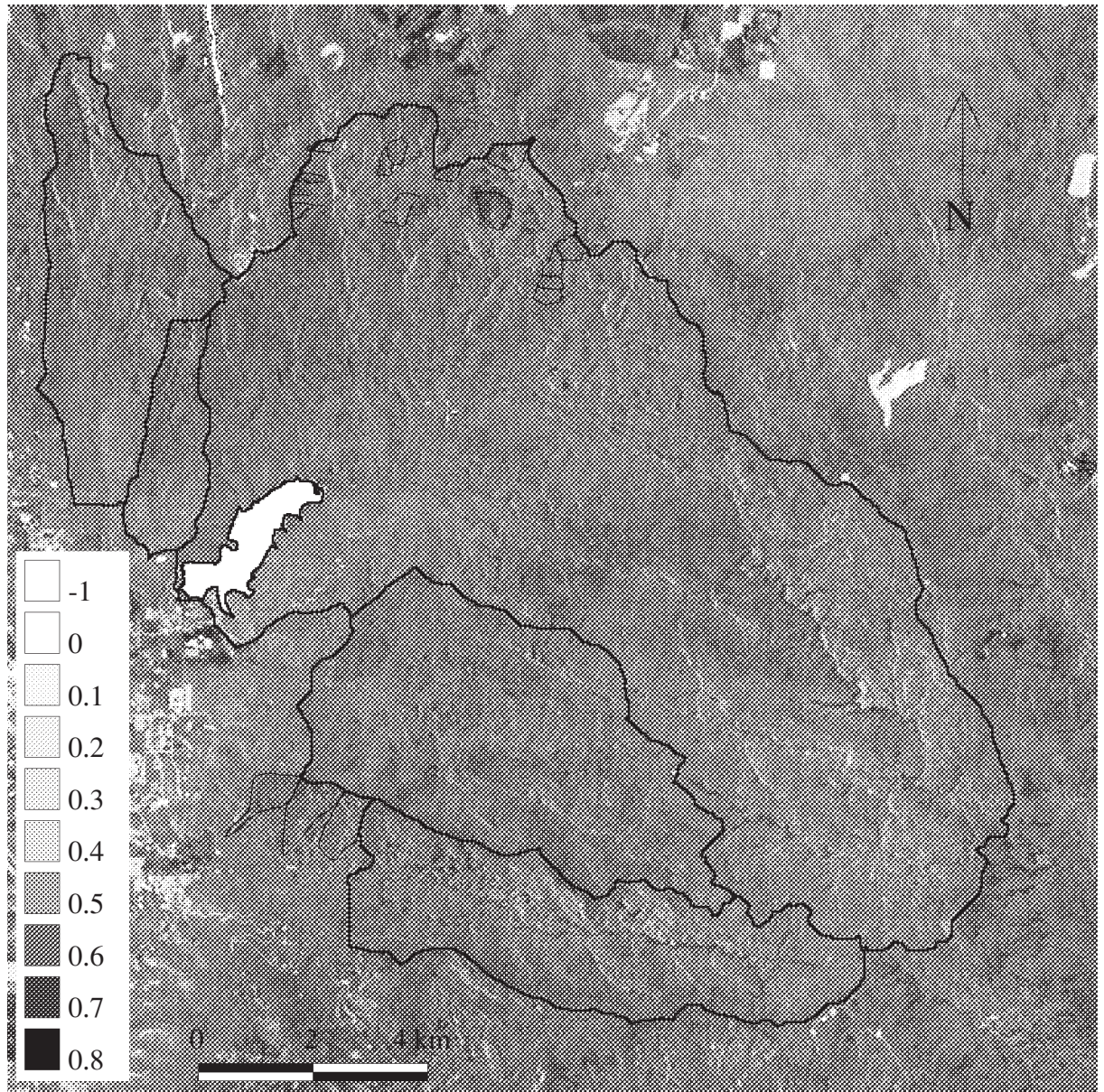
Figure 9.9: Landsat 5 TM NDVI image of the study area for 19th Jan. 1993 *based on shade-corrected data.*

away the sun; when a high mountain lies between the sun and other parts of the study area; and when high trees are between the sun and other areas. These effects are minimal in the imagery, except for obstruction by trees which occurs in many gullies where a low rainforest canopy at the bottom of the gully is surrounded by high Ash forest on all sides.

9.5 Remote sensing of total LAI

Macaque requires separate quantification of canopy and understorey LAI. This is achieved by constructing maps of total and canopy LAI and subtracting one from the other to give understorey LAI. This section deals with mapping *total* LAI.

The *only* data on total LAI which are available are those described in Section 9.3.3.4: Li-Cor PCA measurements made by various workers; and the single destructive measurement made by Beringer (1994). These data are insufficient to enable a map of total LAI to be derived. They must be correlated with some form of spatial data to provide distributed estimates of LAI. Two possibilities were considered. The first was to correlate remote sensing imagery with the ground measurements of LAI to provide a remotely sensed map of LAI. The second was to use the hydro-ecological equilibrium theory reviewed in Section 9.2.1.6. The first possibility is investigated in this Section. The second is perhaps equally viable but is left for future research.

9.5.1 First attempt

Two attempts were made at correlating ground measurements of LAI with remotely sensed imagery. The first was largely unsuccessful but is described here as an important 'negative conclusion', illustrating the problems which can occur with some approaches to remote sensing.

The methodology of this attempt was simple. All available Li-Cor PCA measurements of LAI were plotted against various remotely sensed vegetation indices in search of a correlation. The details are as follows.

For the sites measured by Pfeiffer and Watson (see Section 9.3.3.4), tape measures and clinometers were used to locate the PCA measurement sites relative to known cartographic features such as road bends. This involved tape measurement in dense undergrowth over distances of up to one kilometre. The measurements were drawn on a map and AMG and AHD co-ordinates

were determined from each measurement site. At a small number of sites, geographic co-ordinates were able to be determined using a GPS receiver by O'Sullivan (in prep.) and these were converted to AMG/AHD using the method given by the National Mapping Council of Australia (1972). It is estimated that errors in absolute site co-ordinates are about 50 m with a maximum of 100 m.

Despite the geocoding correction described in Section 9.4.1, it is likely that some parts of the satellite imagery may be miss-coded by about 50 m due to non-uniform elevation-induced distortion across the study area. Thus the error in locating a ground measurement site within the imagery may be about 100 m due to the combined errors of site location relative to AMG and image distortion.

Some GRASS-compliant code was written to sample the imagery within circular areas of defined radius centred on the ground measurement sites and report the average image value within these areas. A 50 m radius was chosen as a compromise between loss of resolution at high radii and the reduced chance of sampling the ground measurement site at low radii.

Figure 9.10 plots shade-corrected NDVI against ground measured LAI. No correlation was apparent. This could be because either shade-corrected NDVI is not related to LAI in the forests of the study area, or the method is flawed. The navigational problems already mentioned could account for the negative result. But there are other, more subtle explanations. It is possible that the random variability in both the shade-corrected NDVI data and the ground data are large relative to the range of NDVI and LAI values which were recorded, such that a relationship exists which can only be observed over large ranges of LAI. There may be considerable 'noise' in the imagery due to atmospheric effects and artefacts in the shading correction associated with DEM inaccuracies. There is also likely to be considerable variability in the Li-Cor PCA data, as has been reported in the literature (see Section 9.2.1.4).

9.5.2 Second attempt

The second attempt at correlating ground measurements of LAI with remotely sensed imagery specifically addressed the major source of systematic variation observable in the imagery: logging coupes. Large changes in LAI occur during and immediately after logging and these can easily be seen in the satellite imagery.
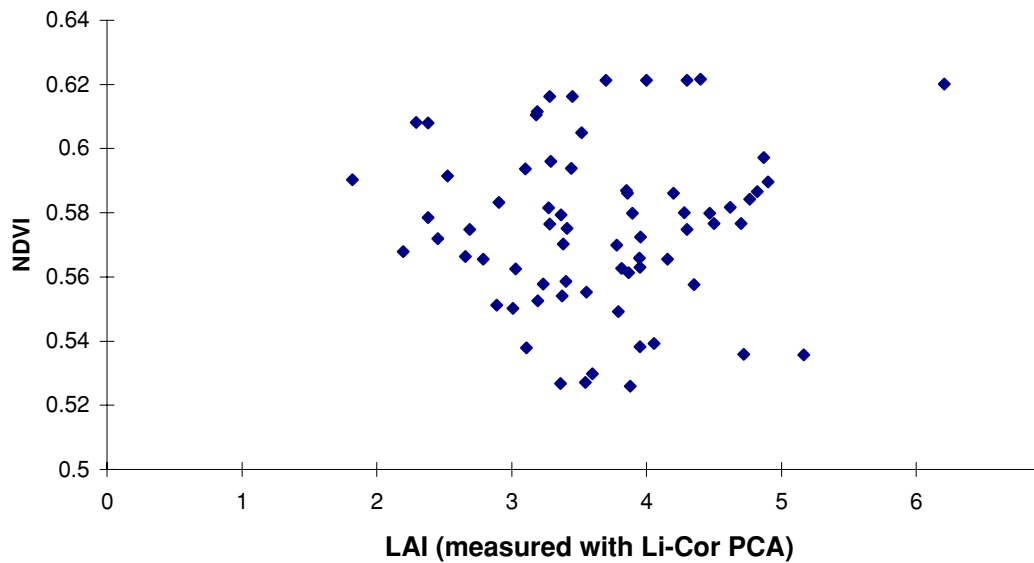
Figure 9.10: 50 m radius-averaged NDVI derived from shade corrected imagery plotted against ground measured LAI using a Li-Cor PCA.

9.5.2.1   Initial observations

Figure 9.11 compares shade-corrected NDVI images of an area of recent logging activity in *E. regnans* forest for the four image acquisition dates. The appearance of new coupes can easily be discerned as a large drop in NDVI, as can their regeneration toward pre-logging NDVI values over two or three years. Close examination reveals a number of areas where NDVI is higher (darker) than normal. These are associated with coupes which are about four or five years old.

Two hypotheses are thus formed:

- For *E. regnans* forests, shade-corrected NDVI decreases to zero upon logging, rapidly rises past pre-logging values to a peak higher than pre-logging values, and then declines to pre-logging values.

- For *E. regnans* forests, LAI is correlated with shade-corrected NDVI and thus follows the same pattern of time.

A quantitative examination of this hypothesis follows:
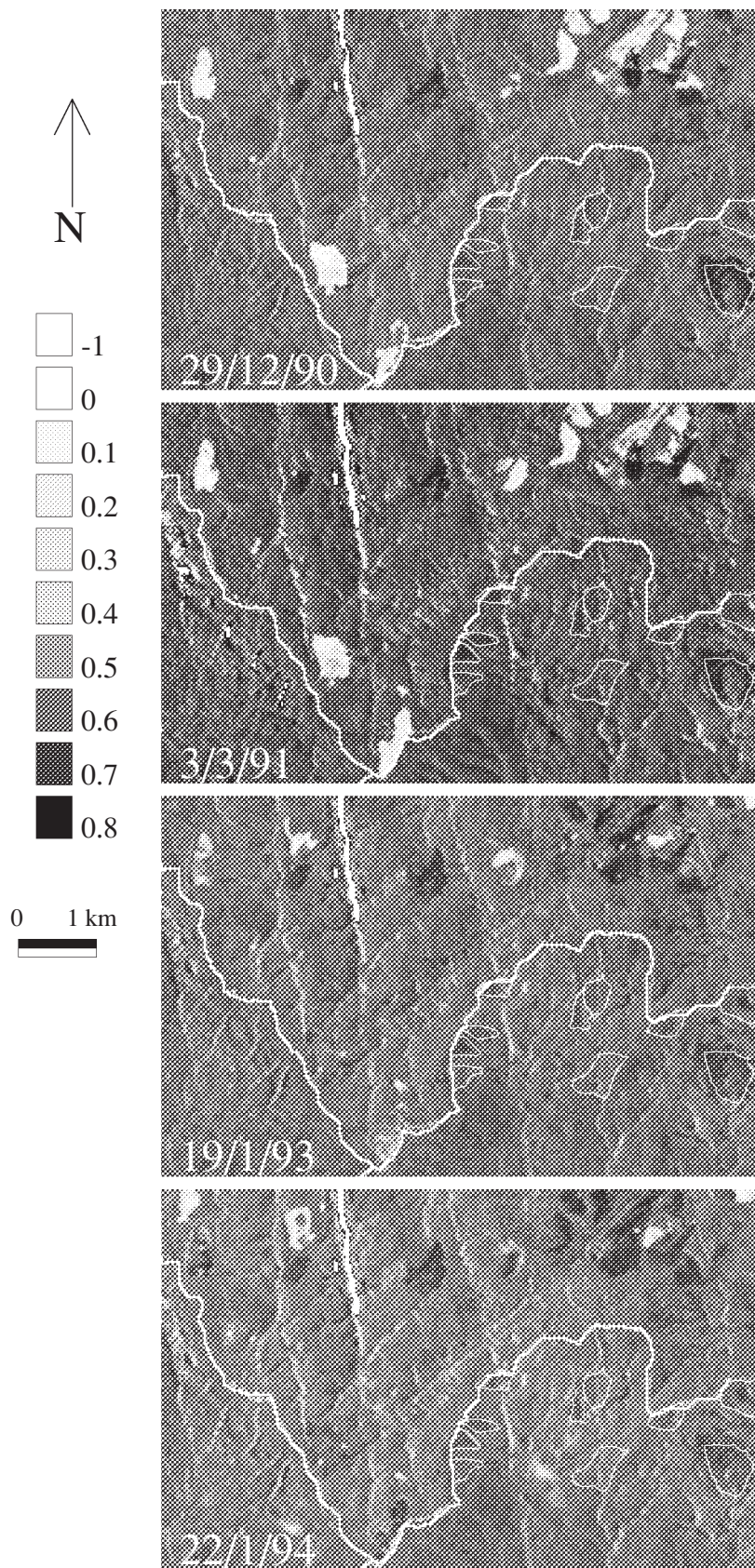
Figure 9.11: Four images of shade-corrected NDVI in a region north of the study area where there is a high concentration of recent *E. regnans* logging coupes (dates shown on figure).

9.5.2.2 NDVI versus forest age

Initially, the relationship between shade-corrected NDVI and forest age was examined. Two sets of NDVI/age data were constructed: by direct examination of NDVI values from logging coupes in the imagery (mostly outside the study area); and by calculation of areally averaged NDVI values for forests of different age mapped across the study area.

The year of logging for all coupes to the north and east of the study area was obtained from the managers of those forests (G. Dash, DNRE, Toolangi; and B. McTavish, DNRE, Marysville; pers. comm.). A selection of 24 coupes was made with logging dates ranging from 1978 to 1994. The radius-averaging code described in Section 9.5.1 was used to give average shade-corrected NDVI values within 50 m radius circular areas centred on sites located in the middle of each coupe (determined from the imagery in conjunction with maps supplied by the forest managers). There are four images, so four values were obtained for each coupe.

The maps of forest origin described in Section 9.3.2 provided an additional source of information on forest age, concentrated on older ages as opposed to the young ages of the logging coupes. Some purpose-written GRASS-compliant code was used to compute the average shade-corrected NDVI value for each forest type and age for each of the four acquisition dates. As before, four values were obtained for each forest origin date.

Figure 9.12 plots all of the resulting (shade-corrected) NDVI versus forest age data for *E. regnans*. Values from single coupes or single forest origin dates were linked by lines of four points, allowing inspection of the progression over time of NDVI data from each source. The Log plot in Figure 9.13 better illustrated the young-aged data but could not show the decline from pre-logging values. Clearly, the data support the first hypothesis outlined above.

9.5.2.3 Total LAI versus forest age

To examine whether the total LAI of *E. regnans* forest has the same relationship with forest age as NDVI, the Li-Cor PCA data were grouped into averages for different forest ages and data sources and plotted against forest age as shown in Figure 9.14. Whilst there were fewer points than in the plot of TNDVI versus age, a relationship was evident. Total LAI was zero at age zero, rose rapidly to a peak at or before 8 years, and thereafter appeared to decline perennially. There were no total LAI data for *E. regnans* forests
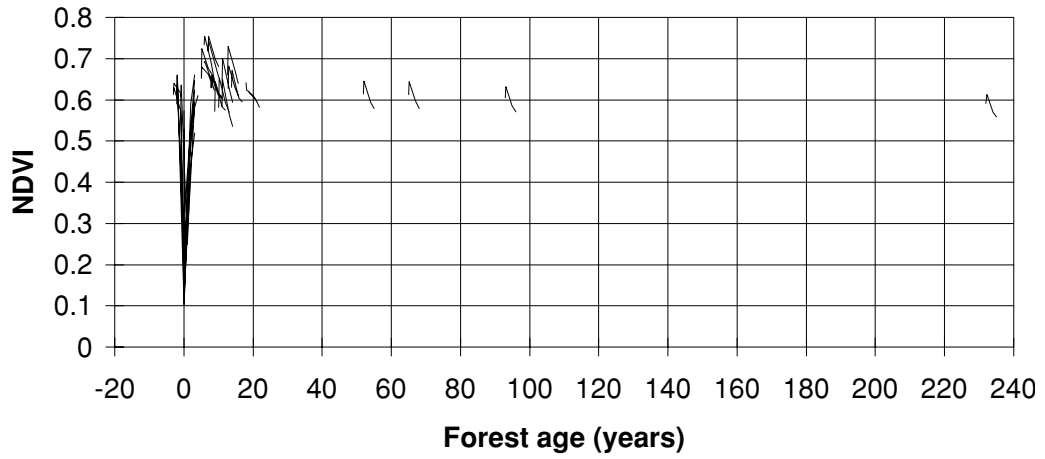
Figure 9.12: The relation between shade-corrected NDVI and forest age for *E. regnans*.
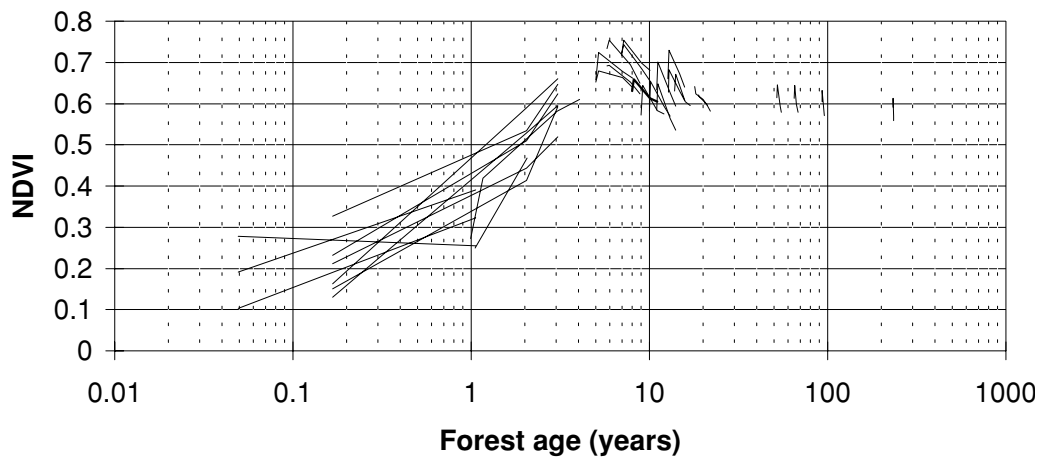
Figure 9.13: As for Figure 9.12 but with a logarithmic time axis. Pre-logging values (with negative ages) can not be shown on this plot.
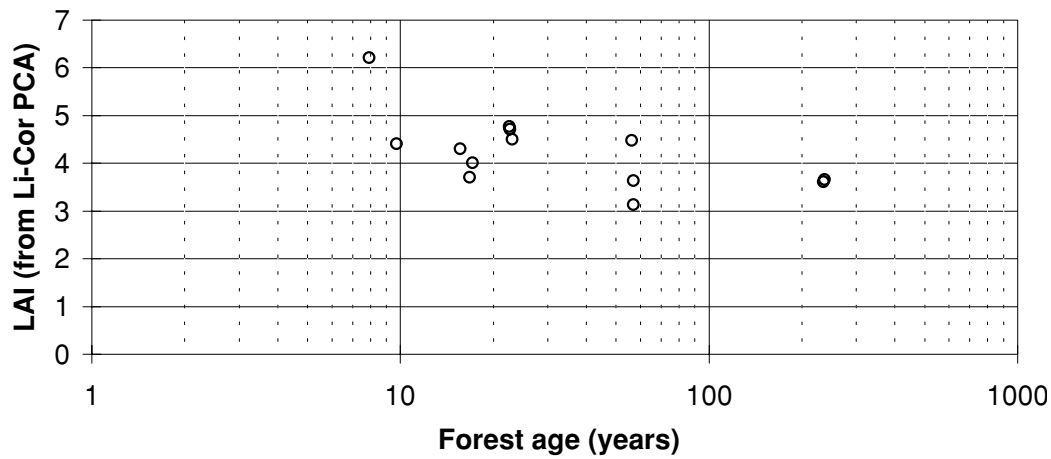
Figure 9.14: Average ground measurements of LAI using a Li-Cor PCA plotted against forest age for *E. regnans* forest. Each point represents the average of between 25 and 1650 measurements as described in Table 9.5.

younger than the 7.94 year old forest measured by Beringer (1994).

9.5.2.4 Correlating NDVI with total LAI

Because of the discontiguous nature of the NDVI and total LAI data, a simple scatter plot of one against the other was not possible. Instead, the plots of each against forest age were overlaid and, in the following section, a continuous function was constructed as a common interpolator for the two data sets.

Beforehand, the shade-corrected NDVI data were transformed to TNDVI values which could be used to directly estimate LAI using the general model cited by Lacaze (1996) (Equation 9.9). The model has three parameters. $NDVI_\infty$ was set to the theoretical maximum value cited by Lacaze (1996). $NDVI_{back}$ was set by eye such that the LAI values estimated for month-old forest were centred about zero. The shape parameter, k, was adjusted by eye to give the best match between estimated and measured LAI.

Figure 9.15 shows the resulting correlation between LAI and TNDVI and Table 9.9 gives the model parameters. It is clear from the correspondence between estimated and measured LAI that the two are correlated and that NDVI can be used to predict the LAI of *E. regnans* forests.

The calibration of Equation 9.9 given in Table 9.9 allows a map of LAI to be calculated, as shown for 1993 in Figure 9.16. Note that this calculation assumed that the LAI/NDVI correlation determined for *E. regnans* forest held for all parts of the study area. As the study area was almost totally
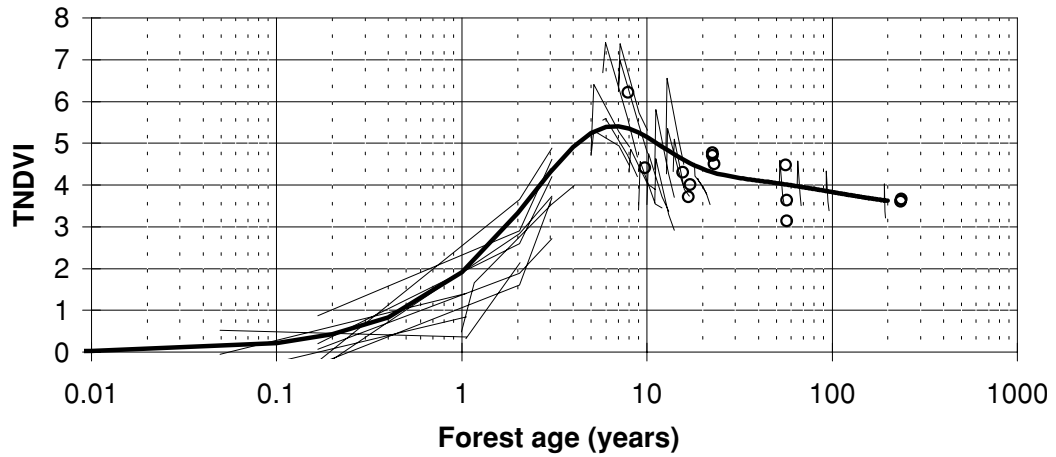
Figure 9.15: Total LAI of *E. regnans* forest. The circles are ground measurements of LAI made using a Li-Cor PCA. The short thin lines are LAI values estimated using (shade-corrected) TNDVI derived from Landsat TM imagery. The long, curved line is an arbitrary functional interpolation through the points (see below).

Parameter	Value
$NDVI_\infty$	0.867
$NDVI_{back}$	0.200
k	0.240

Table 9.9: Parameters used for the general model of LAI versus NDVI given in Equation 9.9. The values apply to shade-corrected TNDVI data only.

covered with closed-canopy eucalypt forest, there was no reason to doubt this assumption in the absence of ground measurements of total LAI in non-*E. regnans* forests. The most notable feature of Figure 9.16 is that *total LAI did not vary greatly* within the largely older than 50 year old forests which covered most of the study area in 1993.

9.5.2.5   A functional relation predicting total LAI from forest age

The above investigation has shown that remote sensing can be used to estimate total LAI in *E. regnans* forests, which is of course useful. It has also shown that total LAI for *E. regnans* forests varies significantly with age, particularly in the first 50 years of growth. This means that unless imagery is available for every year of model simulation, remote sensing can not be used *directly* for model input (for *E. regnans* forests). For long term simulations, an auxiliary, age-sensitive method is required.

The dominant source of variability in total LAI across the study area is forest age and thus, this control should be the basis of *E. regnans* total LAI estimation in the model.

The relation illustrated by Figure 9.15 is characterised by three features: a peak in LAI for young aged forest, a rapid drop shortly after to a period of slow decay, and a climax LAI which is reached after the slow decay. A mathematical equation was developed that approximated this relation. The equation is plotted as the smooth line in Figure 9.15 and is given below:

$$
\begin{aligned}
\text{total } LAI \ &= (LAI_{tot,P} - LAI_{tot,C} - LAI_{tot,D}) \, \frac{e}{\tau_{tot,P}} \, AGE \, e^{\left(\frac{-AGE}{\tau_{tot,P}}\right)} \\
&+ (LAI_{tot,C} + LAI_{tot,D}) \left(\frac{2}{1 + e^{\left(\frac{-AGE}{\tau_{tot,C}}\right)}} - 1 \right) \qquad (9.11) \\
&+ LAI_{tot,D} \left(e^{\left(\frac{-AGE}{\tau_{tot,D}}\right)} - 1 \right)
\end{aligned}
$$

The curve was chosen to be flexible, with six parameters which may be used to adjust the magnitude and timing of peak, decay, and climax LAI values. LAI starts at $LAI = 0$, peaks $LAI \approx LAI_{tot,P}$, then decays quickly and then more slowly to a climax LAI of $LAI_{tot,C}$. The magnitude of the decay is controlled by $LAI_{tot,D}$. The equation is the sum of three terms, representing the three main features of the relation illustrated by Figure 9.15. The first term is similar to the Kuczera curve (Figure 1.1), starting at zero, peaking
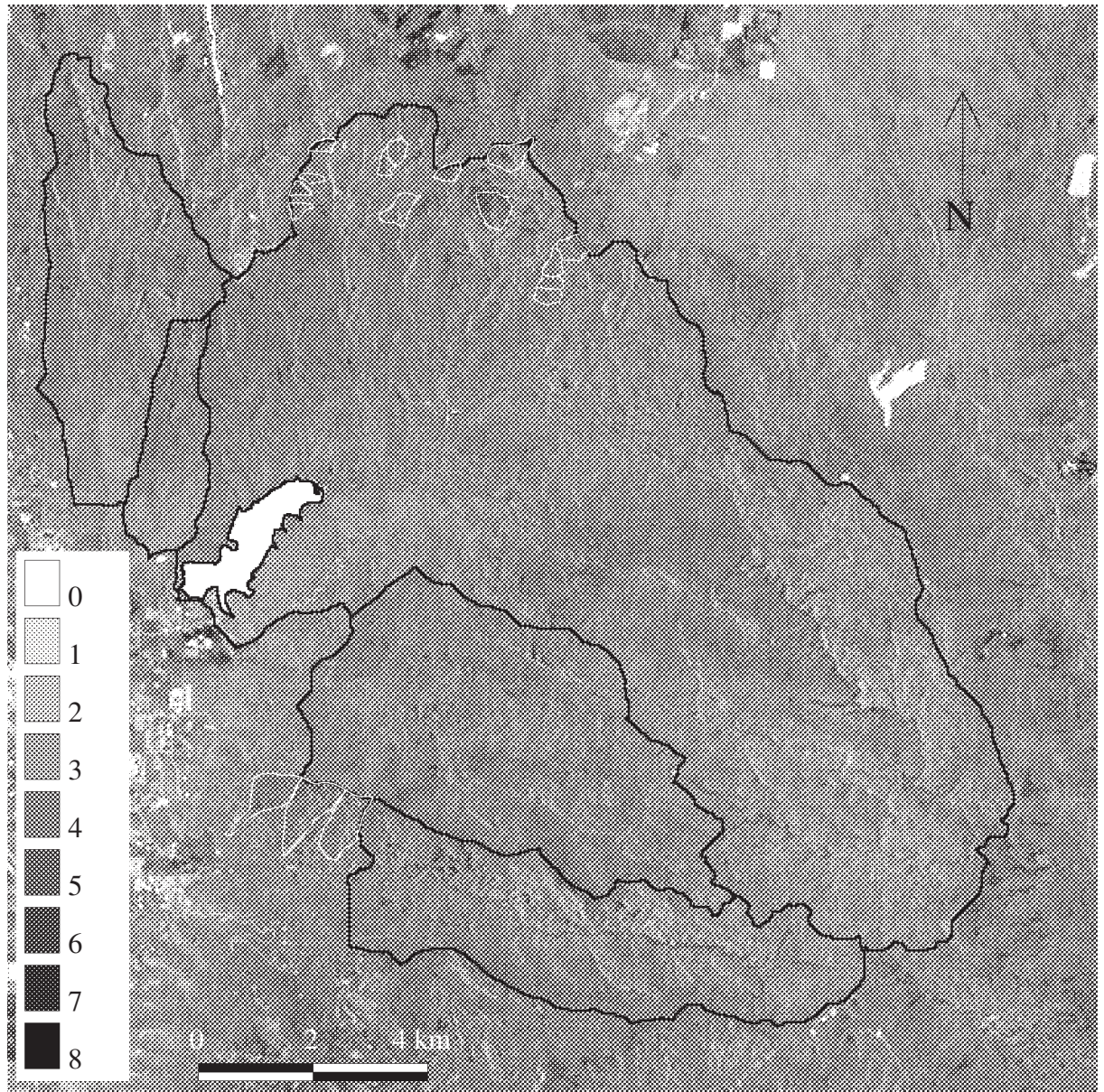
Figure 9.16: Total LAI mapped over the study area for 19th Jan. 1993 by remote sensing using a correlation between shade-corrected TNDVI derived from Landsat 5 TM imagery and ground-based Li-Cor PCA measurements of LAI.

Parameter	Value
$LAI_{tot,P}$	6.0
$\tau_{tot,P}$	4 years
$LAI_{tot,C}$	3.5
$\tau_{tot,C}$	2 years
$LAI_{tot,D}$	0.9
$\tau_{tot,D}$	100 years

Table 9.10: Parameters fitted by eye for the functional relation predicting *E. regnans* total LAI from forest age.

at an age determined by $\tau_{tot,P}$, and decaying back to zero. The second term represents the climax value and is a sigmoid function (Zurada, 1992), which begins at zero and rises to an asymptote over a period determined by $\tau_{tot,C}$. The third term represents the slow decay, starting at zero and decaying slowly at a rate determined by $\tau_{tot,D}$.

The parameters were fitted by eye and are given in Table 9.10.

9.5.2.6 Other influences on *E. regnans* total LAI

It is evident from the imagery that there are secondary controls on the total LAI of *E. regnans* forest apart from forest age. Some of these may be historical or effectively random, whilst others may be linked to environmental influences such as precipitation, radiation, and temperature (see Section 9.2.3). Environmental influences are not *strongly* apparent in the imagery, and their characterisation is left for future research. 'Random' influences are apparent but are unlikely to affect model operation in a systematic manner and thus their inclusion in the model parameterisation process is also left for future work.

9.5.2.7 Total LAI for species other than *E. regnans*

Whilst *E. regnans* dominates the study area, LAI values are still required for the other species present. Some of these are mapped in origin-date classes in Figures 9.1 to 9.4. Others are mapped as having 'unknown' origin. Following the methods and results of the previous sections (including Equation 9.9 and Table 9.9), areal average remotely sensed LAI is plotted for each species with known age in Figure 9.17.

The three Ash type species, *E. regnans*, *E. nitens*, and *E. delegatensis*, appear
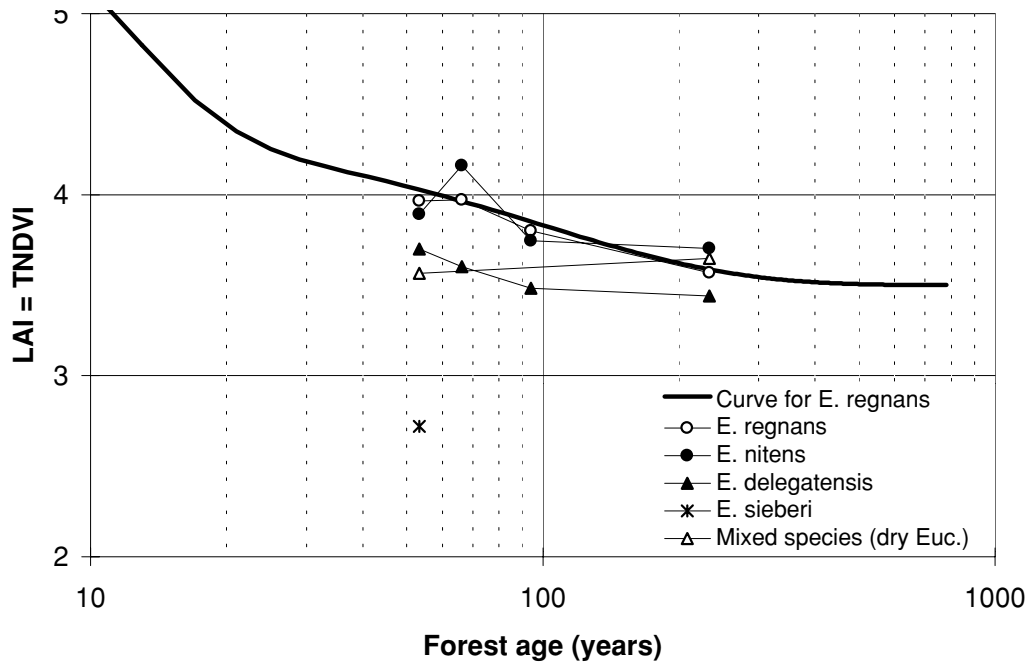
Figure 9.17: Remotely sensed total LAI of all species which were mapped in known forest-origin classes. The fitted curve for *E. regnans* is shown for reference.

to exhibit similar downward trends in LAI with age. In absolute terms *E. nitens* is similar to *E. regnans* whilst *E. delegatensis* exhibits slightly lower total LAI in keeping with its preference for higher, colder sites. As expected, the drier, 'mixed species' forest type exhibits still lower LAI, with insufficient data to reveal any age trend. Finally, *E. sieberi*, which occupies the driest sites, exhibits the lowest LAI of the eucalypt forest types.

For modelling purposes, LAI values were set as follows. *E. nitens* was treated exactly as for *E. regnans. E. delegatensis* was treated similarly but with two parameters reduced: $LAI_{tot,P} = 5.7$, and $LAI_{tot,C} = 3.2$. All other species were treated as being age invariant beyond a short initial growth period. Their climax LAI ($LAI_{tot,C}$) was set according to the areal average remotely sensed LAI for each species. An equation containing only the sigmoid term from Equation 9.11, with parameter $\tau_{tot,C}$ set as above, was used to simulate the growth from zero to climax:

$$\text{non-Ash type total } LAI = LAI_{tot,C} \left(\frac{2}{1 + e^{\left(\frac{-AGE}{\tau_{tot,C}} \right)}} - 1 \right) \qquad (9.12)$$

Equations 9.11 and 9.12 were incorporated directly into Macaque for all prediction of total LAI during model operation. Solely for the purposes of
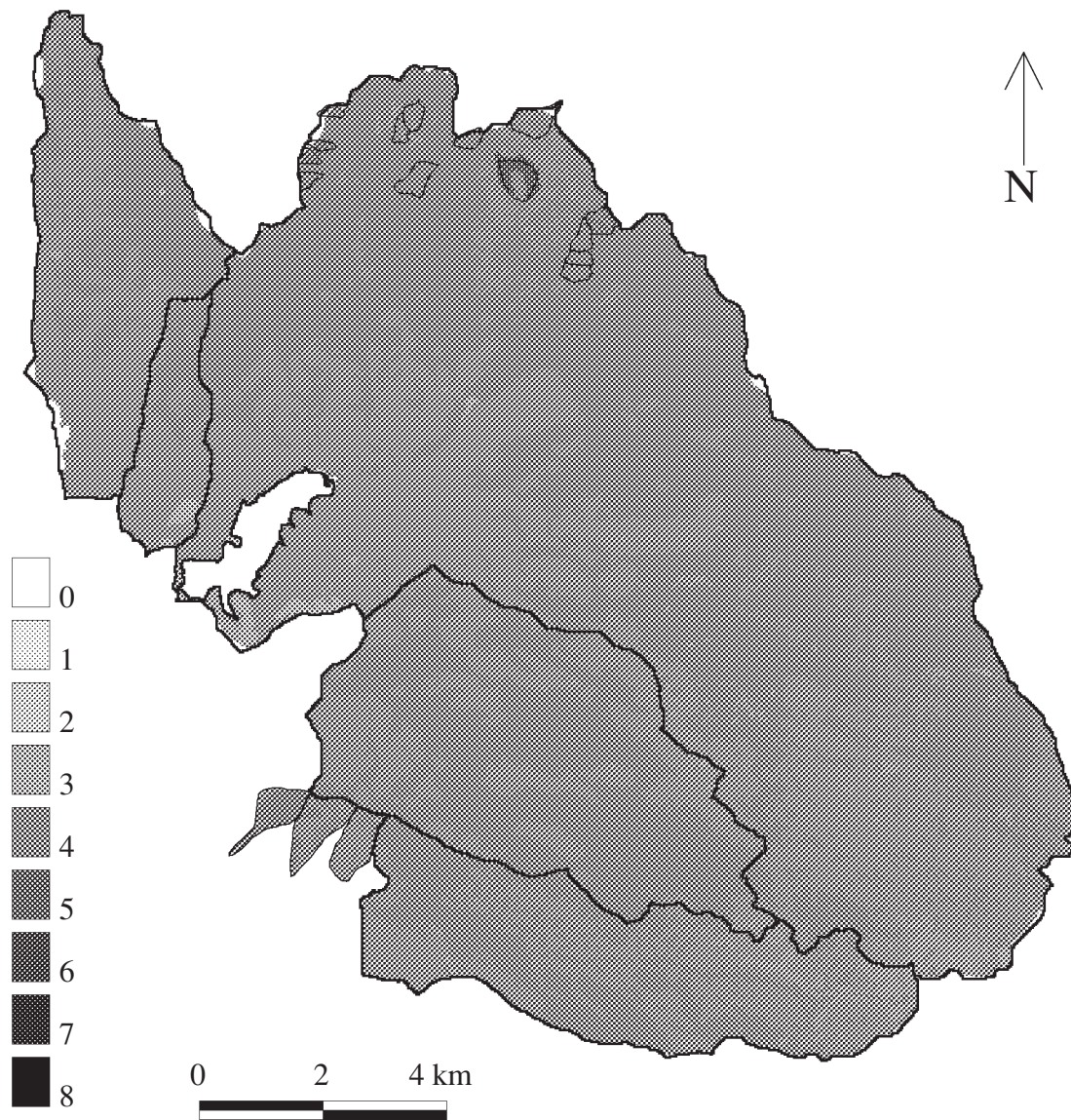
Figure 9.18: Total LAI as modelled within Macaque for 19th Jan. 1993.

comparison with Figure 9.16, these equations were used to compute a map of total LAI modelled for 1993 as shown in Figure 9.18. The two maps are similar in absolute terms and, to an extent, in spatial pattern. However, in the direct remotely sensed map, the spatial pattern predicted by Figure 9.18 is often obscured by 'random' and environmental variability.

9.6   Mapping canopy and understorey LAI

The most comprehensive information on *canopy* LAI for the study area is contained in the *E. regnans* canopy LAI versus age relationship described in

Chapter 8 and represented by Equation 8.45. There is no direct information on the canopy LAI for any other species as they occur *within the study area*. Thus, the simplest possible procedure for mapping canopy LAI was used.

The Ash-type species, *E. regnans*, *E. nitens*, and *E. delegatensis*, were treated as one. Equation 8.45 was used to predict canopy LAI for each of them.

For all other species, canopy LAI was set to be half of the total LAI estimated in Section 9.5. This choice was loosely based on the ratio between canopy and total LAI in *E. regnans* forests between about 50 and 100 years of age. For mixed species forests, the ratio is probably higher, given the barren appearance of the understorey of mixed-species forest. For rainforest, the ratio may be lower. However, at the scale of the study area, which is dominated by Ash-type forests, the choice is unlikely to be important.

Understorey LAI was mapped as the difference between total and canopy LAI.

9.7 Summary and discussion points

9.7.1 Summary

Methods for mapping the leaf area index (LAI) of eucalypt forest over large areas were addressed.

A comprehensive review was presented of the literature on LAI, including aspects of: LAI measurement and estimation, expected values and spatial and temporal patterns of LAI, and finally, remote sensing of LAI. Destructive sampling is the most accurate measurement technique, but is costly and therefore a range of alternatives exist, including: allometry, light interception analysis, remote sensing, and the use of hydrological equilibrium theory.

A survey was made of all eucalypt LAI values given in the literature (Table 9.1). Reported values range from less than one to over six, depending largely on precipitation and drought status. *E. regnans*, the dominant species in the study area, exhibits the highest values in keeping with the high rainfall, high radiation, medium temperature montane environment occupied by this species.

Spatial and temporal variations in LAI are relatively under-studied. Conifer LAI is known to respond to environmental gradients of water stress and temperature, and whilst the same is expected of eucalypts, it has only been

coarsely observed. The extent of apparently random spatial variability is unknown, but there are indications that it is significant. Drought-related temporal variations in LAI from less than one to over five at a single site have been observed for *E. maculata* which grows in slightly drier regions than the study area. Based on the lack of evidence of water-limited transpiration, drought effects are likely to be weaker for *E. regnans*.

A wide range of vegetation indices have been developed for remote sensing of vegetation, and these have been correlated with ground-based measurements of LAI in order to estimate LAI over large areas. The normalised difference vegetation index (NDVI) has proved most successful, particularly using Landsat Thematic Mapper (TM) data over the coniferous forests of the Pacific north west of North America. Work on remote sensing of eucalypts has only recently commenced, and to date, has been successful.

A number of considerations associated with remote sensing of LAI were reviewed, such as:

- limitations due to 'saturation' when sensing high LAI forests,

- the wide range of image correction procedures which permit accurate sensing,

- the effect of and measurement of temporal variations in LAI with respect to remote sensing,

- the problem of registering ground sites to image pixels and use of homogeneous sites to avoid the problem,

- and the use of remotely sensed LAI data in hydro-ecological modelling.

The present LAI sensing exercise was 'data driven', commencing with a survey of all potentially useful data for the study area. Habitat mapping of the study area conducted by DNRE for another project resulted in detailed maps of both canopy species and forest origin date. These formed the spatial basis of the LAI mapping procedure. Supplemental information was gained from a survey of historical fire dates. The large data set and functional relations for *E. regnans* canopy LAI were taken directly from Chapter 8, whilst there were no *direct* data for other canopy species. Understorey LAI data was scarce and generally had to be inferred from the difference between total and canopy LAI. Total LAI data were available mainly from a diverse data set of Li-Cor PCA (ground-based light interception analysis) measurements. Some of these data were collected as part of other studies, and some are

original data collected for the present study. A mosaic of aerial photography was constructed to facilitate better visualisation of vegetation distribution throughout the study area. Finally, four Landsat TM satellite images were obtained.

An extensive suite of image processing procedures was employed in order to convert the satellite data into a useful form. The supplied images were geocoded within the Australian Map Grid (AMG) but poorly so. A *novel* correction scheme was devised and applied which avoided image re-sampling and its associated loss of precision. Standard radiometric correction was applied to convert the data into physical radiance units (W m^{-2} sr^{-1}, sr = steradian). Atmospheric correction is more involved and, whilst likely to be useful, was not able to be applied in the time available. Digital satellite data for forests are not easily displayed or visualised so a *novel* automatic, objective contrast enhancement scheme was devised and applied to enable enhanced true-colour images to be viewed. The LAI estimation procedure which was used (see below) was conceived as a result of this effective visualisation of the imagery. Remote sensing is often avoided in mountainous areas because of the detrimental effects of topographic shading. A non-trivial (i.e. non-Lambertian) shading correction scheme from the literature was applied to the imagery resulting in images with greatly reduced topographic shading features. Finally, NDVI was calculated for each of the four images, giving four snap-shots of the vegetative status of the study area at a 25×25 metre resolution.

Total LAI was mapped using remote sensing. Two attempts based on correlation between satellite and ground-based data were made. The first was unsuccessful because the range of variation in LAI and NDVI values which was sampled was of similar magnitude to the noise in the data. No correlation was evident. If there is environmentally determined variation in LAI within the study area, it may be of similar magnitude to apparently random variation.

The second attempt focused on the major systematic source of variation in LAI within the study area, which is forest age. The true-colour and NDVI images revealed an interesting pattern of vegetative development within the numerous recent logging coupes in and around the study area. In the four images, NDVI could be observed within a wide range of different aged coupes and natural forest, decreasing to very low values immediately following clearing, then rapidly increasing to a peak at about six years of age, and subsequently and gradually decreasing from this youthful peak to a climax value for old-growth forests. A separate analysis of the total LAI data revealed a

pattern which *qualitatively* correlated with the NDVI pattern. This pattern could not immediately be *quantitatively* correlated with LAI data because the NDVI data and LAI data rarely coincided in time, but rather, were scattered across overlapping ranges from very young to very old forest.

A mathematical equation predicting LAI from age was developed as a common interpolator of the two data sets (NDVI and LAI), allowing a form of quantitative correlation. The equation was fitted to both the LAI data and the NDVI data, the latter of which were ultimately scaled to give quantitative prediction of LAI in the form of transformed NDVI (TNDVI) values.

The outcomes of this procedure were thus: a general curve predicting the total LAI of *E. regnans* forests given their age; and a non-linear scaling of satellite based NDVI enabling the spatial prediction of the LAI of eucalypt forests (assuming species generality of the NDVI/LAI relationship established for *E. regnans*).

The way that LAI estimation is encoded within Macaque requires that LAI/age relations are given for each canopy species. This required some generalisation of the results from the above analyses and those presented in the previous chapter. For *E. regnans*, the total LAI curve (above) and canopy LAI curve (previous chapter) were used directly. For other Ash type species, the same or slightly modified curves were used. For non-Ash type species: total LAI was assumed to reach a constant climax LAI value determined directly from the satellite TNDVI predictions after a brief period of growth from clearing; and canopy LAI was assumed to be a constant proportion of total LAI.

9.7.2 Discussion points

In deciduous and coniferous forests, the idea that LAI rises to a peak and then declines to an equilibrium or climax value emerged some time ago (Gholtz et al., 1976, citing Kira and Shidei, 1967, and Ovington, 1957), although in 1976 the idea of a peak still 'awaited confirmation' (Gholtz et al., 1976). Here, strong evidence has been presented now for eucalypt forests supporting a peak and decline in both total and canopy LAI. From the data presented here, it seems likely that total LAI declines to equilibrium, whilst the same may not be true for canopy LAI which may continue to be usurped by an ever burgeoning understorey beyond 250 years of age.

The mapping of LAI as described reproduces the spatial influence of forest clearing and the temporal influence of forest growth which together are the dominant source of spatio-temporal variability in LAI. There has been no

analysis of the accuracy of the subsequent predictions. Additional causes of variability are likely, including environmental controls that operate *within* the range of individual species as well as some apparently random influences. It is likely that seasonal and drought related effects are also present although there is insufficient information at present to quantify this.

Clearly there are many avenues for future improvement. Some suggestions are:

- Take more repeat Li-Cor PCA measurements to counter the high degree of scatter observed in the Li-Cor data.

- Locate Li-Cor PCA sampling sites *after* image processing so that sites can be located in homogeneous image areas and thereby minimise navigation/registration problems (see Walker et al., 1986; Wallace, 1996).

- Measure seasonal variations in LAI using the Li-Cor PCA.

- Consider using allometric measurements of LAI for ground data instead of Li-Cor PCA measurements. Li-Cor measurements are highly variable and difficult to take beneath sunny skies. A large data base of DBH measurements already exists for the study area and surrounding regions as part of Melbourne Water's continuous forest inventory (CFI) programme.

- Incorporate atmospheric correction of the remotely sensed imagery. In particular, this should reduce the inter-annual scatter observed between the four images (unless of course the scatter is associated with drought) (see Peterson et al., 1987; Paltridge and Mitchell, 1990).

- Investigate climax LAI estimation through hydrological equilibrium theory. Given that the climatic and topographic variables upon which climax LAI should depend are the easiest to map spatially, this is potentially accurate, and will offer a new perspective on the problem.

- Implement a one-stage re-sampling of raw (not geocoded, as used above) satellite imagery to the Australian Map Grid using a DEM to compensate for topographic shifts. This will improve the accuracy of spatially aligning satellite data with forest type data and mapped ESUs. In the above analysis alignment errors in the order of 100 metres may be present.

- Extract more information from the spectra of the satellite imagery by overlaying sample sites and LAI values upon band-against-band scatter plots as done by McCloy and Hall (1991) and Walker et al. (1986).

- Commission very-low-level aerial photography to better understand what reflections comprise each pixel 'seen' by a satellite.

- Obtain satellite imagery from more years, and more dates within each year.

Part IV

Model testing and application

Chapter 10

Model testing

Contents

10.1   Introduction

As discussed in Chapter 3, physically based hydrological modelling studies draw frequent criticism for their lack of attention to internal model testing and the resulting uncertainty in model predictions. This chapter attempts to redress the imbalance between model sophistication and model validation. Section 10.2 tests a number of key internal variables against measurements of the same. Following this, Section 10.4 informally examines the sensitivity of key parameters as an indication of appropriate model response to lumped, physical expressions of catchment conditions. Finally, Section 10.5 examines the spatial sensitivity of the model by examining both lumped and spatial responses of streamflow to changes in strategies for mapping key spatial parameters (precipitation, LAI, and topography).

10.2   Testing of model components

Beven (1996b) noted that there are very few hydrological data sets in the world 'with adequate internal state measurements', and goes on to list some contenders. The present study area could be added to the list, offering a

wide variety of already measured data. It provides an excellent opportunity to explore possibilities for internal testing in some detail. Therefore, this section deals with the testing of all internal and external predictions made by Macaque (where 'external' is considered to mean streamflow, 'internal' is everything else). It is organised into sub-sections which, for ease of reference, closely match the structure of the model description in Chapter 4 and the parameter description in Chapter 5.

As a starting point, the model was parameterised and calibrated to the point where it was operating in a generally realistic manner, determined using the following criteria:

- predicted and observed hydrographs matched *approximately* at daily, weekly, monthly, and yearly scales,

- all stream areas marked on a topographical map produced runoff, and runoff was not normally produced from areas not marked as streams,

- the runoff producing areas expanded in winter,

- the upslope and midslope areas of hillslopes did not produce runoff except in the highest rainfall areas,

- upslope water tables remained 10 metres or deeper below the soil surface (observed augering and seismic survey data from the present study in conjunction with Campbell, in prep.),

- near stream water tables remained within a few metres of the soil surface and varied by about one metre annually (observed piezometer data from Campbell, in prep.),

- relative proportions of stormflow and baseflow matched those reflected in the observed hydrograph,

- canopy and understorey transpiration matched observed ranges (observed heat pulse data from O'Sullivan, in prep., and J. Buckmaster, unpublished data, CRCCH),

- canopy conductance remained near observed ranges (observed data from Connor et al., 1977),

- interception of precipitation matched observed totals and temporal patterns (observed data available from numerous studies),

- climatic variables such as precipitation, VPD, and net radiation remained within locally observed ranges and displayed expected spatial patterns throughout the study area (numerous observed data available).

From this starting point, a series of quantitative tests of predictions against observations of internal model data are presented below. Two types of test were used: *independent* tests isolated specific processes and tested them using measured data for input; and *integrated* tests evaluated processes as part of the overall model, using predicted data from some simulated driving process as input instead of measured data. Independent tests were performed for much of the early micro-climate modelling. Integrated tests were used for later processes in the order of simulation where reliable observed input data were not always available.

The test results are intended to emphasise the types of errors that are generated by the model. *At this level of detail* R-squareds or any other form of exact numeric quantification of error are of limited use, because they only apply to particular periods of test data, at particular test data locations. For example if an error value was given for VPD at Lower Coranderrk in Winter, the reader might be tempted to assume that similar error applies to VPD estimates at Mt Donna Buang in summer - which due to differences in radiation, precipitation, ET, and seasonal lapse rates, is most likely not the case. Data are available to test the *character* of errors in model components, and not for detailed statistical quantification.

10.2.1   Topography

Apart from the (trivial) de-convolution of aspect from its mean sine and cosine, there are no internal topographic predictions made by Macaque.

10.2.2   Vegetation

Internal calculations regarding vegetation include age and LAI calculations. From the point of view of internal testing, these are simply applications of equations developed in Chapters 8 and 9. Their validity and accuracy was discussed in those chapters.

10.2.3   Temperature

Testable temperature predictions include: maximum and minimum temperatures as predicted by lapse rate; and conversions of these into 24-hour mean, mean daytime, mean night-time, and soil temperatures. Maximum and minimum temperature prediction were tested first, followed by daytime mean temperature prediction. Soil temperature, 24-hour mean, and night-time mean temperature are used in less critical calculations relating to snowfall, snowmelt, and cold-temperature leaf water potential and were not tested.

The tests shown relate only to the correct estimation of *temporal* variation in temperature from day to day and within days. They are not independent tests of mean annual estimated temperatures because the test data were used in the initial parameterisation of temperature/elevation lapse rates (Section 5.3.4). Too few data were available to withhold data from use in parameterisation for use in independent testing of lapse rates.

10.2.3.1   Maximum and minimum temperature

Figure 10.1 shows predicted versus observed temperature for Blacks' Spur meteorological station from a model run using the Melbourne Regional Office meteorological station as the temperature base station. The scatter about the line is due to both: the mean variation of this station from the regional lapse rate trend ($c.$ $2°$ C), the seasonal variation in lapse rate which is not accounted for in the model ($c.$ $3°$ C, see Section 5.3.4), and daily variation from these mean spatio-temporal trends.

Another perspective may be gained from Figures 10.2 and 10.3 which show daily predicted maxima and minima plotted alongside hourly observed temperature for February and August. For February, maximum temperatures were reasonably well predicted whilst predicted minima were generally too low by up to a few degrees. For August, minima were well predicted whilst maxima were often over-predicted by more than $5°$ C. This is probably due to seasonality in observed lapse rates which are not taken into account within Macaque (see Section 5.3.4).

10.2.3.2   Daytime mean temperature

As noted in Section 4.3.4, daytime mean temperature was estimated from maximum and minimum temperature using a simple sinusoidal assumption from the literature. 'Observed' data were calculated using hourly data from
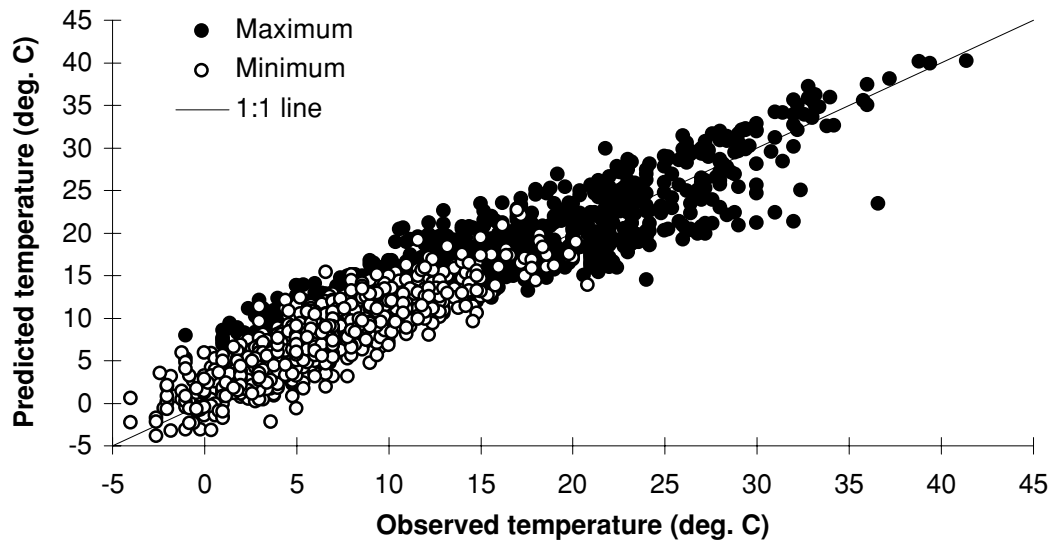
Figure 10.1: Testing the modelling of temperature/elevation lapse rates: predicted versus observed maximum and minimum temperatures from 1982-1984 at Blacks' Spur meteorological station(F1820) (*c.* 55 km separation from base station in Melbourne, F2540).
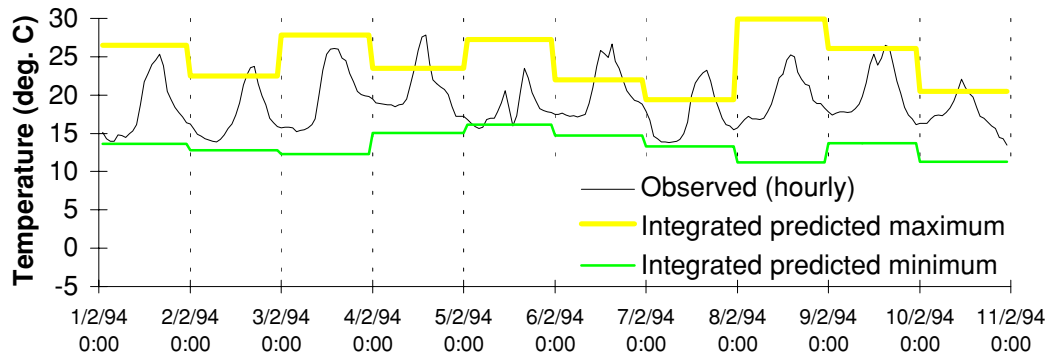
Figure 10.2: Integrated testing of temperature modelling for 10 February days at Upper Coranderrk (F0440): hourly observed data versus daily predicted temperatures using Melbourne Regional Office (F2540) as a base station.
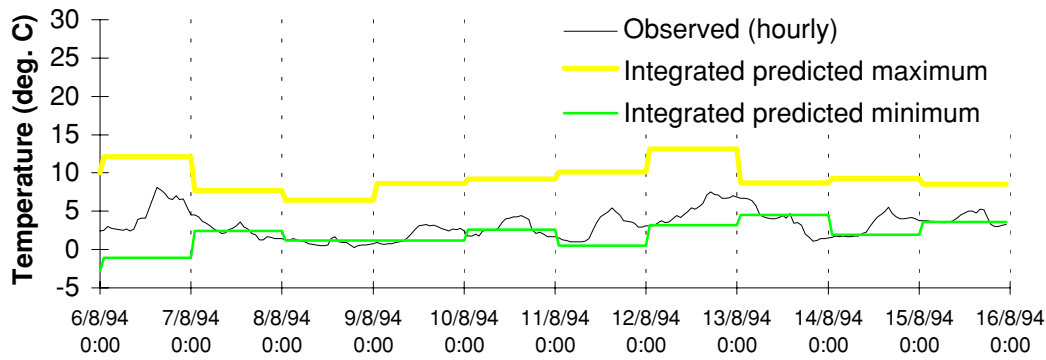
Figure 10.3: As for Figure 10.2 but in August.
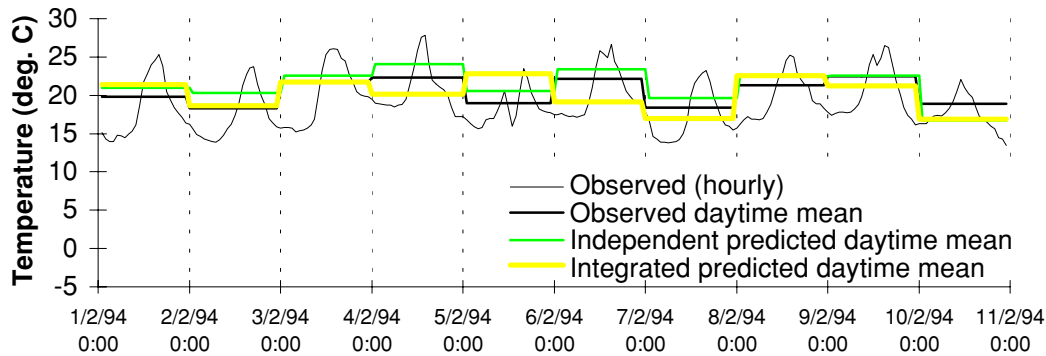
Figure 10.4: Independent testing of daytime mean temperature modelling for 10 February days at Upper Coranderrk.

Upper Coranderrk averaged over daytime periods determined from sunrise and sunset time estimates produced by Macaque. These data were used to test both independent (using Upper Coranderrk maximum and minimum temperature) and integrated (using modelled maximum and minimum temperature) predictions of daytime mean temperature.

The test results for February and August are shown in Figures 10.4 and 10.5. For February, the independent predictions were too high. This is because the hourly observed data did *not* follow the assumed sinusoidal pattern, but rather, were quite peaky with a low mean relative to daily maxima. Curiously, the integrated predictions were more accurate, presumably because over-estimation due to the spiky time signal was balanced by underestimation of minimum temperatures (Section 10.2.3.1). For August, the spikiness was greatly reduced and hence the independent predictions were quite accurate. The integrated predictions were a few degrees too high due to the over-estimated maximum temperatures (Section 10.2.3.1).
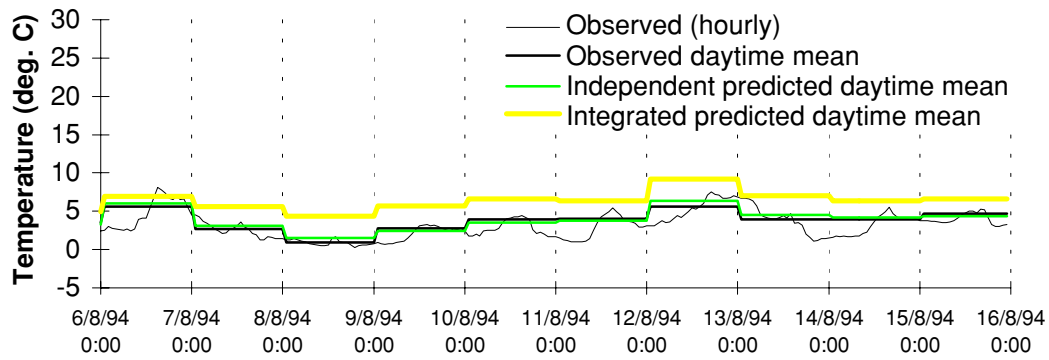
Figure 10.5: As for Figure 10.4 but in August.

10.2.4 Humidity

10.2.4.1 Dewpoint

Humidity calculation started with the calculation of dewpoint temperature from minimum temperature, which is tested first.

It was asserted in Section 4.3.5 that dewpoint remains relatively constant throughout the day, as evidenced by graphical data from Sydney showing variations on the order of only a few degrees (Linacre and Hobbs, 1977, Fig. 6.5). Figures 10.6 and 10.7 test this assertion, and the use of minimum temperature as a proxy for dewpoint. The figures show hourly observations of dewpoint at Upper Coranderrk calculated from wet and dry bulb data using a simple equation from Linacre (1992, Equation 2.4); and both independent and integrated daily predictions of dewpoint from Upper Coranderrk minimum temperature and modelled minimum temperature respectively. The February plot shows daily variations in observed dewpoint of up to seven degrees, which invalidates the assumption of constancy. It is likely that the high evapotranspiration environment in which these February observations were made induces larger daily variations in air moisture content (and hence dewpoint) than occur at stations used in the conventional literature. Independent predictions usually fell within the daily observed range but were a few degrees too low on average. The integrated predictions were consistently low, probably also because of high daytime ET, but mainly because of under-estimated minimum temperature (Section 10.2.3.2). In August, intra-day dewpoint variations were much lower and so did not lead to under-estimation in either independent or integrated predictions. Unlike February, integrated minimum temperature was accurately predicted for August (Section 10.2.3.1), which also contributed to the accurate integrated predictions
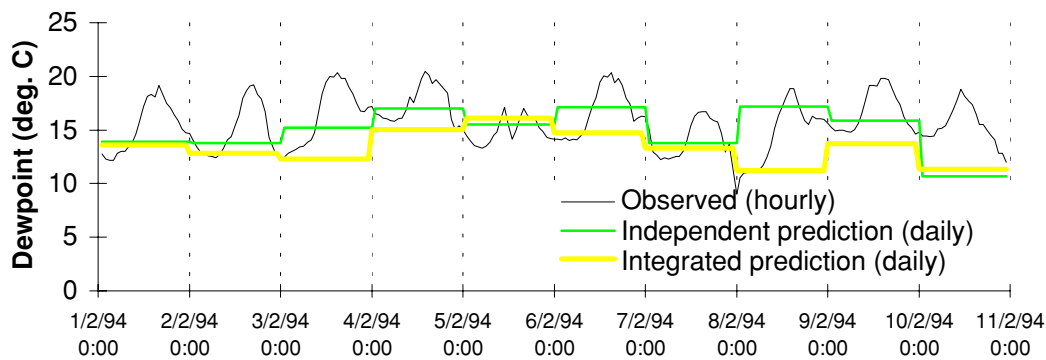
Figure 10.6: Independent testing of dewpoint modelling for 10 February days at Upper Coranderrk: hourly observed data (derived from F0420 and F0440) versus daily predicted dewpoint (derived from F0440).
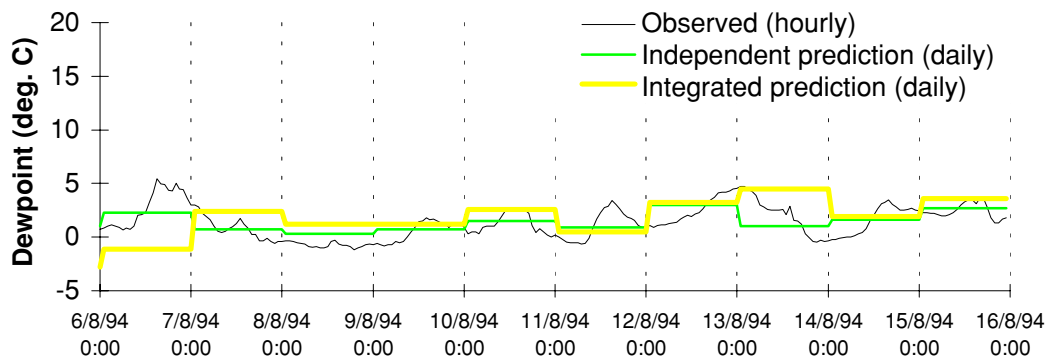
Figure 10.7: As for Figure 10.6 but in August.

of dewpoint shown in Figure 10.7.

10.2.4.2 Vapor pressure deficit

Hourly observed VPD data were derived for Upper Coranderrk from wet and dry bulb data using the Clausius-Clapeyron equation (see Section 4.3.5) to calculate SVP; and Regnault's equation (Linacre, 1992, Eqn 2.3; Smith, 1990, Eqn 15) with an aspiration constant of 0.0008 $°C^{-1}$ to calculate VP. Vapor pressure deficit was then calculated as the difference of the two.

Daytime mean observed VPD were calculated using the same sunrise and sunset time predictions as used in the calculation of observed daytime mean temperature (Section 10.2.3.2).

Daily independent VPD predictions were derived using two instances of the Clausius-Clapeyron equation. The first estimated mean daytime SVP us-
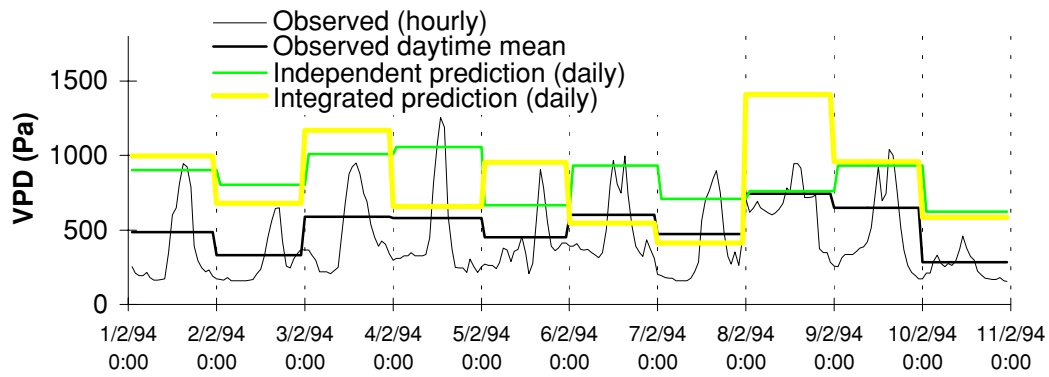
Figure 10.8: Independent and integrated testing of VPD modelling for 10 February days at Upper Coranderrk: both hourly and daily observed data (derived from F0420 and F0440) versus daily predicted dewpoint (using F0440 for independent predictions and F2540 for integrated predictions).

ing, as input, mean daytime temperature calculated from maximum and minimum temperature assuming a sinusoidal temperature oscillation. The second estimated VP from dewpoint using minimum temperature as an estimate of dewpoint. Thus the independent predictions tested a combination of model components, with maximum and minimum temperature at Upper Coranderrk as input. The integrated predictions did the same, but also included the modelling of maximum and minimum temperature using lapse rates.

Figures 10.8 and 10.9 show daily independent and integrated predictions of *mean daytime* VPD versus both hourly and mean daytime observed data for February and August. In February, both independent and integrated predictions were too high, often doubling the observed daytime mean. This is explained by the errors described in the previous sections. In particular, under-estimated dewpoint (noted for both independent and integrated predictions) and over-estimated mean daytime temperature (noted for independent predictions only) both contributed to over-estimated VPD. In August, the independent predictions were accurate, which is due to accurate independent predictions noted for all contributing variables in August. However, the integrated predictions for August were over-estimated as for February. This is due to the over-estimated daytime mean temperature.

Note that no testing was undertaken of the reduction of VPD down through respective vegetation layers due to ET. It would be practical however, in a detailed field campaign, to collect sufficient data to enable testing of these processes.
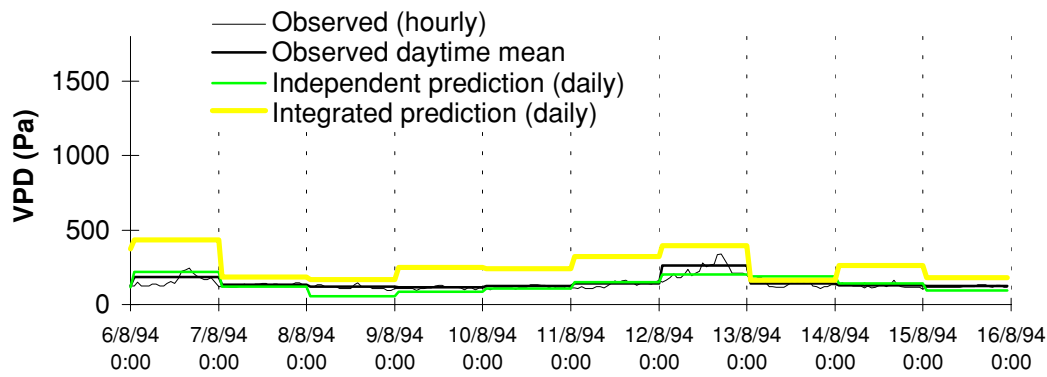
Figure 10.9: As for Figure 10.8 but in August.

10.2.4.3   Interim discussion

Should we proceed with poor estimations of a key model variable such as
VPD? The temperature and humidity components of Macaque could be re-
fined by both including a sinusoidal seasonal lapse rate for maximum temper-
atures, and estimating dewpoint not from minimum temperature but from
some value a degree or two higher than this. This additional complexity
would involve a few more parameters and introduce yet more detail for which
there is minimal testing data with respect to the range of climate in the
study area. The sense of the present work is to get *some* form of whole
catchment simulation operating and not to perfect every sub-component of
the model. The limitations of the temperature and humidity models are suf-
ficiently slight at this stage that they do not detract greatly from the aim to
determine 'whether realistic simulation is possible'. Hence, it is decided to
proceed un-deterred and attempt to draw benefit by observing the influence
of poor VPD estimates on subsequent model processes.

10.2.5   Radiation

10.2.5.1   Total daily solar radiation incident above the canopy

Observed solar radiation data were available from three sites: Upper Coran-
derrk (F0430), Murrindindi (F1510), and Tarrawarra (F1064); whilst net
radiation data were only available from Tarrawarra (F1065).

The Upper Coranderrk data were used to calibrate the 'transmission versus
temperature range' model (Section 5.3.7.1) and are used here for independent
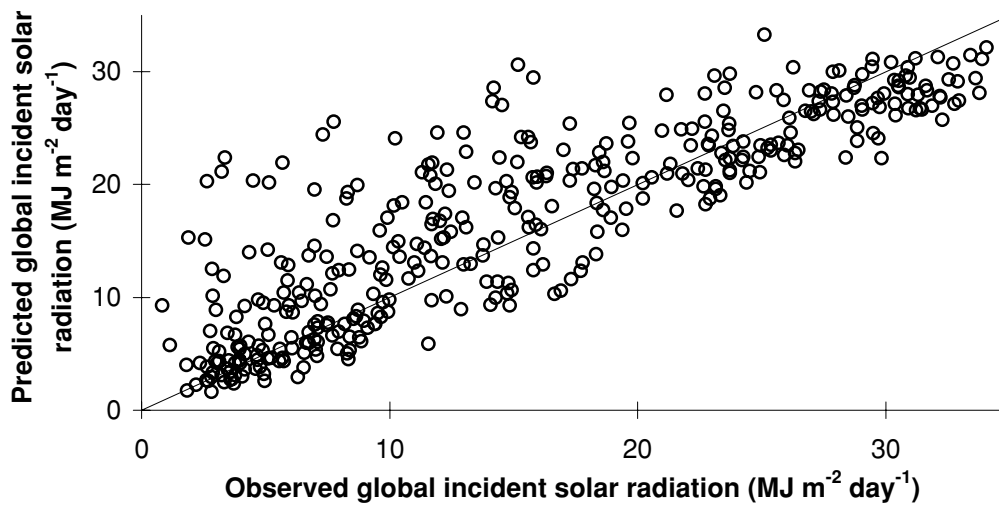
Figure 10.10: Independent testing of global solar radiation modelling: observed daily data for Upper Coranderrk (F0430) versus daily predictions made using temperature data and calibration data for Upper Coranderrk (F0440). A 1:1 line is shown.

testing of global incident solar radiation predictions. Figure 10.10 shows a scatter plot of (independently) predicted and observed global incident solar radiation. Considering that the estimates were based solely on temperature range and time of year, the predictions are surprisingly accurate. However over-estimation by factors of about five was occasionally observed.

For testing of integrated predictions, the Murrindindi data set was used. Thus, in Figure 10.11, full Macaque predictions made using Melbourne Regional Office temperature data are plotted against observed data. The integrated predictions appeared valid, although there was more scatter than was observed for independent prediction. Whilst much of the data clustered about the 1:1 line, there were numerous instances of gross over and under-prediction of solar radiation. Over-prediction was more common, most likely due to over prediction of temperature range which implied less cloudy conditions than reality (Section 10.2.3.1).

The temporal signal of the integrated predictions was examined and is shown in Figure 10.12. Both extra-terrestrial and clear-sky[1] predicted radiation are plotted in addition to the predicted and observed canopy-incident values. The fact that the observed values sat just below the clear-sky predictions provided reassurance of the accuracy of the fundamental calculations of solar

---

[1]Clear-sky values were calculated using Dingman (1994, App. E) with: dewpoint estimated from minimum temperature; mean daily optical air mass estimated by fitting a function to Dingman's Fig. E-4 at the appropriate latitude; albedo, slope, and azimuth set to zero; and the attenuation due to dust set to 0.1.
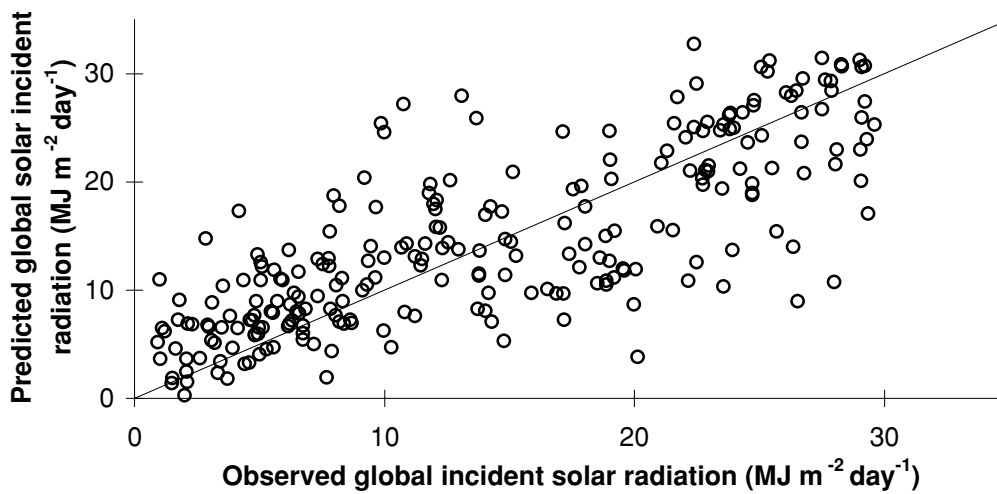
Figure 10.11: Integrated testing of global solar radiation modelling: observed daily data for Murrindindi (F1510) versus daily predictions made using temperature data from Melbourne Regional Office (F2540) and calibration data from Upper Coranderrk. A 1:1 line is shown.

and atmospheric physics. The predicted canopy-incident values generally followed the temporal pattern of the observed values but deviations were common.

10.2.5.2 Net radiation

As noted in Section 5.3.7.3, net radiation data were only available from the lowland pasture field site at Tarrawarra. The data were used to regress net radiation against solar radiation to parameterise the relation within Macaque which predicts one from the other. In this section, the data are again used to evaluate both independent and integrated predictions of net radiation using the relation.

The previous section showed that, using temperature data from Upper Coranderrk, independent predictions of solar radiation could be made for Upper Coranderrk, and integrated predictions of solar radiation could be made for Murrindindi. At the rural Tarrawarra site, independent predictions of global *solar* radiation (not shown) were of similar accuracy to those for Upper Coranderrk (Figure 10.10). However, considerable additional scatter was introduced when integrated predictions were made (not shown), using Macaque driven by temperature data from the Melbourne Regional Office. This may be due to differences between lowland pastoral and mountainous forested sites in the processes which control temperature range and link temperature
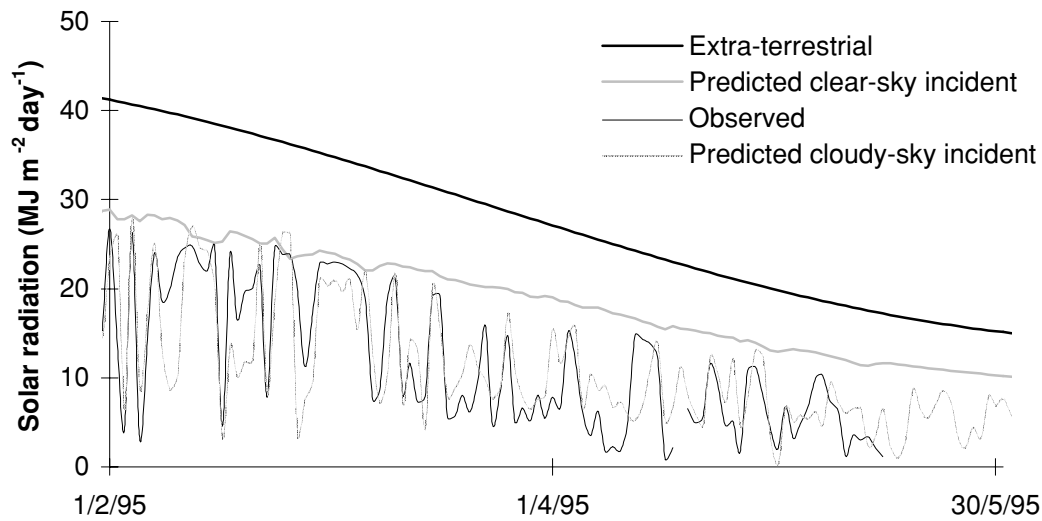
Figure 10.12: As for Figure 10.11 but in time-series form, and with extra-terrestrial and clear-sky values included for comparison.

range to atmospheric transmission of radiation (although note that net radiation is not thought to differ greatly between grassland and eucalypt forest sites, pers. comm., F. Dunin, CSIRO Plant Industry, Perth). As shown in Figure 10.13, the scatter in integrated *solar* radiation predictions propagates to the integrated *net* radiation predictions. The figure shows that independent predictions are accurate in both mean and temporal respects whilst the integrated predictions often are often too high or too low. The high predictions in the winter months are most likely due to over-estimated temperature range in these times (Section 10.2.3.1). In general, considering the remote source data and simple representation of processes, the integrated predictions of net radiation appear adequate.

Note that the propagation of radiation down through the vegetation layers was not tested. As with VPD reduction (above), this should be evaluated by a detailed field campaign.

10.2.6 Daylength

Macaque calculates daylength as an offshoot to an involved sequence of radiation equations incorporating times of sunrise and sunset on sloping surfaces (Sections 4.3.6.1 and 4.3.7). A check on this calculation can be made using a general equation for daylength on horizontal surfaces. Linacre (1992, pp. 148-150) gives perhaps the most direct of these equations:
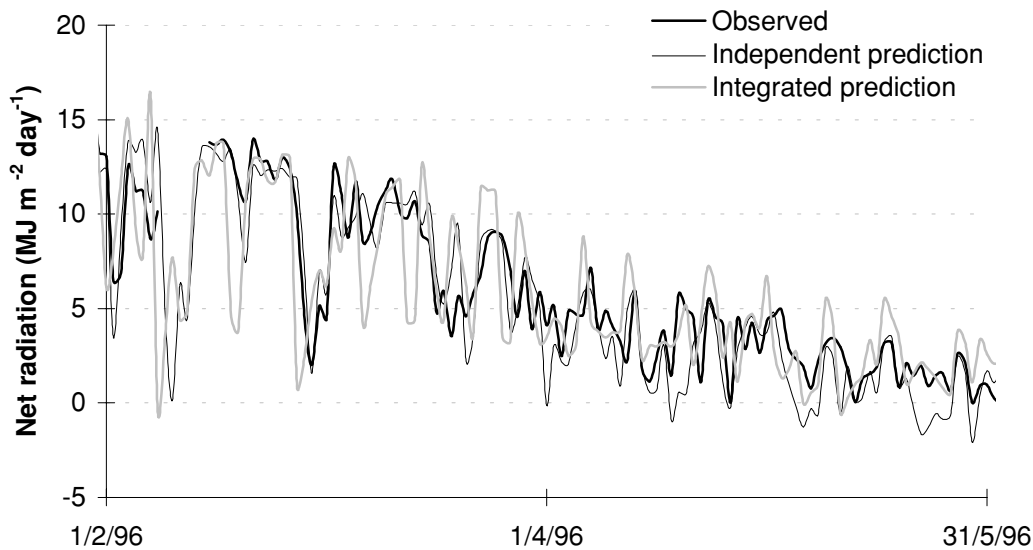
Figure 10.13: Time series of predicted and observed net radiation at the Tarrawarra field site. The independent predictions used local temperature data, and the integrated predictions were made by Macaque using temperature data from Melbourne Regional Office.

daylength check

$$= \frac{3600}{7.5} \arccos\left\{ -\tan lat \times \tan\left[23.45 \sin\left(360 \frac{t_{day} - 80}{365}\right)\right] \right\} \quad (10.1)$$

Here, 3600 (s hour^{-1}) is the number of seconds an hour, the second tan term is the solar declination, 23.45 (°) is the maximum solar declination, 360 (°) is the number of degrees in a circle, 80 is the year-day of March 21st, the equinox in a non-leap-year, 365 (days) is the number of days in a non-leap-year, and 7.5 (°) is half the number of degrees the sun moves in an hour. The equation does note take account of leap years, but this is of little consequence.

Daylength predictions using Linacre's equation and using Macaque were compared for Upper Coranderrk, a site sloping 17° almost due south (207° east of north). As expected, the values were equal at the start and end of the year in the height of summer when the sun rises south of due east and sets south of due west and its beam is uninterrupted by close terrain. In winter however, the sun rises and sets more northward and the high terrain immediately north of Upper Coranderrk causes that site to experience shorter days than horizontal sites. Thus, these simple comparisons indicate that daylength is correctly predicted by the model.
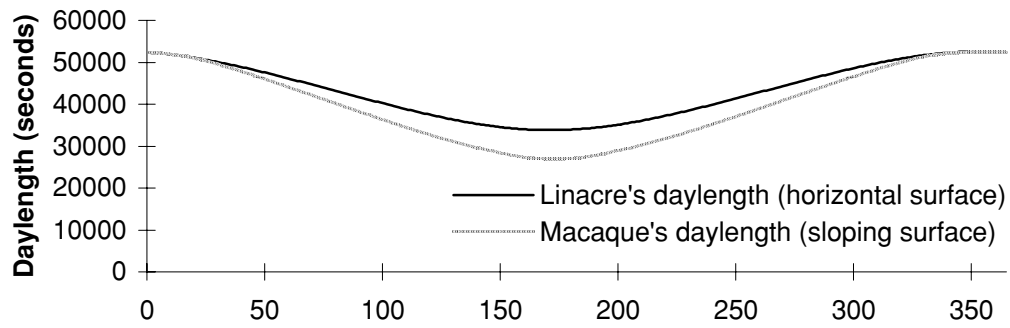
Figure 10.14: Comparison (and hence cross-validation) of two methods of estimating daylength. Macaque takes account of the sloping surface and hence its predictions *should* be lower in winter, as is shown.

10.2.7   Precipitation

Successful daily precipitation estimation requires two things: that bulk or long term estimates are accurate; and that the daily temporal pattern is accurate. The former of these was discussed in Chapter 7 and the latter is briefly addressed here.

The Murrindindi meteorological station provided one of the few daily precipitation records (F1487) in or near the study area which was not used in the initial mapping of MMPI. Precipitation for the site was predicted by Macaque using Maroondah Dam (F0710) as a precipitation base station. Warburton Post Office, F1195, was unsuitable due to excessive missing data in the relevant period. Time series and scatter plots of predicted and observed daily precipitation are shown in Figures 10.15 and 10.16 respectively. The scatter plot indicates that the predictions were often accurate but that large errors were possible. The mean prediction was 26% lower than the mean observation, although this value should be interpreted with caution given that only 246 daily observations were available. Despite the long term error, the time series plot revealed a close correspondence in the temporal pattern of precipitation between Murrindindi and Maroondah Dam. These data serve to warn that long term errors in predicted precipitation can be large. The overall ability of the model to predict water balance will be limited accordingly. Greater emphasis should be placed in future on quantifying and rectifying both long term and temporal errors in precipitation.

It should be noted that Kuczera (1985) deduced from double-mass plots that the Maroondah Dam precipitation gauge (F0700) used as the base station for MMPI calculation had an inconsistency from 1964 onwards. This will lead to an error in MMPI values calculated for stations with significant periods
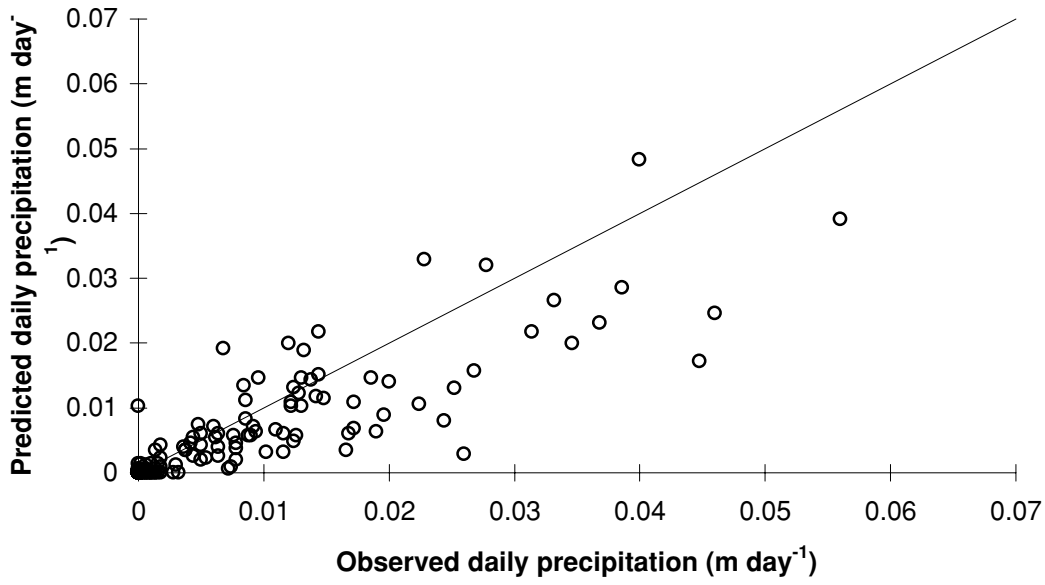
Figure 10.15: Predicted versus observed daily precipitation at Murrindindi (F1487): predictions made by Macaque using Maroondah Dam (F0710) as the precipitation base station (5.5 km separation between stations). A 1:1 line is shown.
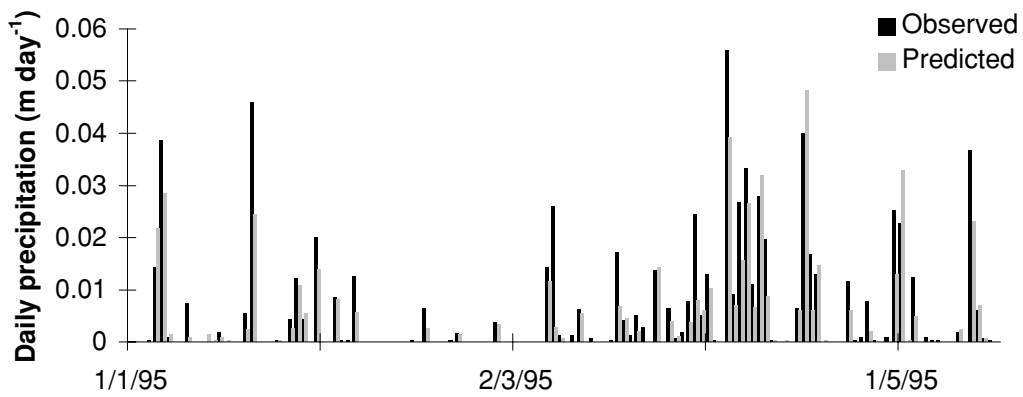
Figure 10.16: Time series of a portion of the data from Figure 10.15.

of record post-1963 (i.e. all of the records from the North Maroondah and Coranderrk experimental areas). In hindsight, this error should have been corrected prior to calculation of MMPI values.

10.2.8 Rainfall, snowfall, and interception

Snowfall and snowmelt processes are less important in the present study than other processes. Hence, their representation within Macaque has not been tested. This section therefore deals only with testing the modelling of rainfall interception by vegetation.

Daily (and sub-daily) throughfall trough data were available from the CR-CCH installations within the Picaninny and Myrtle catchments. Owing to monitoring problems, neither data set was ideal for studying continuous time series of interception. The Myrtle data set, from 8 to 10 year old *E. regnans* forest, was the better of the two and is used here.

Figure 10.17 plots both (integrated) predicted and observed daily throughfall versus precipitation. The 'observed' data points are plotted against precipitation measurements from a 203 mm tipping bucket rain gauge in a clearing about 100 m from the throughfall troughs (F1980). The 'predicted' data are plotted against precipitation predictions from Macaque using Warburton Post Office (F1195) as the precipitation base station and Melbourne Regional Office (F2540) as the temperature base station. In both cases, stemflow was allowed for and was assumed to be 6% of precipitation, as observed by Langford and O'Shaughnessy (1978, Tab. 14).

As expected, the observed data generally fall just beneath the 1:1 line, but there are some obvious erroneous measurements near zero for large precipitation events. The predicted values follow the general pattern of the observed values but do not necessarily match-up on a day to day basis. This is partly because of discrepancies in the predicted and observed precipitation for the site, but mostly due to limitations of the model. In particular, it is likely that the scaling problems due to modelling at daily time step (discussed in Section 5.3.9) prevent the model from accurately predicting throughfall for both low and high precipitation events. Sub-daily modelling would be required to match the very high levels of interception recorded for large precipitation events. If instead larger interception storage was specified, predicted interception would be too high for small events. In general, the data suggest that the interception component of Macaque is working as well as can be expected for a daily model.
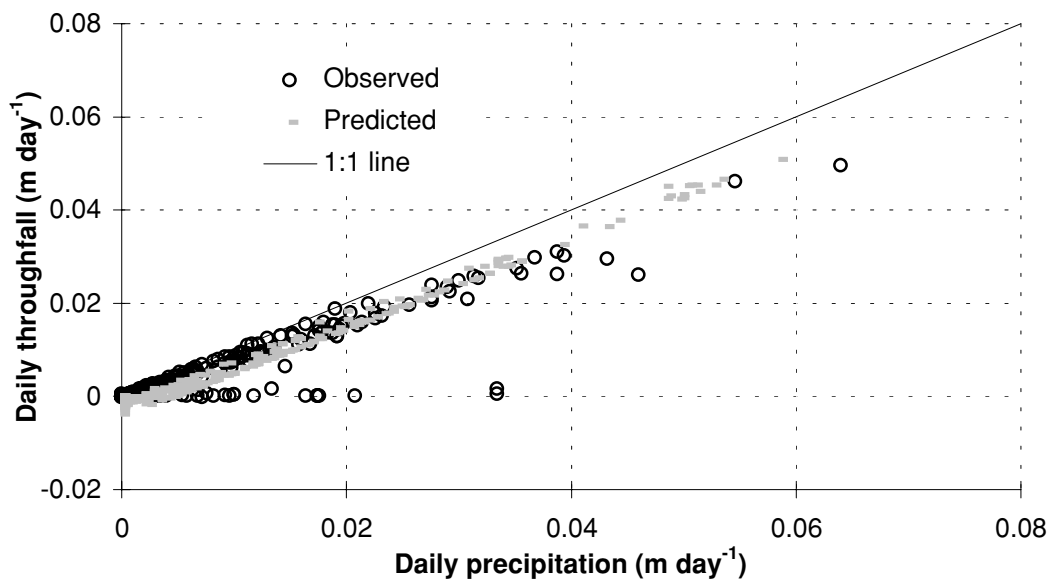
Figure 10.17: Integrated testing of interception modelling at Myrtle 2: predicted versus observed throughfall.

Note that predicted throughfall is occasionally negative for zero precipitation because of evaporation of stored intercepted water on dry days following precipitation.

Total precipitation and interception was accumulated over the first six months of 1994, where there were no missing data. The predicted precipitation in this period (729 mm) was 19% higher than the observed precipitation (612 mm). Predicted interception was 28% of predicted precipitation and observed interception was 6% lower at 22% of observed precipitation. This is an acceptable error given that it is an independent test of the model which was calibrated against a bulk interception ratio from the Coranderrk group pertaining to forest some twenty years younger (see Section 5.3.9).

Note also that separate testing of interception of precipitation by the canopy and understorey was not undertaken. Logistically, this would be very difficult.

10.2.9 Snowpack accumulation and melting

As noted above, the snow related components of Macaque have not been tested. There is scope for future validation of snow-cover predictions in the study area using snow gauge data at Mt Donna Buang (Ruddell et al., 1990) and possibly also remote sensing (Rango, 1985; Roberts, 1993; Engman,

1995).

10.2.10 Evapotranspiration

Using heat pulse sensors, O'Sullivan (in prep.) measured transpiration in a
number of different aged stands of *E. regnans* within the study area over an
18 month period during 1994 and 1995. Some of the data were made available
for the present study. Specifically, intermittent individual tree water use data
for 13 trees in the Ettercon 3 experimental catchment were acquired for the
second half of 1994. One of the trees was a reference tree for which there was
a nearly complete record. The other trees were gauged for short periods. Six
trees had data which overlapped the data for the reference tree.

The data from each of the six overlapping trees were regressed using zero-
intercept linear regression against the reference tree, resulting in a scaling
factor relative to the reference tree for each of the six trees. The scaling
factors were regressed against DBH, and the resulting equation was applied
to the DBH of every tree in a plot of known area to yield an estimated
scaling factor for every tree. These were summed giving a scaling factor for
estimating the daily water use of the entire plot from that of the reference
tree. After dividing by the plot area, the data became 'observed' daily canopy
transpiration values. The method is equivalent to, but slightly more efficient
than that of Vertessy et al. (1997). Note that some gaps in the final daily
time series were supplemented by estimations of reference tree water use
made by O'Sullivan (in prep.) using data from other parts of the study area.

Figure 10.18 shows the observed data along with Macaque predictions cor-
responding to the same location as the observed data (i.e. the ESU from
the Ettercon 3 experimental catchment within which O'Sullivan's plot falls).
Temperature input was derived from Melbourne Regional Office (F2540) and
precipitation input was derived from Warburton Post Office (F1195). Whilst
the winter predictions are of similar magnitude to the observed data, the
summer predictions are nearly three times higher than observed. This dis-
crepancy may be partly due to limitations of the model, but also to problems
with the observed data. This is explained as follows. Vertessy et al. (1997)
made observed daily stand water use for the same species at the same age
at Blacks' Spur. Their Figure 7 shows minimum, mean, and maximum daily
water use (in late spring) of *c.* 0.001, *c.* 0.002, and *c.* 0.004 m day^{-1} respec-
tively. There is thus a factor of two difference between Vertessy et al's and
O'Sullivan's observations. Additionally, as illustrated later in this chapter,
streamflow predictions are accurate for Ettercon 3 but become significantly
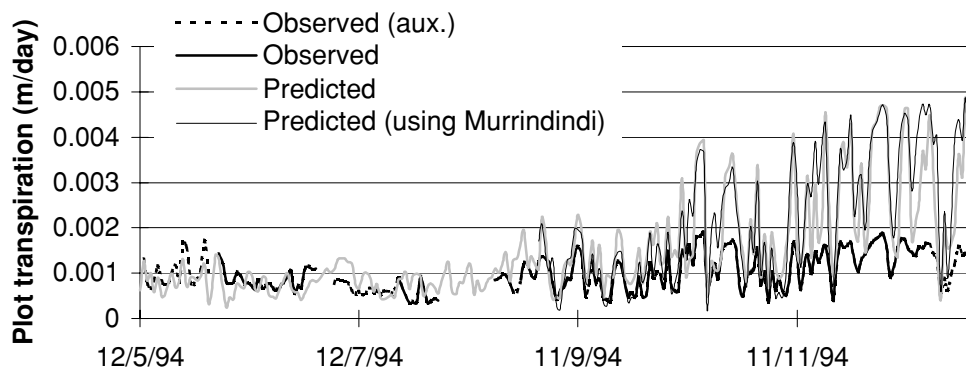
Figure 10.18: Integrated testing of canopy transpiration modelling at Ettercon 3: predictions and observations of stand water use. 'Auxiliary' observations are those supplemented by data from other parts of the study area (see text).

over-estimated if the predicted transpiration is scaled to match the observed data of Figure 10.18. On the other hand, weighing in favour of O'Sullivan's observations is the fact that VPD is known to be over-predicted (see Section 10.2.4) which would lead to over-prediction of transpiration. However, when VPD is reduced, either seasonally or uniformly, by up to a factor of three, the reduction in transpiration is insufficient to match the observed data (analysis not shown). Because of the over-prediction of VPD, it is likely that transpiration was over-predicted to some degree. But it is also likely that most of the discrepancy in Figure 10.18 is due to inaccurate observed data.

Some additional information was gained by using the Murrindindi meteorological station for both temperature and precipitation input. Murrindindi is only a few kilometres from Ettercon 3, at a similar elevation. As shown in Figure 10.18, predictions made using these data (from 31/8/94 only) did not differ significantly from the original predictions. This indicates that errors due to inaccurate daily maximum and minimum temperature prediction do not affect the conclusions of the previous paragraph.

Finally, some encouragement is gained when a detail is taken from Figure 10.18 as in Figure 10.19 where only two months of predictions and observations are plotted. Clearly, despite the mean discrepancies, the temporal patterns of the predicted and observed data are very similar. This suggests that, whilst there may be uncertainty regarding the overall balance, the modelling of canopy transpiration is being driven by the appropriate time-varying inputs, namely: net radiation available after evaporation of intercepted water, reference level VPD, and canopy conductance.

In the future, there may be scope for *spatial* validation of transpiration predictions using remote sensing of surface temperature following, for exam-
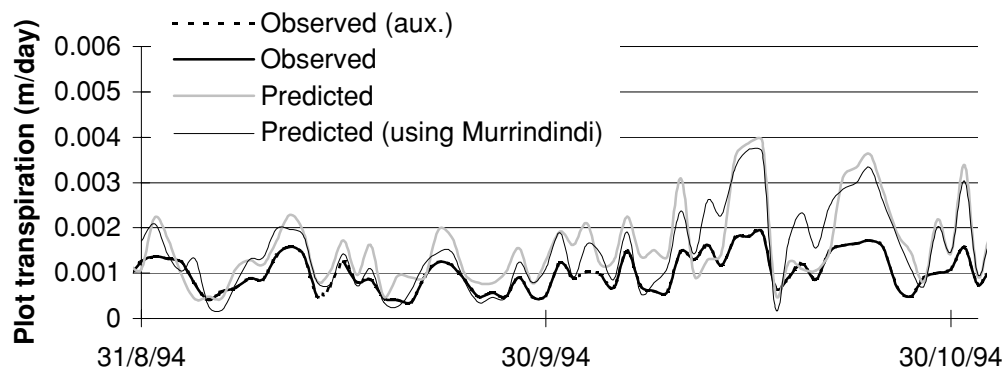
Figure 10.19: Detail taken from Figure 10.18 showing just two months of data.

ple, the ideas of Pierce et al. (1990). The theory underlying these ideas is that transpiration involves latent heat transfer from the leaf surface to the air causing an decrease in leaf surface temperature which may be remotely sensed by thermal infrared scanners (see reviews by Stewart and Finch, 1993; and Engman, 1995).

10.2.11 Soil water fluxes

10.2.11.1 Water table levels

Using capacitance probe piezometers, Campbell (in prep.) monitored water table levels continuously at four locations along each of four short transects in the Ettercon 3 experimental catchment during various periods in 1994 and 1995. Numerous problems with data loggers were encountered and, as a result, useful data were only obtained from eight piezometers comprising one complete and one incomplete transect. For the times when data were concurrently available from all of these eight piezometers, water table profiles could be interpolated from points at 0, 8, 13, 15, 24, 36 and c. 80 metres from the permanent stream.

To relate predicted water table levels to these observations is not at all straightforward, mainly due to differences between the spatial sampling scale of the piezometer network and the scale of Macaque's ESUs. The piezometers were spaced as close as five metres apart whilst typical ESUs for Ettercon 3 were between 25 and 100 metres (1 -4 grid cells) wide. Further, ESUs typically represented areas of about one hectare whilst piezometer measurements were point measurements influenced by water table levels in only the surrounding few square metres. The piezometer data were collected as part of a groundwater process study (Campbell, in prep.), and were never intended

for validation of a model such as Macaque.

Realistic prediction of water table levels is one of the novel features of the limited DFM hillslope modelling approach employed within Macaque. Therefore, an effort was made to relate predicted and observed water table levels using the best information available. This is shown in Figure 10.20. The Figure shows a section view of the hillslope containing the piezometers. The soil surface data were derived from the detailed topographic survey of Ettercon 3 described in Chapter 6. The bedrock data were derived from seismic survey at three locations roughly aligned with the piezometer transects. Bedrock depths were very approximate, owing to the often extensive transition from soil to saprolite, fractured bedrock, and finally 'solid' rock (Campbell, in prep.; Heislers 1993), and also the difficulty of vertically and horizontally aligning the piezometer and seismograph transect co-ordinates. The observed water table levels are shown as an interpolated line connecting mean values for each piezometer over the it's period of measurement (ranging from 40 to 370 days). The bars accompanying each point show the maximum and minimum recorded values. The predicted water table levels were calculated for each of the 14 ESUs in the Ettercon 3 catchment. The bars show maximum and minimum predicted values over the period 1991-1994. Associated *mean* distances to the stream were estimated visually from a map of the ESUs. Thus the predicted values relate to the representation of the entire Ettercon 3 catchment as a conceptual hillslope, whilst the observed values relate specifically to the transect of piezometers.

The important features of Figure 10.20 are as follows. Both predicted and observed water tables remain relatively shallow for the first 10 or twenty metres away from the stream and then become deep (*c.* 15 m) beyond about 30 metres away from the stream. The range of observed water table levels (as indicated by the bars) is quite large (> 2 m) where the water table is shallow, and quite small (*c.* 0.2 m) where the water table is deep. This is expected since shallow water tables are likely to exhibit greater response to annual and daily fluctuations in recharge and evapotranspiration. The predicted water table levels approach a similar pattern, with the largest range being predicted for the shallow water tables, and a smaller (but not small enough) range being predicted for the deep water tables. This variation in range is not able to be predicted by conventional DFMs such as TOPMODEL. As noted in Section 4.3.1, water table variations in Macaque are directly linked to saturated area expansion and hence streamflow production. Conventional DFMs can only vary water table depth uniformly across an entire hillslope. Because most of the hillslope is far away from the stream with deep, static water tables, water table variations predicted by conventional DFMs are under-predicted
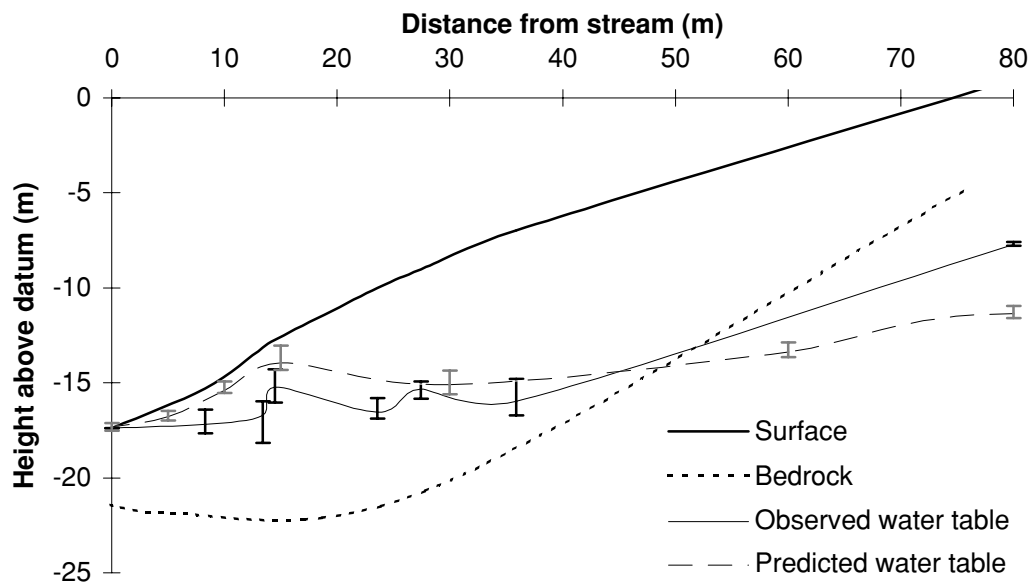
Figure 10.20: Water table levels at Ettercon 3: hillslope section comparing the observed water table profile along a transect with the average predicted water table for Ettercon 3.

near the stream, thus precluding a realistic connection of water table levels, saturated area expansion, and streamflow.

A limitation of the predicted values shown in Figure 10.20 is that the water table gradient near the stream is too steep. This is because the hydraulic gradient used to calculate baseflow exfiltration is held constant within Macaque. Thus, in order to achieve realistic baseflow response, the saturated area response must be over-predicted, because baseflow is the product of hydraulic gradient, saturated area, and surface saturated hydraulic conductivity (Section 4.3.11.6). Over-prediction of saturated area response was achieved by having a steep near stream water table for which a small rise in level led to a large rise in saturated area.

In conclusion, whilst an involved process of quasi-prediction had to be used in order to allow comparisons of predicted and observed water tables, the key features of the observed and predicted water table profiles were able to be shown. The general character of the predictions was accurate, exhibiting shallow, dynamic near-stream water tables and deep, static water tables away from the stream. In analyses not shown, there were indications that *individual and absolute* predictions of water table level were at times in error but this is not considered a great problem considering the statistical nature of the present modelling exercise (i.e. the fact that a model ESU represents the mean water status of an area larger than the circle of influence of a single

borehole observation). One-to-one matching of specific daily predictions and observations is a desirable future step in this part of the investigation, but would probably be fruitless without a piezometer network designed with this purpose in mind.

No validation of water tables in other parts of the study area was attempted. In both larger, steeper valleys and areas with skeletal soils, it is likely that complete re-calibration would be required. In the absence of any data from other areas, the key parameters controlling water table shape (Δ_{sat} and δ) must be calibrated with respect to their influence on hydrographs and some reference to expected realistic values.

10.2.11.2 Soil moisture

Soil moisture measurements were made in the study area by the MMBW at various sites during the 1970's and 1980's using neutron moisture meters (Langford and O'Shaughnessy, 1979b, 1980b; Moran and O'Connell, 1977; Duncan and Heeps, 1980; Jayasuriya and Creaner, 1994). Here, comparison is made with data from the Slip Creek experimental catchment (62.3 ha) (Langford and O'Shaughnessy, 1980b, Table D.2). Three transects of neutron moisture meter holes were located perpendicular to Slip Creek creating a coverage representative of the whole catchment. Measurements at different depths were integrated to provide estimates of total moisture in the top 3.1 m of soil. These were averaged to give values of 'observed' catchment mean soil moisture.

Corresponding predictions by Macaque were derived as the average moisture available to canopy roots, $s_{tot,c}$, for the Slip Creek catchment. As described in Section 5.3.12.1, canopy root depth was set at 4.0 m, which is slightly different to the value of 3.1 m over which the observed data apply. Time series input data were taken from Warburton (F1195) and Melbourne Regional Office (F2540).

Figure 10.21 shows a time series of predicted and observed soil moisture for the full span of the observed data. The 'adjusted' predictions are discussed below. The non-adjusted predictions are accurate in mean terms but show greatly under-estimated seasonal amplitude. This is because only a single-layered unsaturated zone is represented within Macaque. The average predicted water table depth for the catchment and for the period shown is 23.0 m which means that the unsaturated zone is very large. Significant changes in absolute moisture content in this zone will appear as only small changes in moisture content per unit depth, and this is reflected in the predictions.
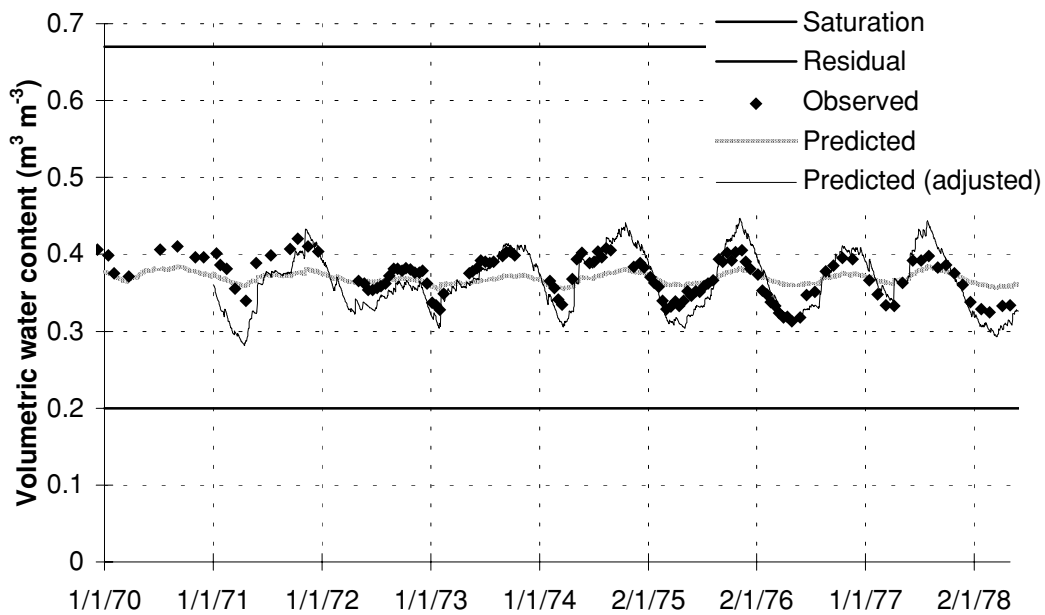
Figure 10.21: Testing modelled soil moisture at Slip Creek: time series of observed and predicted volumetric moisture content. Observed values are 'catchment averages' from 16 spatially distributed neutron moisture meters integrated over top 3.1 m of soil. Predicted values are catchment averages within canopy root zone (in this case, top 4.0 m of soil).

An adjustment can be made to the predictions for the purposes of realistic comparison with the observed data. The assumption is made that moisture levels below the canopy roots are significantly lagged with respect to surface moisture levels. Hence, the absolute moisture content of the unsaturated zone below the canopy rooting depth was set to the 1 year moving average of the initially predicted value. The residual changes in absolute moisture were then applied to the surface soil. Seasonal variations in absolute moisture levels were thus distributed mainly over the top 4.0 m of soil, leading to much greater seasonal amplitude in predicted water content per unit depth for that layer. From Figure 10.21, it can be seen that the adjusted predictions were accurate in both mean and seasonal terms.

It is concluded that accurate predictions were made of annual mean moisture content per unit depth and absolute moisture content. But, due to the single-layered representation of deep unsaturated soil, seasonal variations in moisture content per unit depth were poorly predicted. Adjustment of the initial predictions yielded accurate predictions of this latter quantity indicating, by inference, that the initial predictions of seasonal variation in absolute moisture content were also accurate. The implications of these findings are that the simulated response of processes which depend on absolute moisture

content (e.g. expansion of saturated areas) was realistic, but the simulated response of processes which depend on moisture content per unit depth (e.g. transpiration) were significantly damped. Perhaps most pertinent is that water limited transpiration is not likely to be predicted as often as it occurs in nature. In this regard, the model would benefit from a re-working of the unsaturated zone component, perhaps by including separate root zone and deep unsaturated stores, or perhaps by simply applying an adjustment as above *within* the model itself.

There remains scope for limited *spatial* validation of soil moisture predictions using individual bore data from the MMBW studies cited above, as well as by installing new monitoring networks such as that used in nearby forest by Soste et al. (1996). Alternatively, as reviewed by Engman (1995), investigations into remote sensing of soil moisture are currently popular, and indeed are being undertaken in earnest in a small rural catchment near the study area using Synthetic Aperture Radar (SAR) data which covers the study area (Troch et al., 1997; Wang, 1997). However, the confounding influence of forest cover (Stewart and Finch, 1993), and the limited depth to which SAR is able to penetrate the soil means that the techniques are not currently applicable to present study. Roberts (1993) suggests that improved soil water modelling may enable predictions of deeper soil water conditions from remotely sensed measurements made within the top few centimetres.

10.2.11.3   Streamflow

All testing of model components described thus far was done using the standard parameter set summarised in Table 5.2. The streamflow predictions (hydrographs) which result from this standard parameter set for the Ettercon 3 experimental catchment are shown in Figures 10.22 to 10.25 at a variety of time scales. Precipitation input was taken from the Blacks' Spur nearby (F1790), and temperature input was taken from the Lower Coranderrk meteorological station (F0290).

The daily hydrograph (Figure 10.22) shows a number of desirable features, such as a clear separation of stormflow and baseflow. Stormflow peaks above the baseflow were predicted at the correct times and with correct magnitude. Predicted baseflow rose with the observed baseflow during winter, but dropped away too early. More years are shown in the weekly hydrograph (Figure 10.23), in which both intra- and inter-annual variations in flow were accurately predicted, but the timing problems remain. In particular, predicted baseflow dropped away too early after the wetter winters, and there
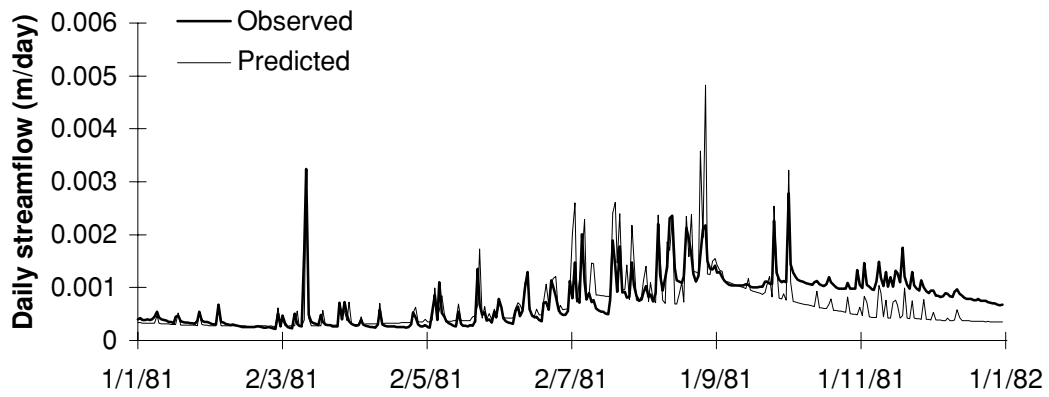
Figure 10.22: Daily predicted and observed hydrographs for Ettercon 3: predictions using standard parameter set.
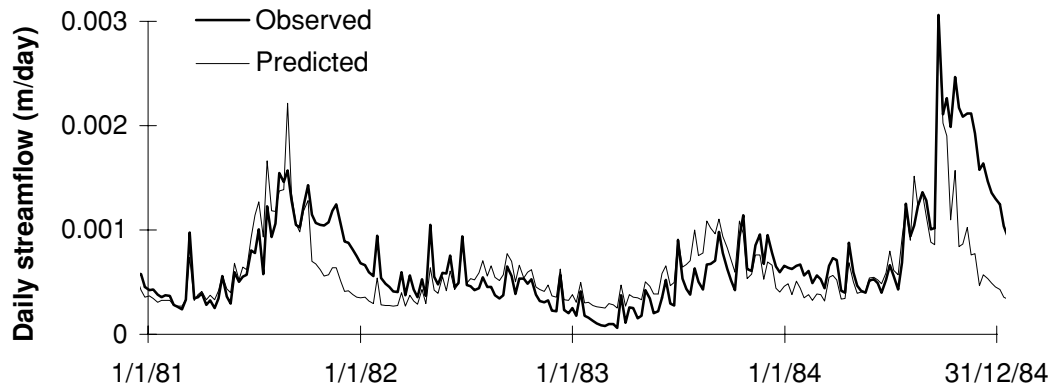
Figure 10.23: Weekly predicted and observed hydrographs for Ettercon 3: predictions using standard parameter set.

was some wandering of the predicted hydrograph in drier years. The monthly and yearly plots (Figure 10.24) reinforce these observations by including extra years in the late 1980's for which streamflow was rather poorly predicted. Errors were present in both the timing and magnitude of seasonal variations in flow.

Despite the problems mentioned, some general encouragement is to be gained from these hydrographs, for they were predicted without *any* free[2] calibration of the parameters which control the overall water balance of the catchment. *In this sense, they are a confirmation of the general validity of the water balance modelling approach taken within Macaque.* By taking only precipitation and temperature as time series inputs, deriving from them a host of

---

[2]As noted in the relevant sections, (non-free) calibration against internal variables was used for some parameters
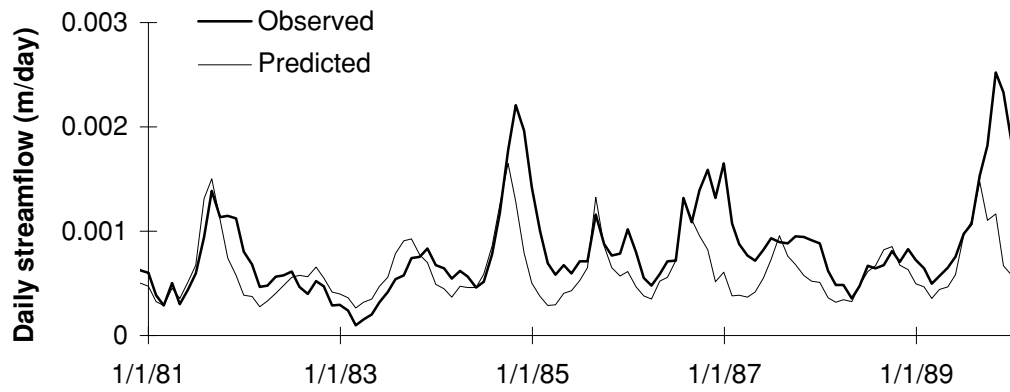
Figure 10.24: Monthly predicted and observed hydrographs for Ettercon 3: predictions using standard parameter set.
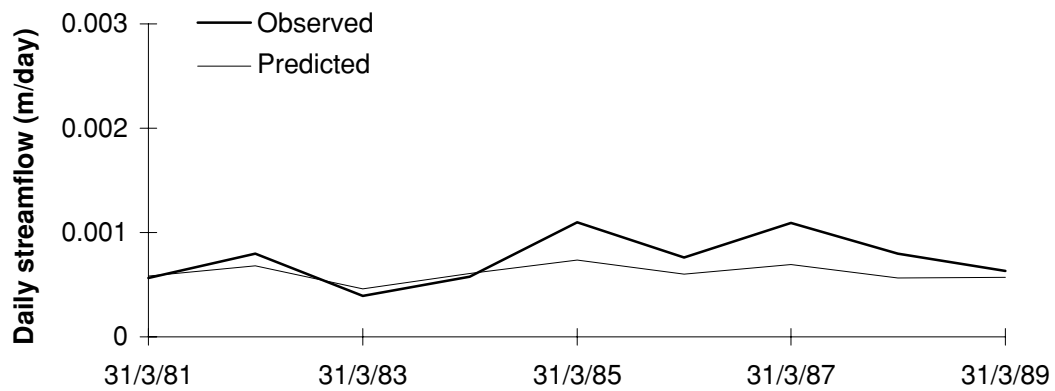
Figure 10.25: Water-yearly predicted and observed hydrographs for Ettercon 3: predictions using standard parameter set.

micro-climatic variables, and using these to drive a three-layered Penman-Monteith representation of evapotranspiration, there is no guarantee that annual or seasonal hydrographs will not be in gross error.

In order to ascertain the model's ability to reproduce observed hydrographs, calibration of two relatively free sub-surface parameters was undertaken. The prescribed rate of change of saturation deficit with wetness index, Δ_{sat}, and the lateral redistribution factor, δ, operate in conjunction to control the depth of the water table, its slope, and its dynamics near the stream. In the standard parameter set they were set to $\Delta_{sat} = -6.5$ m i_{wet}^{-1} and $\delta = 0.001$ day^{-1}. Both manual and automatic calibration was employed to optimise the predicted weekly hydrograph for the period 1981-1984. The manual procedure proved most successful owing to problems defining an objective function which reflected desirable hydrograph features. From the manual procedure, it was determined that greater seasonal variation can be achieved by decreasing either of the above parameters, and preferably both together. This resulted in greater disconnection of ESUs and a more bucket like representation of the catchment. Because each ESU can be partially saturated (rather than totally saturated or not saturated at all), streamflow can occur from all ESUs together, even when none of them is saturated to the surface. This is what occurs under low Δ_{sat} and δ.

The (subjectively) best weekly hydrographs were obtained with: $\Delta_{sat} = -10.5$ m i_{wet}^{-1} and $\delta = 0.0002$ day^{-1}. These are shown in Figures 10.26 to 10.29. The calibrated daily hydrograph was similar to its un-calibrated counterpart except that the decline in baseflow after winter was much better represented. In order to achieve this, higher baseflow was required at the height of winter, and this led to over-predicted stormflow at this time. The weekly hydrograph was much improved with calibration, both in the post-winter decline and during drier times. However, the full length of post-winter decline was still not predicted. The monthly and yearly predictions were also improved, showing greater and more accurate variability in both intra- and inter-annual flow. The latter half of the decade was given less attention during calibration and hence exhibited the greatest prediction error.

In analysis not shown, the effect of calibration on predicted water table level was examined by re-plotting Figure 10.20 using the calibrated parameters. Away from the stream, the more negative values of Δ_{sat} would be expected to produce very deep water tables. However, the concomitant decrease in δ decreased the influence of the distribution function, allowing the water table to stabilise well above the deep level prescribed by the distribution function. The net result was an almost unchanged water table level. Near the stream,
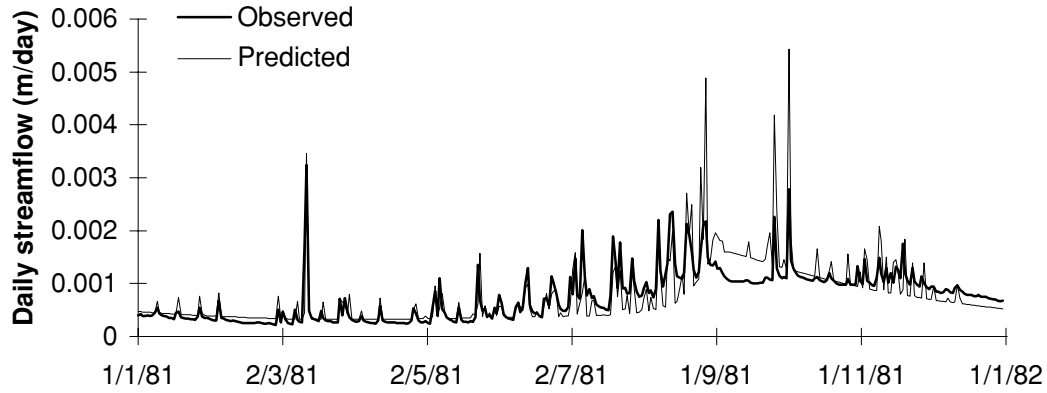
Figure 10.26: Calibrated daily predicted and observed hydrographs for Ettercon 3: predictions using standard parameter set (with calibrated adjustments to Δ_{sat} and δ).
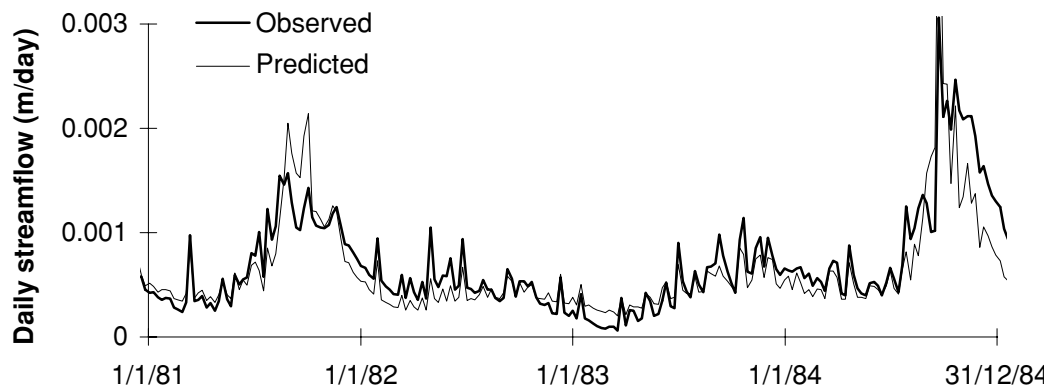
Figure 10.27: Calibrated weekly predicted and observed hydrographs for Ettercon 3: predictions using standard parameter set (with calibrated adjustments to Δ_{sat} and δ).
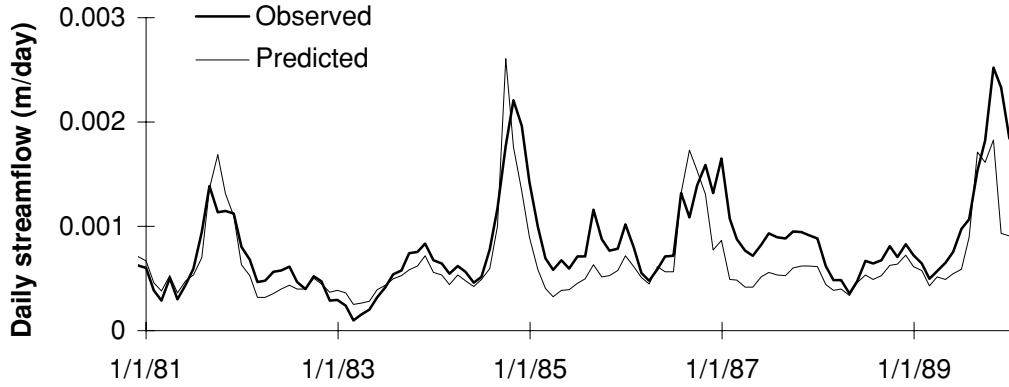
Figure 10.28: Calibrated monthly predicted and observed hydrographs for Etter-con 3: predictions using standard parameter set (with calibrated adjustments to Δ_{sat} and δ).
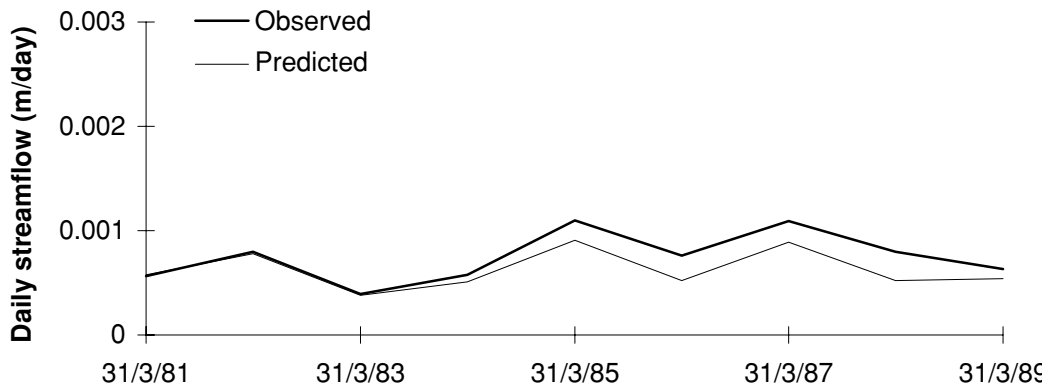
Figure 10.29: Calibrated water-yearly predicted and observed hydrographs for Ettercon 3: predictions using standard parameter set (with calibrated adjustments to Δ_{sat} and δ).

the dynamics were altered considerably. Where before, the wettest ESUs were saturated to the surface (see Figure 10.20), the new parameters lead to *no* fully saturated ESUs but, rather, a greater number of ESUs contributing to streamflow from a point of partial saturation.

Pending more detailed examination, the following *general* conclusions can be made from the streamflow testing process. Generally accurate, un-calibrated predictions indicate a valid representation of water balance processes (at least for small catchments) within Macaque. Improvement in the timing and magnitude of seasonal streamflow variability with the calibration of two parameters indicates that these parameters are useful in that they are effective in changing streamflow dynamics. However, there remains an inability to fully reproduce the seasonal accumulation and drying-up of soil moisture as reflected in the observed baseflow hydrographs. This is most likely related to uncertainty in the assumption of constant near-stream hydraulic gradient, and in the simplistic representation of unsaturated soil moisture storage.

The predictions of water table dynamics shown in Figure 10.20 suggest that the limited DFM approach is a useful alternative to conventional DFMs which cannot simulate realistic near stream water table dynamics in deep soiled catchments. However, the fact that optimal hydrographs were obtained with parameters which greatly de-emphasise the role of the distribution function suggests that a one-dimensional bucket approach may perform as well as a limited DFM but without the conceptual complexity. This is evidence that, in deep soiled catchments, there is no need for either fully distributed models or distribution function models. Large scale, one-dimensional, distributed parameter models similar to ALSIS may be sufficient.

The de-emphasis of the distribution function in this limited DFM context highlights the lack of realism in conventional DFMs such as TOPMODEL which are unable to simulate highly dynamic water tables which change shape. The key to the successful simulation reported above is that accurate hydrographs were modelled as a direct response to realistic water table and saturated area *dynamics* near the stream with a deep, static water table elsewhere. The dynamic, subsurface kinematic wave behaviour normally associated with fully distributed models was reproduced within a parsimonious, DFM context. This is something which conventional DFMs cannot do.

10.3 Other testing

A range of other aspects of the internal operation of the model were tested in analyses not shown here. These include:

- numerical verification that solar, longwave, and net radiation propagate through the vegetation layers in an expected manner which is sensitive to radiation reflection and interception coefficients,

- outputting of maps of mean summer and winter radiation incident across the study area to verify that expected seasonal and topographic sensitivity occurs,

- dynamic visualisation of the expansion and contraction of hillslope saturated areas in both plan and profile view to verify expected dynamic behaviour.

Data on internal variables which is available but which has not been used include: snow depth data for Mount Donna Buang (Ruddell et al., 1990), *temporal* data on LWP and leaf conductance (Connor et al., 1977), time series data on understorey transpiration (R. Vertessy, unpublished data), and *temporal* data on soil evaporation (McJannet et al., 1996).

10.4 Testing model response to lumped parameters

As noted in Table 5.2, there are eight parameters within Macaque which are considered 'highly' sensitive relative to certainty. They are the main controls on model operation once all the other parameters have been set by physical measurement or internal calibration. Their sensitivity is examined in this section.

For the first few parameters examined below, parameter values were varied within acceptable ranges and the effect on streamflow and/or ET is reported. For this purpose, the model was run on the Ettercon 3 experimental catchment for the period 1980-1989. Effects on streamflow and ET are reported with respect to mean daily values from the full period. The standard parameter set (Table 5.2) was used with three changes, calibrated to ensure that the sensitivity results were reported with respect to a parameter set which resulted in accurate longer term (10 year) predictions of ET and streamflow. Specifically, the calibrated values of $\Delta_{sat} = -10.5$ m i_{wet}^{-1} and $\delta = 0.0002$ day^{-1} from Section 10.2.11.3 were retained; and the conductance parameters, $g_{cl,max}$ and $g_{ul,max}$ were calibrated against 10 year total streamflow to a common value of 0.0045 m day^{-1}. Note that Ettercon 3 has a lower than usual streamflow to ET ratio (possibly due to flow beneath the weir), so small percentage changes in ET will be reflected as large percentage changes in streamflow.

10.4.1 Temperature parameter sensitivity

Because of the model's inability to simulate seasonal temperature lapse rates (see Section 5.3.4), and the strong effect of the associated inaccuracy in temperature prediction on a range of derived variables influencing evapotranspiration (see Sections 10.2.3 to 10.2.4), the lapse rate for maximum temperatures is a sensitive parameter relative to its uncertainty.

The standard value used for $\Delta_{T,max}$ was -0.006 °C m^{-1}. An acceptable seasonal range of -0.004 to -0.12 was determined using the sine wave fit from Figure 5.8 which shows seasonal lapse rate variations (for a station biased toward giving high lapse rate values). Model runs spanning this range resulted in +8.8% to -30% changes in ET respectively, which caused -44% to +151% changes in streamflow. These large changes clearly indicate the benefits for model realism which would be gained if a seasonal lapse rate model

was included. However, despite the wide seasonal ranges, the *mean* value of $\Delta_{T,max}$ is reasonably well fixed and so the parameter as such is not used for calibration.

10.4.2   Evapotranspiration parameter sensitivity

Maximum canopy conductance supposedly varies within a relatively narrow range (Körner, 1994). However, the discussion in Section 5.3.12.3 revealed considerable uncertainty in the most appropriate model values. It is unknown whether the parameter varies significantly amongst the *Eucalyptus* species of the study area, and little is known of the maximum conductance of the myriad understorey species. Further, the discussion in Chapter 11 suggests that long term temporal changes in leaf conductance may occur.

In the present study, the two maximum leaf conductance parameters, $g_{cl,max}$ and $g_{ul,max}$, were used as a key control of water balance. They were calibrated within physical ranges to scale ET such that mean streamflow predictions matched those observed. An indication of their sensitivity was given by running the model with each parameter in turn varied in the range 0.0025 to 0.0065 m day^{-1}. With respect to maximum canopy conductance, this led to changes in ET of -10% to +6.7% respectively, and changes in streamflow of +50% to -33% respectively. Slightly less influence was exerted by changes in maximum understorey conductance, which led to changes in ET of -6.9% to +4.8%, and changes in streamflow of +33% to -24%.

A third evapotranspiration parameter which is highly sensitive relative to its certainty is the nominal soil evaporation depth, $z_{s,max}$, mostly due to its low certainty. The parameter is conceptual, unrealistic, and effectively serves as a place-holder until a more suitable representation of soil resistance is developed. Its standard value is 0.003 m, which was derived by calibrating predicted soil evaporation against mean values given by McJannet et al. (1996). For the sake of this discussion, it was varied by a factor of two in each direction (0.0015 to 0.006 m). This resulted in changes in ET of +5.4% to -3.9%, and changes in streamflow of -27% to +28%.

When dealing with the concept of 'sensitivity *relative to certainty*' as introduced in Table 5.2, the aim is to have no highly sensitive parameters. The above analyses have shown that this aim is not met. A number of parameters are able to completely alter the scale of the predicted hydrograph when varied within their respective bounds of certainty. However, this is not considered to be a problem. The soil evaporation sub-model was calibrated as

a relatively closed system, so it is not so important that the physical representation of soil resistance *within* that system is poor. The conductance parameters were used in an 'effective' sense as overall scaling parameters, in some way compensating for the fact that few of the parameters controlling the water balance can be physically measured at large scales. The fact that their calibrated values do not stray from typical physical measurements of leaf conductance actually provides reassurance that essentially point measurements of the inputs to the Penman-Monteith equation can be scaled up to water supply catchments without a great deal of perturbation.

10.4.3   Precipitation parameter sensitivity

Section 10.5 shows that of the spatial parameters of the model, MMPI is the most sensitive relative to its uncertainty. Because much of the catchment is not water limited, the response of streamflow to changes in precipitation is non-linear. For example, in a typical energy limited system where two thirds of the water balance is ET, a 1% increase in precipitation might not lead to any additional ET, and hence would translate as a 3% increase in streamflow. Further, the extent of this non-linearity will vary spatially throughout the study area from dry, water limited areas to the very high rainfall areas near Mount Donna Buang. This is confirmed in Section 10.5 below, where spatial changes in MMPI amounting to a mean increase in precipitation of 12% result in an increase in predicted streamflow of 36%.

10.4.4   Soil parameter sensitivity

As noted in Section 5.3.11.5, the parameter expressing the hydraulic gradient of the water table near the stream, Δ_z, serves to control the rate of baseflow exfiltration. In turn, this directly influences the size of the saturated area (given that ET is relatively unaffected by such changes and hence the same streamflow must find its way out of the basin). Saturated area controls the amount of stormflow, and so, through these connections, Δ_z mainly serves within the model to control the size of stormflow peaks relative to the baseflow. This is illustrated in Figure 10.30 which shows two predicted daily hydrographs for the second half of 1981. Under two different values of Δ_z, baseflow remains unchanged at low flow but changes markedly at high flow. Independent of baseflow however, predicted stormflow peaks are significantly lower when the hydraulic gradient is at the high value (and hence saturated area is low).
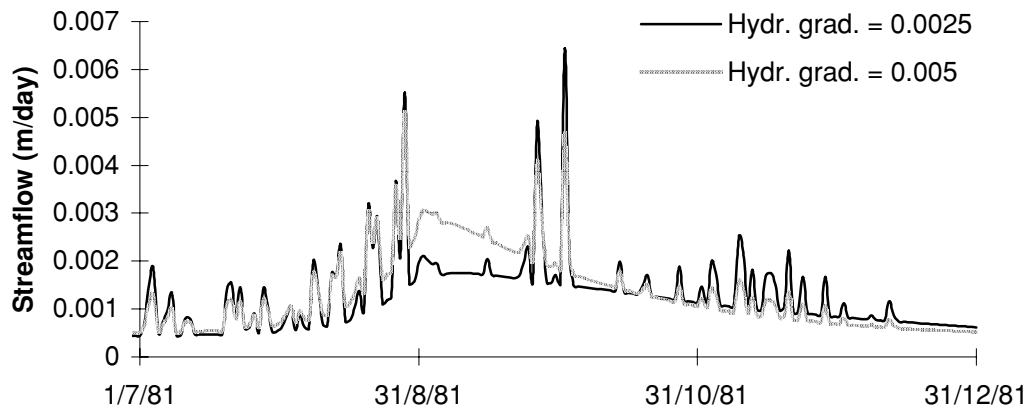
Figure 10.30: Sensitivity of daily streamflow predictions to changes in hydraulic gradient (Δ_z): model runs on Ettercon 3 using standard parameter set with $\Delta_{sat} = -10.5$, $\delta = 0.0002$, and $g_{cl,max} = g_{ul,max} = 0.0045$.

Δ_z is a useful parameter with a strong influence on saturated area and hence hydrograph shape, but relatively little influence on any other model variables. It is listed in Table 5.2 as having high sensitivity relative to certainty because of the high uncertainty inferred from the observation that its calibrated value (0.0025 in the standard parameter set) was lower than most values measured in the field (see Section 5.3.11.5). The inclusion of a variable hydraulic gradient dependent on water table levels would most likely remedy this.

10.4.5 Hillslope and ESU parameter sensitivity

Whilst a detailed analysis of the sensitivity of hillslope and ESU parameters was not undertaken, some general comments can be made given related analyses. In Section 10.2.11.3, the two parameters which control the profile shape of the water table, Δ_{sat} and δ, were shown to work together as a strong control of hydrograph shape as well as water table dynamics. In the following chapter, it is shown that they are also sensitive to scale. In order to match predicted and observed hydrographs, these parameters must be calibrated whenever the wetness index distribution changes, such as in scaling up from experimental to water supply catchments.

As shown in Section 10.5.3 below, the three wetness index parameters, i_{wet}, $i_{wet,range}$, and $\bar{i}_{wet}$, are surprisingly insensitive at the scale of first order basins. At large scales, they may be more sensitive. This is indicated by the need to re-calibrate the model between application to small experimental catchments (this chapter) and large water supply catchments (following chapter). The

change in scale is largely represented by changes in the topographic form of the catchments reflected within the distribution of wetness index values.

10.5 Testing model response to spatial parameters

The previous sections have tested internal and external model components and responses to perturbations in inputs and parameters in a largely *lumped* sense. However, land cover change is usually *spatially variable*, and hence, the spatial response of the model must also be tested. This section tests spatial response by supplying different parameter maps to the model and examining the associated differences in both lumped and spatial predictions of streamflow.

Material is reproduced and paraphrased from a recent journal paper which was written as part of the present study (Watson et al., 1997a). The text of the paper was written by the present author and augmented by R. Grayson. A few paragraphs below contain Grayson's writing. A slightly earlier version of the model was used in the paper and differed mainly by implementing a slightly more primitive model of precipitation interception with a simple radiation control on evaporation of intercepted water (instead of the current Penman control which uses both radiation and VPD). This is unlikely to affect the outcomes of the exercise because both interception schemes were calibrated to the same observations of throughfall, and the spatio-temporal signal of modelled radiation and VPD are similar. Hence it is considered unnecessary to re-do the modelling analysis for the present study.

The spatial response relating to maps of three parameters was investigated: precipitation, LAI, and topography. Initially, the model was run using the standard parameter maps described in Chapters 7, 9, and 6 respectively. Then, each parameter in turn was mapped by some alternative means based on a different type of spatial information, and the model was run using this map. Differences in model operation were assessed by comparing spatial and temporal streamflow predictions.

Results derived using the standard parameter set are given initially. With reference to the parameter mapping techniques described below, this parameter set used 3D precipitation interpolation, LAI mapped according to canopy species, and air-photo interpreted topography. The results may be compared with results derived using alternative parameter sets presented in

the following sections. A three year simulation period was used, spanning the years 1982-1984, and covering a wide range of catchment conditions. The 1982/1983 summer was extremely dry and the 1984 winter was wetter than most winters. Whilst the model operates with a daily time step, weekly hydrographs are presented for clarity. Predictions were made for the three largest water supply catchments (see Figure 2.3) summed as one, the other two water supply catchments being unreliably gauged. Figure 10.31a shows predicted and observed hydrographs and Figure 10.32a maps the associated runoff source areas.

The predicted hydrograph was similar in character to those produced for the Ettercon 3 experimental catchment earlier. Seasonal variations were well predicted but baseflow recession was too quick and stormflow was overestimated in winter. As with Ettercon 3 the same causes are suspected, particularly the assumption of constant hydraulic gradient within the near-stream water table which necessitates excessive saturated areas in order to produce high baseflow during winter.

Predicted streamflow source areas (Figure 10.32a) were generally as expected. All mapped watercourses were represented as source areas, as were broad areas observed in the field as 'soaks'. The high precipitation areas in the south east generated more streamflow from a greater proportion of each hillslope than other areas. A general failing of the model however, was that streamflow was predicted to originate from a number of hillslopes known to be permanently unsaturated, such as the upper slopes of the south west tip of the southern catchment. This is most likely related to the problem of excessive saturated areas noted above.

In the following sections, the model is run using alternative precipitation, LAI, and topographic mapping schemes respectively, and the effects on simulated hydrological response are examined.

10.5.1   Spatial response to precipitation mapping

The standard parameter set used the 3D spline interpolated MMPI (precipitation) map from Figure 7.6. The model response to spatial changes in precipitation mapping was tested by running the model using the 1D linear MMPI map from Figure 7.5 instead. The two maps differ not only spatially but in mean value. Scaling each MMPI map by the mean annual precipitation (MAP) at the base station yields areal average MAP for the study area of 1610 mm using the 1D MMPI map, and 1807 mm using the 3D MMPI
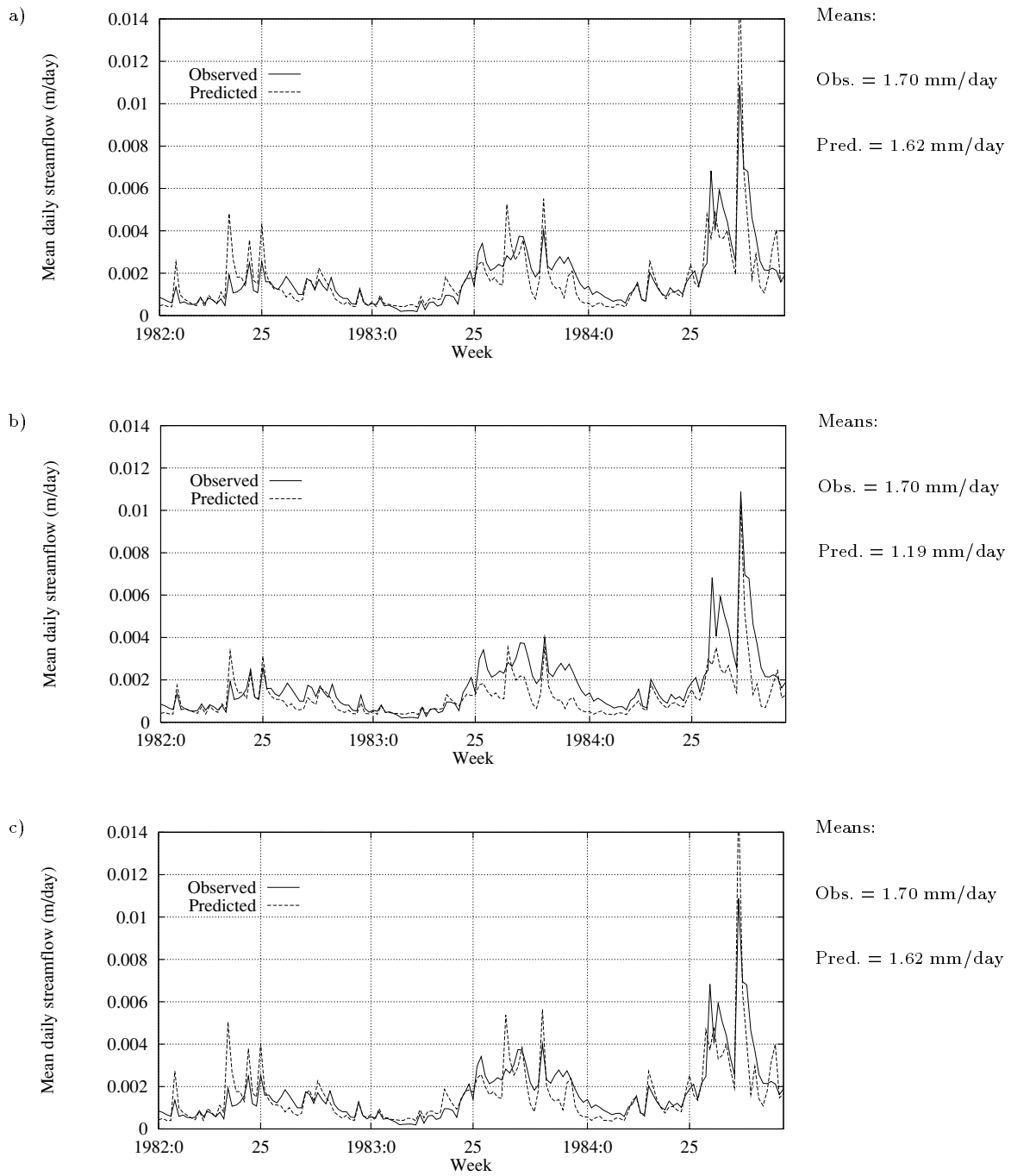
Figure 10.31: Predicted and observed weekly hydrographs aggregated from the three largest water supply catchments (see Figure 2.3) for the period 1982-1984: a) using the standard parameter set; b) using 1D linear instead of 3D spline interpolation of precipitation; and c) using total LAI estimated from TM satellite imagery instead of forest type.
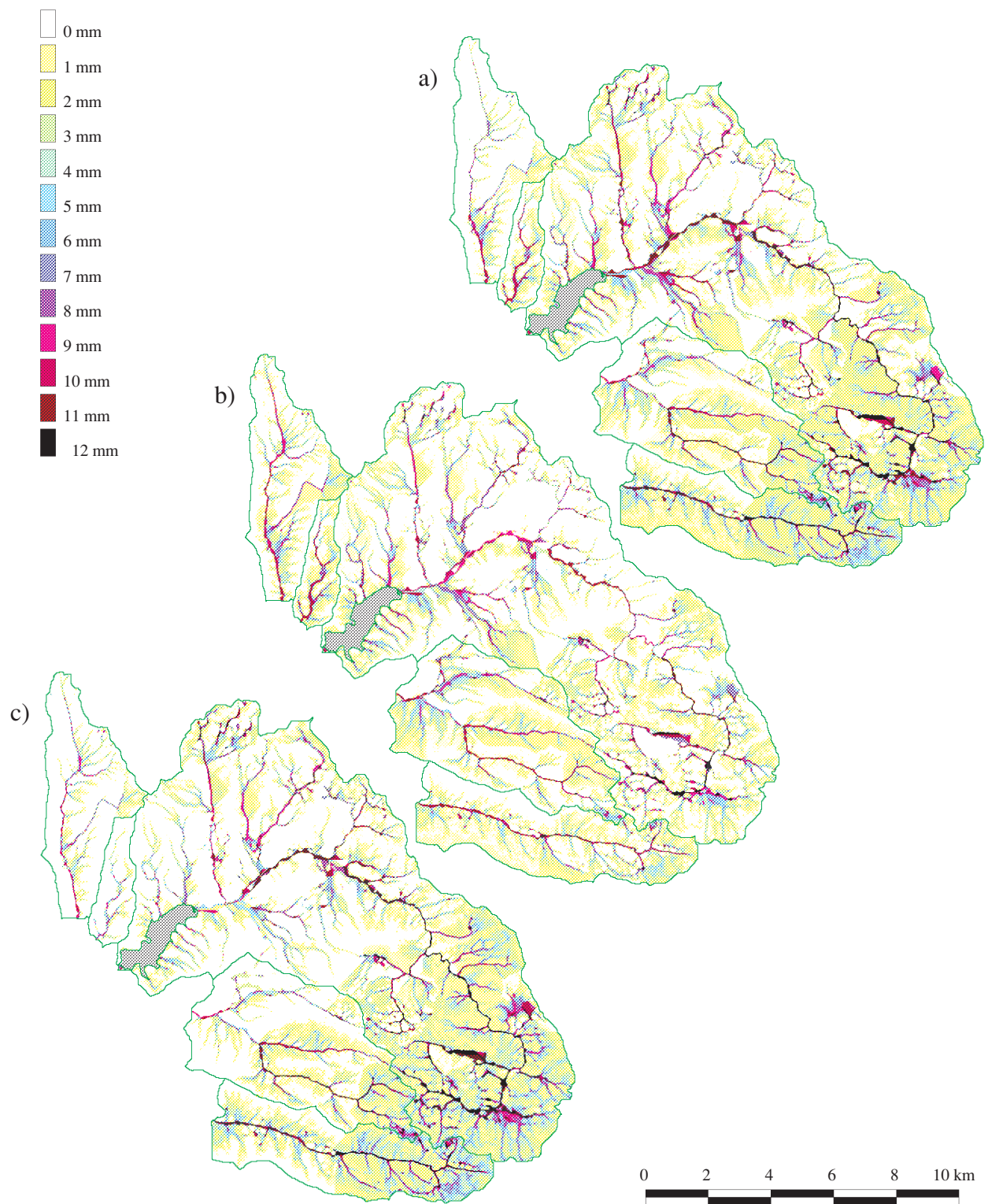
Figure 10.32: Mean daily streamflow source areas for 1984: a) using the reference parameter set; b) with MAP estimated using 1D linear instead of 3D spline interpolation; c) with total LAI estimated from TM imagery instead of forest type.

map (a 12% increase or 11% decrease). The hydrographs produced using 3D spline interpolated MMPI and 1D linear MMPI are shown in Figure 10.31a and Figure 10.31b respectively. The corresponding pair of maps of predicted streamflow source areas are shown in Figures 10.32a and 10.32b. The hydrograph for the 1D linear map is lower and less peaky than that for the 3D spline map. Mean daily flow is 27% lower using the 1D linear map (or 36% higher vice versa). In the south east of the study area, there is a significant reduction in the proportion of hillslopes which generate streamflow under the 1D linear map. These observations all relate to the lower precipitation predicted for the south east by the 1D linear technique. The peakiness and excessive saturation of hillslopes predicted under the 3D spline map were cited earlier as problems with the initial simulation so these observations favour the use of the more simple technique.

There is some uncertainty as to whether the more sophisticated mapping has resulted in improved prediction of streamflow because predictions made under the simpler 1D linear technique exhibited more desirable features than those made using the 'improved', 3D spline technique. Nevertheless, the investigation has highlighted the sensitivity of precipitation mapping. It is important to note that the density of gauges available for this exercise was much greater than is usual, but was still a limiting factor in locations such as Mount Donna Buang where there was only one gauge for quite some distance. The choice of analysis method greatly influenced simulated response, particularly near Mount Donna Buang. Future measurements will need to constrain the prediction of other elements of the water balance to the point where more is able to be said about the true distribution of precipitation.

10.5.2   Spatial response to LAI mapping

The standard LAI map used in this exercise was produced by assigning temporally constant total LAI values to distinct forest types mapped on the basis of canopy species. The resulting map was similar to, although an earlier version of Figure 9.18 which was derived for 1993 using Equation 9.11. Spatial variability was dominated by the distribution of the three major forest types: Mixed Species (low LAI), Ash (medium LAI), and rainforest (high LAI). The mean LAI value for the three largest catchments was 3.78.

An alternative total LAI map was produced directly from satellite NDVI data and was an earlier, similar version of Figure 9.16. The mean value for the three largest catchments was 3.77, which is very close to the average obtained from the species based map.

The differences between the two LAI maps used here and their more up-to-date counterparts in Chapter 9 are slight, and will not affect the results the sensitivity analysis.

The average LAIs predicted by the species based and satellite based maps differ by less than one percent. Spatially, however, the two maps differ significantly. The species based map shows large areas of uniform total LAI, broken only near the major boundary between Ash type and other forests (the latter occurring near the reservoir), and along the bands of rainforest bordering streams in high precipitation areas. The satellite based map exhibits more spatial variability. For example, LAI in the south east corner is shown to be generally lower than in the remainder of the study area, coinciding with a large area of old-growth Ash forest. There is also slight variability associated with topographic aspect and areas which can be identified from aerial photography as having patchy vegetation. The aspect-related variability may be real, or it may be some residual topographic shading effect due to inadequate shading correction, or it may be a combination of both. Insufficient data are available at this stage to clarify this, so there is uncertainty in both maps. The point here is that LAI is a vital parameter in any physical model of forest hydrology and the two maps represent equally viable, yet quite different alternatives to mapping this parameter.

Using the otherwise-unchanged standard parameter set, Macaque was run using each of the two total LAI maps. The hydrographs produced using the species based LAI map and the satellite based LAI map are shown in Figure 10.31a and Figure 10.31c respectively. The corresponding pair of maps of predicted streamflow source areas are shown in Figures 10.32a and 10.32c. There was almost no difference in the shape of the two hydrographs, and no difference in the mean daily streamflow. This is because the mean LAI was virtually the same for the two. Spatial variations in LAI do not affect mean streamflow for the study area. This suggests that evapotranspiration as predicted by Macaque is linearly proportional to LAI and probably not limited by spatially variable influences such as soil moisture stress. Similar results were reported by Nemani et al. (1993a, Tab. 1) who produced two spatially different LAI maps for coniferous forest whose mean difference resulted in identical mean differences in ET predicted using RHESSys. Whilst this observation satisfies our perceptual model of Ash forest behaviour, it may not be appropriate for drier, water-limited forests. There are small differences in the maps of streamflow source areas, with the satellite based map reducing excessive hillslope saturation in drier areas. This indicates that the satellite based map may be a better predictor of LAI, but further testing against observed data is needed before this assessment can be confirmed.
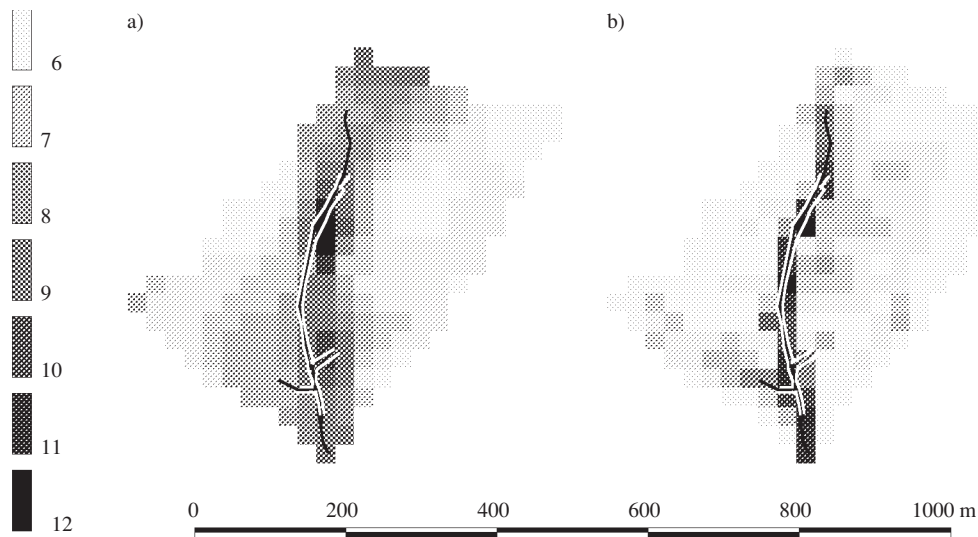
Figure 10.33: ESUs calculated from the $\ln(\frac{a}{\tan\beta})$ wetness index for the Ettercon 3 experimental catchment calculated from: a) the API DEM; and b) the ground surveyed DEM. Both maps are overlaid with ground surveyed stream lines and saturated area boundaries (during a relatively dry period).

10.5.3 Spatial response to topographic mapping

Spatial response to topographic mapping was tested by using each of the two DEMs constructed in Chapter 6 for the Ettercon 3 experimental catchment to create two maps of wetness index. This leads to two separate spatial disaggregations of Ettercon 3 into a number of ESUs. The standard parameter set used the air-photo interpreted (API) DEM of Figure 2.4 which was produced for the whole study area. The alternative DEM was the ground-surveyed one shown in Figure 6.3.

The two DEMs were used to construct two separate maps of the $\ln(\frac{a}{\tan\beta})$ wetness index, which were discretised into ESUs to provide two alternative topographic parameterisation and spatial disaggregation schemes for Ettercon 3. Figure 10.33 shows the disaggregation into ESUs of the wetness index. The smooth representation of topography by the API DEM is reflected in Figure 10.33a which shows only a limited convergence of high wetness areas along the stream. Figure 10.33b on the other hand shows a concentrated gully with high wetness reflecting the incised topography more accurately represented by the ground surveyed DEM. This also more accurately reflects the shape of the ground surveyed saturated zone (during a relatively dry period) which is overlaid on both maps.

Macaque was run on both representations of Ettercon 3 with the otherwise unchanged standard parameter set. The resulting hydrographs are shown in

Figure 10.34, and the predicted streamflow source areas are shown in Figure 10.35. The two predicted hydrographs are almost identical and are reasonably accurate in both shape and mean value. Neither hydrograph predicted the effects of the drought in the summer of 1982/3 very well, and both hydrographs were too variable during the high flow period at the end of 1984. The fact that such a marked difference in the two DEMs used to produce these hydrographs did not induce a marked difference in the hydrographs is perhaps surprising. The maps of runoff source area, however, are quite different. Field observations indicate that Figure 10.35a is an unrealistic simulation of runoff producing area. The smoothing of terrain apparent in the API derived map clearly spreads the saturated area out too much. In a water limited system, this spreading of the saturated area would be expected to result in reduced plant water stress, greater evapotranspiration, and hence, lower streamflow. On close inspection of the hydrographs in Figure 10.34, it can be seen that this difference is in fact predicted by the model, but only to a limited extent (8% lower flow is predicted under the smooth representation of terrain). This suggests that water limitations are controlling simulated evapotranspiration at Ettercon 3 to a limited extent. In general, it appears that whilst the maps of wetness index differ, the statistical representation of topography that the two DEMs effect within the distribution function is almost the same from a hydrological point of view. This indicates that there would be little benefit obtaining more detailed topographic data over the whole catchment because the structure of the distribution function model is unable to exploit the greater detail.

10.5.4 Discussion

In applying large scale spatial models (LSSMs), the user is faced with a myriad of questions regarding the way in which spatial information is to be used. In the case of data such as precipitation, point information must be interpolated whilst variables such as LAI must be derived from surrogate measures such as forest type or reflectance of solar radiation. The way in which the modeller chooses to use the information has important implications for model response. There is always great uncertainty regarding the true nature of spatially variable inputs and it is not always the case that apparently more sophisticated analytical approaches yield more certain results.

The 3D interpolation of precipitation was strongly influenced by data from a particular gauge in the south east of the study area so it was impossible to say whether the resulting rainfall distribution was a more realistic representation or simply an artefact of an unrepresentative gauge.
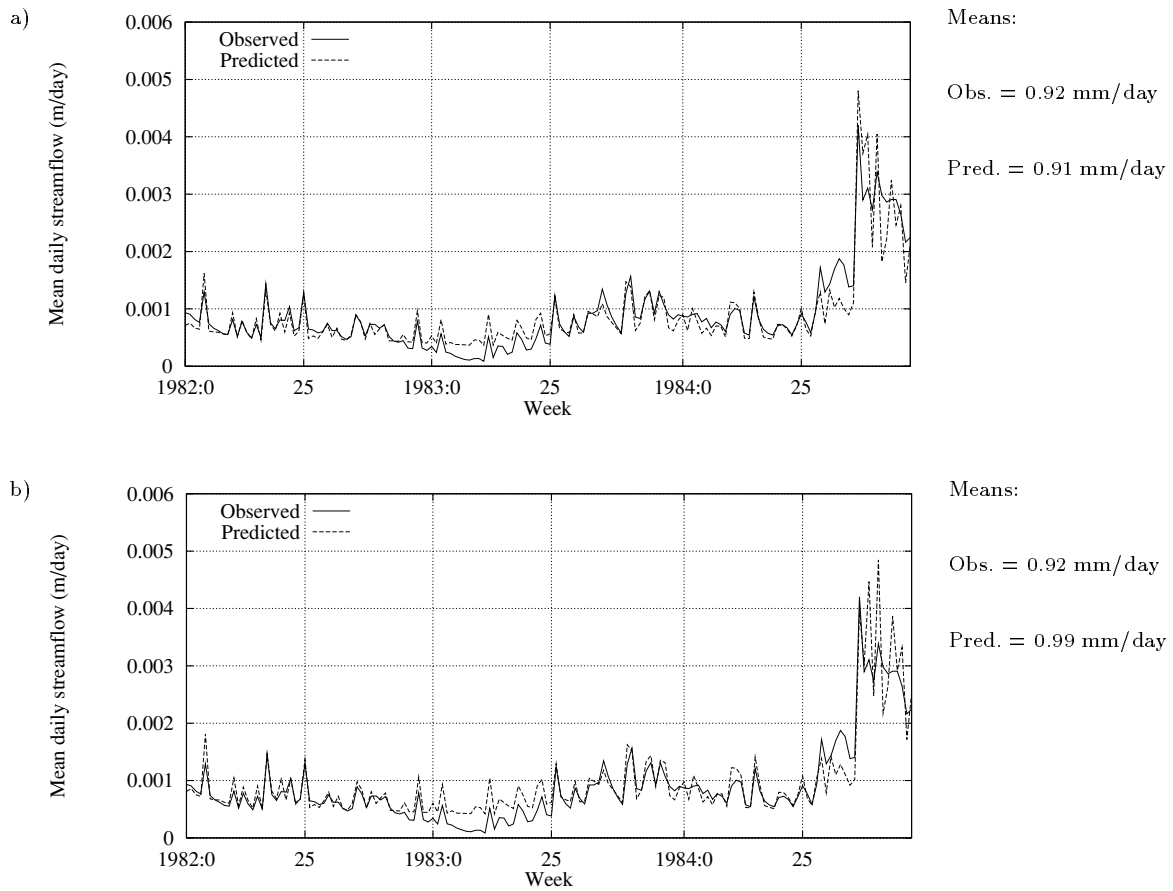
Figure 10.34: Predicted and observed weekly hydrographs for the Ettercon 3 experimental catchment for the period 1982-1984: a) using the API DEM; and b) using the ground surveyed DEM.
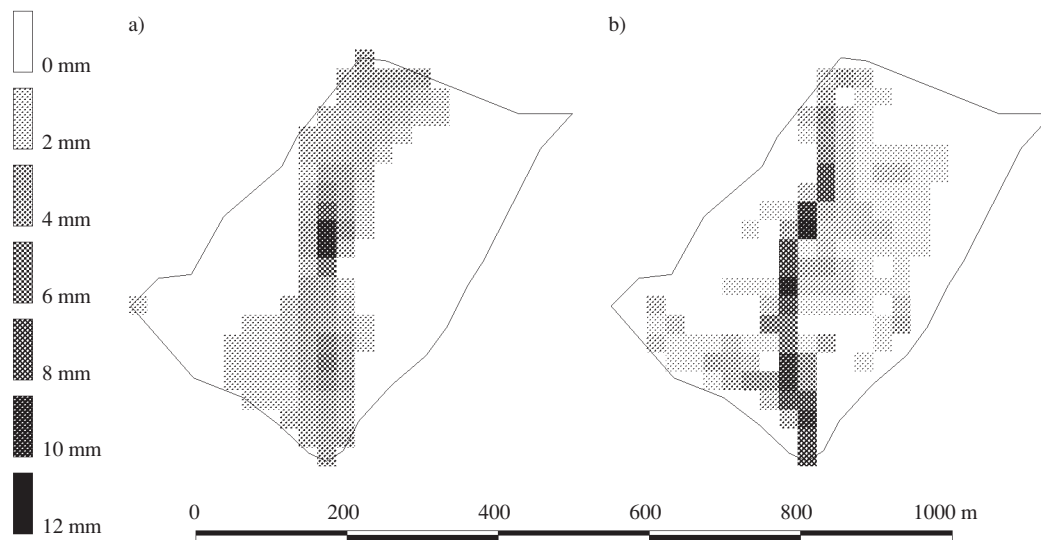
Figure 10.35: Mean daily streamflow source areas for the Ettercon 3 experimental catchment in 1984 using: a) the API DEM; and b) the ground surveyed DEM.

Similar uncertainty existed in the estimation of LAI, a parameter to which hydrological models of forested areas are highly sensitive. Fortunately the mean LAI estimates by the two methods were similar so overall runoff was similar but there were large spatial differences in LAI representation. The spatial variability of the satellite derived data gave a more realistic looking spatial runoff response but there are no direct data to confirm this observation. Ultimately the user must simply accept that by choosing a particular method of representation, certain spatial variability of response is 'locked in'.

It must also be accepted that different model structures can be limited in the extent to which they can exploit more detailed information. In the example given above, more detailed topographic data of a small sub-catchment gave a clearly more realistic estimate of runoff producing area yet, even at this small scale, the impact on the hydrograph was not detectable. This was because the representation of processes (especially evapotranspiration) within the model structure makes little distinction between saturated and almost saturated soil. There would be no point in trying to obtain such detailed topographic data for the entire area. Model users must carefully consider whether the model they are using is able to exploit more detailed information.

Ultimately, the choice of spatial detail depends on the user's ability to assess whether the simulated response is a better representation of reality. This can be both a quantitative and qualitative assessment and should consider not only whether the specific variable of interest is better represented but also whether the simulated response of interest is affected. If the former is true

but the latter is not, there may still be no value in greater spatial detail since the model structure was unable to use the higher level of information.

10.6   Summary

Three aspects of model testing were addressed: testing of individual internal and external model predictions; model sensitivity to key lumped parameters; and model sensitivity to spatial parameters.

Internal testing progressed approximately in the order of model execution, starting with the micro-meteorological predictions made within Macaque. As described below, it was found that seemingly innocuous errors introduced at the start of simulation can be traced through the entire simulation to errors in key predictions such as evapotranspiration and streamflow.

Encouraging evidence of realistic micro-meteorological simulation was revealed in tests of the temperature, humidity, and radiation components of the model. The key errors could be explained by simple, rectifiable deficiencies in the model. For instance, over-prediction of daytime mean vapor pressure deficit (VPD) in summer was caused by both under-prediction of dewpoint and over-prediction of daytime mean temperature. In turn, the former was caused by both an invalid assumption of daily constant dewpoint and under-estimation of minimum temperature, whilst the latter was also caused by under-estimation of minimum temperature as well as an invalid assumption of intra-day sinusoidal temperature patterns. The same problem with minimum temperature estimation was implicated in over-prediction of solar radiation. In winter, both VPD and solar and net radiation were over-estimated, mainly as a result of over-estimated winter maximum temperatures following the assumption of seasonally constant maximum temperature lapse rates.

These problems could be fixed easily, by making simple improvements to maximum and minimum temperature estimation, and adding bias parameters to the assumption of sinusoidal daily temperature and constant daily dewpoint.

The estimated occurrence of precipitation at a location 5.5 km distant from the base station was temporally consistent with observations, although significant under and over-estimation was common. The estimates were sufficiently accurate to permit their use in the reminder of the model as a realistic model input, but the results clearly illustrate that correlations with base sta-

tion precipitation deteriorate well within the breadth of the study area (*c.* 16 km).

Suitable predictions of precipitation interception and throughfall were reported. The accuracy was as good as could be expected for a daily interception storage model, and was sufficient for the modelling exercise as a whole.

The first major test of the internal operation of the model came with comparisons of observed and predicted transpiration. Temporal patterns matched reasonably well except in mid-winter, but the mean seasonal variations in transpiration did not match at all. This was cited as being partly due to the over-estimation of VPD noted earlier, but mostly due to inaccurate observed data. Despite this, the test broadly provided sufficient evidence that the transpiration component of the model is a realistic representation, and would operate correctly given better input and testing data.

A key aim of the limited distribution function modelling (limited DFM) approach to hillslope modelling employed by Macaque is the ability to simulate the dynamics of deep water tables using the a DFM. The criteria for success in this regard are qualitative: that water tables distant from streams are deep (> 10 m) and relatively static, and that near stream water tables are shallow and dynamic, with seasonal depth variations in the order of one metre. Predicted water table levels at various points along the conceptual hillslope representing the Ettercon 3 experimental catchment were compared with data from transects of piezometers within this catchment. Whilst the spatial framework of the observed and predicted data differed, it was possible to establish that the model predictions met the above criteria for success. The model predicted spatio-temporal water table dynamics which matched those observed, in a way not able to achieved by conventional DFMs. This was therefore a validation of the limited DFM approach conceived as part of the present study.

In the unsaturated zone, similar incompatibility existed between the spatial nature of observed and predicted data, but a conversion was devised which facilitated meaningful comparison. The resulting test of predicted versus observed soil moisture revealed accurate prediction of seasonal, and inter-annual soil moisture variations. The need for conversion of the predicted data did however highlight a possible structural limitation of the model, which might be improved by a two layer (root zone and deep soil) representation of the unsaturated zone.

The prediction of streamflow is particularly challenging in physically based long term studies because of the range of time scales which will necessarily

be involved until an *inherently* monthly or annual physical description of the hydro-ecological system emerges. Specifically, it is difficult to simulate simultaneously daily and annual hydrographs spanning one century. Two sets of hydrograph prediction results were presented. The first was based on standard model parameters with the key hillslope parameters calibrated largely against observations of water table dynamics. Daily patterns were accurate, but with increasing temporal aggregation of the results, the amplitude of the simulated hydrograph became progressively under-estimated. This was rectified in the second set of results, where the two parameters controlling water table depth and dynamics were calibrated against observed hydrographs. This calibration involved some deterioration of internal water table predictions, indicating ample scope for improvement of the streamflow generation and water table prediction components of the model.

Each of the tests of internal and external model predictions highlighted limitations and capabilities of the model. None of the limitations are considered so serious as to invalidate the model. Indeed, considering the requirement of just three daily time series inputs, precipitation and maximum and minimum temperature, encouragement is drawn from the ability of the model to simulate daily through to yearly hydrographs through a detailed and validated representation of the key hydro-meteorological controlling processes. Many of the observed errors can be traced back to a single source, in particular, the simplistic representation of maximum and minimum temperature lapse rates. Simple improvements at the most basic meteorological level should propagate as significant improvements throughout the entire model.

A number of lumped parameters known to exhibit high sensitivity relative to certainty were singled out for a basic sensitivity analysis. Gross variations in predicted ET and streamflow were caused by perturbations of the key temperature, ET, and soil parameters within acceptable ranges. In most cases, the implied uncertainty is reduced when additional constraints are introduced through calibration against internal variables such as canopy transpiration, understorey transpiration, soil evaporation, and hydrograph shape. With respect to precipitation parameters, it was argued that the sensitivity of predicted streamflow to precipitation estimation will always be very high in non-water limited, high ET areas such as the study area.

Model sensitivity to spatial parameters was also tested, using various maps of precipitation, LAI, and topography. Very high spatial and lumped sensitivity to different precipitation maps was reported. The possibility was raised that a single gauge may be responsible for this sensitivity, indicating the need for careful consideration of model data sources and the way in which they

are used. The model was spatially sensitive to differences in LAI maps, although to a lesser extent than for precipitation. Lumped sensitivity to LAI is implied but not observable given the similar mean LAI of the two maps. Whilst topographic sensitivity is almost certain (but untested) *at large scales* due to variation in radiation, very little sensitivity in hydrograph prediction was observed as a result of significant differences in the representation of a small (15 ha) first-order catchment by two *small* DEMs. This latter point suggests that, in specific cases, it is possible to reach a limit in spatial model parameterisation where the sophistication in parameter mapping exceeds the ability of models to represent hydrological responses to parameters.

Chapter 11

Application to land cover scenarios

Contents

An earlier version of this Chapter was published as a conference paper (Watson et al., 1997b) which was written by the present author and reviewed by the co-authors.

11.1   Introduction: the 1939 fires

The most influential event in the recent history of the Ash forests of Victoria was the 1939 fires (Paine, 1982). These fires razed most of the forests in the state including most of the study area (see Figure 9.2). As noted in Chapter 1, the ensuing hydrological effects manifested as a long term reduction in water yield and are well known, at least for *E. regnans* forests. The Kuczera curve (Figure 1.1) is based on an analysis of long term hydrographs from a number of affected water supply catchments in the period spanning 1939 and is currently the best description of the effects of the 1939 fires, and of the effects of complete forest regeneration in general.

The fires represent an historical scenario of large scale land cover change which is used in this final non-discussion chapter as a test of Macaque's ability to predict the effects of land cover change using a large scale, physically based modelling approach. Effectively, an attempt is made to model the Kuczera curve.

Perhaps curiously, the hydrological effects of the 1939 fires have never been modelled using a water balance model (pers. comm., H. Duncan, J. Langford, P. O'Shaughnessy, M. Jayasuriya, D. Heeps). This is despite great research interest stimulated by the 1939 fires involving extensive hydrological modelling, experimentation, and hydrograph analysis in the past few decades by Melbourne Water and its predecessor, the MMBW. Note that Williamson (1989) *did* model long term water yield spanning 1939 using forest growth/ET correlations instead of a water balance approach. This approach differs from the present in that the inputs (i.e. forest growth data) are not independent of, and external to the terrestrial hydrological system (as are the climatic inputs of typical water balance models). Williamson's approach could not be used to predict the effects of future land cover scenarios which differed greatly from those already observed.

11.2   Method

Macaque was designed such that the move from short term simulation of small experimental catchments (as in the previous chapter) to long term water balance simulation of the whole study area is simply a matter of supplying long enough records of input data. Hence, there is no specific method associated with the long term simulation process. For convenience however, the relevant methodological points made throughout the present dissertation are

brought together here.

An aim of the present study is to investigate long term water balance simulation *in response to land cover change.* Within the model, the intent is to express land cover change through changes in forest age and hence LAI. Indeed, the only means by which we initially expect to see long term trends in simulated water yield is through the expression of time-dependent LAI curves. As described in Chapters 8 and 9 for the Ash-type forests which dominate the study area, two such curves were constructed and incorporated into Macaque as time-dependent parameters.

The two curves, from Figures 9.15 and 8.26, are combined for ease of comparison and reference below as Figure 11.1. Individual data points relating to the curves are retained in the plot because the error in the curves relative to these points is relevant in discussions below pertaining to the uncertainty of LAI parameterisation.

The total LAI curve for *Eucalyptus regnans* forest was derived through correlation of satellite vegetation index (TNDVI) and ground-based measurements of total LAI. It predicts total LAI rising from zero at age zero to a peak of over 5 at about 8 years of age, declining rapidly to just over 4 at age 20, and then more gradually to about 3.5 during the next two centuries.

The canopy LAI curve for *E. regnans* was derived by combining a series of regression equations linking destructive measurements of LAI with mensurational statistics quantifying DBH, stocking density, and age. It predicts canopy LAI remaining at zero for the first 5 years following clearing, rising rapidly to nearly 4 at just over 10 years of age, and then declining exponentially to below 1.5 during the next two centuries.

The spatial distribution of LAI at any time during the simulation is calculated by applying the time-dependent LAI curves above to the Ash-type forests, and applying temporally constant values to all other species. The distribution of species is known from detailed forest type mapping undertaken by DNRE.

All other parameters of the model were as set out in the table summarising the standard parameter set (Table 5.2), except for the following. As summarised in Table 11.1, The hydrograph/water table calibration parameters, Δ_{sat} and δ, were manually calibrated to maximise the accuracy of annual streamflow predictions whilst retaining acceptable accuracy in daily, weekly, and monthly hydrographs (in the period 1980-1989). The hydraulic gradient, Δ_z, was manually calibrated to yield accurate stormflow peaks in the daily hydrograph, and the maximum canopy conductances, $g_{cl,max}$ and $g_{ul,max}$, were manually calibrated to reduce ET and thereby increase stream-
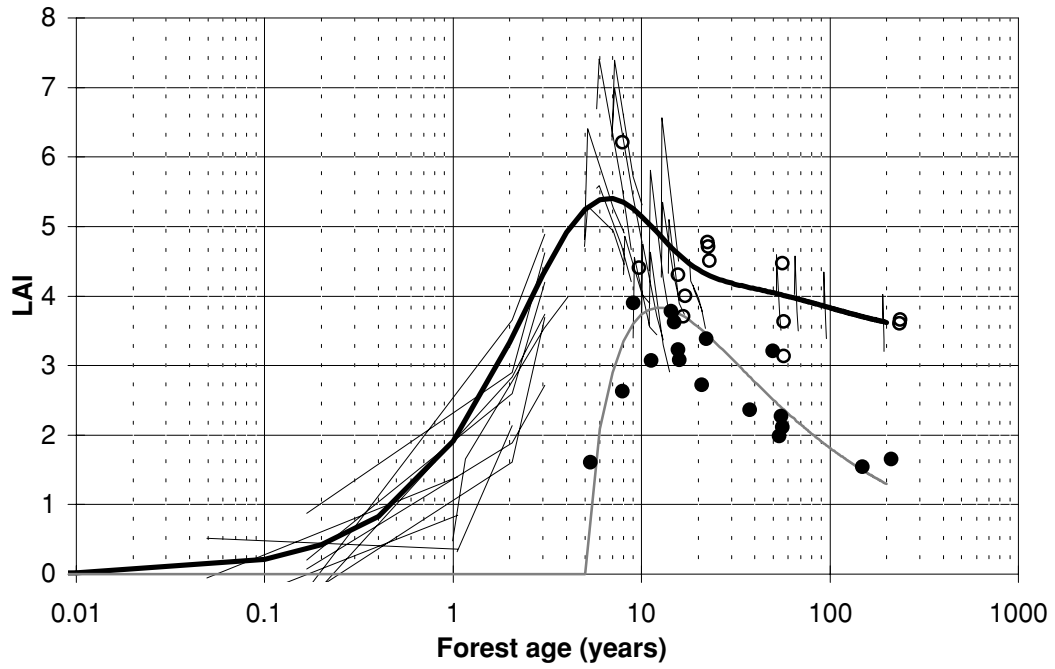
Figure 11.1: Combined plot of total (upper curve) and canopy (lower curve) *E. regnans* LAI curves from Figures 9.15 and 8.26. The auxiliary data points are described with the original Figures.

Parameter	Standard value	Value calibrated during model testing in Chapter 10	Value calibrated for large scale application (present chapter)	Unit
Δ_{sat}	-6.5	-10.5	-3.0	m i_{wet}^{-1}
δ	0.001	0.0002	0.0005	day^{-1}
Δ_z	0.005	-	0.01	-
$g_{cl,max}$	0.005	-	0.0023	m s^{-1}
$g_{ul,max}$	0.005	-	0.0023	m s^{-1}

Table 11.1: Re-calibration of parameters for large scale modelling.

flow to match annual observations in the period 1980-1989. Note that the maximum canopy conductance values are lower than those typically observed for *E. regnans* (see Section 5.3.12.3). This is partly due to the fact that no account is taken within the model of likely reduced maximum conductance of both understorey species and non-Ash type canopy species. All of these changes from the standard parameter set reflect the change of scale and increase in spatial heterogeneity from experimental catchments to water supply catchments. The most appropriate values for the three parameters Δ_{sat}, δ, and Δ_z would be expected to change with hillslope shape (i.e. steepness and degree of convergence). Ideally, they would be varied for each hillslope based on measurements from the DEM. However, the exact relationship with the DEM is not certain, and hence, lumped calibrated values must be chosen reflecting some form of large scale mean hillslope shape. These values are likely to differ from the values calibrated at Ettercon 3 because, as a hillslope, Ettercon 3 is not completely representative of the larger area. Similarly, not enough is known about inter-specific variations of maximum leaf conductance within the plant species of the region to warrant a systematic determination of the spatial variability of maximum leaf conductance. However, such variation is likely to exist at scales such that a difference would be observed between the mean leaf conductance of a small experimental catchment and that of the larger water supply catchments. Depending on spatial structure, spatial variability in land surface parameters can lead to changes in effective means when one moves between scales.

Monthly streamflow data were available for the three largest water supply catchments from 1910 to the present (Watts, F0720; Grace Burn, F0584; and Coranderrk, F0020). The records were summed into a single, aggregated streamflow record representing a combined catchment area of 145 km^2 (F9000). Thrice weekly precipitation data from 1910 to the present were available for a site at Blacks' Spur inside the study area (F1910). These were pro-rated to construct a long term daily record (F1911) using more

frequent data from Warburton post office (F1195). As shown below, the pro-rated data lead to significantly better hydrograph predictions than raw data from less central sites. Daily maximum and minimum temperature data were taken from the Melbourne Regional Office station of the Bureau of Meteorology (F2540). This is the nearest long term record to the study area which spans 1939.

The model was run on the entire study area for the period 1910 to 1993 using the parameters, parameter maps, and time-series inputs as described throughout the present dissertation and summarised above. Initially, results from the calibration are presented to demonstrate that minimal loss of accuracy has occurred during the scaling-up process. Then long term results are presented from a run using temporally constant LAI values to provide a simulation of the *null hypothesis that LAI does not vary with age*. The constant values were determined by evaluating the equations for the LAI curves at age 50. This gave values for LAI_{tot} of 4.05 and 3.75 for *E. regnans/E. nitens* and *E. delegatensis* respectively, and a value for LAI_c of 2.51 for all Ash-type species. Finally, results are presented from a run using the LAI curves as summarised above, effecting the *hypothesis that changes in water yield are caused by changes in ET through its dependence on LAI*. This is followed by an interim discussion of the above results before more simulations are presented.

11.3   Calibration results

Figures 11.2 to 11.5 show predicted and observed hydrographs for the summed water supply catchments at daily to water yearly time scales. Whilst not quite as well matched as the calibrated hydrographs for the Ettercon 3 experimental catchment (see previous chapter), the accuracy of the hydrographs for the water supply catchments is acceptable at all time scales. This indicates that, notwithstanding the fact that five parameters required re-calibration against hydrographs, the scaling-up from experimental to water supply catchment was successful.

11.4   Long term water balance

The simulated total water balance of the summed water supply catchments is plotted yearly in Figure 11.6. The Figure is based on a model run with no temporal variation in LAI or conductance (see below). Later, a similar
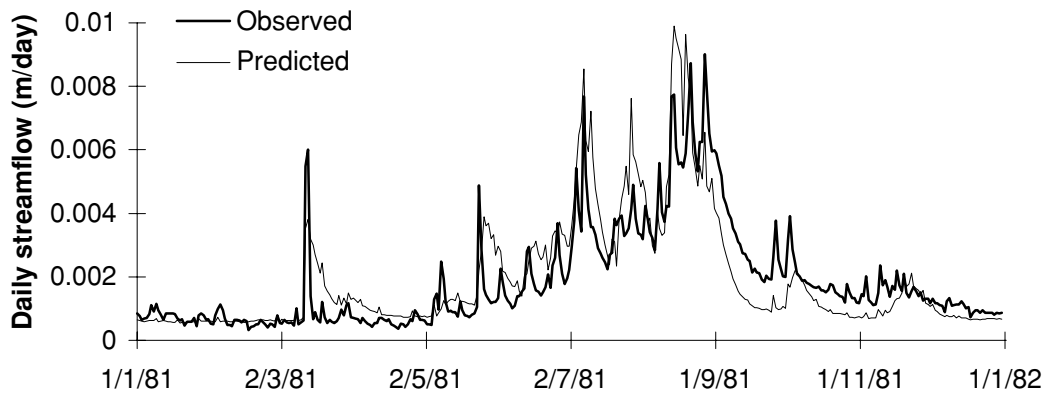
Figure 11.2: Daily predicted and observed hydrographs for the summed water supply catchments.
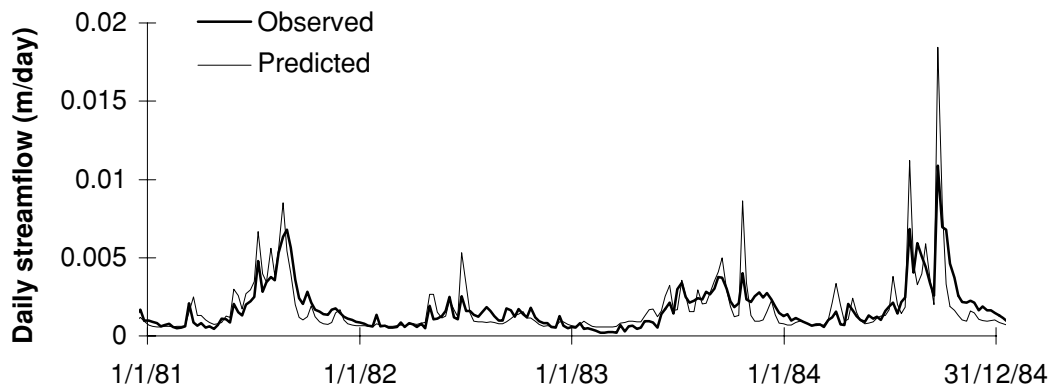
Figure 11.3: Weekly predicted and observed hydrographs for the summed water supply catchments.
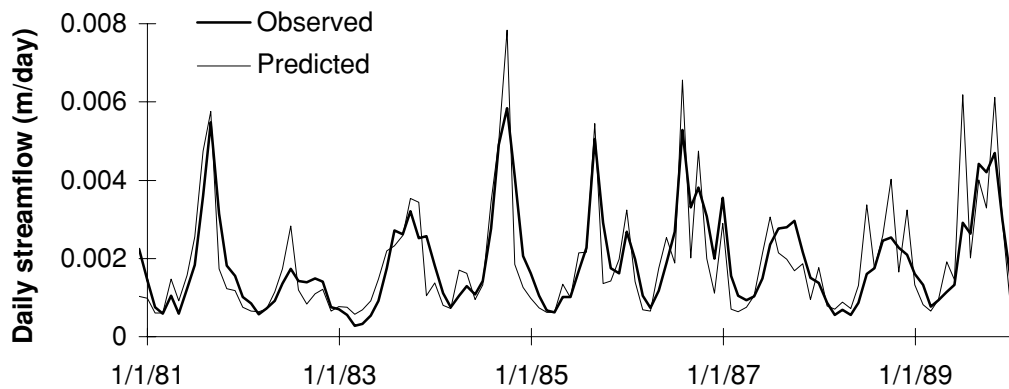
Figure 11.4: Monthly predicted and observed hydrographs for the summed water supply catchments.
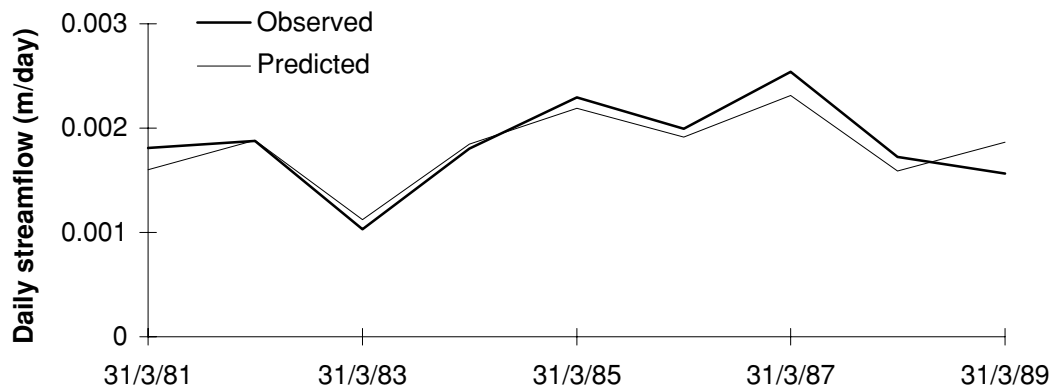
Figure 11.5: Water-yearly predicted and observed hydrographs for the summed water supply catchments.

figure drawn from a more final model run is presented.

The figure provides some additional confirmation that model is operating as expected at large scales. The major components of the water balance are represented as percentages of the simulated precipitation for each year. Thus, all elements should add up to 100% in the long term. The fact that this is so confirms that a water balance is, in fact, achieved and there are no accounting errors within the model. The balance may be in surplus or deficit in any given year due to changes in soil water storage. The largest single component of those represented in the Figure is streamflow, followed by canopy and then understorey transpiration. Soil evaporation and total interception represent smaller fluxes, being around 10% of the water balance each. Changes in storage can be over 20% of the precipitation in some years, but accumulation or depletion of storage rarely persists for longer than one or two years. None of these observations contradict the perceptual model of catchment water balance which may be discerned from the various data sources discussed in the previous chapter.

11.5   Long term hydrographs using constant LAI

Figure 11.7a shows long term predicted and observed streamflow for the summed water supply catchments, and Figure 11.7b shows the percentage error in prediction.

The first thing one notices about these figures is that the idealised form of
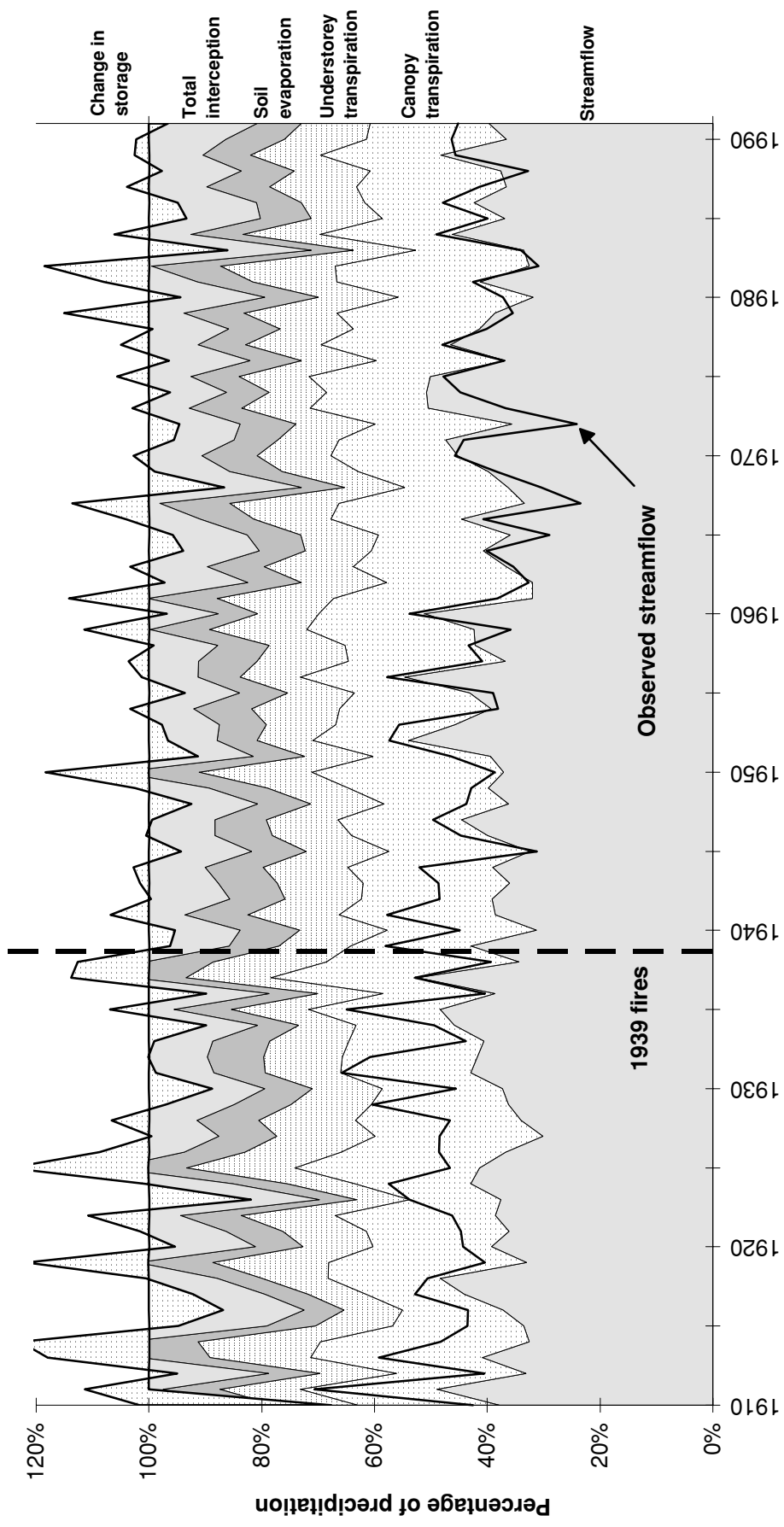
Figure 11.6: Long term simulated water balance of the summed water supply catchments (under constant LAI and constant conductance configuration).
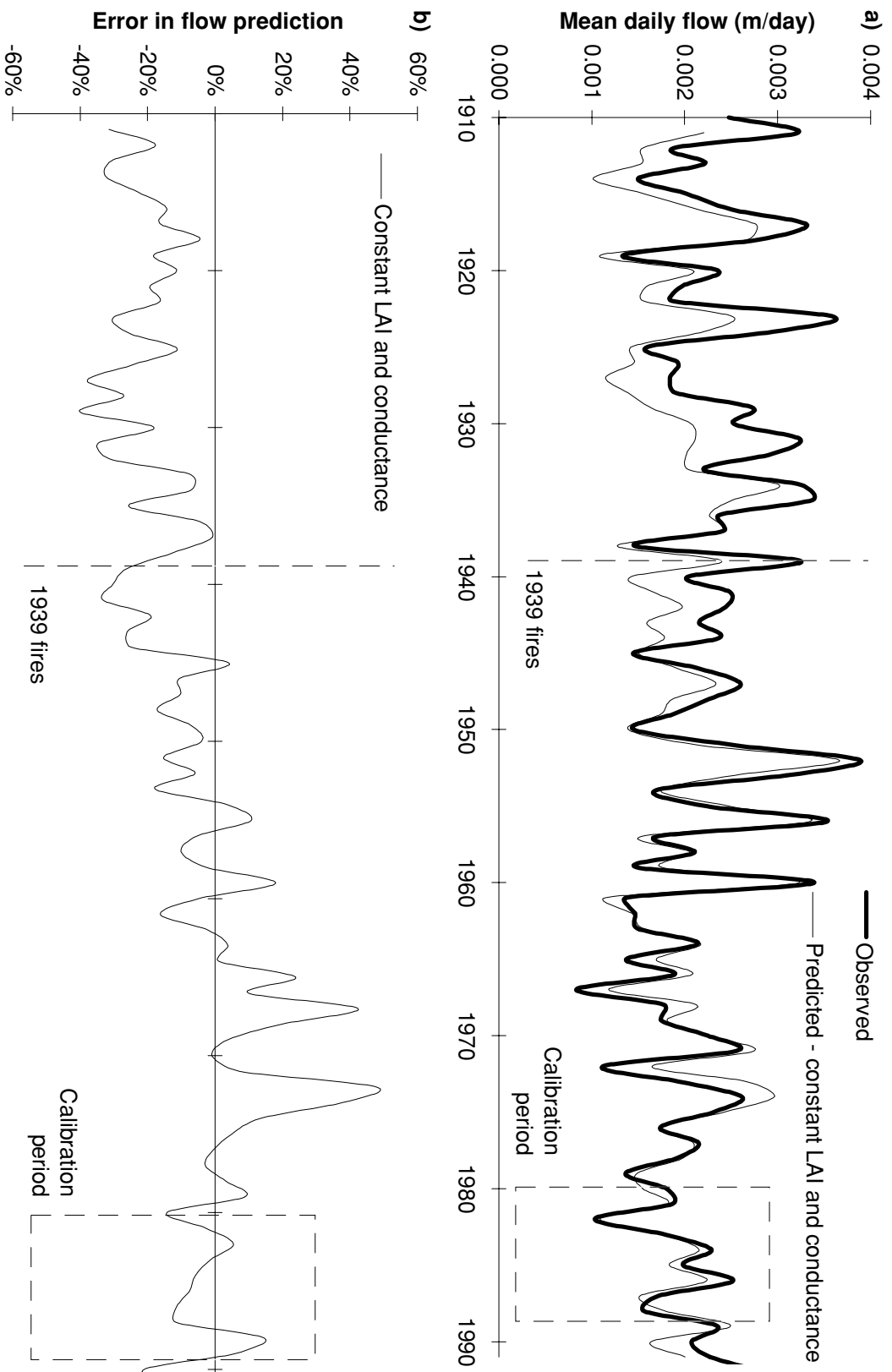
Figure 11.7: Long term water-yearly predicted and observed hydrographs for the summed water supply catchments using constant LAI: a) absolute values; b) prediction error.

the Kuczera curve (Figure 1.1) is not obviously apparent in the *observed* data. There is considerable variability at time scales of around one to two years, and at larger time scales, any drop in flow in the decades following the 1939 fires is apparently quite small. Precipitation accounts for much of the observed short and medium term variability, but even when the observations are expressed as fractions of annual catchment precipitation (not shown), the long term patterns in observed flow are not obvious. As discussed below, possible reasons for this dilution of the patterns approximated by the Kuczera curve include: the fact that not all of the study area was burnt in 1939, nor is all of it forested with Ash-type species (the species to which the Kuczera curve pertains); and, because the extent of the 1926 fires in particular is unknown, it is unknown to what extent the pre-1939 forest was 'old-growth'.

Turning to the simulated data, the short term temporal signals in the predicted and observed hydrographs match well but there are gross absolute errors during various parts of the century. Near the calibration period, the errors are small, but in the period prior to the 1939 fires, when the forest was oldest, the hydrograph is consistently under-predicted. This is expected. The null hypothesis of temporally constant LAI effected by this simulation is expected to result in lower flow for the oldest forests because no decline in LAI (and hence ET) is simulated for these forests. Similarly, over-prediction occurs from about 25 to 40 years after 1939, which is also expected because this is the period of maximum flow reduction predicted by the Kuczera curve. The period of under-prediction immediately following the 1939 fires is longer than expected. This is the time when observed flows would be higher than at other times due to the loss of forest cover. Kuczera (1985) suggests that this period might last two years, but the present data indicate that five years might be a more reasonable figure.

11.6   Long term hydrographs using LAI curves

Simulations conducted using the temporal LAI curves were expected to produce improved predictions of long term water yield trends. The results are shown in Figure 11.8 which overlays the additional results onto the results of the previous simulation. As expected, clear improvement is shown in the pre-1939 period and little change is apparent near the calibration period. Also, the few years immediately following the 1939 fires are better predicted. However, the pre-1939 predictions have not improved enough, and the predictions from 5 to 15 years after the 1939 fires have worsened. This latter period coincides with the peaks in both total and canopy LAI predicted

by the temporal LAI curves above. It is possible that moisture storage in the deep soils of the catchment induce a delay in water yield response of a few years which is not properly simulated by the model. Such delays have been observed in South African studies of the hydrological effects of eucalypt forestry (Scott and Lesch, 1997). However, the most important result here is the gross difference between regrowth and old-growth yield.

This result leads us to question either the shape of the temporal LAI curves, or the hypothesis that the relation between water yield and forest age is explained by LAI changes. They suggest that other factors must be considered before a complete explanation is possible.

11.7   Interim discussion

The only age-variant parameters of the model, as used in Figure 11.8, are total and canopy LAI. There are a number of possibilities as to why LAI changes do not fully explain the observed age/yield relation:

1. Leaf conductance may decline with age. This is discussed below.

2. Currently, canopy and understorey leaf conductance are modelled as being identical. However, canopy leaf conductance may be greater than understorey leaf conductance, and because canopy LAI declines faster than total LAI (see Figures 3 and 4), this would manifest as a greater decline in transpiration with age. This has not yet been tested.

3. Non-Ash type forests may exhibit LAI decline as well as Ash type species. This is likely to be the case, although unlikely to induce the required hydrograph changes because the water yield from, and area covered by these drier forests is small.

4. The aerodynamic resistance, particularly between the understorey air and that above the canopy, may increase as the forest increases in height. Preliminary calculations indicate this increase is insufficient (as a single agent) to reduce ET by the necessary amount. Aerodynamic resistance may also be high in 5 to 15 year old forests which are typically very dense.

5. Moisture saturation may be occurring in younger forests to a greater extent than is currently simulated. The model simulates the reduction of driving moisture gradients for lower evapotranspiring layers by higher layers, but not self-saturation of the atmosphere within a given layer.
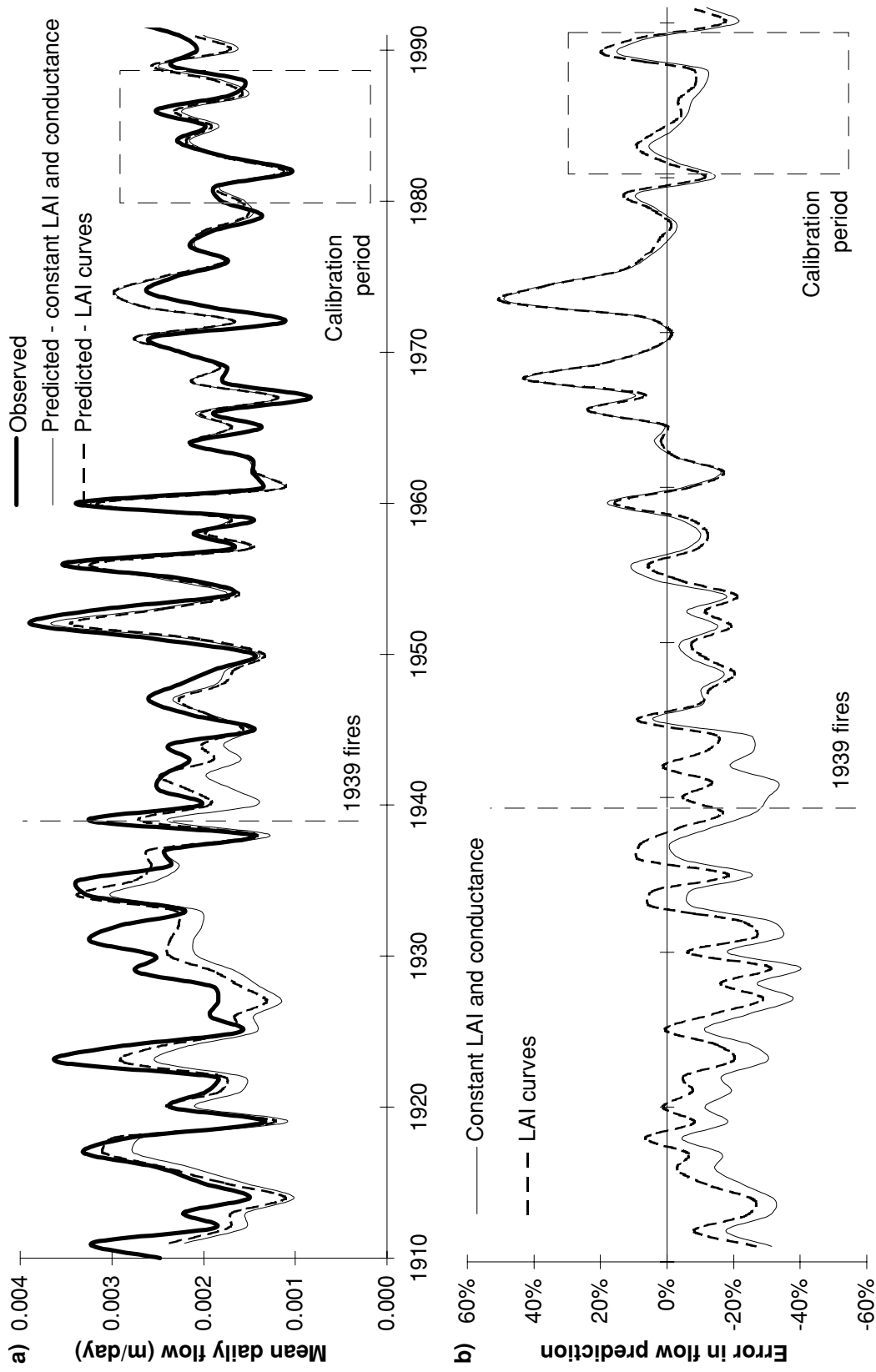
Figure 11.8: Long term water-yearly predicted and observed hydrographs for the summed water supply catchments: as for Figure 11.7 but including results using LAI curves (see text).

These processes, if significant, are likely to be more pronounced in younger, more dense forests.

6. The precipitation and/or streamflow records may contain errors. These possibilities were tested using double mass curves and associated analyses. Apart from the known bias in the Maroondah Dam precipitation record (Kuczera, 1985), which is not used here, there are no major trends in the precipitation data. The streamflow data originate from a network of crude, box-section spillways and aqueduct levels, and typical 'observations' are the sum of a number of gauged intakes and diversions, as well as visual estimates of the level of the Maroondah reservoir. It is possible that this gauging system could introduce significant temporal and mean errors in the observed data. This possibility is partly examined in Section 11.10.1.

7. The model may be wrong.

8. The LAI curves may be wrong. In particular, predicted hydrographs are likely to be quite sensitive to fine tuning of the timing and height of peaks in LAI, and of the rate of long term LAI decline. If the peaks in the total and canopy LAI curves occurred about 15 years later than those represented in Figure 11.1, the problem of under-prediction from 5 to 15 years after fire and over-prediction from 25 to 40 years after fire would be lessened. However, this would require moving the curves significantly away from measured LAI values. Given the scarcity of LAI measurements in old-growth forests, the curves could more easily be adjusted to predict a more severe decline in LAI in the long term.

9. As noted earlier, the fire history presented to the model may be wrong. In particular, the extent of the 1926 fires may have been under-estimated.

11.8 Model run with leaf conductance curve

Possibility (1) above was investigated further as the most logical avenue of improvement:

There is evidence to suggest that mean maximum leaf conductance in *E. regnans* forests declines markedly with age. This evidence centres around two observations discussed below: that stand sapwood area (SA) per unit LAI declines with age; and that mean daily sapwood velocity is constant with age.
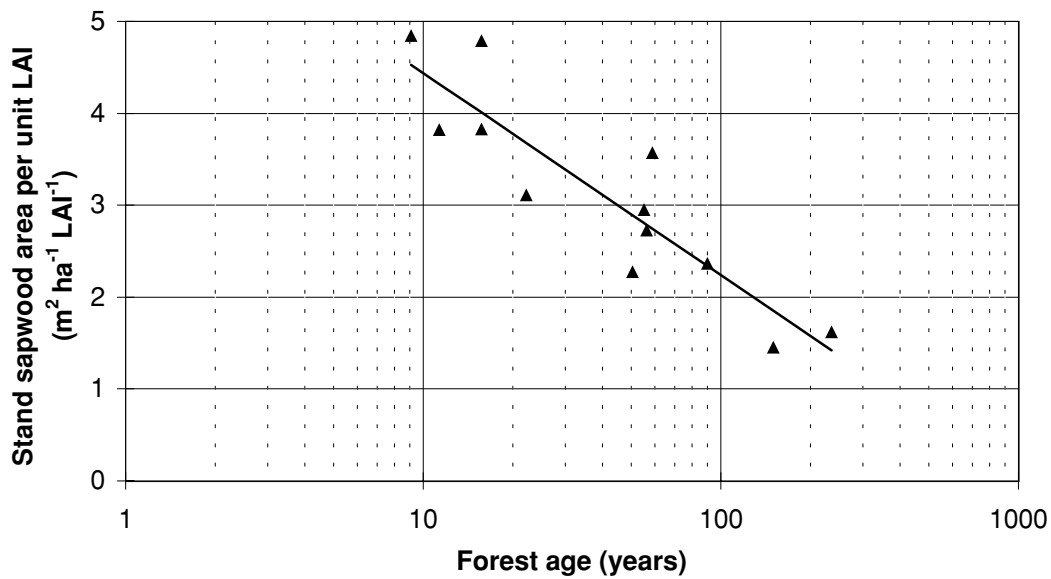
Figure 11.9: Observations of sapwood area per unit LAI plotted against forest age for *E. regnans*.

Data on SA per unit LAI were assembled by R. Vertessy (unpublished analysis) from a range of recent experimental work in the study area (including: Dunn and Connor, 1993; Vertessy et al., 1994b, 1995a, 1997; Haydon et al., 1996; O'Sullivan, in prep.). The data include stand SA values for 13 sites obtained by scaling a sample of direct SA measurements to stand values using site-specific SA/DBH regression equations. Corresponding LAI values were derived using equations relating individual tree leaf area (LA) to DBH. Seven of the LAI values resulted from site-specific LA/DBH equations developed from destructive LA measurement at the site. The remaining six LAI values were obtained using the general *E. regnans* LA/DBH model given in Chapter 8 (Equation 8.29) and published by Watson and Vertessy (1996). Figure 11.9 plots the 13 SA/LAI values against forest age. A clear downward trend is evident and is characterised by the following regression equation:

$$SA/LAI = 6.64 - 0.956 \ln(AGE) \quad n = 13, r^2 = 0.81 \tag{11.1}$$

where SA/LAI is in m^2 ha^{-1} LAI^{-1} and AGE is in years.

The observation that mean daily sapwood velocity in *E. regnans* forest remains constant with age was initially made by Dunn and Connor (1993) based on data from 50, 90, 150, and 230 year old stands. This was later corroborated by additional data from Vertessy et al. (1995a and 1997) in 15 and 56 year old stands.

The most plausible explanation of the observations that stand sapwood area per unit LAI decreases with age whilst sapwood velocity remains constant is that the velocity of water flow through the leaves (the leaf conductance) also decreases. Since external factors controlling *instantaneous* leaf conductance (e.g. radiation, VPD) are unlikely to vary sufficiently between young and old forests, this implies that the mean emphmaximum leaf conductance of *E. regnans* forests declines with age. This may be caused by slower leaf replacement in old forests and hence a greater abundance of older, gummed-up leaves; and/or by increased water stress in the leaves of taller, older forests. The 'old leaf' theory may have some generality, being supported by observations of declining maximum conductance of individual conifer leaves with leaf age (Lee, 1980) and noted in Körner et al's general review of leaf conductance (Körner et al, 1979).

Making the assumption that maximum leaf conductance is directly proportional to SA per unit LAI, Equation 11.1 was modified to predict the maximum leaf conductance of any *E. regnans* forest given its age, and the maximum leaf conductance of a 'standard aged' forest, in this case 50 years. The resulting equation is:

$$g_{cl,max,age} = g_{cl,max} \, \frac{6.64 - 0.956 \, \ln(AGE)}{2.90} \qquad (11.2)$$

where $g_{cl,max}$ is the specified maximum canopy leaf conductance (assumed to be at age 50), $g_{cl,max,age}$ is its age-dependent equivalent, and 2.90 is the value of Equation 11.1 at age 50.

The model was run including the modification to maximum canopy leaf conductance introduced by Equation 11.2. Figure 11.10 shows the resulting simulation.

A significant change in the hydrograph for older forests is evident. The under-prediction of streamflow from 5 to 15 years after 1939 has worsened, whilst the over prediction following that period has remained the same. In mean terms, the under-prediction in the pre-1939 period has been eliminated, but errors remain in certain periods, particularly around the late 1920's. This latter observation again flags the possibility that the extent of the 1926 fires was underestimated in these simulations (see Figures 9.2 to 9.4).

In general, the inclusion of both LAI *and* conductance curves has led to acceptable predictions of long term changes in water yield resulting from land cover change. However, there are still problems in the medium term (first few decades after fire). The accuracy achieved reflects well on the

model validity given the uncertainty resulting from areas such as: lack of knowledge about pre-1939 fire history; and sensitivity to precipitation inputs (see Sections 10.5 and 11.10). The successive improvements resulting from the inclusion of LAI curves, and then conductance curves suggests strongly that changes in both these variables over time must be invoked in order to explain long term changes in water yield. This does not however preclude the influence of long term changes in other variables such as aerodynamic resistance. It is quite possible that a number of influences act in concert (but not necessarily in unison) to cause the observed changes in water yield.

11.9 Final simulated water balance

As noted earlier, a similar water balance plot to that given in 11.6 is presented below in Figure 11.11 based on the final model run above with both LAI curves and conductance curves. Accompanying this in Figure 11.12 is a plot of mean simulated catchment LAI during the modelling period. The water balance plot illustrates a number of expected interactions resulting from the temporal variations in LAI and conductance. The most obvious of these is the large difference in canopy transpiration between the pre- and post- 1939 fires period. This is partly compensated for by an inverse pattern in understorey transpiration. The understorey is most dense beneath the oldest canopies. A slight response in soil evaporation is simulated, this flux being greater beneath more sparse vegetation due to increased penetration of radiation to the forest floor, and less reduction of VPD due to transpiration. Similarly, a slight response in total interception is simulated in response to, and in unison with the LAI changes that cause the response in transpiration. Note that simulated variations in LAI (Figure 11.12) are not as marked as those predicted by the original LAI curves (Figure 11.1) because they are diluted by areas of non-Ash type vegetation for which an approximately constant LAI is simulated. Note also that a *very* slight dip in LAI is simulated for the 1926 fires. Some of the observations discussed elsewhere in this chapter would suggest that a much greater effect is more appropriate and that the area affected by the 1926 fires (see Figures 9.2 to 9.3) has been significantly under-estimated in the present study.
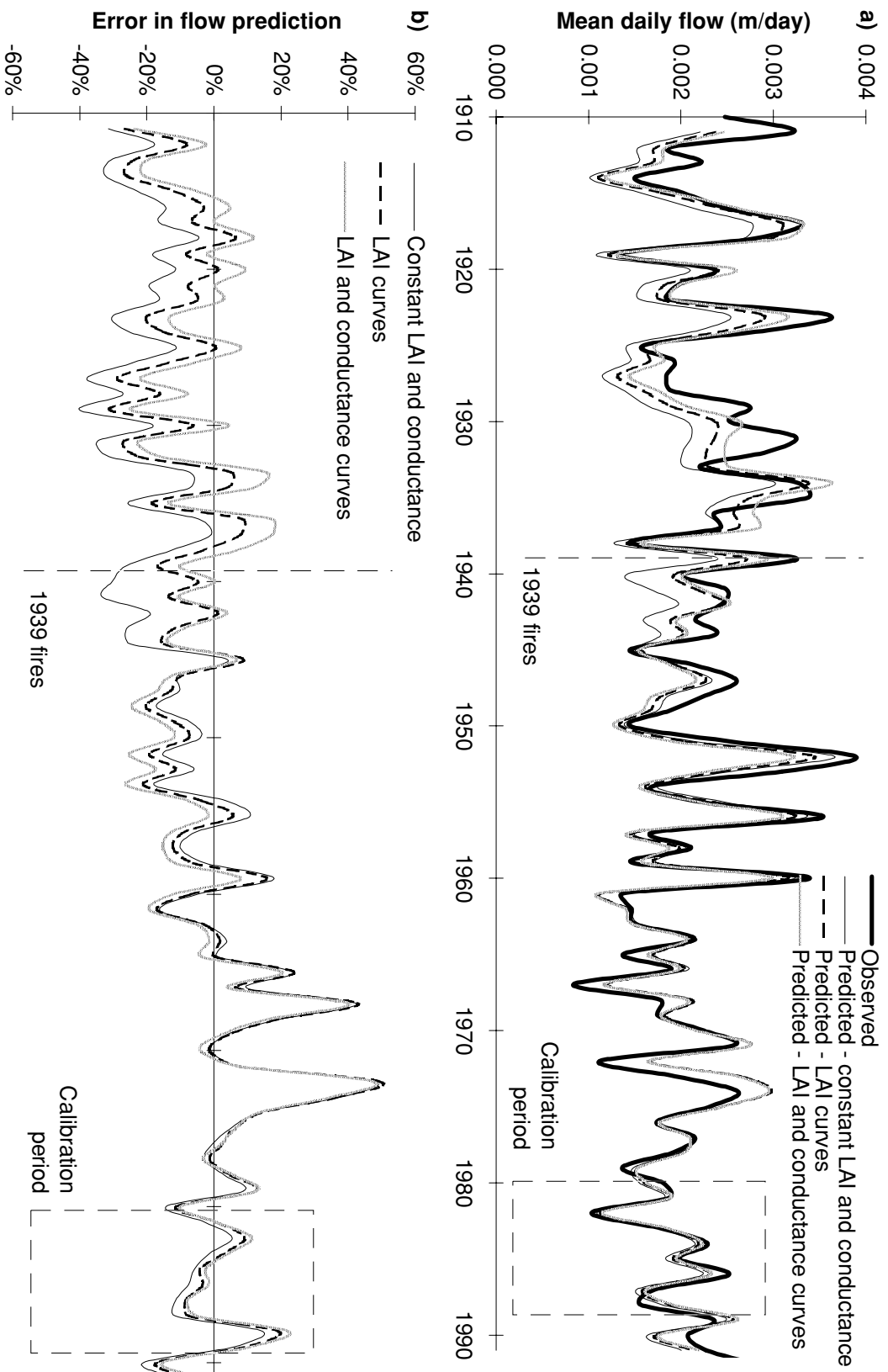
Figure 11.10: Long term water-yearly predicted and observed hydrographs for the summed water supply catchments: as for Figure 11.8 with temporally varying maximum leaf conductance (see text).
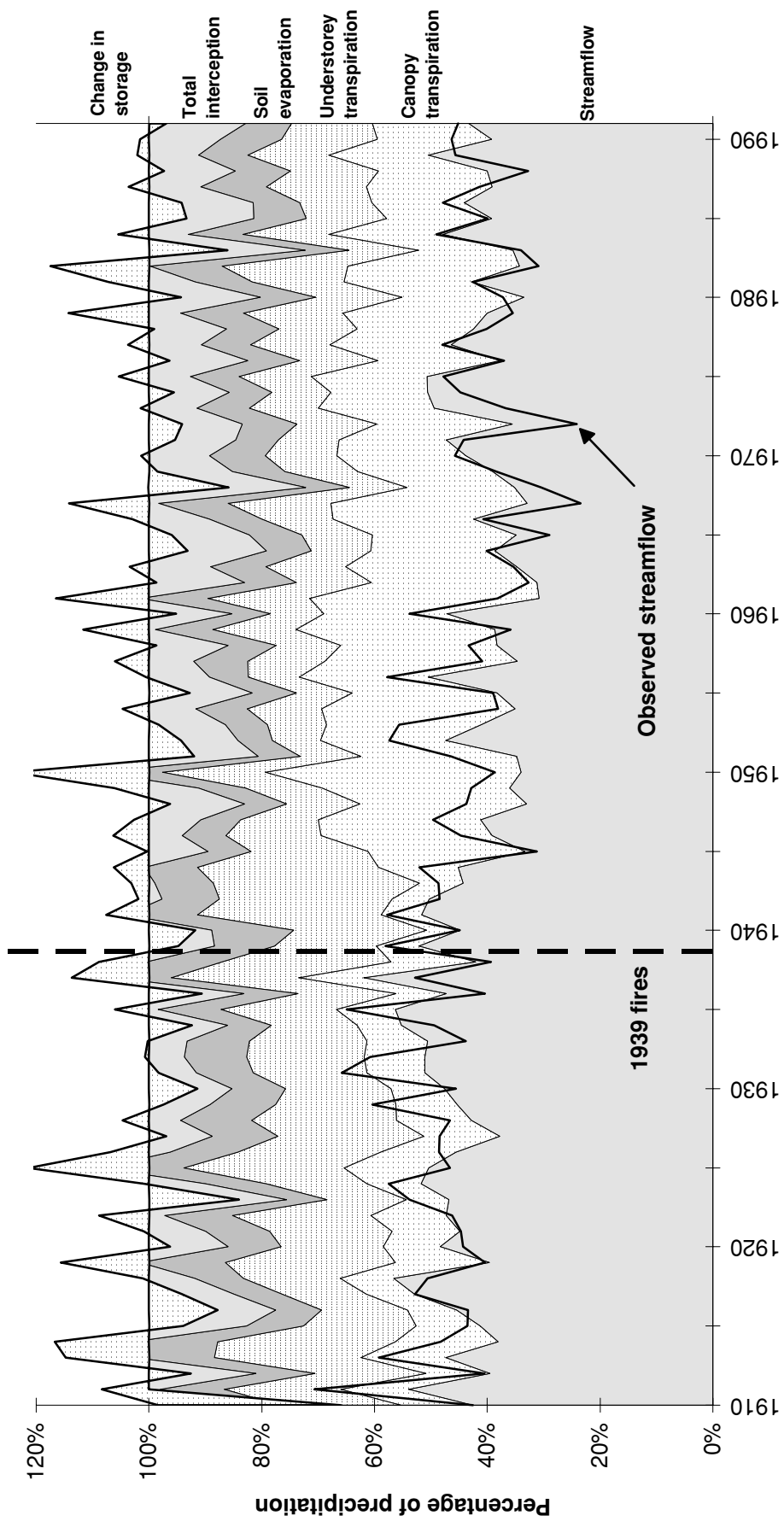
Figure 11.11: Long term simulated water balance of the summed water supply catchments (under configuration with both LAI curves and conductance curves).
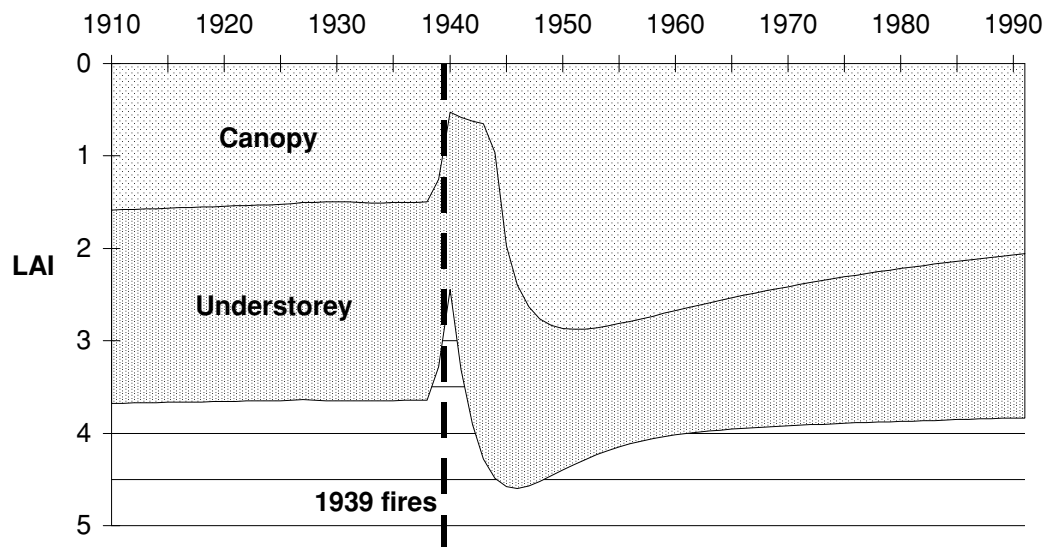
Figure 11.12: Catchment mean simulated canopy and understorey LAI for the final model run with curved LAI and curved conductance.

11.10 Final sensitivity analysis

Model testing and sensitivity analysis was the focus of the previous chapter, but a final, important addition to this process emerged from the present chapter. This concerns the effect on simulated water yield of precipitation variability and the use of different long term precipitation records to drive the model.

The *preliminary* model runs for this chapter were done using the precipitation record from Warburton post office (F1195). At this time it was noticed that there were considerable differences in the short term (one to two years) temporal signals in the predicted and observed hydrographs. As the short term signal is likely to be largely determined by the short term variability of the time-series inputs, it was hypothesised that the inconsistency between predicted and observed water yield was due mostly to either: poor precipitation time-series data, poor extrapolation of this data to areal estimates, or poor hydrographic data. Two of these possibilities are investigated below, starting with an examination of variability in the observed hydrographic data. This is followed by analyses of model sensitivity to the source of precipitation time series input.

11.10.1   Variability in observed hydrographs

Fortunately, the observed hydrograph used in this chapter is actually the sum of three hydrographs (see Section 11.2 from three neighbouring catchments. These hydrographs may differ in temporal pattern from each other either because of inaccurate gauging, or spatial variability in streamflow resulting largely from spatial variability in precipitation. In either case, the accuracy/variability *cannot be quantified at present* and therefore places a limit on accuracy of streamflow predictions which may be expected to be achieved using *any* model. These concerns were examined by:

- constructing regression equations for each of the three catchments between their water yield and the sum of the other two,

- using these equations to construct water yield predictions for each catchment based on the water yield data from the other two,

- and examining the difference between the observed water yields and those expected from the predictions.

Figure 11.13 plots the percentage difference between the water yield of each catchment and the expected value based on the water yield of the other two catchments. The most obvious feature is the period of much higher than expected flow for Grace Burn in 1914-1915. Monthly comparisons using similar techniques revealed that this feature is *not* the result of a single data entry but rather persists in most months from late 1913 to mid 1915. Perhaps the standard hydrographic procedure for Grace Burn was changed during the War? This would indicate a rather severe gauging error.

In the remainder of the plot, individual catchments often vary by $\pm 20\%$ from their expected value. However, the typical variation is the same for each catchment and there are no violent deviations. The clearest long term trend in the plot is the continual decline in flow at Grace Burn (relative to that expected) from about 1924 onwards. This is easily explained by the fact that the Grace Burn catchment was the most affected by the 1939 fires (see Figure 9.2). It therefore exhibits the greatest decline in water yield following the 1939 fires, and possibly also the 1926 fires.

It is conceivable that 20% errors occur in observations of total annual streamflow. As noted in Section 11.7, parts of the streamflow gauging system are crude. On the other hand, it is also quite conceivable that spatial heterogeneity in precipitation can lead to real 20% differences in the temporal streamflow signal between neighbouring water supply catchments (as discussed in
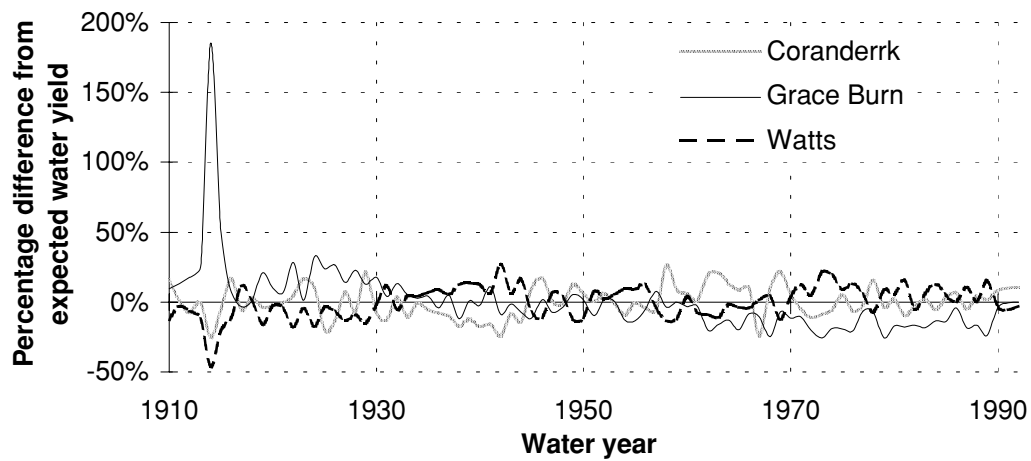
Figure 11.13: Verification of long term observed hydrographs.

Section 10.5.1). The important point is that, whatever the source of variability in observed hydrographic data, about 20% of it cannot be quantified.

11.10.2   Sensitivity to source of precipitation time-series

Attacking the problem from the opposite direction, simulations of water yield for the summed catchment were conducted using different precipitation stations in order to quantify the model's sensitivity to the spatial location of input precipitation data. In addition to the (artificial) Blacks' Spur precipitation data (from inside the study area) used in the final simulation above, model runs were conducted using precipitation data from Warburton post office (F1195) just south of the study area, and Mount St Leonard (F0970) on the northern edge of the study area.

The sensitivity was examined using two plots. Figure 11.14 shows the hydrograph prediction error under the three different precipitation inputs, and Figure 11.15 shows the difference in the hydrographs predicted using the two alternate precipitation records relative to that predicted using the Blacks' Spur record. The first of these figures clearly shows that the model is very sensitive to the source of precipitation time-series input. The three error signals are often completely un-correlated. In the worst years, such as 1927, two of the precipitation records lead to more than 25% *over*-prediction in the same year, whereas the other record results in nearly 25% *under*-prediction. In general, the two alternative records lead to greater errors than the chosen Blacks' Spur record. But there are notable exceptions, such as 1967 and 1972, where the Blacks' Spur record produces the worst predictions (note that these
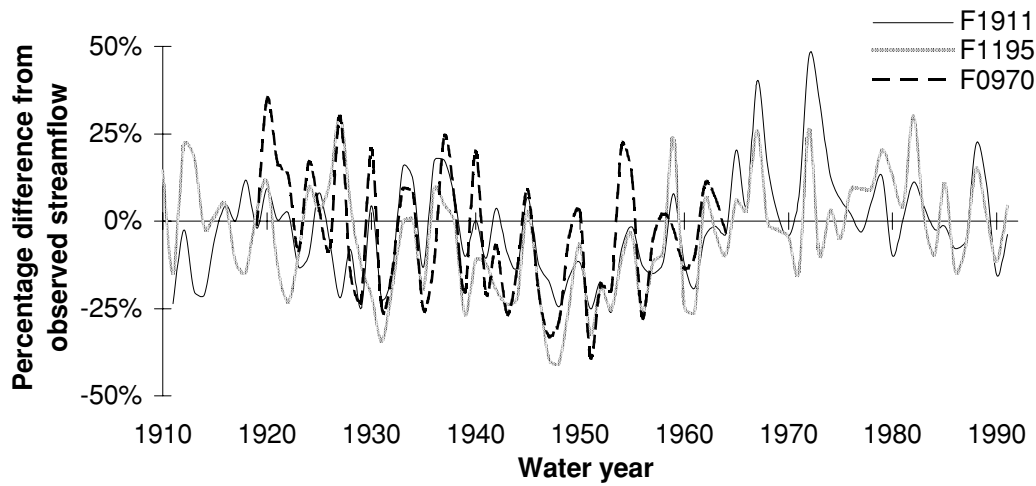
Figure 11.14: Error in predicted hydrographs for the summed water supply catchments: using three different precipitation stations for input.

two years are also the worst predicted of any in the final model run above). Perhaps curiously, moving averages fitted over the data (not shown) indicate that the mean prediction is no better than any of the individuals.

The second plot (Figure 11.15) shows that by choosing an alternative precipitation record, typically 20% and at worst over 60% differences in predicted streamflow will result. These figures are commensurate with the observations of hydrograph variability in the previous section. In concert, the two sets of observations indicate that the typically 20% errors in the final predicted hydrograph do not reflect so much on the ability of the model *per se* to simulate large scale hydrology, but on the precipitation data, the extrapolation to areal precipitation data, and the hydrographic data used to validate the model.

The areal precipitation estimation scheme employed here used a spatial precipitation pattern based on numerous gauges, but a temporal scheme based on only one gauge. This scheme was chosen because only a single long term daily precipitation record was deemed suitable for driving simulations. The daily record at Maroondah Dam wall (F0710) began in 1940, which is too late to span the 1939 fires. The daily record at nearby Mount St Leonards (F0970) finished too early (1965). The record at Warbuton Post Office (F1195) was considered too distant from the study area. The Blacks' Spur data is not daily but thrice weekly, but was used to pro-rate the Warburton Post Office data in order to provide the hybrid record used in the final simulations (see Section 11.2).

It would be interesting to see if a superior scheme could be constructed which
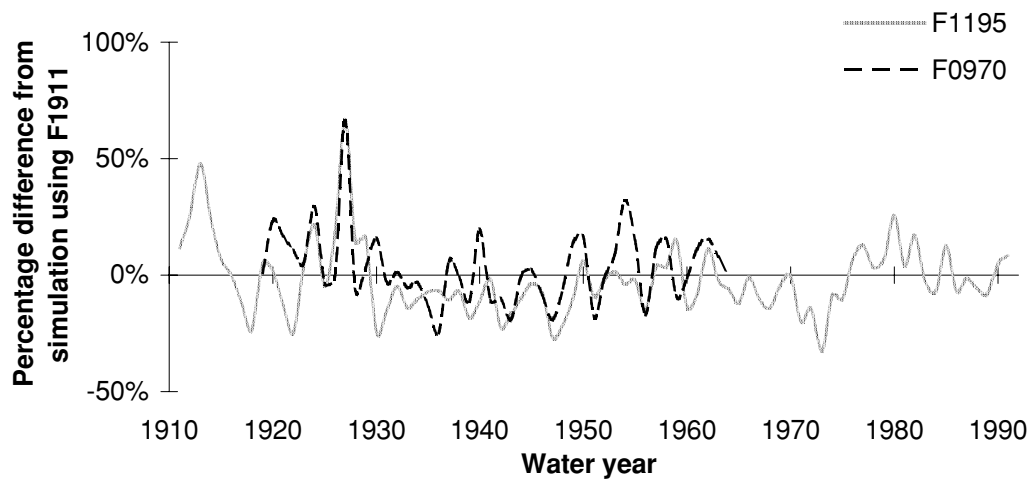
Figure 11.15: Percentage differences from the final simulated streamflow above resulting from equivalent simulations using two different precipitation stations for input.

would reduce the error in predicted streamflow. Recent work by Thornton et al. (1997) highlights an alternative approach to large scale daily climate estimation, where complexity in spatial interpolation (e.g. splines) is foregone in favour of increased use of temporal data. In a modernised version of MTCLIM, these authors perform daily spatial interpolations of precipitation data by passing a truncated gaussian weighting filter over a spatial field of 498 daily gauging records, including a daily-regressed linear adjustment of gauged data to offset elevation differences. This scheme was applied over a 400 000 km^2 area and operates much quicker than would a scheme employing daily spline interpolation. It does however rely on a substantial amount of daily precipitation data, far more than is available at Maroondah for a period spanning 1939.

For the present study area, a compromise is needed. Perhaps a number of psuedo-daily records could be constructed by regressing various existing records against each other and using real daily temporal signals whenever possible. If, say, three such records were constructed, then three spline surfaces of associated weighting coefficients could be interpolated from correlation coefficients based on monthly data (which are more widely distributed). The daily estimate of precipitation at a given location would then be a linear combination of weights for that location and daily precipitation values from the three records.

11.11 Simulation in the absence of climatic noise

As a final illustration of the model's performance, synthetic climate data were used to simulate the Kuczera curve (Figure 1.1) in the absence of climatic noise.

The long term records of precipitation and temperature used above were inspected for a representative year. The year 1958 was selected because it differed in mean annual precipitation and mean maximum and minimum temperature from the respective long term means by less than 3%. Additionally, the temporal pattern of precipitation for this year appeared 'typical' when plotted. A synthetic climate record was constructed where the data for 1958 were repeated for 100 years. Standard parameters were supplied to the model except that all ESUs were assigned forest origin dates such that old-growth forest existed at the start of the 100 year period and that the entire study area was burnt at Year 40 of the 100 year period.

A particular form of the Kuczera curve was selected to best match the conditions of the simulation. Kuczera's (1987) regional curve was parameterised assuming that an area comprising 72% Ash forest was entirely burnt at Year 40. The value 72% was inferred from Kuczera's Table 1 (1987) for the three largest catchments in the study area (Watts, Grace Burn, and Coranderrk) and is preferable to more recent estimates because it is one of the values used in the formulation of Kuczera's model. A value must be given for the old-growth water yield. This does not alter the shape or magnitude of the yield decline predicted by the curve and is immaterial in the context of simulation using synthetic climate data. For convenience it was set to the simulated yield just before Year 40 of 1060 mm year^{-1}, which is similar to the value of 1100 mm typically assumed (originally from Ronan and Duncan, 1980, p. 84).

Figure 11.16 compares the simulated yield decline with that predicted by the Kuczera curve. It is encouraging that the majority of the simulated curve falls within the 90% confidence limits of the Kuczera curve. The magnitude of the yield decline is well predicted by the model, but the time to minimum yield is less than for the Kuczera curve. This matches the results of the conventional simulations presented earlier in Sections 11.6 to 11.8. Possible explanations for the discrepancy in timing include:

- inaccurate timing of peaks in canopy and total LAI curves,
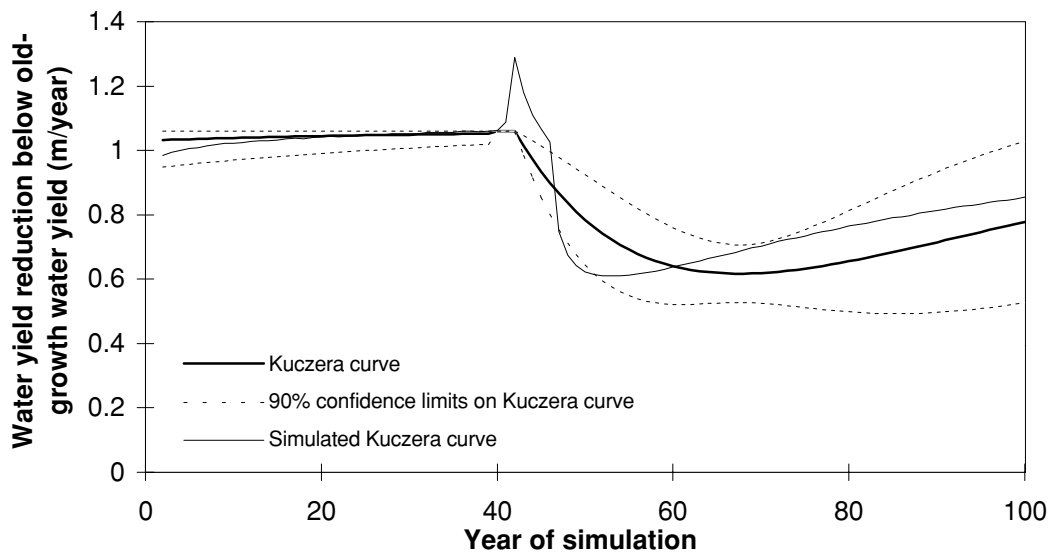
Figure 11.16: Simulation of the Kuczera curve using Macaque supplied with synthetic, noiseless climate data.

- inaccuracy in the Kuczera curve,

- unmodelled long term influences on forest water balance such as temporal dynamics in aerodynamic resistance, and

- limitations in the model's ability to simulate long term moisture storage effects which may act as a buffer or delay mechanism between tree water use and streamflow.

An obvious difference between the curves is the omission from the Kuczera curve of the peak in yield in the 5 years immediately following the fire. Kuczera considered including this peak (1985, p. 148) but decided that whilst it is strong in certain small experimental catchments, there was insufficient evidence of it in large catchments. The simulation suggests that a peak should occur at large scales, but this is subject to uncertainty resulting from the crude representation of canopy LAI for young aged forest (see Chapter 8).

In general, the comparison is a further, encouraging indication of the model's ability to convert accurately information on long term forest dynamics to long term predictions of changes in water yield.

11.12 Discussion

The simulations presented in this chapter were built from the bottom up. The model was designed around the wide array of hydro-ecological processes observed scales of about 0.1 to 100 metres. Its parameters were derived from a diverse set of measurements made at these scales, and then a number of detailed parameter mapping exercises were undertaken in order to scale-up to a catchment-wide representation. A daily time step was chosen in order that model realism could be validated at a level of detail commensurate with the spatial scale of process representation, but the key application of the model relates to periods of over a century. Apart from the use of hydrographs, which integrate over large spatial scales, the testing of individual model components was restricted to small spatio-temporal scales. It is then encouraging to find that the integration of these individual model components and the aggregation of predictions to large scales resulted in simulated long term, large scale hydrographs with errors that did not exceed the errors in our ability to measure the input data (e.g. precipitation) and validation data (streamflow), in a way where nothing grossly unrealistic was predicted by the internal variables of the model.

The long term simulation results with constant LAI indicated, as expected, that climatic variability as represented by the time-series input to the model is not sufficient to explain long term trends in water yield. Simulations with physically based LAI curves partly explained the long term trends by improving streamflow predictions for the oldest forests. However, accompanying this improvement was a deterioration of accuracy in water yield prediction for younger forests, particularly in the period 5 to 15 years after the 1939 fires. The addition of temporal curves for maximum canopy leaf conductance (also physically based), enhanced these changes, the end-point being reasonably accurate prediction of the drop in water yield from 50 to about 200 year old forest, but persisting problems with predictions for forests younger than 50 years. Simulations with synthetic climate data which were devoid of inter-annual 'noise' confirmed a discrepancy in the timing of minimum water yield predicted respectively by the model and the Kuczera curve. A number of possible explanations were given for this.

The results presented here represent perhaps the first time the dynamics of forest evapotranspiration have been investigated at such long (*c*. 200 years) time scales in the context of physical process understanding and simulation. I suggest that in order to achieve realistic simulation, we may need to re-define some conventional paradigms such as the assumption in long term studies of

temporal constancy of both leaf conductance (as investigated above) and aerodynamic resistance (as noted in the possibilities listed in Section 11.7). Complex process interactions may be occurring at very long time scales. For example, the period of high LAI and high leaf conductance enjoyed by younger forests may, to some extent, be cancelled by high aerodynamic resistance, self-shading, and moisture saturation within the extremely dense canopies exhibited at this time. Traditionally, aerodynamic resistance in particular has been viewed as an insensitive parameter in *forest* ET simulation (see Section 5.3.12.4), but this view is rooted in studies where the forests do not grow from zero to over 100 metres in height during their lifetime.

The sensitivity of yield predictions to physically based measurements of LAI and conductance trends is encouraging. It is possible, and perhaps likely, that such sensitivity is sufficient to explain long term water yield trends given some further improvement in the measurement and representation of LAI and conductance. This may simply mean adjustment of the timing and magnitude of peaks, and the rates of long term decline in the respective curves. The current situation is that the long term water yield trends expressed by the Kuczera curve have been *approximately* simulated using a large scale physically based model operating in a physically realistic manner.

Part V

Summary and conclusion

Chapter 12

Summary and conclusion

Contents

12.1 Research question and aim

Recall Chapter 1 where it was asked: *Is it possible to realistically and spatially simulate the water balance of forests at large scales for long periods in a way that responds to land cover change?*

The aim of the present work was to determine whether this kind of simulation is possible by attempting to construct a model which achieves it. This aim was broken into the following steps:

- design a model structure which represents the key catchment processes which are believed to occur,

- parameterise the model through measurement, and where this is not possible, through calibration against observations of internal variables,

- map key spatial parameters,

- test and validate the model against observations of both internal and external variables,

- apply the model to a large scale, long term scenario.

12.2 Summary

The remainder of the dissertation presented the results of conducting each of the above steps in turn and is summarised in the following sections.

12.2.1 Study area

A large (163 km^2) study area containing five water supply catchments was chosen from the Melbourne water supply region. The area exhibits forest cover, terrain, and climate typical of the region. It is the site of a rich and diverse database on surface hydrological processes, and is therefore ideal for testing ideas about the realistic representation such processes within models.

12.2.2 Existing models

A review of existing models revealed that there are very few models which fit the constraints of realistic, large scale, and long term simulation. The models RHESSys, DHVM, SHE, and Topog offer many suitable features and were selected for discussion. Various elements of these models are well suited to the task at hand. But each has a limitation which precludes its use here. RHESSys is ideally suited to large scale modelling through its parsimonious representation of spatial heterogeneity using implicit lateral connections between spatial elements defined by hydrological similarity. But it represents only a single evaporating layer. The present research problem would be better served by a three layer representation of evapotranspiration (ET) because of long term changes in the balance between evapotranspiration from canopy, understorey, and soil layers. DHVM offers a suitably detailed ET model, but uses a regular grid based representation of horizontal space with explicit lateral connections between grid cells. This can lead to limitations such as

high computation time, redundancy and duplicated representation in some locations, and overly coarse representation in others. This is not in keeping with the present study's requirement for parsimony. SHE is also unsuitable because its representation of ET is similar to that of RHESSys, and its representation of horizontal space is similar to DHVM. Topog has a detailed representation of ET which is well suited to the present study. But it uses a particularly fine, contour-based spatial structure with many redundant spatial elements. It is normally applied to small catchments where this does not pose a computational problem and where parsimony is less important. Topog also uses a highly detailed representation of vertical unsaturated soil water flux which is incompatible with the level of detail which is desirable in a large scale study.

In designing a new model structure, a review of approaches to spatial modelling was conducted. The distribution function modelling (DFM) concepts employed by RHESSys and TOPMODEL were seen as desirable due to their parsimony. Due to difficulties applying DFMs in deep soiled catchments, a modification termed 'limited DFM' was developed which allows the lateral redistribution of water within hillslopes to be slowed down according to a lateral redistribution factor.

12.2.3   Model structure

The model is named Macaque. It works with a hierarchy of spatial units, in the present case: regions, catchments, hillslopes, and elementary spatial units (ESUs). Subsurface lateral flow between ESUs occurs along conceptual soil catenas represented as 'hillslopes'.

Time series input to the model is limited to precipitation and maximum and minimum temperature at a base station.

Within each ESU the structural elements which are represented include two vegetation layers, a snowpack, and two soil layers. Precipitation falling on successive vegetation layers may be intercepted, stored, and evaporated, or become throughfall reaching the forest floor. Within the soil an unsaturated zone lies above a saturated zone. If the water table at the boundary of these is shallow, it is considered to intersect the surface in some parts of the ESU, in which case baseflow is released from the 'saturated portion'. Throughfall falling on this portion becomes saturation excess flow (stormflow). All evaporation and transpiration is calculated using the Penman-Monteith equation driven by both net radiation and vapor pressure deficit (a humidity vari-

able). Transpiration from either vegetation layer may be drawn from either soil layer. In addition to radiation and humidity controls, transpiration is controlled by canopy conductance which, in turn, is controlled by leaf area index (LAI), soil water status, temperature, and additional radiation and humidity controls.

The model also implements a detailed micro-meteorological simulation for each ESU. This includes calculation of variables such as: precipitation and daytime mean temperatures at locations distant from the base station, solar and net radiation for each evaporating layer, humidity above the canopy, and whether precipitation is rain or snow.

12.2.4   Model parameterisation

Macaque has over 70 parameters. In order to give the best chance of physically realistic model operation, every effort was made to provide parameter values through measurement or calibration against observations of internal model variables. Nearly half the parameters were measured locally, ten were calibrated against local internal measurements, and 16 were derived from measurements and internal calibrations in the literature. A few others were derived from mixed sources, defaulted from other values, or not used. In this style of modelling, the idea is to avoid calibrating parameters solely against streamflow observations. Whilst this was achieved, there remained eight parameters which were considered highly sensitive relative to the certainty with which their values were known. Three in particular were initialised from measured data but were then adjusted considerably within the range of measurement uncertainty to achieve an accurate simulation of hydrograph shape and annual streamflow. These were the maximum canopy leaf conductance, and two parameters related to subsurface lateral hydraulic conductivity and soil depth.

12.2.5   Parameter mapping

A number of key *spatial* parameters were mapped over the study area rather than treated as lumped values. Elevation was mapped using standard surface fitting techniques. The accuracy of the resulting DEM was tested against detailed ground data which revealed significant smoothing of valley bottoms. The effect of this is noted below.

Precipitation was mapped using similar surface fitting techniques, which, al-

though standard in climatological investigations, have rarely been used in hydrological modelling. A literature review highlighted numerous potential difficulties in accurately estimating precipitation over large catchments. These range from problems in the measurement of precipitation at a single site, to high degrees of unpredictable spatio-temporal variability at a variety of scales. A large bulk precipitation data set was compiled and input to a spline interpolation procedure to produce a mean precipitation map which was superior to that produced using simpler linear techniques. Both maps were submitted to sensitivity analyses as noted below.

A detailed and involved vegetation mapping process was undertaken, focusing on leaf area index (LAI) as the key variable describing the vegetative status of forests. Based on an extensive database of ground and remote sensing measurements of both canopy and total (canopy and understorey) LAI measurements in forests of different age, a series of original techniques were developed to produce curves expressing the LAI of Mountain Ash forest as a function of forest age. In simple terms, the curves match the shape of an inverted Kuczera curve, rising from zero at age zero to a peak in the first decade or so, and declining steadily over the following centuries. Related and simplified curves were estimated for the remaining species in the study area which are less well understood and less important for water production.

The spatial aspect of the vegetation mapping process was derived from a detailed map of forest species and age produced by the Department of Natural Resources and Environment. During execution, Macaque checks the dominant species and most recent fire or logging date of each ESU, and then determines the canopy and total LAI by calculating the age and looking up the LAI value from the appropriate curve.

12.2.6 Model testing

Model testing produced mixed results. Comparisons were made between time series of predictions and observations of internal variables such as mean daytime temperature, vapor pressure deficit (VPD), throughfall, transpiration, soil moisture, and water table levels. In most cases a good match was shown between the daily temporal patterns of predicted and observed data. This indicates that modelled responses to short term controls reflect reality. However, mean values and seasonal variation often differed between predicted and observed data. In particular, the model generally over-estimated VPD, radiation, and transpiration. This was due largely to a single limitation in the modelling of temperature lapse rates. In other cases, such as errors in the

predicted seasonal pattern of transpiration, inaccuracies in the *observed* data were implicated. In all cases, errors in model performance could be explained logically by factors such as limitations in the model structure which could be remedied. In no cases were errors inexplicable and indicative of unrealistic representation of catchment conditions and processes.

Initial streamflow predictions matched observed hydrographs at daily, weekly, monthly, and yearly time scales. Because these predictions were made without any free calibration against hydrographs, *they demonstrate the general validity and realism of the model structure and parameterisation.*

Re-calibration of two key subsurface parameters against observed hydrographs produced better predictions. The resulting parameter values de-emphasised the role of lateral subsurface redistribution of water in the model, and raised questions about how important this process is in reality for deep soiled catchments.

There remains much room for improvement and 'tightening up' within the model. A simple sensitivity analysis against lumped parameters revealed that streamflow predictions can be extremely sensitive to variations in a small number of key parameters which are within the bounds of certainty for those parameters. Similar sensitivity was revealed by varying the pattern of certain spatial parameters. The model was shown to be very sensitive to spatial patterns of precipitation (as expressed by the two maps of mean precipitation distribution described above), to be sensitive in an expected, linear way to spatial patterns of LAI (as expressed using both satellite and species based mapping techniques), and, surprisingly insensitive to variations in topography at the scale of first order basins (as expressed by the two DEMs described above).

12.2.7 Model application

All parts of the present study came together in an example application of the model where long term changes in water yield resulting from the widespread 1939 wildfires were simulated for three largest catchments in the Maroondah study area (145 km^2). After re-calibration of hydrograph-sensitive parameters to account for the scaling-up to large catchments, hydrographs were accurately predicted at daily, weekly, monthly, and yearly time scales. Three simulations were run. The first did not implement any long term changes in land cover, i.e. no fire or logging was simulated, and LAI was held constant. As expected, the predicted annual hydrograph was accurate near the

1980-1989 calibration period, but was consistently under-predicted prior to the 1939 fires. In the second run, the LAI curves were incorporated into the model and historical fires were simulated. The simulation improved for the pre-1939 period and remained accurate near the calibration period. However, there remained some under-prediction in the pre-1939 period. This suggests that changes in LAI only partly account for changes in water yield due to land cover change. Of a number of possibilities, long term changes in leaf conductance were suggested as an additional influence. Data were gathered on this and incorporated into the model, resulting in a suitably improved prediction.

Whilst long term changes in water yield were able to be accounted for by changes in land cover through these simulations, the shorter term 'noise' in the predicted hydrograph remained considerable. This would limit any more precise analyses. Sensitivity analyses using different observed hydrographs and different precipitation gauges indicated that the hydrograph noise could be accounted for by variability in the precipitation input to the model. Thus improvement in this area is paramount. Such improvement could be achieved by using more than one daily precipitation gauge to drive the temporal aspect of precipitation estimation. Methods exist which use multiple gauges, and whilst these are too data demanding for the present study area, a compromise scheme was suggested which may be able to make better use of the limited long term daily precipitation records for the region.

12.3   Implications for model realism

In the research question, it is the word 'realistically' which is of key interest. Clearly, this dissertation has shown that is possible to spatially simulate the water balance of forests at large scales for long periods in a way that responds to land cover change? But was it done realistically?

To answer this, a definition of 'realism' must first be adopted. Here, realistic simulation is defined as occurring when: every variable represented by the model is well defined in a physical sense; the interactions between these variables are defined in terms of real physical processes; and, at all times during simulation, the value of each variable reflects its real value in nature.

It is difficult to formulate a logic which allows us to determine with certainty whether or not the simulation is realistic because the evidence often appears contradictory. There are results which support model realism and results which cause us to question it.

Support for model realism is gained from the following results.

- Whilst streamflow data were used in combination with other data in determining values for three of the parameters, no model parameters were calibrated *solely* against streamflow.

- Most key spatial variables were successfully mapped, including topography, precipitation, and LAI.

- Internal testing of model variables was successful. Whilst discrepancies occurred, an acceptable match was obtained between predictions and observations of key model variables such as VPD, transpiration, soil moisture, and water table levels.

- Initial small scale streamflow predictions did not involve free calibration against streamflow data but were nevertheless accurate.

- Large scale long term simulations responded in an expected way to physically expressed changes in land cover, matching observed changes in water yield.

Uncertainty about model realism arise from the following results.

- Mapping of soil parameters was unsuccessful and so spatially uniform soil properties had to be assumed. Due to the influence of soil parameters on water table levels and saturated area dynamics, and hence, on simulated hydrographs, it is likely that, whilst *integrated* catchment hydrographs were accurately predicted, hydrographs from certain ungauged hillslopes were inaccurately predicted.

- The response of transpiration to environmental controls such as soil moisture stress, temperature, VPD, and radiation was not tested. This affects the predicted spatial distribution of transpiration, which was also not able to be validated.

- Errors in estimation of spatial precipitation remained despite an advanced spatial interpolation procedure, and typically led to 20% errors in predicted annual streamflow.

In defence of the above list is the fact that, in each case, a reasonable path toward improvement was able to be suggested. The following conclusion is thus offered. The model behaved realistically in a broad sense, but upon

closer inspection of specific processes or specific spatial configurations, errors indicate that unrealistic simulation also occurred. In all cases, the errors explicable and indicative of a situation with potential for realistic simulation, and therefore, where not currently so, the model is deemed *potentially realistic*.

This may be said of many models. But there are certain advantages which make the present approach useful for particular types of application. It was intended that the model be able to respond to changes in land cover expressed spatially, and with respect to the interaction between land cover and environmental influences such as precipitation and radiation. The scale at which we understand these processes is small, in the order of 0.1 to 100 metres. As stated in Section 1.2, they are unlikely to integrate to larger scales in a linear way, and so, until we are able to explicitly re-express our knowledge of these interactions at larger scales, a spatial model such as Macaque provides the only means of integrating the effects of large scale land cover change on the water balance in situations where both the land cover and its environment are spatially heterogeneous.

This point is illustrated by the testing of model sensitivity to spatial variations in precipitation at the scale of individual mountains, where significant non-linear sensitivity was shown (Section 10.5.1). Variability in radiation occurs at the smaller scale of terrain facets and is also a non-linear influence on water balance because of the co-dependence of ET on factors such as soil moisture as well as radiation. At still smaller scales, we observe heterogeneity in land cover change resulting from the exclusion of vegetation buffer strips around streams during logging operations. Once again, a non-linear response is likely, because of the biased location of buffer strips to valley bottom areas with high moisture supply and a direct connection to streams. Lumped models cannot represent this heterogeneity. Semi-spatial, conceptual models such as MODHYDROLOG, which simulate catchments as a group of one dimensional sub-catchments, are able to account for variability at the scale of mean precipitation distribution, but no smaller. More detailed models such as LASCAM employ spatial units which are sufficiently small to be able to represent variability in radiation at a coarse level. But only models employing fully-distributed or distribution function approaches such as that used in the present study are able to represent features as small as buffer strips, and thereby match the scale of process representation (0.1 to 100 metres) with the scale of the smallest model spatial units.

The above arguments in favour of the detailed modelling approach employed here assume that detailed spatial data are available. In practice, this is

not always the case. Frequently there is much uncertainty in spatial data. The present study benefited from a large amount of both spatial and non-spatial data which reduced the uncertainty to a level where realistic model operation was observed in specific situations and, in the general case, is possible. Application at other sites may be limited by data availability to the extent that realistic model operation is never apparent. Detailed large scale physically based modelling of this kind is thus appropriate where good data are available, but in less data-rich situations it may not be a good idea.

Macaque, through its detailed representation of vertical hydrological processes, is able to represent the interactions between land cover change and a range of environmental influences, and through its detailed disaggregation of space, it is able to represent the spatial heterogeneity of both land cover change and environmental influences with sufficient parsimony that integration is possible up to the scale of large water supply catchments. This dissertation has shown that there is no reason to question that it is possible to realistically and spatially simulate the water balance of forests at large scales for long periods in a way that responds to land cover change, and that the present approach is a worthwhile way to do so.

Chapter 13

References

Abbott, M.B. & Refsgaard, J.C. (eds) (1996), Distributed Hydrological Modelling. Kluwer, Dordrecht, 321 pp.

Abbott, M.B., Bathurst, J.C., Cunge, J.A., O'Connell, P.E., & Rasmussen, J. (1986), An introduction to the European Hydrological System - Systeme Hydrologique Europeen 1: History and philosophy of a physically-based, distributed modelling system. J. Hydrol., 87:45-59.

Abbott, M.B., Bathurst, J.C., Cunge, J.A., O'Connell, P.E., & Rasmussen, J. (1986), An introduction to the European Hydrological System - Systeme Hydrologique Europeen 2: Structure of a physically-based, distributed modelling system. J. Hydrol., 87:61-77.

Adamson, D., Selkirk, P., & Mitchell, P. (1983), The role of fire and lyre birds in the sandstone landscape of the Sydney Basin. In: Young, R.W. & Nanson, G.C. (eds.), Aspects of Australian Sandstone Landscapes, Wollongong, University of Wollongong, 81-93.

Ambroise, B., Beven, K., & Freer, J. (1996), Toward a generalisation of the TOPMODEL concepts: Topographic indices of hydrological similarity. Water Resources Research, 32:7:2135-2145.

Ambroise, B., Freer, J., & Beven, K. (1996), Application of a generalized TOPMODEL to the small Ringelbach catchment, Vosges, France. Water Resources Research, 32:7:2147-2159.

Anderson, M.C. (1981), The geometry of leaf distribution in some south-eastern Australian forests. Agric. Meteorol., 25:195-205.

Anderson, M.G. & Rogers, C.C.M. (1987), Catchment scale distributed hydrological models: a discussion of research directions. Progr. in Phys. Geog., 11:1:28-52.

Andrew, M.H., Noble, I.R., & Lange, R.T. (1979), A non-destructive method for estimating the height of forage and shrubs. Aust. Rangeland J., 1:225-231.

Anon. (1995), ANUSPLIN Implementor's Guide. Centre for Resource and Environmental Studies (CRES), Aust. Nat. Univ., Canberra, Australia, 13 pp.

Anon. (c. 1918), Reports on Forestry in Victoria: 1887-1918. Compilation held in library of Dept. of Nat. Res & Environ., Victoria.

Arino, O., Brockman, C., Veraini, B., & Pittella, G. (1995), ESA Products and Processing Algorithms for Landsat TM. Earthnet online, http://gds.esrin.esa.it/tm (1st Jul. 1997).

Arnold, J.G. & Williams, J.R. (1995), SWRRB - A watershed scale model for soil and water resources management. In: Singh, V.P. (ed.), Computer Models of Watershed Hydrology, Water Resources Publications, Highlands Ranch, Colorado, 847-908.

Ashton, D.H. (1975), The root and shoot development of Eucalyptus regnans F Muell.. Aust. J. Bot., 23:867-887.

Ashton, D.H. (1976), The development of even aged stands of Eucalyptus regnans F Muell. in central Victoria. Aust. J. Bot., 24:397-414.

Ashton, D.H. & Attiwill, P.M. (1994), Tall open-forests. In: Groves, R.H. (ed.), Australian Vegetation (2nd ed.), Cambridge University Press, Cambridge, U.K., pp. 157-196.

Asrar, G., Fuchs, M., Kanemasu, E.T., Hatfield, J.L. (1984), Estimating absorbed photosynthetic radiation and Leaf Area Index from spectral reflectance in wheat. Agronomy Journal, 76:300-306.

Aston, A.R. (1979), Rainfall interception by eight small trees. J. Hydrol., 42:383-396.

Aston, A.R. (1984), Evaporation from eucalypts growing in a weighing lysimeter: a test of the combination equations. Agric. & For. Meteorol., 31:241-249.

Aston, A.R. (1985), Heat storage in a young eucalypt forest. Agricultural and Forest Meteorology, 35:281-297.

Attiwill, P.M. (1962), Estimating branch dry weight and leaf area from measurements of branch girth in Eucalyptus. Forest Science, 8:2:132-141.

Attiwill, P.M. (1991), Productivity of Eucalyptus regnans forest regenerating after bushfire. In: Schonau, A.P.G. (ed.), Symposium on Intensive Forestry: The Role of Eucalypts, IUFRO P2. 02-01 Productivity of Eucalypts, Printed in: South African Forestry Journal, 160:1-6.

Attiwill, P.M. & Leeper, G.W. (1987), Forest Soils and Nutrient Cycles. Melbourne University Press, Melbourne.

Auer, A.H., Jr. (1974), The rain versus snow threshold temperatures. Weatherwise, 27:67.

Ball, J.T., Woodrow, I.E., & Berry, J.A. (1987), A model predicting stomatal conductance and its contribution to the control of photosynthesis under different environmental conditions. In: Biggins, J. (ed.), Progress in Photosynthesis Research, Vol. IV, Martinus Nijhoff Publishers, Netherlands, 221-224.

Band, L.E. (1993), Effect of land surface representation on forest water and carbon budgets. J. Hydrol., 150:749-772.

Band, L.E., Patterson, P., Nemani, R., & Running, S. (1993), Forest ecosystem processes at the watershed scale: incorporating hillslope hydrology. Agric. For. Meteorol., 63:93-126.

Band, L.E., Peterson, D.L., Running, S.W., Coughlan, J., Lammers, R., Dungan, J., & Nemani, R. (1991), Forest ecosystem processes at the watershed scale: basis for distributed simulation. Ecol. Model., 56:171-196.

Banks, J.C. (1993), Tree-Ring Analysis of Two Mountain Ash Trees Eucalyptus regnans F. Muell. from the Watts and O'Shannassy Catchments, Central Highlands, Victoria. A Report to the Central Highlands Old Growth Forest Project. August 1993. Flora Unit, Dept. of Conservation and Natural Resources, Melbourne.

Baret, F., Olioso, A., Luciani, J.L., & Hanocq, J.F. (1989), Estimation de l'énergie photosynthétiquement active absorbée par une culture de blé à partir de données radiométriques. Agronomie, 9:885-895.

Barling, R.D., Moore, I.D., & Grayson, R.B. (1994), A quasi-dynamic wetness index for characterizing the spatial distribution of zones of surface saturation and soil water content. Wat. Resour. Resear., 30:4:1029-1044.

Barrett, E.C. & Curtis, L.F. (1992), Introduction to Environmental Remote Sensing (3rd ed.). Chapman & Hall, London, 426 pp.

Barros, A.P. & Lettenmaier, D.P. (1994), Dynamic modeling of orographically induced precipitation. Rev. Geophys., 23:3:265-284.

Barry, R.G. (1992), Mountain Weather and Climate (2nd ed.). Routledge, London, pp. 402.

Bathurst, J.C. (1986), Physically based distributed modelling in an upland catchment using the Systeme Hydrologique European. J. Hydrol., 87:79-102.

Bathurst, J.C. & O'Connell, P.E. (1992), Future of distributed modelling: The Systeme Hydrologique Europeen. In: Beven, K.J. & Moore, I.B. (eds.), Terrain Analysis and Distributed Modelling in Hydrology, Wiley, Chichester, pp. 213-226.

Bathurst, J.C., Wicks, J.M., & O'Connell, P.E. (1995), The SHE/SHESED basin scale water flow and sediment modelling system. In: Singh, V.P. (ed.), Computer Models of Watershed Hydrology, Water Resources Publications, Highlands Ranch, Colorado, 563-594.

Bergström, S. (1991), Principles and confidence in hydrological modelling. Nordic Hydrol., 22:123-136.

Bergström, S. (1995), The HBV model. In: Singh, V.P. (ed.), Computer Models of Watershed Hydrology, Water Resources Publications, Highlands Ranch, Colorado, 443-476.

Beringer, J. (1994), Preliminary Evaluation of Leaf Area Index Using the LICOR LAI-2000 Plant Canopy Analyser in a Eucalyptus regnans Forest. Unpublished manuscript, 11 pp.

Beven, K.J. (1985), Distributed models. In: Anderson, M.G. & Burt, T.P. (eds.), Hydrological Forecasting, Wiley, Chichester, 405-435.

Beven, K.J. (1986), Hillslope runoff processes and flood frequency characteristics. In: Abrahams, A.D. (ed.), Hillslope Processes, Allen and Unwin, Winchester, MA, 187-202.

Beven, K.J. (1989), Changing ideas in hydrology - the case of physically-based models. J. Hydrol., 105:1:157-172.

Beven, K.J. (1993), Prophesy, reality and uncertainty in distributed hydrological modelling. Advances in Water Resources, 16:41-51.

Beven, K.J. (1996), A discussion of distributed hydrological modelling. In: Abbot, M.B. & Refsgaard, J.C. (eds), Distributed Hydrological Modelling, Ch. 13A, Kluwer, Dordrecht, 255-278.

Beven, K.J. (1996), Response to comments on 'a discussion of distributed hydrological modelling' by J C Refsgaard et al. In: Abbot, M.B. & Refsgaard, J.C. (eds), Distributed Hydrological Modelling, Ch. 13C, Kluwer, Dordrecht, 289-295.

Beven, K.J. & Binley, A.B. (1992), The future of distributed models: model calibration and uncertainty prediction. Hydrol. Processes, 6:279-298.

Beven, K.J. & Kirkby, M.J. (1979), A physically based, variable contributing model of basin hydrology. Hydrol. Sci. Bull., 24:43-69.

Beven, K.J., Lamb, R., Quinn, P., Romanowicz, R., & Freer, J. (1995), TOPMODEL. In: Singh, V.P. (ed.), Computer Models of Watershed Hydrology, Water Resources Publications, Highlands Ranch, Colorado, 627-668.

Bloschl, G. & Sivapalan, M. (1995), Scale issues in hydrological modelling: a review. Hydr. Proc., 9:251-290.

Bouma, J. (1985), Soil variability and soil survey. In: Nielsen, D.R. & Bouma, J. (eds.), Soil Spatial Variability, Proceedings of a Workshop of the ISSS and the SSSA, Las Vegas, USA, 30 Nov.-1 Dec., 1984, Pudoc, Wageningen, the Netherlands.

Brack, C.L., Dawson, M.P., & Gill, A.M. (1985), Bark, leaf and sapwood dimesnions in Eucalyptus. Aust. Forest. Res., 15:1-7.

Bren, L.J. (1997), Effects of slope vegetation removal on the diurnal variations of a small mountain stream. Water Resources Research, 33:321-331.

Bristow, K.L. & Campbell, G.S. (1984), On the relationship between incoming solar radiation and daily maximum and minimum temperature. Agric. For. Meteorol., 31:159-166.

Brookes, J.D. & Turner, J.S. (1963), Hydrology and Australian forest catchments. In: Water Resources - Use and Management, Proceedings of the Aust. Acad. Sci. Symposium, Canberra, 1963, Melbourne Univ. Press, pp. 390-398.

Burt, T.P. & Butcher, D.P. (1985), Topographic controls of soil moisture distributions. J. Soil Sci., 36:469-486.

Campbell, G.S. (1977), An Introduction to Environmental Biophysics. Springer-Verlag, New York, 159 pp.

Campbell, R. (in prep.), Groundwater Behaviour in a Small Forested Catchment. MSc thesis, Hydrogeology and Environmental Science, Univeristy of Melbourne, Australia..

Carbon, B.A., Bartle, G.A., & Murray, A.M. (1979), A method for visual estimation of leaf area. For. Sci., 25:53-58.

Carbon, B.A., Bartle, G.A., & Murray, A.M. (1979), Leaf area index of some eucalypt forests in southwest Australia. Aust. For. Res., 9:323-326.

Carver, M. (1972), Forestry in Victoria, 1838-1919, Vols A-E.

Cecil, M.K. (1977), An Investigation of Two Slope Mantles in Victoria. Unpub. B.Sc. (Hons) Thesis, Dept. Earth Sci., Monash Univ., Australia.

Cheesman, J. & Petch, J. (1996), Interpolation of precipitation data in small upland catchmnets of north west England, for utilization within a catchment yield model. HydroGIS 96, Applications of Geographical Information Systems in Hydrology and Water Resources Management (Poster paper volume from the Vienna Conference, Vienna, Austria, April, 1996), IAHS, 45-59.

Chiew, F.H.S, Stewardson, M.J., & McMahon, T.A. (1993), Comparison of six rainfall-runoff modelling approaches. J. Hydrol., 147:1-36.

Chiew, F.H.S. & McMahon, T.A. (1990), Estimating groundwater recharge using a surface watershed model: Sensitivity analyses. J. Hydrol., 114:305-325.

Chiew, F.H.S. & McMahon, T.A. (1990), Estimating groundwater recharge using a surface watershed modelling approach. J. Hydrol., 114:285-304.

Chiew, F.H.S. & McMahon, T.A. (1994), Application of the daily rainfall-runoff model MODHYDROLOG

to 28 Australian catchments. J. Hydrol., 153:383-416.

Chiew, F.H.S., McMahon, T.A., & O'Neill, I.C. (1992), Estimating groundwater recharge using an integrated surface and groundwater modelling approach. J. Hydrol., 131:151-186.

Chiew, F.H.S., Wang, Q.J., McMahon, T.A., Bates, B.C., & Whetton, P.H. (1996), Potential hydrological responses to climate change in Australia. In: Jones, J.A.A., Liu, C., Woo, M-K., & Kung, H-T. (eds), Regional Hydrological Response to Climate Change, Kluwer, Dordrecht, The Netherlands, p. 337-349.

Choudhury, B.J. (1989), Estimating evaportaion and carbon assimilation using infrared temperature data: vistas in modeling. In: Asrar, G. (ed.), Theory and application of optical remote sensing, Wiley, New York, pp. 628-690.

Choudhury, B.J. & Monteith, J.L. (1988), A four-layer model for the heat budget of homogeneous land surfaces. Q. J. R. Meteorol. Soc., 114:373-398.

Clark, B.P. (1986), New look-up tables. EOSAT Landsat Tech. Notes 1:2-8.

Colls, K. & Whitaker, R. (1990), The Australian Weather Book. National Book Distributors, Sydney.

Colosimo & Mendicino (1996), Scale definition in an integrated GIS hydrological model: a case study. HydroGIS 96: Application of Geographic Informations Systems in Hydrology and Water Resources Management (Proc. of the Vienna Conference, April 1996). IAHS Publ. no. 235.

Connor, D.J., Legge, N.J., & Turner, N.C. (1977), Water relations of Mountain Ash (Eucalyptus regnans F. Muell.) forests. Aust. J. Plant Physiol., 4:753-762.

Cooper, E. (1876), Forest Culture and Eucalyptus Trees. Cubery & Co., San Fransisco.

Coops, N., Delahaye, A., & Pook, E. (1997), Estimation of eucalypt forest leaf area index on the south coast of New South Wales using Landsat MSS data. Aust. J. Bot., in press.

Costa, F.D.S., Damazio, J.M., Neves, F.P.D., & Simabuguro, M.D.F.R. (1996), Linking a synthetic storm generation model with the IDRISI GIS. HydroGIS 96: Application of Geographic Information Systems in Hydrology and Water Resources Management, Proceedings of the Vienna Conference, April, 1996, IAHS Publ. No. 235, 107-113.

Costa-Cabral, M.C. & Burges, S.J. (1994), Digital Elevation Model Networks (DEMON): A model of flow over hillslopes for computation of contributing and dispersal areas. Water Resources Research, 30:6:1681-1692.

Costermans, L. (1983), Native Trees and Shrubs of South-Eastern Australia. Weldon Publishing, Sydney.

Cowpertwait, P.S.P., O'Connell, P.E., Metcalfe, A.V., & Mawdsley, J.A. (1996), Stochastic point process modelling of rainfall. I. Single-site fitting and validation. J. Hydrol., 175:17-46.

Cowpertwait, P.S.P., O'Connell, P.E., Metcalfe, A.V., & Mawdsley, J.A. (1996), Stochastic point process modelling of rainfall. II. Regionalisation and dissaggregation. J. Hydrol., 175:47-65.

Craigie, R. (1981), A study of the Application of Geostatistics to Estimation Problems in the Hydrological and Earth Sciences. Unpub. M.App.Sc. thesis, Environmental Engineering, Faculty of Engineering, University of Melbourne, Melbourne, Australia, 108 pp.

Crawford, A. (1995), A special heritage cut down. Forests for the Future, A Sunday Age Display Advertising Feature, Sunday Age, 17th Sept. 1995, Victoria, Australia.

Creutin, J.D. & Obled, C. (1982), Objective analyses and mapping techniques for rainfall fields: an objective comparison. Wat. Resour. Res., 18:413-431.

Crombie, D.S., Tippett, J.T., & Hill, T.C. (1988), Dawn water potential and root depth of trees and understorey species in South-western Australia. Aust. J. Bot., 36:621-631.

CSIRO Division of Atmospheric Research (1996), Climate Chnage Scenarios for the Australian Region. Climate Impact Group, Report available from CSIRO Division of Atmospheric Research, Mordialloc, 3195, Australia, 6 pp..

Curran, P.J. (1994), Attempts to drive ecosystem simulation models at local to regional scales. In: Foody, G.M. & Curran, P.J. (eds), Environmental Remote Sensing From Regional to Global Scales, Wiley, Chichester, 149-166.

Curran, P.J., Dungan, J.L., & Gholz, H.L. (1992), Seasonal LAI in slash pine estimated with Landsat TM. Remote Sensing of Environment, 39:3-13.

Davis, S.H. (in prep.), Measurement of soil hydraulic properties and implications for catchment modelling. PhD thesis, Dept of Civil Engineering, Monash University, Melbourne, Australia.

Davis, S.H., Vertessy, R.A., & Silberstein, R. (1997), The sensitivity of a catchment model to soil hydraulic properties obtained by using different measurement techniques. Proc., Int. Congr. on Modelling and

Simulation, MODSIM 97, December,1997, Hobart, Australia, 311-316.

Davis, S.H., Vertessy, R.A., Dunkerly, D.L., & Mein, R.G. (1996), The influence of scale on the measurement of saturated hydraulic conductivity in a forest soil. 23rd Hydrology and Water Resources Symposium, Hobart, Australia, 21-24 May 1996, 103-108.

Dawes, W. & Hatton, T.J. (1993), TOPOG_IRM, 1. Model Description. CSIRO, Div. of Water Resources, Tech. memo. 93/5, 33 pp.

Dawes, W.R., Zhang, L., Hatton, T.J., Reece, P.H., Beale, G.T.H., & Packer, I. (1997), Evaluation of a distributed parameter ecohydrological model (TOPOG_IRM) on a small cropping rotation catchment. J. Hydrol., 191:64-86.

De Laine, R.J. (1969), Measuring rainfall on forest catchments. J. Hydrol., 9:103-112.

Department of State Forests (1911), Report for the Year Ended 30th June, 1911. In: Anon., Reports on Forestry in Victoria: 1887-1918.

Dickinson, R.E., Henderson-Sellers, A., Kennedy, P.J., & Wilson, M.F. (1986), Biosphere-Atmosphere Transfer Scheme (BATS) for the NCAR Community Climate Model. NCAR Technical Note: NCAR/TN-275+STR, 69 pp.

Dickinson, R.E., Henderson-Sellers, A., Rosenzweig, C., & Sellers, P.J. (1991), Evapotranspiration models with canopy resistance for use in climate models, A review. Agric. For. Meteorol., 54:373-388.

Dingman, S.L. (1994), Physical Hydrology. Macmillan, New York, 575 pp.

Dingman, S.L., Seely-Reynolds, D.M., & Reynolds III, R.C. (1988), Application of kriging to estimating mean annual precipitation in a region of orographic influence. Water. Resour. Bull., 24:329-339.

Dozier, J. & Frew, J. (1989), Rapid calculation of terrain parameters for radiation modelling from digital elevation data. Proc. Int. Remote Sens. Symp., 89:1760-1774.

Dozier, J., Bruno, J., & Downey, P. (1981), A faster solution to the horizon problem. Comp. Geosci., 7:145-151.

Droesen, W.J. & Geelen, L.H.W.T. (1993), Application of fuzzy sets in hydroecological expert modelling. HydroGIS 93: Application of Geographic Information Systems in Hydrology and Water Resources (Proceedings of the Vienna Conference, April 1993). IAHS Publ. no. 211.

Duncan, H.P. (1980), Streamflow chacteristics. In: Langford, K.J. & O'Shaughnessy, P.J. (eds.), Second Progress Report - Coranderrk, Water Supply Catchment Hydrology Research, Melbourne and Metropolitan Board of Works, Rep. No. MMBW-W-0010, pp. 163-172.

Duncan, H.P. & Heeps, D.P. (1980), Soil Moisture. In: Langford, K.J. & O'Shaughnessy, P.J. (eds.), Second Progress Report - Coranderrk, Water Supply Catchment Hydrology Research, Melbourne and Metropolitan Board of Works, Rep. No. MMBW-W-0010, Ch. 7, pp. 133-146.

Duncan, H.P. & Langford, K.J. (1977), Streamflow characteristics. In: Langford, K.J. & O'Shaughnessy, P.J. (eds.), First Progress Report - North Maroondah, Water Supply Catchment Hydrology Research, Melbourne and Metropolitan Board of Works, Rep. No. MMBW-W-0005, pp. 215-229.

Duncan, H.P., Heeps, D.P., & Langford, K.J. (1977), Calibrations. In: Langford, K.J. & O'Shaughnessy, P.J. (eds.), First Progress Report - North Maroondah, Water Supply Catchment Hydrology Research, Melbourne and Metropolitan Board of Works, Rep. No. MMBW-W-0005, pp. 233-255.

Duncan, H.P., Heeps, D.P., & Langford, K.J. (1979), Calibration of the Monda Catchments. In: Langford, K.J. & O'Shaughnessy, P.J. (eds.), Second Progress Report - North Maroondah, Water Supply Catchment Hydrology Research, Melbourne and Metropolitan Board of Works, Rep. No. MMBW-W-0009, pp. 7-48.

Duncan, H.P., Heeps, D.P., & Langford, K.J. (1980), Streamflow Yield. In: Langford, K.J. & O'Shaughnessy, P.J. (eds.), Second Progress Report - Coranderrk, Water Supply Catchment Hydrology Research, Melbourne and Metropolitan Board of Works, Rep. No. MMBW-W-0010, pp. 147-162.

Duncan, H.P., Langford, K.J., & O'Shaughnessy, P.J. (1978), A comparitive study of canopy interception. Hydrol. Symp. 1978, Canberra, 5-7 Sep. 1978, Preprints of Papers, Inst. Eng. Aust., 150-154.

Dunin, F.X. & Mackay, S.M. (1982), Evaporation of eucalypt and coniferous forest communities. The First Nat. Symp. on Forest Hydrol., Melbourne, 11-13 May 1982, Preprints of Papers, Inst. Eng. Aust., 18-25.

Dunin, F.X., O'Loghlin, E.M., & Reyenga, W. (1988), Interception loss from eucalypt forest: lysimeter determination of hourly rates for long term evaluation. Hydrol. Processes., 2:315-329.

Dunn, G.M. & Connor, D.J. (1991), Transpiration and Water Yield in Mountain Ash Forest. Land and Water Resources Research and Development Corporation/Melbourne Water Partnership Programme Project P88/37, Final Report, 61 pp.

Dunn, G.M. & Connor, D.J. (1993), An analysis of sap flow in mountain ash (Eucalyptus regnans) forests of different age. Tree Physiol., 13:321-336.

Dunn, S.M. & Mackay, R. (1995), Spatial variation in evapotranspiration and the influence of land use on catchment hydrology. J. Hydrol., 1995:49-73.

Eagleson, P.S. (1982), Ecological optimality in water limited natural soil-vegetation systems. 1. Theory and hypothesis. Wat. Resour. Res., 18:325-340.

Edwards, A.B. (1932), The geology and petrology of the Black Spur area (Healesville). Proc. Roy. Soc. Vic., 44:49-76.

Engman, E.T. (1995), Recent advances in remote sensing in hydrology. Rev. of Geophys., Supplement, July 1995, 967-975.

Evans, R.S. & Joyce, E.B. (1974), Some areas of landslide activity in Victoria, Australia. Proc. Roy. Soc. Vic., 88:95.

Ezekiel, M. & Fox, K.A. (1959), Methods of Correlation and Regression Analysis (3rd ed.). Wiley, New York, 548 pp.

Famiglietti, J.S., Wood, E.F., Sivapalan, M., & Thongs, D.J. (1992), A catchment scale water balance model for FIFE. J. Geophys. Res., 97(D17), 18997-19007.

Faures, J-M., Goodrich, D.C., Woolhiser, D.A., Sorooshian, S. (1995), Impact of small-scale spatial rainfall variability on runoff modeling. J. Hydrol., 173:309-326.

Federer, C.A. (1995), BROOK 90: A Simulation Model for Evaporation, Soil Water, and Streamflow, Version 3.1. Computer freeware and documentation, USDA Forest Service, PO Box 640, Durham, New Hampshire, 03824.

Federer, C.A. & Lash, D. (1978), BROOK: A Hydrologic Simulation Model for Eastern Forests. Research Report No. 19, Water Resource Research Center, Univ. of New Hampshire, Durham, New Hampshire, 94 pp.

Feller, M.C. (1980), Biomass and nutrient distribution in two eucalypt forests systems. Aust. J. Ecol., 309-333.

Feller, M.C. (1981), Catchment nutrient budgets and geological weathering in Eucalyptus regnans ecosystems in Victoria. Aust. J. Ecol., 6:65-77.

Feller, M.C. (c. 1978), Nutrient Cycling in Eucalypt Forest Ecosystems and the Effects of Pine Planting on Nutrient Cycling and Soil Fertility. Unpub., Faculty of Agriculture and Forestry, University of Melbourne, Australia, 237 pp..

Ferguson, I.S. (1995), Timber production and streamflow benefits: a contrary analysis of options. Australian Forestry, 58:142-146.

Finlayson, B.L. & Wong, N. R. (1982), Storm runoff and water quality in an undisturbed forested catchment in Victoria. Aust. For. Res., 12:303-15.

Fiske, K.F., Higgins, R.W., O'Connell, M.J., & Szirom, L.F. (1977), Instrumentation and filed procedures. In: Langford, K.J. & O'Shaughnessy, P.J., First Progress Report: North Maroondah, Water Supply Catchment Hydrology Research, Melbourne and Metrpolitan Board of Works, Rep. MMBW-W-0005, pp 71-89.

Foley, J.C. (1947), A Study of Meterological Conditions Associated with Bush and Grass FIres and Fire Protection Strategy in Australia. Bureau of Meterorology, Bulletin No. 38, Australia.

Foley, J.D., van Dam, A., Feiner, S.K., & Hughes, J.F. (1990), Computer Graphics: Principles and Practice (2nd ed.). Addison-Wesley, Reading, Massachusetts, 1175 pp.

Foufoula-Georgiou, E. & Georgakakos, K.P. (1991), Hydrologic advances in space-time precipitation modeling and forecasting. In: Bowles, D.S. & O'Connell, P.E. (eds), Racent Advances in the Modeling of Hydrologic Systems, Kluwer, Dordrecht, pp. 47-65.

Franks, S.W., Beven, K.J., Chappell, N.A., Gineste, P. (1997), The utility of multi-objective conditioning of a distributed hydrological model using uncertain estimates of saturated areas. Proc., Int. Congr. on Modelling and Simulation, MODSIM 97, December,1997, Hobart, Australia, 335-340.

Freeman, T.G. (1991), Calculating catchment area with divergent flow based on a regular grid. Comp. Geosci., 17:3:413-422.

Freeze, R.A. & Cherry, J.A. (1979), Groundwater. Prentice-Hall, Englewood Cliffs, New Jersey, 604 pp.

French, M.N., Krajewski, W.F., & Cuykendall, R.R. (1992), Rainfall forecasting in space and time using a neural network. J. Hydrology, 137:1:1-31.

Gamon, J.A., Field, C.B., Goulden, M.L., Griffin, K.L., Hartley, A.E., Joel, G., Penuelas, J., & Valentini, R. (1995), Relationships between NDVI, canopy structure, and photosynthesis in three Californian vegetation types. Ecological Applications, 5:28-41.

Garen, D.C. & Daly, C. (1996), Spatially distributed preciptation and temperature fields in mountainous regions estimated from surface observations. Holzmann, H. & Nachtnebel, H.P. (eds.), Int. Conf. on Applic. of Geographical Information Systems in Hydrol. and Wat. Resour. Manag., HydroGIS '96, Vienna, Austria, April 16-19, 1996, Vol. of Poster Papers, IAHS, 122-128.

Gates, D.M. (1980), Biophysical Ecology. Springer-Verlag, New York, 611 pp.

Gholtz, H.L. (1982), Environmental limits on aboveground net primary production, leaf area, and biomass in vegetation zones of the Pacific Northwest. Ecology, 63:467-481.

Gholz, H.L., Fitz, F.K., & Waring, R.H. (1976), Leaf area difference associated with old-growth forest communities in the western Oregon Cascades. Canadian Journal of Forest Research, 6:49-57.

Gigliotti, P., Blake, P., & Gan, K. (1994), A Study of Severe Fire Weather Conditions in the Thomson Catchment and Central Areas of Victoria. Draft Report, Meterological Study 49, Bureau of Meterology, Melbourne.

Givone, C. & Meignien, X. (1990), Influence of topography on spatial distribution of rain. Hydrology of Mountainous Areas, Proceedings of the Strbske Pleso Workshop, Czechoslovakia, June 1988, IAHS Publ. no. 190, 57-65.

Goodrich, D.C., Faures, J-M., Woolhiser, D.A., & Sorooshian, S. (1995), Measurement and analysis of small-scale convective storm rainfall variability. J. Hydrol., 173:283-308.

Gray, D.M. & Prowse, T.D. (1993), Snow and floating ice. In: Maidment, D.R. (ed.), Handbook of Hydrology, Ch. 7, McGraw-Hill Inc., New York, 7.1-7.58.

Grayson, R.B. & Moore, I.D. (1992), Chapter 7, Effect of land surface configuration on catchment hydrology. In: Parsons, A.J. & Abrahams, D. (eds), Overland Flow: Hydraulics and Erosion Mechanics. University College London Press Ltd., London, pp. 147-175.

Grayson, R.B., Bloschl, G., Barling, R.D., & Moore, I.D. (1993), Process, scale and constraints to hydrologic modelling in GIS. HydroGIS 93: Application of Geographic Information Systems in Hydrology and Water Resources, Proceedings of the Vienna Conference, April 1993, IAHS Publ. no. 211, 83-92.

Grayson, R.B., Moore, I.D., & McMahon, T.A. (1992), Physically based hydrologic modeling. 1. A terrain-based model for investigative purposes. Water Resources Research, 28:10:2639-2658.

Grayson, R.B., Moore, I.D., & McMahon, T.A. (1992), Physically based hydrologic modeling. 2. Is the concept realistic?. Water Resources Research, 28:10:2659-2666.

Greacen, E.L. & Williams, J. (1983), Physical properties and water relations. In: CSIRO, Division of Soils, Soils: An Australian Viewpoint, CSIRO, Melbourne; Academic Press, London, 928 pp, 499-530.

Greaves, B.L. & Spencer, R.D. (1993), An evaluation of spectroradiometry and multispectral scanning for differentiating forest communities. Aust. For., 56:1:68-79.

Grier, C.C. & Running, S.W. (1977), Leaf area of mature north-western coniferous forests: relation to site water balance. Ecology, 58:893-899.

Grier, C.C. & Waring, R.H. (1974), Conifer foliage mass related to sapwood area. Forest. Sci., 20:205-206.

Griffiths, T. (1992), Secrets of the Forest: Discovering History in Melbourne's Ash Range. Allen & Unwin, St Leonards, NSW.

Gu, X.F. (1988), Mise en relation des luminances measurées par SPOT avec les réflectances de surfaces agricoles measurées au sol. Mémoire DEA Méthodes physiques en télédétection, Univ. Paris 7.

Guiness Publishing (1997), The Guiness Book of Records 1998. 384 pp.

Guyot, G. (1990), Optical properties of vegetation canopies. Clarke, J.A. and Steven, M.D. (eds), Applications of Remote Sening in Agriculture, Butterwoths, London, 19-43.

Hanson, C.L. & Woolhiser, D.A. (1990), Precipitation simulation model for mountainous areas. American Society of Civil Engineers, New York, pp. 578-583.

Hardy, A.D. (1911), Giant Trees of Victoria. In: Department of State Forests (1911), Report for the Year Ended 30th June, 1911, In: Anon., Reports on Forestry in Victoria:1887-1918.

Hardy, A.D. (1935), Australia's great trees. Victorian Naturalist, 51:231-241.

Harrison, B.A. & Jupp, D.L.B. (1990), Introduction to Image Processing, Part Two of the microBRIAN Resource Manual. CSIRO, Division of Water Resources, Canberra, Australia.

Hatton, T.J. & Wu, H.I. (1995), Scaling theory to extrapolate individual tree water use to stand water

use. Hydrol. Process., 9:527-540.

Hatton, T.J., Dyce, P., Zhang, L., & Dawes, W. (1995), WAVES - An Ecohydrological Model of the Surface Energy and Water Balance: Sensitivity Analysis. Tech. Memo. 95.2, CSIRO, Institute of Natural Resources and Environment, Division of Water Resources, Canberra.

Hatton, T.J., Pierce, L.L., & Walker, J. (1993), Ecohydrological changes in the Murray-Darling Basin. II. Development and tests of a water balance model. J. of Applied Ecol., 30:274-282.

Hatton, T.J., Salvucci, G.D., & Wu, H.-I (in press.), Eagleson's ecological optimality theory: quo vadis?. Functional Ecology, in press.

Hatton, T.J., Walker, J., Dawes, W., & Dunin, F.X. (1992), Simulations of hydroecological responses to elevated CO_2 at the catchment scale. Aust. J. Bot., 40:679-696.

Hay, L. & Knapp, L. (1996), Integrating a geographic information system, a scientific visualization system and an orographic precipitation model. HydroGIS 96: Application of Geographical Information Systems in Hydrology and Water Resources Management, Proceedings of the Vienna Conference, April 1996, IAHS Publ. no. 235, 123-131.

Hay, L.E., Battaglin, W.A., Branson, M.D., & Leavesley, G.H. (1993), Application of GIS in modelling winter orographic precipitation, Gunnison River Basin, Colorado, USA. HydroGIS 93: Application of Geographic Information Systems in Hydrology and Water Resources (Proceedings of the Vienna Conference, April 1993). IAHS Publ. no. 211.

Haydon, S.R. (1993), Modelling of annual streamflow yield changes. In: O'Shaughnessy, P.J., Benyon, R., & Lucas, A. (eds.), The Crotty Creek Project, Second Prog. Rep., Cons. & Nat Resour. - For. Serv. Res. Rep. 358, Melbourne Water - Rep. No. MMBW-W-0020, pp. 26-38.

Haydon, S.R. & Jayasuriya, M.D.A. (1993), The hydrologic response to strip thinning in a Mountain Ash catchment: The Crotty Creek Experiment. Hydrol. & Wat. Res. Symp., Newcastle, June 30 - July 2, 1993, 81-86.

Haydon, S.R., Benyon, R.G., & Lewis, R. (1996), Variation in sapwood area and throughfall with forest age in mountain ash (Euaclyptus regnans F.Muell.). J. Hydrol., 187:351-366.

Heislers, D. (1993), Groundwater in the Central Victorian Highlands. Dept. Cons. Nat. Res., Water Division, Melbourne, Rep. no. 87.

Herwitz, S.R., Peterson, D.L., & Eastman, J.R. (1990), Thematic mapper detection of changes in the leaf area of closed canopy pine plantations in central massachusetts. Remote Sensing of Environment, 29:129-140.

Hevesi, J.A., Flint, A.L., & Istok, J.D. (1992), Precipitation estimation in mountainous terrain using multivariate geostatistics. Part II: Isohyetal maps. J. Appl. Meteorol., 31:677-88.

Hevesi, J.A., Istok, J.D., & Flint, A.L. (1992), Precipitation estimation in mountainous terrain using mulivariate geostatistics. Part I: Structural analysis. J. Appl. Meteorol., 31:661-76.

Hillis, W.E. & Brown, A.G. (eds) (1984), Eucalypts for wood production. CSIRO Academic Press, Sydney, 434 pp.

Hills, E.S. (1975), Physiography of Victoria: An Introduction to Geomorphology (new ed.). Whitcombe & Tombs, Marrickville, NSW, Australia, 373 pp.

Holmgren, P. (1994), Multiple flow direction algorithms for runoff modelling in grid based elevation models: An empirical evaluation. Hydr. Proc., 8:327-334.

Hookey, G.R., Loh, I.C., & Bartle, J.R. (1987), Water Use of Eucalypts Above Saline Groundwater. Water Authority of Wetsern Australia, Report No. WH 32.

Horn, B.K.P. (1981), Hill shading and the reflectance map. Proc. IEEE 69:14-47.

Howard, J.A. (1991), Remote Sensing of Forest Resources: Theory and Application. Chapman & Hall, London, 420 pp.

Howard, N. & O'Shaughnessy, P. (1971), Coranderrk Experimental Area: First Progress Report, Pre-treatment Calibration. Water Supply Catchment Hydrology Research, Melbourne Metropolitan Board of Works, Rep. No. MMBW-W-0001.

Hughes, D.A. & Sami, K. (1994), A semi-distributed, variable time interval model of catchment hydrology - structure and parameter estimation procedures. J. Hydrol., 155:265-291.

Hutchinson, M.F. (1983), A new objective for spatial interpolation of meteorological variables from irregular networks applied to the estimation of monthly mean solar radiation, temperature, precipitation and windrun. In: Fitzpatrick, E.A. & Kalma, J.D. (eds.), Need for climatic and hydrologic data in agriculture of Southeast Asia, Proceedings of a United Nations Univ. Workshop, 12-15 Dec. 1983, CSIRO Div. Wat.

Res., Canberra.

Hutchinson, M.F. (1987), Methods of generation of wethaer sequences. In: Bunting, A.H. (ed.), Agricultural Environments: Chracterization, Classification and Mapping, Ch. 16, CAB International, Wallingford, U.K., pp. 149-157.

Hutchinson, M.F. (1988), Calculation of hydrologically sound digital elevation models. Proc. Third. Int. Symp. on Spatial Data Handling, Sydney, 1988, pp. 117-133.

Hutchinson, M.F. (1989), New procedure for gridding elevation and stream line data with automatic removal of spurious pits. J. Hydrol., 106:3:211-232.

Hutchinson, M.F. (1991), Climatic analyses in data sparse regions. In: Muchow, R.C. & Bellamy, J.A. (eds.), Climatic Risk in Crop Production, CAB International, Wallingford, pp. 55-71.

Hutchinson, M.F. (1991), The application of thin plate smoothing splines to continent-wide data assimilation. In: Jasper, J.D., Data Assimilation Systems: Papers Presented at the Second BMRC Modelling Workshop, September, 1990, Bureau of Meteorology Research Centre, Melbourne, Australia, 259 pp., pp.104-113.

Hutchinson, M.F. (1993), Development of a continent-wide DEM with applications to terrain and climate analysis. In: Goodchild, M.F., Parks, B.O., & Steyaert, L.T. (eds.), Environmental Modelling with GIS, Oxford Univ. Press, New York, 392-400.

Hutchinson, M.F. (1995), Interpolating mean rainfall using thin plate splines. Int. J. Geographical Information Systems, 9:4:385-403.

Hutchinson, M.F. (1995), Stochastic space-time weather models from ground-based data. Agricultural and Forest Meterorology, 73:237-264.

Hutchinson, M.F. & Gessler, P.E. (1994), Splines - more than just a smooth interpolator. Geoderma, 62:45-67.

Hutchinson, M.F. & Bischof, R.J. (1983), A new method for estimating the spatial distribution of mean annual rainfall applied to the Hunter Valley, New South Wales. Aust. Meteorol. Mag., 32:179-184.

Hutchinson, M.F. & Dowling, T.I. (1991), A continental hydrological assessment of a new grid-based digital elevation model of Australia. Hydrol. Proc., 5:45-58.

Hutchinson, M.F., Kalma, J.D., & Johnson, M.E. (1984), Monthly estimates of wind speed and wind run for Australia. J. Climatology, 4:311-324.

Hutchinson, M.F., Kesteven, J.L., & Nix, H.A. (1997), New Australian climate surfaces for natural resource assessment. Australian Collaborative Land Evaluation Program (ACLEP), Newsletter, Vol. 6, No. 4, pp. 2-5.

Incoll, W.D. (1969), Root excavations of *Eucalyptus regnans*. Res. Activ. For. Commn. Vict., 69:15-16.

Iqbal, M. (1983), An Introduction to Solar Radiation. Academic Press, Toronto, 390 pp.

Jackson, E. (1991), Soil moisture distribution and tree mortality in Shaver Hollow, Shenandoah National Park, Virginia. M.Sc. Thesis, Dept. of Env. Science, Univ. of Virginia, Charlottesville, VA.

Jakeman, A.J. & Hornberger, G.M. (1993), How much complexity is warranted in a rainfall-runoff model?. Wat. Resour. Res., 29:2637-2649.

Jakeman, A.J., Hornberger, G.M., Littlewood, I.G., Whitehead, P.G., & Harvey, J.W. (1992), A systematic approach to modelling the dynamic linkage of climate, physical catchment descriptors and hydrologic response components. Mathematics and Computers in Simulation, 33:359-366.

Jakeman, A.J., Littlewood, I.G., & Whitehead, P.G. (1990), Computation of the instantaneous unit hydrograph and identifiable component flows with application to two small upland catchments. J. Hydrol., 117:275-300.

Jarvis, P.G. & McNaughton, K.G. (1986), Stomatal control of transpiration: scaling up from a leaf to a region. Adv. Ecol. Res., 15:1-49.

Jarvis, T. & Leslie, D. (1988), Using Sapwood Area to Estimate Leaf Area Index in Old Growth Stands of Mountain Ash (Eucalyptus regnans F. Muell). Unpub., Maroondah Leaf Area Study Report, Melbourne Metropolitan Board of Works, Upper Yarra Regional Office, Forestry Section, 9 pp.

Jayasuriya, M.D.A. (1994), Effects of forest treatment on total streamflow. In: O'Shaughnessy & Jayasuriya, M.D.A., P.J. (eds.), Third Progress Report - North Maroondah, Water Supply Catchment Hydrology Research, Melbourne Water, Rep. No. MMBW-W-0017, pp. 123-138.

Jayasuriya, M.D.A. (1994), Streamflow characteristics. In: O'Shaughnessy & Jayasuriya, M.D.A., P.J. (eds.), Third Progress Report - North Maroondah, Water Supply Catchment Hydrology Research, Melbourne Water, Rep. No. MMBW-W-0017, pp. 94-112.

Jayasuriya, M.D.A. & Creaner, S.J. (1994), Analysis of soil moisture data. In: O'Shaughnessy, P.J. & Jayasuriya, M.D.A. (eds), Third Progress Report - North Maroondah, Melbourne Water, Water Supply Catchment Hydrology Research, Report No. MMBW-W-0017, Ch. 7, pp 113-122.

Jayasuriya, M.D.A. & O'Shaughnessy, P.J. (1988), The use of mathematical models in evaluating forest treatment effects on streamflow. Hydrol. & Wat. Resour. Symp., A.N.U., Canberra, 1-3 Feb. 1988, Preprints of Papers, Inst. Eng. Aust., 135-139.

Jayasuriya, M.D.A., Dunn, G.M., Benyon, R., & O'Shaughnessy, P.J. (1993), Some factors affecting water yield from mouintain ash (Eucalyptus regnans) dominated forests in southeast Australia. J. Hydrol., 150:345-367.

Jensen, K.H. & Mantoglou, A. (1992), Future of distributed modelling. In: Beven, K.J. & Moore, I.B. (eds.), Terrain Analysis and Distributed Modelling in Hydrology, Wiley, Chichester, pp. 203-212.

Jensen, K.H., Bitsch, K., & Bjerg, P.L. (1993), Large scale dispersion experiments in a sandy aquifer in Denmark: observed tracer movements and numerical analysis. Wat. Resour. Res., 28:269-284.

Jones, J.A.A. (1986), Some limitations to the a/s index for predicting basin-wide patterns of soil water drainage. Z. Geomorph., 60:7-20.

Journet, A.R.P. (1979), The water status of Eucalyptus blakelyi M. under field conditions. Annals of Botany, 44:125-128.

Jupp, D.L. & Strahler, A.H. (1991), A hotspot model for leaf canopies. Rem. Sens. of the Environ., 38:3:193-210.

Körner, Ch. (1994), Leaf diffusive conductances in the major vegetation types of the globe. In: Schulze, E.-D. & Caldwell, M.M. (eds), Ecophysiology of Photosynthesis, Ecological Studies Vol. 100, Springer, Heidelberg, pp. 463-490.

Körner, Ch., Scheel, J.A., Bauer, H. (1979), Maximum diffusive leaf conductance in vascular plants. Photosynthetica, 13:45-82.

Kaufmann, M.R. & Troendle, C.A. (1981), The relationship of leaf area and foliage biomass to sapwood conducting area in four subalpine forest tree species. Forest Sci., 27:477-482.

Kelliher, F.M., Leuning, R., Raupach, M.R., & Schulze, E.-D. (1995), Maximum conductances for evaporation from global vegetation types. Agricultural and Forest Meteorology, 73:1-16.

King, A.R. (1963), The Influence of Colonization in the forests and the prevalence of bush fires in Australia. CSIRO Division of Physical Chemistry, Melbourne, Victoria.

Kira, T. & Shidei, T. (1967), Primary production and turnover of organic matter in different forest ecosystems of the Western Pacific. Jap. J. Ecol., 17:70-87.

Kite, G.W. (1995), The SLURP model. In: Singh, V.P. (ed.), Computer Models of Watershed Hydrology, Water Resources Publications, Highlands Ranch, Colorado, 521-562.

Knisel, W.G. & Williams, J.R. (1995), Hydrology components of CREAMS and GLEAMS models. In: Singh, V.P. (ed.), Computer Models of Watershed Hydrology, Water Resources Publications, Highlands Ranch, Colorado, 1069-1114.

Kuczera, G.A. (1983), Improved parameter inference in catchment models. 1. Evaluating parameter uncertainty. Wat. Resour. Resear., 19:5:1151-1162.

Kuczera, G.A. (1983), Improved parameter inference in catchment models. 2. Combining different kinds of hydrologic data and testing thier compatability. Wat. Resour. Resear., 19:5:1163-1172.

Kuczera, G.A. (1984), Forecasting monthly runoff in the Thomson catchment using the revised SDI model. Unpub., Internal Report, Melbourne and Metropolitan Board of Works.

Kuczera, G.A. (1985), Prediction of Water Yield Reductions Following a Bushfire in Ash - Mixed Species Eucalypt Forest. Melbourne Metropolitan Board of Works, Water Supply Catchment Hydrology Research, Rep. No. MMBW-W-0014.

Kuczera, G.A. (1987), Prediction of water yield reductions following a bushfire in ash-mixed species eucalypt forest. J. Hydrol., 94:215-236.

Kuczera, G.A. (1988), On the revision of the Soil Dryness Index streamflow yield model. Civ. Eng. Trans., Inst. Eng. Aust., CE30:2: 79-86.

Kuczera, G.A. (1988), The soil dryness index streamflow yield model: An overview of its development an capabilities. Hydr. & Wat. Res. Symp., ANU, Canberra, 1-3 Feb. 1988, Preprints of Papers, 103-107.

Kuczera, G.A., Raper, G.P., Brah, N.S., & Jayasuriya, M.D.A. (1993), Modelling yield changes after strip thinning in a mountain ash catchment: an exercise in catchment model validation. J. Hydrol., 150:433-457.

Lacaze, B. (1990), The relationships between remotely sensed vegetation indices and plant canopy properties. In: Barrett, E.C., Power, C.H., & Micallef, A. (eds), Satellite Remote Sening for Hydrology and Water Management: The Mediterranean Coasts and Islands, Proc. of an Int. Training Course, Rabat, Malta, 2-12 Oct., 1988, Gordon & Breach, New York, 137-151.

Lacaze, B. (1996), Spectral characterisation of vegetation communities and practical approaches to vegetation cover changes monitoring. Remote Sensing for Land Degradation and Desertification Monitoring in the Mediterranean Basin, Workshop Proceedings, Valencia, 13-15 June 1994, in press.

Lacey, G.C. (1996), The Scaling of Baseflow. Cooperative Research Centre for Catchment Hydrology, Working Document 96/1, Melbourne, 35 pp.

Lamb, R. (1996), Distributed hydrological prediction using generalised TOPOMDEL concepts. PhD Thesis, Lancaster University, U.K.

Lamb, R. & Beven, K. (1997), Using interactive recession curve analysis to specify a general catchment storage model. Hydrology and Earth System Sciences, 1:101-114.

Lamb, R., Beven, K., & Myrabo, S. (1996), A generalised topographic-soils hydrological index. In: Lane, S.N., Richards, K.S., & Chandler, J.H. (eds), Landform Monitoring, Modelling and Analysis, Ch. 12, Wiley, Chichester.

Lamb, R., Beven, K., & Myrabo, S. (1997), Discharge and water table predictions using a generalised TOPMODEL formulation. Hydr. Proc., 11:1131-1144.

Lammers, R.B. & Band, L.E. (1990), Automating object representation of drainage basins. Comp. Geosci., 16:6:787-810.

Lang, A.R.G., Xiang, Y., & Norman, J.M. (1985), Crop structure and the penetration of direct sunlight. Agric. For. Meteorol., 35:83-101.

Langford, K.J. (1974), Change in Yield of Water Following a Bushfire in a Forest of Eucalyptus Regnans. Water Supply Catchment Hydrology Research, Melbourne Metropolitan Board of Works, Rep. No. MMBW-W-0003.

Langford, K.J. (1976), Change in yield of water following a bushfire in a forest of Eucalyptus regnans. J. Hydrol., 29:87-114.

Langford, K.J. & O'Shaughnessy, P.J. (eds.) (1977), First Progress Report: North Maroondah. Water Supply Catchment Hydrology Research, Melbourne Metropolitan Board of Works, Rep. No. MMBW-W-0005.

Langford, K.J. & O'Shaughnessy, P.J. (eds.) (1978), A Study of Canopy Interception in Native Forests and Conifer Plantations. Melbourne Metropolitan Board of Works, Water Supply Catchment Hydrology Research, Rep. No. MMBW-W-0007.

Langford, K.J. & O'Shaughnessy, P.J. (eds.) (1979), Second Progress Report: North Maroondah. Melbourne Metropolitan Board of Works, Water Supply Catchment Hydrology Research, Rep. No. MMBW-W-0009.

Langford, K.J. & O'Shaughnessy, P.J. (eds.) (1979), Soil moisture depletion rates in 1939 regrowth Mountain Ash over a summer drying period. Melbourne Metropolitan Board of Works, Water Supply Catchment Hydrology Research, Rep. No. MMBW-W-0008.

Langford, K.J. & O'Shaughnessy, P.J. (eds.) (1980), A Study of the Coranderrk Soils. Water Supply Catchment Hydrology Research, Melbourne Metropolitan Board of Works, Rep. No. MMBW-W-0006.

Langford, K.J. & O'Shaughnessy, P.J. (eds.) (1980), Second Progress Report: Coranderrk. Melbourne Metropolitan Board of Works, Water Supply Catchment Hydrology Research, Rep. No. MMBW-W-0010.

Langford, K.J., Duncan, H.P., & Heeps, D.P. (1977), Evaluation and use of a balance model. Hydrol. Symp. 1977: The Hydrology of Northern Australia, Brisbane, 28-30 June 1977, Inst. Eng. Aust., 151-155.

Langford, K.J., Duncan, H.P., & Heeps, D.P. (1978), Forecasting streamflow and storage using a soil dryness index model. Melbourne Metropolitan Board of Works, Rep. No. MMBW-W-0031.

Langford, K.J., Moran, R.J., & O'Shaughnessy, P.J. (1982), The Coranderrk Experiment - The effects of roading and timber harvesting in a mature mountain ash forest on streamflow yield and quality. The First National Symposium on Forest Hydrology, 11-13 May, 1982, Melbourne, pp. 92-102.

Laslett, G.M. (1994), Kriging and splines: an empirical comparison of their predictive performance in some applications. J. Am. Stat. Assoc., 89:391-409.

Lathrop, Jr., R.G. & Pierce, L. (1991), Ground-based canopy transmittance and satellite remotely sensed measurements for estimation of coniferous forest canopy structure. Remote Sensing of Environment, 36:179-188.

Lau, J.A., Vandenberg, W.G., & Willig, R.U. (1994), Visual and spatial techniques in multiple-use forest planning. New opportunities best practice, Proceedings, Resource technology 94, University of Melbourne, Australia, pp. 154-179.

Lau, J.A., Vandenberg, W.G., & Willig, R.U. (1996), The integration of visualization, spatial and operation research techniques into a single forest planning system. Proc. Southern Forestry Geographical Information Systems Conference, University of Georgia, Athens, USA, pp. 103-114.

Lau, J.A., Vandenberg, W.G., Willig, R.U., & Chikumbo, O. (1995), Visual and spatial approach to large scale forest modelling in multiple-use forest planning - Australian (Victorian) experience. Proc. International Seminar on Large Scale Foresry Scenario Models, Experience, and Requirements, Joensuu, Finland, pp. 261-273.

Leavesley, G.H. & Stannard, L.G. (1995), The precipitation-runoff modeling system - PRMS. In: Singh, V.P. (ed.), Computer Models of Watershed Hydrology, Water Resources Publications, Highlands Ranch, Colorado, 281-310.

Lebel, T., Bastin, G., Obled, C., & Creutin, J.D. (1987), On the accuracy of areal rainfall estimation: a case study. Wat. Resour. Res., 23:2123-2134.

Leblon, B., Granberg, H., Ansseau, C., & Royer, A. (1993), A semi-emperical model to estimate the biomass production of forest canopies from spectral variables. Part 1: Relationship between spectral variables and light interception efficiency. Remote Sensing Reviews, 7:109-125.

Lee, R. (1980), Forest Hydrology. Columbia University Press, New York.

Leeper, G.W. & Uren, N.C. (1993), Introduction to soil science (5th ed.). Melbourne University Press, Melbourne.

Lees, B.G. & Ritman, K. (1991), Decision-tree and rule-induction approach to integration of remotely sensed and GIS data in mapping vegetation in disturbed or hilly environments. Environ. Manag., 15:6:823-831.

Legge, N.J. (1980), Aspects of transpiration in mountain ash (*Eucalyptus regnans* F. Muell.). PhD thesis, Latrobe Univ., Victoria, Australia.

Legge, N.J. (1985), Relating water potential gradients in mountain ash (Eucalyptus regnans F. Muell.) to transpiration rate. Aust. J. Plant. Physiol., 12:89-96.

Leuning, R. (1995), A critical appraisal of a combined stomatal-photosynthesis model for C_3 plants. Plant Cell Environ., 18:339-355.

Leuning, R., Kriedemann, P.F., & McMurtis, R.F. (1991), Simulation of evapotranspiration by trees. Agric. Wat. Manag., 19:3:205-221.

Linacre, E. (1992), Climate Data and Resources: A Reference and Guide. Routledge, London, 366 pp.

Linacre, E. & Hobbs, J. (1977), The Australian Climatic Environment. Wiley, Brisbane, Australia, 354 pp.

Lindenmayer, D.B. (1996), Wildlife and Woodchips: Leadbeater's Possum - a test case for sustainable forestry. Univ. of New South Wales Press, Sydney, 156 pp.

Liu, C.Y. & Krajewski, W.F. (1993), Interpolated accumulation of radar-rainfall estimation (abstract). EOS, Transactions, Am. Geophys. Union, 74:43:250.

Lorieri, D., Vertessy, R.A., Elsenbeer, H., & Davis, S.H. (1997), Saptial variability in the saturated hydraulic conductivity of soils in the Ettercon 3 catchment. Cooperative Research Centre for Catchment Hydrology, Report in prep., Monash University, Melbourne.

Loukas, A. & Quick, M.C. (1996), Spatial and temporal distribution of storm precipitation in southwestern British Columbia. J. Hydrol., 174: 37-56.

Ludquist, D., Christophersen, N., & Neal, C. (1990), Towards developing a new short-term model for the Birkenes catchment. Lessons learned. J. Hydrol., 116:391-401.

Mackay, D.S. & Band, L.E. (1997), Forest ecosystem processes at the watershed scale: dynamic coupling of distributed hydrology and canopy growth. Hydr. Proc., 11:1197-1217.

Markham, B.L. & Barker, J.L. (1986), Landsat MSS and TM post-calbration dynamic ranges, exoatmospheric reflectances and at-satellite temperatures. EOSAT Landsat Tech. Notes 1:3-8.

Martinez-Cob, A. (1996), Multivariate geostatistical analysis of evapotranspiration and precipitation in mountainous terrain. J. Hydrol., 174:19-35.

McBratney, A.B., De Gruijter, J.J., & Brus, D.J. (1992), Spacial prediction and mapping of continuous soil classes. Geoderma, 54:39-64.

McCloy, K.R. & Hall, K.A. (1991), Mapping the density of woody vegetative cover using Landsat MSS digital data. Int. J. Rem. Sens., 12:9:1877-1885.

McDonald, R.C. & Isbell, R.F. (1990), Soil profile. In: McDonald, R.C., Isbell, R.F., Speight, R.F., Walker, J.G., & Hopkins, M.S., Australian Soil and Land Survey Field Handbook (2nd ed.), Inkata Press, Melbourne, 198 pp., pp. 103-152.

McDonnell, J.J., Freer, J., Hooper, R., Kendall, C., Burns, D., Beven, K., & Peters, J. (1996), New method developed for studying flow on hillslopes. EOS, Transactions, American Geophysical Union, 77:47:465.

McJannet, D.L., Vertessy, R.A., Tapper, N.J., O'Sullivan, S.K., Beringer, J., & Cleugh, H. (1996), Soil and Litter Evaporation BEneath Re-growth and Old-growth Mountain Ash Forest. Report 96/1, Cooperative Research Centre for Catchment Hydrology, Department of Civil Engineering, Monash University, Clayton, Victoria, Australia, 59 pp.

McKenzie, N.J. & Austin, M.P. (1993), A quantitative Australian approach to medium and small scale surveys based on soil stratigraphy and environmental correlation. Geoderma, 57:329-355.

McLaughlin, R.J.W. (1988), Upper Devonian to Lower Carboniferous provinces: Central Victorian Volcanic Cauldron Province. In: Ferguson, J.A. & Douglas, J.G. (eds.), Geology of Victoria, Vic. Div., Geol. Soc. of Aust. Inc., 655 pp, 151-169.

McMurtie, R.E. (1993), Modelling of canopy carbon and water balance. In: Hall, D.O., Scurlock, J.M.O., Bolhar-Nordenkampf, H.R., Leegood, R.C., & Long, S.P. (eds), Photosynthesis and Production in a Changing Environment: a field and laboratory manual, Chapman & Hall, London, 220-231.

McMurtie, R.E. & Landsberg, J.J. (1992), Using a simulation model to evaluate the effects of water and nutrients on the growth and carbon partitioning of $Pinus$ $radiata$. Forest Ecology and Management, 52:243-260.

McMurtie, R.E., Benson, M.L., Linder, S., Running, S.W., Talsma, T., Crane, W.J.B., & Myers, B.J. (1990), Water/nutrient interactions affecting the productivity of stands of $Pinus$ $radiata$. Forest Ecology and Management, 30:415-423.

McMurtie, R.E., Leuning, R., Thompson, W.A., & Wheeler, A.M. (1992), A model of canopy photosynthesis and water use incorporating a mechanistic formulation of leaf CO_2 exchange. Forest Ecology and Management, 52:261-278.

McMurtie, R.E., Rook, D.A., & Kelliher, F.M. (1990), Modelling the yield of $Pinus$ $radiata$ on a site limited by water and nitrogen. Forest Ecology and Management, 30:381-413.

McNaughton, K.G. & Black, T.A. (1973), A study of evapotranspiration from a Douglas Fir forest using the energy balance approach. Water. Resour. Res., 9:1579-1590.

McVicar, T.R. (1997), The Use of Remote Sensing to Aid Decisions on Drought Exceptional Circumstances. Report to Bureau of Resource Sciences, Dept. of Primary Industries and Energy, CSIRO Division of Water Resources, Consultancy Report 97-14, Canberra, 83 pp.

McVicar, T.R., Jupp, D.L.B., & Williams, N.A. (1996), Relating AVHRR Vegetation Indices to Landsat TM Leaf Area Index Estimates. CSIRO Division of Water Resources, Tech. Memo. 96.15, Canberra, 32 pp.

McVicar, T.R., Jupp, D.L.B., Reece, P.H., & Williams, N. (1996), Relating Landsat TM Vegetation Indices to in $situ$ Leaf Area Index Measurements. CSIRO Division of Water Resources, Tech. Memo. 96.14, Canberra, Australia, 80 pp.

McVicar, T.R., Walker, J., Jupp, D.L.B., Pierce, L.L., Byrne, G.T., & Dallwitz, R. (1996), Relating AVHRR Vegetation Indices to in $situ$ Measurements of Leaf Area Index. CSIRO Division of Water Resources, Tech. Memo. 96.5, Canberra, Australia, 54 pp.

Melbourne Metropolitan Board of Works (MMBW) (1980), Summary of Technical Conclusions to 1979. Water Supply Catchment Hydrology Research, Rep. No. MMBW-W-0012.

Merot, Ph., Ezzahar, B., Walter, C., & Aurousseau, P. (1995), Mapping waterlogging of soils using digital terrain models. Hydr. Proc., 9:27-34.

Michaud, J.D., Auvine, B.A., & Penalba, O.C. (1995), Spatial and elevational variations of summer rainfall in the southwestern United States. J. Appl. Met, 34:2689-2703.

Minnaert, M. (1941), The reciprocity principle in lunar photometry. The Astrophysical Journal, 93:403-410.

Mitasova, H. & Hofierka, L. (1993), Interpolation by regularized spline with tension: II. Application to terrain modeling and surface geometry analysis. Mathematical Geology, 25:6:657-669.

Mitasova, H. & Mitas, L. (1993), Interpolation by regularized spline with tension I. Theory and imple-

mentation. Mathematical Geology, 25:6:641-655.

Mitchell, N.D. (1991), The derivation of climatic surfaces for New Zealand, and their application to the bioclimatic analysis of the distribution of kauri (Agathis australis). J. of the Roy. Soc. of N.Z.

Monteith, J.L. & Unsworth, M.H. (1990), Principles of Environmental Physics (2nd ed.). Routledge, Chapman and Hall, New York, 291 pp.

Moore, I.D. & Mein, R.G. (1975), An evaluation of three rainfall-runoff models. Proc., Hydrol. Symp. 1975, Armidale N.S.W., Inst. Eng. Aust., 122-126.

Moore, I.D., Burch, G.J., & Mackenzie, D.H. (1988), Topographic effects on the distribution of surface soil water and the location of ephemeral gullies. Trans., A.S.A.E., 31:4:1098-1107.

Moore, I.D., Grayson, R.B., Ladson, A.R. (1991), Digital terrain modelling: a review of hydrological, geomorphological, and biological applications. Hydrological Processes, 5, 3-30.

Moore, I.D., Mackay, S.M., Wallbrink, P.J., Burch, G.J., & O'Loughlin, E.M. (1986), Hydrologic characteristics and modelling of a small forested catchment in southeastern New South Wales. Prelogging condition. J. Hydrol., 83:307-335.

Moore, I.D., Norton, T.W., & Williams, J.E. (1993), Modelling environmental heterogeneity in forested landscapes. J. Hydrol., 150:717-747.

Moore, R.D. & Thompson, J.C. (1996), Are water table variations in a shallow forest soil consistent with the TOPMODEL concept?. Water Resources Research, 32:3:663-669.

Moore, R.J. (1985), The probability-distributed principle and runoff production at point and basin scales. Hydrol. Sci. J., 30:273-297.

Moran, R.J. & O'Connell, M.J. (1977), Soil moisture. In: Langford, K.J. & O'Shaughnessy, P.J. (eds), First Progress Report - North Maroondah, Melbourne and Metropolitan Board of Works, Water Supply Catchment Hydrology Research, Report MMBW-W-0005, Ch. 7, pp 157-167.

Moran, R.J. & O'Shaughnessy, P.J. (1984), Determination of the evapotranspiration of E. regnans forested catchments using hydrological measurements. Agricultural Water Management, 8:57-76.

Moran, R.J. & Ronan, M. (1978), Soil moisture depletion rates in 1939 regrowth Mountain Ash over a summer drying period. Hydrol. Symp. 1978, Canberra, 5-7 Sep. 1978, Preprints of Papers, Inst. Eng. Aust., 163-167.

Morris, C.J.G., Nunez, M., Montes, S. (1995), A field study of orographic precipitation anomalies during high velocity winds usings an aerofoil rain gauge. Theoretical and Applied Climatology, 51:139-151.

Morton, F.I. (1965), Potential evaporation and river basin evaporation. J. Hydraul. Eng., 91:HY6:67-97.

Morton, F.I. (1969), Potential evaporation as a manifestation of regional evaporation. Water Resour. Res., 5:1244-1255.

Morton, F.I. (1975), Estimating evaporation and transpiration from climatological observations. J. Appl. Meteorol., 14:488-497.

Morton, F.I. (1983), Operational estimates of areal evaporation and their significance to the science and practice of hydrology. J. Hydrol., 66:1-76.

Mount, A.B. (1972), The Derivation and Testing of a Soil Dryness Index Using Runoff Data. Tasmanian Forestry Commision, Bulletin No. 4.

Mount, A.B. (1980), Estimation of evaporative losses from forests: A proven simple model with wide applications. Hydrol. & Wat. Resour. Symp. 1980, Adelaide, 4-6 Nov. 1980, Preprints of Papers, Inst. Eng. Aust., 101-105.

Mroczkowski, M. & Kuczera, G. (1996), On model identification for catchments undergoing land use change. 23rd Hydrology and Water Resources Symposium, Hobart, Australia, 21-24 May 1996, 89-95.

Munro, R.K., Lyons, W.F., Shao, Y., Wood, M.S., Hood, L.M., & Leslie, L.M. (1997), Modelling land surface-atmosphere interactions over the Australian continent with an emphasis on the role of soil moisture. Proc., Int. Congr. on Modelling and Simulation, MODSIM 97, December,1997, Hobart, Australia, 246-252.

Murray, F.W. (1967), On the computation of saturation vapor pressure. J. Appl. Meteorol., 6:203-204.

Myeni & Williams (1994), On the relationship between FAPAR and NDVI. Rem. Sens. of Environ., 49:200-211.

Myers, D.E. (1994), Spatial interpolation: an overview. Geoderma, 62:17-28.

Naden, P., Crooks, S., & Broadhurst, P. (c. 1996), Impact of Climate and Land Use Chnage on the Flood Response of Large Catchments. Unpublished, informal manuscipt, Institute of Hydrology, Wallingford,

UK.

National Mapping Council of Australia (1972), The Australian Map Grid - Technical Manual - Special Publication 7. Aust. Gov't. Publ. Service, Canberra.

Nemani, R., Pierce, L., Band, L.E., & Running, S.W. (1993), Forest ecosystem processes at the watershed scale: Sensitivity to remotely sensed leaf area index observations. Int. J. Rem. Sens., 14:2519-2534.

Nemani, R., Running, S.W., Band, L.E., & Peterson, D.L. (1993), Regional hydroecological simulation system: An illustration of the integration of ecosystem models in a GIS. In: Goodchild, M.F., Parks, B.O., & Steyaert, L.T. (eds.), Environmental Modelling with GIS, Oxford Univ. Press, New York, 296-304.

Nemani, R.R. & Running, S.W. (1989), Testing a theoretical climate-soil leaf area hydrologic equilibrium of forests using satellite data and ecosystem simulation. Agric. & For. Meteorol., 44:245-260.

Niemann, O. (1993), Automated forest cover mapping using Thematic Mapper images and ancillary data. Applied Geography, 13:86-95.

Northcote, K.H. (1961), Atlas of Australian Soils. Sheet 2. Melbourne - Tasmania area. CSIRO, Division of Soils, Canberra, Australia.

O'Connell, M.J. & O'Shaughnessy, P.J. (1975), The Wallaby Creek fog drip study. Melbourne and Metropolitan Board of Works, Water Supply Catchment Hydrology Research, Rep. No. MMBW-W-0004.

O'Loughlin, E.M. (1986), Prediction of surface saturation zones in natural catchments by topographic analysis. Water Resources Research, 22:5:794-804.

O'Shaughnessy, P.J. & Jayasuriya, M.D.A. (1991), Water Supply Catchment Hydrology Research: Status Report 1991. Melbourne Water, 16 pp..

O'Shaughnessy, P.J., Moran, R.J., & Flinn, D.W. (eds.) (1981), The Crotty Creek Project: The Effects of Strip Thinning Eucalyptus Regnans on Water Yield. Melbourne Metropolitan Board of Works, Water Supply Catchment Hydrology Research, Rep. No. MMBW-W-0013. Forests Comission Victoria, Misc. Pub. No. 9.

O'Sullivan, S.K. (in prep.), The Relationship Between Leaf Area, Transpiration and Canopy Interception in Various Age Classes of Eucalyptus regnans. PhD thesis, Department of Civil Engineering, Monash University, Melbourne, Australia.

Obled, Ch., Wendling, J., & Beven, K. (1994), The sensitivity of hydrological models to spatial rainfall patterns: an evaluation using observed data. J. Hydrol., 159:305-333.

Oke, T.R. (1987), Boundary Layer Climates (2nd ed.). Routledge, London, 435 pp.

Ord, S. (1985), North Maroondah Experimental Catchments, Myrtle II Timber Utilisation and Regeneration 1984/85. Unpublished report, Melbourne Water.

Orr, S., Bennett, D., Snodgrass, J., Hoenen, J., Winter, G., & Burley, C. (1986), A leaf area index for Eucalyptus regnans age 15 years. Coranderrk Leaf Area Project Report, Melbourne Metropolitan Board of Works, Internal Report, Melbourne.

Ostendorf, B., Quinn, P., Beven, K.J., & Tenhunen, J.D. (1995), Hydrological controls on ecosystem gas exchange in an arctic landscape. In: Reynolds, J.R. & Tenhunen, J.D. (eds), Landscape function and disturbance in Arctic tundra, Ecological Studies 120, Springer Verlag, Berlin, 369-386.

Ovington, J.D. (1957), Dry-matter production by Pinus sylvestris L.. Ann. Bot. (London), N.S., 21:287-314.

Paine, D.W.M. (1982), Bushfires. In: Duncan, J.S. (ed.), Atlas of Victoria, Victorian Government Printing Office, Melbourne.

Paltridge, G.W. & Mitchell, R.M. (1990), Atmospheric and viewing angle correction of vegetation indices and grassland fuel-moisture content derived from NOAA/AVHRR. Rem. Sens. of Environ., 31:1:121-135.

Parton, W.J. & Logan, J.E. (1981), A model for diurnal variation in soil and air temperature. Agric. Meteorol., 23:205-216.

Peirce, J.D. (1890), The Giant Trees of Victoria. Melbourne.

Petch, R.A. (1988), Soil saturation patterns in steep, convergent hillslopes under forest and pasture vegetation. Hydr. Proc., 2:93-103.

Peterson, D.L., Spanner, M.A., Running, S.W., & Teuber, K.B. (1987), Relationship of thematic mapper simulator data to leaf area index of temperate coniferous forests. Rem. Sens. of Environ., 22:323-341.

Peterson, D.L., Westman, W.E., Stephenson, N.J., Ambrosia, V.G., Brass, J.A., & Spanner, M.A. (1986), Analysis of forest structure using Thematic Mapper Simulator data. IEEE Trans. on Geoscience and

Remote Sensing, 24:113-121.

Pfeiffer, C. & Watson, F.G.R. (1996), Spatial Variability of Leaf Area Index in the Maroondah Experimental Area. Unpublished rep., Cooperative Research Centre for Catchment Hydrology, Univ. of Melbourne, Australia.

Piñol, J., Beven, K., & Freer, J. (1997), Modelling the hydrological response of mediteranean catchments, Prades, Catalonia. The use of distributed models as aids to hypothesis formulation. Hydrol. Proc., 11:1287-1306.

Pierce, L.L. & Running, S.W. (1988), Rapid estimation of coniferous forest leaf area index using a portable integrating radiometer. Ecology, 69:1762-1767.

Pierce, L.L., Running, S.W., & Riggs, G.A. (1990), Remote detection of canopy water stress in coniferous forests using the NS001 Thematic Mapper simulator and the thermal infrared multispectral scanner. Photogrammetric Engineering and Remote Sensing, 56:5:579-586.

Pietsch, S.D. (1975), Plant water relations of *Eucalyptus regnans* F. Muell. (mountain ash). Honours Thesis, School of Agriculture, La Trobe University.

Pitkethly, A. & Pitkethly, D. (1988), N.J. Caire, Landscape Photographer. Anne and Don Pikethly, 37 Stanton Cres., Rosanna, Victoria, Australia, 112 pp.

Pittock, A.B. (1975), Climatic change and the pattern of variation in Australian rainfall. Search, 6:498-503.

Pittock, A.B. (1983), Recent climatic change in Australia: implications for a CO_2 warmed earth. Climate Change, 5:321-340.

Polarski, M. (1997), A distributed rainfall-runoff model incorporating channel extension and gridded digital maps. Hydr. Proc., 11:1-11.

Polglase, P.J. & Attiwill, P.M. (1992), Nitrogen and phosphorus cycling in relation to stand age of Eucalyptus regnans F. Muell. - I. Return from plant to soil in litterfall. Plant and Soil, 142:157-166.

Polglase, P.J., Attiwill, P.M. & Adams, M.A. (1992), Nitrogen and phosphorus cycling in relation to stand age of Eucalyptus regnans F. Muell. - II. N mineralization and nitrification. Plant and Soil, 142:167-176.

Polglase, P.J., Attiwill, P.M. & Adams, M.A. (1992), Nitrogen and phosphorus cycling in relation to stand age of Eucalyptus regnans F. Muell. - III. Labile inorganic and organic P, phosphatase activity and P availability. Plant and Soil, 142:177-185.

Pook, E.W. (1984), Canopy dynamics of *Eucalyptus maculata* Hook. I. Distribution and dynamics of leaf populations. Aust. J. Bot., 32:387-403.

Pook, E.W. (1984), Canopy dynamics of speciesEucalyptus maculata Hook. II. Canopy leaf area balance. Aust. J. Bot., 32:405-13.

Pook, E.W. (1985), Canopy dynamics of *Eucalyptus maculata* Hook. III. Effects of drought. Aust. J. Bot., 33:65-79.

Porter, J.W. & McMahon, T.A. (1971), A model for the simulation of streamflow data from climatic records. J. Hydrol., 13:297-324.

Porter, J.W. & McMahon, T.A. (1975), Application of a catchment model in southeastern Australia. J. Hydrol., 24:121-134.

Post, D.A. & Jakeman, A.J. (1996), Relationships between catchment attributes and hydrological response characteristics in small Australian mountain ash catchments. Hydr. Proc., 10:877-892.

Post, D.A., Jakeman, A.J., Littlewood, I.G., Whitehead, P.G., & Jayasuriya, M.D.A. (1993), Modelling land cover induced variations in hydrologic response: Picaninny Creek, Victoria. In: Proc. Int. Congr. on Modelling & Simulation, Univ. of Western Australia, Dec. 6-10 1993, 43-48.

Post, D.A., Jones, J.A., & Grant, G.E. (1997), Improving predictions of daily hydrologic response for ungauged catchments by incorporating water yield predictions on an inter-annual timestep. Proc., Int. Congr. on Modelling and Simulation, MODSIM 97, December,1997, Hobart, Australia, 259-264.

Powell, B., McBratney, A.B., & MacLeod, D.A. (1992), Fuzzy classification of soil profiles and horizons from the Lockyer Valley, Queensland, Australia. Geoderma, 52:173-197.

Price, D. (1996), Modelling the evapoartive losses from the Lake Malawi catchment using a GIS approach. Holzmann, H. & Nachtnebel, H.P. (eds.), Int. Conf. on Applic. of Geographical Information Systems in Hydrol. and Wat. Resour. Manag., HydroGIS '96, Vienna, Austria, April 16-19, 1996, Vol. of Poster Papers, IAHS, 239-247.

Priestly, C.H.B. & Taylor, R.J. (1972), On the assessment of surface heat flux and evaporation using large scale parameters. Mon. Weather Rev., 100:81-92.

Quick, M.C. (1995), The UBC watershed model. In: Singh, V.P. (ed.), Computer Models of Watershed Hydrology, Water Resources Publications, Highlands Ranch, Colorado, 233-280.

Quinn, P.F., Beven, K.J., & Lamb, R. (1995), The ln (a/tan β) index: how to calculate it and how to use it within the TOPMODEL framework. Hydrol. Proc., 9:161-182.

Rango, A. (1985), Assessment of remote sensing input to hydrologic models. Wat. Resour. Bull., 21:423-432.

Rango, A. (1992), Worldwide testing of the snowmelt runoff model with applications for predicting the effects of climate change. Nordic Hydrology, 23:155-172.

Rao, C.R.N. (1987), Prelaunch calibration of channels 1 and 2 of the Advanced Very High Resolution Radiometer. NOAA Tech. Rep. 36, U.S. Dept. of Commerce, 66 pp.

Rawls, W.J. & Brakensiek, D.L. (1989), Estimation of soil water retention and hydraulic properties. In: Morel-Seytoux, H.J. (ed.), Unsaturated Flow in Hydrologic Modelling - Theory and Practice, Kluwer Academic, Dordrecht.

Rawls, W.J., Ahuja, L.R., Brakensiek, D.L., & Shirmohammadi, A. (1993), Infiltration and soil water movement. In: Maidment, D.R. (ed.), Handbook of Hydrology, Ch. 5, McGraw-Hill Inc., New York, 5.1-5.51.

Read Sturgess & Associates (1992), Evaluation of the Economic Values of Wood and Water for the Thomson Catchment. Unpub. Consultancy Report, Read Sturgess & Associates, 89 Gladstone St, Kew, Victoria, Australia.

Read Sturgess & Associates & Tasman Economic Research Pty. Ltd. (1994), Phase Two of the Study into the Economic Evaluation of Wood and Water for the Thomson Catchment. Unpub. Consultancy Report for Melbourne Water & Dept. Cons. & Nat. Res., Kew, Australia.

Refsgaard, J.C. (1996), Terminology, modelling protocol and classification of hydrological model codes. In: Abbot, M.B. & Refsgaard, J.C. (eds), Distributed Hydrological Modelling, Ch. 2, Kluwer, Dordrecht, 17-39.

Refsgaard, J.C. (1997), Parameterisation, calibration and validation of distributed hydrological models. J. Hydrol., 198:69-97.

Refsgaard, J.C. & Storm, B. (1995), MIKE SHE. In: Singh, V.P. (ed.), Computer Models of Watershed Hydrology, Water Resources Publications, Highlands Ranch, Colorado, 809-846.

Rich, P.M. (1990), Characterizing plant canopies with hemispherical photographs. Remote Sensing Reviews, 5:1:13-29.

Rich, P.M., Clark, D.B., Clark, D.A., & Oberbauer, S.F. (1993), Long-term study of solar radiation regimes in a tropical wet forest using quantum sensors and hemispherical photography. Agronomy Journal, 83:818-825.

Richardson, C.W. (1978), Generation of daily precipitation over an area. Water. Resour. Bull., 14:1035-1047.

Roberts, G. (1993), A Review of Remote Sensing within the Institute of Hydrology. Unpublished report, Institute of Hydrology, Crowmarsh Gifford, Wallingford, UK, 47 pp.

Roberts, J., & Rosier, P.T.W. (1994), Comparative estimates of transpiration of ash and beech forest at a chalk site in southern Britain. J. Hydrol., 162:229-245.

Roberts, S. (in prep.), Transpiration and Water Yield in *Eucalyptus sieberi* forests. PhD thesis, Dept. of Civil & Environmental Engineering, Univ. of Melbourne, Australia.

Rogers, R. & Hinckley, T.M. (1979), Foiar weight and area related to current sapwood in oak. Forest Sci., 25:298-303.

Ronan, N.M. (1984), Leaf Area Studies. Unpublished report, Melbourne and Metropolitan Board of Works, 27 pp.

Ronan, N.M. & Duncan, H.P. (1980), Production of timber and water. In: Langford, K.J. & O'Shaughnessy, P.J. (eds), A Case Study of Maroondah Catchment, Melbourne and Metropolitan Board of Works, Rep. No. MMBW-W-0011, pp. 71-94.

Ross, J. (1981), The Radiation Regime and Architecture of Plant Stands. Dr W. Junk Publishers, The Hague, 391 pp.

Rouse, J.W., Haas, R.H., Schell, J.A., & Deering, D.W. (1973), Monitoring vegetation systems in the great plains with ERTS. Third ERTS Symposium, Vol. 1.

Rouse, J.W., Haas, R.H., Schell, J.A., Deering, D.W., & Harlan, J.C. (1974), Monitoring the veral advancement and retrogradation (greenwave effect) of natural vegetation. NASA/GSFC Type III Final

Report, Greenbelt, Maryland, USA.

Ruddell, A.R., Budd, W.F., Smith, I.N., Kege, P.L., Jones, R. (1990), The South East Australian Alpine Climate Study. Univ. of Melb..

Running, S.W. & Coughlan, J.C. (1988), A general model of forest ecosystem processes for regional applications. I. Hydrologic balance, canopy gas exchange and primary production processes. Ecol. Model., 42:125-154.

Running, S.W. & Gower, S.T. (1991), FOREST-BGC, a general model of forest ecosystem processes for regional applications, II. Dynamic carbon allocation and nitrogen budgets. Tree Physiol., 9:147-160.

Running, S.W. & Hunt, Jr., E.R. (1993), Generalization of a forest ecosystem process model for other biomes, BIOME-BGC, and an application for global-scale models. In: Ehleringer, J.R. & Field, C. (eds.), Scaling Physiological Processes: Leaf to Globe, Academic Press, San Diego, California, USA, 141-158.

Running, S.W., Nemani, R., & Hungerford, R.D. (1987), Extrapolation of synoptic meteorological data in mountainous terrain and its use for simulating forest evapotranspiration and photosynthesis. Can. J. For. Res., 17:472-483.

Running, S.W., Nemani, R.R., Peterson, D.L., Band, L.E., Potts, D.F., Pierce, L.L., & Spanner, M.A. (1989), Mapping regional forest evapotranspiration and photosynthesis by coupling satellite data with ecosystem simulation. Ecology, 70:4:1090-1101.

Running, S.W., Peterson, D.L., Spanner, M.A., & Teuber, K.B. (1986), Remote sensing of coniferous forest leaf area. Ecology, 67:273-276.

Rutter, A.J., Kershaw, K.A., Robins, P.C., & Morton, A.J. (1971), A predictive model of rainfall interception in forests: 1. Derivation of the model from observations in a plantation of Corsican pine. Agric. Meteorol., 9:367-384.

Sadek, T. (1997), Modelling streamwater turbidity using GIS and remote sensing. PhD thesis, Dept. of Civil and Environmental Engineering, Univ. of Melbourne.

Sader, S.A. (1986), Analysis of effective radiant temperatures in a Pacific Northwest forest using thermal infrared multispectral scanner data. Remore. Sens. Environ., 19:105-115.

Salisbury, F.B. & Ross, C.W. (1992), Plant Physiology (4th ed.). Wadsworth Pub. Co., Belmont, California, 682 pp.

Schaap, M.G. & Bouten, W. (1997), Forest floor evaporation in a dense Douglas fir stand. J. Hydrol., 193:97-113.

Schulze, R.E. (1976), On the application of trend surfaces of precipitation to mountainous areas. Water S A, 2:110-18.

Scuderi, L.A., Barker-Schaff, C., Orth, K.U., & Band, L.E. (1993), Alpine treeline growth variability: simulation using an ecosystem process model. Arctic and Alpine Research, 25:175-182.

Sefton, C.E.M., Whitehead, P.G., Eatherall, A., Littlewood, I.G., & Jakeman, A.J. (1993), Dynamic response characteristics of the plynlimon catchments and preliminary analysis of relationships to physical descriptors. In: Proc. Int. Congr. on Modelling & Simulation, Univ. of Western Australia, Dec. 6-10 1993, 49-54.

Sellers, P.J. (1991), Modelling and observing land-surface-atmosphere interactions on large scales. Surveys in Geophysics, 12:85-114.

Sellers, P.J., Mintz, Y., Sud, Y.C., & Dalcher, A. (1986), A simple biosphere model (SiB) for use within general circulation models. J. Atmos. Sci., 43:505-531.

Shah, S.M.S., O'Connell, P.E., & Hosking, J.R.M. (1996), Modelling the effects of spatial variability in rainfall on catchment response. 1. Formulation and calibration of a stochastic rainfall field model. J. Hydrol., 175:67-88.

Shah, S.M.S., O'Connell, P.E., & Hosking, J.R.M. (1996), Modelling the effects of spatial variability in rainfall on catchment response. 2. Experiments with distributed and lumped models. J. Hydrol., 175:89-111.

Shao, Y., Leslie, L.M., Munro, R.K., Irannejad, P., Lyons, W.F., Morison, R., Short, D., & Wood, M.S. (1997), Soil moisture prediction over the Australian continent. Metorol. Atmos. Phys., 63:195-215.

Shao, Y., Munro, R.K., & Irannejad, P. (1997), Surface energy fluxes on different scales. Proc., Int. Congr. on Modelling and Simulation, MODSIM 97, December,1997, Hobart, Australia, 271-276.

Shaw, E.M. (1994), Hydrology in Practice (3rd ed.). Chapman & Hall, London, 569 pp.

Shaw, E.M. & Lynn, P.P. (1972), Areal rainfall evaluation using two surface fitting techniques. Bull. of the Int. Assoc. of Hydrological Sciences, 17:4:419-433.

Shuttleworth, W.J. (1991), Evaporation models in hydrology. In: Schmugge, T.J. & Andre, J-C. (eds), Land Surface Evaporation: Measurement and Parameterisation, Springer-Verlag, New York, 93-120.

Shuttleworth, W.J. (1993), Evaporation. In: Maidment, D.R. (ed.), Handbook of Hydrology, McGraw-Hill Inc., New York, pp. 4.1-4.53.

Shuttleworth, W.J. & Wallace, J.S. (1985), Evaporation from sparse crops - an energy combination theory. Q. J. R. Meteorol. Soc., 111:839-855.

Silberstein, R.P. & Sivapalan, M. (1995), Estimation of terrestrial water and energy balances over heterogeneous catchments. Hydrol. Process., 9:613-630.

Silberstein, R.P. & Sivapalan, M. (1996), A Small-Catchment Scale Model Coupling Water and Energy Balances. Centre for Water Research Report: ED 712RS, Dept. of Environ. Engin., Univ. of Western Australia, 35 pp.

Silbertsein, R.P. & Sivapalan, M. (1993), Modelling vegetation heterogeneity effects on terrestrial water and energy balances. In: Proc. Int. Congr. on Modelling & Simulation, Univ. of Western Australia, Dec. 6-10 1993, 37-42.

Sinclair, R. (1980), Water potential and stomatal conductance of three *Eucalyptus* species in the Mount Lofty Ranges, South Australia: responses to summer drought. Aust. J. Bot., 28:499-510.

Singh, B. & Szeicz, G. (1980), Predicting the canopy resistance of a mixed hardwood forest. Agric. Meteorol., 21:49-58.

Singh, V.P. (ed.) (1995), Computer Models of Watershed Hydrology. Water Resources Publications, Highlands Ranch, Colorado, 1130 pp.

Sivapalan, M. & Viney, N.R. (1994), Application of a nested catchment model for predicting the effects of changes in forest cover. In: Ohta, T. (ed.), Proc. of the Int. Symp. on Forest Hydrology, Univ. Tokyo, Tokyo, IUFRO, Oct. 24-28 1994, 315-322.

Sivapalan, M. & Viney, N.R. (1994), Large scale catchment modelling to predict the effects of land use and climate. Water: Official Journal of the Australian Water and Wastewater Association, 21:1:33-37.

Sivapalan, M., Beven, K., & Wood, E.F. (1987), On hydrologic similarity 2. A scaled model of storm runoff production. Water Resour. Res., 23:2266-2278.

Sivapalan, M., Ruprecht, J.K., Viney, N.R. (1996a), Water and salt balance modelling to predict the effects of land use changes in forested catchments. 1. Small catchment water balance model. Hydrol. Proc., 10:393-411.

Sivapalan, M., Viney, N.R., & Jeevaraj, C.G. (1996c), Water and salt balance modelling to predict the effects of land use changes in forested catchments. 3. The large catchment model. Hydrol. Proc., 10:429-446.

Sivapalan, M., Viney, N.R., & Ruprecht, J.K. (1996b), Water and salt balance modelling to predict the effects of land use changes in forested catchments. 2. Coupled model of water and salt balances. Hydrol. Proc., 10:413-428.

Slatyer, R.O. (1976), Water Deficits in Timberline Trees in the Snowy Mountains of South-Eastern Australia. Oecologia, 24, 357-366.

Smith, J., Lin, T., & Ranson, K. (1980), The Lambertian assumption and Landsat data. Photogrammetric Engineering and Remote Sensing, 46:9:1183-1189.

Smith, J., Pert, P., & McFarlane, M. (1996), Leadbeater's Possum: Collection and Analysis of Habitat Resource Information. Final report to: The Australian Nature Conservation Agency (ANCA), Endangered Species Program (ESP), 24 pp.

Smith, M. (1990), Report on the Expert Consultation on Revision of FAO Methodologies for Crop Water Requirements. Rome, Italy, 28-31 May, 1990, Land and Water Development Division, Food and Agriculture Organization of the United Nations, 59 pp.

Smith, R.B. & Woodgate, P.W. (1985), Appraisal of fire damage and inventory for timber salvage by remote sensing in mountain ash forests in Victoria. Aust. For., 48:252-263.

Soste, L., Cooper, S., Monacella, M., & Jolly, T. (1996), Topographic indicators of soil moisture variation in forested mountain catchments. 23rd Hydrol. and Water Resources Symp., Institution of Engineers, Australia, pp. 707-708.

Spanner, M.A., Pierce, L.L., Peterson, D.L., & Running, S.W. (1990), Remote sensing of temperate forest leaf area index: Influence of canopy closure, understory vegetation and background reflectance. Int. J. Rem. Sens., 11:96-111.

Spanner, M.A., Pierce, L.L., Running, S.W., & Peterson, D.L. (1990), The seasonality of AVHRR data

of temperate coniferous forests: Relationship with leaf area index. Remote Sensing of Environment, 33:97-112.

Steven, M.D., Malthus, T.J., Demetriades-Shah, T.H., Danson, F.M., & Clark, J.A. (1990), High-spectral resolution indices for crop stress. Clarke, J.A. and Steven, M.D. (eds), Applications of Remote Sening in Agriculture, Butterwoths, London, 209-228.

Stewart, J.B. (1988), Modelling surface conductance of pine forest. Agric. For. Meteorol., 43:17-35.

Stewart, J.B. & Finch, J.W. (1993), Application of remote sensing to forest hydrology. J. Hydrol., 150:701-716.

Storm, B. & Refsgaard, A. (1996), Distributed physically-based modelling of the entire land phase of the hydrological cycle. In: Abbot, M.B. & Refsgaard, J.C. (eds), Distributed Hydrological Modelling, Ch. 4, Kluwer, Dordrecht, 55-69.

Sun News-Pictorial (1939), Bush Fires - A Pictorial Survey of Victoria's Most Tragic Week, January 8-15, 1939.

Swaminathan, R. (1994), Relationship between leaf area index and forest age using remote sensing techniques. Unpublished draft, Major Project, Graduate Diploma in Land Data Management, RMIT, Melbourne.

Tabios, G.Q. & Salas, J.D. (1985), A comparative analysis of techniques for spatial interpolation of precipitation. Wat. Resour. Bull., 21:365-380.

Teillet, P.M. (1986), Image correction for radiometric effects in remote sensing. Int. J. Remote Sensing, 7:1637-1651.

Teixeira Filho, J., Rambal, S., Lacaze, B., & Lointier, M. (1996), Mapping maximal canopy transpiration over a Mediterranean watershed. Parlow, E., (ed.), Progress in Environmental Remote Sensing Research and Applications, Proc. of the 15th EARSel Symp., Basel, Switz., 4-6 Sept. 1995, Balkema, Rotterdam, 379-384.

Teskey, R.O. & Sheriff, D.W. (1996), Water use by Pinus radiata trees in a plantation. Tree Physiol., 16:273-279.

Tetens, O. (1930), Uber einige meteorologische Begriffe. Zeitschrift Geophysic, 6:297-309.

The Illustrated Australian News (1878), Special edition for the Paris exhibition. 10 June 1878, Melbourne.

Thom, A.S. (1975), Momentum, mass and heat exchange of plant communities. In: Monteith, J.L. (ed.), Vegetation and the Atmosphere, Academic Press, London, Vol. 1, pp. 57-109.

Thornton, P.E., Running, S.W., & White, M.A. (1997), Generating surfaces of daily meterological variables over large regions of complex terrain. J. Hydrol., 190:214-251.

Tian, G.L. (1989), Spectral signatures and vegetation indices of crops: Based on the 11 channels of the Daedalus airborne thematics mapper scanner. CSIRO, Div. of Wat. Resour., Div. Rep. 89/4.

Todini, E. (1996), The ARNO rainfall-runoff model. J. Hydrol., 175:339-382.

Tolhurst, K.G. (1994), An assessment of the amount of biomass burning in Australia from 1983 to 1992. To be published in: Dept. Environment, Sport & Territories, Australian Methodology for the Estimation of Greenhouse Gas Emissions: Workbook for Non CO_2 Gases from the Biosphere, Canberra.

Trenberth, K.E. (ed.) (1992), Climate System Modelling. Cambridge University Press, Cambridge, 788 pp.

Troch, P.A., Mancini, M., Paniconi, C., & Wood, E.F. (1993), Evaluation of a distributed catchment scale water balance model. Wat. Resour. Res., 29:6:1805-1817.

Troch, P.A., De Troch, F.F., Grayson, R.B., Western, A., Derauw, D., & Barbier, C. (1997), Spatial organization of hydrological processes in small catchments derived from advanced SAR image processing: Field work and preliminary results. Proc. 3rd ERS symposium on Space at the service of our Environment, European Space Agency SP-414, Florence, Italy, pp. 93-97.

Turk, L.J. (1975), Diurnal fluctations of water tables induced by atmospheric pressure changes. J. Hydrol., 26:1-16.

Vörösmarty, C.J. & Moore III, B. (1991), Modelling basin-scale hydrology in support of physical climate and global biogeochemical studies: An example of the Zambezi river. Surverys in Geophysics, 12:271-311.

Valdes, J.B., Rodriguez-Iturbe, I., & Gupta, V.K. (1985), Approximation of temporal rainfall from a multidimensional model. Water. Res. Research, 21:8:1259-1270.

van de Griend, A.A. & van Boxel, J.H. (1989), Water and surface energy balance model with a multilayer canopy representation for remote sensing purposes. Water Resour. Res., 25:949-971.

Varley, M.J., Beven, K.J., & Oliver, H.R. (1996), Modelling solar radiation in steeply sloping terrain. Int. J. Climatology, 16:93-104.

Vertessy, R.A., Benyon, R.G., & Haydon, S. (1994), Melbourne's forest catchments: Effect of age on water yield. Water, Journal of the Australian Water & Wastewater Association, 21:2:17-20.

Vertessy, R.A., Benyon, R.G., O'Sullivan, S.K., & Gribben, P.R. (1994), Leaf Area and Tree Water Use in a 15 Year Old Mountain Ash Forest, Central Highlands, Victoria. Report 94/3, Cooperative Research Centre for Catchment Hydrology, Australia, 31 pp.

Vertessy, R.A., Benyon, R.G., O'Sullivan, S.K., & Gribben, P.R. (1995), Relationships between stem diameter, sapwood area, leaf area and transpiration in a young mountain ash forest. Tree Physiol., 15:559-567.

Vertessy, R.A., Hatton, T.J., Benyon, R.J., & Dawes, W.R. (1995), Long term growth and water balance predictions for a mountain ash (Eucalyptus regnans) forest catchment subject to clearfelling and regeneration. Tree Physiol., 16:221-232.

Vertessy, R.A., Hatton, T.J., O'Loughlin, E.M., & Broph, J.H. (1991), Water balance simulation in the Melbourne water supply area using a terrain analysis-based catchment model. Australian Centre for Catchment Hydrology, Consultancy Report 91/32, CSIRO Division of Water Resources, Australia, 55 pp.

Vertessy, R.A., Hatton, T.J., O'Shaughnessy, P.J., & Jayasuriya, M.D.A. (1993), Predicting water yield from a mountain ash forest catchment using a terrain analysis based catchment model. J. Hydrol., 150:665-700.

Vertessy, R.A., Hatton, T.J., Reece, P., O'Sullivan, S.K., & Benyon, R.G. (1997), Estimating stand water use of large mountain ash trees and validation of the sap flow measurement technique. Tree Physiology, 17:747-756.

Vertessy, R.A., O'Loghlin, E., Bevely, C., & Butt, T. (1994), Australian experiences with the CSIRO Topog model in land and water resources management. Proceedings, International UNESCO Symposium, Water Resources Planning in a Changing World, Karlsruhe, Germany, June 28-30, 1994, III-135 - III-144.

Wahba, G. & Wendelberger, J. (1980), Some new mathematical methods for variational objective analysis using splines and cross validation. Monthly Weather Review, 108:1122-1143.

Walker, J., Jupp, D.L.B., Penridge, L.K., & Tian, G. (1986), Interpretation of vegetation structure in Landsat MSS imagery: A case study in disturbed semi-arid Eucalypt woodlands. Part 1. Field data analysis. J. Environ. Manag., 23:19-33.

Wallace, J. (1996), Relationships Between Satellite Image Data and Leaf Area Index in Jarrah Forest. A report to Alcoa Australia, CSIRO Mathematical and Information Sciences, 16 pp.

Wang, L. (1997), Investigation of the Feasability of the ERS-1/2 SAR for High Spatial Resolution Soil Moisture Mapping. M. App. Sci., Department of Geomatics, University of Melbourne, Melbourne, Australia.

Waring, R.H., Emmingham, W.H., Gholz, H.L., & Grier, C.C. (1978), Variation in maximum leaf area of coniferous forests in Oregon and its ecological significance. Forest Science, 24:131-140.

Watson, F.G.R. & Vertessy, R.A. (1996), Estimating leaf area index from stem diameter measurements in Mountain Ash forest. Report 96/7, Cooperative Research Centre for Catchment Hydrology, Dept. of Civil Engineering, Monash University, Clayton, Victoria, Australia, 102 pp.

Watson, F.G.R., Grayson, R.B., Vertessy, R.A., & McMahon, T.A. (1997), Large scale distribution modelling and the utility of detailed ground data. Hydrol. Proc., in prep.

Watson, F.G.R., Vertessy, R.A., & Band, L.E. (1996), Distributed parameterization of a large scale water balance model for an Australian forested region. HydroGIS 96: Application of Geographic Information Systems in Hydrology and Water Resources Management, Proceedings of the Vienna Conference, April, 1996, IAHS Publ. No. 235, 157-166.

Watson, F.G.R., Vertessy, R.A., & Grayson, R.B. (1997), Large scale, long term, physically based prediction of water yield in forested catchments. Proc., Int. Congr. on Modelling and Simulation, MODSIM 97, December,1997, Hobart, Australia, 397-402.

Watson, F.G.R., Vertessy, R.A., & Grayson, R.B. (1998), Large scale modelling of forest hydrological processes and their long term effect on water yield. Submitted to Hydr. Proc.

Watson, F.G.R., Vertessy, R.A., Grayson, R.B., Band, L.E., & McMahon, T.A. (1997), Macaque: Regional scale modelling of water yield from forested basins. Water, Journal of the Australian Water and Wastewater Association, 24:9.

Welles, J.M. & Norman, J.M. (1991), Instrument for indirect measurement of canopy architecture. Agronomy J., 83:818-825.

Western, A.W. & Grayson, R.B. (1997), The Tarrawarra data set: Soil moisture patterns, soil characteristics and hydrological flux measurements. Submitted to Geophysical Review Letters.

Whitford, K.R., Colquhoun, I.J., Lang, A.R.G., & Harper, B.M. (1995), Measuring leaf area index in a sparse eucalypt forest: A comparison of estimates from direct measurement, hempispherical photography, sunlight transmittance and allometric regression. Agric. For. Meteorol., 74:237-249.

Wigmosta, M.S., Lettenmaier, D.P., & Vail, L.W. (1994), A distributed hydrology vegetation model for mountainous catchments. In: Rosso, R., Peano, A., Becchi, I., & Bemporad, G.A. (eds), Advances in Distributed Hydrology, Selected papers from the International Workshop, Bergamo, Italy, June 25-26, 1992, Water Resources Publications, 359-378.

Williamson, R.J. (1989), Growth rates as an index of hydrological change. Hydrology and Water Resources Symposium, Christchurch, N.Z., 23-30 Nov. 1989, 1-5.

Wise, S.M. (1995), The effect of interpolation errors on the use of DTMs in geomorphology. In: British Geomorphological Research Group, Annual Conference, Abstracts, 15th-17th Sep., 1995, University of Cambridge, 79 pp., p. 39.

Wong, S.C. & Dunin, F.X. (1987), Photosynthesis and transpiration of trees in a eucalypt forest stand: CO_2 light and humidity responses. Aust. J. Plant Physiol., 14:619-632.

Wood, E.F., Sivapalan, M. & Beven, K.J. (1990), Similarity and scale in catchment storm response. Reviews of Geophysics, 28:1:1-18.

Wood, E.F., Sivapalan, M., Beven, K., & Band, L. (1988), Effects of spatial variablity and scale with implications to hydrologic modeling. J. Hydrol., 102:29-47.

Woods, R.A., Sivapalan, M., & Robinson, J.S. (1997), Modeling the spatial variability of subsurface runoff using a topographic index. Water Resources Research, in press.

Woodward, F.I. (1987), Climate and Plant Distribution. Cambridge Univ. Press, Cambridge, 174 pp.

Wu, A.Y.K., Papworth, M.P., & Flinn, D.W. (1984), The Effects of Some Forest Practices on Water Quality and Yield in the Reefton Experimental Area, Victoria. Hydrology Section, Soil Conservation Authority, Melbourne, Victoria.

Yates, S.R. & Yates, M.V. (1990), Geostatistics for Waste Management: A User's Manual for the GEOPACK (Version 1.0) Geostatistical Software System. U.S. Environ. Prot. Agency, Office for R. & D., Robert S. Kerr Environ. Res. Lab., Ada, Oklahoma, 70 pp.

Zaslavsky, D. & Sinai, G. (1981), Surface hydrology: I- Causes of lateral flow. Journal of the Hydraulics Division, Proc. Am. Soc. Civ. Engineers, 107:37-52.

Zhao, R.J. (1992), The Xinanjiang model applied in China. J. Hydrol., 135:371-381.

Zhao, R.J., Zuang, Y.L, Fang, L.R., Liu, X.R., & Zhang, Q.S. (1980), The Xinanjiang model. Hydrological Forecasting, Proc. Oxford Symp., April, 1980, IAHS Publ. 129, 351-356.

Zhu, A. (1994), Soil Pattern Inference Using GIS Under Fuzzy Logic. PhD thesis, Department of Geography, University of Toronto.

Zhu, A. & Band, L.E. (1995), Automated soil inference under fuzzy logic. Ecol. Modelling, 90:123-145.

Zierholz, C. (1994), Runoff and soil erosion following wildfire. Abstract of informal workshop (W4) presentation, Water Down Under 94, Adelaide Convention Centre, 21st Nov., 1994.

Zimmerman, H.-J. (1991), Fuzzy set theory - and its applications (2nd rev. ed.). Kluwer-Nijhoff Publishers, Boston. Ma., U.S.A., 399 pp.

Zurada, J.M. (1992), Introduction to Artificial Neural Systems. West Pub. Co., St. Paul, USA, 683 pp.

Part VI

Appendices

Appendix A

Publications

The following publications have arisen from this study:

Refereed journals

Watson, F.G.R., Grayson, R.B., Vertessy, R.A., & McMahon, T.A. (1997a) Large scale distribution modelling and the utility of detailed ground data. Invited paper, in press., Hydrological Processes (special issue on GIS Applications in Hydrology).

Conference papers

Watson, F.G.R., Vertessy, R.A., & Band, L.E. (1996) Distributed parameterization of a large scale water balance model for an Australian forested region. HydroGIS 96: Application of Geographic Information Systems in Hydrology and Water Resources Management (Proc. of the Vienna Conf. April 1996), IAHS Publication No 235, pp 157-166.

Watson, F.G.R., Vertessy, R.A., & Grayson, R.B. (1997b) Large scale, long term, physically based prediction of water yield in forested catchments. To be presented at International Congress on Modelling and Simulation (MODSIM 97), Hobart, Tasmania, 8-11 December, 1997.

Research reports

Watson, F.G.R. & Vertessy, R.A. (1996) Estimating leaf area index from stem diameter measurements in Mountain Ash forest. Cooperative Research Centre for Catchment Hydrology. Melbourne. Report 96/7, November 1996, 102 pp.

Industry magazines

Watson, F.G.R., Vertessy, R.A., Grayson, R.B., Band, L.E., & McMahon, T.A. (1997c) Macaque: Regional scale modelling of water yield from forested basins. Water, Journal Australian Water & Wastewater Assoc., 24:9.

Appendix B

Time series data

Table B.1: Time series data used in the present study. Note that data used in the calculation of MMPI values are summarised in Table 7.1.

F-num.	Record name	Easting (m)	Northing (m)	Elevation (m)
F0020	Coranderrk streamflow (MW-est.)	375000	5827875	305
F0290	Coranderrk Site 10 temperature	373475	5827750	232
F0420	Coranderrk Site 11 humidity (wet bulb mean/max./min.)	374675	5829150	692
F0430	Coranderrk Site 11 radiation	374675	5829150	692
F0440	Coranderrk Site 11 temperature (mean/max./min.)	374675	5829150	692
F0584	Grace Burn streamflow (MW-est.)	374225	5831300	215
F0710	Maroondah dam (nearby) rainfall	372000	5832500	155
F0720	Maroondah Reservoir natural inflow (mostly Watts R.) (MW-est.)	372075	5833200	140
F0970	Mount St Leonard (summit - just south) rainfall	369675	5840975	1007
F1064	Tarrawarra Field Site global radiation	362500	5831200	100
F1065	Tarrawarra Field Site net radiation	362500	5831200	100
F1195	Warburton Post Office rainfall	384400	5820600	152
F1487	Murrindindi rainfall	373000	5838300	880
F1510	Murrindindi radiation	373000	5838300	880
F1790	North Maroondah Site 10 rainfall	379375	5838275	567
F1820	North Maroondah Site 10 temperature	379375	5838275	567
F1910	North Maroondah Site 15 rainfall	378350	5838475	570
F1911	North Maroondah Site 15 rainfall - modulated	378350	5838475	570
F1980	North Maroondah Site 16 rainfall	377700	5839600	715
F2540	Melbourne (BOM Latrobe St) max and min temperature	321300	5813600	35
F9000	Combined streamflow from Watts, Grace Burn and Coranderrk	-	-	-

Appendix C

List of symbols, variables, and units used by Macaque

The following two tables list the symbols used throughout this report. The first table summarises the subscripts and facilitates the interpretation of the full symbol list given in the second table.

Table C.1: Summary of subscripts used with the symbols listed in Table C.2.

Subscript	Meaning
Roman	
a	absorbed radiation
$aero$	aerodynamic
age	age of vegetation
air	air
atm	atmosphere
$avail$	available (volumetric water content)
b	balance of radiation
$base$	baseflow
$below$	below (down the hillslope)
c	canopy, canopy level
cl	canopy leaves
$close$	(stomatal) closure
con	(solar) constant
$dist$	saturation zone distribution function
day	day, daytime
dd	degree days (of snowpack)
dew	dewpoint
E	east
eff	effective value
eq	equilibrium
$eqiv$	equivalent (latitude)
et	evapotranspiration
$evap$	evaporation
ex	extraterrestrial
f	relative leaf conductance
$fall$	total water falling on soil
$flow$	total flow
hor	horizontal (surface)

421

inf	infiltration of water into soil
int	interception of precipitation
l	leaf
lon	longitude
mound	saturated zone mound
max	maximum
min	minimum
night	night-time
origin	origin of vegetation
p	pressure
P	precipitation
par	(solar) parameter
param	a parameter
ref	boundary layer reference level
res	residual (water content of soil)
R	net (or unspecified) radiation
rain	rain
rech	recharge
redist	redistribution (implicit lateral flow)
rise	sunrise
s	soil, soil level
S	solar radiation
sat	saturated zone within soil, saturated water content of soil, saturated air
set	sunset
slop	sloping (surface)
snow	snow, snowpack
stn	value from the climatic base station
sub	sublimation
surf	surface (of soil)
T	temperature
thresh	threshold
thru	throughfall
tom	tomorrow
tot	total water (combined from saturated and unsaturated zones), total radiation (incident above canopy), total LAI
tran	transpiration
u	understorey, understorey level
ul	understorey leaves
unsat	unsaturated zone within soil
v	water vapor
vap	vaporisation
w	water
W	west
wet	wetness
wt	water table
xs	saturation excess
year	year
z	depth within soil

Greek

μ	snowmelt
ψ	water potential

Table C.2: Symbols, variable names, variable descriptions, and units used by Macaque. Where variable names are missing, the quantity is expressed as a numerical constant in the code. Where units are missing, the quantity is dimensionless. Where substances quantified in the units may be ambiguous, the substance is named in parentheses: e.g. '(water)' or '(soil)'.

Symbol	Variable name	Description	Unit
Roman			
a	`p_bristow_and_campbells_a`	Bristow and Campbell's A parameter for atmospheric transmission	-
A	`a_area`	area of a spatial unit	m^2
A_{hill}	-	area of a hillslope	m^2
b	`p_bristow_and_campbells_b`	Bristow and Campbell's B parameter for atmospheric transmission	-
c	`p_bristow_and_campbells_c`	Bristow and Campbell's C parameter for atmospheric transmission	-
c_p	-	specific heat of air at constant pressure	$J\ kg^{-1}\ K^{-1}$
C_R	`p_intercept_net_vs_solar_rad`	intercept of the net (versus) solar radiation relation	$J\ m^{-2}\ day^{-1}$
d	`w_declination`	declination of the sun's observed path	$°$
d_v	-	molecular diffusion coefficient for water vapor in air	-
D_c	`w_canopy_vapor_pressure_-deficit`	mean daytime vapor pressure deficit at canopy level	Pa
$D_{eq,c}$	`w_equilibrium_canopy_-vapor_pressure_deficit`	mean daytime equilibrium vapor pressure deficit at canopy level	Pa
$D_{eq,u}$	`w_equilibrium_understorey_-vapor_pressure_deficit`	mean daytime equilibrium vapor pressure deficit at understorey level	Pa
$D_{eq,s}$	`w_equilibrium_soil_vapor_-pressure_deficit`	mean daytime equilibrium vapor pressure deficit at soil level	Pa
D_{ref}	`w_reference_vapor_-pressure_deficit`	mean daytime vapor pressure deficit at reference level above canopy boundary layer	Pa
D_s	`w_soil_vapor_pressure_-deficit`	mean daytime vapor pressure deficit at soil level	Pa
D_u	`w_understorey_vapor_-pressure_deficit`	mean daytime vapor pressure deficit at understorey level	Pa
$dayl$	`w_daylength`	number of seconds in a day for which the sun is above the horizon	$s\ day^{-1}$
e	`w_vapor_pressure`	vapor pressure of water in air	Pa
e_{sat}	`w_saturation_vapor_pressure`	mean daytime saturation vapor pressure of water in air	Pa

E_c	`w_canopy_transpiration_rate`	canopy transpiration rate	m s^{-1}
E_s	`w_soil_evaporation_rate`	soil evaporation rate	m s^{-1}
E_u	`w_understorey_-` `transpiration_rate`	understorey transpiration rate	m s^{-1}
f	`p_saturated_hydraulic_-` `conductivity_shape`	shape parameter in equation for saturated hydraulic conductivity of soil	m^{-1}
g_c	`w_canopy_conductance`	conductance to vapor transfer of entire canopy	m s^{-1}
g_{cl}	`w_final_canopy_leaf_-` `conductance`	conductance to vapor transfer of canopy leaf surfaces (final stage in calculation)	m s^{-1} leaf_side^{-1} LAI^{-1}
$g_{cl,1}$	`w_first_canopy_leaf_-` `conductance`	conductance to vapor transfer of canopy leaf surfaces (first stage in calculation)	m s^{-1} leaf_side^{-1} LAI^{-1}
$g_{cl,2}$	`w_second_canopy_leaf_-` `conductance`	conductance to vapor transfer of canopy leaf surfaces (second stage in calculation)	m s^{-1} leaf_side^{-1} LAI^{-1}
$g_{cl,3}$	`w_third_canopy_leaf_-` `conductance`	conductance to vapor transfer of canopy leaf surfaces (third stage in calculation)	m s^{-1} leaf_side^{-1} LAI^{-1}
$g_{cl,max}$	`p_maximum_canopy_leaf_-` `conductance`	maximum conductance to vapor transfer of canopy leaf surfaces	m s^{-1} leaf_side^{-1} LAI^{-1}
$g_{cl,max,age}$	`p_maximum_canopy_leaf_-` `conductance`	forest age dependent version of $g_{cl,max}$	m s^{-1} leaf_side^{-1} LAI^{-1}
$g_{cl,min}$	`p_minimum_canopy_leaf_-` `conductance`	minimum conductance to vapor transfer of canopy leaf surfaces	m s^{-1} leaf_side^{-1} LAI^{-1}
g_u	`w_understorey_conductance`	conductance to vapor transfer of entire understorey	m s^{-1}
g_{ul}	`w_final_understorey_leaf_-` `conductance`	conductance to vapor transfer of understorey leaf surfaces (final stage in calculation)	m s^{-1} leaf_side^{-1} LAI^{-1}
$g_{ul,1}$	`w_first_understorey_leaf_-` `conductance`	conductance to vapor transfer of understorey leaf surfaces (first stage in calculation)	m s^{-1} leaf_side^{-1} LAI^{-1}
$g_{ul,2}$	`w_second_understorey_leaf_-` `conductance`	conductance to vapor transfer of understorey leaf surfaces (second stage in calculation)	m s^{-1} leaf_side^{-1} LAI^{-1}
$g_{ul,3}$	`w_third_understorey_leaf_-` `conductance`	conductance to vapor transfer of understorey leaf surfaces (third stage in calculation)	m s^{-1} leaf_side^{-1} LAI^{-1}
$g_{ul,max}$	`p_maximum_understorey_-` `leaf_conductance`	maximum conductance to vapor transfer of understorey leaf surfaces	m s^{-1} leaf_side^{-1} LAI^{-1}
$g_{ul,min}$	`p_minimum_understorey_-` `leaf_conductance`	minimum conductance to vapor transfer of understorey leaf surfaces	m s^{-1} leaf_side^{-1} LAI^{-1}
h	`p_elevation`	elevation of a spatial unit	m
h_{stn}	`master->base_elevation_-` `temperature`	elevation of the climatic base station	m
i_{wet}	`p_wetness_index`	wetness index of a spatial unit	arbitrary (not necessarily dimension
$\bar{i}_{wet}$	`p_mean_wetness_index`	mean wetness index of a number of spatial units	arbitrary (not necessarily dimension

Symbol	Code name	Description	Units
$i_{wet,range}$	`p_wetness_index_range`	range of wetness index values within the current spatial unit	arbitrary (not necessarily dimensionless)
I_{con}	-	solar constant	W m^{-2}
I_{ex}	`w_extraterrestrial_-radiation_sloping_surface`	extraterrestrial solar radiation incident on a horizontal surface	W m^{-2}
I_{par}	-	solar parameter	W m^{-2}
I'_{ex}	`w_extraterrestrial_-radiation_horizontal_-surface`	extraterrestrial solar radiation incident on a sloping surface	W m^{-2}
k_{rain}	`p_rain_interception_coeff`	rainfall interception coefficient	m LAI^{-1}
k_{snow}	`p_snow_interception_coeff`	snow interception coefficient	m LAI^{-1}
$k_{R,c}$	`p_canopy_radiation_-extinction_coeff`	canopy radiation extinction coefficient	-
$k_{R,u}$	`p_understorey_radiation_-extinction_coeff`	understorey radiation extinction coefficient	-
$K_{sat,surf}$	`p_surface_saturated_-hydraulic_conductivity`	saturated vertical hydraulic conductivity of soil at the soil surface	m day^{-1}
$K_{sat,min}$	`p_minimum_saturated_-hydraulic_conductivity`	saturated vertical hydraulic conductivity of soil at large depths	m day^{-1}
$K_{sat,wt}$	`w_table_saturated_-hydraulic_conductivity`	saturated vertical hydraulic conductivity of soil at the water table	m day^{-1}
K_{wt}	`w_table_hydraulic_-conductivity`	vertical hydraulic conductivity of soil at the water table	m day^{-1}
$L_{a,c}$	`w_long_rad_canopy_absorbed`	balance of longwave radiation absorbed by the canopy	J m^{-2} day^{-1}
$L_{a,snow}$	`w_long_rad_snow_absorbed`	balance of longwave radiation absorbed by the snowpack	J m^{-2} day^{-1}
$L_{a,s}$	`w_long_rad_soil_absorbed`	balance of longwave radiation absorbed by the soil	J m^{-2} day^{-1}
$L_{a,u}$	`w_long_rad_understorey_-absorbed`	balance of longwave radiation absorbed by the understorey	J m^{-2} day^{-1}
L_b	`w_long_rad_balance_down`	balance of downward and upward longwave radiation measured in the downward direction	J m^{-2} day^{-1}
LAI_c	`w_canopy_lai`	canopy LAI	m^2(leaf) m^{-2}(ground)
$LAI_{c,lookup}$	`w_canopy_lai`	canopy LAI read from a lookup table	m^2(leaf) m^{-2}(ground)
LAI_{tot}	`w_total_lai`	total LAI reported after LAI calculations	m^2(leaf) m^{-2}(ground)
$LAI_{tot,lookup}$	`w_total_lai`	total LAI read from a lookup table	m^2(leaf) m^{-2}(ground)
$LAI_{tot,param}$	`p_total_lai`	total LAI if supplied as an input parameter	m^2(leaf) m^{-2}(ground)
LAI_u	`w_understorey_lai`	understorey leaf area index (LAI)	m^2(leaf) m^{-2}(ground)
$LAI_{tot,P}$	-	magnitude of peak in total LAI curve	m^2(leaf) m^{-2}(ground)
$LAI_{tot,D}$	-	magnitude of long term decline from peak to climax total LAI value	m^2(leaf) m^{-2}(ground)
$LAI_{tot,C}$	-	climax total LAI value	m^2(leaf) m^{-2}(ground)
lat	`p_latitude`	latitude of site	$°$north

lat_{eqiv}	`w_equivalent_latitude`	the latitude of the horizontal surface which faces the same way as the current sloping surface	°
$MMPI$	`p_mean_monthly_-` `precipitation_index`	Index of mean monthly precipitation relative to some base station	-
$MMPI_{stn}$	`master->base_mean_monthly_-` `precipitation_index`	Index of the mean monthly precipitation of the current base station relative that of the base station which was used to derive the original MMPI data	-
n	`p_van_genuchten_n`	Van Genuchten's n parameter for the shape of unsaturated hydraulic conductivity of soil with variation in Θ	-
N	`numsubunits`	the number of ESUs in the current hillslope	-
O_{dd}	`s_snowpack_degree_days`	a measure of energy stored within the snowpack	°C.days
$O_{dd,min}$	`p_min_snowpack_degree_days`	minimum allowable snowpack energy	°C.days
p_{sat}	`w_saturated_proportion`	proportion of a spatial unit whose soil is saturated to the surface	-
$p_{c,sat}$	`p_sat_canopy_-` `transpiration_proportion`	nominal proportion of canopy transpiration to be drawn from saturated zone	-
$p_{u,sat}$	`p_sat_understorey_-` `transpiration_proportion`	nominal proportion of understorey transpiration to be drawn from saturated zone	-
q_{base}	`f_baseflow`	baseflow exfiltrated from soil	m day^{-1}
q_{et}	`f_total_evapotranspiration`	total evapotranspiration	m day^{-1}
q_{evap}	`f_soil_evaporation`	soil evaporation	m day^{-1}
$q_{evap,sat}$	`f_soil_evaporation_from_sat`	soil evaporation from the saturated store	m day^{-1}
$q_{evap,unsat}$	`f_soil_evaporation_from_-` `unsat`	soil evaporation from the unsaturated store	m day^{-1}
q_{fall}	`f_total_water_falling_on_-` `soil`	total water (throughfall and snow melt) falling on the soil	m day^{-1}
q_{flow}	`f_totalflow`	total streamflow	m day^{-1}
q_{inf}	`f_infiltrated`	total water infiltrated into the soil	m day^{-1}
q_{int}	`f_total_interception`	total interception of precipitation which results in vaporisation/sublimation to the atmosphere	m day^{-1}
q_{melt}	`f_snowpack_melt_total`	total meltwater from the snowpack	m day^{-1}
$q_{melt,R}$	`f_snowpack_melt_rad`	snowpack meltwater caused by radiation	m day^{-1}
$q_{melt,T}$	`f_snowpack_melt_temperature`	snowpack meltwater caused by high temperatures	m day^{-1}
q_P	`f_precipitation`	precipitation (rain and snow)	m day^{-1}
$q_{P,stn}$	`nextin->yesterdays_-` `precipitation`	precipitation at the base station	m day^{-1}
q_{rain}	`f_rain`	rainfall	m day^{-1}
q_{rech}	`f_recharge`	recharge from the unsaturated store to the saturated store	m day^{-1}

q_{redist}	`w_sat_redistribution`	implicit lateral flow redistributing saturated zone water to/from the current ESU from/to some other part of the hillslope	m day^{-1}
q_{snow}	`f_snow`	snowfall	m day^{-1}
$q_{sub,c}$	`f_canopy_sublimated_snow`	snowfall intercepted by the canopy and subsequently sublimated	m day^{-1}
$q_{sub,u}$	`f_understorey_sublimated_-snow`	snowfall intercepted by the understorey and subsequently sublimated	m day^{-1}
$q_{thru,c,rain}$	`f_canopy_thrufall_rain`	rain falling through the canopy	m day^{-1}
$q_{thru,c,snow}$	`f_canopy_thrufall_snow`	snow falling through the canopy	m day^{-1}
$q_{thru,u,rain}$	`f_understorey_thrufall_rain`	rain falling through the understorey	m day^{-1}
$q_{thru,u,snow}$	`f_understorey_thrufall_snow`	snow falling through the understorey	m day^{-1}
$q_{tran,c}$	`f_canopy_transpiration`	canopy transpiration	m day^{-1}
$q_{tran,c,sat}$	`f_canopy_transpiration_-from_sat`	canopy transpiration taken from the saturated store	m day^{-1}
$q_{tran,c,unsat}$	`f_canopy_transpiration_-from_unsat`	canopy transpiration taken from the unsaturated store	m day^{-1}
$q_{tran,u}$	`f_understorey_transpiration`	understorey transpiration	m day^{-1}
$q_{tran,u,sat}$	`f_understorey_-transpiration_from_sat`	understorey transpiration taken from the saturated store	m day^{-1}
$q_{tran,u,unsat}$	`f_understorey_-transpiration_from_unsat`	understorey transpiration taken from the unsaturated store	m day^{-1}
$q_{vap,c}$	`f_canopy_vaporised_rain`	rainfall intercepted by the canopy and subsequently vaporised	m day^{-1}
$q_{vap,pot,c}$	`f_potential_canopy_-vaporised_rain`	potentially vaporisable canopy intercepted rain	m day^{-1}
$q_{vap,u}$	`f_understorey_vaporised_-rain`	rainfall intercepted by the understorey and subsequently vaporised	m day^{-1}
$q_{vap,pot,u}$	`f_potential_understorey_-vaporised_rain`	potentially vaporisable understorey intercepted rain	m day^{-1}
q_{xs}	`f_saturation_excess_flow`	saturation excess flow	m day^{-1}
$r_{aero,c,ref}$	`p_canopy_reference_-aerodynamic_resistance`	aerodynamic resistance to vapor transfer between the canopy and the reference level	s m^{-1}
$r_{aero,s,u}$	`p_soil_understorey_-aerodynamic_resistance`	aerodynamic resistance to vapor transfer between the soil and the understorey	s m^{-1}
$r_{aero,u,c}$	`p_understorey_canopy_-aerodynamic_resistance`	aerodynamic resistance to vapor transfer between the understorey and the canopy	s m^{-1}
r_s	`w_soil_resistance`	soil resistance to vapor transfer	s m^{-1}
R	`w_net_rad`	net radiation incident above the canopy	J m^{-2} day^{-1}
$R_{a,c}$	`w_net_rad_canopy_absorbed`	net radiation absorbed by the canopy	J m^{-2} day^{-1}
$R_{a,c,sub}$	`w_net_rad_canopy_for_sublim`	net radiation absorbed by the canopy and used for sublimation of intercepted snow	J m^{-2} day^{-1}

Symbol	Variable name	Description	Units
$R_{a,c,tran}$	`w_net_rad_canopy_for_transp`	net radiation absorbed by the canopy and used for transpiration	J m^{-2} day^{-1}
$R_{a,c,vap}$	`w_net_rad_canopy_for_vapor`	net radiation absorbed by the canopy and used for vaporisation of intercepted rain	J m^{-2} day^{-1}
$R_{a,snow}$	`w_net_rad_snow_absorbed`	net radiation absorbed by the snowpack	J m^{-2} day^{-1}
$R_{a,s}$	`w_net_rad_soil_absorbed`	net radiation absorbed by the soil	J m^{-2} day^{-1}
$R_{a,u}$	`w_net_rad_understorey_-absorbed`	net radiation absorbed by the understorey	J m^{-2} day^{-1}
$R_{a,u,sub}$	`w_net_rad_understorey_for_-sublim`	net radiation absorbed by the understorey and used for sublimation of intercepted snow	J m^{-2} day^{-1}
$R_{a,u,tran}$	`w_net_rad_understorey_for_-transp`	net radiation absorbed by the understorey and used for transpiration	J m^{-2} day^{-1}
$R_{a,u,vap}$	`w_net_rad_understorey_for_-vapor`	net radiation absorbed by the understorey and used for vaporisation of intercepted rain	J m^{-2} day^{-1}
rot	-	angular speed of rotation of Earth	$^{\circ}$s^{-1}
s_c	`s_canopy_interception`	canopy precipitation interception store	m(water)
s_{snow}	`s_snow`	snowpack depth	m(water)
s_{sat}	`s_sat`	saturation deficit of soil	m
$\bar{s}_{sat}$	`parent_s_sat`	the hillslope-wide area-weighted mean saturation deficit of the soil	m
$s_{sat,0}$	`w_sat_at_zero_exfiltration`	saturation deficit of soil when baseflow exfiltration exactly equals zero	m
$s_{sat,c}$	`w_sat_water_available_to_-canopy_roots`	water from the saturated zone available for canopy transpiration	m
$s_{sat,dist}$	`w_sat_distribution`	saturation deficit of soil given by distribution function	m
$s_{sat,s}$	`w_sat_water_available_for_-evaporation`	water from the saturated zone available for soil evaporation	m
$s_{sat,u}$	`w_sat_water_available_to_-understorey_roots`	water from the saturated zone available for understorey transpiration	m
$s_{sat,mound}$	`w_sat_mound`	size of water table 'mound': the difference between s and s_d	m
s_u	`s_understorey_interception`	Understorey precipitation interception store	m(water)
s_{unsat}	`s_unsat`	water depth contained within the unsaturated store	m
$s_{unsat,c}$	`s_unsat_water_available_to_-canopy_roots`	water from the unsaturated zone available for canopy transpiration	m
$s_{unsat,s}$	`s_unsat_water_available_-for_evaporation`	water from the unsaturated zone available for soil evaporation	m
$s_{unsat,u}$	`s_unsat_water_available_to_-understorey_roots`	water from the unsaturated zone available for understorey transpiration	m
$s_{tot,c}$	`w_water_available_to_-canopy_roots`	total water available for canopy transpiration	m

Symbol	Code name	Description	Units
$s_{tot,c,max}$	`w_canopy_root_zone_capacity`	maximum water that canopy roots can access	m
$s_{tot,s}$	`w_water_available_for_-evaporation`	total water available for soil evaporation	m
$s_{tot,s,max}$	`w_evaporation_capacity`	nominal maximum amount of water that can be made available for soil evaporation	m
$s_{tot,u}$	`w_water_available_to_-understorey_roots`	total water available for understorey transpiration	m
$s_{tot,u,max}$	`w_understorey_root_zone_-capacity`	maximum water that understorey roots can access	m
$S_{a,c}$	`w_solar_rad_canopy_absorbed`	solar radiation absorbed by the canopy	J m^{-2} day^{-1}
$S_{a,snow}$	`w_solar_rad_snow_absorbed`	solar radiation absorbed by the snow-pack	J m^{-2} day^{-1}
$S_{a,s}$	`w_solar_rad_soil_absorbed`	solar radiation absorbed by the soil	J m^{-2} day^{-1}
$S_{a,u}$	`w_solar_rad_understorey_-absorbed`	solar radiation absorbed by the understorey	J m^{-2} day^{-1}
S_{dif}	`w_diffuse_rad`	diffuse solar radiation incident above the canopy (on either a horizontal or sloping surface)	J m^{-2} day^{-1}
S_{dir}	`w_sloping_direct_rad`	direct solar radiation incident above the canopy on a sloping surface	J m^{-2} day^{-1}
$S_{thresh,c}$	`p_canopy_leaf_conductance_-radiation_threshold`	amount of net radiation below which canopy leaf conductance is radiation limited	J m^{-2} day^{-1} LAI^{-1}
$S_{thresh,u}$	`p_understorey_leaf_-conductance_radiation_-threshold`	amount of net radiation below which understorey leaf conductance is radiation limited	J m^{-2} day^{-1} LAI^{-1}
S_{tot}	`w_solar_rad`	total solar radiation incident above the canopy on a sloping surface	J m^{-2} day^{-1}
S'_{dir}	`w_direct_rad`	direct solar radiation incident above the canopy	J m^{-2} day^{-1}
S'_{tot}	`w_horizontal_global_rad`	total solar radiation incident above the canopy on a horizontal surface	J m^{-2} day^{-1}
t_{date}	`w_date`	current fractional year	years A.D.
t_{day}	`loop->day`	current day of year - 1st Jan. is Day 1	days
$t_{hor,set}$	`w_horizontal_surface_-sunset_time`	time of sunset on a horizontal surface (since noon)	s
$t_{slop,rise}$	`w_sloping_surface_sunrise_-time`	time of sunrise on a sloping surface (since noon)	s
$t_{slop,set}$	`w_sloping_surface_sunset_-time`	time of sunset on a sloping surface (since noon)	s
t_{year}	`loop->year`	current year	years A.D.
T_{dew}	`w_dewpoint`	dewpoint temperature	°C
$\bar{T}_{day}$	`w_mean_day_temperature`	mean daylight air temperature	°C
T_{max}	`w_todays_max_temperature`	today's maximum air temperature	°C
$T_{max,stn}$	`nextin->yesterdays_base_-max_temperature`	today's maximum air temperature at the base station	°C

$\bar{T}$	`w_mean_temperature`	mean daily air temperature	°C
T_{min}	`w_todays_min_temperature`	today's minimum air temperature	°C
$T_{min,stn}$	`in->todays_base_min_-` `temperature`	today's minimum air temperature at the base station	°C
$T_{min,tom}$	`w_tomorrows_min_temperature`	tomorrow's minimum air temperature	°C
$T_{min,tom,stn}$	`nextin->wtomorrows_base_-` `min_temperature`	tomorrow's minimum air temperature at the base station	°C
$\bar{T}_{night}$	`w_mean_night_temperature`	mean night time air temperature	°C
T_s	`w_soil_temperature`	soil temperature	°C
V_c	`p_canopy_species`	canopy species	species_code
V_u	`p_understorey_species`	understorey species	species_code
y_{age}	`w_vegetation_age`	age of vegetation (since cessation of fire or logging)	years
y_{growth}	`p_vegetation_growth_time_-` `constant`	time constant of vegetation growth	years
$y_{origin,1}$	`p_origin_1`	most recent origin date of vegetation (date of cessation of fire or logging)	years A.D.
$y_{origin,2}$	`p_origin_2`	2nd most recent origin date of vegetation (date of cessation of fire or logging)	years A.D.
$y_{origin,3}$	`p_origin_3`	3rd most recent origin date of vegetation (date of cessation of fire or logging)	years A.D.
z_{wt}	`w_water_table_depth`	depth of the water table (or: saturation deficit in soil metres)	m(soil)
$z_{c,max}$	`p_canopy_root_depth`	maximum depth of canopy roots	m(soil)
$z_{s,eff}$	`w_depth_of_air_dry_soil`	effective depth at which soil evaporation is taking place	m(soil)
$z_{s,max}$	`p_evaporation_depth`	nominal maximum depth of soil from which soil evaporation can take place	m(soil)
$z_{u,max}$	`p_understorey_root_depth`	maximum depth of understorey roots	m(soil)

Greek

α_c	`p_canopy_reflection_-` `coefficient`	canopy reflection coefficient (albedo) for solar radiation	-
α_{snow}	`p_snow_reflection_-` `coefficient`	snow reflection coefficient (albedo) for solar radiation	-
α_s	`p_soil_reflection_-` `coefficient`	soil reflection coefficient (albedo) for solar radiation	-
α_u	`p_understorey_reflection_-` `coefficient`	understorey reflection coefficient (albedo) for solar radiation	-
β	`p_slope`	slope or inclination of a sloping surface	°
β_E	`p_east_horiz`	Angle above the horizontal of the eastern visible horizon at the point of sunrise	°

β_W	`p_west_horiz`	Angle above the horizontal of the western visible horizon at the point of sunset	°
γ	`w_psychrometer_constant`	psychrometer constant	Pa K^{-1}
Γ	`w_day_angle`	day angle (angle of Earth's orbit relative to its position on 1st January)	°
δ	`p_lateral_distribution_-factor`	factor controlling lateral redistribution of water within a hillslope	day^{-1}
$\Delta_{e_{sat}}$	`w_slope_saturation_vapor_-pressure_vs_temperature`	rate of change of saturation vapor pressure with temperature	Pa K^{-1}
$\Delta_{f,cl,D}$	`p_slope_canopy_relative_-leaf_cond_vs_vpd`	relative rate of change of canopy leaf conductance with vapor pressure deficit	Pa^{-1}
$\Delta_{f,ul,D}$	`p_slope_understorey_-relative_leaf_cond_vs_vpd`	relative rate of change of understorey leaf conductance with vapor pressure deficit	Pa^{-1}
$\Delta_{f,T}$	`p_slope_rel_leaf_cond_vs_-warm_temp`	relative rate of change of canopy leaf conductance with above freezing temperature	°C^{-1}
$\Delta_{g,T}$	`p_slope_leaf_cond_vs_cold_-temp`	rate of change of canopy leaf conductance with below freezing temperature	m s^{-1} °C^{-1}
Δ_{lon}	`w_delta_longitude`	difference in longitude between the current sloping surface and the horizontal surface facing the same direction	°
Δ_R	`p_slope_net_vs_solar_rad`	slope of the net (versus) solar radiation relation	-
Δ_z	`p_hydraulic_gradient`	subsurface hydraulic gradient operative at the point of baseflow exfiltration	-
Δ_{sat}	`p_slope_sat_vs_wetness_index`	Rate of change of saturation deficit (according to distribution function) with wetness index	m arbitrary_unit^{-1}
$\Delta_{T,max}$	`p_max_temperature_-elevation_lapse_rate`	temperature elevation lapse rate for daily maximum temperatures	°C m^{-1}
$\Delta_{T,min}$	`p_min_temperature_-elevation_lapse_rate`	temperature elevation lapse rate for daily minimum temperatures	°C m^{-1}
$\Delta_{\psi,l}$	`p_slope_leaf_water_-potential_vs_rel_water_-availability`	rate of change of leaf water potential with relative water availability	Pa
ϵ	`w_epsilon`	$\epsilon = \Delta/\gamma$ is a convenient variable in transpiration calculations	-
θ	`w_volumetric_water_content`	volumetric water content of unsaturated zone	m(water) m^{-1}(soil)
$\theta_{avail,max}$	`w_maximum_available_-volumetric_water_content`	maximum available volumetric water content of soil	m(water) m^{-1}(soil)
θ_{res}	`p_residual_volumetric_-water_content`	residual (air dry) volumetric water content of soil	m(water) m^{-1}(soil)
θ_{sat}	`p_saturated_volumetric_-water_content`	saturated volumetric water content of soil	m(water) m^{-1}(soil)

Θ	`w_normalised_volumetric_-` `water_content`	normalised volumetric water content of unsaturated zone	-
λ	`w_latent_heat_of_-` `vaporisation_of_water`	latent heat of vaporisation of water	J kg^{-1}
$\mu_{snow,R}$	`p_snowmelt_coeff_rad`	coefficient scaling snowmelt caused by net radiation	-
$\mu_{snow,T}$	`p_snowmelt_coeff_-` `temperature`	coefficient scaling snowmelt as influenced by ambient temperature	m(water) $^\circ$C^{-1} day^{-1}
ρ_{air}	`w_air_density`	density of air including water vapor	kg m^{-3}(air)
ρ_w	-	density of liquid water	kg m^{-3}(water)
τ	`p_soil_evaporation_-` `tortuosity_factor`	tortuosity of soil through soil evaporation vapor transfer occurs	?
τ_{atm}	`w_transmission`	transmission of the atmosphere to solar radiation	-
τ_c	`p_canopy_transmission_-` `coefficient`	canopy transmission coefficient for solar radiation	-
τ_u	`p_understorey_-` `transmission_coefficient`	understorey transmission coefficient for solar radiation	-
$\tau_{tot,P}$	-	time to peak total LAI	years
$\tau_{tot,D}$	-	time constant of long term decline from peak to climax total LAI values	years
$\tau_{tot,C}$	-	time constant of period before climax total LAI can be reached	years
ϕ	`p_sin_aspect, p_cos_aspect,` `w_aspect`	aspect or azimuth of a sloping surface	$^\circ$
ψ_{cl}	`w_pre_dawn_canopy_leaf_-` `water_potential`	pre-dawn canopy leaf water potential	Pa
$\psi_{cl,close}$	`p_canopy_leaf_water_-` `potential_at_stomatal_-` `closure`	canopy leaf water potential at stomatal closure	Pa
$\psi_{cl,max}$	`p_canopy_leaf_water_-` `potential_maximum`	maximum canopy leaf water potential	Pa
ψ_{ul}	`w_pre_dawn_understorey_-` `leaf_water_potential`	pre-dawn understorey leaf water potential	Pa
$\psi_{ul,close}$	`p_understorey_leaf_water_-` `potential_at_stomatal_-` `closure`	understorey leaf water potential at stomatal closure	Pa
$\psi_{ul,max}$	`p_understorey_leaf_water_-` `potential_maximum`	maximum understorey leaf water potential	Pa
$\omega_{c,sat}$	`w_weighted_sat_canopy_-` `transpiration_factor`	water availability weighted factor controlling amount of canopy transpiration to be drawn from saturated zone	-
$\omega_{c,unsat}$	`w_weighted_unsat_canopy_-` `transpiration_factor`	water availability weighted factor controlling amount of canopy transpiration to be drawn from unsaturated zone	-
$\omega_{u,sat}$	`w_weighted_sat_-` `understorey_transpiration_-` `factor`	water availability weighted factor controlling amount of understorey transpiration to be drawn from saturated zone	-

$\omega_{u,unsat}$	`w_weighted_unsat_-`
	`understorey_transpiration_-`
	`factor`
		water availability weighted factor controlling amount of understorey transpiration to be drawn from unsaturated zone	-

$\Omega_{c,u}$	`w_canopy_understorey_-` `decoupling_coefficient`	amount of aerodynamic de-coupling between canopy and understorey layers	-
$\Omega_{ref,c}$	`w_reference_canopy_-` `decoupling_coefficient`	amount of aerodynamic de-coupling between reference and canopy layers	-
$\Omega_{u,s}$	`w_understorey_soil_-` `decoupling_coefficient`	amount of aerodynamic de-coupling between understorey and soil layers	-

Appendix D

Physical constants used by Macaque

Table D.1: Physical constants used by Macaque

Symbol	Description	Value and unit	Reference
c_p	specific heat of air at constant pressure	1010 J kg^{-1} K^{-1}	Oke, 1987, p. 44
I_{con}	solar constant	1367 W m^{-2}	Linacre, 1992, p. 152
rot	angular speed of rotation of Earth	4.167×10^{-3} °s^{-1}	Dingman, 1994, p. 532
ρ_w	density of liquid water	1.0×10^3 kg m^{-3}	Oke, 1987, p. 393
-	volumetric latent heat of fusion of water	0.334×10^9 J m^{-3}	Oke, 1987, p. 392
-	volumetric latent heat of sublimation of water	2.83×10^9 J m^{-3}	Oke, 1987, p. 392
-	volumetric latent heat of vaporisation of water	2.50×10^9 J m^{-3}	Oke, 1987, p. 392

Appendix E

Acronyms

Table E.1: Acronyms used.

Acronym	Meaning
AHD	Australian Height Datum
AMG	Australian Map Grid
ATM	(Daedalus) Airborne Thematic Mapper
AVHRR	Advanced Very-High Resolution Radiometer
BOM	Bureau of Meteorology
CFI	Continuous Forest Inventory (programme of Melbourne Water)
CHWP	constant head well permeameter
CRCCH	Cooperative Research Centre for Catchment Hydrology
CVE	calibrated visual estimation (of LAI)
DBH	diameter at breast height (over bark)
DFM	distribution function model
DNRE	Victorian Department of Natural Resources and Environment (formerly Department of Conservation and Natural Resources (DNCR), formerly Department of Conservation Forests and Lands (DCFL) and Forests Commission Victoria (FCV))
EDM	electronic distance measurement system
EM	electro-magnetic
ESU	elementary spatial unit
FDM	fully distributed model
GCV	generalised cross validation
GDF	generalised distribution function
GIS	geographic information system
GLM	generalised linear modelling
GLUE	generalised likelihood uncertainty estimation
HPA	hemispherical photo analysis
LA	leaf area
LAI	leaf area index
LWP	leaf water potential
MAP	mean annual precipitation
MMBW	Melbourne and Metropolitan Board of Works
MMPI	mean monthly precipitation index
MSS	Multi-spectral Scanner
NA	not available/applicable
NOAA	National Oceanic and Atmospheric Administration
PAR	photosynthetically absorbed radiation
PCA	(Li-Cor) Plant Canopy Analyser
RHESSys	Regional Hydro-Ecological Simulation System
SA	sapwood area
SAR	Synthetic Aperture Radar

SVP	saturation vapor pressure
TDR	time domain reflectometry
TM	Thematic Mapper
USA	United States of America
VP	vapor pressure
VPD	vapor pressure deficit

Appendix F

Scientific and common names for plant species

Table F.1: Scientific and common names for plant species.
References: Hillis and Brown (1984), Costermans (1983).

Scientific name	Common name
Acacia longifolia	Sallow Wattle
Eucalyptus botryoides	Southern Mahogany
Eucalyptus calophylla	Marri
Eucalyptus cinerea	Argyle Apple
Eucalyptus diversicolor	Karri
Eucalyptus dives	Broad-leaved Peppermint
Eucalyptus globoidea	White Stringybark
Eucalyptus grandis	Flooded Gum
Eucalyptus gummifera	Bloodwood
Eucalyptus maculata	Spotted Gum
Eucalyptus mannifera	Brittle Gum / Red Spotted Gum
Eucalyptus marginata	Jarrah
Eucalyptus melliodora	Yellow Box
Eucalyptus microcarpa	Grey Box
Eucalyptus obliqua	Messmate
Eucalyptus pauciflora	Snow Gum
Eucalyptus regnans	Mountain Ash
Eucalyptus rossii	Scribbly Gum
Eucalyptus saligna	Sydney Blue Gum
Eucalyptus sideroxylon	Red Ironbark
Eucalyptus viminalis	Manna Gum
Pinus radiata	Radiata Pine
Sequoia sempervivens	Coastal Redwood

Appendix G

Error analyses used in Chapter 8

G.1 Confidence limits for the model of inter-stand variability in mean ln(LA)

Following the method described in Ezekiel and Fox[1] (1959) we can place 95% confidence limits on the regression of mean ln(LA) against mean ln(DBH) (see Section 8.7.2) by 'estimating the reliability of an individual forecast' as:

$$CL_{\hat{\nu}_s.\mu_s} = \pm 1.960 \, SE_{\hat{\nu}_s - \hat{\nu}_s} \tag{G.1}$$

where $CL_{\hat{\nu}_s.\mu_s}$ is the confidence limit for an estimate of $\hat{\nu}_s$ given μ_s, and $SE_{\hat{\nu}_s - \hat{\nu}_s}$ is the standard error of that estimate given by:

$$SE^2_{\hat{\nu}_s - \hat{\nu}_s} = SE^2_{\hat{\bar{\nu}}_s} + (SE_\beta(\mu_s - \bar{\mu}))^2 + \widehat{SE}^2_{\hat{\nu}_s.\mu_s} \tag{G.2}$$

with:

$$\bar{\mu} = \frac{1}{S} \sum_{s=1}^{S} \mu_s \tag{G.3}$$

---

[1]Refer to Ezekiel and Fox's Equations 1.1, 1.2, 1.4, 2.1, 5.6, 17.1, 17.3, and 19.1.

where $SE_{\bar{\hat{\nu}}_s}$ is the standard error of the estimate of the mean value of $\hat{\nu}_s$, SE_β is the standard error of the estimate of β, and $\widehat{SE}_{\hat{\nu}_s.\mu_s}$ is the (estimated) standard error of the estimates of $\hat{\nu}_s$ from μ_s. The corresponding calculated values are as follows:

$$SE_{\bar{\hat{\nu}}_s} \;=\; 0.127 \tag{G.4}$$

$$SE_\beta \;=\; 0.072 \tag{G.5}$$

$$\widehat{SE}_{\hat{\nu}_s.\mu_s} \;=\; 0.255 \tag{G.6}$$

G.2 Confidence limits for the model of intra-stand variability in residual ln(LA)

Ninety-five percent confidence limits for the mean line of best fit to residuals (see Section 8.7.3) are calculated from the associated standard error in a similar fashion to Equations G.1 and G.2 with two differences. The squared standard errors for the three component lines of best fit are averaged. Also, because the three lines of best fit were fitted to residual data and are hence *effectively* constrained to have zero intercepts, a term for the independent variable, $x - \mu_s$, is used instead of that value's deviation from its mean. The resulting equation is:

$$SE^2_{(\hat{y}-\hat{\nu}_s)-(y-\hat{\nu}_s)} =$$
$$\frac{1}{3}\sum_{s=1}^{3} SE^2_{\overline{\hat{y}_{s,j}-\hat{\nu}_s}} + \left(SE_{\delta_s}(x - \mu_s)\right)^2 + \widehat{SE}^2_{(y_{s,j}-\hat{\nu}_s).(x_{s,j}-\mu_s)} \tag{G.7}$$

where $SE_{(\hat{y}-\hat{\nu}_s)-(y-\hat{\nu}_s)}$ is the standard error of an estimate of $y - \hat{\nu}_s$ given x, and for each stand, $SE_{\overline{\hat{y}_{s,j}-\hat{\nu}_s}}$ is the standard error of the estimate of the mean value of $y - \hat{\nu}_s$, SE_{δ_s} is the standard error of the estimate of δ_s, and $\widehat{SE}_{(y_{s,j}-\hat{\nu}_s).(x_{s,j}-\mu_s)}$ is the standard error of the estimates of $y_{s,j} - \hat{\nu}_s$ from $x_{s,j} - \mu_s$. The corresponding calculated values are as follows:

$$SE_{\overline{\hat{y}_{1,j}-\hat{\nu}_1}} \quad = \quad 0.063 \qquad\qquad \text{(G.8)}$$

$$SE_{\overline{\hat{y}_{2,j}-\hat{\nu}_2}} \quad = \quad 0.146 \qquad\qquad \text{(G.9)}$$

$$SE_{\overline{\hat{y}_{3,,j}-\hat{\nu}_3}} \quad = \quad 0.406 \qquad\qquad \text{(G.10)}$$

$$SE_{\delta_1} \quad = \quad 0.062 \qquad\qquad \text{(G.11)}$$

$$SE_{\delta_2} \quad = \quad 0.226 \qquad\qquad \text{(G.12)}$$

$$SE_{\delta_3} \quad = \quad 0.271 \qquad\qquad \text{(G.13)}$$

$$\widehat{SE}_{(y_{1,j}-\hat{\nu}_s).(x_{1,j}-\mu_s)} \quad = \quad 0.089 \qquad\qquad \text{(G.14)}$$

$$\widehat{SE}_{(y_{2,j}-\hat{\nu}_s).(x_{2,j}-\mu_s)} \quad = \quad 0.377 \qquad\qquad \text{(G.15)}$$

$$\widehat{SE}_{(y_{3,j}-\hat{\nu}_s).(x_{3,j}-\mu_s)} \quad = \quad 0.295 \qquad\qquad \text{(G.16)}$$

G.3 Confidence limits for the full LA model

Ninety-five percent confidence limits for the full model are calculated from the associated standard error in a similar fashion to Equation G.1, with $SE_{\hat{y}-y}$, the standard error of an estimate of y given x and μ_s, calculated as:

$$SE^2_{\hat{y}-y} = SE^2_{\hat{\nu}_s-\hat{\nu}_s} + SE^2_{(\hat{y}-\hat{\nu}_s)-(y-\hat{\nu}_s)} \qquad\qquad \text{(G.17)}$$